Title

Microfluidic Technologies for Positron Emission Tomography (PET) radiopharmaceutical microvolume production and analysis: How low can we go?

Author

Laferriere-Holloway, Travis S.

Publication Date

2022

Peer reviewed|Thesis/dissertation

UNIVERSITY OF CALIFORNIA

Los Angeles

Microfluidic Technologies for Positron Emission Tomography (PET) radiopharmaceutical microvolume production and analysis: How low can we go?

A dissertation submitted in partial satisfaction of the

requirements for the degree Doctor of Philosophy in

Molecular and Medical Pharmacology

by

Travis Scott Laferriere-Holloway

2022

ABSTRACT OF THE DISSERTATION

Microfluidic Technologies for Positron Emission Tomography (PET) radiopharmaceutical production and analysis: How low can we go?

by

Travis Scott Laferriere-Holloway

Doctor of Philosophy in Molecular and Medical Pharmacology

University of California Los Angeles, 2022

Professor R. Michael van Dam, Chair

The increasing use of quantitative imaging in the understanding of the pathophysiological processes, monitoring disease progression, and assessment of responses to treatment has become evident in modern healthcare in the past decade. Using short-lived radionuclides, positron emission tomography (PET) harnesses the ability to visualize and quantify specific biochemical processes *in vivo* non-invasively. However, despite the increasing importance of PET, cost-restrictive and complex production is undermining due to the use of highly specialized facilities needed for conventional macroscale radiosynthesis systems. To reduce the cost associated with PET, centralized production of large batches of radiopharmaceuticals has been leveraged to achieve economies of scale. While cost-effective, this production pathway severely limits the diversity of PET radiopharmaceuticals that are available for routine use.

In recent years, microfluidic technologies have hinted at the possibility replace macroscale vial-based reactors and to restructure the current centralized production of PET

radiopharmaceuticals. Microvolume syntheses, allow the reduction of reagents utilized, reduce the overall synthesis time, and in some cases have led to higher yield. While many initial advances were achieved with micro-flow devices, and micro-batch devices, the complexity of operation, poor robustness, and high cost of prototyping have led to limited use. Instead, our group has recently pioneered the use microfluidic reactors that allow the use of sessile droplets for microvolume radiosyntheses. With these devices our lab has improved radiochemical yield, lowered reagent use, allowed high molar activity to be achieved with low reaction activities, shortened synthesis time, all in a compact and low-cost apparatus. These initial studies highlighted the possibility of clinical scale production. Despite these advances, there are some aspects that require further improvement before widespread use. The current reliance on conventional chromatography systems with a large footprint, undermine the advances in miniaturization and cost-reduction of the droplet microfluidic system. Second, though clinical-scale production has been achieved, it Is not as reliable or easy to use as other aspects of the droplet system. Third, the adaption of tracer synthesis protocols to this platform requires tedious optimization since reaction conditions at the microscale are usually different from conventional vial-based reactors. Several advances are necessary to allow the advances seen with the sessile microvolume droplet reactors pioneered by our group to achieve the cost effective on demand syntheses of PET radiopharmaceuticals.

We describe here several advances toward addressing these shortcomings. One development is the creation of new high-throughput methodologies that allow the synthesis of PET radiopharmaceuticals in a massively parallel fashion, with dozens of times greater throughput than possible with conventional technology, allowing the fine tuning of reaction parameters to increase yields, reduce reagent consumption, and shorten reaction times. In conjunction, we developed high-throughput methodologies for the analysis of

radiopharmaceuticals via radio-TLC, and the development of approaches (PRISMA) to achieve high chromatographic resolution on par with conventional HPLC systems.

Once an optimized droplet synthesis protocol is achieved, it can be immediately used for routine production in a droplet-based radiosynthesizer. We explore novel, more robust methods of radionuclide concentration that have allowed scaling to clinically-relevant batches of a diverse range of radiopharmaceuticals. We have also developed miniaturized methods for purification and formulation based on high-resolution radio-TLC that can potentially replace HPLC-based purification protocols. This novel method enabled compact, fast, and high-efficiency purification of PET radiopharmaceuticals, and, furthermore, eliminated the need for a separate formulation step since the purified radiopharmaceutical is provided in a biocompatible buffer solution, enabling further simplification of the system and reduction of overall synthesis time.

The improved radio-TLC methods were also applied to the assessment of the metabolism of radiopharmaceuticals in tissue such as blood. Compared to HPLC, SPE, or earlier TLC analysis approaches, we achieved high sensitivity by using commercially available channeled TLC plates with concentrating zones to permit the deposition of large sample volumes without adversely affecting resolution. In fact, we showed for the first time that TLC-based analysis has sufficient sensitivity for analysis of clinical plasma samples to profile the metabolism of [^{18}F]FEPPA as a function of time.

In addition to the microreactor systems, we also developed novel radiolabelling techniques. Experimental approaches with electrochemistry are also described for the fluorination of electron rich moieties that are not able to be directly labelled through conventional radiochemistry strategies.

Finally, we describe the development of synthesis protocols for the routine production of a potentiometric PET radiopharmaceutical, [^{18}F]FBnTP, to study mitochondrial membrane dysfunction in the context of lung cancer metabolism. Initial studies reveal that tumors feature

metabolic heterogeneity not assessable through conventionally accepted clinical profiling. Further studies suggested that tumors with high oxidative phosphorylation (OXPHOS), feature distinct compartments of mitochondrial networks. This data suggests in lung cancers, mitochondrial networks are compartmentalized into distinct subpopulations that govern bioenergetic capacity. These studies elucidate a potential treatment pathway for tumors, that harness mitochondrial complex inhibitors. Our group is currently surveying microscale radiosynthesis methods for the production of [^{18}F]FBnTP to leverage the high interest of the community in this radiopharmaceutical. Not described in this dissertation, we conducted further studies to develop novel potentiometric analogues of [^{18}F]FBnTP that could measure mitochondrial dysfunction in the brain.

The dissertation of Travis Scott Laferriere-Holloway is approved.

Giuseppe Carlucci

Yoram Cohen

Vasilios Manousiouthakis

Jennifer Murphy

R. Michael van Dam, Chair

University of California, Los Angeles

2022

Dedicated to the love of my life, Tyler

Table of Contents

LIST OF FIGURES

LIST OF TABLES

ACKNOWLEDGEMENTS

I want to start by thanking the funding sources that supported my doctoral work: the National Institute of Biomedical Imaging and Bioengineering (R21 EB024243), and the National Cancer Institute (R21 CA212718, R33 CA240201).

I would like to take this chance to thank my past and present lab members in the van Dam lab both past and present. Dr. Jia Wang for her help in learning the operations surrounding microfluidic radiochemistry. Dr. Philip Chao for his help in learning the concentration processes further develop in this work. Dr. Ksenia Lisova for discussions about microfluidic radiochemistry that were helpful in directing some of the research described in this work. Dr, Jason Jones for his help in machining materials for various projects. Dr. Alejandra Rios, for her help in completing a major portion of the work presented. Dr. Rios was a joy to work and learn with, and I count her as a close friend and colleague – my time in graduate school would neither have been as productive or enjoyable without her companionship. Yingqing Lu for her extremely valuable conversation about the chemistry underlying the radiochemistry projects described. Chelsea Okoro for the privilege to act as a mentor in the lab and transfer the passion of science. Dr. Adrian Gomez, for all of the scientific work surrounding [^{18}F]FBnTP, and his friendship throughout the years of graduate school. Drs. Sadeghi and Shackelford for the opportunity to contribute to the work surrounding [^{18}F]FBnTP. Finally, I would like to express my profound gratitude to Prof. R. Michael van Dam for his years of mentorship and the ability to develop novel projects and for the help in learning how to successfully direct them. I would like to further thank Prof. R. Michael van Dam for the scientific discussions over the years that have allowed me to venture into a new field of research.

I am extremely grateful to each collaborator I have had the privilege to work with during my time at UCLA. The true breadth of talent in this community made me grow as a scientist, and I would like to extend my thanks to: Edythe London, Catherine Cahill, Mark Mandelkern, Judah

Farahi, and Yvonne Yang. I am also grateful to CNSI cleanroom staff Lorna Tokunaga, Krissy Do and Tony Wright for their help and advice related to fabrication questions. I thank Emily Fitch for her help with the documents and providing detailed answers to any related questions and Karen Lum, Cecilia Canadas and Erika Corrin for their help with purchasing/reimbursements and administrative matters. Moreover, I appreciate the help received from everyone at the Crump Preclinical Imaging Technology Center. Thank you to Drs. Jason Lee and Shili Xu for providing in-depth discussion about preclinical image techniques and specific results and lessons on image and data analysis. Thank you to the staff of the UCLA Biomedical Cyclotron facility and Jeffrey Collins for generously providing [^{18}F]fluoride ion for the radiochemistry studies.

Outside of the lab, the years have been filled with many friends that along the way helped to push me through graduate school. I would like to thank Edythe Sato and her husband Raihei, for being some of my most long-term friends, your friendship over the years has been invaluable. I would like to also thank Leticia Malavasi and Bonita Goh for their friendship over the years, I have truly enjoyed every minute. I would like to thank Shane Cullen and Dean Schinderle who in Los Angeles, are our best friends, some of the best moments of my time in LA have been spent with you both. I would like to thank soon to be Drs. Elizabeth Fernandez and Allyson Terry (along with Ben Shotaki) for their years of friendship and understanding of the graduate school journey. My thank yous for other friendships exceed this short list, and for the many I call friend, thank you so much for your support on my journey to completing my time at UCLA.

I would like to thank my family who has been supportive throughout my life, and the many years through school. Ashlee Rogers, her husband Josh, son Logan, and daughter Lillian, thank you for the years of memories. My grandfather Ken Puryear, who was always interested in my journey during graduate school. My parent in laws, Tim and Penny Laferriere, I have absolutely loved our time together over the years, and am happy to call you parents. To my parents, Scott, and Valerie Holloway, thank you for all your love and support throughout my years, I am finally

finished with school. Finally, and most prominently I would like to thank my husband, Tyler Laferriere-Holloway who has been my companion and listened to me throughout my time in graduate school. If there was a possibility to award an honorary doctorate, there would be no one more worthy. I look forward to the beginning of this new journey with you.

Lastly, I want to thank my doctoral committee for advising me with my research, and for collaborations. Thank you, Drs. Carlucci, Cohen, Manousiouthakis, Murphy, and van Dam. Your help in discussions of my work led to the ability to complete them. I am also thankful for the discussions surrounding my work as I think this made me a much stronger scientist. Thank you. In the words of Frank Sinatra, “The best is yet to come, and won’t that be fine”.

Chapter 2: Microfluidic radiochemistry: synthesis in sessile droplets is a modified version of:
Rios A, Laferriere-Holloway TS, Wang J, van Dam RM. Optimization of radiochemical reactions using droplet arrays. *JoVE*. 2021. I helped to develop methodologies underlying the optimization of radiochemical reactions.

Chapter 3: Utilizing droplet radiochemistry methods for the production of [^{18}F]FDOPA is a modified version of:
Wang, J.; Holloway, T.; Lisova, K.; Dam, R. M. van. Green and Efficient Synthesis of the Radiopharmaceutical [18F]FDOPA Using a Microdroplet Reactor. React. Chem. Eng. 2020, 5 (2), 320–329. I helped to define the reaction parameter space for optimization work and performed preliminary experiments.

Chapter 4: Microliter-scale reaction arrays for economical, high-throughput experimentation in radiochemistry is a modified version of:
Rios A, Laferriere-Holloway TS, Chao PH, De Caro C, Okoro CC, van Dam RM. Microliter-scale reaction arrays for economical, high-throughput experimentation in radiochemistry. Sci. Rep. 2022;12:10263. I helped to design and perform experiments, to perform the massively parallel reaction described.

Chapter 6: Impact of aqueous phases in the analysis of radiopharmaceuticals via radio-TLC is a modified version of:
Laferriere-Holloway TS, Rios A, van Dam RM. Detrimental impact of aqueous phases in 18F-labelled radiopharmaceutical analysis via radio-TLC. Under revision. I designed and performed experiments described.

Chapter 7: A rapid and systematic approach for the optimization of radio thin-layer chromatography resolution is a modified version of:
Laferriere-Holloway, T. S.; Rios, A.; Lu, Y.; Okoro, C. C.; van Dam, R. M. A Rapid and Systematic Approach for the Optimization of Radio Thin-Layer Chromatography Resolution. Journal of Chromatography A 2022, 463656. I designed and performed experiments described.

Chapter 8: Rapid purification and formulation of radiopharmaceuticals via thin-layer chromatography is a modified version of:
Laferriere-Holloway, T. S.; Rios, A.; Carlucci, G.; van Dam, R. M. Rapid Purification and Formulation of Radiopharmaceuticals via Thin-Layer Chromatography. Molecules 2022, 27 (23), 8178. I designed and performed experiments described.

Chapter 9: Detection of radiometabolites in human blood using a high-performance, high-throughput thin-layer chromatography method is a modified version of:
Laferriere-Holloway TS, Rios A, Kibaly C, Farahi J, Xu S, Yang Y, Mandelkern M, Cahill C, London E, and van Dam RM. Detection of radiometabolites in human blood using a high-performance, high-throughput thin-layer chromatography method. Submitted. I designed and performed experiments described.

Chapter 10: Electrochemical flash fluorination and radiofluorination is a modified version of:
Balandeh M, Rios A, Allison N, Shirazi D, Gomez AL, Rambaran L, Holloway TS, Sadeghi S. Electrochemical flash fluorination and radiofluorination. *Chem. Electro. Chemi.* 2018;5:3353-3356. I helped to perform analysis of electrochemical reactions, and data analysis.

Chapter 11: Electrochemical radiofluorination of thioethers is a modified version of:
Allison N, Balandeh M, Holloway TS, Gomez AL, Rios A, Waldmann C, Lebedev A, Sadeghi S. Electrochemical no-carrier added radiofluorination of thioethers. *J. Fluor. Chem.* 2022;257-258:10988. I helped to perform analysis of electrochemical reactions, and data analysis.

Chapter 12: *In vivo* Imaging of Mitochondrial Membrane Potential in Non-Small Cell Lung Cancer is a modified version of:
M. Momcilovic, A. Jones, S. T. Bailey, C. M. Waldmann, R. Li, J. Lee, G. Abdelhady, A. Gomez, T. Holloway, E. Schmid, D. Stout, M. C. Fishbein, L. Stiles, D. V. Dabir, S. M. Dubinett, H. Christofk, O. Shirihai, C. M. Koehler, S. Sadeghi, D. Shackelford. In Vivo Imaging of Mitochondrial Membrane Potential in Non-Small Cell Lung Cancer. Nature, 2019, 575, 380—384. I helped to perform the radiochemical production of [^{18}F]FBnTP.

Chapter 13: 3-dimensional mapping of mitochondrial networks defines diverse bioenergetic phenotypes in lung cancer is a modified version of:
Han M, Bushong EA, Wolf DM, Tiard A, Wong A, Brady MR, Momcilovic M, Segawa M, Zhang R, Petcherski A, Madany M, Xu S, Lee JT, Poyurovsky MV, Olszewski K, Holloway T, Gomez A, John MS, Lisberg A, Dubinett SM, Koehler CM, Shirihai O, Stiles L, Soatto S, Sadeghi S, Ellisman MH, Shackelford DB. 3-dimensional maping of mitochondrial networks defines diverse bioenergetic phenotypes in lung cancer. Submitted. I helped to perform the radiochemical production of [^{18}F]FBnTP.

Curriculum Vitae

EDUCATION

Washington State University — **B.S.** Chemical Engineering, 2017
Whitworth University — **B.A.** Chemistry, 2015

Work Experience

University of California Los Angeles, David Geffen School of Medicine - Graduate Research Student 2017-2022

- Developed novel microfluidic devices and techniques to produce Positron Emission Tomography (PET) imaging tracers. Additionally, developed techniques for the quantitative assessment of PET tracer metabolism

University of California Los Angeles, Technology Development Group - Senior Technology Development Fellow 2020-2022

- Led the marketing of all pre-clinical life science technologies at UCLA over a cohort of Ph.D. students and drafted technology transfer agreements encompassing term-sheet agreements, CDAs, IIAs, and MTAs

Technology Development Fellow 2018-2020

- Partnered in the marketing of pre-clinical life science technologies and physical science technologies through the drafting of non-confidential disclosures (NCDs), marketing analysis reports, and company pitch decks

Merck, Translational Imaging Biomarkers - Intern 2017

- Developed various radiotracers for PET imaging studies focused on neuroimaging, encompassing a breadth of radionuclides, including C-11, F-18, Cu-64, Ga-68, and Zr-89. All developed tracers were translated to in vivo studies

Washington State University - Research Assistant 2015-2017

- Developed multi-modal radio (Single Photon Emission Computed Tomography (SPECT)) and optical imaging agents that utilized Tc-99m tri and bi-carbonyl cores, targeting prostate-specific membrane antigen (PSMA)

Whitworth University - Research Assistant 2014-2015

- Developed a novel pH-sensitive rhenium tri-carbonyl complex for fluorescent imaging studies

Book Chapters

Laferriere-Holloway TS, van Dam RM. Radio-TLC: Recent technical advances and applications. In Progress.

Publications

Laferriere-Holloway TS, Rios A, Kibaly C, Farahi J, Xu S, Yang Y, Mandelkern M, Cahill C, London E, and van Dam RM. Detection of radiometabolites in human blood using a high-performance, high-throughput thin-layer chromatography method. Submitted.
Laferriere-Holloway TS, Rios A, Carlucci G, van Dam RM. Rapid purification and formulation of radiopharmaceuticals via thin-layer chromatography. Submitted.
Laferriere-Holloway TS, Rios A, Lu Y, Okoro CC, van Dam RM. A rapid and systematic approach for the optimization of radio-TLC resolution. Submitted.

Laferriere-Holloway TS, Rios A, van Dam RM. Detrimental impact of aqueous phases in 18F-labelled radiopharmaceutical analysis via radio-TLC. Submitted.
Han M, Bushong EA, Wolf DM, Tiard A, Wong A, Brady MR, Momcilovic M, Segawa M, Zhang R, Petcherski A, Madany M, Xu S, Lee JT, Poyurovsky MV, Olszewski K, **Holloway T**, Gomez A, John MS, Lisberg A, Dubinett SM, Koehler CM, Shirihai O, Stiles L, Soatto S, Sadeghi S, Ellisman MH, Shackelford DB. 3-dimensional maping of mitochondrial networks defines diverse bioenergetic phenotypes in lung cancer. Submitted.
Rios A, Wang J, **Laferriere-Holloway TS**, Chao PH, De Caro C, Okoro CC, van Dam RM. Microliter-scale reaction arrays for economical, high-throughput experimentation in radiochemistry. Sci. Rep. 2022;12:10263.
Allison N, Balandeh M, **Holloway TS**, Gomez AL, Rios A, Waldmann C, Lebedev A, Sadeghi S. Electrochemical no-carrier added radiofluorination of thioethers. J. Fluor. Chem. 2022;257-258:10988.
Rios A, **Laferriere-Holloway TS**, Wang J, van Dam RM. Optimization of radiochemical reactions using droplet arrays. JoVE. 2021.
Wang, J.; **Holloway, T**.; Lisova, K.; Dam, R. M. van. Green and Efficient Synthesis of the Radiopharmaceutical [18F]FDOPA Using a Microdroplet Reactor. React. Chem. Eng. 2020, 5 (2), 320–329.
M. Momcilovic, A. Jones, S. T. Bailey, C. M. Waldmann, R. Li, J. Lee, G. Abdelhady, A. Gomez, **T. Holloway**, E. Schmid, D. Stout, M. C. Fishbein, L. Stiles, D. V. Dabir, S. M. Dubinett, H. Christofk, O. Shirihai, C. M. Koehler, S. Sadeghi, D. Shackelford. In Vivo Imaging of Mitochondrial Membrane Potential in Non-Small Cell Lung Cancer. Nature, 2019, 575, 380—384.
Balandeh M, Rios A, Allison N, Shirazi D, Gomez AL, Rambaran L, **Holloway TS**, Sadeghi S. Electrochemical flash fluorination and radiofluorination. Chem. Electro. Chemi. 2018;5:3353-3356.

Conference Presentations

Holloway, T. S.; Rios, A.; Okoro, C.; van Dam, R. M. SP-053 - Replacing High-Performance Liquid Chromatography (HPLC) with High-Resolution Thin Layer Chromatography (TLC) for Rapid Radiopharmaceutical Analysis. Nuclear Medicine and Biology 2021, 96–97, S63.
Holloway, T. S.; Rios, A.; Okoro, C.; van Dam, R. M. SP-054 - Thin Layer Chromatography for Rapid Purification and Reformulation of Microfluidically-Produced Radiopharmaceuticals. Nuclear Medicine and Biology 2021, 96–97, S63–S64.

Patents

T. S. Holloway, A. Rios, C. Okoro, R.M. van Dam. Systems and methods for the purification of radiopharmaceuticals using thin layer chromatography (TLC) plates. Patent Application WO2022098584 A1.

Chapter 1: Introduction

1.1 Positron emission tomography

Molecular imaging has improved our understanding of biochemical processes *in vivo*: stratifying disease[1–3], determining the effectiveness of treatment[4,5], and understanding their underlying pathophysiological processes[6,7]. By utilizing short-lived radionuclides tagged to biologically active molecules (known as radiopharmaceuticals), positron emission tomography (PET) allows the *in vivo* assessment of these processes[8]. There are two potential decay possibilities for neutron deficient radionuclides, positron emission (β+) or electron capture (EC)[9]. Fluorine-18 is the most utilized PET radionuclide due to its high positron decay ration (97%), short half-life (109.8 min), low positron energy (635 keV), and wide availability[10–12]. Inside the body, the emitted positron is slowed by tissue through collisions, allowing it to reach a speed where annihilation with an electron can occur (**Figure** 1**-**1). Two near co-linear gamma-rays of 511 keV are generated. The gamma rays are detected using a ring of scintillator crystals[9], and coincidence, and sometimes, time of flight (TOF), are used to partially localize the annihilation event. The scintillator crystals emit a burst of light that is detected by photomultiplier tubes. Computerized readout is able to reconstruct images of the decay events, giving biodistribution of radioactivity in the body.

In recent decades, the increased use of PET and development of numerous novel radiopharmaceuticals have transformed the clinical understanding of a myriad of diseases. In 2020, it was estimated that 2.2 million PET scans were performed in the U.S. alone[13]. Many of these scans utilize 2-[^{18}F]fluoro-2-deoxy-D- glucose ([^{18}F]FDG); a radiopharmaceutical that has been in routine use since the 1970s[14–16]. Many novel radiopharmaceuticals, though providing promising imaging, have not advanced to widespread clinical application. One of the main underlying reasons for this is the very high cost of PET radiopharmaceutical production, and the

insufficient demand of new radiopharmaceuticals to allow coordination of schedules for centralized production and distribution of these compounds, which are the keys to the low cost of [^{18}F]FDG[17]. Furthermore, the specialized facilities required to handle the radioactivity necessary to produce radiopharmaceuticals have great initial cost and high maintenance costs[18,19]. Production is carried out primarily using specialized automated radiosynthesizers that operate within radiation shielded "hot cells" to perform multi-step synthesis protocols in milliliter volumes. To increase accessibility to diverse PET tracers, and to facilitate the production of novel tracers for early studies, advances are needed in radiosynthesis technology that make it possible to affordably produce smaller batches of radiopharmaceuticals on demand, perhaps by avoiding the needed for specialized facilities and expensive instrumentation.

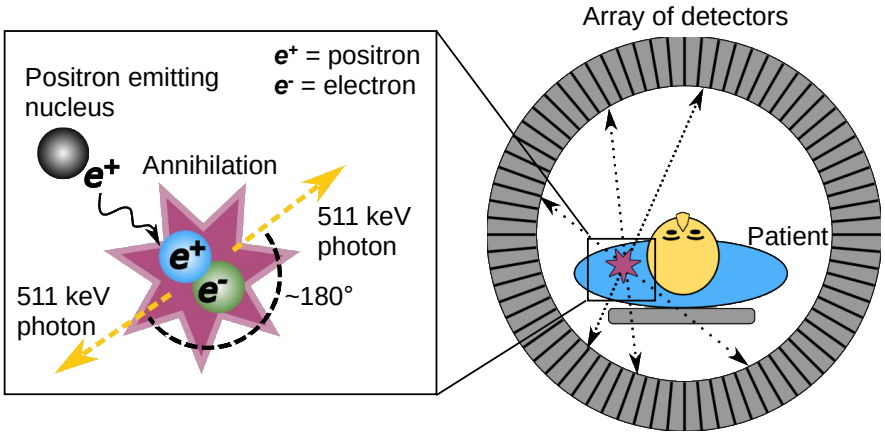

Figure 1-1. Mechanism of PET imaging.
PET image is formed based on detection of sets of coincident 511 keV photons emitted upon annihilation events after positron decays. PET scan image courtesy of National Cancer Institute.

1.2 History of microfluidic radiosynthesis of PET tracers

In recent years, there has been significant development of microfluidic devices to perform radiochemical synthesis of PET radiopharmaceuticals[20,21]. The quantity of PET tracer needed for imaging is typically in the nmol to pmol range, and thus useful quantities can be produced even in the tiny volume scale of microvolume devices. One increasingly popular methodology of microfluidic radiosynthesis utilize "flow chemistry" in which reagent streams flow through a mixer

and a thermally controlled capillary or channel. Reactions in this high surface to volume regime have been observed to be rapid[22–24]. Custom and commercially available flow systems have been used with a wide array of PET radionuclides: carbon-11, nitrogen-13, fluorine-18, copper-64, gallium-68, zirconium-89, and lutetium-177[25–29]. However, these systems are bulky and expensive and often utilize additional bulky external macroscale systems ahead of the flow reactor (e.g., azeotropic activation of [^{18}F]fluoride) and downstream of the flow reactor (e.g. HPLC purification)[30,31] or require the scaling up of overall volumes and reagent amounts for increased activity scales[32,33]. These limitations have limited the usefulness of flow-based systems in achieving a cost-effective pathway to on demand PET radiopharmaceutical production.

Among the various approaches that have been explored, batch-mode systems may provide the greatest potential for cost reduction in PET radiopharmaceutical production on demand[34,35]. It is possible to reduce the cost of reagents by 2-3 orders of magnitude by performing reactions at the microliter scale (compared to the milliliter scale of conventional radiosynthesizer technologies and microfluidic flow chemistry approaches). Furthermore, miniaturization of the synthesizer can result in a significant reduction in the cost of specialized radiation-shielded facilities (e.g., hot cells or minicells) and equipment. Moreover, the small volume scale used limits contamination of reactions with fluorine-19 derived from reagents[36]. As a result, ^{18}F-labeled tracers can be produced with high molar activities (as determined by the ratio between radioactive molecules and non-radioactive molecules[37]). High molar activity can be achieved even when the PET tracer is produced in small batches; whereas conventional systems require large quantities of tracer to achieve satisfactory molar activity. It is particularly important to use high molar radioactivity in early tracer development and preclinical research because it allows injection of sufficient activity (for high signal-to-noise ratio images) without inducing pharmacologic effects. Generally, small animals are injected with much higher concentrations of the tracer than humans to achieve sufficient signal for small animal scanners that have small voxel sizes[38,39]. Due to the greatly reduced quantities of reagents and small volume (10 microliters) of crude product, microvolume

radiosynthesis facilitates the simple purification of crude products by using radio-high-performance liquid chromatography (radio-HPLC) on an analytical scale rather than semi-preparative scale. A more rapid purification process is provided by analytical-scale chromatography (shorter retention times), and a smaller volume is collected of the pure product, which simplifies the formulation of the tracer into an injectable solution downstream. There is, however, still a need for advancements in microscale purification due to the large footprint and high cost of the HPLC system, which hinders many of the attributes of microfluidic devices. Some advances by the Reichert group have shown the ability to radiolabel with the radiometals Cu-64, Ga-68, and Zr-89 in PDMS devices[26,40]. Similar advances have been made by the Pamme[31] and Manning[41] groups.

1.3 Batch-scale microfluidic devices

Lee *et al.* reported the first batch-based microfluidic system for multistep radiochemistry (**Figure 1-2**)[42]. Utilizing this system the successful production of a small quantity (10s of μCi) of [^{18}F]FDG in a chip with 40 nL reactor volume was achieved. Poly(dimethylsiloxane) (PDMS) was used to fabricate the integrated microfluidic chip according to well-established “soft lithography” procedures[43,44]. Several pneumatically actuated micromechanical valves on the chip were used to separate distinct regions, to accelerate diffusion-dominated mixing by peristaltically pumping liquid around a ring-shaped reaction loop, as well as to create an in-situ ion-exchange resin bed to concentrate radionuclides. Due to the gas-permeable nature of PDMS, it was possible to perform solvent exchange steps (evaporatively). Despite the integrated radionuclide concentration, the small size and slow flow rates of this chip limited the ability of the chip to produce larger quantities of tracer.

.

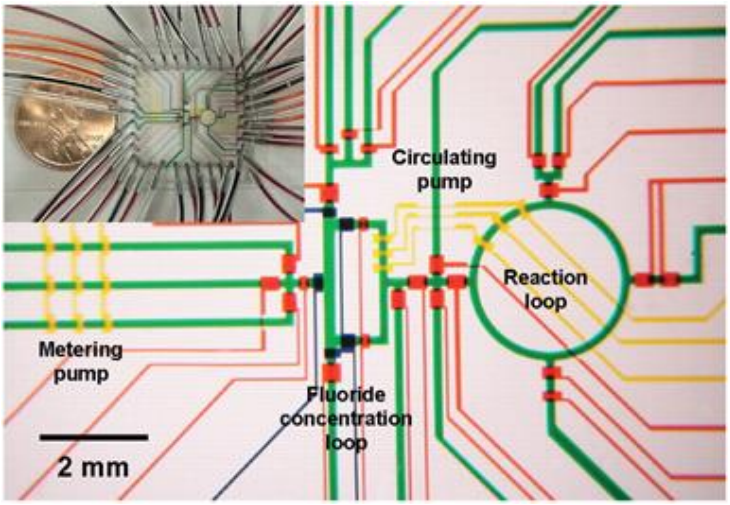

Figure 1-2. Optical micrograph of the batch-based microfluidic system.
The various channels have been loaded with food dyes to help visualize the different components of the microfluidic chip. Green channels contain the reagents and reaction mixture. Red channels are microvalves. Yellow channels are triplets of microvalves used as peristaltic pumps. Inset: View of the whole device positioned beside a penny (diameter 18.9 mm) for scale comparison. Figure adapted from Lee *et al.* © 2005 Science[42].

Later, Elizarov *et al.* developed a scaled-up version of this chip featuring a 5 L cylindrical ("coin-shaped") reaction chamber for the synthesis of [^{18}F]FDG up to the mCi level[45] (**Figure 1-3**). The new version of the chip featured an additional layer of channels, in addition to the previous two-layer design (i.e., with a flow layer and a valve control layer): the new layer contained channels just beneath the reaction chamber to which vacuum is applied. Gas transport across the membrane was accelerated due to the very thin layer of PDMS between the reaction chamber and these channels. This resulted in the rapid removal of trapped gas when initially filling the chamber with reagents and the rapid removal of solvent vapor during solvent evaporation. Additionally, air could be applied to the vent channels during reactions to minimize unwanted evaporation. The radionuclide concentration process was also moved to an off-chip column so that a faster flow rate (2 mL/min) could be used to trap more radionuclide before introduction into the microfluidic device. However, the layers are still constructed of PDMS elastomer, which has low chemical resistance to many organic solvents commonly used for radiosynthesis. This limits

their potential for radiochemical reactions. As a result of PDMS reacting with [^{18}F]fluoride under certain conditions, a large amount of radioactivity was not recovered from the chip[46].

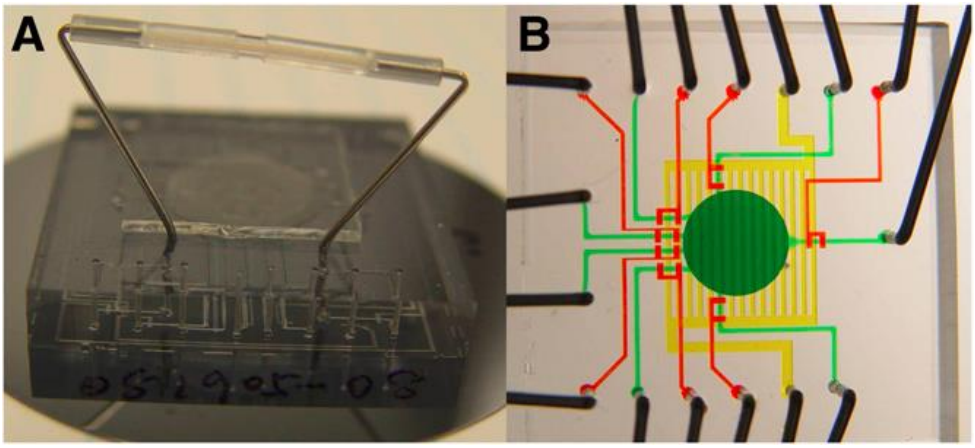

Figure 1-3. The coin-shaped reactor for scaled-up radiosynthesis.
(A) Photograph of chip with off-chip ion exchange column controlled by on-chip valves. (B) Zoomed in photograph of the chip. The channels are filled with dyes for visualization: the fluid channel network is shown in green, control valves in red, and the vent channel in yellow. Figure adapted from Elizarov *et al.* © 2010 Journal of Nuclear Medicine[45].

In order to overcome the chemical compatibility issue with PDMS, van Dam et al. developed a new generation of the 5-litre "coin-shaped" reactor using polydicyclopentadiene (pDCPD), a rigid, transparent material[47]. The microfluidic chip (**Figure 1-4**) consisted of three layers - a flexible gasket layer (PDMS coated with an optimized perfluoropolyether) between a fluidic layer (pDCPD) and a vent layer (pDCPD). In contrast to the previous version with a thin layer of PDMS between the reaction chamber and vent channels, the new composite gasket material provided both good vapor permeability and excellent chemical resistance. The layers of this chip were not bonded together, requiring a different approach to implement diaphragm microvalves on the chip. Linearly actuated metal rods either allowed the membrane to deflect (open valve) or prevented it from deflecting (closed valve). With this reactor, a human dose (~16 mCi) of [^{18}F]FDG was produced. Despite this, the speed of operation was still limited by the transport of vapor across the gasket layer. While further advances to this approach led to the successful synthesis of a wide range of PET radiopharmaceuticals[48,49], even in one instance producing a dose of [^{18}F]Fallypride sufficient

for clinical use[50], the need for a bulky external system limit its practicality in miniaturizing on demand production.

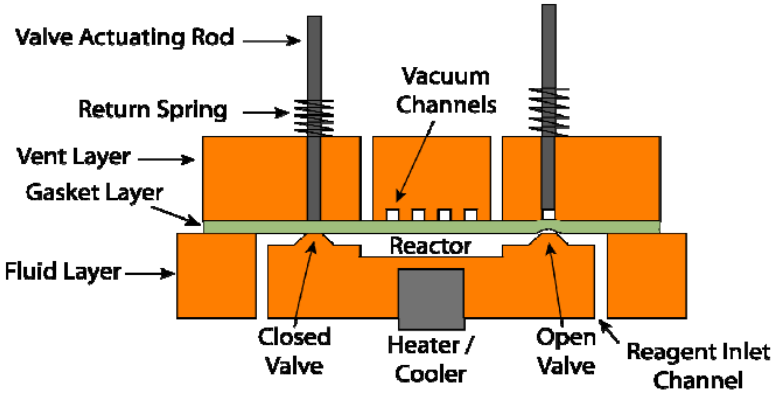

Figure 1-4: The new coin-shaped reactor fabricated from inert materials.
Cross-section of microfluidic chip illustrating the main features in each layer and the architecture of the on-chip diaphragm valves. Figure adapted from van Dam *et al.* © 2007 NSTI Nanotechnology Conference[47].

In order to develop a more compact and disposable microfluidic system for PET radiopharmaceutical production, our lab has utilized droplet-based electrowetting-on-dielectric (EWOD)[51–54]. As shown in **Figure 1-5**, the EWOD chip has a bottom plate with a pattern of individual electrodes that is two-dimensional. The chip can control droplet movement by applying local electric fields via the electro-wetting phenomenon (reduction in contact angle between droplet and surface during the application of electrical potential). A ground electrode is provided by a cover plate. The two plates are coated with a conductor layer, a dielectric layer, and a hydrophobic layer (Teflon), which facilitates droplet movement and provides excellent compatibility with various solvents and reagents. In the EWOD microfluidic chips, sequential electrode activation is used to transport reagent droplets (surrounded by air), as they are required, from fixed reagent loading sites to a central, temperature-controlled zone where evaporation and reaction processes are carried out to perform multi-step radiosynthesis (**Figure 1-6**).

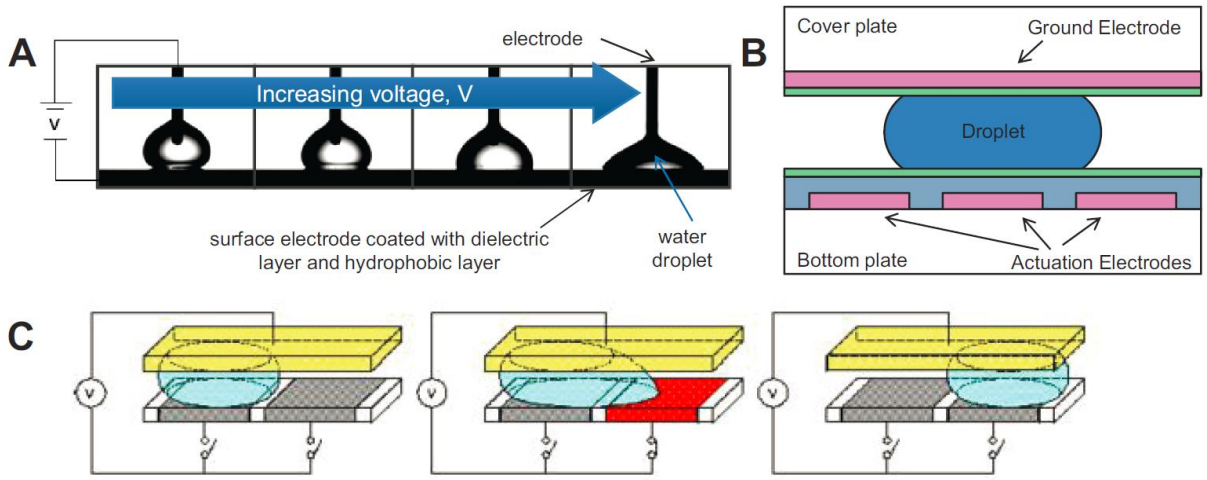

Figure 1-5. Structure and operation of EWOD microfluidic chips.
(A) Electronic control of the droplet interaction with the surface due to electrowetting effect. (B) In a typical EWOD device, the droplet is sandwiched between two plates with the electrode configuration as shown. The blue layer is an insulating dielectric layer and the green layer is a hydrophobic coating. (C) By applying a voltage to one end of a droplet with an actuation electrode, a force is generated, pulling the droplet toward the activated electrode, allowing linear transport, splitting, and other manipulations of droplets. Figure adapted from Keng *et al.* © 2015 Digital Microfluidics[35].

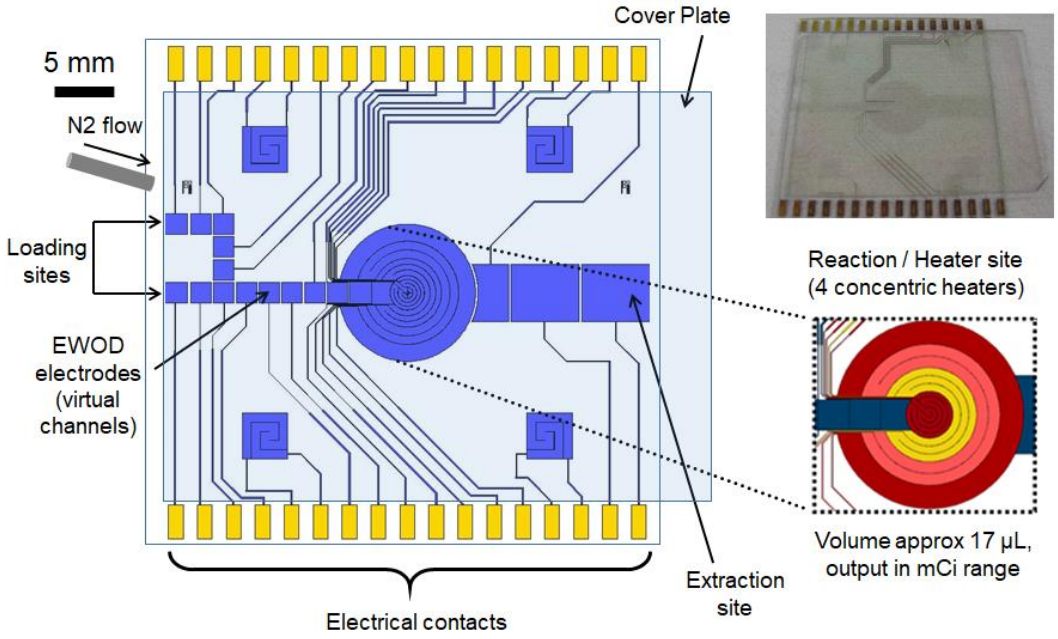

Figure 1-6. Schematic of the EWOD radiosynthesis chip.
The schematic shows electrode pattern of the central reaction size (with concentric resistive heaters) and reagent pathways. A photograph of the actual device is shown at the top right of the figure. Figure adapted from Keng *et al.* © 2015 Digital Microfluidics[35].

Multiple tracers have been successfully synthesized with the EWOD system and used for preclinical imaging, including [^{18}F]fallypride[53], [^{18}F]FDG[55], 3'-fluoro-3'-[^{18}F]fluorodthymidine ([^{18}F]FLT[56]), and [^{18}F]SFB[52]. However, the complex production pathway of EWOD devices, with high fabrication failure rates, limit their disposability, posing an issue for cost-effective PET radiopharmaceutical production.

1.4 Next-generation droplet radiosynthesis

Another example of active droplet manipulation for the radiosynthesis of PET radiopharmaceuticals is the use of magnetic droplet microfluidics[57]. At the beginning of the synthesis, a volume of [^{18}F]fluoride solution (up to 1 mL) and droplets of reagents (~50 µL) are manually placed atop a hydrophobic Teflon sheet mounted on a plastic stage. By addition of magnetic particles into a droplet, that droplet can be manipulated by robotically moving a magnet mounted under the stage. Despite its capability of moving aqueous droplets and conducting room temperature reactions (mixture of water and t-BuOH) under aqueous conditions, it has yet to be proven that it can extend to additional radiosyntheses involving organic solvents, elevated temperatures, or moisture-sensitive precursors.

Our lab has instead utilized a simplified version of EWOD chips, that utilize Teflon coated silicon chips, to create a series of hydrophilic trap reaction sites, that contained manually added reagents[58]. These simple Teflon-glass chips could in fact also be used for manually carrying out the entire production of tracers for imaging[36,59]. Heating was provided by placing the chip atop a temperature control platform (Figure 1-7). The chip was mounted on a temperature control platform which in turn was mounted off-center on a compact rotation stage, which was used to align the reaction site under different reagent dispensers or product collection tubing. Piezoelectric dispensers were used to load reagent droplets directly onto the reaction site. After the chip was heated to perform an evaporation or reaction step, the chip was then rotated to align the reaction site under the dispenser containing the next reagent to be added. Once the synthesis

was finished, the resulting crude product was collected by aligning the reaction site under a stainless-steel tube and transferring the droplet off the chip via application of vacuum.

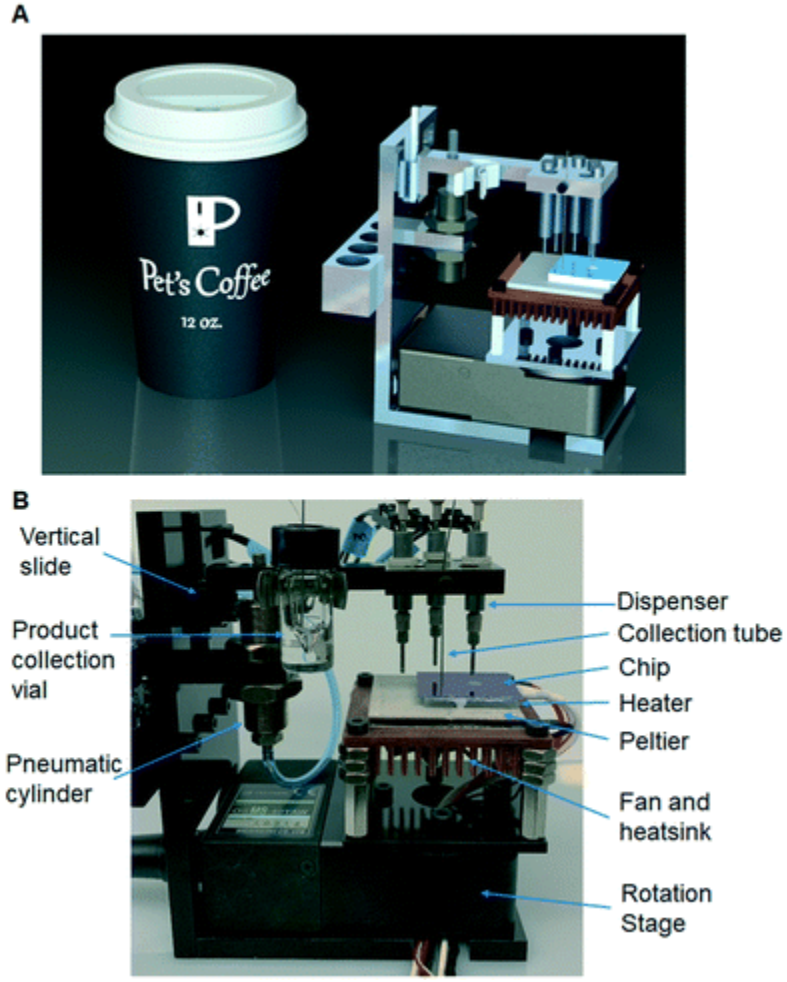

Figure 1-7. A compact and automated droplet radiochemistry system.
(A) A CAD rendering of the system alongside a 12 oz. coffee cup. (B) A photograph of the synthesizer, including the reagent dispensing, product collection, temperature control, and rotation subsystems. Figure adapted from Wang *et al.* © 2019 Lab on a Chip[58].

This novel droplet radiosynthesizer holds enormous potential in the cost-effective, on-demand production of PET radiopharmaceuticals. As our lab and others continue to explore droplet radiochemistry, we expect there will be continued translation of known tracers from macroscale methods to droplet-based reactors, and eventually synthesis development could occur on the droplet platform itself to take advantage of the reagent economy and simple operation. Initial clinical scale has been shown for these droplet reactor systems[60].

1.5 Reaction Optimization

Droplet reactions also provide significant advantages for radiosynthesis development. In particular, the reduced consumption of reagents can enable ~2 orders of magnitude more experiments to be performed (for synthesis optimization or production of batches for in vitro and in vivo studies) with a single macroscale reaction quantity of precursor. This is particularly valuable at early stages when the precursor is scarce. However, due to the nature of radiochemistry systems, and the contamination of apparatus after use, it can take a long time and high cost (i.e., many batches of radioisotope, significant labor cost) to optimize radiochemical processes on the system, suffering the same issues as conventional radiosynthesizers.

Toward the concept of optimization, our group recently developed a high-throughput chip that has multiple hydrophilic traps (Figure 1-8) to perform up to 16 reactions simultaneously[61]. The reagent loading and product collection were performed manually on a temperature-controlled platform (**Figure 8B**). Further studies remain to determine the effectiveness of these multi-reaction chips for optimization of a diverse range of radiopharmaceuticals. Preliminary use of these platforms also highlighted the need for improvements to the available methods for the analysis of reaction mixtures, especially throughput.

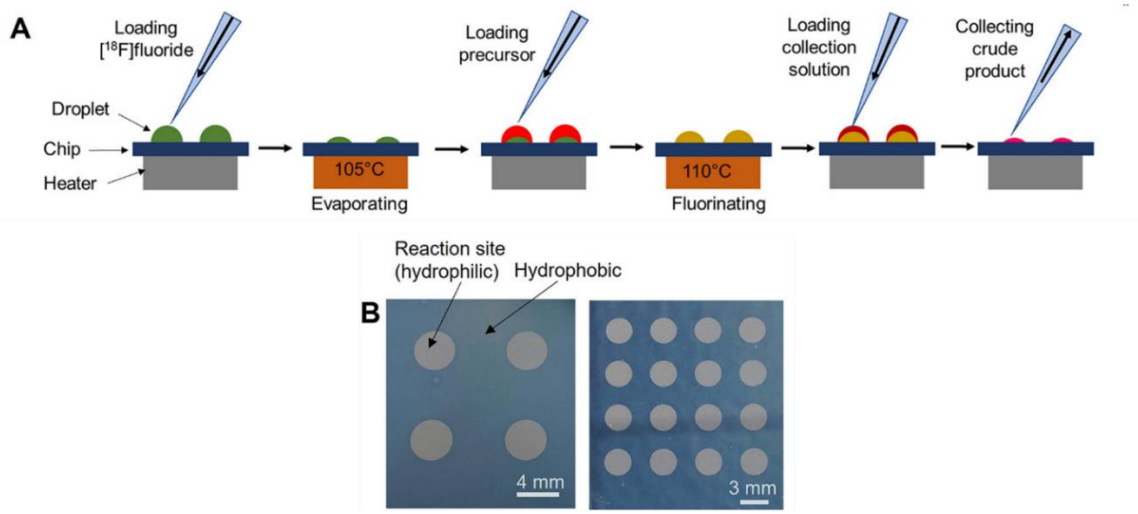

Figure 1-8. High-throughput methodology for the reaction of multiple sessile reactions on a single reactor chip.
(A) Schematic process to perform multiple simultaneous radiosynthesis using multi-reaction chips. (B) Top view photographs of multi-reaction chips with 4 reaction sites (diameter 4 mm, pitch 9 mm) and 16 reaction sites (diameter 3 mm, pitch 5 mm). First, at each site, a droplet (8 µL) of [^{18}F]fluoride mixed with phase transfer catalyst was added and then dried using heat. Then, a droplet of precursor solution (6 µL) was added and reacted at elevated temperature. Finally, 20 µL of collection solution was loaded on the reaction site to dissolve resulting compounds and collected from the chip. Each site was collected for independent analysis via 3 repeats of the collection process. Figure adapted from Wang *et al.* © 2020 Molecular Imaging[62].

1.6 The history of TLC

The history of liquid chromatography dates back to the early 1900s, with its first description by Mikhail Tsvet for the separation of plant pigments[63], further descriptions of this work have been covered by Sherma[64]. This seminal work described the use liquid-adsorption chromatography with the use of calcium carbonate as a stationary phase (absorbent phase), and mixtures of petroleum ether and ethanol as a mobile phase (eluent) for the separation of chlorophylls and carotenoids. The underlying methodology of this method, the use of a stationary phase, and mobile phase for the differential adsorption and elution of chemical entities has translated to many modern chromatographic techniques: TLC[65], paper chromatography[64], adsorption chromatography[63], partition chromatography[66], ion-exchange chromatography[67], affinity chromatography[68], gel filtration gas chromatography[69], and high-performance liquid

chromatography[70]. One of the simplest cases of chromatography, TLC, remains one of the most utilized techniques across a myriad of disciplines.

While the origins of TLC can be traced back to work by Izmailov and Schraiber in 1938 for the separation of medicinal compounds, this technique does not bear high similarity to familiar TLC methods of today[71]. Instead, in this work, glass plates coated with alumina were used to separate applied mixtures of compounds applied as droplets. The advent of modern TLC as we visualize it today, instead can be traced back to the late 1950s, by work from Kirchner and colleagues at the U.S. Department of Agriculture[72]. Kirchner utilized silica gel adhered to glass plates through the aid of binding agents. This silica gel was coated with a fluorescence indicator to visualize the separation of chemical species that are UV-active. These plates utilized vertical development, which at the time, was conventionally used with paper chromatography. This simplification in the separation of compounds was a departure from other popularized methods of the time. Importantly, Kirchner standardized the TLC materials (e.g., backing material – glass, aluminum; stationary phase – silica, alumina), procedures (e.g., sample deposition and plate development), and nomenclature (underlying terms that are still in use today). Commercial companies helped to lead the widespread adoption of TLC, with standardized plates and developing apparatuses – which are currently in use today.

1.7 The basic principles of TLC

The principles and basic protocol of TLC outlined by Kirchner are still used today (**Figure 1-9**). A small aliquot of sample is placed onto the stationary phase at a defined origin. Once the spotted sample is dried, the bottom edge of the TLC plate, near the spotted sample, is placed into a developing chamber containing a small amount of mobile phase. The developing chamber is closed to limit mobile phase evaporation and prevent drying of the TLC plate or demixing of multi component mobile phases. When the mobile phase has migrated the desired distance along the plate, normally pre-defined by marking the face of the TLC plate (denoted as the solvent front),

the plate is removed from the developing chamber. The mobile phase is then evaporated from the TLC plate (e.g., by ambient evaporation or heating of the plate). Visualization of the separated components of the sample can be achieved through many different methods. The most employed method, fluorescence, utilizes willemite that is embedded into the stationary phase, that when exposed to UV light (e.g., short wave - 254 nm and long wave – 365 nm), is excited and fluoresces a brilliant green. If a chemical analyte absorbs UV light is present, it will quench the natural fluorescence of the plate, producing dark bands of contrast. While this technique is commonly employed, its use is limited to analytes that are UV active. Other visualization methods include the use of chemical stains that the plate is dipped into and which cause a color change if there are species present on the plate with certain functional groups. It should be kept in mind that these methods are often destructive and can't be used in conjugation with recovery of analytes from the TLC plate. The differential migration distances of different chemical species up the length of the TLC plate are the result of different affinities for the analytes in equilibrium between the stationary and mobile phases. While various separation mechanisms are involved for silica stationary phases, the predominant forces have been elucidated by Snyder[73] and colleagues and include proton donation affinity, proton acceptor affinity, and dipole interactions.

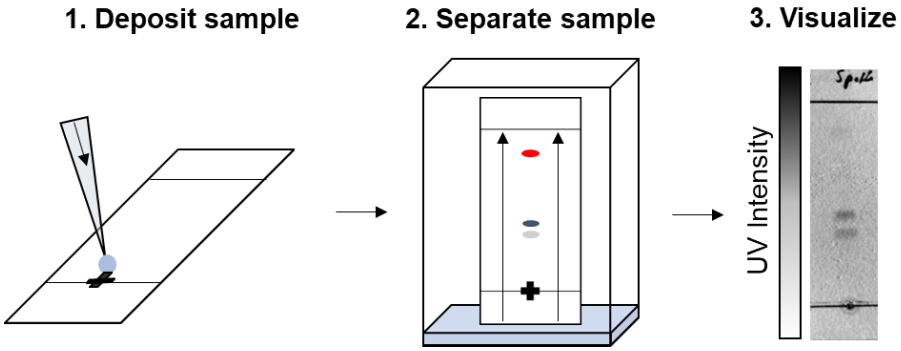

Figure 1-9. The basic procedure for the development of TLC plates.

1.8 TLC analysis of radiopharmaceuticals

While many disciplines utilize TLC, no field, like that of radiochemistry, utilizes the method as a core technique for as many applications. This is likely because of the simplicity of TLC, and

the rapidity of separation, as time is critical when working with short-lived compounds. Radio-TLC is useful in determining the incorporation of radionuclide into the target radiopharmaceutical (i.e. assessing the reaction yield). For the case of fluorine-18 labeling, it is generally the case that unreacted radionuclide is sequestered at the origin, while the radiopharmaceutical of interest (and impurities) are mobilized away from the origin with an appropriate mobile phase. Determining the relative abundance of radionuclide and label species allows reaction metrics like the radiochemical conversion to be calculated[74]. In a similar fashion, quality control (QC) analysis of the final formulated radiopharmaceutical relies on the separation of the product from the radionuclide and impurities to determine the radiochemical purity of the formulated radiopharmaceutical[75]. Further, when radio-TLC is coupled with staining procedures, spot testing of formulated radiopharmaceuticals can be used to determine the residual presence of toxic phase transfer catalysts[76]. Radio-TLC has also been utilized to profile the *in vivo* metabolism of injected radiopharmaceuticals to enable quantitative analysis of PET images[77]. Radio-TLC can be used to determine the relative abundance of intact radiopharmaceutical (versus radioactive metabolites) in tissues such as plasma. These measurements in tandem with gamma counting of blood samples taken at multiple timepoints after injection of the tracer allows accurate determination of the arterial input function (AIF), i.e. the concentration of available radiopharmaceutical[78].

1.9 Factors affecting chromatographic resolution of radio-TLC

While there are numerous factors that can be optimized for increased chromatographic resolution between species in TLC, due to the short-lived nature of radiopharmaceuticals, the selection of the stationary and mobile phases remains the most impactful factors in the resolution of radio-TLC. (Factors such as separation length are not often considered as small changes in separation length can add significantly to the separation time.) Conventionally, silica has been utilized in PET radiochemistry due to most syntheses utilizing organic reaction solvents that are

miscible with common mobile phases. There are some notable cases in the literature that make use of reverse-phase sorbents as stationary phases, for the separation of highly polar chemical species. However, in some cases, the reaction solvent is incompatible with mobile phases used for these stationary phases – often leading to poor chromatographic behavior. The mobile phases utilized in radio-TLC are usually experimentally determined, seeking to separate the radiopharmaceutical from the sequestered radionuclide at the origin[79–82]. However, substantial optimization and validation is rarely performed, and it is often the case that multiple different mobile phase may be found in the literature for studies of the same radiopharmaceutical[80,83]. A gap in the literatures remains for a systematic determination of mobile phase conditions suitable for radiopharmaceuticals with diverse chemical properties.

1.10 Radio-TLC readout

After the radio-TLC plates are developed they are read out for analysis of the radiochemical species distribution across the plate. 1-dimensional TLC scanners are predominantly used. This basic TLC scanner consists of a flatbed scanning table, that moves the plate under a radiation detector. One detector configuration consists of a radiation-shielded gas-based radiation detector that is sensitive to gamma radiation and beta particles. Notably, this detector suffers from the need for a continuous gas supply and the need for periodic calibration. Due to these issues, increased use of lead shielded crystal scintillators that emit light when excited (e.g., gamma emission or positron interaction) are recorded by photodiodes. A chromatogram is generated by plotting the radiation signal as a function of distance along the plate. The spatial resolution of these systems is a function of the type of radiation being measured. Resolution is high for short-ranged particles (e.g., alpha and beta) when employing detectors sensitive to short decay distances. Longer-ranged particles (e.g., gamma rays) often result in lower resolution, but can be improved with the use of collimators, at the expense of sensitivity.

Some commercially available 2-dimensional scanners (e.g., AR-2000) allow the automated scanning of multiple lines along the TLC plates to give an 'image' of the distribution of radioactivity on the plate, or to scan multiple TLC plates placed on the scanner bed[84]. Of course, scanning multiple plates is performed sequentially, requiring longer readout times for larger TLC plates or larger numbers of plates. Alternatively, autoradiography has been used as a radio-TLC readout method. The TLC plate once developed (or multiple plates) is placed into contact with a phosphor imaging screen, effectively capturing an image of the radioactivity distribution on the TLC plate(s) all at once. The screen is subsequently read out with a phosphor imaging system[85]. While capable of parallel imaging of many plates, this method is time-consuming and cumbersome.

1.11 Technical advances of radio-TLC readout

Other readout methods have also been employed, including the advent of imaging-based readout. One category of such approaches is solid-state imagine devices. Jeon et al. utilized a 64x1 array of scintillator crystals above a photodiode array to quantify sample at multiple locations using different radionuclides (e.g., F-18 and Tc-99m)[86]. Maneuski *et al.* used a pixelated solid-state timepix silicon detector to obtain a 2D image of a partial radio-TLC plate spotted with fluorine-18[87]. These methods, however, are small and too expensive to scale to image multiple TLC plates.

Autoradiography studies have been conducted with instant imaging systems (e.g., Canberra Packard) that have a large-area multiwire proportional counter detector, on which multiple radio-TLC plates can be imaged simultaneously. This system has been used with many different radionuclides (e.g., C-11, F-19, Cu-64, Tc-99m, and I-124)[88–91].

Optical imaging utilizing light derived from radionuclide decay, namely Cerenkov luminescence imaging (CLI), has recently been used to read out TLC plates[92,93]. As a charged particle traverses a dielectric medium at speed greater than light's phase velocity, Cerenkov

luminescence occurs[94]. In general, light emitted from a particle is in a cone, and its spectrum is proportional to the inverse wavelength squared. Material properties limit the wavelength ranges and intensities of emitted light. The low light level makes the detection of Cerenkov luminescence rather difficult, as it typically requires the same type of imaging system as bioluminescence, which is a high-sensitivity charge-coupled device (CCD) coupled to a focusing optics and placed in a light-tight environment.

Originally, CLI was reported by Park et al. for the read out of TLC plates spotted with radionuclides. However, Wang et al. recently reported that the method could be used for the massive read out of multiple samples developed on radio-TLC plates (**Figure 1-10**). This work additionally showed a very low-cost readout method using an inexpensive camera. It had much smaller field of view than small animal imaging systems but was large enough for multilane TLC plates. The benefits of this imaging approach are numerous. The larger field of view allows multiple lanes developed in parallel to be readout simultaneously. This allows the timely analysis of a great number of samples, that would not be achievable by other analysis means.

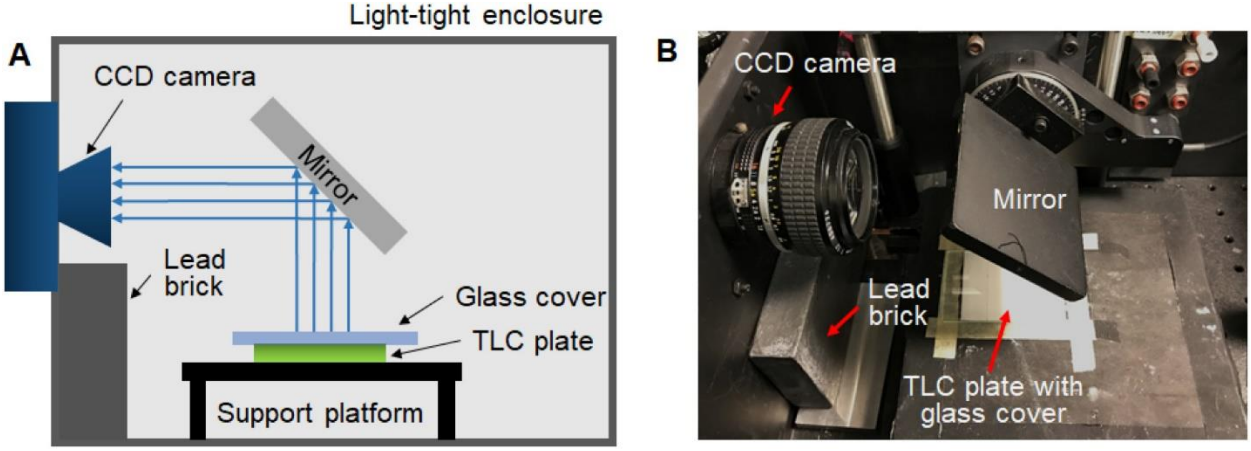

Figure 1-10. Cerenkov luminescence imaging setup within a light-tight enclosure.
(A) Schematic. (B) Photograph. Figure adapted from Wang *et al.* © 2020 Nuclear Medicine and Biology[93].

In contrast to simple 1D TLC scanners, the ability to image the plate allows the ability to assess the quality of the separation and to detect anomalies across the face of the TLC due to

irregular development or contamination (Figure 1-11). When the CLI image is combined with other optical imaging techniques like brightfield imaging, its further possible to better archive data, and compute the Retention factor (R_f) of analytes across the TLC plate.

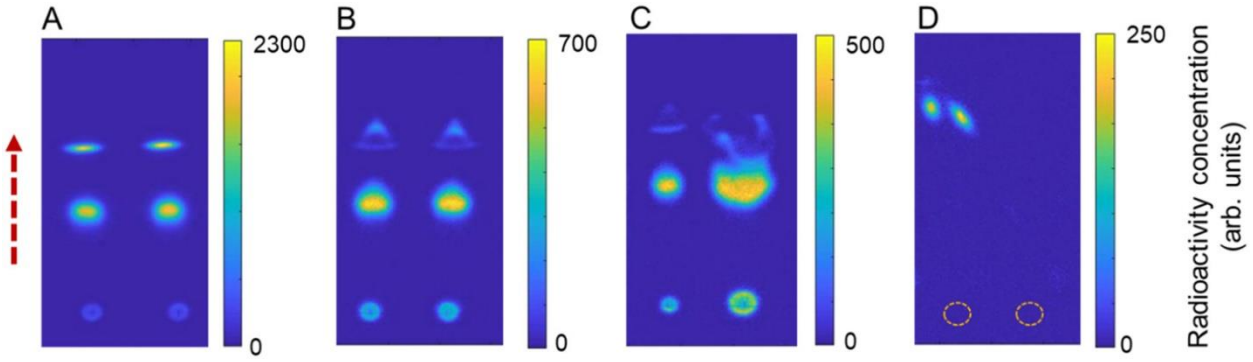

Figure 1-11. Assessing quality of the TLC spotting and developing process.
(A) Cerenkov image of developed plate after spotting of two replicates (1 µL) each of crude [^{18}F]FET product. This image indicates a normal spotting and developing process. (B) Separation artifacts visible in most distant spots when the plate was not completely dried prior to developing. (C) Separation artifacts due to a combination of incomplete drying as well as abnormally large sample volume (right spot 2.0 µL). (D) Separation artifacts arising from liquid contamination at the right edge of the TLC plate during developing, causing the main solvent flow to be deflected to the left. The TLC plate in this case was spotted, at the positions marked with dash circles, with two replicates (1 µL each) of crude [^{18}F]Fallypride product. Figure adapted from Wang *et al.* © 2020 Nuclear Medicine and Biology[93].

In the work by Wang et al. conventional radio-TLC scanner readout was compared with CLI imaging readout[93]. While single well separated peaks showed good correlation between the methods, quantitation of overlapping bands was improved with CLI imaging due to improved readout resolution, and improved ability to quantity the radioactivity in the entirety of each band, and not just the center line. The quantification of the two overlapping radiochemical analytes with conventional radio-TLC scanning differed from that quantified with CLI imaging, especially for overlapping bands that significantly differed in intensity (abundance).

While imaging-based readout methods provide high resolution readout, resolution among different chemical species is still dictated by the underlying chromatographic resolution of radio-TLC, which is typically rather low compared to other chromatographic approaches such as radio-HPLC. This is especially important given the fact that many radiochemical syntheses are late-

stage nucleophilic substitution reactions where the precursor used to produce radiopharmaceuticals has high structural similarity to the product. Given the harsh reaction conditions necessary to promote these reactions, many side products of high structural similarity can also be generated. Therefore, a major unmet need to develop a systematic approach to enhance the chromatographic resolution of radio-TLC remains. This method should take into account the various intermolecular forces that govern the resolution of radio-TLC.

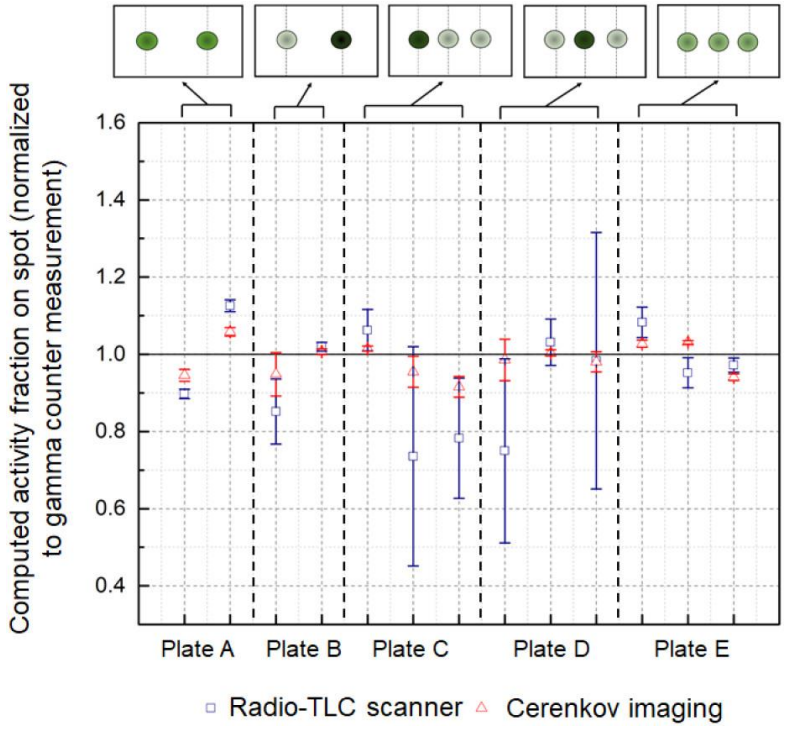

Figure 1-12. Radio-TLC readout performance comparison of radio-TLC scanner.
The data points show the average activity fraction in each spot (averaged over the analysis performed by n = 8 participants) normalized by the activity fraction determined by gamma counting. The normalized activity fraction provides a measure of accuracy. Values close to 1.0 indicate high accuracy, i.e., close agreement between the result from the radio-TLC scanner or Cerenkov luminescence analysis and the gamma counter measurement of the radioactivity in a particular spot. The error bars show the relative standard deviations and indicate the precision. The black dashed vertical lines separate the data from each of the five radio-TLC plates. Cartoons of the activity distribution are shown at the top of the graph (darker green spots represent higher activity level). Figure adapted from Wang *et al.* © 2020 Nuclear Medicine and Biology[93].

1.12 Summary of Dissertation

Next-generation droplet microfluidic radiosynthesizers have shown enormous promise for cost-effective, on-demand production of radiopharmaceuticals. Reductions in costs are possible

due to vastly lowered reagent use. High molar activity values can be achieved for all batches, even those with low activities, which could allow the cost-effective production of small batches of radiopharmaceuticals for applications where receptor density of the biological target of interest may be low. Reductions in synthesis time are also attractive. Further reductions in the mass scale of reactions lead to cleaner synthetic reactions, that can employ lower capacity chromatographic methods, shortening the purification and reformulation processes to produce radiopharmaceuticals. Furthermore, it has been shown in many preliminary reports that the radiochemical yield of conventional macroscale literature reported radiopharmaceuticals can be matched. Finally, the small footprint of the droplet radiosynthesizer is attractive for use in clinical locations, that may only utilize small shielding apparatuses, obviating the need for highly specialized facilities that are too expensive for the use of PET in many exploratory studies. All of these advantages promise the ability to provide a diverse catalogue of radiopharmaceuticals at low cost on demand. With the advent of droplet microfluidic radiosynthesizers that allow multiple parallel reactions to be run simultaneously, high-throughput reaction optimization studies are possible, enabling rapid translation of known macroscale synthesis protocols to the droplet format. It is conceivable that this capability could be leveraged to optimize synthesis protocols where conventional yields are low, perhaps providing improved reaction conditions and improved manufacturing methods. The ability of high-throughput methods for the development of microscale reaction conditions could have enormous implications in the cost-effective production of radiopharmaceuticals, however, to leverage these methods, the need for equally high-throughput and resolution analysis techniques remains.

In **Chapter 2**, I describe the methodology for high throughput experimentation that enables the rapid optimization of droplet radiochemical syntheses. This method is applied to the optimization of a previously reported droplet radiosynthesis of [^{18}F]Fallypride, showing an increase in yield due to optimization. In **Chapter 3**, we explore the utilization of this high-throughput methodology for the optimization of [^{18}F]FDOPA. The synthesis of [^{18}F]FDOPA

presents a challenge not seen with [^{18}F]Fallypride, due to the need for a secondary optimization of the deprotection reaction. Utilizing this method, we were able to increase the yield of [^{18}F]FDOPA. In **Chapter 4**, we explore the use of a radiosynthesizer system that features multiple heating elements. Using the high-throughput methodology we performed over 1000 reactions in a 14-day time-period – a feat unachievable with conventional macroscale systems. The radiosyntheses of [^{18}F]FEPPA, [^{18}F]PBR-06, [^{18}F]FMZ, and [^{18}F]Fallypride were all adapted from the macroscale and optimized in the microfluidic droplet format. In **Chapter 5**, we explore the ability to increase the radiosynthesis activity scale of optimized radiotracers in the microvolume droplet scale to product clinically-relevant quantities of radiotracers. Previous reports by our lab have shown that activity yield decreases as a function of the activity scale used for reactions. However, a universal base free concentration method was developed that in principle allows scaling activity to arbitrary levels of radioactivity in droplet reactions, and which decouples the conditions for the concentration step (i.e., base amount) from the downstream reaction step using a volatile base. Starting in **Chapter 6**, I begin to describe our efforts to develop improved techniques for radio-TLC. First, we assess the effects of utilizing aqueous components for mobile phases used with silica-based TLC plates. Conventionally, water is used in radiochemistry as a mobile phase component to mobilize polar compounds. However, we show that the use of water can in fact lead to ambiguous results, that render radio-TLC unhelpful in the analysis of radiopharmaceuticals. In **Chapter 7**, we introduce a systematic approach (PRISMA) for developing mobile phase conditions to achieve high chromatographic resolution in a set of radiopharmaceuticals with a diverse range of chemical properties. In the series of radiopharmaceuticals tested, complete baseline separation of radiopharmaceuticals from impurities (e.g., radioactive, and UV-active) was achievable. In **Chapter 8**, leveraging the low mass scale of microvolume droplet reactions, along with the high resolution of TLC achievable with CLI and PRISMA, to explore the use of TLC separation as a means for the *purification* of microscale produced radiopharmaceuticals without the need for expensive and bulky radio-HPLC

apparatus. Purification of [^{18}F]PBR-06 and [^{18}F]Fallypride was achievable with high efficiency. Furthermore, the ability to recover purified radiopharmaceuticals in saline obviated the need for conventional downstream reformulation, significantly shortening the purification timeline. In **Chapter 9**, we describe the application of the TLC advances to the analysis radio-metabolites. Using separation conditions that givehigh chromatographic resolution between [^{18}F]FEPPA and impurities, we successfully analyzed intact [^{18}F]FEPPA fraction in rat plasma samples. Using channeled radio-TLC plates large deposition volumes could be achieved without affecting radiopharmaceutical resolution and used autoradiography readout to increase signal-to-noise ratio, and also extended this method to the analysis of clinical samples, where the radioactivity concentration in plasma is much lower than for small animals. Finally, an automated sample deposition manifold was developed to allow the parallel spotting of samples onto TLC plates, further reducing the analysis time of radiometabolites and simplifying the procedure for potential routine clinical use. In **Chapter 10-Chapter 11**, we explore the electrochemical fluorination of electron rich moieties, like thioethers. Under conventional nucleophilic fluorination pathways, the ability to label thioethers is not achievable. These successful methods are being translated to further reduced scale volumes, can could be attractive for microvolume droplet reactors. In **Chapter 12-Chapter 13**, we explore the use of charged radiopharmaceutical ([^{18}F]FBnTP) for the assessment of mitochondrial membrane potential. Interestingly, it was found that tumors can have different metabolic profiles that are not fully captured by the clinically recognized standard [^{18}F]FDG. Further studies elucidated the role that [^{18}F]FBnTP can have in the assessment of the metabolic pathway of OXPHOS. Together, these findings hold enormous impact for the next-generation profiling of metabolism in tumors, and their susceptibilities to novel treatments. Our lab is currently researching methods to produce [^{18}F]FBnTP in the microvolume droplet format. This dissertation is concluded with **Chapter 14**, that looks at potential outlooks of microvolume reactors, utilizing the findings of this dissertation for a truly microscale radiosynthesizer for the cost-effective on-demand production of radiopharmaceuticals.

Chapter 2: Microfluidic radiochemistry: synthesis in sessile droplets

2.1 Introduction

Positron-emission tomography (PET) radiopharmaceuticals are widely used as research tools to monitor specific in vivo biochemical processes and study diseases, and for the development of new drugs and therapies. Moreover, PET is a critical tool for diagnosing or staging disease and monitoring a patient's response to therapy[95–97]. Due to the short half-life of PET radioisotopes (e.g., 110 min for fluorine-18-labeled radiopharmaceuticals) and radiation hazard, these compounds are prepared using specialized automated systems operating behind radiation shielding and must be prepared just before use.

Current systems used to synthesize radiopharmaceuticals are designed to produce large batches that are divided up into many individual doses to share the production cost. While current systems are suitable for the production of widely used radiotracers like [^{18}F]FDG (because multiple patient scans and research experiments can be scheduled in a single day), these systems can be wasteful for the production of novel radiotracers during early-stage development, or less commonly used radiotracers. Volumes that conventional systems use are typically in the 1-5 mL range, and the reactions require precursor amounts in the 1-10 mg range. Furthermore, using conventional radiosynthesizers is generally cumbersome during optimization studies since the apparatus becomes contaminated after use and the user must wait for radioactivity to decay before performing the next experiment. Aside from equipment cost, the cost of the radioisotope and reagents can, therefore, become very substantial for studies requiring production of multiple batches. This can occur, for example, during the optimization of synthesis protocols for novel radiotracers to achieve sufficient yield and reliability for initial in vivo imaging studies.

Microfluidic technologies have been increasingly used in radiochemistry to capitalize on several advantages over conventional systems[20,25,98]. Microfluidic platforms, including those based on 1-10 µL reaction volumes[35,58,99], have shown a significant reduction of reagent volumes and consumption of expensive precursors, as well as short reaction times. These reductions lead to lower costs, faster heating and evaporation steps, shorter and more straightforward downstream purification, an overall "greener" chemistry process[61], and higher molar activity of the produced radiotracers[36]. These improvements make it more practical to perform more detailed optimization studies by lowering the reagent cost of each synthesis. Further benefits can be achieved by performing multiple experiments from a single batch of radioisotope in a single day. For example, microfluidic flow chemistry radiosynthesizers operating in "discovery mode" can sequentially perform dozens of reactions, each using only 10s of µL reaction volume[100].

Inspired by these advantages, a multi-reaction droplet array chip in which microvolume reactions are confined to an array of surface-tension traps on a silicon surface, created using a patterned Teflon coating, was developed. These chips enable multiple reactions at the 1-20 µL scale to be performed simultaneously, opening the possibility to explore 10 s of different reaction conditions per day, each with multiple replicates. In this paper, the utility of this new high-throughput approach for performing rapid and low-cost radiochemistry optimizations is demonstrated. Using multi-reaction droplet chips allows for convenient exploration of the impact of reagent concentrations and reaction solvent, and the use of multiple chips could enable the study of reaction temperature and time, all while consuming very low amounts of precursor.

2.2 Protocol

2.2.1 Microfluidics in Radiochemistry

NOTE: Batches of multi-reaction microdroplet chips are fabricated from 4" silicon wafers using standard photolithography techniques (**Figure 2-1**). This procedure will produce 7 chips each with 4x4 array of reaction sites.

2.2.1.1 Place silicon wafer on the spin-coater chuck, ensuring that it is centered. Deposit 3 mL of polytetrafluoroethylene solution at the center of the wafer with a transfer pipette and coat wafer at a 1000 rpm for 30 s (500 rpm/s ramp).

2.2.1.2 To solidify the coating, place the wafer on a 160 °C hotplate for 10 min and then transfer to a 245 °C hotplate for 10 min.

2.2.1.3 Anneal the coating in a high-temperature oven at 340 °C for 3.5 h under nitrogen atmosphere, followed by cooling to 70 °C at a 10 °C/min ramp

2.2.1.4 Place the silicon wafer on the spin-coater chuck, ensuring that it is centered. Pour 2 mL of positive photoresist at the center of the wafer using a transfer pipette, and then perform coating at 3000 rpm for 30 s (1000 rpm/s ramp).

2.2.1.5 Solidify the photoresist by performing a soft bake of the wafer on a 115 °C hotplate for 3 min.

2.2.1.6 Install the wafer and photomask in a mask aligner and perform a 14 s exposure at 12 mW/cm2 lamp intensity and 356 nm wavelength in hard contact mode. This step uses a transparency mask containing the negative final polytetrafluoroethylene pattern, i.e., a 4" diameter pattern of 4 copies of the 16-reaction chip, with reaction sites transparent and all other regions in opaque color.

2.2.1.7 Submerge the wafer using 20 mL of photoresist developer solution in a glass container for 3 min with slight agitation to develop the exposed pattern.

2.2.1.8 Rinse away the developing solution by submerging the wafer in a glass container with 20 mL of DI water for 3 min with slight agitation. Dry the wafer with a nitrogen gun.

2.2.1.9 Remove the exposed polytetrafluoroethylene regions via reactive-ion etching (RIE) with oxygen plasma under the following conditions: 30 s exposure, 100 mTorr pressure, 200 W power, and 50 sccm oxygen flow.

2.2.1.10 Dice the wafer into individual chips (7 total per wafer) using a silicon wafer cutter.

2.2.1.11 Submerge each chip in acetone for 1 min to remove the photoresist, then isopropanol for 1 min. Finally, dry each chip with a nitrogen gun.

2.2.1.12 Place dry chips in a glass container and cover with aluminum foil for storage until use.

2.2.2 Planning of the optimization study

NOTE: In this protocol, synthesis of the radiopharmaceutical [^{18}F]fallypride is used as an example to illustrate high-throughput optimization (**Figure 2-2**). With a single chip, 16 simultaneous reactions can be performed, for example, with varied precursor concentration (8 different concentrations, n=2 replicates each). The conditions are mapped to reaction sites in **Figure 2-3A**. Adjustments can be made to this protocol to optimize other reaction parameters (e.g. reaction solvent, reaction volume, amount of $TBAHCO_3$, etc.) or other radiopharmaceuticals.

2.2.2.1 Select the reaction parameter(s) to be varied, the specific values to be used, and the number of replicates.

2.2.2.2 Compute the number of chips needed to perform the experiment.

2.2.2.3 For each chip, prepare a map of which reaction conditions will be used at each reaction site to assist with reagent preparation and performing the droplet reactions.

2.2.3 Preparation of reagents and materials for optimizing the radiosynthesis of [^{18}F]Fallypride

NOTE: The droplet-based radiosynthesis of [^{18}F]fallypride (**Figure 2-2**) begins with the addition of [^{18}F]fluoride and phase transfer catalyst ($TBAHCO_3$) to the reaction site, followed by heating to evaporate water and leave a dried residue. Next, a droplet of precursor (tosyl-fallypride) in reaction solvent (thexyl alcohol and acetonitrile) is added and heated to perform the radiofluorination reaction. Finally, the crude product is collected from the chip for analysis. The reagent preparation and synthesis procedures should be adapted if performing optimization of a different tracer.

2.2.3.1 Prepare a 30 µL stock solution of precursor (tosyl-fallypride) in the reaction solvent with the maximum concentration to be explored (77 mM). Ensure that the volume is enough to perform the planned experiment. In this example optimization, ~30 µL is sufficient.

2.2.3.2 Prepare a stock solution of the reaction solvent, consisting of thexyl alcohol and acetonitrile in a 1:1 by volume mixture. Ensure that the volume is enough to create the planned dilution series. In this example optimization, ~30 µL is sufficient.

2.2.3.3 From the precursor stock solution and reaction solvent, perform 2x serial dilutions to prepare the different concentrations of the precursor solution. Ensure that the volume of each dilution is enough to perform the desired number of replicates for each condition. In this example optimization, ~15 µL of each concentration is sufficient.

2.2.3.4 Prepare microcentrifuge tubes to collect each crude reaction product using a permanent marker to label each tube with a unique number. Ensure that the total number of microcentrifuge tubes matches the number of conditions multiplied by the number of replicates (8 x 2 = 16).

2.2.3.5 Prepare a stock of collection solution (10 mL) comprising 9:1 methanol:DI water (v/v). Aliquot 50 µL into each of 16 additional labeled microcentrifuge tubes (one per reaction site on the chip).

2.2.3.6 Prepare a [^{18}F]fluoride stock solution in a 500 µL microcentrifuge tube by mixing [^{18}F]fluoride/[^{18}O]H_2O (~260 MBq [7 mCi]) with 75 mM $TBAHCO_3$ solution (56 µL) and diluting with DI water up to 140 µL. 8 µL of this solution will be loaded to each reaction site (containing ~15 MBq [0.40 mCi] of activity, and 240 nmol of $TBAHCO_3$).

2.2.4 Parallel synthesis of [^{18}F]Fallypride with different precursor concentrations

NOTE: The chip is operated atop a heating platform (constructed as previously described13) consisting of a 25 mm x 25 mm ceramic heater, controlled using an on-off temperature controller using the internal thermocouple signal for feedback. Heater surface temperatures were calibrated using thermal imaging. If such a platform is not available, a pair of hot plates can be used (one at 105 °C and one at 110 °C).

2.2.4.1 Load [^{18}F]fluoride stock solution (with phase transfer catalyst).

2.2.4.2 Using a micropipette, load an 8 µL droplet of [^{18}F]fluoride stock solution on the first reaction spot of a multi-reaction chip. Measure the activity of the chip by placing it in a dose calibrator and record the time at which measurement is conducted.

2.2.4.3 Remove the chip from dose calibrator and then load an 8 µL droplet of [^{18}F]fluoride stock solution on the second reaction spot. Measure the activity on the chip by placing it once again in the dose calibrator and record the time at which measurement is conducted.

2.2.4.4 Repeat for all other reaction sites on the chip.

2.2.4.5 Calculate the activity loaded per reaction spot by taking the activity measurement after loading the radioisotope and subtracting the previous measurement (decay-corrected) before that site was loaded.

2.2.4.6 Align the multi-reaction chip on the heater.

2.2.4.7 Add a thin layer of thermal paste on top of the ceramic heater.

2.2.4.8 Carefully place the chip on top of the heater using tweezers to avoid the spill of the droplets, aligning the reference corner of the chip with the reference corner of the heater (as shown in Figure 3B). The chip will overhang the heater by a small amount.

2.2.4.9 Dry the [^{18}F]fluoride and phase transfer catalyst.

2.2.4.10 Heat the chip for 1 min by setting the heater to 105 °C in the control program to evaporate the droplets to dryness leaving a dried residue of [^{18}F]fluoride and $TBHACO_3$. After 1 min, cool the chip by setting the heater to 30 °C and turning on the cooling fan with the control program.

2.2.4.11 Add the precursor solution.

2.2.4.12 Using a micropipette, add a 6 µL solution of fallypride precursor on top of the dried residue on the first reaction site.

2.2.4.13 Repeat for all other reaction sites on the chip. Use the optimization plan to determine which concentration of the dilution series is used for each reaction site.

2.2.4.14 Perform fluorination reaction.

2.2.4.15 Heat each chip to 110 °C for 7 min using the control program to perform radiofluorination reaction. Afterwards, cool the chip by setting the heater to 30 °C and turning on cooling fan with the control program.

2.2.4.16 Collect the crude products from the reaction sites.

2.2.4.17 Collect the crude product at the first reaction site by adding 10 µL of collection solution from the designated microcentrifuge tube via micropipette. After waiting for 5 s, use the micropipette (with the same tip installed) to aspirate the diluted crude product and transfer to its corresponding labeled collection microcentrifuge tube.

2.2.4.18 Repeat this process a total of 4 times using the same pipette tip for all operations.

2.2.4.19 Repeat the collection process for all other reaction sites on the chip.

2.2.5 Synthesis analysis to determine reaction performance and optimal conditions

2.2.5.1 Determine the "collection efficiency" for the first reaction on the chip.

2.2.5.2 Place the microcentrifuge tube with the collected crude product of the first reaction spot in the dose calibrator to measure the activity. Record the measurement and time of the measurement. Repeat this process for each of the collected crude products.

2.2.5.3 Calculate the collection efficiency by dividing the activity of the collected crude product by the starting activity measured for the same reaction site (decay-correcting the activity values to the same timepoint).

2.2.5.4 Repeat for all other reaction sites on the chip.

2.2.5.5 Analyze the composition (fluorination efficiency) of each collected crude product.

NOTE: To make practical the analysis of all samples in a short time, fluorination efficiency is analyzed using a previously described high-throughput radio-thin layer chromatography (radio-

TLC) approach[93]. This technique allows up to eight samples to be processed in parallel by spotting then side by side (5 mm pitch, 0.5 µL per spot) on a single TLC plate, then developing together, and performing readout together using Cerenkov imaging[93,101]. For the example optimization with 16 parallel reactions, 2 TLC plates are needed. Another option is to use radio- high-performance liquid chromatography (radio-HPLC) for analysis, though the time for separation, cleaning, and equilibration may limit the number of samples that can be analyzed.

2.2.5.6 For each TLC plate (50 mm x 60 mm), with a pencil, draw a line at 15 mm away from one 50 mm edge (bottom), and another line 50 mm away from the same edge. The first line is the origin line; the second is the solvent front line. Draw 8 small "X"s along the origin line at 5 mm spacing to define the sample spotting position for each of 8 "lanes".

2.2.5.7 Using a micropipette, transfer 0.5 µL of the first crude product onto the TLC plate at the "X" for the first lane.

2.2.5.8 Repeat for additional crude products (up to 8 per TLC plate).

2.2.5.9 Wait for the crude product spots to dry on the TLC plate.

2.2.5.10 For each TLC plate, develop using a mobile phase of 60% MeCN in 25 mM NH_4HCO_2 with 1% TEA (v/v) until the solvent front reaches the solvent front line.

2.2.5.11 Wait for the solvent on the TLC plate to dry and then cover with a glass microscope slide (76.2 mm x 50.8 mm, 1 mm thick).

2.2.5.12 Obtain a radioactivity image of each TLC plate by placing the plate in a Cerenkov imaging system for a 5 min exposure. Perform standard image corrections (dark current subtraction, flat field correction, median filtering, and background subtraction).

2.2.5.13 Use region of interest (ROI) analysis for the first lane of the first TLC plate. Draw regions around each band visible in the lane. The software will compute the fraction of integrated intensity of each region (band) compared to the total integrated intensity of all regions (bands).

2.2.5.14 With this mobile phase, the following bands are expected at the indicated retention factors: R_f = 0.0: Unreacted [^{18}F]fluoride; R_f = 0.9: [^{18}F]fallypride; R_f = 0.94: Side product. Determine the fluorination efficiency as the fraction of activity in the [^{18}F]fallypride band.

2.2.5.15 Repeat this analysis for all other lanes on all TLC plates.

NOTE: If a Cerenkov imaging chamber is not available, a small animal (preclinical) in vivo optical imaging system can be used to image the TLC plates. Alternatively, a 2-dimensional TLC scanner can be used. Alternatively, if only a 1-dimensional TLC scanner is available, the TLC plates can be analyzed by cutting into strips with scissors (1 per lane), and scanning each strip individually.

2.2.5.16 Determine the crude radiochemical yield (crude RCY) for each reaction site.

2.2.5.17 Determine the crude RCY for the first crude product by multiplying the collection efficiency by the fluorination efficiency.

2.2.5.18 Repeat for all other reaction sites.

2.2.5.19 Analyze the results.

2.2.5.20 Aggregate values for any replicate experiments into an average and standard deviation.

2.2.5.21 Plot the collection efficiency, fluorination efficiency, and crude RCY as a function of the parameter that was varied (precursor concentration in this example).

2.2.5.22 Select the optimal conditions based on the desired criteria. Typically, this is the maximum crude RCY. Additionally, the point is often chosen in a region where the slope of the graph is relatively flat, indicating it is insensitive to small changes in the parameter, providing a more robust protocol.

2.3 Representative results

A representative experiment was performed to illustrate this method. Using 16 reactions, optimization studies of the radiopharmaceutical [^{18}F]fallypride were performed by varying precursor concentration (77, 39, 19, 9.6, 4.8, 2.4, 1.2, and 0.6 mM) in thexyl alcohol:MeCN (1:1, v/v) as the reaction solvent. Reactions were performed at 110 °C for 7 min. Collection efficiency, sample composition (i.e., proportions of [^{18}F]fallypride product, unreacted [^{18}F]fluoride, and side product) are tabulated in Table 2-1 and are summarized graphically in Figure 2-4.

The study showed that the fluorination efficiency (proportion of [^{18}F]fallypride) increases with increasing precursor concentration, and that the remaining unreacted [^{18}F]fluoride varied inversely (**Figure 2-4A**). There was a small amount of a radioactive side product at low precursor concentrations, but the proportion decreased to near zero at the higher precursor concentrations

(**Figure 2-4A**). The collection efficiency was nearly quantitative for most conditions, though it dropped slightly at low precursor concentrations.

From these results, the highest RCY can be achieved with ~230 nmol of precursor (i.e., 39 mM concentration in a 6 µL droplet). At this condition, the fluorination efficiency was 96.0 ± 0.5% (n=2) and the crude RCY was 87.0 ± 2.7 (n=2), and there was no observed radioactive side product formation. While the use of 77 mM precursor showed similar results, in general it is desirable to use a lower amount of precursor to reduce cost and simplify downstream purification steps.

2.4 Discussion

Due to limitations of conventional radiochemistry systems that allow only one or a small number of reactions per day and consume a significant quantity of reagents per data point, only a tiny portion of the overall reaction parameter space can be explored in practice, and many times results are reported with no repeats (n=1). Compared to conventional systems, this multi-reaction droplet radiosynthesis platform makes it practical to accomplish more comprehensive and rigorous studies of radiosynthesis conditions while consuming very little time and amount of precursor, potentially enabling new insights on parameters that impact product yield and side-product formation. The information can be used to choose the conditions that result in the highest product yield or the most robust synthesis. The low precursor consumption may be especially useful in the early development of novel radiotracers when only a small amount of precursor may be available or when the precursor is expensive. While the open nature of the chips contributes to rapid synthesis time and ease of access via pipette, it can lead to substantial losses of volatile molecules and may not be practical when optimizing the synthesis of radiopharmaceuticals that have volatile precursors, intermediates, or products.

Due to the hazard of radiation exposure, it should be reiterated that these experiments should be performed only with suitable training and approvals and should be conducted behind radiation shielding, preferably in a ventilated hot cell. Due to the short half-life of the radioisotopes, it is important to perform the experiments quickly and efficiently. Pipetting reagents to the chip and collecting products from the chip should be practiced under non-radioactive conditions to become familiar with the reduced access and visibility in a hot cell. Similarly, installing and removing the chip, and making measurements of the chip with the dose calibrator should also be practiced. In addition, it is critical to be organized, with a detailed experiment map (i.e., specific reaction conditions at each site on the chip). It is also helpful to prepare in advance a table of results to be filled in as measurements are made. To ensure reproducibility, especially with the possibility of human error, multiple replicates of each set of conditions should be performed. It is important to be especially careful during the step of collecting the crude samples from the chip to avoid spilling liquid outside the reaction site and causing cross-contamination with adjacent reaction sites. If any errors are noticed, it is important to flag these reaction sites so the data can be excluded from the eventual analysis.

In this example study, the amount precursor consumed for 16 data points was 1.1 mg (~70 µg each), compared to 4 mg per data point using a conventional radiosynthesizer. Furthermore, all 16 reactions were completed in 25 min all in a single experiment. In comparison, the synthesis of crude [^{18}F]fallypride on a conventional radiosynthesizer requires ~15-20 min per reaction[79,102].

This representative experiment demonstrated the utility of a multi-reaction microdroplet chip with 16 reactions to optimize conditions for the radiosynthesis of the radiopharmaceutical [^{18}F]fallypride by exploring 8 different precursor concentrations (n=2 replicates for each condition) in a fast and economical manner. Other variables that can be conveniently optimized using a multi-reaction chip include the amount of radioactivity, type of phase transfer catalyst, amount of phase transfer catalyst, evaporation/drying conditions (e.g., number of azeotropic drying steps), reaction solvent, etc. By using multiple multi-reaction chips, it also is possible to explore the

influence of reaction temperature and reaction time, in addition to conditions such as evaporation/drying temperature and time. Such studies would need to be performed sequentially using the single heater or could be parallelized by operating multiple heaters at the same time.

The underlying droplet synthesis method has been shown to be compatible with a wide range of ^{18}F-labeled radiopharmaceuticals, such as[^{18}F]fallypride[61], [^{18}F]FET[103], [^{18}F]FDOPA[104], [^{18}F]FBB[105] and it can be used for the optimization of the majority of other ^{18}F-labeled compounds and compounds labeled with other isotopes. Moreover, the resulting optimized droplet-based reactions intrinsically leverage the advantages of microvolume radiochemistry, including reduced precursor consumption, faster process times, and compact instrumentation, and can offer these same advantages for routine production of large batches. Larger batches simply require scaling up the amount of activity initially loaded at the start of the reaction. To prepare a tracer suitable for use in in vitro or in vivo assays, the crude product must be purified (e.g., using analytical-scale HPLC) and formulated (e.g. via evaporative or solid-phase solvent exchange[60]) Alternatively, it may be possible to adapt the optimal conditions from droplet-scale to a conventional vial-based radiosynthesizer. Investigation of this possibility is ongoing.

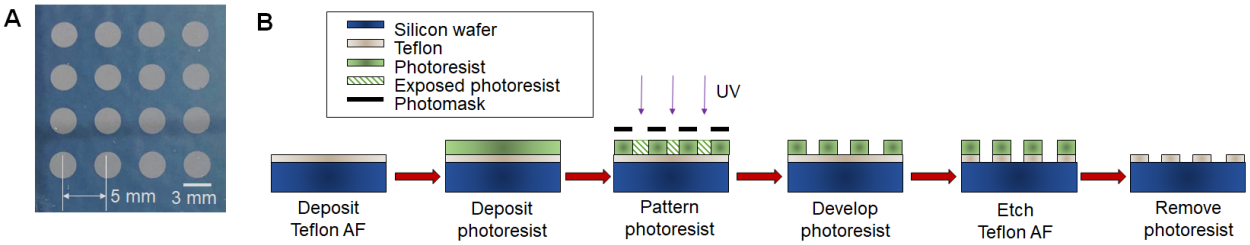

Figure 2-1. Droplet reaction chip fabrication.
(A) Photograph of multi-reaction microdroplet chip with 4x4 array of reaction sites. The chip consists of Teflon-coated silicon with circular regions of Teflon etched away to create the hydrophilic reaction sites. (B) Schematic of fabrication procedure. A silicon wafer is spin-coated with Teflon AF 2400 solution and baked to solidify the coating. Next, photoresist is spin-coated, and patterned via photolithography to produce an etch mask. Photoresist is developed with photoresist developing solution. The exposed Teflon is then removed via dry etching with oxygen plasma. The wafer is diced into individual chips and photoresist is stripped.

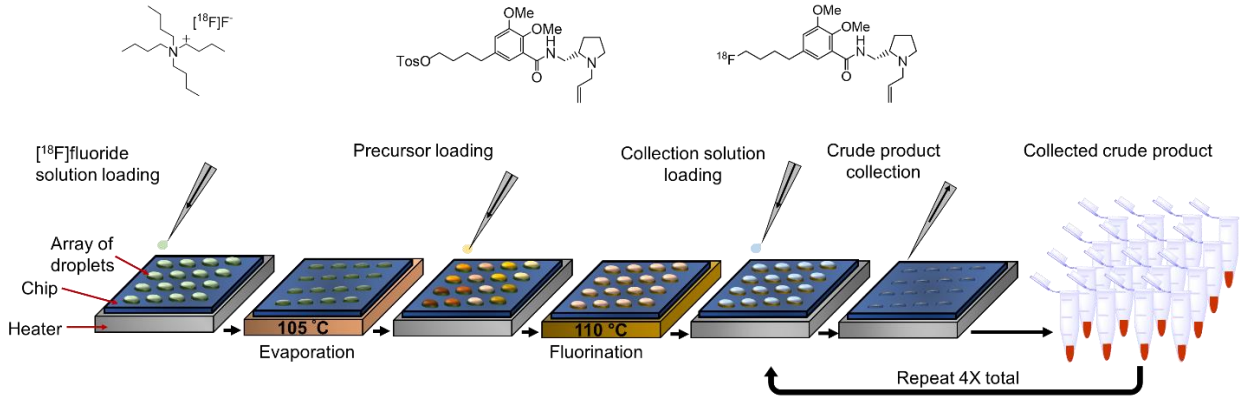

Figure 2-2. Experimental procedure for performing 16 parallel syntheses of the radiopharmaceutical [^{18}F]fallypride on a multi-reaction chip. In this example, the precursor concentration is varied for each reaction.

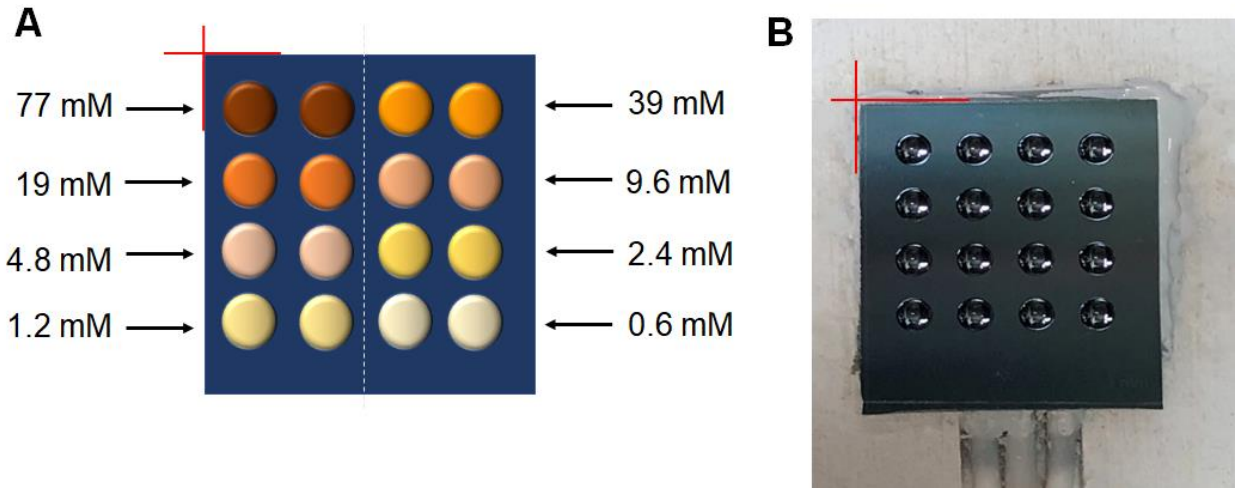

Figure 2-3. Precursor concentration study overview.
(A) Experimental design to explore the influence of precursor concentration on the radiofluorination of tosyl fallypride using a single 16-reaction chip (top view). Eight different concentrations were explored, each with n=2 replicates. Other reaction conditions were held constant (temperature: 110 °C; time: 7 min; solvent: thexyl alcohol:MeCN; amount of $TBAHCO_3$: 240 nmol). Each reaction was performed with ~14 MBq of activity. (B) Photograph of the ceramic heater platform with a 16-reaction chip installed. Red lines represent the reference corner of the chip used for alignment with the reference corner of the heater.

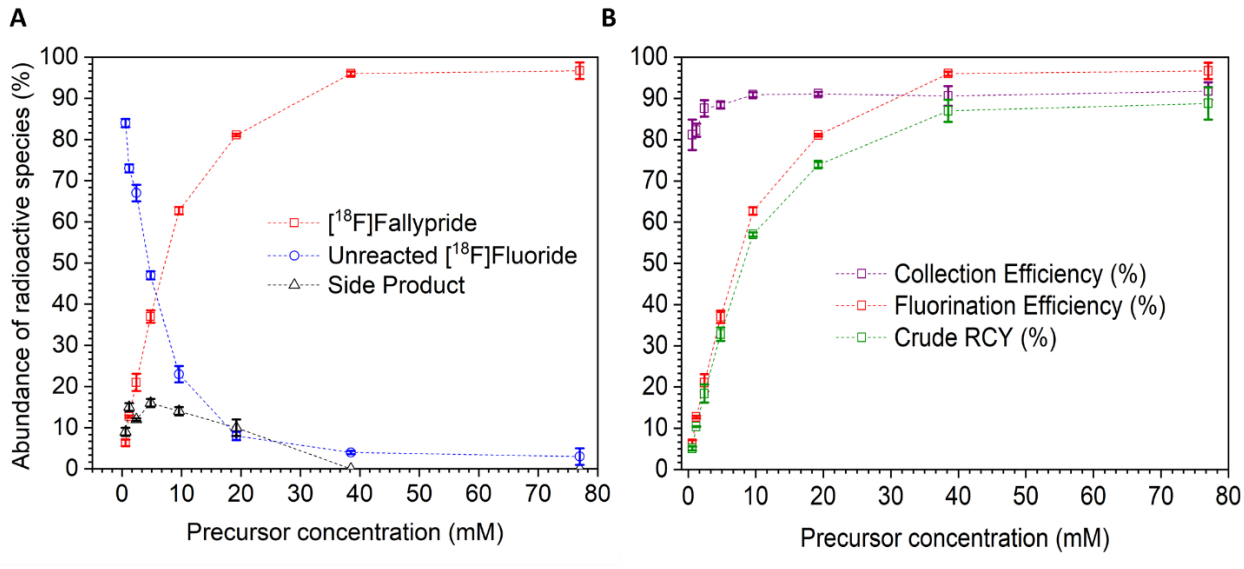

Figure 2-4. Influence of precursor concentration on the microdroplet synthesis of [^{18}F]Fallypride.
(A) Proportion of radioactive species present in the collected crude reaction product, i.e. [^{18}F]Fallypride, side product, or unreacted [^{18}F]fluoride. (B) Synthesis performance. Collection efficiency, fluorination efficiency, and crude RCY are plotted as a function of precursor concentration. In both graphs, data points represent the average of n=2 replicates, and error bars represent the standard deviation.

Table 2-1. Data obtained from study of precursor concentration. All values are averages ± standard deviations computed from n = 2 replicates.

Precursor concentration (mM)	Collection efficiency (%)	Fluorination efficiency (%)	Crude RCY (%)	Unreacted [^{18}F]fluoride (%)	Side product (%)
77	91.8 ± 2.1	96.7 ± 2.0	88.8 ± 3.9	3.3 ± 2.0	0.0 ± 0.0
39	90.6 ± 2.4	96.0 ± 0.5	87.0 ± 2.7	4.0 ± 0.5	0.0 ± 0.0
19	91.1 ± 0.5	81.1 ± 0.3	73.9 ± 0.7	8.4 ± 1.2	10.5 ± 2.0
9.6	90.9 ± 0.6	62.7 ± 0.9	57.0 ± 0.5	23.3 ± 2.1	14.0 ± 0.9
4.8	88.4 ± 0.8	37.0 ± 1.5	32.8 ± 1.6	47.3 ± 0.8	15.7 ± 1.0
2.4	87.6 ± 2.0	21.0 ± 2.1	18.4 ± 2.2	67.4 ± 2.1	11.6 ± 1.0
1.2	82.3 ± 1.6	12.7 ± 0.3	10.4 ± 0.1	72.8 ± 0.7	14.5 ± 1.0
0.6	81.2 ± 3.7	6.3 ± 0.8	5.1 ± 0.5	84.3 ± 0.2	9.4 ± 1.0

Chapter 3: Droplet radiosynthesis production of [^{18}F]FDOPA

3.1 Introduction

The amino acid positron-emission tomography (PET) tracer 3,4-dihydroxy-6-[^{18}F]fluoro-L-phenylalanine ([^{18}F]FDOPA) is mainly applied to the clinical imaging of Parkinson's disease[106], brain tumors[107,108] and diseases related to dopaminergic system. Recently, there has also been increasing interest in the use of [^{18}F]FDOPA to image various neuroendocrine tumors (NETs)[109], in which the uptake of [^{18}F]FDOPA through the transmembrane amino acid transporter systems is upregulated significantly It has been demonstrated that [^{18}F]FDOPA has high sensitivity and precision for imaging of carcinoid tumors, medullary thyroid cancer and et al. [110–112].

Even though [^{18}F]FDOPA has wide application in molecular imaging, its usage is limited due to its complicated synthesis. The earliest methods relied on a straightforward synthesis pathway involving electrophilic fluorination (which requires the production of [^{18}F]F_2 [113]) and deprotection. However, the low availability of [^{18}F]F_2 contributes to poor accessibility. Thus, many groups have been exploring alternative production pathways based on nucleophilic fluorinations using [^{18}F]fluoride [114]. High radiochemical yield (RCY ~40%) has been reported using two-step copper-mediated approaches[115], but these methods require a high amount (~40 mg) of the expensive precursor, which can complicate purification. Furthermore, the toxicity of copper also complicates purification and testing for clinical use. Libert *et al.* described a five-step radiosynthesis employing a chiral phase-transfer catalyst and successfully produced more than 45 GBq [1.2 Ci] [^{18}F]FDOPA after 65 min synthesis time with 36 ± 3% (n=8) (decay corrected) RCY[116]. However, the preparation of the catalyst is difficult and expensive, and the synthesis can be difficult to implement on some synthesizers because two reaction steps are performed on solid supports. Kuik *et al.* reported a simple 2-step diaryliodonium salt synthesis method to produce [^{18}F]FDOPA with RCY of 14 ± 4% [117]. The overall synthesis time was still relatively long (~117 min as reported

by Kuik *et al*., and ~71 min as reported by us[102]) due to the need for an intermediate purification step.

To overcome the limitations of current synthesis methods for [^{18}F]FDOPA, we explored the feasibility of synthesizing [^{18}F]FDOPA using microfluidics. Our group has previously demonstrated the successful production of multiple tracers (e.g. [^{18}F]fallypride, [^{18}F]FDG, [^{18}F]FET, [^{18}F]SFB, etc.) using microdroplet reactors, including devices based on electrowetting-on-dielectric (EWOD)[35,52] and passive droplet transport by patterned wettability[99]. By performing syntheses in the microscale, 10s to 100s times less reagents are needed, which can significantly reduce the production cost and increase the molar activity (by reduction of [^{19}F]fluoride contamination)[36]. Moreover, rapid purification is possible via analytical-scale HPLC instead of semi-preparative HPLC due to the reduced quantity of unreacted reagents and side products. By integrating a radionuclide concentrator[118], microdroplet-based syntheses can be scaled to clinically-relevant levels[119].

Here, we implement the diaryliodonium salt based method[117] of synthesizing [^{18}F]FDOPA to microdroplet format. We focused on this method due to the simple synthesis process and the commercial availability of the precursor. We optimized the synthesis protocol by testing various parameters, including concentrations of base and precursor, and reaction temperature. In addition, we investigated the use of the radical scavenger 2,2,6,6-tetramethyl-1-piperidinyloxy (TEMPO) to increase yield through prevention of precursor decomposition during the reaction[120]. Furthermore, we automated the synthesis on a newly developed ultra-compact microdroplet reactor (similar in size to a small (12 oz) coffee cup).

3.2 Materials and Methods

3.2.1 Planning of the optimization study

Anhydrous acetonitrile (MeCN, 99.8%), methanol (MeOH, 99.9%), ethanol (EtOH, 99.5%), diethylene glycol dimethyl ether (diglyme, 99.8%), TEMPO (98%), potassium carbonate (K_2CO_3,

99%), 4,7,13,16,21,24-hexaoxa-1,10-diazabicyclo[8.8.8]hexacosane (K_{222}, 98%), hydrocholoric acid (HCl, 37%), sulfuric acid (H_2SO_4, 99.99%), ethylenediaminetetraacetic acid (EDTA, 99%), acetic acid (99%), L-ascorbic acid and perchloric acid ($HClO_4$) were purchased from Sigma-Aldrich. Both 6-Fluoro-L-DOPA hydrochloride (reference standard for L type [^{18}F]FDOPA) and 6-Fluoro-D,L-DOPA hydrochloride (reference standard for mixture of D and L type [^{18}F]FDOPA) were purchased from ABX Advanced Biochemical Compounds (Radeberg, Germany). ALPDOPA precursor was obtained from Ground Fluor Pharmaceuticals (Lincoln, NB, USA). DI water was obtained from a Milli-Q water purification system (EMD Millipore Corporation, Berlin, Germany). No-carrier-added [^{18}F]fluoride in [^{18}O]H_2O was obtained from the UCLA Ahmanson Biomedical Cyclotron Facility.

Prior to synthesis of [^{18}F]FDOPA, several stock solutions were prepared. Base stock solution was prepared by dissolving K_{222} (22.8 mg) and K_2CO_3 (4.08 mg) in a 9:1 (v/v) mixture of DI water and MeCN (600 µL). [^{18}F]fluoride stock solution (containing 8.4mM K_{222} and 4.1mM K_2CO_3) was prepared by mixing [^{18}F]fluoride/[^{18}O]H_2O (10 µL, ~220 MBq [~6.0 mCi]), base solution (10 µL) and DI water (100 µL). Precursor stock solution (containing 9mM ALDOPA) was prepared by dissolving ALDOPA (0.96 mg) in in diglyme (120 µL, 75 mol% TEMPO). Finally, a collection solution to dilute the crude product prior to collection from the chip was prepared from a 4:1 (v/v) mixture of MeOH and DI water (500 µL).

3.2.2 Microscale synthesis of [^{18}F]FDOPA

The initial microscale [^{18}F]FDOPA synthesis protocol was adapted from the macroscale synthesis method reported by Kuik *et al.*[117]. Experiments were first performed on multi-reaction microfluidic chips to optimize the protocol in a more high-throughput fashion, and then the synthesis with optimal conditions was automated. Optimization experiments were performed on microfluidic chips comprising a 2x2 arrays of circular hydrophilic reaction sites (4 mm diameter, 9 mm pitch) patterned in a hydrophobic substrate (25 mm x 27.5 mm) (**Figure 3-1A**). The patterned chips were prepared as described previously[99] (except that no final acid treatment step was used)

by coating silicon wafers with Teflon AF, and then etching away the coating to leave exposed silicon regions. The microfluidic chip was affixed atop of a heater platform to control temperature, and reagent addition and crude product collection were performed with a micro-pipette. Each chip was used once and then discarded after use.

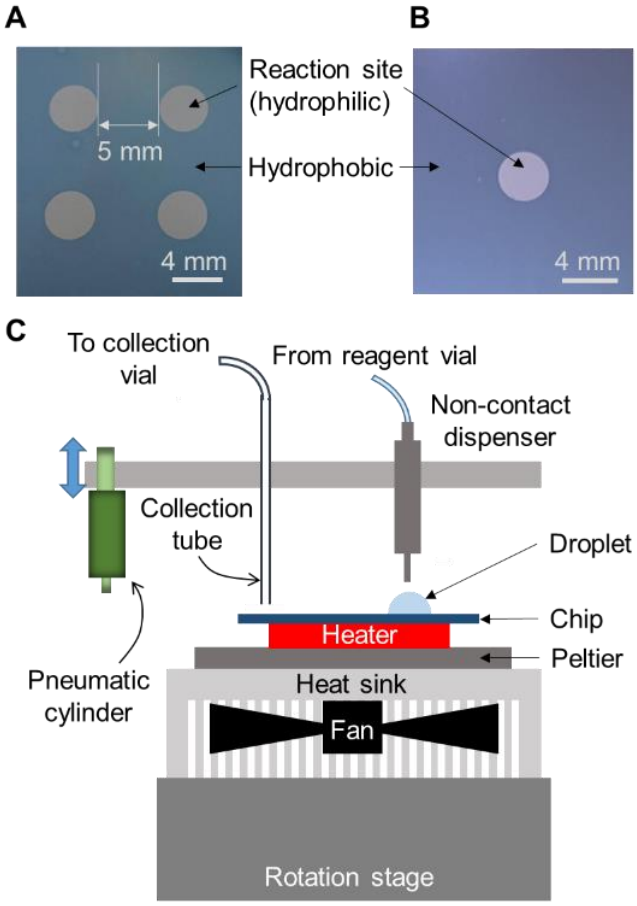

Figure 3-1. Microfluidic chips and experiment setup.
(A) Photograph of the microfluidic chip with four hydrophilic liquid traps serving as the reaction sites. Diameter of the site is 4 mm and pitch is 9 mm. (B) Photograph of the microfluidic chip comprising a Teflon-coated silicon wafer with one hydrophilic liquid trap serving as the reaction site. Diameter of the site is 4 mm. (C) Schematic of the side view of the experimental setup for the microdroplet reactor.

The details of the microscale synthesis are shown in **Figure 3-2B**. Briefly, a 10µL droplet of [^{18}F]fluoride stock solution (~11MBq, 84 nmol K_{222} / 41 nmol K_2CO_3) was first loaded on each reaction site, and the chip was heated to 105°C for 1min to form the dried [^{18}F]KF/K_{222} complex at each site. Then, a 10µL droplet of precursor solution was added to reach reaction site and the chip was heated to 100°C to perform the fluorination step. During the 5 min reaction, the solvent

was replenished at all sites by adding droplets (~7 µL) of diglyme every 30 s. Following fluorination, a 10 µL droplet of H_2SO_4 (6M) was added to each reaction site and the mixtures were heated to 125°C for 5 min to perform the deprotection step. Finally, for each individual reaction site, a 20 µL droplet of collection solution was loaded at each site to dilute the resulting crude product, which was then recovered via pipette. The dilution and collection process was repeated 4x in total to maximize the radioactivity recovery.

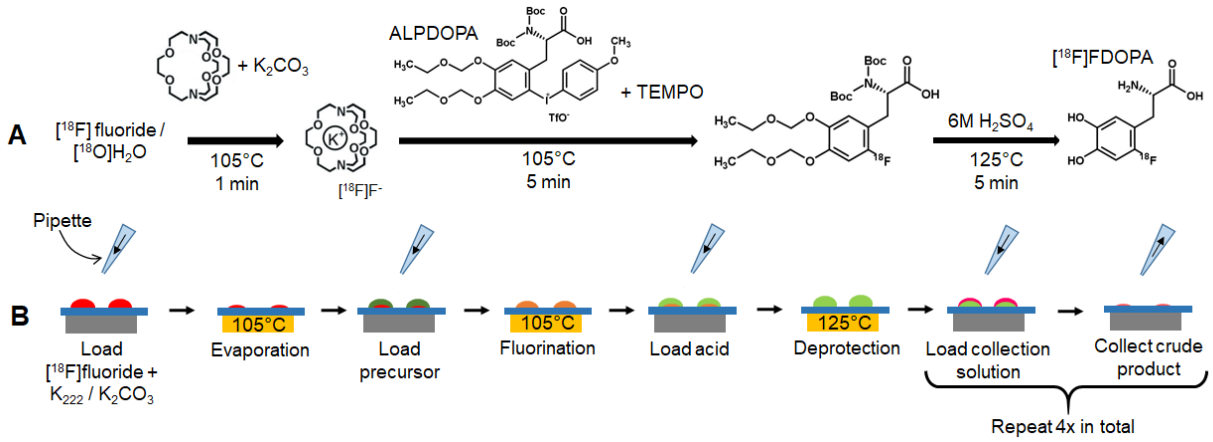

Figure 3-2. Multi-step radiochemical synthesis of [^{18}F]FDOPA.
(A) Synthesis scheme. (B) Schematic of manual [^{18}F]FDOPA synthesis process using the multi-reaction chip.

3.2.3 Automated synthesis using the microdroplet reactor

To increase safety and to facilitate routine production, we next automated the synthesis. Automated syntheses were conducted on chips with a single reaction site (**Figure 3-1B**) operated using a custom-built compact framework (**Figure 3-1C**), consisting of a rotating, temperature-controlled platform, a set of reagent dispensers, and a collection system to remove the reaction droplet at the end of the synthesis. The rotating stage positions the reaction site as desired under a carousel in which reagent dispensers and product collection tube are mounted. More details about the ultra-compact microdroplet reactor were previously described.

Prior to synthesis, reagent vials connected to the reagent dispensers were loaded with the [^{18}F]fluoride stock solution, precursor stock solution, replenishing solution (diglyme), deprotection

solution (6M H_2SO_4) and collection solution. An illustration of the automated microdroplet radiosynthesis is shown in **Figure 3-3**. The chip was first rotated to position the reaction site below the dispenser 1 for [^{18}F]fluoride stock solution and ten 1 µL droplets of [^{18}F]fluoride stock solution (~18.5 MBq; ~0.5 mCi) were sequentially loaded onto the chip (total time < 10s). The chip was rotated 45° counterclockwise (CCW) and heated to 105 °C for 1 min to evaporate the solvent and leave a dried residue of the [^{18}F]KF/K_{222} complex at the reaction site. Then, the chip was rotated 45° CCW to position the reaction site under the precursor dispenser and ten 1 µL droplets of precursor solution were loaded to dissolve the dried residue. Next, the chip was rotated 45° CCW to position the reaction site under the replenishing dispenser (diglyme) and heated to 100 °C for 5 min to perform the fluorination reaction. Solvent was replenished by adding a 1 µL droplet of diglyme every 10 s. Afterwards, the chip was rotated 45° CCW to position the reaction site under the deprotection solution dispenser, twenty 0.5 µL droplets of deprotection solution were loaded on the reaction site and the chip was heated to 125 °C for 5 min to perform deprotection step. Finally, the chip was rotated 45° CCW to position the reaction site under the collection solution dispenser, and twenty 1 µL droplets of collection solution were deposited to dilute the crude product. After rotating the chip 45° CCW to position the reaction site under the collection tube, the diluted solution was transferred into the collection vial by applying vacuum. The collection process was repeated a total of four times to minimize the residue on the chip (i.e., by rotating the chip 45° CW back to the collection solution dispenser, loading more collection solution, etc.).

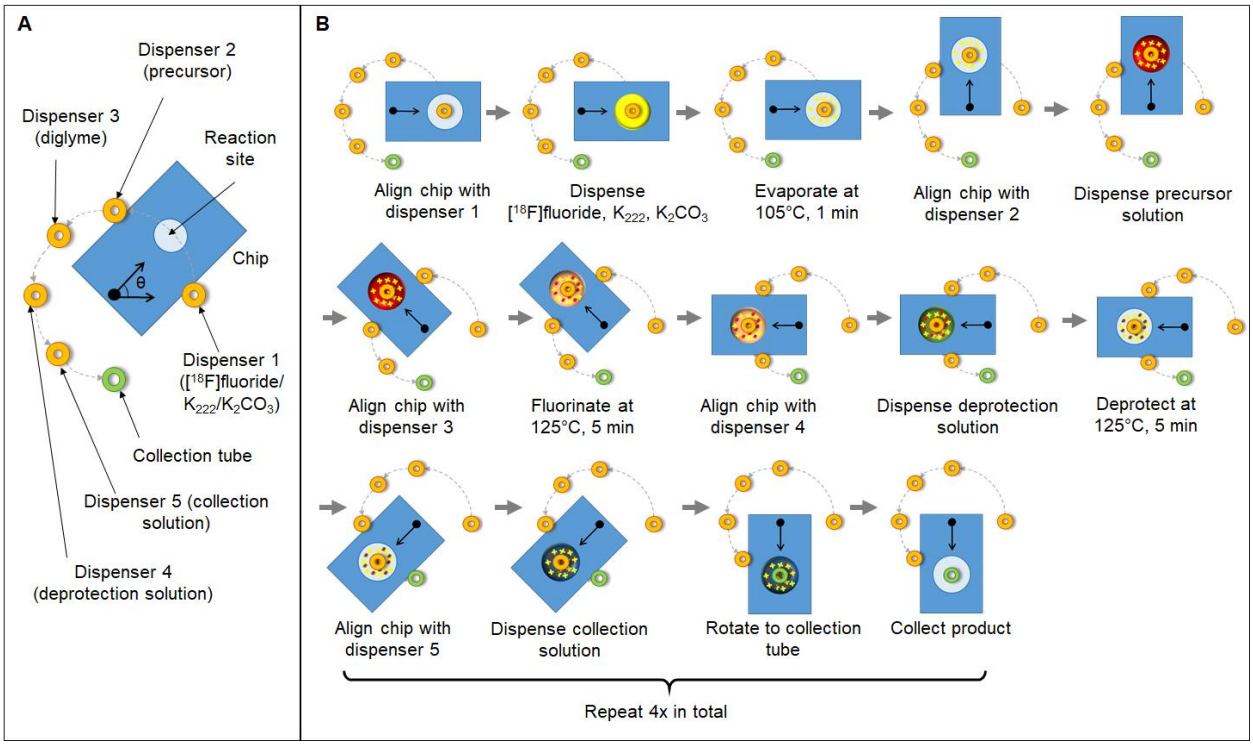

Figure 3-3. Schematic of the automated microdroplet radiosynthesis.
(A) Top view schematic of the microfluidic chip mounted on the rotating heating platform and the fixed locations of reagent dispensers and the collection tube above the chip. (B) Schematic of automated [^{18}F]FDOPA synthesis process with the microdroplet reactor setup.

3.2.4 Analytical methods

Performance of the fluorination step was assessed through measurements of radioactivity using a calibrated dose calibrator (CRC-25R, Capintec, Florham Park, NJ, USA) at various stages of the synthesis process, and measurements of fluorination efficiency using radio thin-layer chromatography (radio-TLC). All radioactivity measurements were corrected for decay. Radioactivity recovery was calculated as the ratio of radioactivity of the collected crude product to the starting radioactivity on the chip after loading the [^{18}F]fluoride stock solution. Residual activity on the chip was the ratio of radioactivity on the chip after collection to the starting radioactivity on the chip. Fluorination efficiency of the crude product collected from the chip was determined via radio-TLC. Fluorination yield (decay-corrected) was defined as the radioactivity recovery times the fluorination efficiency.

To accelerate the analysis, radio-TLC was performed using recently-developed parallel analysis methods. Groups of 4 samples were spotted via pipette (1 µL each, 1 mm pitch) onto each TLC plate (silica gel 60 F_{254} TLC plate, aluminum backing (Merck KGaA, Darmstadt, Germany)). TLC plates were dried in air and developed in the mobile phase (95:5 v/v MeCN : DI water). After separation, the multi-sample TLC plate was read out by imaging (5 min exposure) with a custom-made Cerenkov luminescence imaging (CLI) system[101]. To determine the fluorination efficiency, regions of interest (ROIs) were drawn on the final image (after image corrections and background subtraction) to enclose the radioactive regions/spots. Each ROI was integrated, and then the fraction of the integrated signal in that ROI (divided by the sum of integrated signal in all ROIs) was computed. Two radioactive species were separated in the samples: [^{18}F]fluoride (R_f = 0.0) and the fluorinated intermediate (R_f = 1.0).

Analysis of samples (crude reaction mixture or purified product) was performed on a Smartline HPLC system (Knauer, Berlin, Germany) equipped with a degasser (Model 5050), pump (Model 1000), a UV detector (Eckert & Ziegler, Berlin, Germany) and a gamma-radiation detector and counter (B-FC- 4100 and BFC-1000; Bioscan, Inc., Poway, CA, USA). Injected samples were separated with a C18 column (Luna, 5 µm pore size, 250 x 4.6 mm, Phenomenex, Torrance, CA, USA). The mobile phase consisted of 1 mM EDTA, 50 mM acetic acid, 0.57 mM L-ascorbic acid and 1% v/v EtOH in DI water. The flow rate was 1.5 mL/min and UV absorbance detection was performed at 280 nm. The retention times of [^{18}F]fluoride, [^{18}F]FDOPA and the fluorinated intermediate were 2.4, 6.2, and 25.8 min, respectively. [^{18}F]FDOPA conversion was determined via dividing the area under the [^{18}F]FDOPA peak by the sum of areas under all three peaks.

For purification, the collected crude product (~ 80 µL) was first diluted with 80 µL of the mobile phase, and then separated under the same conditions as above.

3.3 Results and discussion

3.3.1 Optimization of manual synthesis

Before developing our multi-reaction microfluidic chips, we performed some initial studies of the fluorination step with varied reaction conditions to establish a baseline set of conditions upon which further fine-grained optimizations could be made. The initial studies examined reaction temperature (85 – 125 °C), reaction time (5 – 15 min), reaction solvent (DMF, MeCN, DMSO, diglyme), precursor concentration (9 – 71 mM), base amount (21 – 168 nmol of K_{222} and 10 - 82 nmol of K_2CO_3). The highest fluorination yield (~7%) was observed using 84 nmol K_{222} / 41 nmol K_2CO_3, 9 mM precursor, diglyme as reaction solvent, 105°C temperature, and 5 min reaction time, but the yield exhibited poor day to day consistency.

Previously, Carroll *et al.* reported that the yield and reproducibility of the fluorination of diaryliodonium salts could be improved by adding TEMPO as a radical scavenger to improve the stability of the diaryliodonium salt precursor[120]; we investigated whether this approach could be potentially used to improve the yield and consistency of [^{18}F]FDOPA synthesis using the multi-reaction chips.

Initially we added 20 mol% TEMPO into the precursor solution, and performed a detailed study of the effect of precursor concentration on the fluorination yield (**Figure 3-4A**) with 5 min reaction time and 105 °C reaction temperature. The highest yields were obtained with moderate precursor concentrations. At 9 mM and 18 mM, the fluorination yields were 12.0 ± 1.7 % (n=3) and 11.6 ± 0.3 % (n=3), respectively. We chose 12 mM for subsequent experiments to study of the effect of TEMPO concentration on the fluorination step (**Figure 3-4B**). The fluorination yield was only 6.5 ± 0.1 % (n=2) without any TEMPO but nearly tripled (18.8 ± 0.2 % (n=2)) when 80 mol% TEMPO was added. The improvement was mainly due to an increase in fluorination efficiency from 23 ± 1 % (n=2) to 53 ± 2 % (n=2), respectively, though a small increase in radioactivity recovery (from 28 ± 2 % (n=2) to 35 ± 2 % (n=2), respectively) was also observed. Next, we studied the effect of

the amount of base, keeping the ratio of K_{222} at K_2CO_3 fixed at 2.05. (**Figure 3-4C**). As the amount of base was increased, starting from 21 nmol K_{222} / 10 nmol K_2CO_3, the fluorination yield rose sharply and reached the maximum, 21.89 ± 0.02 % (n=2) at 84 nmol K_{222} / 41 nmol K_2CO_3). The fluorination yield remained relatively constant up to ~252 nmol K_{222} / 123 nmol K_2CO_3 (18.8 ± 1.7 % (n=2)), and then began to drop significantly as base amount was further increased. Thus, for the later deprotection study, we picked 75 mol% TEMPO, 9 mM precursor solution, 84 nmol K_{222} / 41 nmol K_2CO_3 as base amount.

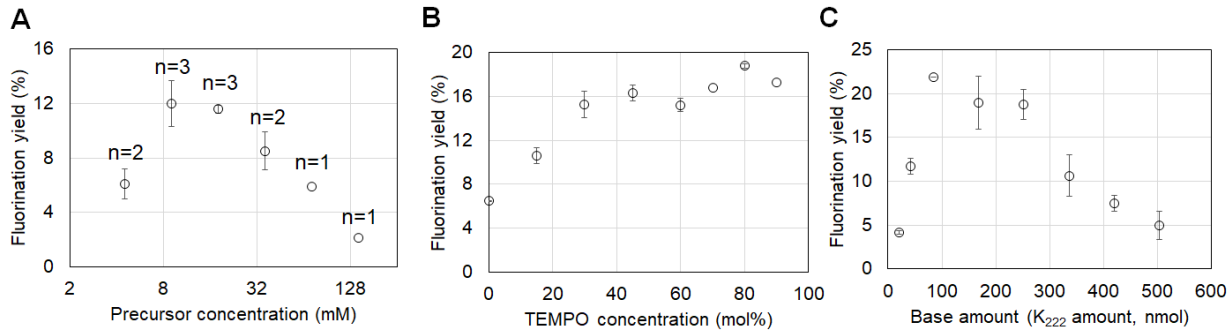

Figure 3-4. Optimization of microdroplet synthesis of [^{18}F]FDOPA using the manual setup. (A) Effect of precursor concentration. (B) Effect of TEMPO concentration. (C) Effect of base amount, represented by K_{222} amount, which is 2.05 times of K_2CO_3 amount. Data points represent average values and error bars represent standard deviations. For 70 and 90 mol % datapoints in (B), n=1, and the rest of datapoints have n=2. For datapoints in (C), n = 2.

Deprotection was performed immediately after fluorination, with no intermediate purification step. To assess the performance of this step, the [^{18}F]FDOPA conversion after deprotection was assessed via radio high-performance liquid chromatography (HPLC). Crude radiochemical yield (RCY, decay-corrected) was defined as the radioactivity recovery times the [^{18}F]FDOPA conversion. Isolated RCY was defined as the ratio of radioactivity of the purified product (recovered from the same analytical-scale radio-HPLC) to the starting radioactivity on the chip.

Preliminary optimization of the deprotection step (deprotection reagent, concentration, reaction temperature and reaction time) is summarized in the **Appendix 3.5, Table 3-2**. Even though the overall crude RCY and isolated RCY were below 10% due to performing these experiments starting with non-optimal fluorination conditions (i.e. 20 mol% TEMPO, 36 mM precursor, 84 nmol

K_{222} / 41 nmol K_2CO_3), comparative conclusions could still be drawn. Performing deprotection with 6 M H_2SO_4 at 115 °C enabled the highest RCY. Combining these conditions with the optimal fluorination conditions, [^{18}F]FDOPA could be produced on the chip with crude RCY of 11% (n=1) and isolated RCY of 7.2 % (n=1). By adding a cover plate over the droplet during deprotection (**Appendix 3.5, Figure 3-6 and Table 3-3**), the crude RCY and isolated RCY could be further increased to 14.3 ± 0.5 % (n=2) and 10.0 ± 0.7 % (n=2), respectively. Noting that the [^{18}F]FDOPA conversion was only 84 ± 5 % (n=2) at 115 °C, indicating the deprotection reaction was not complete, we increased the deprotection temperature to 125 °C and the conversion improved to 95% (n=1).

Finally, we performed full (manual) syntheses including analytical-scale HPLC purification and formulation. The fluorination conditions were 75 mol% TEMPO, 9 mM precursor solution, 84 nmol K_{222}/41 nmol K_2CO_3 at 105°C for 5 min, and the deprotection conditions were 6M H_2SO_4 at 125 °C for 5 min (with cover plate). The resulting crude RCY and isolated RCY were 20.5 ± 3.5 % (n=3) and 15.1 ± 1.6 % (n=3), respectively (**Table 3-1**). An example of a radio-HPLC chromatogram of the crude product is shown in the **Appendix 3.5, Figure 3-7A**, and a co-injection with L-DOPA and D-DOPA reference standards to determine enantiomeric purity (98.0 ± 0.2 (n=3)) is shown in the **Appendix 3.5, Figure 3-7B**. The retention time of [^{18}F]FDOPA was ~6 min, and the chromatogram was relatively clean with no nearby side-product peaks, despite omission of the intermediate cartridge purification between fluorination and deprotection steps [117]. The overall synthesis time was only ~40 min, including ~25 min for initial drying of [^{18}F]fluoride and the two reactions, ~7 min for purification and ~8 min for formulation.

3.3.2 Optimization of automated synthesis

Considering the accuracy of droplet volume dispensed by the dispensers (~10%) studied previously, we adjusted some concentrations so the overall synthesis would be more robust and repeatable, and tolerant of volume errors. The optimal condition was selected where the slope of

the optimization curves (in **Figure 3-4**) was close to zero. Automated syntheses were performed with 80 mol% TEMPO, 12 mM precursor solution and 101 nmol K_{222} / 49 nmol K_2CO_3.

Benefiting from the automated dispensing system, the frequency of replenishing solvent during heated reactions could be increased (up to several droplets per second, compared to one droplet per ~7 s via manual dispensing), and we therefore briefly explored higher fluorination temperatures. As shown in **Figure 3-5**, with the increase of reaction temperature from 100 °C to 140°C, even though the fluorination efficiency increases from 58 ± 3 % (n=3) to 95 ± 1 % (n=2), the radioactivity recovery fell from 36 ± 4 % (n=3) to 27.3 ± 0.3 % (n=2). Due to these opposite effects, the overall fluorination yield was relatively constant (~26%) for temperatures above 105 °C. Overall, 120 °C reaction temperature resulted in the highest fluorination yield of 26.9 ± 1.3 % (n=2) and was chosen as the optimal reaction temperature for the automated synthesis. As shown in **Table 3-1**, with full automated synthesis, the crude RCY and isolated RCY were 15.2 ± 2.1 % (n=3) and 10.3 ± 1.4 % (n=3), respectively. Both are slightly lower than the manual synthesis, which is commonly occurs when transferring from manual to automated synthesis protocol. We note that the [^{18}F]FDOPA conversion was lower for the automated synthesis (i.e., 78 ± 4 % (n=3) vs 95.6 ± 0.4 % (n=3), respectively), likely due to the absence of the cover plate, which was omitted to avoid the need for manual intervention during operation, while the radioactivity recoveries of both methods were comparable (20 ± 2 % (n=3) vs 21 ± 4 % (n=3), respectively). To further increase the [^{18}F]FDOPA conversion, we attempted performing the deprotection step at even higher temperature (130 °C), but significant side products appeared.. The synthesis time was ~22 min, which was slightly faster than the manual synthesis (~25 min) due to the automation steps.

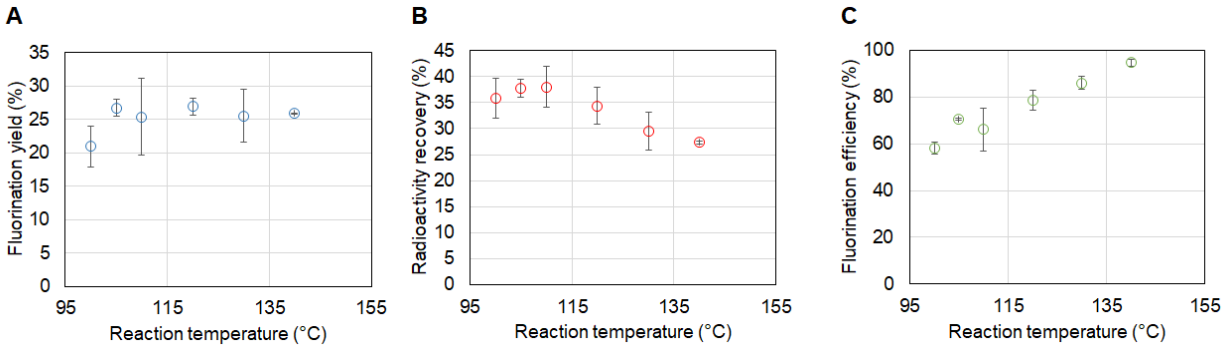

Figure 3-5. Optimization of reaction temperature.
(A) Effect on the fluorination yield. (B) Effect on the radioactivity recovery. (C) Effect on the fluorination efficiency. Datapoints represent average values and error bars represent standard deviations. For 100, 105, 110, 120, 130, and 140 °C datapoints, the number of replicates is n = 3, 2, 3, 3, 2, 2, respectively.

Compared to macroscale methods for [^{18}F]FDOPA synthesis using the same precursor and route, the microscale method, with 10 µL reaction volume, used significantly less precursor, i.e. 0.12 µmol versus 16.8 µmol [102] or 13.4 µmol[117]. The small mass of reagents and small volume collected from the chip (~80 µL) furthermore facilitated the use of analytical-scale HPLC to perform purification. This enabled rapid purification (~7 min) and needed only a short time for formulation (~8 min). Overall the synthesis time with the microdroplet reactor was ~37 min, compared to ~71 min[102], or ~117 min[117] in conventional radiosynthesizers. In fact the isolated non-decay-corrected yield of the microscale method 8.2 ± 1.1 % (n=3) (was higher than both macroscale approaches, i.e. 2.9 ± 0.8 % (n=3) [102] and 6.7 % ± 1.9 % (n =?)[117].

Table 3-1. Comparison of microscale [^{18}F]FDOPA synthesis performance using manual and automated approaches.
All values are averages ± standard deviations for the indicated number of replicates. All percentages are decay-corrected. N.M. indicates the quantity was not measured.

	Manual synthesis (n=3)	**Automated synthesis (n=3)**
Starting activity (MBq)	4.4 ~ 12.2	12.6 ~ 22.9
Synthesis time including purification (min)	~40	~37
[^{18}F]FDOPA conversion (%)	95.6 ± 0.4	78 ± 4
Crude RCY (%)	20.5 ± 3.5	15.2 ± 2.1
Isolated RCY (%)	15.1 ± 1.6	10.3 ± 1.4
Enantiomeric purity (%)	98.0 ± 0.2	N.M.
Total activity loss during overall synthesis (%)	50 ± 5	78 ± 2
Unrecoverable activity on cover chip (%)	24.7 ± 0.3	NA
Unrecoverable activity on bottom chip (%)	2.1 ± 0.4	2.9 ± 0.2
Radioactivity recovery (%)	21 ± 4	20 ± 2

3.4 Conclusion

A straightforward synthesis for [^{18}F]FDOPA using the diaryiodonium salt-based route was implemented in microscale for the first time. Through optimizing various parameters (base amount, precursor concentration, reaction temperature, etc.…) and adding a radical scavenger (i.e., TEMPO), a moderate yield could be achieved reliably. With manual operation, the isolated RCY (decay corrected) was ~15%, which slightly exceeded the highest reported macroscale synthesis (~14%)[117]. Furthermore, the non-decay corrected isolated RCY of manual synthesis was 11.9%, significantly higher than 6.7% [117] and 2.9%[102] of the diaryliodonium precursor-based macroscale synthesis The synthesis was automated using a novel, ultra-compact microdroplet reactor. By performing synthesis in the microdroplet, the tedious and time-consuming solid-phase extraction process and evaporative solvent exchange (for intermediate purification between fluorination and deprotection) could be eliminated while still achieving comparable yields and a crude product that could be easily purified with analytical-scale HPLC. Due to this change and the rapid heating, cooling, and evaporation of small volumes, the overall synthesis time was shortened significantly (~37 min vs ~71 min or ~117 min). Another prominent benefit brought by this microscale synthesis was substantial reduction (> 100x) reduction in precursor consumption, which could significantly lower the cost per batch of [^{18}F]FDOPA. At the time of writing, the retail price of the precursor is ~$600 per batch using the macroscale approach. While the volume of the droplet reactor is very small, integration with a radionuclide concentrator[119] can be used to safely increase the production scale to clinically-relevant levels, while also providing advantages of a very compact system (enabling easy shielding) and the possibility of performing multiple syntheses in a single day.

3.5 Appendix

3.5.1 Optimization of deprotection step

Using single-reaction microfluidic chips, the influence of several deprotection reaction parameters was investigated, including type of acid (HCl and H_2SO_4), acid concentration, reaction time, and reaction temperature. These experiments were performed prior to complete optimization of the fluorination step, and used 84 nmol K_{222}, 41 nmol K_2CO_3, 36 mM precursor, and 20 mol% TEMPO. Results are tabulated in **Table 3-2**.

Table 3-2. Effect of various deprotection conditions (without cover plate).
Radioactivity loss indicates the combined activity losses (due to formation of volatile species) during evaporation, fluorination and deprotection steps. Percentages are corrected for decay. For most conditions, only n=1 experiment was performed. * indicates n=2 replicates were performed, and values indicate average ± standard deviation.

Deprotection reagent	HCl				H_2SO_4			
Concentration (M)	6				3	6		
Deprotection time (min)	5	10	15	15	5	5		
Deprotection temperature (°C)	90	90	90	100	100	120*	130	140
Radioactivity loss (%)	86	88	86	88	78	84 ± 3	90	87
Residual activity on chip (%)	3	1	2	1	3	3 ± 1	2	2
Radioactivity recovery (%)	8	8	10	8	15	9 ± 1	6	7
[^{18}F]FDOPA conversion (%)	24	37	53	72	42	87 ± 1	83	92
Crude RCY (%)	2.0	3.1	5.2	5.5	6.3	7.2 ± 0.5	4.9	6.8
Isolated RCY (%)	1.4	2.7	4.0	4.5	4.5	4.8 ± 0.6	3.2	3.7

For some experiments, a cover chip consisting of a Teflon-coated glass slide (25 mm x 25 mm) was positioned 150 µm above (resting on spacers along the chip edges) above the reaction mixture to reduce evaporation (**Figure 3-6**). In this experiments, extra dilution and collection processes were performed to recover the crude product from the cover chip as well as the (bottom) chip. A detailed comparison of the reaction performance with and without the cover plate is summarized in **Table 3-3**.

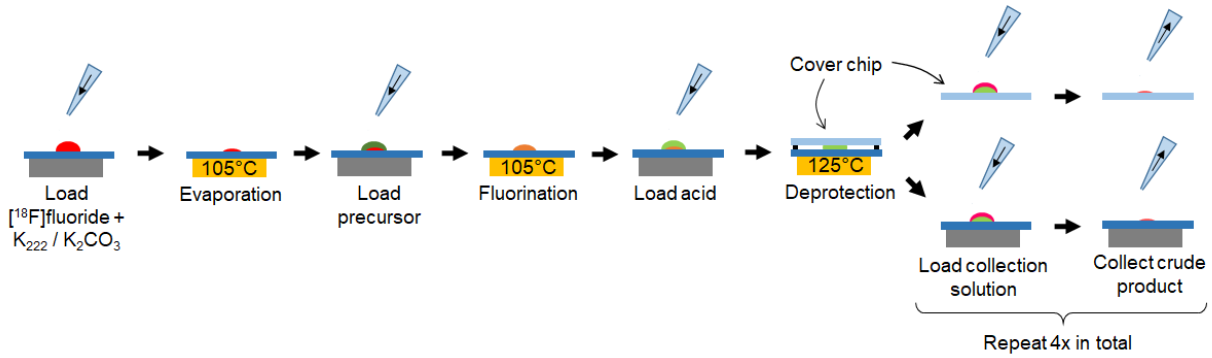

Figure 3-6. Schematic of [^{18}F]FDOPA synthesis process when a cover plate is used during the deprotection step.

Table 3-3. Effect of cover plate on the synthesis performance.
Radioactivity loss indicates the combined activity losses (due to formation of volatile species) during evaporation, fluorination and deprotection steps. Percentages are corrected for decay. Values of the group with cover plate indicate average ± standard deviation computed from the indicated number of replicates.

	No cover plate (n=1)	**With cover plate (n=2)**
Radioactivity loss (%)	84	53.7 ± 0.4
Residual activity on cover chip (%)	NA	26 ± 2
Residual activity on bottom chip (%)	3	1.5 ± 0.2
Radioactivity recovery (%)	12	17 ± 2
[^{18}F]FDOPA conversion (%)	91	84 ± 5
Crude RCY (%)	11.0	14.3 ± 0.5
Isolated RCY (%)	7.2	10.0 ± 0.7

3.5.2 Example radio-HPLC chromatograms

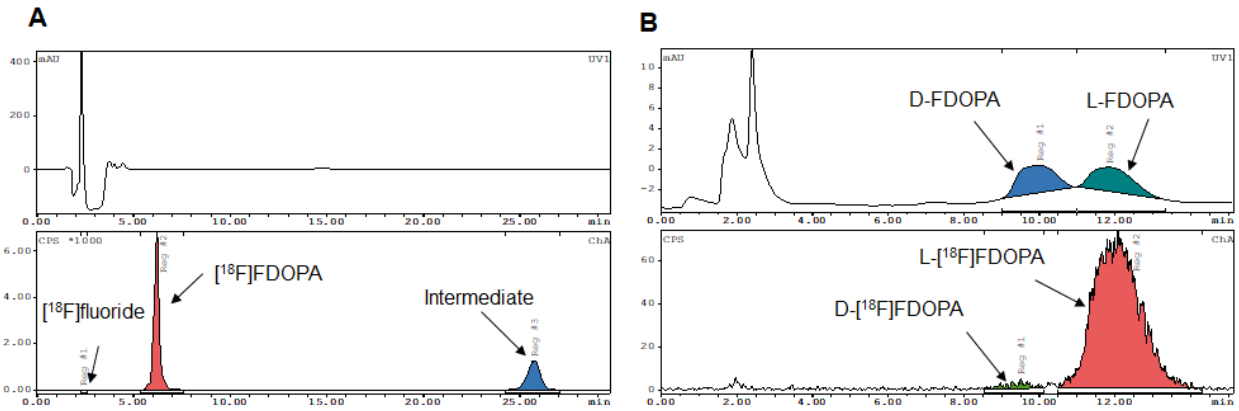

Figure 3-7. Examples of analytical radio-HPLC chromatograms.
(A) crude [^{18}F]FDOPA product, (B) purified [^{18}F]FDOPA product coinjected with a mixture of reference standards of both D-FDOPA and L-FDOPA.

Chapter 4: Microliter-scale reaction arrays for economical, high-throughput experimentation in radiochemistry

4.1 Introduction

The field of molecular imaging has created positron emission tomography (PET) and single-photon emission computed tomography (SPECT)[97]for the visualization and quantification of biochemical processes in living subjects. The use of biologically active molecules tagged with short-lived radionuclides enables such imaging to be performed non-invasively at the whole-body level. PET is used in a wide range of research in small animals and humans to help understand disease pathways[121,122], measure pharmacokinetics, confirm the biological effects of new therapeutic compounds[6,123], monitor disease progression, or monitor the response to treatment[124–126]. Common radioisotopes used in PET include C-11 ($t_{1/2}$ = 20.4 min), F-18 ($t_{1/2}$ = 109.8 min), and Ga-68 ($t_{1/2}$ = 67.7 min), among others.

Radiopharmaceuticals are typically prepared using automated synthesizers to limit radiation exposure to personnel and improve reproducibility[127]. Preparing a batch of a radiopharmaceutical is expensive due to the high cost of the radiosynthesizer, radiation shielding, reagents, radioisotope, and skilled personnel. These costs are greatly multiplied for optimization studies, which require many syntheses to be performed under different conditions. Furthermore, most radiosynthesizers are designed for only one or a few consecutive radiosyntheses per day, thus optimization studies can take weeks or months which further increase labor cost, resource usage, and radioisotope cost.

Recently, multiple approaches have been described to significantly improve the throughput of radiochemistry experiments. Zhang *et al.* performed reactions without radioactivity but mimicked the ultra-low concentrations associated with radionuclides, and leveraged the high sensitivity of

LC-MS/MS analysis to assess product yield[128]. While avoiding the use of radioactivity increased the throughput of experiments, the reliance on conventional reaction volumes still consumed significant time and reagents to obtain each data point. As an alternative, microfluidic platforms and miniaturized radiochemistry techniques provide promising avenues to increase throughput while minimizing reagent consumption[20,25,36,41] by borrowing concepts from high-throughput experimentation in organic chemistry[129–131]. Several groups have shown that dozens of small-scale radiochemical reactions (i.e. 10s of µL each, compared to the ~0.5 – 2.0 mL used in conventional setups) can be sequentially performed using flow-chemistry capillary reactor platforms with crude products collected and analyzed offline[31,33,100,132]. While parameters like temperature and reagent flow rates can be readily studied in a high-throughput manner, others, such as reaction solvent or the conditions for the drying/activation of the [^{18}F]fluoride, cannot. Another optimization platform used a polydimethylsiloxane (PDMS) microfluidic chip to prepare ultra-small batches (~100 nL each) for screening of aqueous protein radiolabeling conditions but was limited to varying reagent ratios and pH[133,134].

Small-volume vial-based reactions have also been used for optimization[135] and enable a wider range of parameters to be studied. Recently, Laube *et al.* reported the use of multi-vial heating blocks to perform up to ~50 radiofluorinations per day, each involving drying a small aliquot of [^{18}F]fluoride eluted from a QMA cartridge, followed by reaction at the 25-50 µL scale[136]. While demonstrating parallelism and low reagent consumption, this technique required significant manual handling of vials, including installation and removal of vial caps. In addition, it is well known that the detailed heating characteristics of the system are essential to consider[137], and after optimization in small vials the conditions may have to be adapted to a conventional synthesizer for routine automated production.

Our group recently pioneered a microfluidic platform, in which reactions are performed at an even smaller scale (i.e. 1-10 µL) in droplets confined in surface-tension traps patterned on a

surface[58]. Under these conditions, droplet reactions typically have yields comparable to conventional methods but allow shorter synthesis time and up to ~100x lower reagent consumption per reaction[62,103,138]. Of particular note, after optimization under low activity conditions, larger scale production (e.g. one or a few clinical doses) can be achieved under identical conditions using an automated droplet-based radiosynthesizer[60,139] by a simple increase of starting activity. To increase throughput, we created chips with multiple reaction sites for performing up to 16 droplet-based syntheses in parallel, all with the same reaction temperature and time but with varying volumes or concentrations of reagents[61]. A preliminary study showed the possibility of optimizing several parameters in the synthesis of [^{18}F]Fallypride, including the amount of base, precursor concentration, and droplet reaction volume. In this paper, throughput and flexibility are further increased by introducing an array of 4 independent heaters, enabling operation of 4 chips in parallel. This improved platform allows the parallel exploration of additional reaction variables (reaction temperature and time) that cannot be conveniently studied with a single chip at a time

4.2 Materials and reagent preparation

4.2.1 Analysis of reaction performance

Anhydrous N,N-dimethylformamide (DMF, 99.8%) purchased from Fisher Scientific, anhydrous dimethyl sulfoxide (DMSO, ≥99.9%), anhydrous acetonitrile (MeCN, 99.8%), 2,3-dimethyl-2-butanol (thexyl alcohol,98%), 4,7,13,16,21,24-hexaoxa-1,10-diazabicyclo[8.8.8]hexacosane (K_{222}, 98%), triethylamine (TEA, 99%), trifluoroacetic acid (TFA, >99%), tetrahydrofluran (THF, >99.9%, inhibitor-free), hexanes (95%), dichloromethane (DCM, >99.8%), acetone (99.5%), ammonium formate (NH_4HCO_2: 97%) N-methyl-2-pyrrolidone (NMP, 99.5% anhydrous), 1,3-dimethyl-3,4,5,6-tetrahydro-2(1H)-pyrimidinone (DMPU, 98%), ethylene glycol (99.8%) and potassium carbonate (K_2CO_3, 99.995%) were purchased from Sigma-Aldrich (St. Louis, MO, USA). n-butanol (nBuOH, 99%) was purchased from Alfa Aesar (Ward Hill, MA, USA).

Tetrabutylammonium bicarbonate ($TBAHCO_3$, 75mM in ethanol), ethyl-5-methyl-8-nitro-6-oxo-5,6-dihydro-4*H*-benzo[f]imidazo[1,5-*a*][1,4]diazepine-3-carboxylate (nitromazenil; precursor for [^{18}F]Flumazenil, > 97%) and Flumazenil (reference standard, >99%), 2-((2,5-dimethoxybenzyl)(2-phenoxyphenyl)amino)-2-oxoethyl-4-methylbenzenesulfonate ([^{18}F]PBR06 precursor, >95%), 2-fluoro-N-(2-methoxy-5-methoxybenzyl)-N-(2-phenoxyphenyl)acetamide (reference standard for [^{18}F]PBR06, >95%), (*S*)-2,3-dimethoxy-5-[3-[[4-methylphenyl)-sulfonyl]oxy]-propyl]-N-[[1-(2-propenyl)-2-pyrrolidinyl]methyl]benzamide (Fallypride precursor, >90%), Fallypride (reference standard, >95%), 2-(2-((*N*-4-phenoxypyridin-3-yl)acetamido)methyl)phenoxy)ethyl-4-methylbenzenesulfonate ([^{18}F]FEPPA precursor, >90%), and *N*-[[2-(2-fluoroethoxy)phenyl]methyl]-*N*-(4-phenoxypyridin-3-yl)acetamide (reference standard for [^{18}F]FEPPA, >95%) were purchased from ABX Advanced Biochemical Compounds (Radeberg, Germany). DI water was obtained from a Milli-Q water purification system (EMD Millipore Corporation, Berlin, Germany). No-carrier-added [^{18}F]fluoride in [^{18}O]H_2O was obtained from the UCLA Ahmanson Biomedical Cyclotron Facility and Crump Cyclotron Facility.

1% Teflon AF 2400 solution was purchased from Chemours. Positive photoresist (MEGAPOSIT SPR 220-7.0) and developer (MEGAPOSIT MF-26A) were purchased from MicroChem (Westborough, USA). Additional solvents and chemicals used for microfluidic chip fabrication, including methanol (MeOH, Cleanroom LP grade), acetone (Cleanroom LP grade), isopropanol (IPA, Cleanroom LP grade), sulfuric acid (96%, Cleanroom MB grade) and hydrogen peroxide (30%, Cleanroom LP grade), were purchased from KMG Chemicals (Fort Worth, USA).

4.2.2 Reagent preparation

The following stock solutions were prepared daily to carry out droplet reactions. The [^{18}F]fluoride stock solution contained either 60 mM $TBAHCO_3$ and 1.8 MBq/µL (48 µCi/µL) of [^{18}F]fluoride in water (i.e. for [^{18}F]Flumazenil, [^{18}F]PBR06, [^{18}F]Fallypride, and [^{18}F]FEPPA), or 60 mM of K_{222} with 30 mM of K_2CO_3 and 1.8 MBq/µL (48 µCi/µL) of [^{18}F]fluoride in water (i.e. for [^{18}F]Flumazenil and [^{18}F]PBR06), or 60 mM of K_{222} with 30 mM of Cs_2CO_3 and 1.8 MBq/µL (48

μCi/μL) of [^{18}F]fluoride in water (i.e. for [^{18}F]Flumazenil). [^{18}F]Flumazenil precursor stock solution contained 70 mM precursor in either DMSO, DMF, NMP, DMPU, or ethylene glycol. [^{18}F]PBR06 precursor stock solution contained 70 mM precursor in either DMSO or a 1:1 v/v mixture of thexyl alcohol and MeCN. [^{18}F]Fallypride stock solution contained 77 mM of precursor in a 1:1 v/v mixture of thexyl alcohol and MeCN. [^{18}F]FEPPA stock solution contained 30 mM of precursor in a 1:1 v/v mixture of thexyl alcohol and MeCN. For [^{18}F]Flumazenil, the collection stock solution was a 2:1 v/v mixture of reaction solvent and water when using DMSO or DMF as the reaction solvent, or a 9:1 v/v mixture of MeOH and H_2O collection stock solution when using NMP, DMPU, or ethylene glycol as the reaction solvent. For [^{18}F]PBR06, [^{18}F]Fallypride, and [^{18}F]FEPPA, the collection stock solution was a 9:1 v/v mixture of MeOH and H_2O.

4.3 Analytical methods

4.3.1 Analysis of reaction performance

Radioactivity measurements were made using a calibrated dose calibrator (CRC-25R, Capintec, Florham Park, NJ, USA). To calculate the starting activity on each reaction site, we measured the activity on the chip after loading the initial [^{18}F]fluoride solution to each individual spot (via dose calibrator) and subtracted the previous measurement of chip activity. All measurements were decay-corrected to a common timepoint. Collection efficiency was determined by dividing the activity of the collected crude sample from an individual spot by the starting activity used in that same reaction site (corrected for decay). Fluorination efficiency was analyzed using radio-TLC. Crude radiochemical yield (crude RCY) was calculated by multiplying the collection efficiency by the fluorination efficiency. The total residual activity left on the chip was measured by placing the chip in a dose calibrator after collection of the crude products from each reaction site. To compute the residual activity left on the chip at each individual reaction site, the activity distribution on the chips was first determined via Cerenkov imaging[61,99,101]. For Cerenkov imaging, a glass microscope slide (76.2 mm x 50.8 mm, 1 mm thick; C&A Scientific;

Manassas, VA, USA) was placed on top of the chip, and the acquisition time was 5 min. Raw images were corrected as previously described[93]. Residual activity for a particular reaction site on the chip was computed with the aid of a custom region-of-interest (ROI) analysis software written in MATLAB (MathWorks, Natick, MA). For each reaction site, an ROI was drawn and the integrated Cerenkov signal was computed from the image. To quantify the amount of residual activity at a particular reaction site, the corresponding ROI integrated signal was divided by the sum of integrated signal for all ROIs and multiple by the measured total residual radioactivity on the chip. This value could then be expressed as a fraction of starting radioactivity by dividing the residual activity for a particular reaction site by the starting activity used at that particular reaction site (correcting for decay).

4.3.2 Thin-layer chromatography

Performing 64 simultaneous reactions presents a significant challenge for analysis. Typical methods of spotting one sample per TLC plate for typically used TLC plates lengths and conditions require 2-7 min per sample separation and readout and cannot be practically scaled to 64 samples. To accelerate the analysis, TLC plates (silica gel 60 F254; Merck KGaA, Darmstadt, Germany) were spotted with multiple samples (8 samples at 0.5 mm pitch), with all samples separated in parallel and read out simultaneously via Cerenkov imaging using methods we have previously reported[93]. Briefly, 8 samples (0.5 µL each) were spotted onto a 50 mm x 60 mm (W x L) TLC plate, with adjacent spots separated by 5 mm. Developed TLC plates were read out by covering the TLC plate with a scintillator plate (50 mm x 35 mm, 1 mm thick, BC-400, Saint-Gobain, OH, USA) or a glass microscope slide (76.2 mm x 50.8 mm, 1 mm thick, A&C Scientific) to obtain images of the emitted light. The solvent front took ~2 min to travel 45 mm (corresponding to 30 mm separation distance). The mobile phase to separate the [^{18}F]Flumazenil crude sample was 100% MeCN, for [^{18}F]PBR06 crude samples 13:10:24:54 (v/v) dichloromethane:chloroform:acetone:hexanes as the mobile phase, for [^{18}F]FEPPA crude samples 25.6:37.5:36.5:0.4 (v/v) nBuOH:THF:hexanes:TEA as the mobile phase, and

[^{18}F]Fallypride crude samples were separated using 60% MeCN in 25 mM HN_4HCO_2 with 1% TEA (v/v), as previously reported[61]. More information on R_f values and TLC separation studies can be found in **Appendix 4.7.4**, under the radio-TLC methods.

4.3.3 High-performance liquid chromatography (HPLC)

Analytical radio-HPLC was used to identify the product of each synthesis (via co-injection with reference standard) and to isolate pure products to confirm the R_f value of the product bands in radio-TLC. The radio-HPLC system setup comprised a Smartline HPLC system (Knauer, Berlin, Germany) equipped with a degasser (Model 5050), pump (Model 1000), UV detector (254 nm; Eckert & Ziegler, Berlin, Germany) and gamma-radiation detector, and counter (B-FC- 4100 and BFC-1000; Bioscan, Inc., Poway, CA, USA). All HPLC separations used a C_{18} Gemini column (Kinetex, 250 x 4.6 mm, 5 µm, Phenomenex, Torrance, CA, USA). Using a mobile phase of 3:1 H_2O:MeCN with 0.1% TFA (v/v) and a flow rate of 1.0 mL/min, the retention time of [^{18}F]Flumazenil was 11 min. For [^{18}F]PBR06, the retention time was 8 min using a mobile phase of 60:40 (v/v) MeCN:20 mM sodium phosphate buffer (pH = 5.8) with a flow rate of 1.5 mL/min. [^{18}F]Fallypride samples were separated with a mobile phase of 60% MeCN in 25 mM HN_4HCO_2 with 1% TEA (v/v) and a flow rate of 1.5 mL/min resulting in a retention time of 4.5 min. [^{18}F]FEPPA samples were separated with a mobile phase of 70:30 v/v H_2O:EtOH with 0.1% H_3PO_4 at 0.8 mL/min, giving a retention time of 15.5 min.

4.4 Results

4.4.1 Platform Design

Arrays of reactions were performed in droplet format on 25.0 x 27.5 mm^2 Teflon-coated silicon "chips" (**Figure 4-1**). Each reaction was confined to a 3 mm diameter circular hydrophilic site (made by etching away the Teflon coating) that acts as a surface tension trap. Details of the chip fabrication have been previously reported[61] and shown in **Chapter** Error! Reference source not found..

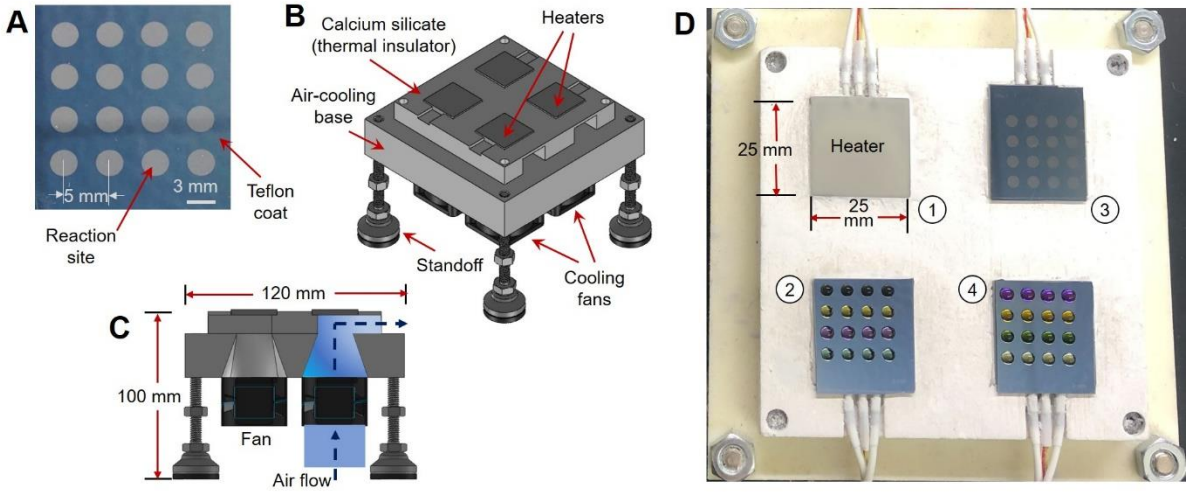

Figure 4-1. High-throughput reaction apparatus.
(A) Photograph of multi-reaction chip. (B) CAD model showing platform components. (C) Cross-section view of the multi-heater platform showing the path of forced-air cooling. (D) Photograph of the platform (from above) with multi-reaction chips installed.

Multiple chips were operated in parallel using a custom-built four-heater platform (**Figure 4-1B-D**). To provide radiation protection, the platform was operated inside a hot cell, but the control system could be placed outside to minimize the footprint. The platform comprised four 25 mm ceramic heaters glued with epoxy on top of a thermally insulating frame CNC-machined from a calcium silicate composite, which was in turn affixed atop of a 3D-printed nylon piece to direct cooling air to each heater from a set of four 36 mm 12V DC fans (**Appendix 4.7.3** and **Figure 4-8**). Thermal simulations were performed to determine an appropriate heater spacing to avoid

thermal crosstalk from neighboring heaters (**Appendix 4.7.3** and **Figure 4-9-12**). The chips were affixed to the heaters with a thin layer of thermal paste.

Each heater (and fan) was independently controlled, enabling the set of reactions on each multi-reaction chip to be performed at a unique temperature or duration (**Figure 4-8**). For each heater, the signal from the integrated K-type thermocouple was amplified and connected to an analog input of a data acquisition module (DAQ). Heaters were powered with 120VAC switched by a solid-state relay driven by a digital output of the DAQ using an on-off controller implemented in LabView (National Instruments). After the desired heating time, forced-air cooling was activated using a digital output of the DAQ to power the corresponding fan via a Darlington driver circuit.

After calibrating the heaters, temperature stability was assessed by monitoring the integrated thermocouple with respect to time (**Figure 4-13**). At each setpoint tested, heating took only ~5 s, and temperature exhibited <1 °C fluctuation once stabilized (**Table 4-2**). Forced-air cooling to 30 °C took ~3 min from 140 °C, ~2.5 min from 100 °C, and ~1.2 min from 50 °C. In addition, spatial temperature distribution of each heater was visualized via thermal imaging. All heaters exhibited uniform surface temperature (Figure 4-14**,** Figure 4-15**,** and Table 4-3), except near the edges (where deviation >2% from the mean was observed). In all cases, the extent of this unusable region was limited to <1.5 mm on each edge of the heater. Thus, the multi-reaction chips were designed with a 2.4 mm unused boundary, ensuring that all 16 reaction sites were entirely located within the uniform portion of the heater surface (Figure 4-16)[61]. A previous study confirmed the consistency of reactions at different sites on the chip and the negligible degree of cross-contamination from one site to another[61]. With the platform, up to 64 radiochemical syntheses could be performed in parallel, each reaction using ~100x less reagents than conventional approaches. Because all steps, including [^{18}F]fluoride drying, are performed on-chip, the conditions used in any part of the synthesis can be explored in a high-throughput fashion.

4.4.2 Synthesis optimization

We used this new platform to perform extensive studies of the syntheses of several clinically relevant PET tracers: [^{18}F]Flumazenil ([^{18}F]FMZ), [^{18}F]PBR06, [^{18}F]Fallypride, and [^{18}F]FEPPA.

For each radiopharmaceutical, an extensive set of experiments was performed to compare the influence of different reaction conditions related to [^{18}F]fluoride drying and the radiofluorination reaction. Our goals were to better understand the influence of various reaction parameters and to develop efficient microscale synthesis protocols for these tracers. Initial droplet reaction conditions were determined essentially by reducing volumes ~100x from conventional macroscale protocols. In general, experiments were performed in batches of 64 simultaneous reactions (4 chips x 16 reactions each), exploring 16 different conditions, each with n=4 replicates.

Figure 4-2 illustrates the synthesis scheme for each tracer and the generalized process for one set of 16 reactions. At each site, an 8 µL droplet of [^{18}F]fluoride stock solution ([^{18}F]fluoride mixed with the desired amount and type of base and phase-transfer catalyst) is added to the reaction site and dried. (Though drying parameters to eliminate residual water could also be studied, drying was performed for 1 min at 105 °C in all experiments.) Next, 8 µL of precursor solution (6 µL for [^{18}F]Fallypride) with the desired concentration and reaction solvent is added to the dried residue and reacted at elevated temperature for the desired time. Reaction volume could also be studied as a parameter but was not explored here. After the reaction is complete, crude product is collected. Though collecting parameters could be optimized to minimize residual activity on the chip, we performed product collection in all cases by dispensing 10 µL of collection solution to the reaction site and aspirating the volume and repeating these steps 4x for a total of 40 µL of collected crude product. The reaction performance was determined by measuring both the conversion of [^{18}F]fluoride to product via radio-TLC, as well as the recovered activity from each reaction (compared to starting activity, i.e. collection efficiency) to determine an overall crude radiochemical yield (RCY). TLC analysis was performed using recently reported multi-lane methods with 8 samples per plate[93].

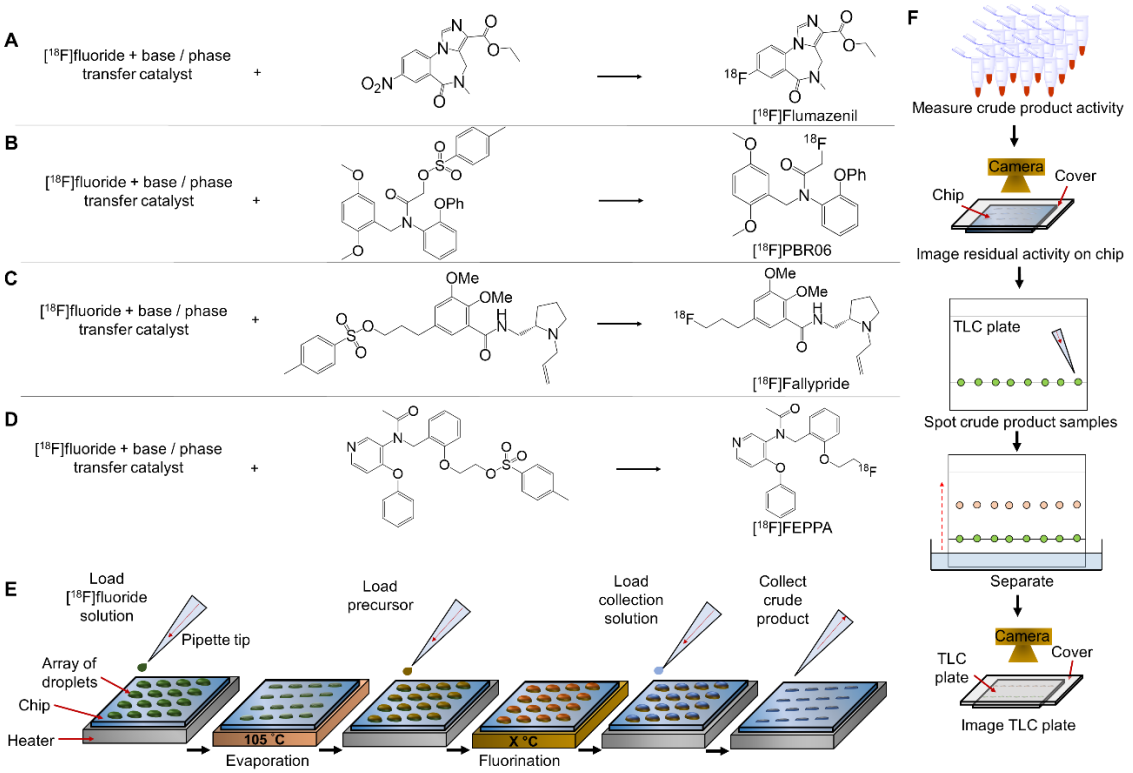

Figure 4-2. Optimization process.
(A) Scheme for the radiosynthesis of [^{18}F]Flumazenil. (B) Synthesis of [^{18}F]PBR06. (C) Synthesis of [^{18}F]Fallypride. (D) Synthesis of [^{18}F]FEPPA. (E) Experimental procedure for performing parallel radiosyntheses using a (4x4) multi-reaction microdroplet chip. Concentrations, solvents, and volumes can be varied from site to site, and temperature and heating time can be varied from chip to chip. (F) Procedure for reaction performance analysis. Activities of collected crude samples are measured using a dose calibrator and compared with starting activity to determine collection efficiency. Residual activity on chip is analyzed via Cerenkov imaging. Crude samples are analyzed via radio-TLC to determine the fluorination efficiency.

4.4.3 Optimization of [^{18}F]Flumazenil

[^{18}F]Flumazenil is used to quantify changes in the density of $GABA_A$ receptors associated with Alzheimer's disease, Schizophrenia, neuronal plasticity, and sensory processes[140]. We focused on the route from the commercially-available nitromazenil precursor[33,141–145], for which reported isolated yields are in the range of 8 to 30%[141–145]. Though other synthesis routes have led to higher yields, they were not pursued here due to the lack of commercial availability of the diaryliodonium tosylate precursor[146] or the very low molar activity (0.37 GBq/μmol [0.01 Ci/μmol]) of the isotopic exchange method[147]. Previous optimization studies using macroscale and flow chemistry

approaches (**Table 4-1**) have typically compared just a couple of values for parameters studied and often with few if any replicates[33,141–145].

Table 4-1. Summary of parameters and conditions tested in reports of optimization of [^{18}F]Flumazenil using nitromazenil as precursor in microscale and macroscale platforms.

	This work	**Wong et al[33]. (2012)**	**Nasirzadeh et al[142]. (2016)**	**Mandap et al[143]. (2009)**	**Massaweh et al[144]. (2009)**	**Ryzhikov et al[145]. (2005)**
Synthesizer type	Microscale (droplet format)	Microscale (flow format)	Macroscale	Macroscale (microwave)	Macroscale	Macroscale
Solvents	DMSO, DMF, NMP, DMPU, ethylene glycol	DMSO, DMF, MeCN	DMF	DMSO, DMF, MeCN	DMF	DMSO, DMF
Reaction times (min)	0.5, 1, 2, 3, 4, 5, 6, 7	2.5	15, 30	2, 5, 10	30	15, 30
Temperatures (°C)	100, 120, 140, 160, 180, 200, 220, 240	110, 120, 130, 140, 160	150	90, 140, 160, 180, 200*	160	130, 160
Base types	$TBAHCO_3$, K_{222} / K_2CO_3, K_{222} / Cs_2CO_3	K_{222} / $KHCO_3$	K_{222} / K_2CO_3	K_{222} / K_2CO_3	K_{222} / K_2CO_3	K_{222} / K_2CO_3
Base amounts (nmol)	480, 320, 240, 160, 80, 40, 20, 10 and 240/120	2850 / 2590	25000 / 12000	12000 / 6000[#]	2800/ 1200	25000 / 12000[+]
Precursor amounts (nmol)	560, 400, 280, 160, 80, 40, 20, 10	1500	24220, 12000, 5100, 3030	24000, 15000, 12000, 51000, 3000	18000, 21000	6000, 12000, 13000, 13000, 19000, 24000, 25000, 25000, 25400, 36000
Total number of different conditions tested	85	13	3	19	1	14
Total number of experiments performed	335	13	23	52	15	14

[#]Not reported but the amount of K_{222} was computed based on the amount of precursor and an indicated precursor to K_{222} / K_2CO_3 molar ratio of 0.5:1. Ratio of K_{222} to K_2CO_3 needed to calculate K_2CO_3 was inferred from a paper they referenced[148]

†Based on 1:1 precursor to K_{222} / K_2CO_3 molar ratio. Note: different volumes of solvent were used as an additional parameter (0.5, 1.0, 1.5, and 2.0 mL)
*In the microwave reactor, the pressure was also varied (0, 100, and 200 kPa).

Leveraging the increased throughput of our platform, we performed a series of experiments to explore more comprehensive ranges of each parameter with finer granularity (typically 8 values each) and more replicates. Parameters explored included: (i) reaction temperature, (ii) amount of base, (iii) amount of precursor, (iv) reaction time, (v) reaction solvent, and (vi) type of base and phase-transfer catalyst. Full details and results for each set of experiments can be found in **Appendix 4.4.3**. Since most literature reported the use of the solvents N,N-dimethylformamide (DMF) and dimethyl sulfoxide (DMSO)[33,143], the studies we performed for parameters i – iv were carried out using each of these solvents. As an example of how each experiment was set up, **Figure 4-3** shows how four chips were used to explore reaction temperature. The figure also shows the images of residual radioactivity on the chips after synthesis, and the Cerenkov images of the TLC plates used to evaluate conversion.

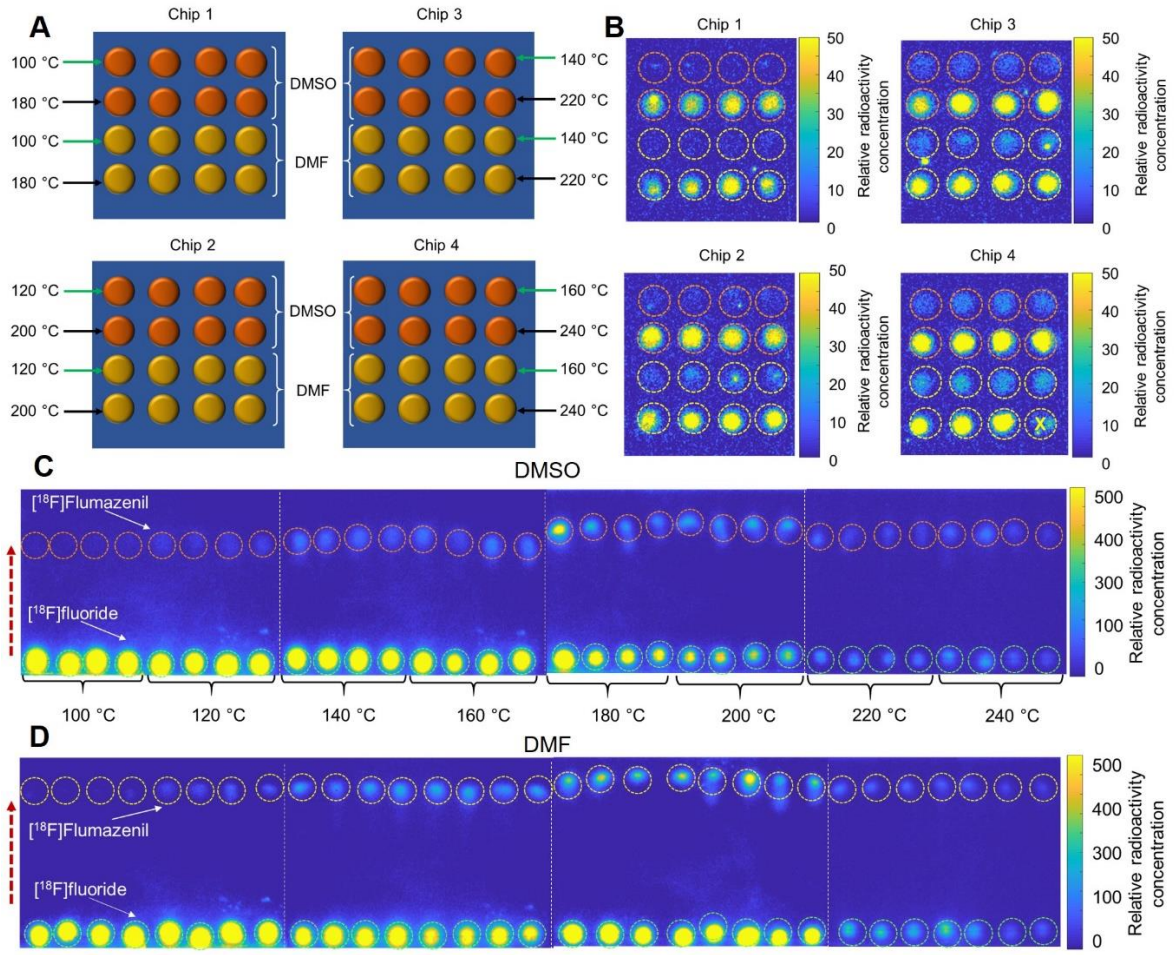

Figure 4-3. Experimental set up for one batch of experiments that explored the influence of reaction temperature (8 values) and solvent (2 types) for the synthesis of [^{18}F]Flumazenil.
(A) Assignment of 64 reaction sites. Half of the reaction sites were used first to explore 4 different temperatures in the first set of 32 simultaneous reactions. Then the other half of the sites were used for the remaining 4 temperatures. (B) Cerenkov images show the distribution of the residual activity on each chip after collecting the crude products. Radioactivity signal is decay-corrected to a common timepoint for all images. The reaction marked with an "X" was not analyzed (by mistake the precursor droplet was not added to reaction site). (C) Cerenkov images of developed TLC plates (each containing 8 samples) for reactions that used DMSO as the reaction solvent. (D) Separated crude samples using DMF as the reaction solvent. Dashed circles indicate the ROIs used for analysis. The dashed red arrow indicates the direction of solvent movement during development. White dotted lines represent the boundary of each multi-sample plate.

The resulting performance calculations for each condition are tabulated in **Appendix 4.7.5 Table 4-4** and the performance is plotted in **Figure 4-4A**. The fluorination efficiency increased strongly with temperature. However, unlike other droplet-based reactions, volatile losses during the fluorination reaction, as well as residual activity stuck to the chip after collection, led to

declining collection efficiency with increasing temperature. (Generally, the amount of volatile loss dominated and was about 15 - 10x higher than the residual loss.) The resulting crude RCY exhibited a peaking behavior with a maximum of 13.5 ± 0.6 (n=4) at 200 °C (with DMF). Consistent with these trends, Wong *et al.* found temperature of a flow reactor to be an essential factor with fluorination efficiency increasing from ~0% at 120 °C to ~20% at 160 °C using DMF as the solvent, and from ~0% to ~5% using DMSO[33]. Mandap *et al.*, using a microwave reactor, also found that fluorination efficiency increased substantially with temperature to a maximum value and then declining somewhat at higher temperatures[143].

We should point out that typically only the radiofluorination efficiency (as determined by radio-HPLC or radio-TLC) and/or radiochemical yield is reported in optimization experiments, making it difficult to make detailed comparisons with droplet reactions. Reporting only radiofluorination efficiency can be misleading as many potential losses (e.g. volatile losses or residual activity stuck on vials or tubing, which can be significant[149]) are not accounted for. Reporting only radiochemical yield accounts for losses, but all the losses (from various synthesis steps or purification) are lumped together. Significant discrepancies have been reported between radiochemical conversional and radiochemical yield for [^{18}F]Flumazenil[141,142,144]. For example, Vaulina *et al.* observed fluorination efficiency (TLC) of 25% but obtained only a 2% isolated yield after HPLC purification and SPE formulation, or 9% after SPE-based purification/formulation[141]. Massaweh *et al.* found that despite a fluorination efficiency (TLC) of 27-35%, isolated yield was only 2-5% [145], though it improved to 15-20% after mobile phase optimization[144]. While these discrepancies may reflect high losses during the purification/formulation step[141], these reports do not contain sufficient details or data to rule out other losses (e.g. residual activity on reaction vessel or tubing, volatile losses, etc.)

The temperature was fixed at 200 °C for subsequent experiments. With increasing base amount (**Figure 4-4B**), we observed the fluorination efficiency to increase from near zero and

plateau at a maximum value when base amount reached ~150-200 nmol. Collection efficiency exhibited an inverse behavior, and the overall crude RCY for DMF (the higher performing solvent) exhibited a sharp increase and then plateau starting at ~160 nmol of base. 240 nmol (where the crude RCY was only marginally lower) was selected as the optimal amount to provide robustness against pipetting errors. Study of increasing precursor amount (**Figure 4-4C**) showed rapid increases up to ~80 nmol and then a plateau, for fluorination efficiency, collection efficiency and crude RCY. The highest crude RCY (with DMF, the higher performing solvent) occurred at a precursor amount of 280 nmol, which was selected as the optimal condition. The strong impact of precursor amount below the plateau is consistent with Mandap *et al.*, who reported low fluorination efficiency (<3%, n = 1) for 1 mg of precursor in DMF at 160°C, and high values (~30%) with 2-8 mg of precursor. Ryzhikov *et al.* also found marked differences in fluorination efficiency in pairwise comparisons of precursor amounts[145]. Unfortunately, the reaction volume is given as a range in both papers, making it impossible to compare the concentration values. In many reactions, the ratio of base to precursor is a relevant parameter and we thus plotted the reaction performance as a function of this ratio in Figure 4-24. Ratios in the range ~1-3 gave the highest crude RCY, with a rapid drop for lower ratio values and a gradual drop for higher values. When exploring increasing reaction time (**Figure 4-4D**), fluorination efficiency exhibited a gradual increase, and the collection efficiency exhibited an inverse trend (mostly due to volatile activity loss). The resulting crude RCY in DMF (the better performing solvent) exhibited a decrease with time, with a maximum of 15.4 ± 0.9% (n = 4) for a 0.5 min reaction. Though reaction time has not been extensively studied in the literature, longer times seemed to improve the synthesis performance in closed reactors. Ryzhikov *et al.* observed an increase in fluorination efficiency from 39% (n = 1) to 80% (n = 1) when increasing the time from 15 to 30 min[145].

Considering the high volatile losses at high temperatures and longer reaction times, we explored additional high boiling point reaction solvents (**Figure 4-4E**), including N-methyl-2-

pyrrolidone (NMP), 1,3-dimethyl-3,4,5,6-tetrahydro-2(1H)-pyrimidinone (DMPU), and ethylene glycol, which have been used in other radiosyntheses[150,151]. Fluorination efficiency and crude RCY were significantly improved using NMP compared to DMF. As a final test we compared the influence of the type of base and phase-transfer catalyst (**Figure 4-4F**) in the reaction solvents DMF, DMSO, and NMP. The best combination was NMP with $TBAHCO_3$; much lower performance was observed with K_{222}/K_2CO_3 and K_{222}/Cs_2CO_3. The optimized conditions (NMP reaction solvent, 240 nmol base ($TBAHCO_3$), and 280 nmol precursor in an 8 µL droplet at 200 °C for 0.5 min) resulted in fluorination efficiency of 37.5 ± 0.8 (n = 4), collection efficiency of 51 ± 1 (n = 4) and crude RCY of 19.1 ± 0.6% (n = 4). Purification via analytical HPLC (Figure 4-50) for a batch that had a crude RCY of 18.0% gave an isolated yield of 11.6% (n = 1). Further optimization of purification may lead to modest improvements but was not investigated. Notably, the droplet-based synthesis could achieve useful isolated yields that are only slightly below the isolated yields reported by others (**Table 4-12**) while offering multiple advantages, including completion within only ~35 min (20 min for synthesis and HPLC purification, with an estimated ~15 min needed for formulation[152]) instead of 55-80 min [143–145], and 100x reduced precursor consumption[143–145].

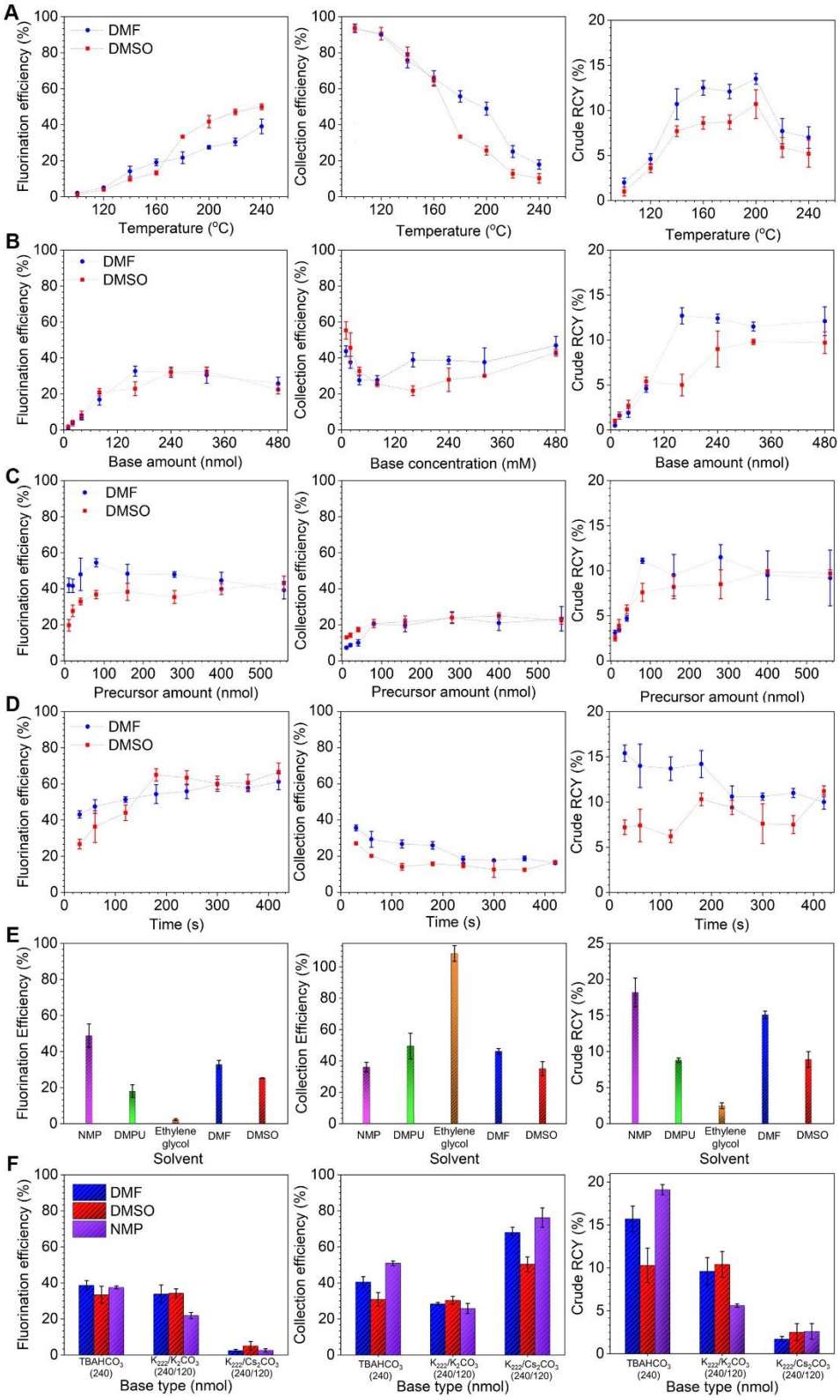

Figure 4-4. Influence of reaction parameters on the performance of the microdroplet radiosynthesis of [^{18}F]Flumazenil.

For each parameter, influence on fluorination efficiency, collection efficiency, and crude RCY are plotted individually. (A) Effect of temperature (and solvent). Precursor amount: 280 nmol. Reaction volume: 8 µL. Base amount: 480 nmol. Reaction time: 2 min. (B) Effect of amount of base (and solvent). Precursor amount: 280 nmol. Reaction volume: 8 µL. Reaction temperature: 200 °C. Reaction time: 2 min. (C) Effect of precursor concentration (and solvent). Reaction volume: 8 µL. Base amount: 240 nmol. Reaction time: 2 min. Reaction temperature 200 °C. (D) Effect of reaction time (and solvent). Precursor amount: 280 nmol. Reaction volume: 8 µL. Base amount: 240 nmol. Reaction temperature: 200 °C. (E) Effect of reaction solvent. Precursor amount: 280 nmol. Reaction volume: 8 µL. Base amount: 240 nmol. Reaction temperature: 200 °C. Reaction time: 0.5 min. (F) Effect of the base type (and solvent). Precursor amount: 280 nmol. Reaction volume: 8 µL. Base amount: 240 nmol. Reaction temperature: 200 °C. Reaction time: 0.5 min.

4.4.4 Optimization of [^{18}F]PBR06 radiosynthesis

To demonstrate versatility of the high-throughput approach, we next used the platform to perform an optimization of the radiosynthesis of [^{18}F]PBR06. This tracer detects microglial activation by targeting the translocator protein (TSPO) and is used for monitoring treatment response in Huntington's disease[153], imaging neuroinflammation, and monitoring tumor progression[154]. Using the commercially-available tosylate precursor for the radiosynthesis, isolated yields of [^{18}F]PBR06 in the range 30-60% have been reported in literature[154,155]; however, to our knowledge, no studies have been reported on the influence of different reaction conditions on the radiosynthesis performance.

Full details of all parameters we explored (precursor amount, base amount, temperature, reaction time, and type of base / phase transfer catalyst) are included in the **Appendix 4.7.6**. Similarly to [^{18}F]Flumazenil, studies of each parameter were performed in the following two different reaction solvents: DMSO (commonly reported in literature[154,155]), and a 1:1 (v/v) mixture of thexyl alcohol and MeCN (used in aliphatic radiofluorinations of other tosylate precursors[61]). In the study of precursor amount (**Figure 4-5A**), reactions in the mixed solvent showed a rapidly increasing fluorination efficiency with increasing precursor amount, reaching a plateau of ~100% at ~100-200 nmol of precursor, and the collection efficiency was consistently high. The resulting crude RCY increased rapidly as precursor amount was increased, reaching a plateau of 91 ± 4% (n = 4) at 160 nmol of precursor. Interestingly, for reactions performed in DMSO, the trends were

similar for precursor amounts below ~100-200 nmol precursor, but for higher precursor amounts, the fluorination efficiency, collection efficiency, and crude RCY showed gradual to moderate decrease instead of leveling off. Still, the maximum crude RCY using DMSO (86 ± 6%, n = 4) was similar to that obtained using the mixed solvent.

In the studies of base amount (**Figure 4-5B**), fluorination efficiency, collection efficiency, and crude RCY were relatively unaffected, showing only modest reductions when the amount of base was lower than ~150 nmol. The crude RCY was maximal at 240 nmol of base. In the study of reaction temperature (**Figure 4-5C**), the fluorination efficiency was relatively independent of temperature when using the mixed reaction solvent. When using DMSO, the fluorination was highest from 90 – 130 °C. Collection efficiency was consistently high across all temperatures (and for both solvents), and the crude RCY mirrored the fluorination efficiency**.** A temperature of 100 °C was selected. The reaction time (**Figure 4-5D**) had almost no impact, with high crude RCY in all cases except for DMSO at 0.5 min, where the crude RCY was substantially lower. Finally, we found no significant difference when using $TBAHCO_3$ compared to the typically reported phase transfer catalyst K_{222}/K_2CO_3 when using the mixed solvent; however, when using DMSO as the reaction solvent, the fluorination efficiency and crude RCY were slightly lower when using K_{222}/K_2CO_3 compared to $TBAHCO_3$ (**Figure 4-5E**). The results for DMSO were lower overall due to the suboptimal reaction time used in this comparison.

Overall, the optimal conditions (240 nmol of $TBAHCO_3$, 160 nmol of precursor in 8 µL of thexyl alcohol: MeCN (1:1 v/v), 100 °C, 0.5 min) gave a fluorination efficiency of 97.4 ± 0.2% (n = 4) and crude RCY of 94 ± 2% (n = 4). Compared to conventional methods (**Table 4-19**), our optimal conditions were significantly quicker (0.5 vs 15 min reaction time)[154] and milder (100 vs 140 °C)[154]. We performed purification via analytical-scale radio-HPLC (**Figure 4-51**) and obtained an isolated yield of 75.8 % (n=1). Though we did not perform formulation to determine the overall RCY, this compares favorably with the overall RCY values (30-60%) reported in literature[154,155], consumed 10-30x less precursor[154,155], and was a shorter synthesis process (~35min, i.e. 20 min for

synthesis and HPLC purification, plus an estimated ~15 min needed for formulation[152]), compared to 50 min reported in literature[155].

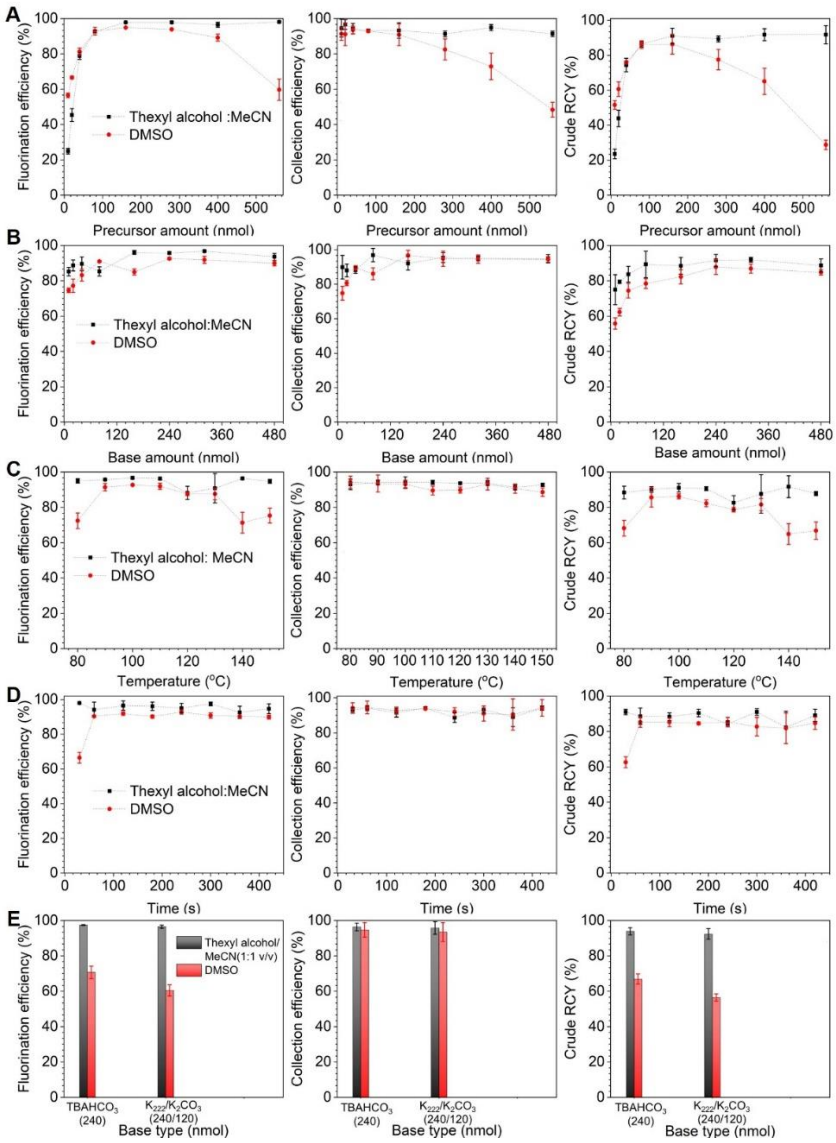

Figure 4-5. Influence of reaction parameters on the performance of the microdroplet radiosynthesis of [^{18}F]PBR06.

For each parameter, influence on fluorination efficiency, collection efficiency, and crude RCY are plotted individually. (A) Effect of precursor concentration (and solvent). Reaction volume: 8 µL. Base amount: 240 nmol. Reaction time: 5 min. Reaction temperature 100 °C. (B) Effect of amount of base (and solvent). Precursor amount: 160 nmol. Reaction volume: 8 µL. Reaction temperature: 100 °C. Reaction time: 5 min. (C) Effect of temperature (and solvent). Precursor amount: 160 nmol. Reaction volume: 8 µL. Base amount: 240 nmol. Reaction time: 5 min. (D) Effect of reaction time (and solvent). Precursor amount: 160 nmol. Reaction volume: 8 µL. Base amount: 240 nmol. Reaction temperature: 100 °C. (E) Effect of the base type. Precursor amount: 160 nmol. Reaction volume: 8 µL. Base amount: 240 nmol. Reaction temperature: 100 °C. Reaction time: 0.5 min.

4.4.5 Optimization of [^{18}F]Fallypride radiosynthesis

[^{18}F]Fallypride is used to study diseases associated with the dopaminergic system, such as Parkinson's, Huntington's, and Alzheimer's diseases[156,157]. We previously performed a preliminary study of the droplet synthesis of [^{18}F]Fallypride from the tosylate precursor exploring the impact of the base amount, precursor amount, and reaction volume[61]. However, with only a single heater operating a single chip, reaction temperature and time could not previously be studied conveniently. Using the expanded capabilities of the multi-heater platform described here, we studied the impact of temperature and reaction time in combination with precursor concentration. Full details are in **Appendix 4.7.7**. As a function of increasing precursor concentration, the fluorination efficiency and crude RCY exhibit a rapid increase from near zero and reach a plateau, while the collection efficiency is consistently high. Surprisingly, nearly identical behavior was observed for reaction temperatures of 95, 110, and 125 °C; but at 80 °C it was evident that a higher precursor concentration was needed to achieve the maximal fluorination efficiency and crude RCY (**Figure 4-6A**). Maximum crude RCY occurred at 110 °C and 39 mM precursor. When examining the combined effect of precursor concentration and reaction time (**Figure 4-6B**), the impact of reaction time was nearly negligible, only leading to discernable differences when the precursor concentration was below ~20 mM. The highest crude RCY (93 ± 5%, n = 2) was obtained when running the reaction at 110 °C for 1.0 min, 240 nmol of $TBAHCO_3$, and 39 mM precursor in 6 µL of thexyl alcohol: MeCN (1:1 v/v). After purification by analytical HPLC (Figure 4-52) the isolated yield was 74% (n = 1). The ability to perform a kinetic study like this in one set of simultaneous experiments is a significant advantage compared to the typical lengthy series of sequential studies with conventional instruments or microfluidic flow chemistry systems[158–160]. This approach likely also provides more reliable reaction times and temperatures than when repeatedly cooling and opening a single reaction to extract samples at different timepoints[161].

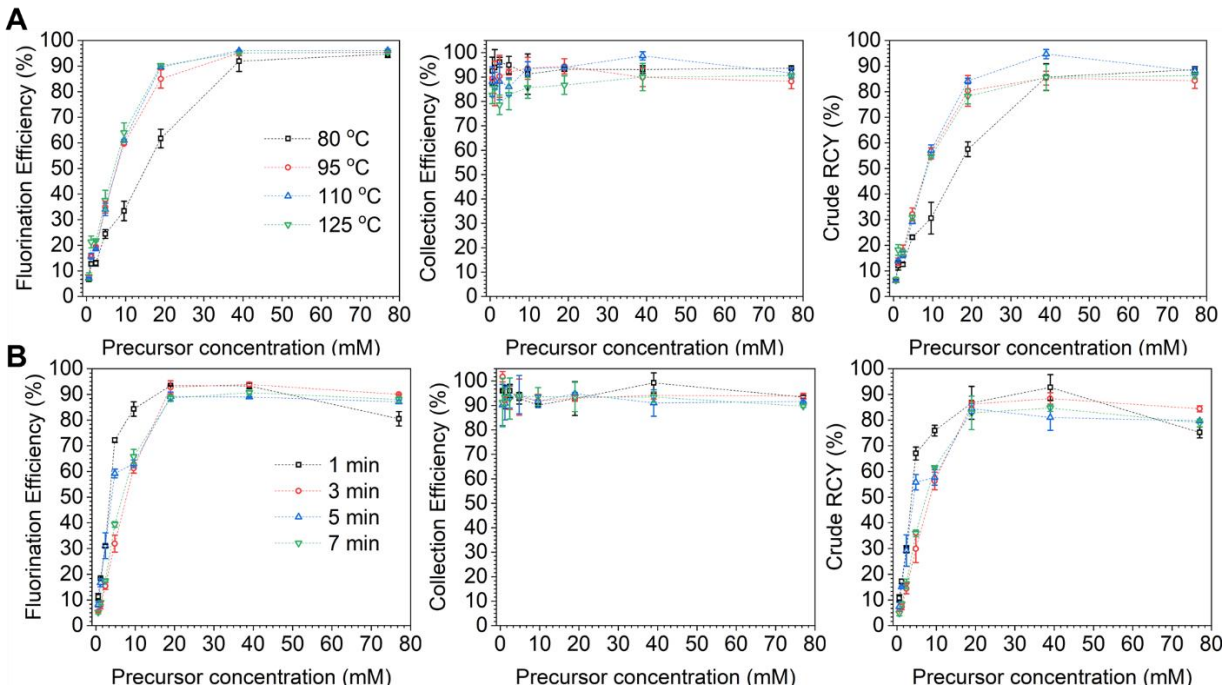

Figure 4-6. Influence of temperature and reaction time on [^{18}F]Fallypride production. (A) Investigation of [^{18}F]Fallypride synthesis performance reaction performance as a function of reaction temperature and precursor concentration. Reaction volume: 6 µL. Base amount: 240 nmol. Reaction time: 7 min. Reaction solvent: thexyl alcohol and MeCN (1:1 v/v) (B) Investigation of reaction performance as a function of reaction time and precursor concentration. Reaction volume: 6 µL. Base amount: 240 nmol. Temperature: 110°C. Reaction solvent: thexyl alcohol and MeCN (1:1 v/v).

4.4.6 Optimization of [^{18}F]FEPPA radiosynthesis

As a final example, we performed a very limited optimization of the synthesis of [^{18}F]FEPPA, a radiopharmaceutical that has been used in several pre-clinical and clinical settings in recent years[162–166] to look at the overexpression of TSPO, which is known to be associated with a variety of neurodegenerative disorders. With the aid of the high-throughput platform to explore the influence of temperature (**Appendix 4.7.8**), we translated the synthesis into droplet format to leverage the advantages of small-volume reactions. We started with conditions like past droplet studies for other tracers using tosylate precursors. Since literature reports include a range of 9 to 45 mM precursor concentration[162–164,167], we chose an initial value of 30 mM. As a function of increasing temperature (**Figure 4-7**), the fluorination efficiency was ~10% at 60 °C and sharply increased to reach a plateau after 90 °C. The collection efficiency was consistently high at all

temperatures, and the resulting crude RCY showed a similar trend to the fluorination efficiency. The highest crude RCY (77 ± 2%, n = 4) was observed at a temperature of 110 °C for 2.0 min, 30 mM precursor in 8 µL of thexyl alcohol: MeCN (1:1 v/v) solvent and 240 nmol of base ($TBAHCO_3$). Compared to literature methods (**Table 4-23**), the reaction time is shorter (2 min vs 10 min[162–164,167]), the droplet reaction consumes 40-50x less precursor, and the overall synthesis is shorter and has higher yield[162–164,167]. A batch was purified by analytical-scale HPLC (Figure 4-53) and the collected fraction was diluted (1:3, v/v) with 9 mM $NaHCO_3$ to produce an isotonic solution appropriate for injection containing 440 MBq [12 mCi], sufficient for multiple preclinical studies. The overall 30 min synthesis had an RCY of 67% (n = 1).

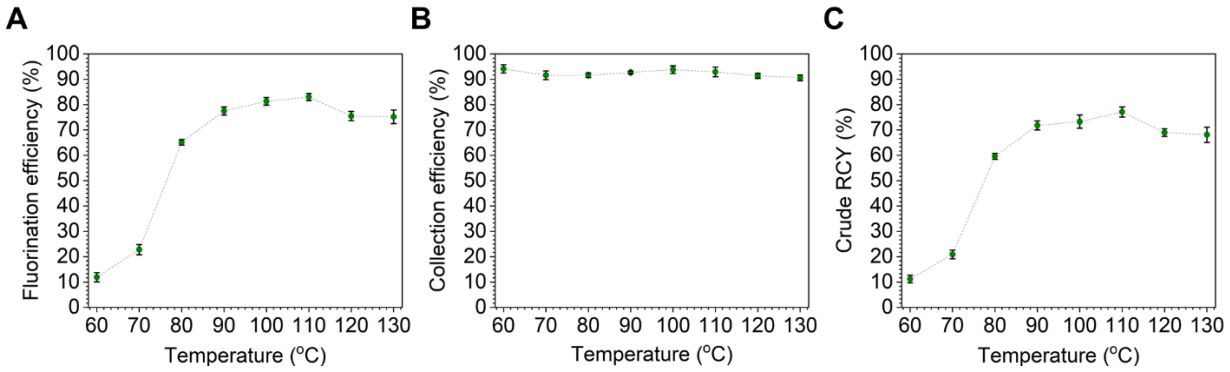

Figure 4-7. Effect of temperature on the performance of [^{18}F]FEPPA synthesis. Reaction volume: 8 µL. Base amount: 240 nmol. Precursor amount: 240 nmol. Reaction time: 2 min. Reaction solvent: thexyl alcohol and MeCN (1:1 v/v).
(A) Effect on fluorination efficiency. (B) Effect on collection efficiency. (C) Effect on crude RCY.

4.4.7 Clinical-scale radiosynthesis

The optimization experiments in this work were performed with ~14 MBq [0.38 mCi], where each reaction often yielded enough product for multiple mouse scans[168,169]. Nevertheless, we wanted to explore whether one of the optimized compounds ([^{18}F]PBR06) could be scaled to clinically-relevant levels without changing any reaction conditions other than the amount of starting radioactivity. We've previously reported that significant scale-up is possible for [^{18}F]Fallypride (7.2 GBq demonstrated)[60], as well as O-2-[^{18}F]fluoroethyl-L-tyrosine ([^{18}F]FET) and [^{18}F]Florbetaben (up to 0.8 GBq demonstrated for each)[139]. Experiments with increasing starting

activity up to 3.2 GBq (86 mCi) are described and shown in the **Figure 4-54**. While the crude RCY showed a slight reduction as starting activity increased due to a decrease in fluorination efficiency, the final quantities after purification and formulation would still be sufficient for several clinical doses.

These results reinforce the ability to optimize small-scale reactions in a high-throughput fashion using the platform described here, and then scale up the starting activity to increase the output of a droplet radiosynthesis. In fact, the starting activity itself could be varied as a reaction parameter and studied with high throughput using the platform described in this paper. Studies are currently underway in our laboratory to explore in more detail how scale-up influences the performance.

4.5 Comparison to other optimization approaches

With the platform presented here for performing parallel radiosyntheses in droplet format, we were able to rapidly and conveniently study the influence of various reaction parameters to obtain a detailed map of conditions that influence the synthesis performance. Each radiopharmaceutical synthesis could be extensively investigated (100s of data points) in a few days, requiring only a few batches of radioisotope. In total, for the four example compounds, 820 experiments were completed in 15 experiment days, with an average of 55 reactions per day. While the maximum number of experiments completed in a single day was 64, it is probably feasible to increase this number to ~96. The limiting factor is the tedious manual adding of reagents, collecting crude products, and performing TLC analysis. An automated platform for high-throughput experimentation is currently being developed, which could address these issues and perhaps increase reaction throughput further while also reducing radiation exposure and the chance for human error[170]. Performing many reactions per day saves on total time (and thus labor and other costs) for optimization and requires far fewer batches of radioisotope, significantly reducing radioisotope production and/or purchase and shipping costs. Importantly, since day-to-day

variation such as radioisotope quality or reagent preparation can sometimes also affect results[171], reducing the total number of experimental days (and radioisotope batches) also reduces the confounding effects of this variability. Furthermore, using small-scale droplet reactions (i.e., 6-8 µL) compared to conventional reactors (0.5-2.0 mL), reagent usage per datapoint was reduced by ~10-100x. The total amount of precursor consumed was only 30 mg for 355 data points for [^{18}F]Flumazenil, 20 mg for 296 data points for [^{18}F]PBR06, 6 mg for 128 data points for [^{18}F]Fallypride, and 4 mg for 32 data points for [^{18}F]FEPPA. These amounts are equivalent to just 12 macroscale reactions for [^{18}F]Flumazenil (5 mg each), 6-7 for [^{18}F]PBR06 (3 mg each), 3 for [^{18}F]Fallypride (2 mg each), and one for [^{18}F]FEPPA. Moreover, the amount of product activity in some cases is sufficient for *in vitro* or pre-clinical *in vivo* imaging studies. This could be a tremendous advantage for new radiotracer development where the precursor is in short supply. The droplet platform allows the possibility of performing both optimization and initial preliminary biological studies in the shortest time using only a few mg of precursor.

Aside from conventional radiosynthesizers, rapid and economical optimizations have also been performed using continuous-flow microfluidic platforms. Small boluses of reagents (10s of µL) are reacted sequentially under different conditions[100,172] (up to 25 experiments per day have been reported[173]). While convenient for studying the influence of residence time, reactant concentrations and ratios (via changes in relative flow rates), and reaction temperature, varying other conditions (e.g. solvent) is cumbersome, requiring manual intervention and cleaning procedures for each change. In addition, some aspects (e.g. [^{18}F]fluoride drying conditions) cannot be explored in a high-throughput fashion since they are performed outside the flow-chemistry workflow. Droplet reactors are suitable for studying all of these variables and can perform reactions in parallel rather than sequentially. An additional advantage of optimization using droplet reactions is that the multi-heater platform is compact (120 x 120 x 100 mm^3), allowing operation in a small part of a hot cell or mini-cell. Its low weight (~900 g) makes the

system portable and easy to move in and out of a hot cell and occupies space only when optimization efforts are needed. In contrast, conventional radiosynthesizers and flow chemistry systems are typically much larger and integrated into infrastructure (gases, vacuum) and cannot easily be moved.

A unique feature of the open microdroplet system is the convenience of visualizing and quantifying the radioactivity distribution on the chip surface via Cerenkov imaging at different stages of the synthesis process. This information enables a more comprehensive assessment of the performance of each step. While some macroscale systems include radiation detectors near reaction vessels and cartridges that enable straightforward activity measurements on these components to help pinpoint losses[149], other systems require removing / disassembling components to make activity measurements, which may be infeasible or inconvenient and increases radiation exposure. In comparison, this data can be readily gathered in parallel for many reactions at once in our high-throughput approach, saving significant time, reducing radiation exposure, and reducing the chance for errors.

On the other hand, a limitation of this approach is that the open droplet format had significant volatile losses for some syntheses. While volatile losses were very low for [^{18}F]PBR06, [^{18}F]Fallypride, and [^{18}F]FEPPA in droplet format (as well as many other tracers[99,103,152]), losses were significant for [^{18}F]Flumazenil and were found to occur during the radiofluorination step. In contrast, in macroscale systems, the reactor is usually closed for the duration of the reaction, and losses during this step are generally likely to be lower. Of course, both droplet systems and conventional systems can exhibit volatile losses at other stages of the radiosynthesis process, such as during solvent evaporation steps. Despite the volatile loss, meaningful and repeatable experiments could still be performed. Moreover, the isolated yield for [^{18}F]Flumazenil (which had substantial volatile loss) was only slightly below the range of isolated yields (before formulation) reported by others, suggesting that loss of the volatile species was not very detrimental to the

overall reaction performance, or perhaps that the reaction loss was offset by other improvements (e.g. perhaps the use of an analytical instead of semi-preparative HPLC column reduced the degree of purification loss). Of course, the volatile losses present a hazard that needs to be mitigated by operation of the system within an appropriate hot cell.

While studies here were performed using a one variable at a time (OVAT) method, further optimization efficiency improvements might be achieved by integrating concepts like the design of experiments (DoE)[171] and reaction modeling. In addition to the reactions optimized here, the droplet format is compatible with other ^{18}F-labeled radiopharmaceuticals[59,103,138,152]. It can likely be used with other isotopes, including radiometals. Although designed for operation in a radiochemistry laboratory, the platform could possibly also be used for reagent-economical optimization of a wide range of chemical reactions outside the field of radiochemistry. Recently, several new platforms and techniques have been reported for performing screening of organic reactions in volumes of 1.5 –100 µL[129,130], and our platform could provide an enhanced ability to vary reaction temperatures and times for different simultaneous reactions.

4.6 Conclusion

In this work, we have developed a platform for radiosynthesis optimization relying on droplet-based reaction arrays that enables many reactions (up to 64) to be performed in parallel, each with minimal reagent consumption. Combined with high-throughput analysis methods[93], it is practical to perform hundreds of experiments in a matter of days. While similar in throughput to flow-chemistry-based optimization methods[174], this platform allows studies of all stages of the synthesis process, including [^{18}F]fluoride drying/activation, and it has been shown in previous work that the chips are also compatible with optimization of reactions having at least 2 synthetic steps[138,152]. It also allows reaction solvent and reagent amounts to be readily varied without the constraints of flow-based systems. Finally, product amounts can be scaled up after optimization by varying the starting activity.

As examples, we used the platform to perform the rapid optimization of the production of [^{18}F]Flumazenil, [^{18}F]PBR06, [^{18}F]Fallypride, and [^{18}F]FEPPA from their commercially-available precursors. Using the platform, a series of syntheses using different conditions (85 for [^{18}F]Flumazenil, 74 for [^{18}F]PBR06, 64 for [^{18}F]Fallypride, and 8 for [^{18}F]FEPPA), spanning 6 different reaction parameters, were performed. Replicate studies were performed for each condition and the small standard deviation computed for each set of replicates indicated that the platform has high reproducibility. For [^{18}F]Flumazenil, the observed trends were comparable to optimization studies performed using conventional radiosynthesizers. For other tracers there is limited optimization data in the literature.

This platform conveniently brings the power and efficiencies of high-throughput experimentation to the field of radiochemistry. It could find use in: (i) rapid refinement and optimization of radiosynthesis protocols for existing or novel radiopharmaceuticals, (ii) translation of known macroscale protocols into droplet format, and (iii) studies of novel labeling methods. The high throughput platform allows exploration of many more reaction conditions within the available parameter space, which can potentially lead to discovery of favorable reaction conditions that might not otherwise be attempted with conventional methods due to time, cost, and low throughput. The small amount of precursor required for each reaction is a crucial advantage, particularly in the early stages of novel radiopharmaceutical development where only a small amount of the starting material may be available; the high-throughput platform enables the development of syntheses within a short timeframe at low cost.

4.7 Appendix

4.7.1 Multi-heater platform

The platform was assembled as described in the manuscript from the following components: ceramic heaters (Ultramic CER-1-01-00093, Watlow, St. Louis, MO, USA), , epoxy glue (JB weld, Sulphur Springs, TX, USA), calcium silicate thermal insulation material (McMaster-Carr; Atlanta,

GA), 3D-printed nylon piece (Fictiv Inc., San Francisco, CA, USA), DC fans (Sanyo Denki model 9GV3612G301), thermocouple amplifier board (AD8495 Breakout Board, Adafruit, New York, NY, USA), data acquisition module (DAQ; NI USB-6003, National Instruments, Austin, TX, USA), and solid-state relay (SSR, Model 240D05, Sensata-Crydom). Thermal paste (OT-201-2, OMEGA, Norwalk, CT, USA) was used to enhance thermal conductivity between the heaters and the multi-reaction chips.

Figure 4-8 shows a photograph of the entire platform composed of the high-throughput microdroplet apparatus and a separate control box (250 mm x 204 mm x 200 mm) that can be placed outside the shielding or hot cell. CAD models of the platform will be provided upon request.

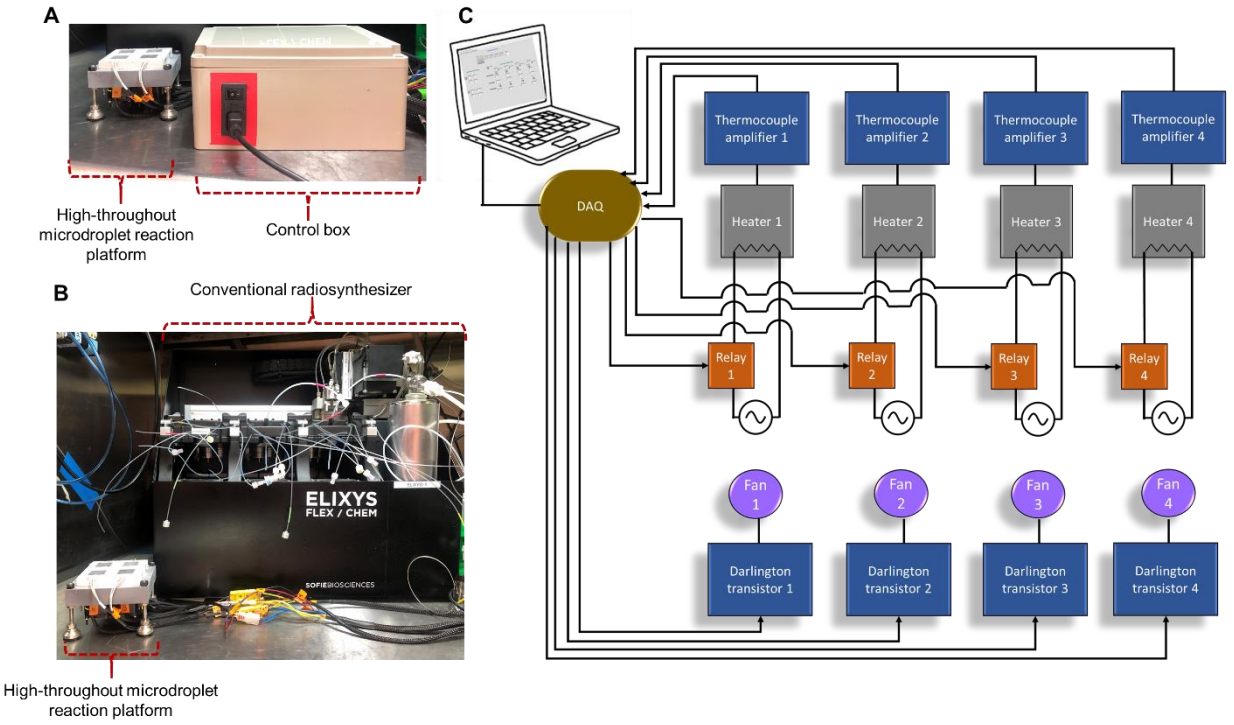

Figure 4-8. High-throughput microdroplet reaction platform.
(A) Photograph of fully assembled high-throughput apparatus with control box inside a hot cell. (B) Photograph with control box located outside the cell to illustrate the small system footprint compared to a conventional radiosynthesizer (ELIXYS, Sofie, Inc., Culver City, CA, USA). C) Electronic wiring diagram of the high-throughput platform.

4.7.2 Thermal simulations

To prevent thermal crosstalk between heaters (i.e., one heater affecting the temperature of a neighboring heater), the heaters were mounted to a frame made of thermally insulating material.

Two different types of thermal insulation were explored: Thermo-12 Gold (Johns Manville, Brunswick, GA, USA) and Firetemp – X (Johns Manville). We chose to use Firetemp-X as it could be readily machined, in contrast to Thermo-12 Gold, which we found too flaky and fibrous. To understand if the spacing of the heaters (19.3 mm gap) was enough to prevent thermal crosstalk, thermal modeling was performed on a simplified CAD model of the platform using Solidworks (Dassault Systems, Vélizy-Villacoublay France) with the Solidworks Simulation add-in. The model includes the thermal insulation frame and the heaters. The heaters were modeled as aluminum nitride blocks having a thermal conductivity of 285 W/m-K. The frame was modeled as Firetemp–X; according to manufacturer specifications, the thermal conductivity of this material depends on operating temperature, so we chose a value of 0.094 W/m-K, which corresponds to an estimated operating temperature range of 60-150°C. The model included a thin layer (200 μm) of JB Weld epoxy between the heaters and insulating material, with thermal conductivity of 0.2 W/m-K. A thermal resistivity value of the interface between the heater and the insulation was set to be 0.001 m^2K/W. This value is derived from both the thermal conductivity of the epoxy and the contact area (allowing for heat transfer) of the heater and insulating material. Bulk ambient temperature and starting temperatures in the model were set to 298 K, and the convective coefficient for stagnant air was modeled as 25 W/m^2-K. A convection boundary condition using the convective coefficient listed above was applied to all outward-facing surfaces. Each heater was defined to have a heater power of 150 W. A high-quality mesh was applied to the model resulting in 17239 nodes and 9796 total elements.

A simple steady-state thermal simulation was performed to analyze the overall temperature distribution of the construct with each of the four heaters set to different temperatures. The resulting temperature distribution from the simulation can be seen in **Figure 4-9.**

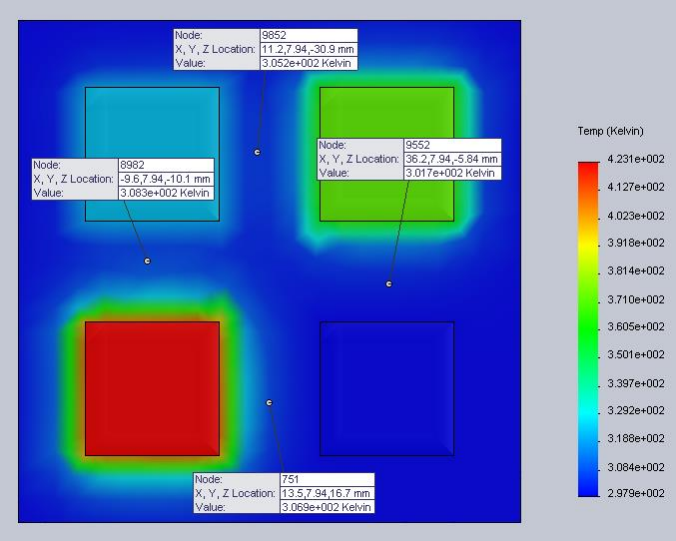

Figure 4-9. Temperature influence from heater to heater.
Steady-state temperature distribution of the four-square heaters mounted in the insulating construct, with setpoints of 323, 373, 298, and 423 K (clockwise, starting at top left). The annotated probe points represent approximate midpoints between adjacent heaters.

The simulation shows that with the designed spacing, heaters are not affected by their neighbors, even for the room temperature (298 K) heater operated adjacent to the hottest (423 K) heater. When probing the insulating material between different pairs of heaters, the highest temperature increase at the midpoint was 10.3 K (between 423 K and 323 K heaters), and the lowest was 3.7 K (between 373 K and 298 K heaters). The temperature change of the insulating material right near the edge of the heater set to 298K was zero confirming adequate insulation of the heater from neighboring heaters

The model results were verified empirically on the heating platform through thermal imaging. The heaters on the heating platform were set to different temperatures, and the system was allowed to reach a steady-state. In this study, heaters 1 to 4 (i.e., counterclockwise, starting from the top right) were set to 373K, 323K, 413K, and 305K, respectively. The thermal IR plot can be seen in **Figure 4-10**. Positions probed between adjacent heaters on the insulating material show a maximum increase of 5.1 K compared to the temperature of the heater set to the lowest temperature (305 K), suggesting that the insulating material can adequately prevent thermal crosstalk.

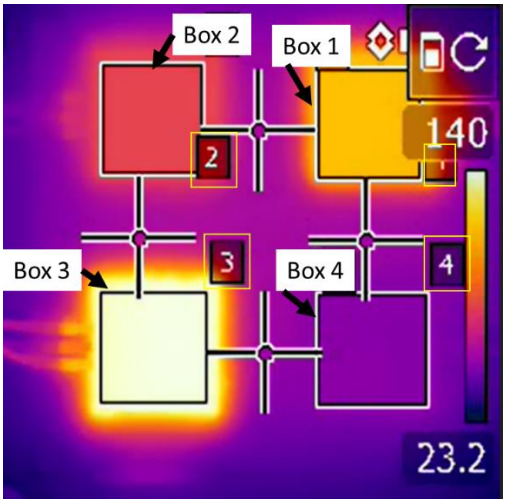

Figure 4-10. Thermal image of the heater platform.
Box 1 through 4 corresponds to areas within heaters 1 through 4. Locations of spot probes between heaters are also shown.

Following the initial steady-state simulation, a transient simulation was performed to estimate the cooling time required for the system to reach room temperature. The model was set up similar to that of the static heating model mentioned above with some minor modifications. The transient model was performed over 600 s with a 1 s step size. Different simulations were performed using different starting temperatures (413 K, 373 K, 323 K) applied to all heaters. The bulk ambient temperature was set to 298 K. To mimic active cooling using fans, a convective coefficient of 200 W/m^2-K was applied to all surfaces in contact with the cooling airflow. The surfaces are highlighted in **Figure 4-11** by the green cones**.** All the other exposed surfaces were set with a convective coefficient for stagnant air modeled as 25 W/m^2-K. A solid mesh was applied consisting of 21594 nodes and 12641 elements.

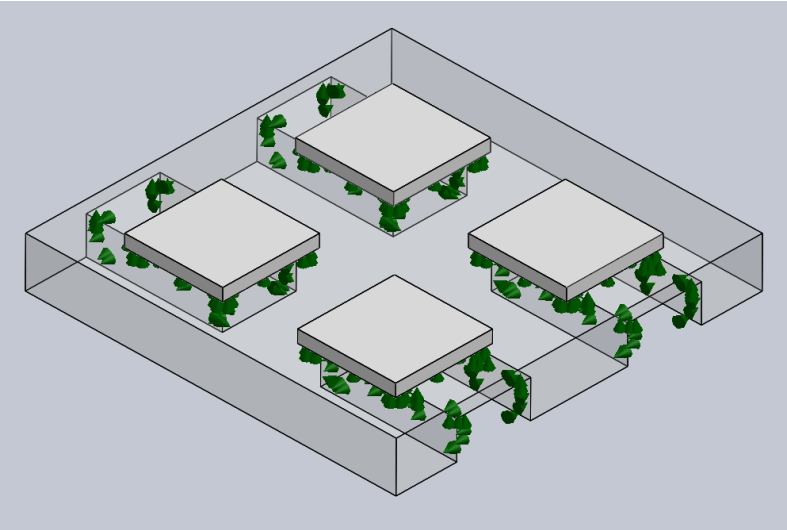

Figure 4-11. CAD model of the insulating material with embedded heaters.
The green cones indicate the surfaces affected by active fan cooling.

For each simulation, temperature readings positioned at the center of each heater were measured as a function of cooling time. Due to symmetries in the geometry, all heaters behaved identically. Cooling temperature profiles for heater 1 as a function of different starting temperatures can be seen in **Figure 4-12**. The required cooling time (to 303K) decreases as we decrease the starting temperature. For starting temperatures of 413K, 373K, and 323K, the cooling times were 108 s, 93 s, and 55 s, respectively. Empirical performance (presented in the main paper) was found to have a slower cooling time than the simulation.

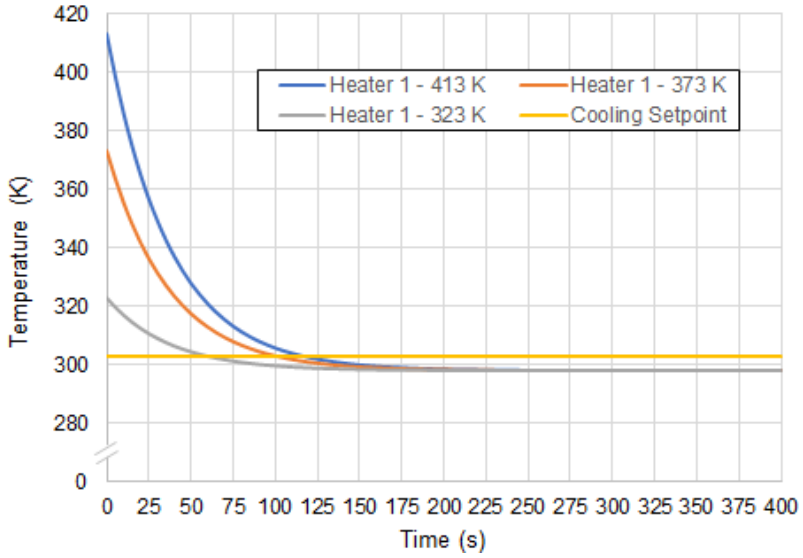

Figure 4-12. Simulated cooling temperature profiles as a function of time for different starting temperatures.
The cooling setpoint temperature is plotted as a yellow line to visualize better when this setpoint temperature has been reached.

4.7.3 Heater calibration and characterization

We initially performed a 2-point linear calibration of thermocouple signal versus temperature by submerging each heater in 2 different water baths (ice water: 0°C; boiling water: 100°C) and measuring the output voltage from the corresponding thermocouple amplifier. Water baths were prepared in 500 mL glass beakers with stir bars, and the temperature was measured independently with a calibrated digital thermometer (53 II B, Fluke, Everett, WA, USA). The temperature stability of the heaters was assessed by setting each heater to a set temperature (50, 100, and 140 °C) and observing the integrated thermocouple measurement for 5 min (**Figure 4-13**). Temperature data were recorded every 0.5 s using the DAQami program (National Instruments) and plotted to examine the heating rate, cooling rate, and temperature stability at the setpoint.

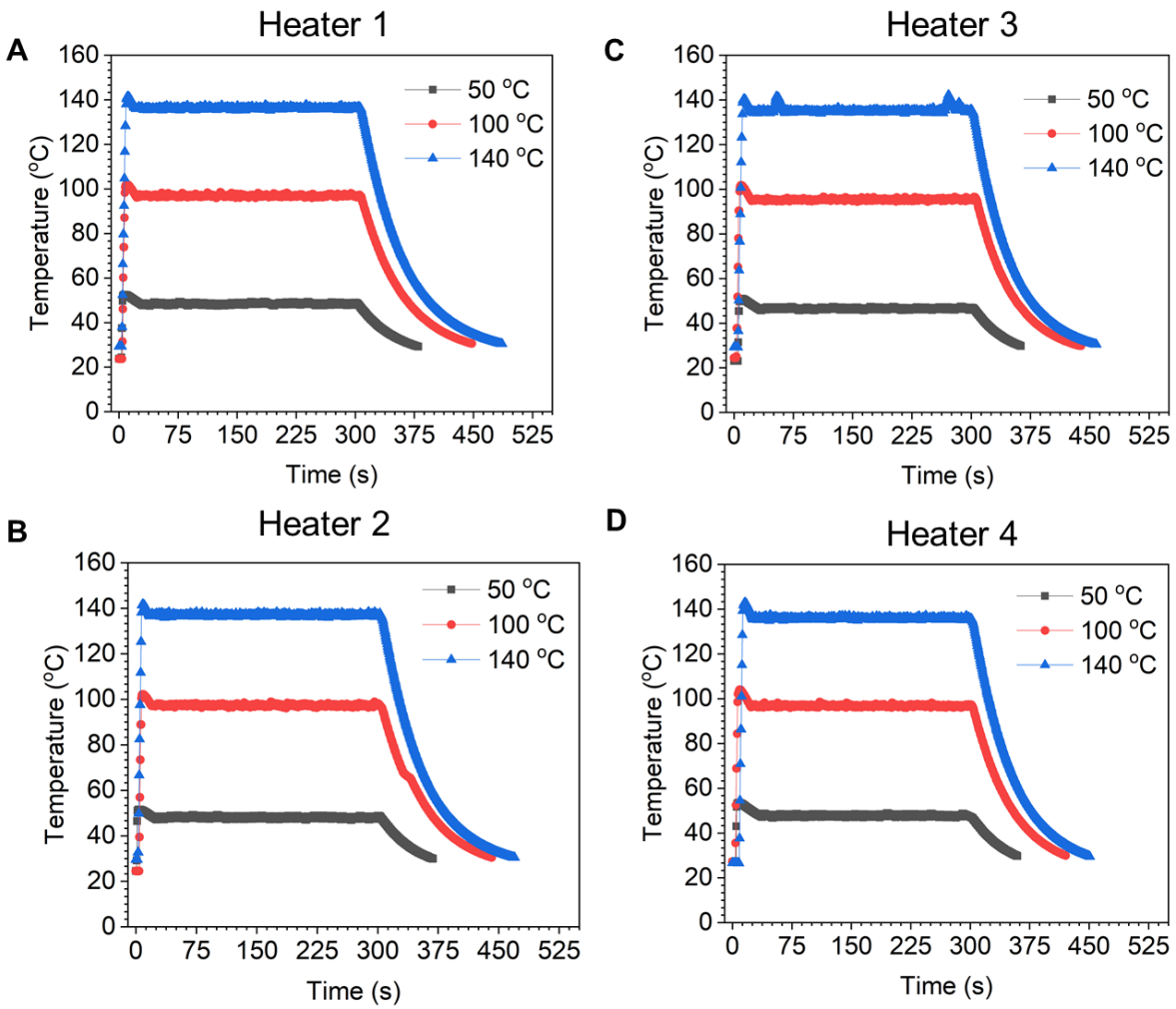

Figure 4-13. Temperature stability of the four heaters at three different temperatures. In each case, the heater was activated, and once it reached the setpoint, it was maintained at that temperature for 5 min, followed by forced-air cooling. (A) Heater 1; (B) Heater 2; (C) Heater 3; (D) Heater 4.

To improve accuracy, a 3-point linear calibration was later performed using a thermal camera (T440-25, FLIR, Wilsonville, OR, USA) to measure the average temperature on the heater surfaces (set at 50, 100, 140 °C, using the original calibration). For each thermal image, the temperature was allowed to stabilize for 5 min before recording the image. The spatial uniformity of temperature distribution was assessed via thermal imaging after this final calibration. **Table 4-2** shows the average thermocouple reading and standard deviation for the plots in **Figure 4-14** and **Figure 4-15**. Average and standard deviation were computed from the 5 min region where the

temperature had stabilized. All heater temperatures exhibited a standard deviation of <1 °C over time.

Table 4-2. Average heater temperatures during 5 min heating.

	Average ± standard deviation (°C)				
Setpoint (°C)	**Heater 1**	**Heater 2**	**Heater 3**	**Heater 4**	**All Heaters**
50	48.5 ± 0.4	48.1 ± 0.5	46.6 ± 0.5	47.9 ± 0.6	47.8 ± 0.8
100	97.0 ± 0.5	97.4 ± 0.5	95.4 ± 0.4	96.9 ± 0.5	96.7 ± 0.9
140	136.3 ± 0.5	137.1 ± 0.5	135.5 ± 1.4	136.0 ± 0.5	136.2 ± 0.7

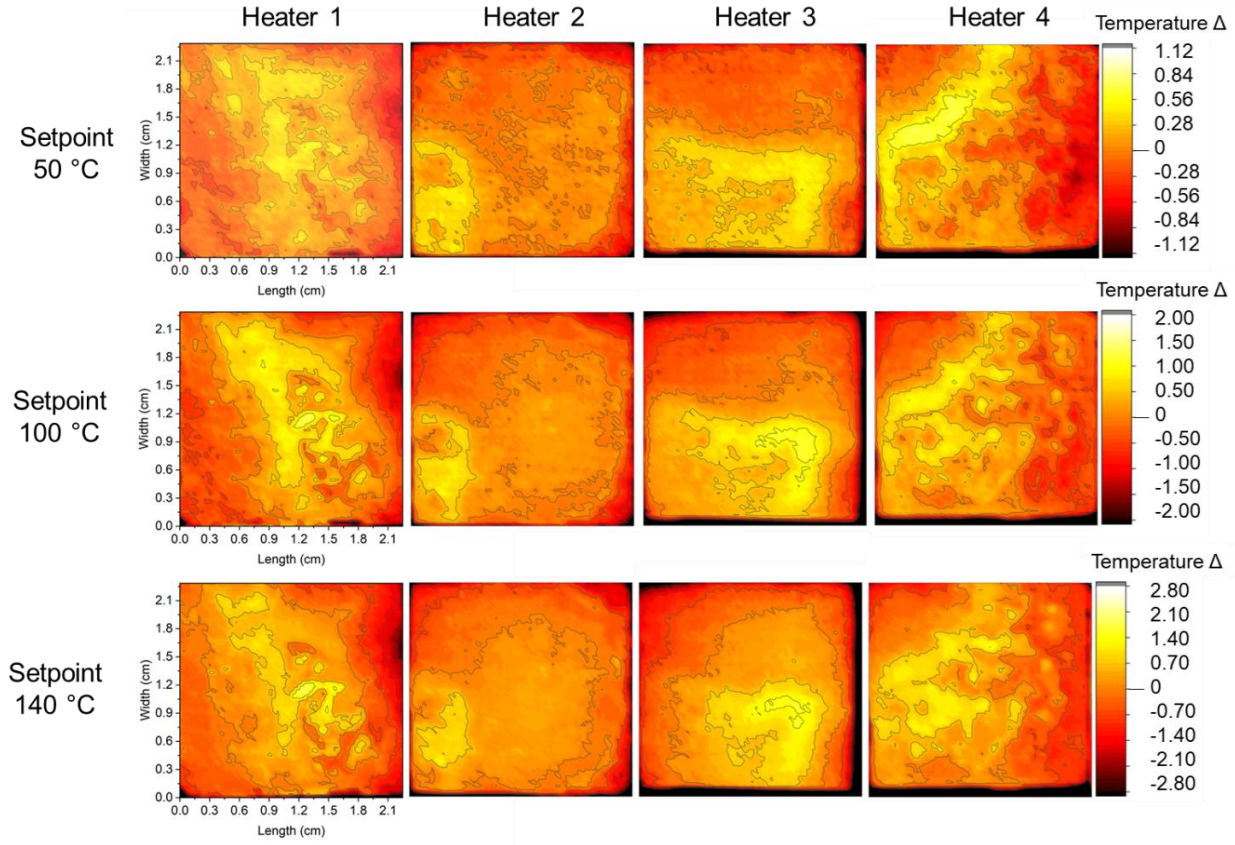

Figure 4-14. Thermal images of all four ceramic heaters (columns) surface at three different temperature setpoints (rows).
The color represents the deviation of each pixel from the mean temperature. The dark areas show the pixels that deviate by >2% from the mean.

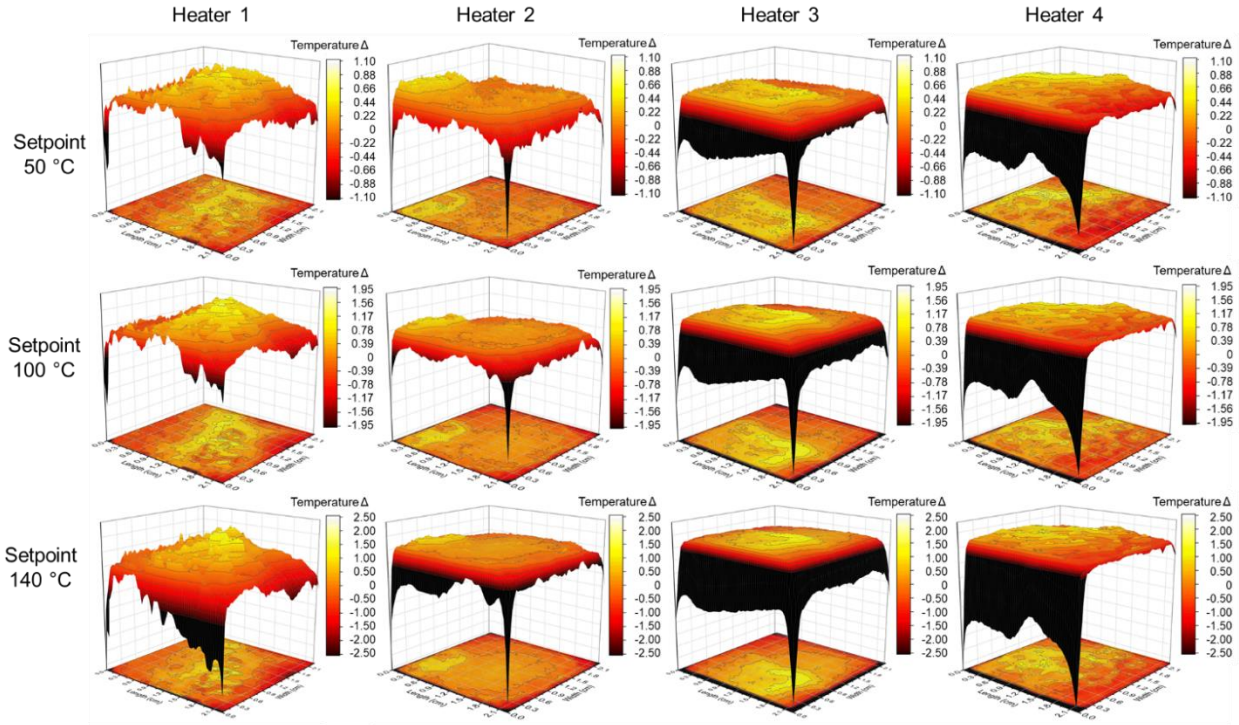

Figure 4-15. The same data as Figure 5.14 was replotted in 3D to provide a different illustration of uniformity.

Regions of the heater with deviations >2% were considered to be unusable. **Table 4-3** summarizes the size of unusable regions of each heater at different set temperatures. The maximum width of the unusable region was 1.5 mm across all heaters and temperature setpoints. The maximum fraction of unusable heater surface was 8.3% (always at the edges).

Table 4-3. Summary of unusable regions of heaters, defined as areas where temperature value deviated >2% above or below the mean temperature of each heater (computed from thermal images).

	Unusable fraction of heater area (%)				Max. width of unusable area (mm)			
Setpoint (°C)	**Heater 1**	**Heater 2**	**Heater 3**	**Heater 4**	**Heater 1**	**Heater 2**	**Heater 3**	**Heater 4**
50	0.27	0.43	3.88	4.01	0.38	0.38	0.76	1.15
100	0.33	0.98	6.85	3.90	0.38	0.38	1.15	1.14
140	1.01	2.81	8.27	4.89	0.38	0.76	1.52	1.52

Since the maximum width of the unusable region was 1.5 mm, we designed the multi-reaction chips such that the outermost 2.4 mm border was unused, and all reaction sites were entirely

located within the usable portion of the heater surface. **Figure 4-16** shows the detailed chip design. Chips are installed onto the heater platform in the orientations shown in **Figure 4-17.**

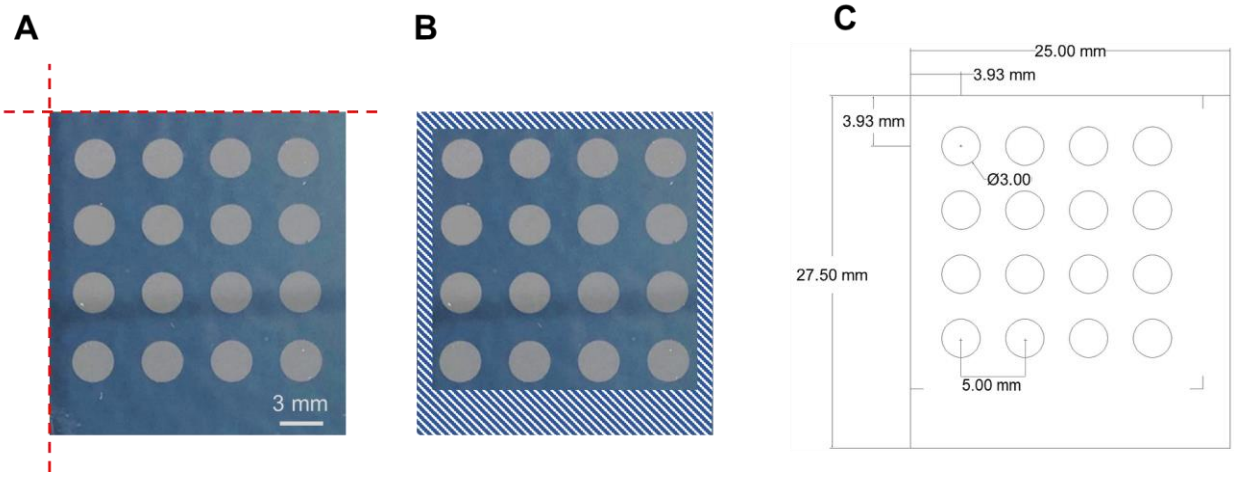

Figure 4-16. Chip dimensions.
(A) Photograph of the chip with 16 reactions sites. The chip is made from silicon coated with Teflon AF, and then the Teflon AF layer is etched away in the circular regions. (B) The hatched region shows the unusable region of the chip (due to >2% temperature deviation from the mean temperature of the heater in these regions). (C) Detailed chip design.

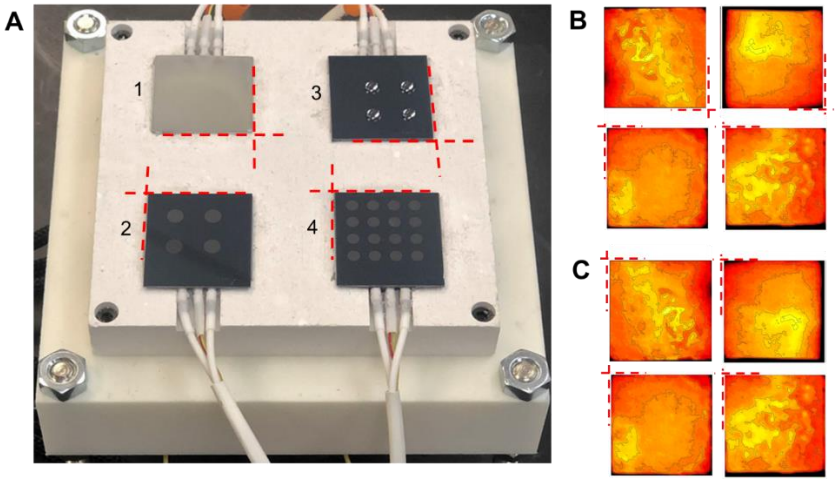

Figure 4-17. Chip positioning on heaters.
(A) Orientation of heaters. Red dashed lines indicate the reference corner for the alignment of chips to heaters. (B) Example thermal images from heater surfaces, shown in the actual heater orientation. (C) Thermal images in this paper are all rotated such that reference corner is located at the top left of each image.

4.7.4 Radio-TLC Methods

In order to use high-throughput radio-TLC for analysis of [^{18}F]Flumazenil, we first investigated different types of TLC plates (normal and RP-18 versions of silica gel 60 F_{254}, Merck KGaA

Darmstadt, Germany) and mobile phases from literature[141–143,145] (**Figure 4-18**). Crude samples were prepared in DMSO:water (2:1 v/v), and 1 μL samples were deposited on the TLC plates. Bands were identified by comparing their R_f values with the R_f values for samples of isolated (via HPLC purification) product. The best separation between [^{18}F]fluoride, [^{18}F]Flumazenil, and an unknown impurity was achieved using (normal) silica gel 60 F_{254} plates with 100% MeCN as the mobile phase. Due to the proximity of the impurity to the product under several conditions, it is possible that the bands might not be well resolved using some readout methods such as conventional radio-TLC scanners. When using DMSO as the reaction solvent, [^{18}F]Flumazenil samples exhibited up to 3 bands: [^{18}F]fluoride (R_f = 0), [^{18}F]Flumazenil (R_f = 0.7), and an unknown impurity (R_f = 0.9), but while using DMF, only 2 bands were observed: [^{18}F]fluoride (R_f = 0) and [^{18}F]Flumazenil (R_f = 0.8), with no impurity evident (also not observed using radio-HPLC).

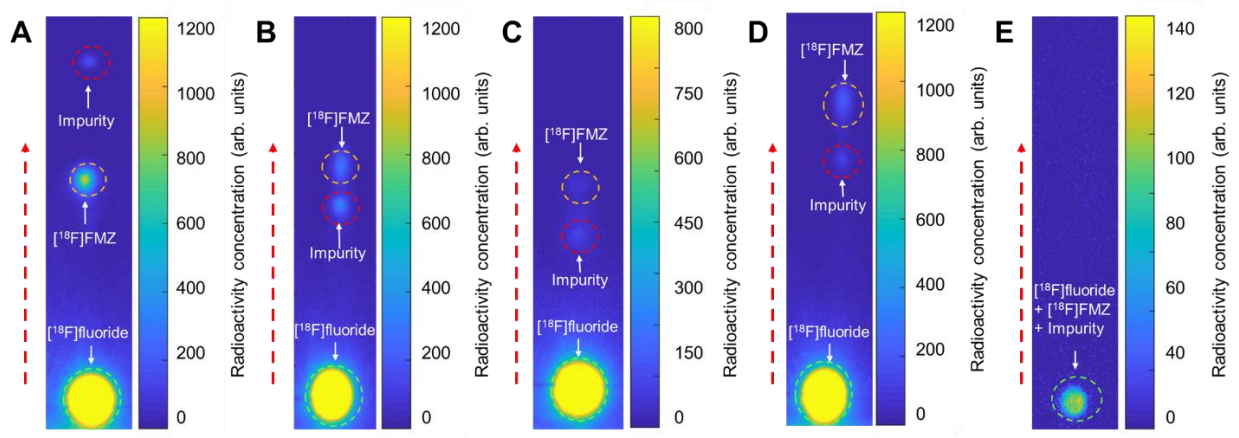

Figure 4-18. Development of radio-TLC separation method for crude [^{18}F]Flumazenil ([^{18}F]FMZ).
(A) Silica gel 60 F_{254} plate with mobile phase of 100% MeCN. (B) Silica gel 60 F_{254} plate with mobile phase of ethyl acetate: ethanol (80:20 v/v) as reported in Ryzhikov *et al.*[145]. (C) Silica gel 60 F_{254} plate with mobile phase ethyl acetate: ethanol: water (80:15:5 v/v) as reported in Vaulina *el al*.[141] and Nasirzadeh *et al*.[142]. (D) RP-18 silica gel 60 F_{254} plate with mobile phase ethyl acetate: ethanol (95:5 v/v) as reported in Mandap *et al.*[143]. (E) RP-18 silica gel 60 F_{254} plate with mobile phase MeCN: water (90:10 v/v). Dashed circles represent the ROIs for analysis. The dashed arrow represents the direction of solvent flow during development.

[^{18}F]PBR06 samples were spotted on silica gel 60 F_{254} plates and separated using 13:10:24:54 (v/v) dichloromethane:chloroform:acetone:hexanes as the mobile phase. Chromatograms exhibited up to 2 bands: [^{18}F]fluoride (R_f = 0) and [^{18}F]PBR06 (R_f = 0.4). [^{18}F]FEPPA samples were spotted on silica gel 60 F_{254} plates and separated using 25.6:37.5:36.5:0.4 (v/v) nBuOH:THF:hexanes:TEA as the mobile phase. Chromatograms exhibited up to 2 bands: [^{18}F]fluoride (R_f = 0) and [^{18}F]FEPPA (R_f = 0.6). Figure 4-19 shows example TLC images confirming the separation.

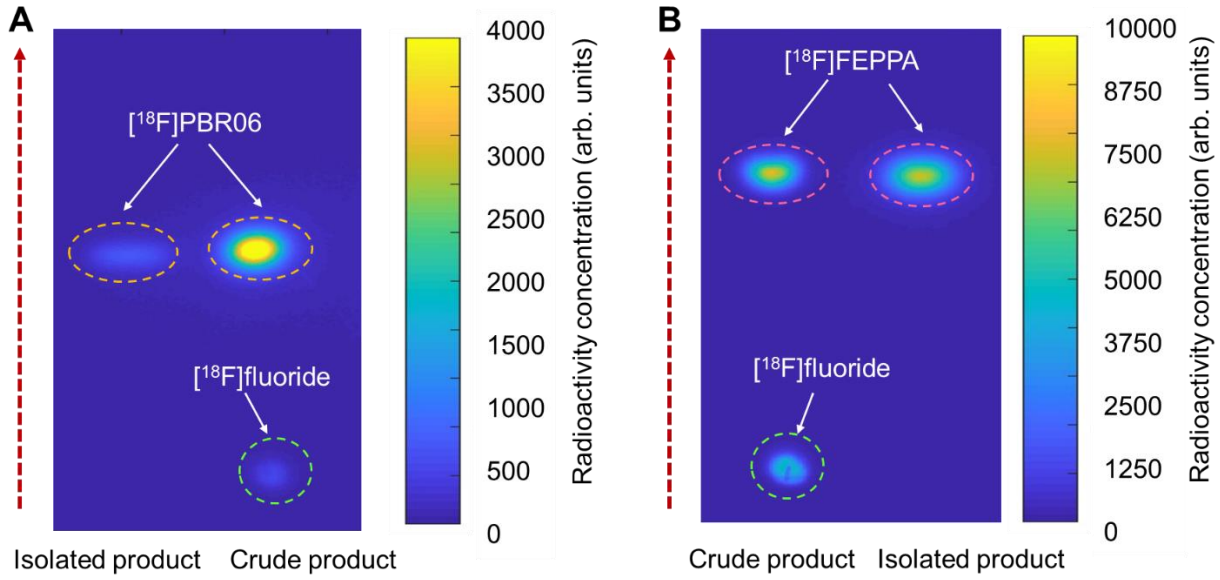

Figure 4-19. Cerenkov images of TLC plates confirming separation for [^{18}F]PBR06 and [^{18}F]FEPPA.
(A) Isolated [^{18}F]PBR06 (left lane) and the crude product after the end of synthesis (right lane). (B) Crude [^{18}F]FEPPA (left lane) and isolated product (right lane). The dashed red arrows indicate the direction of solvent movement during development. (To show more details of bands, images are cropped and do not include the full extent of the TLC plate.)

[^{18}F]Fallypride samples were spotted on silica gel 60 F_{254} plates and separated using 60% MeCN in 25 mM HN_4HCO_2 with 1% TEA (v/v), as previously reported[61]. [^{18}F]Fallypride chromatograms exhibited up to 3 bands: [^{18}F]fluoride (R_f = 0), [^{18}F]Fallypride (R_f = 0.8), and an impurity was previously reported when using high base amounts for the reaction (R_f = 0.9)[61].

4.7.5 Optimization of [^{18}F]Flumazenil synthesis

4.7.5.1 Reaction temperature and solvent

Experiments were performed by drying of [^{18}F]fluoride/[^{18}O]H_2O under identical conditions (13-15 MBq [0.35-0.40 mCi], mixed with 480 nmol of $TBAHCO_3$), and then performing fluorination at different temperatures and in different solvents. The first batch of experiments was performed with heaters 1 – 4 set at 100, 120, 140, and 160 °C, respectively, and a second batch was performed with heaters 1 – 4 set at 180, 200, 220, and 240 °C, respectively (**Figure 4-3A**). Other parameters in the reaction were chosen to be similar to other syntheses we have adapted to droplet format, i.e., 8 µL reaction volume, 480 nmol of $TBAHCO_3$, and 280 nmol of precursor[61,103,138]. The initial reaction time was chosen to be 2 min, matching the condition reported for a flow microreactor[33]. The crude [^{18}F]Flumazenil product was then collected with 40 µL of 2:1 v/v solvent/water mixture (i.e., the same solvent as used in the reaction). The collection solution loading and collecting were 10 µL at a time and were repeated a total of 4 times to minimize the residue left behind at the reaction. Cerenkov images of chips showing residual activity after collection are shown in **Figure 4-3B** of the main paper and radio-TLC data are shown in **Figure 4-3C & D.** Detailed analyses for each individual reaction (collection efficiency, fluorination efficiency, crude RCY, and activity left on-chip) are tabulated in **Table 4-4.**

Table 4-4. Summary of data acquired when exploring the effects of temperature and solvent in the radiosynthesis of [^{18}F]Flumazenil.

Solvent	Temperature (°C)	Collection efficiency (%) n=4	Fluorination efficiency (%) n=4	Crude RCY (%) n=4	Activity left on chip (%) n=4
DMSO	100	93.4 ± 1.7	1.1 ± 0.5	1.0 ± 0.5	0.6 ± 0.1
	120	90.6 ± 3.5	4.0 ± 0.4	3.6 ± 0.5	1.1 ± 0.2
	140	78.8 ± 4.4	9.7 ± 0.9	7.7 ± 0.6	1.6 ± 0.1
	160	64.6 ± 2.5	13.3 ± 1.1	8.6 ± 0.7	1.8 ± 0.2
	180	33.4 ± 0.7	26.1 ± 2.0	8.7 ± 0.8	1.7 ± 0.2
	200	25.7 ± 2.5	41.7 ± 3.4	10.7 ± 1.6	2.2 ± 2.0
	220	12.8 ± 2.3	47.1 ± 1.6	5.9 ± 1.1	8.9 ± 2.6
	240	10.3 ± 2.7	50.0 ± 1.6	5.2 ± 1.5	8.9 ± 2.5
DMF	100	93.6 ± 2.4	2.1 ± 0.5	2.0 ± 0.5	1.0 ± 0.2
	120	90.0 ± 0.3	5.1 ± 0.6	4.6 ± 0.6	2.0 ± 0.4
	140	75.8 ± 4.2	14.2 ± 2.8	10.7 ± 1.7	2.3 ± 0.5

	160	65.7 ± 4.3	19.1 ± 1.8	12.5 ± 0.8	2.5 ± 0.2
	180	55.8 ± 3.2	21.7 ± 0.9	12.1 ± 0.8	2.9 ± 0.2
	200	49.0 ± 3.6	27.5 ± 0.9	13.5 ± 0.6	3.1 ± 0.5
	220	25.1 ± 3.3	30.5 ± 2.1	7.7 ± 1.4	5.4 ± 1.0
	240	17.9 ± 2.6*	39.1 ± 4.1*	7.0 ± 1.2*	5.7 ± 1.5 *

*One reaction was performed incorrectly, and so only n=3 repeats are summarized

4.7.5.2 Base amount and solvent

Experiments to explore the effect of base amount were conducted by mixing [^{18}F]fluoride/[^{18}O]H_2O (13-15 MBq [0.35-0.40 mCi]) with different amounts of the base $TBAHCO_3$ for the drying step as shown in **Figure 4-20A**. Chip 1 and 2 explored different base amounts using DMF as the solvent, and chips 3 and 4 explored different base amounts using DMSO as the solvent. All reactions were performed using 280 nmol of precursor in 8 μL of solvent and reacting for 2 min at 200 °C. Cerenkov images of chips showing residual activity after collection are shown in **Figure 4-20B** and radio-TLC data from reactions is shown in **Figure 4-21**. Detailed analyses for each reaction are tabulated in **Table 4-5.**

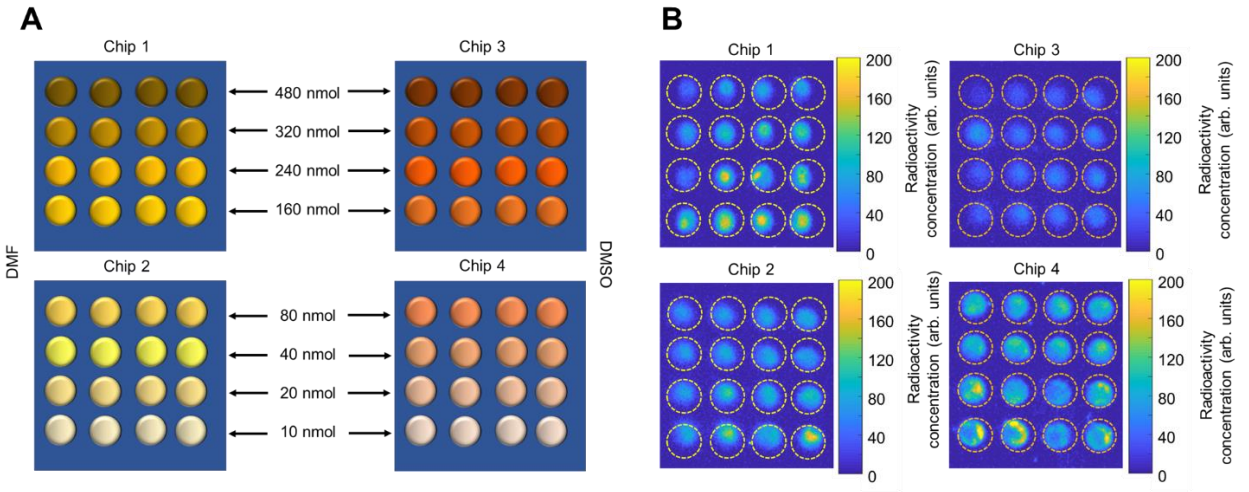

Figure 4-20. Experimental setup for the exploration of base amount and solvent.
(A) Experimental setup for one batch of experiments that explored the influence of base amount (8 values) and solvent (2 types) on the synthesis of [^{18}F]Flumazenil. All 64 reactions were run simultaneously. (B) Cerenkov images showing the distribution of the residual activity on each chip after the collection of all the crude samples. Brightness is decay-corrected to a common timepoint for all images.

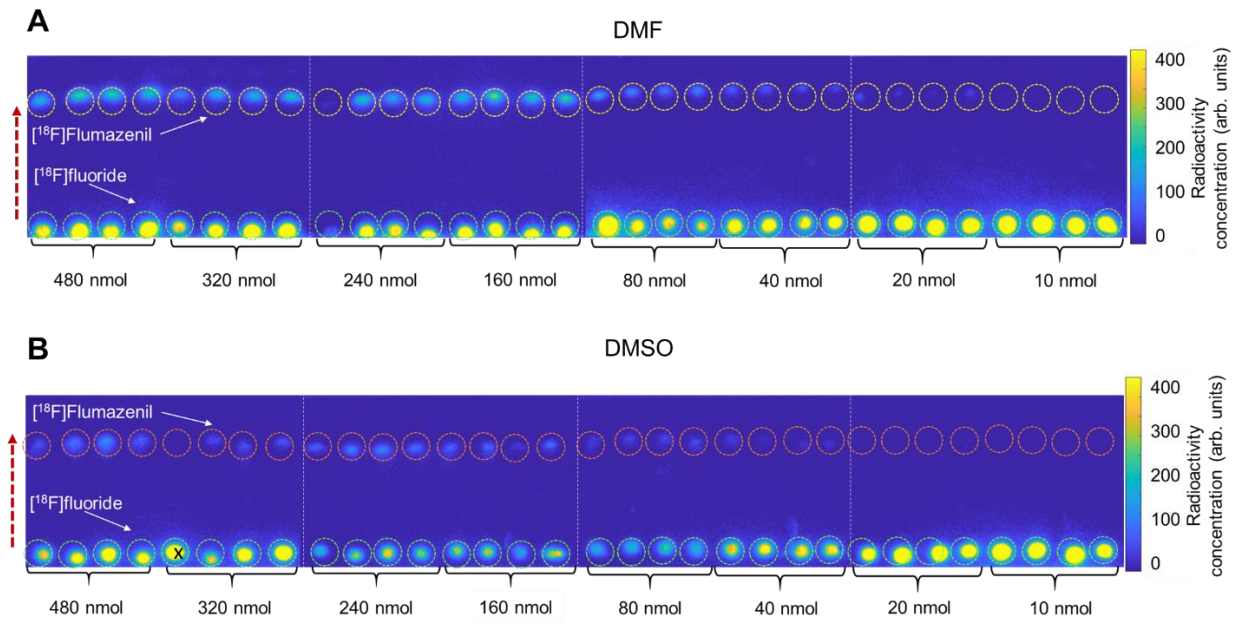

Figure 4-21. Cerenkov images of TLC plates (each containing 8 samples) after developing. In this case, each TLC plate contains samples from two different base amounts in one reaction solvent (n=4 replicates each). White dotted lines show the edges of each separate multi-sample TLC plate. (A) Spotted crude samples using DMF as the reaction solvent. (B) Spotted crude samples using DMSO as the reaction solvent. Dashed circles indicate the ROIs used for analysis. The dashed red arrow indicates the direction of solvent movement during development. The "X" represents an experimental error and was excluded from further analysis.

Table 4-5. Summary of data acquired when exploring the effect of the base amount in the radiosyntheses of [^{18}F]Flumazenil in two different solvents.

Solvent	Base amount (nmol)	Collection efficiency (%) n=4	Fluorination efficiency (%) n=4	Crude RCY (%) n=4	Activity left on chip (%) n=4
DMF	480	47.0 ± 5.0	25.8 ± 3.6	12.1 ± 1.6	3.7 ± 1.9
	320	37.7 ± 8.0	30.5 ± 4.5	11.5 ± 0.5	5.4 ± 0.7
	240	38.7 ± 2.2	32.1 ± 2.8	12.4 ± 0.5	6.0 ± 2.0
	160	39.0 ± 3.9	32.7 ± 2.8	12.7 ± 0.9	7.9 ± 1.0
	80	27.7 ± 2.5	16.9 ± 3.1	4.6 ± 0.4	4.6 ± 0.2
	40	27.6 ± 2.5	7.0 ± 1.4	1.9 ± 0.5	4.9 ± 0.4
	20	37.6 ± 3.3	4.3 ± 0.7	1.6 ± 0.1	5.7 ± 0.7
	10	43.8 ± 3.0	1.1 ± 0.4	0.5 ± 0.1	6.8 ± 1.0
DMSO	480	43.0 ± 2.0	22.5 ± 2.5	9.7 ± 1.2	3.9 ± 1.0
	320	30.1 ± 0.5	32.5 ± 2.3	9.8 ± 0.3	5.2 ± 0.3
	240	27.9 ± 6.5	32.2 ± 1.8	9.0 ± 2.0	5.3 ± 0.8
	160	21.8 ± 2.7	22.9 ± 3.8	5.0 ± 1.2	5.2 ± 0.6
	80	25.6 ± 1.5	21.0 ± 2.0	5.4 ± 0.5	5.1 ± 0.3
	40	32.7 ± 2.2	8.2 ± 2.2	2.7 ± 0.6	5.3 ± 0.4
	20	45.6 ± 8.4	3.8 ± 1.5	1.6 ± 0.4	5.9 ± 1.3
	10	55.3 ± 4.8	1.9 ± 0.5	1.0 ± 0.2	6.9 ± 1.5

*One reaction was performed incorrectly, and so only n=3 repeats are summarized

4.7.5.3 Precursor amount and solvent

Effect of precursor amount experiments were conducted as depicted in **Figure 4-22A**. Drying of [^{18}F]fluoride/[^{18}O]H_2O was performed under identical conditions (13-15 MBq [0.35-0.4 mCi], mixed with 240 nmol of $TBAHCO_3$), and the subsequent fluorination reactions were performed with different amounts of precursor dissolved in the 8 μL droplet and reacted at 200 °C for 2 min. Chips 1 and 2 used DMF as the solvent, while chips 3 and 4 used DMSO. Cerenkov images of chips showing residual activity after collection are shown in **Figure 4-22B** and radio-TLC data is shown in **Figure 4-23**. Detailed analyses for each individual reaction are tabulated in **Table 4-6**.

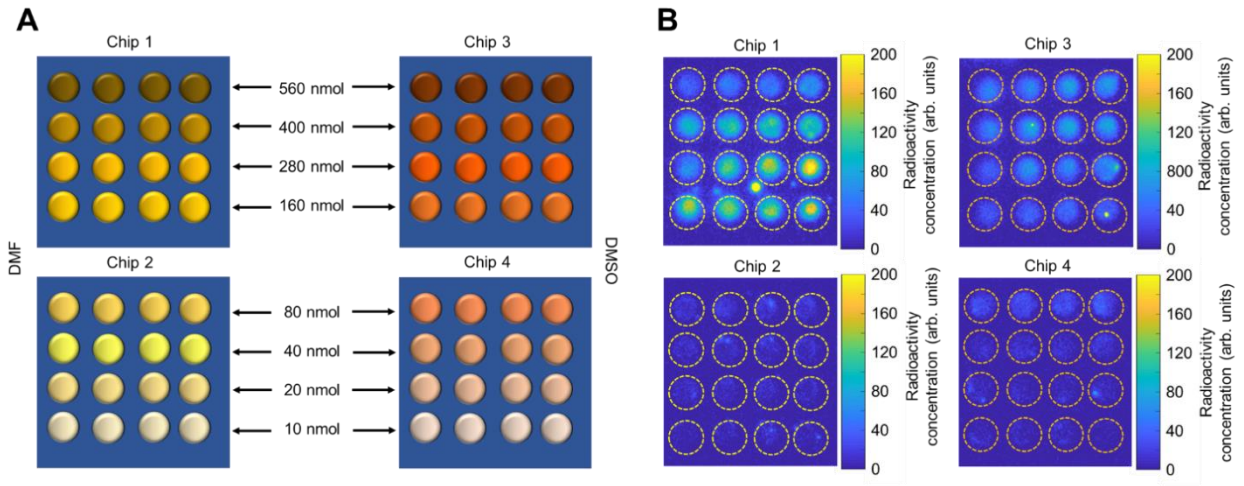

Figure 4-22. Experimental setup for the exploration of precursor amount and solvent.
(A) Experimental setup for one batch of experiments that explored the influence of precursor amount (8 values) and solvent (2 types) on the synthesis of [^{18}F]Flumazenil. All 64 reactions were performed simultaneously. (B) Cerenkov images show the distribution of the residual activity on each chip after collecting all the crude samples. Brightness is decay-corrected to a common timepoint for all images.

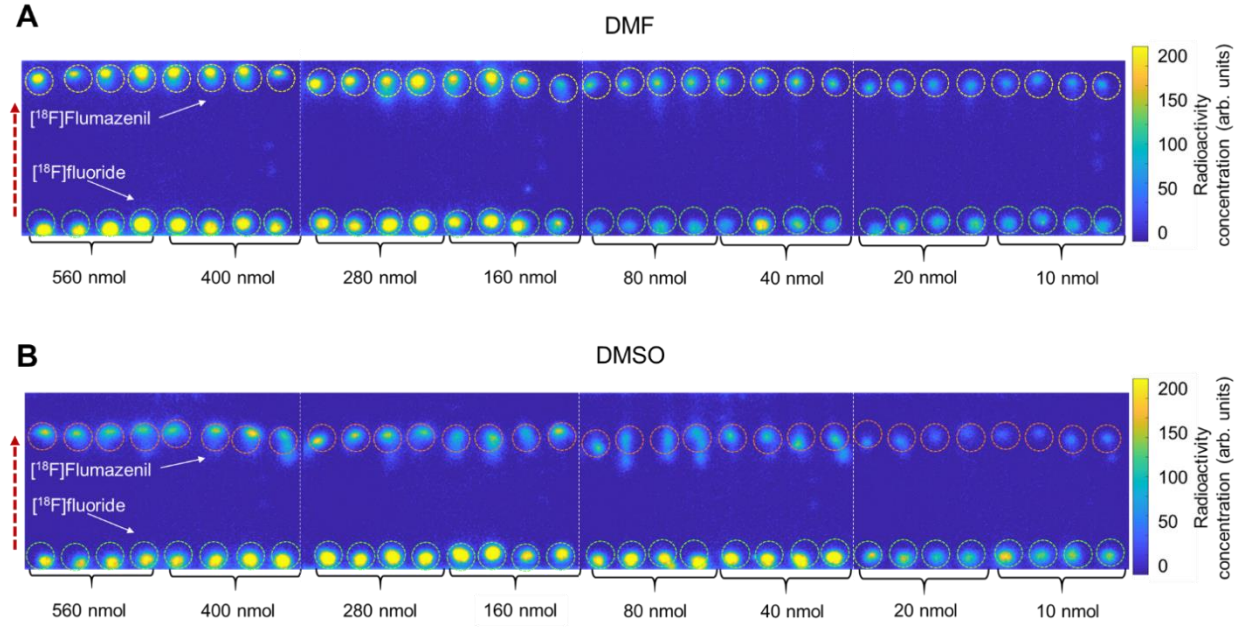

Figure 4-23. Cerenkov images of TLC plates (each containing 8 samples) after developing in the mobile phase.
In this case, each TLC plate contains samples from two different precursor amount conditions in one reaction solvent (n=4 replicates each). White dotted lines show the edges of each separate multi-sample TLC plate. (A) Spotted crude samples using DMF as the reaction solvent. (B) Spotted crude samples using DMSO as the reaction solvent. Dashed circles indicate the ROIs used for analysis. The dashed red arrow indicates the direction of solvent movement during development.

Table 4-6. Summary of data acquired when exploring the effect of precursor amount in the radiosyntheses of [^{18}F]Flumazenil.

Solvent	Precursor amount (nmol)	Collection efficiency (%) n=4	Fluorination efficiency (%) n=4	Crude RCY (%) n=4	Activity left on chip (%) n=4
DMF	560	23.3 ± 6.8	39.2 ± 4.9	9.2 ± 3.1	2.7 ± 0.5
	400	21.0 ± 4.2	44.6 ± 4.6	9.5 ± 2.7	5.3 ± 0.5
	280	24.0 ± 3.3	47.9 ± 1.6	11.5 ± 1.4	6.1 ± 1.9
	160	19.6 ± 3.5	48.3 ± 5.3	9.5 ± 2.3	6.6 ± 0.6
	80	20.4 ± 0.5	54.5 ± 2.3	11.1 ± 0.3	5.9 ± 0.3
	40	10.0 ± 1.8	48.0 ± 9.0	4.7 ± 0.3	4.9 ± 0.7
	20	8.7 ± 0.9	41.6 ± 3.7	3.4 ± 0.2	4.3 ± 0.3
	10	7.3 ± 0.7	41.9 ± 4.0	3.1 ± 0.3	3.7 ± 1.0
DMSO	560	22.3 ± 1.9	43.9 ± 4.0	9.7 ± 0.4	5.5 ± 0.6
	400	24.9 ± 1.7	39.8 ± 3.0	9.9 ± 0.2	6.3 ± 0.8
	280	23.9 ± 2.8	35.4 ± 3.6	8.5 ± 1.6	5.6 ± 1.6
	160	21.6 ± 3.3	38.3 ± 4.8	8.2 ± 1.3	3.9 ± 0.7
	80	20.7 ± 2.3	36.8 ± 2.3	7.6 ± 1.0	9.1 ± 0.6
	40	17.3 ± 1.2	32.9 ± 1.8	5.7 ± 0.5	4.2 ± 0.8
	20	14.2 ± 1.2	27.7 ± 3.2	3.9 ± 0.7	3.6 ± 1.0
	10	13.0 ± 0.8	19.7 ± 3.3	2.5 ± 0.3	2.7 ± 0.7

4.7.5.4 Effect of base to precursor ratio

Figure 4-24 summarizes the effect of base to precursor ratio on collection efficiency, fluorination efficiency, and crude RCY. This data has all been previously presented above, but here it is reorganized to show the dependence on base to precursor ratio. **Table 4-7** tabulates the values of base to precursor ratio used as the x-axis in **Figure 4-24.**

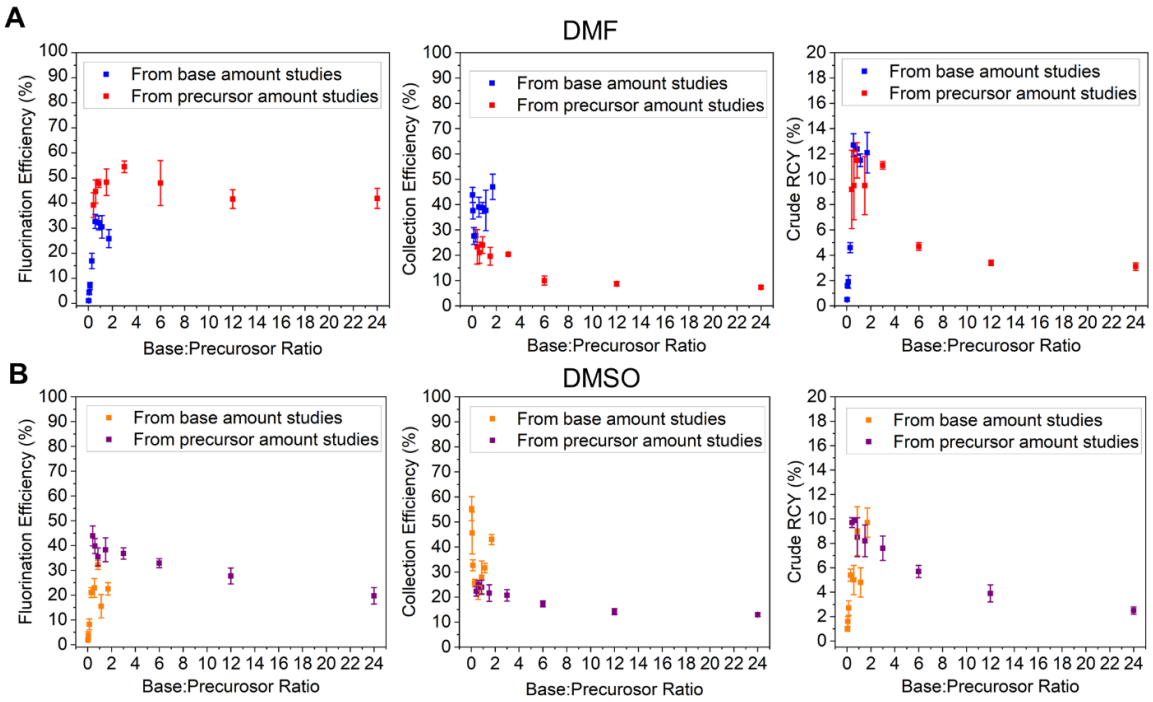

Figure 4-24. Summary of the impact of the base to precursor molar ratio on the synthesis of [^{18}F]Flumazenil.
Data points are derived from other experiments as indicated. Graphs in (A) used DMF as a reaction solvent. Graphs in (B) used DMSO as the reaction solvent.

Table 4-7. Tabulated values of the base to precursor ratios used in both DMF and DMSO.

	Base:Precursor (nmol:nmol)	Base:Precursor ratio		Base:Precursor (nmol:nmol)	Base:Precursor Ratio
Data from base amount study	480:280	1.71	**Data from precursor amount study**	240:560	0.43
	320:280	1.14		240:400	0.60
	240:280	0.86		240:280	0.86
	160:280	0.57		240:160	1.50
	80:280	0.29		240:80	3.00
	40:280	0.14		240:40	6.00
	20:280	0.07		240:20	12.0
	10:280	0.04		240:10	24.0

4.7.5.5 Reaction time and solvent

The study of the effect of reaction time on the synthesis of [^{18}F]Flumazenil was conducted as shown in **Figure 4-25A**. First, [^{18}F]fluoride/[^{18}O]H_2O was dried under identical conditions (13-15 MBq [0.35-0.40 mCi], mixed with 240 nmol of $TBAHCO_3$), and then the fluorinations were carried out for different amounts of time and in different solvents. All fluorinations used 280 nmol of

precursor in 8 μL of reaction solvent and were carried out at 200 °C. A first batch of experiments used reaction times of 30, 60, 120, and 180 s on heaters 1 – 4, respectively, followed by a second batch with reaction times of 240, 300, 360, and 420 s. Cerenkov images of chips showing residual activity after collection are shown in **Figure 4-25B** and radio-TLC data are shown in **Figure 4-26.** Detailed analyses for each individual reaction are tabulated in **Table 4-8**.

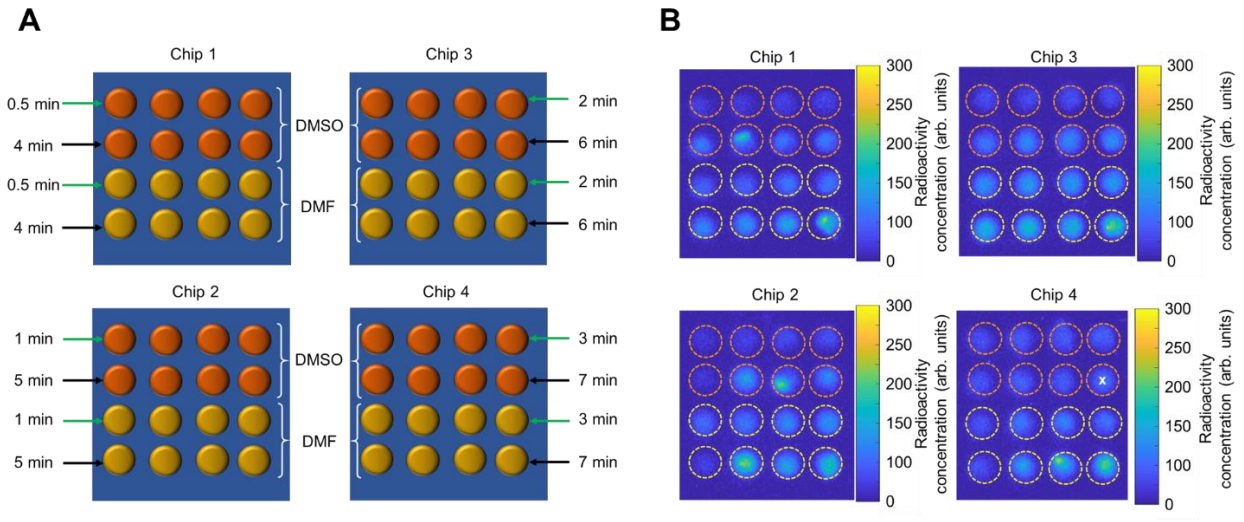

Figure 4-25. Experimental setup for to study the effects of time and reaction solvent. (A) Experimental setup for one batch of experiments that explored the influence of reaction time (8 values) and solvent (2 types) on the synthesis of [^{18}F]Flumazenil. (B) Cerenkov images showing the distribution of the residual activity on each chip after collection of all the crude samples. Brightness is decay-corrected to a common timepoint for all images. The reaction marked with an "X" was not analyzed as a mistake was made in the reaction.

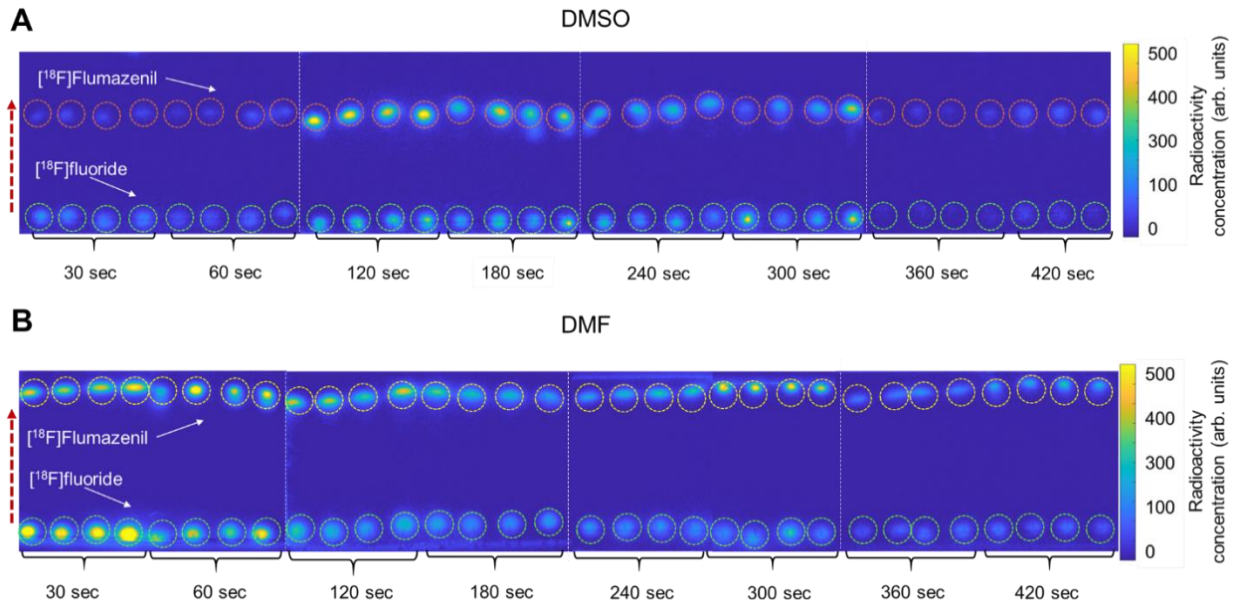

Figure 4-26. Cerenkov images of TLC plates (each containing 8 samples) after developing in the mobile phase.

In this case, each TLC plate contains samples from two different time conditions in one reaction solvent (n=4 replicates each). White dotted lines represent the boundary of each multi-sample plate. (A) Spotted crude samples using DMSO as the reaction solvent. (B) Spotted crude samples using DMF as the reaction solvent. Dashed circles indicate the ROIs used for analysis. The dashed red arrow indicates the direction of solvent movement during development.

Table 4-8. Summary of data acquired when exploring the effect of reaction time and solvent in the radiosyntheses of [^{18}F]Flumazenil.

Solvent	Time (min)	Collection efficiency (%) n=4	Fluorination efficiency (%) n=4	Crude RCY (%) n=4	Activity left on chip (%) n=4
DMSO	0.5	27.1 ± 0.7	26.7 ± 2.7	7.2 ± 0.8	2.5 ± 0.1
	1.0	20.2 ± 0.6	36.4 ± 8.8	7.4 ± 1.8	2.8 ± 0.6
	2.0	14.2 ± 1.9	44.1 ± 4.3	6.2 ± 0.7	4.5 ± 0.4
	3.0	15.8 ± 1.0	65.0 ± 3.4	10.3 ± 0.7	4.5 ± 0.4
	4.0	14.9 ± 1.2	63.4 ± 3.9	9.4 ± 0.8	5.1 ± 0.9
	5.0	12.7 ± 4.4	60.1 ± 4.2	7.6 ± 2.2	7.7 ± 2.9
	6.0	12.5 ±0.8	60.8 ± 4.5	7.5 ± 1.0	5.2 ± 0.6
	7.0	16.8 ± 0.4*	66.7 ± 4.9*	11.2 ± 0.6*	7.2 ± 0.9*
DMF	0.5	35.7 ± 1.6	43.1 ± 2.0	15.4 ± 0.9	4.9 ± 0.2
	1.0	29.4 ± 4.4	47.5 ± 3.8	14.0 ± 2.4	5.1 ± 0.9
	2.0	26.8 ± 2.2	51.4 ± 1.6	13.7 ± 1.3	6.2 ± 0.5
	3.0	26 ± 2.1	54.4 ± 5.2	14.4 ± 1.5	6.7 ± 1.5
	4.0	18.3 ± 1.7	55.9 ± 4.0	10.6 ± 1.2	5.8 ± 0.2
	5.0	17.7 ± 0.3	59.8 ± 2.8	10.6 ± 0.4	6.0 ± 0.2
	6.0	18.8 ± 1.3	57.8 ± 2.1	11.0 ± 0.5	5.5 ± 0.3
	7.0	16.3 ± 0.8	61.2 ± 4.4	10.0 ±0.8	6.4 ± 0.4

*Reaction was performed incorrectly and so only n=3 repeats are summarized

4.7.5.6 Further studies of reaction solvent and temperature

We further explored the use of different aprotic solvents with a high boiling point for reactions at 200°C. In addition to DMF and DMSO, the solvents tested were N-methyl-2-pyrrolidone (NMP; BP: 202 °C), 1,3-dimethyl-3,4,5,6-tetrahydro-2(1H)-pyrimidinone (DMPU; BP: 247 °C), and ethylene glycol (BP: 197 °C). The experimental design is described in **Figure 4-27A.** Experiments were performed by drying of [^{18}F]fluoride/[^{18}O]H_2O under identical conditions (13-15 MBq [0.35-0.40 mCi], mixed with 240 nmol of $TBAHCO_3$), and then performing fluorination in different solvents (each replicated n=3 times). Cerenkov image of the chip showing residual activity after collection is shown in **Figure 4-27B**, and radio-TLC data is shown in **Figure 4-28.** Detailed analyses for each individual reaction are tabulated in **Table 4-9.**

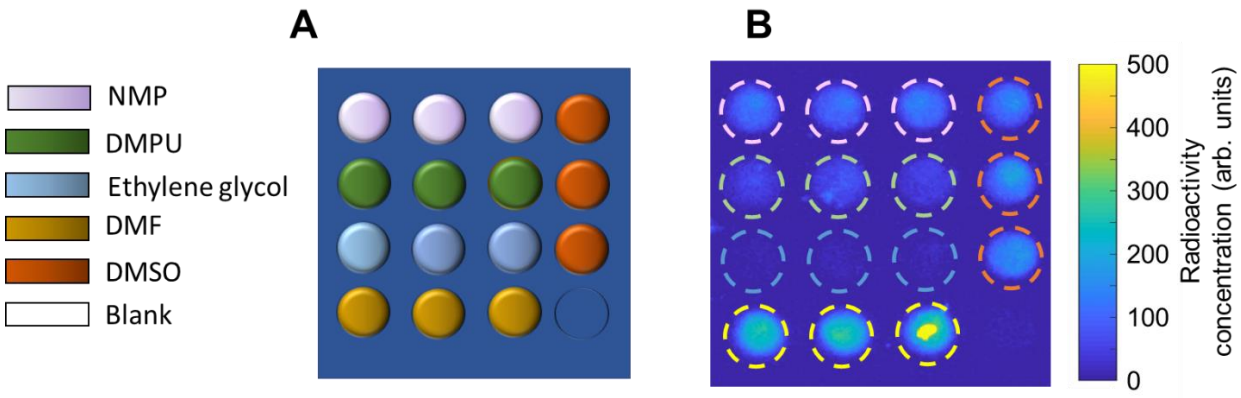

Figure 4-27. Solvent effect experimental set up.
(A) Experimental setup for one batch of experiments that explored the influence of type of solvent (5 types) on the synthesis of [^{18}F]Flumazenil. (B) Cerenkov images showing the distribution of the residual activity on each chip after collection of all of the crude samples.

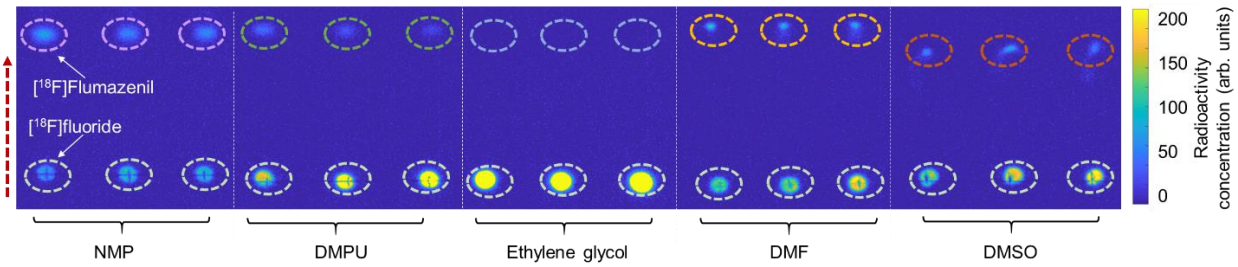

Figure 4-28. Cerenkov images of TLC plates (each containing 3 samples) after developing in the mobile phase.
In this case, each TLC plate contains samples using one of the reaction solvents (n=3 replicates each). Dashed circles indicate the ROIs used for analysis. The dashed red arrow indicates the direction of solvent movement during development.

Table 4-9. Summary of data acquired when exploring the effect of type of base and reaction solvent in the radiosyntheses of [^{18}F]Flumazenil.

Solvent	Collection efficiency (%) n=3	Fluorination efficiency (%) n=3	Crude RCY (%) n=3	Activity left on chip (%) n=3
NMP	37.4 ± 1.1	48.8 ± 6.5	18.2 ± 2.0	5.0 ± 0.3
DMPU	49.5 ± 8.2	18.1 ± 3.5	8.8 ± 0.3	3.1 ± 0.8
Ethylene glycol	108.5 ± 5.0	2.3 ± 0.5	2.5 ± 0.4	0.6 ± 0.1
DMF	46.1 ± 1.8	32.8 ± 2.3	15.1 ± 0.5	10.5 ± 2.9
DMSO	35.1 ± 4.5	25.3 ± 0.2	8.9 ± 1.1	5.7 ± 0.6

We then explored the effect of temperature using NMP as reaction solvent for the radiosynthesis of [^{18}F]Flumazenil, as shown in **Figure 4-29A.** Experiments were performed by drying of [^{18}F]fluoride/[^{18}O]H_2O under identical conditions (13-15 MBq [0.35-0.40 mCi], mixed with 240 nmol of $TBAHCO_3$), and then performing fluorination at different temperatures. Though this experiment could be implemented using 4 chips on 4 heaters, since only 4 reaction sites were needed per temperature value, the experiment was instead performed using just 2 chips in multiple batches. The first batch of experiments was performed with heaters 1 and 2 set at 100 and 120 °C, respectively, a second batch with temperatures of 140, 160 °C, the third batch with temperatures of 180 and 200 °C, and a final batch with temperatures of 220 and 240 °C. All reactions were performed in 8 µL volume, with 240 nmol base, 280 nmol precursor, and 0.5 min reaction time. Cerenkov images of chips showing residual activity after collection are shown in **Figure 4-29B**, and radio-TLC data are shown in **Figure 4-30**. Detailed analyses for each

individual reaction are tabulated in **Table 4-10**, and the results are plotted in **Figure 4-31**. The optimal temperature was 200 °C, giving a crude RCY of 19.1 ± 0.6% (n=4).

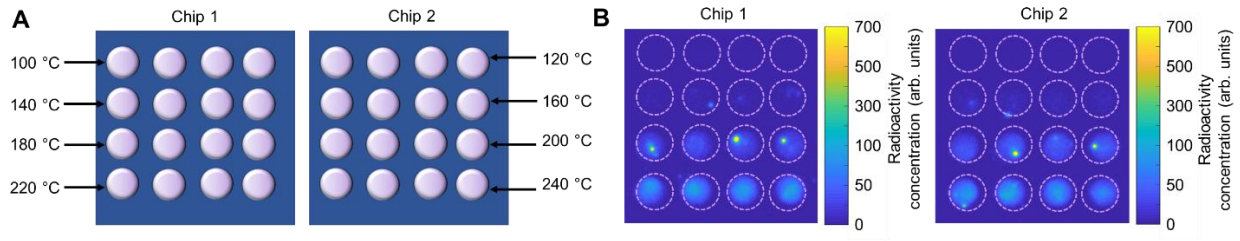

Figure 4-29. NMP solvent and temperature study.
(A) Experimental setup for one batch of experiments that explored the influence of reaction temperature (8 values) in NMP as reaction solvent on the synthesis of [^{18}F]Flumazenil. (B) Cerenkov images showing the distribution of the residual activity on each chip after collection of all the crude samples. Brightness is decay-corrected to a common timepoint for all images.

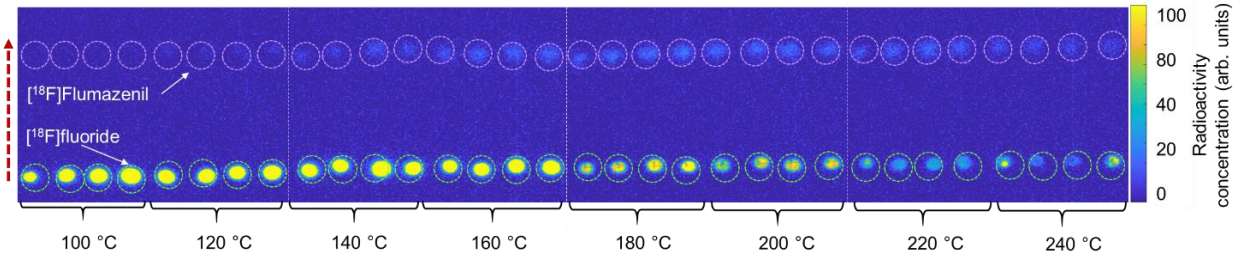

Figure 4-30. Cerenkov images of TLC plates (each containing 8 samples) after developing in the mobile phase.
In this case, each TLC plate contains samples from two different temperatures (n=4 replicates each). White dotted lines show the edges of each separate multi-sample TLC plate. Dashed circles indicate the ROIs used for analysis. The dashed red arrow indicates the direction of solvent movement during development.

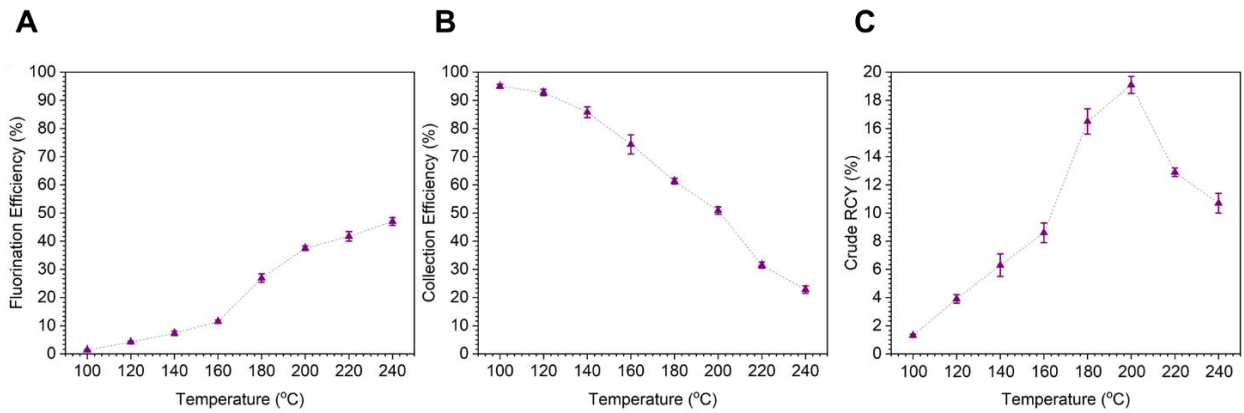

Figure 4-31. Effect of temperature on the performance of [^{18}F]Flumazenil synthesis with NMP as the reaction solvent.
(A) Effect on fluorination efficiency. (B) Effect on collection efficiency. (C) Effect on crude RCY.

Table 4-10. Summary of data acquired when exploring the effect of temperature (with NMP as reaction solvent) on the radiosyntheses of [^{18}F]Flumazenil.

Temperature (°C)	Collection efficiency (%) n=4	Fluorination efficiency (%) n=4	Crude RCY (%) n=4	Activity left on chip (%) n=4
100	95.0 ± 0.7	1.4 ± 0.1	1.3 ± 0.1	0.11 ± 0.01
120	92.8 ± 1.1	4.2 ± 0.3	3.9 ± 0.3	0.24 ± 0.03
140	85.8 ± 1.9	7.3 ± 0.8	6.3 ± 0.8	0.9 ± 0.2
160	74.4 ± 3.4	11.3 ± 0.5	8.6 ± 0.7	1.4 ± 0.4
180	61.3 ± 1.0	26.9 ± 1.5	16.5 ± 0.9	7.4 ± 0.9
200	50.9 ± 1.3	37.5 ± 0.8	19.1 ± 0.6	8.1 ± 1.7
220	31.5 ± 1.1	41.7 ± 1.7	12.9 ± 0.3	12.7 ± 0.1
240	22.8 ± 1.3	47.0 ± 1.9	10.7 ± 0.7	11.1 ± 2.1

4.7.5.7 Base type and solvent

Finally, we explored the use of different types of base/phase transfer catalyst, comparing Kryptofix (K_{222}) with K_2CO_3, K_{222} with Cs_2CO_3, and $TBAHCO_3$, as well as three different solvents (DMF, DMSO, and NMP). Only 2 chips were used for this study. For the drying step, 13-15 MBq [0.35-0.40 mCi] of [^{18}F]fluoride/[^{18}O]H_2O was loaded to each reaction site. The experiment was organized as shown in **Figure 4-32A**. After drying, the subsequent fluorinations were performed with 280 nmol of precursor in 8 µL of DMF, DMSO, or NMP and reacted at 200°C for 0.5 min. Cerenkov image of the chip showing residual activity after collection is shown in **Figure 4-32B**, and radio-TLC data is shown in **Figure 4-33**. Detailed analyses for each individual reaction are tabulated in **Table 4-11**.

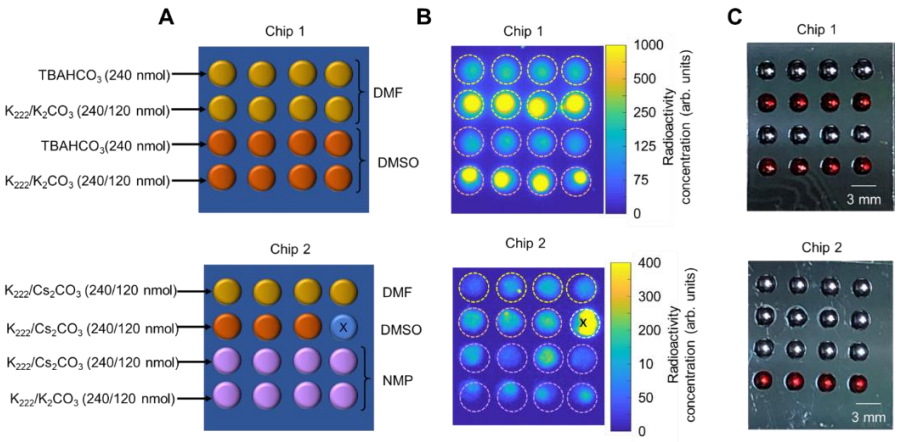

Figure 4-32. Base type study.
(A) Experimental setup for one batch of experiments that explored the influence of type of base (3 types) and solvent (3 types) on the synthesis of [^{18}F]Flumazenil. (B) Cerenkov images showing the distribution of the residual activity on each chip after the collection of all of the crude samples.

(C) Photograph of chips showing the different droplet colors (during fluorination) depending on which base was initially dried on the chip. The reaction marked with an “X” was not analyzed as a mistake was made in the reaction.

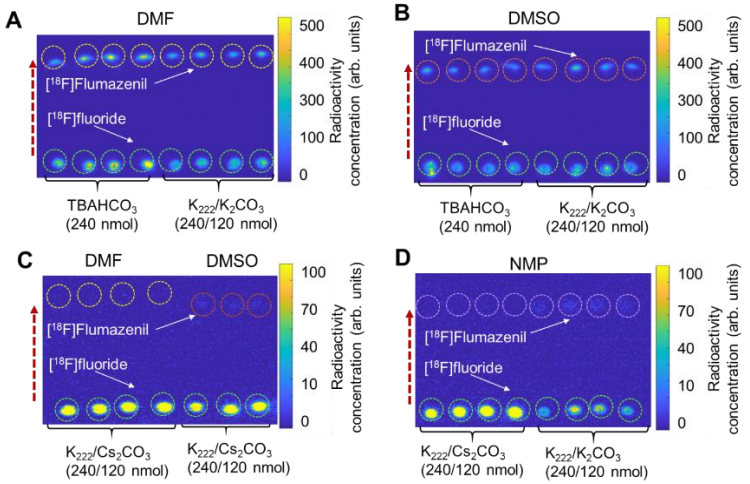

Figure 4-33. Cerenkov images of TLC plates after developing. Each TLC plate contains data from 2 different combinations of solvent and base/phase transfer catalyst (n=4 replicates each).

Dashed circles indicate the ROIs used for analysis. The dashed red arrow indicates the direction of solvent movement during development. (A) Separated crude samples using DMF as the reaction solvent. (B) Separated crude samples using DMSO as the reaction solvent. (C) Separated crude samples using DMF or DMSO as the reaction solvent. (D) Separated crude samples using NMP as the reaction solvent.

Table 4-11. Summary of data acquired when exploring the effect of type of base and reaction solvent in the radiosyntheses of [^{18}F]Flumazenil.

Solvent	Base type and amount (nmol)	Collection efficiency (%) n=4	Fluorination efficiency (%) n=4	Crude RCY (%) n=4	Activity left on chip (%) n=4
DMF	$TBAHCO_3$ (240)	40.5 ± 3.0	38.6 ± 2.6	15.7 ± 1.5	3.3 ± 0.2
	K_{222}/K_2CO_3 (240/120)	28.4 ± 0.8	33.8 ± 5.1	9.6 ± 1.6	8.9 ± 0.9
	K_{222}/Cs_2CO_3 (240/120)	68.1 ± 2.9	2.5 ± 0.6	1.7 ± 0.3	3.7 ± 1.1
DMSO	$TBAHCO_3$ (240)	30.8 ± 3.8	33.4 ± 4.7	10.3 ± 2.0	2.8 ± 0.3
	K_{222}/K_2CO_3 (240/120)	30.8 ± 2.2	34.2 ± 2.5	10.4 ± 1.5	6.6 ± 1.4
	K_{222}/Cs_2CO_3 (240/120)	50.3 ± 4.1*	5.1 ± 2.4*	2.5 ± 1.0*	6.1 ± 0.4*
NMP	$TBAHCO_3$ (240)	50.9 ± 1.3#	37.5 ± 0.8#	19.1 ± 0.6#	8.1 ± 1.7#
	K_{222}/K_2CO_3 (240/120)	25.8 ± 2.8	21.9 ± 1.7	5.6 ± 0.2	3.1 ± 0.6
	K_{222}/Cs_2CO_3 (240/120)	76.2 ± 5.4	3.4 ± 1.3	2.6 ± 0.9	4.2 ± 1.9

*One reaction was performed incorrectly, and so only n=3 repeats are summarized

4.7.5.8 Comparison to literature methods

Table 4-12. Comparison of optimized droplet conditions with literature reports for conventional and flow chemistry synthesis of [^{18}F]flumazenil.

	This work	Wong et al[33]. (2012)	Vaulina et al[141]. (2018)	Nasirzadeh et al[142]. (2016)	Mandap et al[143]. (2009)	Massaweh et al[144]. (2009)	Ryzhikov et al[145]. (2005)
Synthesizer type	Microscale (droplet format)	Microscale (flow format)	Macroscale	Macroscale	Macroscale	Macroscale	Macroscale
Base type	$TBAHCO_3$	K_{222} / $KHCO_3$	K_{222} / K_2CO_3	K_{222} / K_2CO_3	K_{222} / K_2CO_3	K_{222} / K_2CO_3	K_{222} / K_2CO_3
Base amount (nmol)	240	2850 / 2590#	18900 / 10100	25000 / 12000	12100 / 1800	27700 / 1200	25000 / 12000
Precursor amount (nmol)	280	1500	4500	3000-6100‡	6100	18000-21000	25000
Reaction solvent	NMP	DMF	DMF	DMF	DMF	DMF	DMF
Reaction volume (mL)	0.008	0.10	1.5	0.7	0.5-2.0‡	0.6	0.5-1.0
Temperature (°C)	200	160	140	150	160	150-160	160
Reaction time (min)	0.5	2.5 (residence time)	20	15	5	30	30
Synthesis time (min)	35§	N. R.	53	50	55-60	80 Δ	75-80 Δ
Starting activity (MBq [mCi])	13.7 [0.37]	400 [10.8]	10000-2700 [270-730]‡	2000-3000 [54-81]‡	N.R.	50000-56000 [1350-1510]	1800 [49]
Fluorination efficiency (%)	42 ± 7 (n=7)	20 (n=1)	23 ± 5 (n=10)	30 ± 7 (n=9)	40 ± 5 (n=7)	27-35 (n=15)	80 (n=1)
Crude RCY (decay-corrected; %)	19.1 ± 0.6 (n=4)	–	–	–	–	–	–
RCY (decay-corrected; %)	11.6 (n=1)Δ	N.R.	9.0 ± 1.0 (n=6)*	8	26 ± 4	15-20Δ	30Δ

‡ The value corresponding to the optimized condition is not clearly specified, so the whole range reported in the paper is indicated

Not reported, but amount of $KHCO_3$ was computed based on the amount of precursor and an indicated 1.9:1 molar ratio of base to precursor. The amount of K_{222} was in turn computed based on the reported 1.1:1 molar ratio of K_{222} to $KHCO_3$.

N.R. = Not Reported

* Calculated from shorter and higher-yield SPE purification method instead of HPLC

Δ Isolated yield (i.e., not formulated)

§ 20 min for radiosynthesis and HPLC purification plus an estimated ~15 min additional time for formulation[152]

4.7.6 Optimization of [^{18}F]PBR06 synthesis

4.7.6.1 Precursor amount and solvent

Effect of precursor amount experiments were conducted as depicted in **Figure 4-34A**. Drying of [^{18}F]fluoride/[^{18}O]H_2O was performed under identical conditions (13-15 MBq [0.35-0.4 mCi], mixed with 240 nmol of $TBAHCO_3$). The subsequent fluorination reactions were performed with different amounts of precursor dissolved in the 8 μL droplet and reacted at 100 °C for 5 min. Chips 1 and 2 used thexyl alcohol: MeCN (1:1, v/v) as the solvent while chips 3 and 4 used DMSO. Cerenkov images of chips showing residual activity after collection are shown in **Figure 4-34B**, and radio-TLC data is shown in **Figure 4-35**. Detailed analyses for each individual reaction are tabulated in **Table 4-13.**

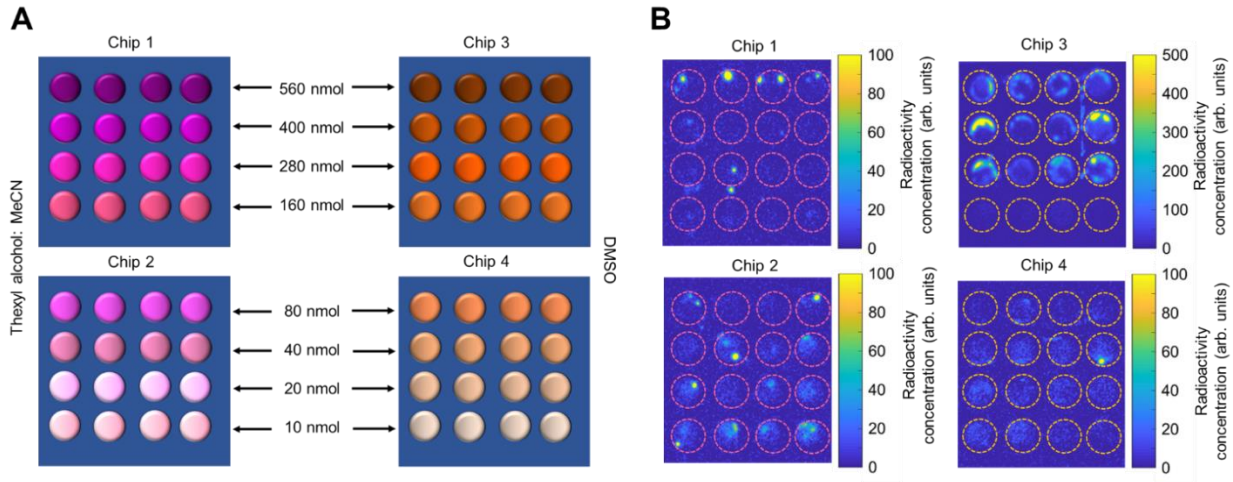

Figure 4-34. Precursor amount and solvent study.
(A) Experimental setup for one batch of experiments that explored the influence of precursor amount (8 values) and solvent (2 types) on the synthesis of [^{18}F]PBR06. All 64 reactions were performed simultaneously. (B) Cerenkov images showing the distribution of the residual activity on each chip after collection of all of the crude samples. Brightness is decay-corrected to a common timepoint for all images.

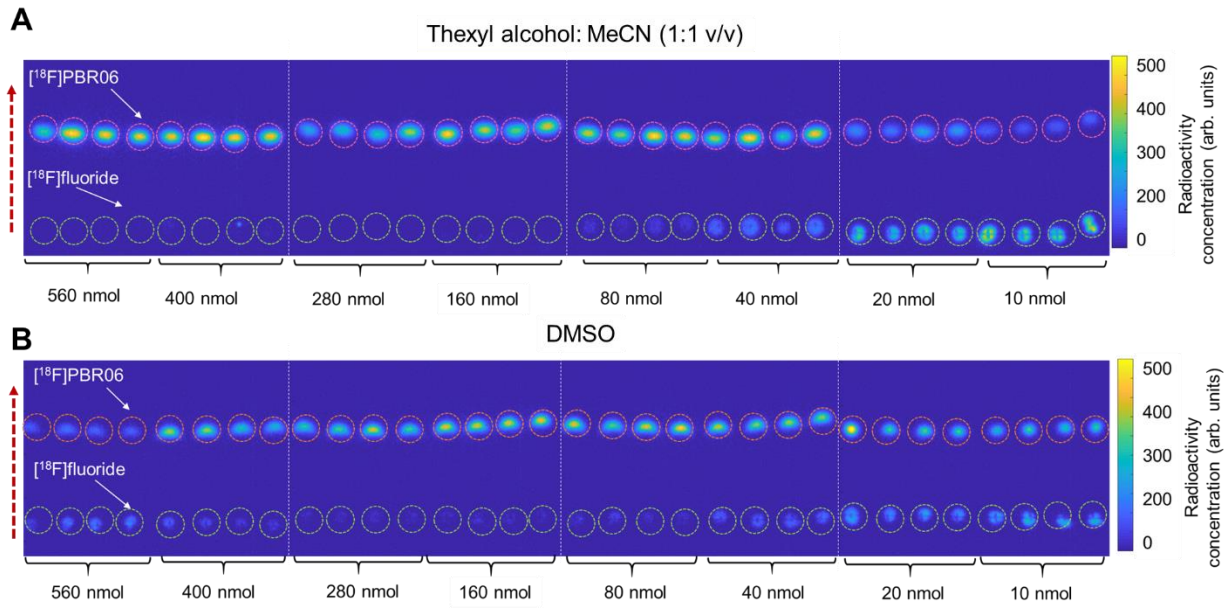

Figure 4-35. Cerenkov images of TLC plates (each containing 8 samples) after developing in the mobile phase. In this case, each TLC plate contains samples from two different precursor amounts in one reaction solvent (n=4 replicates each).
White dotted lines show the edges of each separate multi-sample TLC plate. (A) Image of separated crude samples when using thexyl alcohol:MeCN (1:1 v/v) mixture as the reaction solvent. (B) Image of separated crude samples when using DMSO as the reaction solvent. Dashed circles indicate the ROIs used for analysis. The dashed red arrow indicates the direction of solvent movement during development.

Table 4-13. Summary of data acquired when exploring the effect of precursor amount in the radiosyntheses of [^{18}F]PBR06.

Solvent	Precursor amount (nmol)	Collection efficiency (%) n=4	Fluorination efficiency (%) n=4	Crude RCY (%) n=4	Activity left on chip (%) n=4
Thexyl alcohol: MeCN (1:1 v/v)	560	91.4 ± 1.5	98.0 ± 0.4	91.8 ± 5.2	4.6 ± 1.4
	400	94.9 ± 1.7	96.5 ± 1.5	91.8 ± 3.4	1.2 ± 0.8
	280	91.3 ± 1.6	97.8 ± 0.7	89.3 ± 1.7	2.3 ± 2.1
	160	93.2 ± 4.4	97.8 ± 0.1	91.1 ± 4.3	1.2 ± 0.2
	80	93.1 ± 0.9	92.7 ± 0.8	86.3 ± 1.5	2.4 ± 1.7
	40	94.3 ± 2.9	78.8 ± 1.9	74.4 ± 3.9	2.8 ± 1.2
	20	96.6 ± 2.7	45.4 ± 3.6	43.9 ± 4.7	3.5 ± 1.2
	10	94.6 ± 5.0	24.9 ± 1.6	23.6 ± 2.8	5.0 ± 2.0
DMSO	560	48.4 ± 4.2	59.7 ± 6.0	28.8 ± 2.7	4.6 ± 0.7
	400	72.9 ± 7.5	89.2 ± 2.0	65.1 ± 7.5	8.5 ± 6.3
	280	82.5 ± 5.9	93.9 ± 0.4	77.5 ± 5.8	6.7 ± 2.7
	160	90.8 ± 6.1	94.9 ± 0.3	86.3 ± 5.7	0.5 ± 0.2
	80	92.9 ± 0.7	92.8 ± 2.2	86.1 ± 2.2	1.9 ± 1.3
	40	93.5 ± 2.3	81.3 ± 2.1	76.0 ± 0.8	5.3 ± 2.9
	20	91.1 ± 6.4	66.6 ± 0.8	60.7 ± 4.2	4.2 ± 0.8
	10	91.3 ± 3.6	56.5 ± 1.3	51.6 ± 2.5	3.4 ± 1.2

4.7.6.2 Base amount and solvent

Investigation of the effect of base amount was conducted by mixing [^{18}F]fluoride/[^{18}O]H_2O (13-15 MBq [0.35-0.40 mCi]) with different amounts of the base $TBAHCO_3$ for the drying step as shown in **Figure 4-36A**. In the subsequent fluorination, chips 1 and 2 used thexyl alcohol:MeCN (1:1 v/v) mixture as a reaction solvent and chips 3 and 4 used DMSO. All reactions used 160 nmol of precursor and were performed at 100°C for 5 min. Cerenkov images of chips showing residual activity after collection are shown in **Figure 4-36B**, and radio-TLC data from reactions is shown in **Figure 4-37**. Detailed analyses for each individual reaction are tabulated in **Table 4-14**.

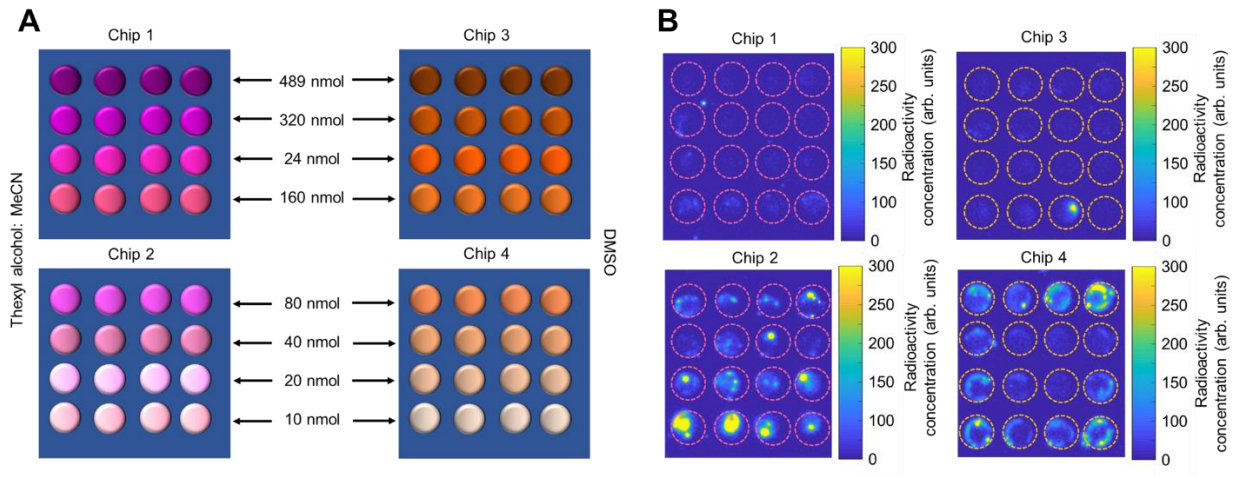

Figure 4-36. Base amount and solvent study.
(A) Experimental setup for one set of experiments that explored the influence of base amount (8 values) and solvent (2 types) on the synthesis of [^{18}F]PBR06. All 64 reactions were run simultaneously. (B) Cerenkov images showing the distribution of the residual activity on each chip after collection of all the crude samples. Brightness is decay-corrected to a common timepoint for all images.

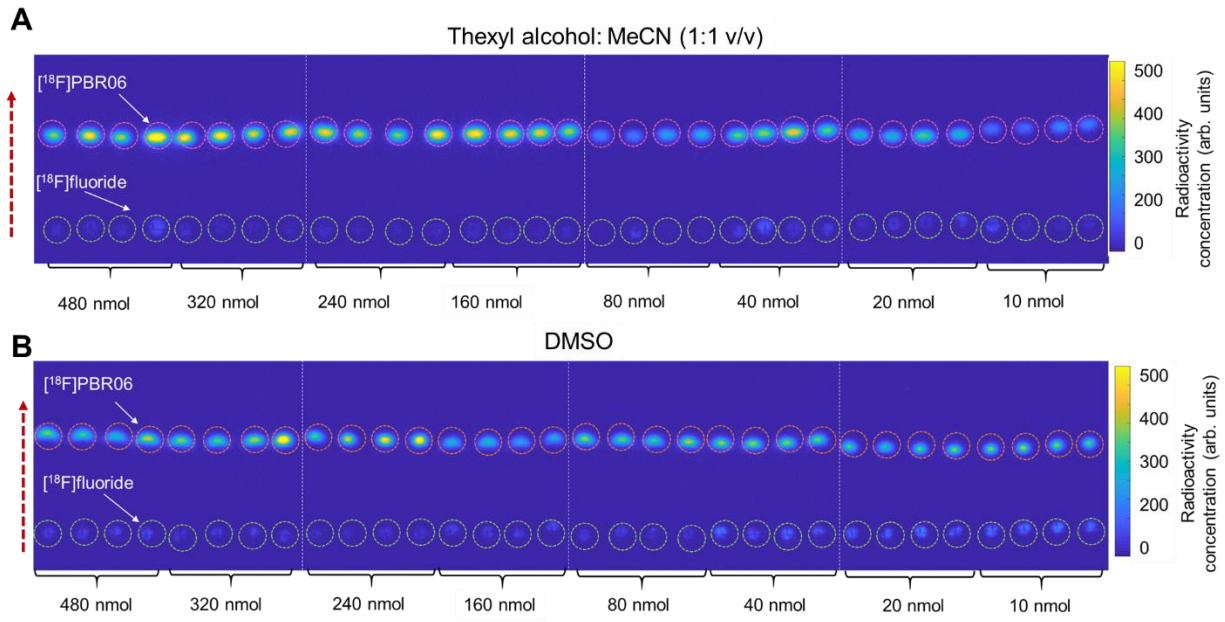

Figure 4-37. Cerenkov images of TLC plates (each containing 8 samples) after developing in the mobile phase. In this case, each TLC plate contains samples from two different base amount conditions in one reaction solvent (n=4 replicates each).
White dotted lines show the edges of each separate multi-sample TLC plate. (A) Image of separated crude samples when using thexyl alcohol:MeCN (1:1 v/v) mixture as the reaction solvent. (B) Image of separated crude samples when using DMSO as the reaction solvent. Dashed circles indicate the ROIs used for analysis. The dashed red arrow indicates the direction of solvent movement during development.

Table 4-14. Summary of data acquired when exploring the effect of the base amount in the radiosyntheses of [^{18}F]PBR06 in two different solvents.

Solvent	Base amount (nmol)	Collection efficiency (%) n=4	Fluorination efficiency (%) n=4	Crude RCY (%) n=4	Activity left on chip (%) n=4
Thexyl alcohol:MeCN	480	94.8 ± 2.4	93.6 ± 2.0	88.7 ± 3.7	1.9 ± 0.7
	320	95.0 ± 1.4	96.8 ± 0.5	91.9 ± 1.4	2.4 ± 2.1
	240	95.5 ± 2.9	95.7 ± 0.6	91.5 ± 3.4	2.0 ± 0.8
	160	92.1 ± 3.9	96.0 ± 1.1	88.5 ± 4.7	5.9 ± 2.0
	80	96.9 ± 3.9	85.3 ± 2.6	98.3 ± 7.5	2.7 ± 1.3
	40	88.2 ± 1.9	89.6 ± 3.9	83.7 ± 4.5	2.1 ± 1.3
	20	88.0 ± 3.7	88.7 ± 3.1	79.4 ± 0.9	4.0 ± 1.6
	10	89.9 ± 6.8	85.2 ± 2.4	75.0 ± 8.5	9.0 ± 4.4
DMSO	480	94.4 ± 1.6	89.9 ± 1.5	84.8 ± 1.5	2.7 ± 0.6
	320	94.6 ± 2.4	91.9 ± 2.0	86.9 ± 2.6	2.4 ± 0.6
	240	94.8 ± 4.4	92.6 ± 0.7	87.8 ± 4.2	1.5 ± 0.2
	160	96.8 ± 2.9	85.0 ± 1.7	82.3 ± 4.0	5.0 ± 4.8
	80	86.1 ± 3.4	91.0 ± 0.6	78.4 ± 2.8	7.9 ± 4.5
	40	89.5 ± 1.3	83.2 ± 3.4	74.4 ± 4.1	1.6 ± 0.7
	20	80.7 ± 1.5	77.2 ± 3.8	62.3 ± 2.1	3.0 ± 1.9
	10	74.8 ± 4.0	74.6 ± 1.3	55.8 ± 3.2	5.9 ± 3.0

4.7.6.3 Reaction temperature and solvent

The experimental design for exploring temperature and solvent effect on the radiosynthesis of [^{18}F]PBR06 was described in **Figure 4-38A.** Experiments were performed by drying of [^{18}F]fluoride/[^{18}O]H_2O under identical conditions (13-15 MBq [0.35-0.40 mCi], mixed with 240 nmol of $TBAHCO_3$) , and then performing fluorination at different temperatures and in different solvents. A first batch of experiments was performed with heaters 1 – 4 set at 80, 90, 100, and 110 °C, respectively, and a second batch was performed with heaters 1 – 4 set at 120, 130, 140, and 150 °C, respectively. All fluorinations used 160 nmol of precursor in 8 µL of solvent and were reacted for 5 min. Cerenkov images of chips showing residual activity after collect are shown in **Figure 4-38B**, and radio-TLC data are shown in **Figure 4-39**. Detailed analyses for each individual reaction (collection efficiency, fluorination efficiency, crude RCY, and activity left on chip) are tabulated in **Table 4-15**.

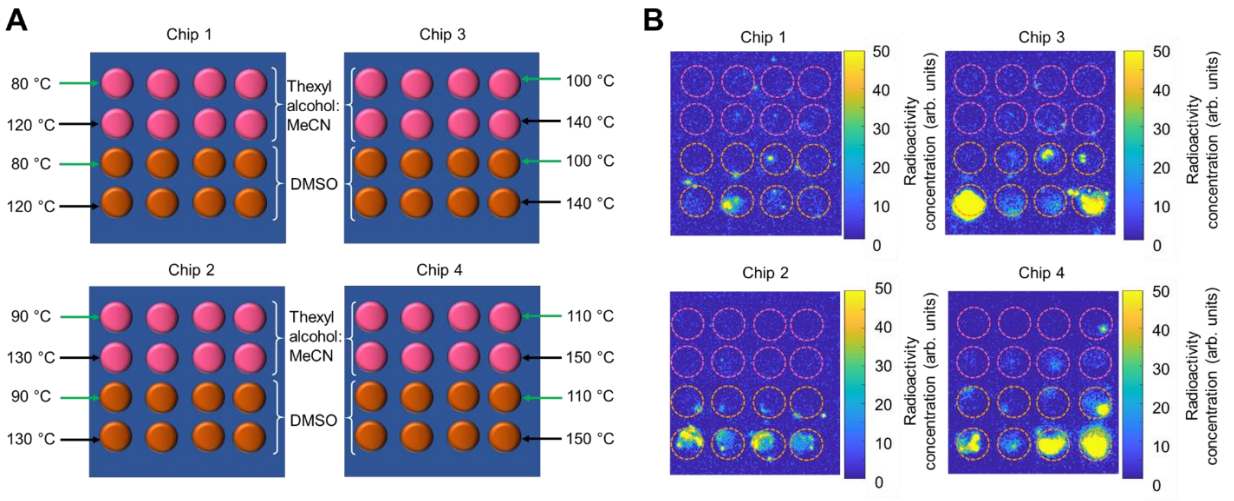

Figure 4-38. Temperature and solvent test.
(A) Experimental setup for one batch of experiments that explored the influence of reaction temperature (8 values) and solvent (2 types) on the synthesis of [^{18}F]PBR06. Half of the reaction sites were used first to explore 4 different temperatures in a first set of 32 simultaneous reactions, and then the other half of the sites were used to explore 4 additional temperatures in a second set of 32 simultaneous reactions. (B) Cerenkov images showing the distribution of the residual activity on each chip after collection of all the crude samples. Brightness is decay-corrected to a common timepoint for all images.

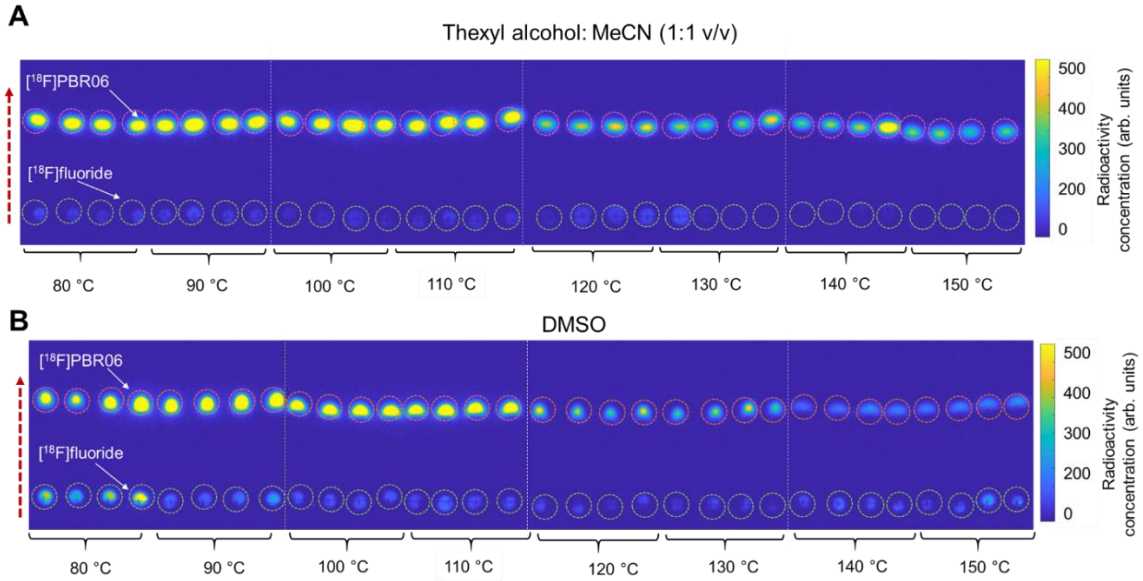

Figure 4-39. Cerenkov images of TLC plates (each containing 8 samples) after developing in the mobile phase. In this case, each TLC plate contains samples from two different temperature conditions in one reaction solvent (n=4 replicates each).
White dotted lines represent the boundary of each multi-sample plate. (A) Image of separated crude samples when using thexyl alcohol:MeCN (1:1 v/v) as the reaction solvent. (B) Image of separated crude samples when using DMSO as the reaction solvent. Dashed circles indicate the ROIs used for analysis. The dashed red arrow indicates the direction of solvent movement during developing.

Table 4-15. Summary of data acquired when exploring the effect of temperature and solvent in the radiosyntheses of [^{18}F]PBR06.

Solvent	Temperature (°C)	Collection efficiency (%) n=4	Fluorination efficiency (%) n=4	Crude RCY (%) n=4	Activity left on chip (%) n=4
Thexyl alchohol: MeCN	80	93.0 ± 3.0	95.0 ± 1.2	88.4 ± 3.6	1.1 ± 0.4
	90	94.1 ± 1.4	95.7 ± 0.4	90.1 ± 1.6	0.6 ± 0.1
	100	94.2 ± 3.1	95.7 ± 0.6	91.1 ± 2.4	0.4 ± 0.2
	110	94.1 ± 1.2	96.3 ± 0.6	90.6 ± 1.1	0.4 ± 0.5
	120	93.6 ± 0.6	88.2 ± 3.7	82.6 ± 4.0	1.3 ± 0.4
	130	93.8 ± 1.4	90.8 ± 8.3	87.5 ± 10.9	0.5 ± 0.2
	140	91.3 ± 1.4	96.4 ± 0.7	91.7 ± 6.2	0.8 ± 0.3
	150	92.7 ± 0.9	94.7 ± 1.1	87.8 ± 1.2	0.9 ± 0.3
DMSO	80	94.3 ± 3.4	72.4 ± 4.4	68.2 ± 4.4	3.7 ± 1.1
	90	93.5 ± 4.8	91.4 ± 2.1	85.6 ± 5.5	2.0 ± 0.4
	100	93.0 ± 2.4	92.7 ± 0.5	86.2 ± 1.9	1.8 ± 1.1
	110	89.5 ± 2.5	91.9 ± 1.8	82.3 ± 1.9	2.5 ± 2.8
	120	89.1 ± 1.7	87.6 ± 1.0	78.7 ± 1.3	5.0 ± 4.1
	130	93.1 ± 3.3	87.6 ± 3.3	81.6 ± 3.5	9.6 ± 2.4
	140	90.6 ± 2.6	71.3 ± 5.9	64.9 ± 5.9	8.5 ± 6.4
	150	88.6 ± 2.4	75.3 ± 4.2	66.8 ± 4.9	8.4 ± 5.0

4.7.6.4 Reaction time and solvent

The study of the effect of reaction time on the synthesis of [^{18}F]PBR06 was conducted as shown in **Figure 4-40A**. First, [^{18}F]fluoride/[^{18}O]H_2O was dried under identical conditions (13-15 MBq [0.35-0.40 mCi], mixed with 240 nmol of $TBAHCO_3$), and then the fluorinations were carried out for different amounts of time and in different solvents. All fluorinations used 160 nmol of precursor in 8 μL of reaction solvent of thexyl alcohol:MeCN (1:1 v/v) mixture or DMSO and were carried out at 100 °C. A first batch of experiments used reaction times of 30, 60, 120, and 180 s on heaters 1 – 4, respectively, followed by a second batch of experiments with reaction times of 240, 300, 360, and 420 s on heaters 1 – 4, respectively. Cerenkov images of chips showing residual activity after collection are shown in **Figure 4-40B** and radio-TLC data are shown in **Figure 4-41.** Detailed analyses for each individual reaction are tabulated in **Table 4-16**.

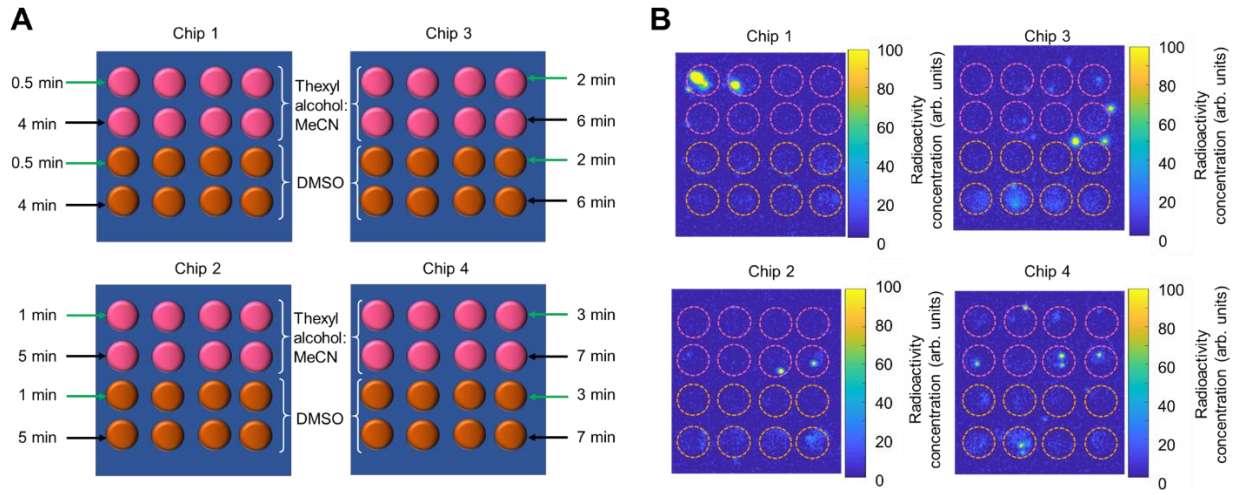

Figure 4-40. Time and solvent test.
(A) Experimental setup for one batch of experiments that explored the influence of reaction time (8 values) and solvent (2 types) on the synthesis of [^{18}F]PBR06. Half of the reaction sites were used first to explore 4 different times in 32 simultaneous reactions, and then the other half of the sites were used to explore 4 additional times in 32 simultaneous reactions. (B) Cerenkov images showing the distribution of the residual activity on each chip after collection of all the crude samples. Brightness is decay-corrected to a common timepoint for all images.

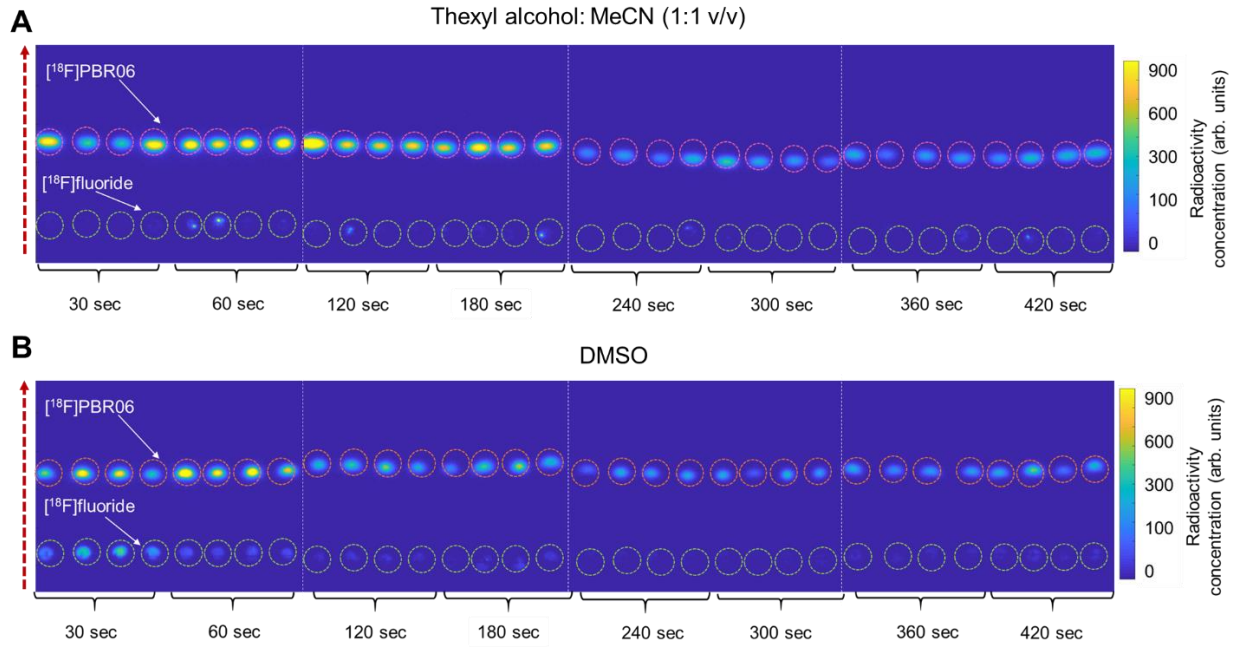

Figure 4-41. Cerenkov images of TLC plates (each containing 8 samples) after developing in the mobile phase. In this case, each TLC plate contains samples from two different time conditions in one reaction solvent (n=4 replicates each).
White dotted lines represent the boundary of each multi-sample plate. (A) Image of separated crude samples when using thexyl alcohol:MeCN (1:1 v/v) mixture as the reaction solvent. (B) Image of separated crude samples using DMSO as the reaction solvent. Dashed circles indicate the ROIs used for analysis. The dashed red arrow indicates the direction of solvent movement

during developing. Red dashed circle represents an area of contamination that was inadvertently on the cover plate when imaging the TLC plates.

Table 4-16. Summary of data acquired when exploring the effect of reaction time and solvent in the radiosyntheses of [^{18}F]PBR06.

Solvent	Time (min)	Collection efficiency (%) n=4	Fluorination efficiency (%) n=4	Crude RCY (%) n=4	Activity left on chip (%) n=4
Thexyl alcohol: MeCN	0.5	92.9 ± 1.6	98.0 ± 0.1	91.0 ± 1.5	2.2 ± 2.0
	1.0	94.1 ± 1.4	94.1 ± 4.4	88.6 ± 4.6	0.5 ± 0.1
	2.0	91.5 ± 2.5	96.5 ± 2.7	88.3 ± 2.2	0.9 ± 0.2
	3.0	94.1 ± 0.9	96.1 ± 2.4	90.4 ± 2.1	0.8 ± 0.2
	4.0	88.7 ± 2.7	95.1 ± 2.7	84.3 ±1.7	0.5 ± 0.2
	5.0	93.3 ± 2.0	97.5 ± 1.0	91.0 ± 1.9	2.6 ± 2.1
	6.0	89.0 ± 5.4	92.6 ± 3.5	82.3 ± 9.1	0.8 ± 0.2
	7.0	94.1 ± 1.2	94.7 ± 2.8	89.1 ± 3.4	2.7 ± 1.7
DMSO	0.5	94.2 ± 3.0	66.5 ± 3.1	62.6 ± 3.1	0.6 ± 0.3
	1.0	94.5 ± 3.6	90.4 ± 0.6	85.3 ± 3.0	3.7 ± 2.6
	2.0	92.7 ± 2.0	91.9 ± 1.0	85.2 ± 2.5	0.9 ± 0.4
	3.0	93.8 ± 0.6	90.2 ± 0.9	84.6 ± 0.8	3.8 ± 2.0
	4.0	92.0 ± 2.4	92.8 ± 1.2	85.3 ± 2.6	1.7 ± 0.7
	5.0	91.0 ± 4.3	90.8 ± 1.5	82.7 ± 5.2	3.4 ± 1.8
	6.0	90.5 ± 8.9	90.3 ± 0.6	81.8 ± 8.6	1.5 ± 0.2
	7.0	94.2 ± 4.8	89.9 ± 1.1	84.7 ± 3.5	3.7± 3.3

4.7.6.5 Base type and solvent

Finally, we explored the use of different type of base / phase transfer catalyst, comparing Kryptofix (K_{222}) and K_2CO_3 versus $TBAHCO_3$ as shown in **Figure 4-42A**. Only one chip was used for this study. For the drying step, 13-15 MBq [0.35-0.40 mCi] of [^{18}F]fluoride/[^{18}O]H_2O was loaded to each reaction site. For half of the spots, the fluoride was mixed with 240 nmol of TBAHCO3. For the other half of the spots, the fluoride was mixed with 240 nmol of K_{222} and 120 nmol of K_2CO_3. After drying, the subsequent fluorinations were performed with 280 nmol of precursor in 8 µL of either thexyl alcohol:MeCN (1:1 v/v) mixture or DMSO, and reacted at 100°C for 0.5 min. Cerenkov image of the chip showing residual activity after collection are shown in **Figure 4-42B**, and radio-TLC data is shown in **Figure 4-43**. Detailed analyses for each individual reaction are tabulated in **Table 4-17**.

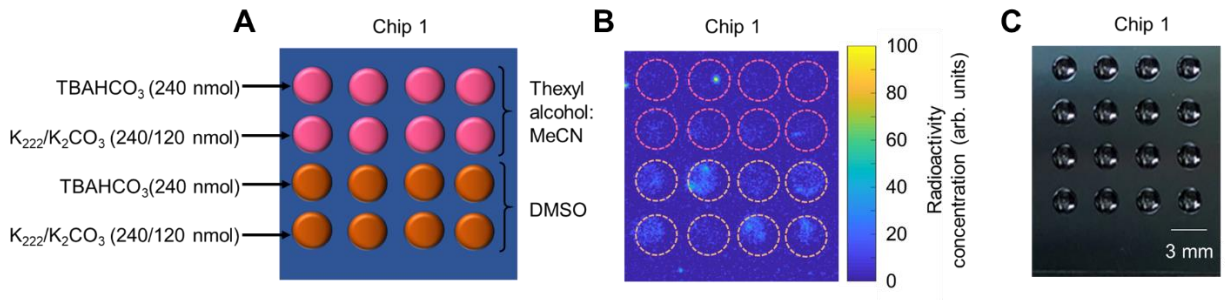

Figure 4-42. Base type and solvent test.
(A) Experimental setup for one batch of experiments that explored the influence of type of base (2 values) and solvent (2 types) on the synthesis of [^{18}F]PBR06. (B) Cerenkov images showing the distribution of the residual activity on each chip after collection of all the crude samples. (C) Photograph of chip after precursor is loaded, showing absence of base-dependent color difference (seen for [^{18}F]Flumazenil).

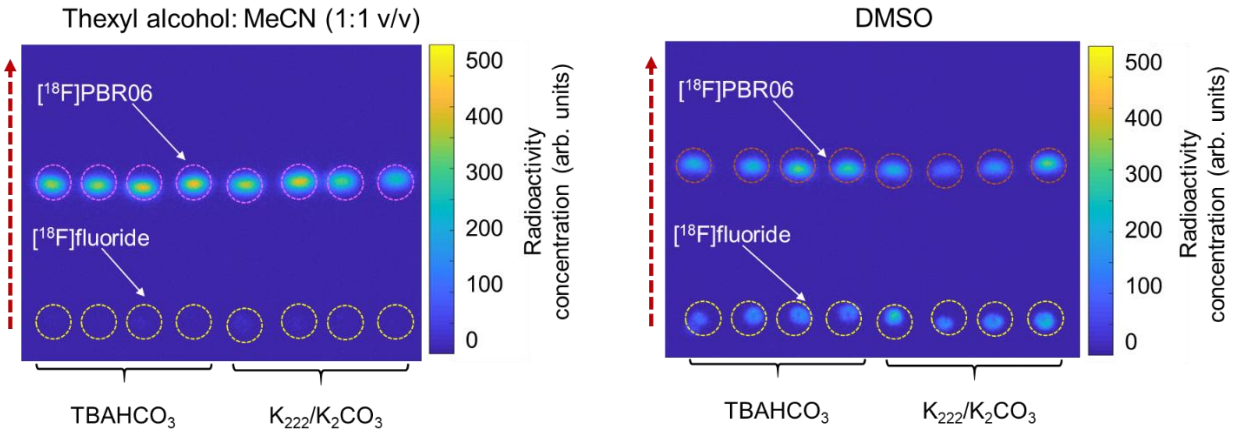

Figure 4-43. Cerenkov images of TLC plates (each containing 8 samples) after developing in the mobile phase. In this case, each TLC plate contains samples from two different base type conditions in one reaction solvent (n=4 replicates each).
Dashed circles indicate the ROIs used for analysis. The dashed red arrow indicates the direction of solvent movement during developing. (A) Image of separated crude samples when using thexyl alcohol:MeCN (1:1 v/v) mixture as the reaction solvent. (B) Image of separated crude samples when using DMSO as the reaction solvent.

Table 4-17. Summary of data acquired when exploring the effect of type of base and reaction solvent in the radiosyntheses of [^{18}F]flumazenil.

Solvent	Base type and amount (nmol)	Collection efficiency (%) n=4	Fluorination efficiency (%) n=4	Crude RCY (%) n=4	Activity left on chip (%) n=4
Thexyl alcohol: MeCN	$TBAHCO_3$ (240)	96.4 ± 2.2	97.4 ± 0.2	93.9 ± 2.0	0.7 ± 0.1
	K_{222}/K_2CO_3 (240/120)	95.8 ± 3.5	96.5 ± 0.9	92.4 ± 3.0	1.63 ± 0.03
DMSO	$TBAHCO_3$ (240)	94.7 ± 4.1	70.7 ± 3.5	66.9 ± 2.9	4.4 ± 1.1
	K_{222}/K_2CO_3 (240/120)	93.5 ± 5.3	60.5 ± 3.2	56.5 ± 2.0	4.3± 1.9

4.7.6.6 Additional studies of reaction temperature

Using thexyl alcohol: MeCN (1:1 v/v) as a reaction solvent exhibited high crude RCY at 80 °C in a 5 min reaction, and high crude RCY at 100 °C in a 0.5 min reaction. We were interested whether short reactions (0.5 min) at lower temperatures would also give good performance. Experiments were performed by drying of [^{18}F]fluoride/[^{18}O]H_2O under identical conditions (13-15 MBq [0.35-0.40 mCi] with 240 nmol of $TBAHCO_3$), followed by fluorination with 160 nmol of precursor in 8 µL of solvent for 0.5 min at different temperatures. To conserve chips, temperatures were explored sequentially, using 4 fresh reaction sites each time. (Two chips were needed in total.) Radio-TLC data are shown in **Figure 4-44**. Detailed analyses for each individual reaction are tabulated in **Table 4-17** and the results are plotted in **Figure 4-45**. We observed that the temperature could be lowered to 90 °C without compromising performance. **Table 4-18** compares our approach with other literature macroscale reports.

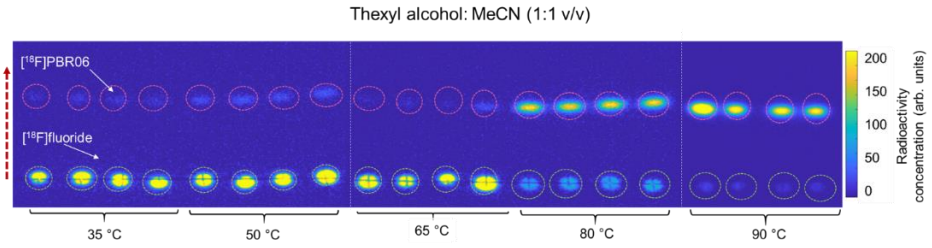

Figure 4-44. Cerenkov images of TLC plates (two containing 8 samples and one containing 4 samples) after developing in the mobile phase.
In this case, each TLC plate contains samples from up to two different temperatures (n=4 replicates each). White dotted lines show the edges of each multi-lane TLC plate. Dashed circles indicate the ROIs used for analysis. The dashed red arrow indicates the direction of solvent movement during developing.

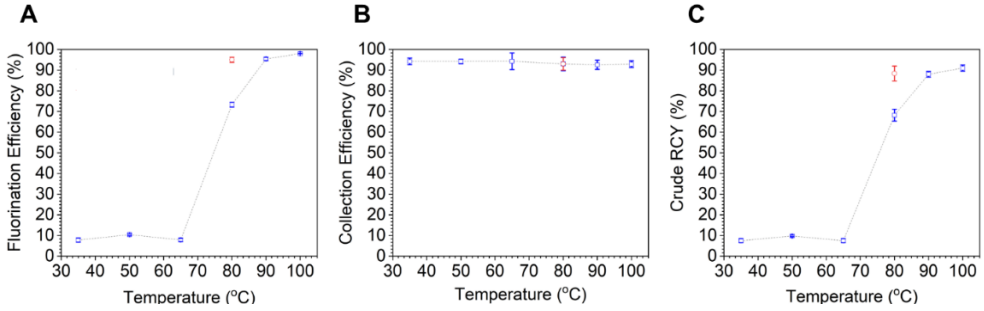

Figure 4-45. Temperature studies of [^{18}F]PBR06.
(A) Fluorination efficiency. (B) Collection efficiency. (C) Crude RCY. The blue markers represent 0.5 min reactions, and the red data points represent 5 min reactions.

Table 4-18. Summary of data acquired when exploring the effect of temperature in the radiosyntheses of [^{18}F]PBR06 (for 0.5 min reactions).

Solvent	Temperature (°C)	Collection efficiency (%) n=4	Fluorination efficiency (%) n=4	Crude RCY (%) n=4	Activity left on chip (%) n=4
Thexyl alchohol: MeCN	35	94.2 ± 1.6	7.8 ± 1.0	7.5 ± 1.0	2.2 ± 0.2
	50	94.2 ± 1.1	10.4 ± 0.4	9.8 ± 0.4	3.5 ± 1.0
	65	94.3 ± 4.0	7.9 ± 0.8	7.5 ± 1.0	1.5 ± 0.8
	80	93.0 ± 3.3	73.3 ± 1.2	68.2 ± 2.9	1.0 ± 0.6
	90	92.6 ± 2.2	95.4 ± 0.8	88.0 ± 1.4	2.5± 0.7

4.7.6.7 Comparison to literature methods

Table 4-19. Comparison of optimized droplet conditions with literature reports for conventional synthesis of [^{18}F]PBR06.

	This work (2021)	Wang et al.[154] (2011)	Zhang et al.[155] (2019)
Synthesizer type	Microscale (droplet format)	Macroscale	Macroscale
Base type	$TBAHCO_3$	K_{222} / K_2CO_3	K_{222} / K_2CO_3
Base amount (nmol)	240	27000/ 12000	40000/10000
Precursor amount (nmol)	160	1800	5500
Reaction solvent	Thexyl alcohol: MeCN (1:1 v/v)	DMSO	DMSO
Reaction volume (mL)	0.008	1	1
Temperature (°C)	100	140	140
Reaction time (min)	0.5	15	15
Synthesis time (min)	35 #	50-60	50
Starting activity (MBq [mCi])	13.8 [0.375]	N.R.	N.R.
Fluorination efficiency (%)	98.0 ± 0.1 (n=4)	N.R.	N.R.
Crude RCY (decay-corrected; %)	93.9 ± 2.0 (n=4)	N.R.	N.R.
RCY (decay-corrected; %)	75.8 (n=1)*	30-60	40-60

* Isolated yield (i.e., not formulated)
# 20 min for radiosynthesis and purification plus an estimated ~15 min additional time for formulation[152]
N.R. = Not reported

4.7.7 Optimization of [^{18}F]Fallypride synthesis

4.7.7.1 Precursor concentration and reaction temperature

A set of experiments to explore the effect of precursor concentration and temperatures were conducted as depicted in **Figure 4-46A**. Drying of [^{18}F]fluoride/[^{18}O]H_2O was performed under identical conditions (13-15 MBq [0.35-0.4 mCi], mixed with 240 nmol of $TBAHCO_3$), and the subsequent fluorination reactions were performed with different amounts of precursor dissolved in the 6 μL droplet, for 7 min. Chip 1 was run at 80 °C, chip 2 at 95 °C chip 3 at 110°C, and chip 4 at 125 °C. All reactions were conducted using thexyl alcohol:MeCN (1:1 v/v) mixture as solvent. Cerenkov images of chips showing residual activity after collected are shown in **Figure 4-46B**, and graphical representation is shown in **Table 4-6A** in the main paper. Detailed analyses for each individual reaction are tabulated in **Table 4-20**.

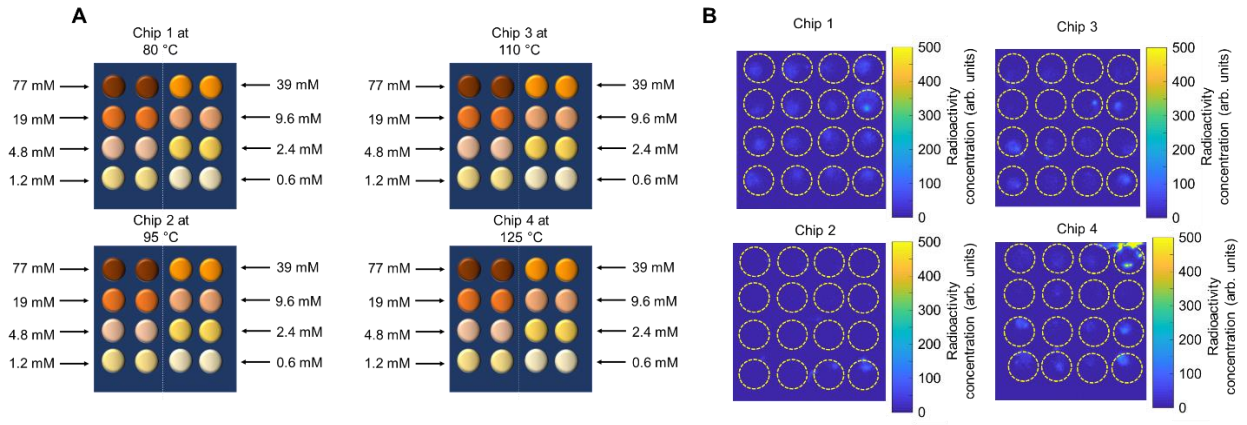

Figure 4-46. Precursor concentration and temperature test.
(A) Experimental setup for one batch of experiments that explored the influence of precursor concentration (8 values) and temperature (4 types) on the synthesis of [^{18}F]Fallypride. Each chip explored 8 different precursor concentrations at one particular temperature. (B) Cerenkov images showing the distribution of the residual activity on each chip after collection of all the crude samples. Brightness is decay-corrected to a common timepoint for all images.

Table 4-20. Summary of data acquired when exploring the effect of precursor concentration and temperature on the radiosyntheses of [^{18}F]Fallypride.

Temperature (°C)	Precursor concentration (mM)	Collection efficiency (%) n=2	Fluorination efficiency (%) n=2	Crude RCY (%) n=2	Activity left on chip (%) n=2
80	77	93.64 ± 0.05	94.7 ± 1.3	88.6 ± 1.2	4.1 ± 0.4
	39	93.1 ± 1.6	91.9 ± 4.0	85.7 ± 5.2	4.2 ± 2.4
	19	93.2 ± 0.8	61.7 ± 3.6	57.5 ± 2.9	3.1 ± 1.2
	9.6	91.2 ± 8.3	33.4 ± 3.8	30.6 ± 6.2	5.8 ± 4.4
	4.8	94.9 ± 3.6	24.4 ± 1.7	23.1 ± 0.8	3.4 ± 1.2
	2.4	96.1 ± 2.0	13.0 ± 1.1	12.5 ± 0.7	4.3 ± 0.1
	1.2	93.9 ± 7.4	12.7 ± 0.8	12.0 ± 1.7	3.4 ± 0.7
	0.6	92.5 ± 5.7	6.7 ± 0.7	6.2 ± 0.3	3.8 ± 0.8
95	77	88.2 ± 3.0	95.5 ± 0.1	84.3 ± 3.0	4.6 ± 0.7
	39	89.8 ± 3.8	95.1 ± 1.0	85.3 ± 2.7	2.1 ± 1.0
	19	94.4 ± 3.1	85.0 ± 3.6	80.3 ± 6.0	1.4 ± 0.2
	9.6	93.6 ± 4.5	59.7 ± 0.5	55.9 ± 2.2	0.75 ± 0.02
	4.8	92.0 ± 1.2	34.9 ± 2.3	32.1 ± 2.5	1.3 ± 0.2
	2.4	90.3 ± 8.6	19.4 ± 0.4	17.2 ± 2.5	1.0 ± 0.3
	1.2	87.4 ± 9.1	15.9 ± 0.5	13.6 ± 1.4	1.0 ± 0.3
	0.6	89.3 ± 0.8	7.4 ± 0.8	6.6 ± 0.8	8.6 ± 5.5
110	77	91.7 ± 2.1	96.1 ± 0.5	88.1 ± 1.5	3.6 ± 0.2
	39	98.7 ± 1.7	96.0 ± 0.2	94.7 ± 1.8	2.1 ± 0.4
	19	94.0 ± 0.8	89.6 ± 0.4	84.2 ± 1.1	1.3 ± 0.4
	9.6	93.5 ± 2.8	61.0 ± 0.4	57.1 ± 2.1	4.6 ± 0.3
	4.8	86.0 ± 3.5	34.0 ± 2.4	29.2 ± 0.8	6.4 ± 3.1
	2.4	88.2 ± 7.4	18.6 ± 0.3	16.3 ± 1.1	3.4 ± 0.5
	1.2	88.6 ± 3.4	15.7 ± 1.1	13.9 ± 0.4	3.9 ± 1.6
	0.6	88.1 ± 6.1	7.1 ± 0.4	6.2 ± 0.1	5.0 ± 3.3
125	77	90.6 ± 0.5	95.3 ± 0.6	86.3 ± 1.0	1.34 ± 0.01
	39	90.0 ± 5.6	95.1 ± 0.3	85.5 ± 5.1	3.1 ± 2.8
	19	86.7 ± 3.8	90.2 ± 0.5	78.2 ± 3.0	0.6 ± 0.1
	9.6	85.6 ± 4.3	64.0 ± 3.8	54.7 ± 0.5	0.4 ± 0.1
	4.8	82.8 ± 6.2	37.5 ± 4.0	30.9 ± 0.9	1.7 ± 1.4
	2.4	78.6 ± 4.0	21.8 ± 0.2	17.1 ± 1.0	2.0 ± 1.3
	1.2	85.6 ± 0.7	21.3 ± 2.3	18.2 ± 2.1	2.6 ± 0.4
	0.6	82.6 ± 3.5	7.8 ± 1.5	6.4 ± 1.0	2.6 ± 2.3

4.7.7.2 Precursor concentration and reaction time

Another study of the impact of precursor concentration and reaction time was conducted as depicted in **Figure 4-47A**. Drying of [^{18}F]fluoride/[^{18}O]H_2O was performed under identical conditions (13-15 MBq [0.35-0.4 mCi], mixed with 240 nmol of $TBAHCO_3$), and the subsequent fluorination reactions were performed with different amounts of precursor dissolved in the 6 μL

droplet, at 110 °C. All reactions were conducted using thexyl alcohol:MeCN (1:1 v/v) mixture as solvent. Samples on each chip were reacted for different times. Cerenkov images of chips showing residual activity after collection are shown in **Figure 4-47B**. Detailed analyses for each individual reaction are tabulated in **Table 4-21**, and the results are plotted in **Figure 4-6B.**

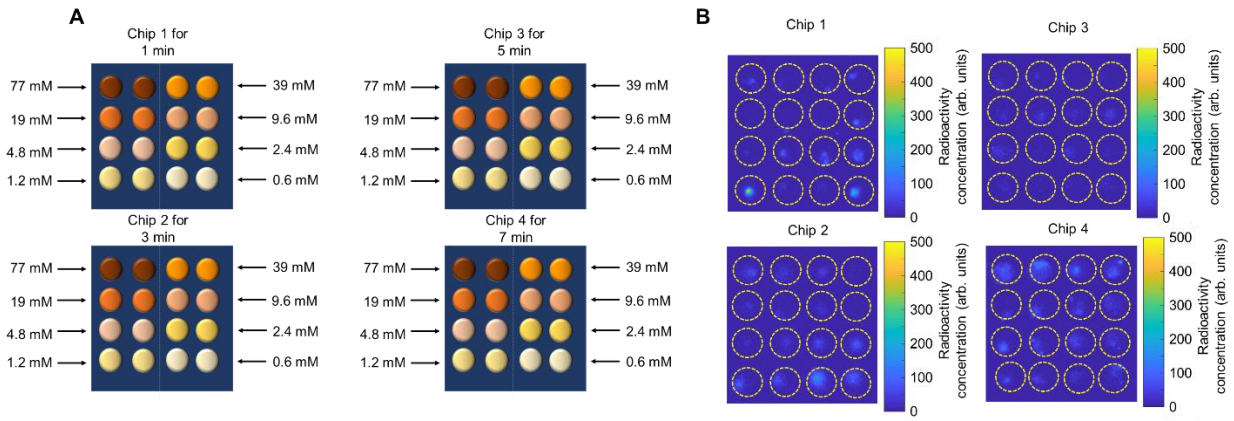

Figure 4-47. Precursor concentration and reaction time test.
(A) Experimental setup for one set of experiments that explored the influence of reaction precursor amount (8 values) and reaction time (4 types) on the synthesis of [^{18}F]Fallypride. (B) Cerenkov images showing the distribution of the residual activity on each chip after collection of all the crude samples. Brightness is decay-corrected to a common timepoint for all images.

Table 4-21. Summary of data acquired when exploring the effect of precursor amount and reaction time on the radiosyntheses of [^{18}F]Fallypride.

Time (min)	Precursor concentration (mM)	Collection efficiency (%) n=2	Fluorination efficiency (%) n=2	Crude RCY (%) n=2	Activity left on chip (%) n=2
1.0	77	93.4 ± 0.7	80.5 ± 2.8	75.2± 2.1	4.1 ± 1.0
	39	99.2 ± 4.1	93.3 ± 1.1	92.7 ± 5.0	2.8 ± 0.5
	19	92. ± 6.9	93.4 ± 0.1	86.7 ± 6.4	1.7 ± 0.5
	9.6	90.1 ± 0.5	84.3 ± 2.8	75.9 ± 2.1	3.8 ± 1.0
	4.8	92.9 ± 2.3	72.2 ± 0.9	67.0 ± 2.5	3.6 ± 3.2
	2.4	95.9 ± 2.7	31.0 ± 0.6	29.7 ± 1.4	5.7 ± 2.6
	1.2	93.4 ± 4.7	18.4 ± 0.1	17.2 ± 1.3	5.8 ± 5.4
	0.6	95.9 ± 0.4	11.2 ± 1.3	10.7 ± 1.3	5.6 ± 4.9
3.0	77	93.8 ± 1.2	90.0 ± 0.1	84.4 ± 1.2	3.7 ± 0.5
	39	94.1 ± 1.5	93.9 ± 0.8	88.4 ± 2.2	1.7 ± 1.0
	19	92.9 ± 1.2	92.8 ± 2.5	86.2 ± 1.2	1.9 ± 0.2
	9.6	91.8 ± 2.7	61.3 ± 1.9	56.3 ± 3.4	1.4 ± 0.8
	4.8	93.4 ± 7.4	31.9 ± 3.3	29.9 ± 5.4	2.3 ± 1.3
	2.4	93.1 ± 4.8	15.4 ± 1.3	14.4 ± 2.0	3.6 ± 0.3
	1.2	92.3 ± 1.1	7.9 ± 1.3	7.3 ± 1.1	4.5 ± 0.3
	0.6	101.7 ± 2.1	5.5 ± 0.2	5.6 ± 0.1	8.7 ± 2.4
5.0	77	91.61 ± 0.01	87.0 ± 0.7	79.7 ± 0.7	2.4 ± 0.7
	39	91.0 ± 5.4	89.0 ± 0.2	81.0 ± 5.0	2.4 ± 0.7
	19	94.8 ± 0.4	89.2 ± 1.7	84.5 ± 1.9	3.4 ± 0.7
	9.6	91.6 ± 2.5	63.0 ± 1.5	57.7 ± 3.0	3.7 ± 1.3
	4.8	94.4 ± 7.8	59.2 ± 1.7	55.8 ± 3.0	3.5 ± 2.9
	2.4	93.5 ± 4.6	31.1 ± 5.0	29.2 ± 6.1	2.5 ± 1.2
	1.2	90.8 ± 6.7	16.7 ± 1.6	15.1 ± 0.3	2.1 ± 0.8
	0.6	90.2 ± 8.4	8.2 ± 1.0	7.4 ± 1.6	2.5 ± 1.1
7.0	77	89.7 ± 0.5	88.0 ± 1.1	78.9 ± 1.5	8.0 ± 1.0
	39	93.4 ± 2.1	90.7 ± 0.6	84.7 ± 1.3	5.2 ± 0.6
	19	93.5 ± 6.0	88.5 ± 1.2	82.8 ± 6.5	2.1 ± 0.8
	9.6	93.6 ± 3.7	64.8 ± 2.8	61.5 ± 0.2	2.85 ± 0.04
	4.8	93.8 ± 0.8	39.4 ± 1.1	35.9 ± 1.3	3.31 ± 0.03
	2.4	92.8 ± 8.4	17.5 ± 0.4	10.2 ± 1.9	2.9 ± 0.6
	1.2	93.3 ± 3.3	9.0 ± 0.7	8.4 ± 0.9	2.27 ± 0.05
	0.6	91.2 ± 9.9	5.2 ± 0.6	4.8 ± 1.0	2.7 ± 1.3

4.7.8 Optimization of [^{18}F]FEPPA synthesis

Experiments to explore the effect of reaction temperature were conducted as shown in **Figure 4-48A**. Drying of [^{18}F]fluoride/[^{18}O]H_2O was performed under identical conditions (13-15 MBq [0.35-0.4 mCi], mixed with 240 nmol of $TBAHCO_3$), and the subsequent fluorination reactions were performed at 8 different temperatures for 2 min using 240 nmol of precursor dissolved in the 8 μL droplet in thexyl alcohol: MeCN (1:1, v/v). Though this experiment could be implemented

using 4 chips on 4 heaters, since only 4 reaction sites were needed per temperature value, the experiment was instead performed using just 2 chips as follows. A first batch of experiments was performed with heaters 1 and 2 set at 60 and 100 °C, respectively, a second batch with temperatures of 70, 110 °C, a third batch with temperatures of 80 and 120 °C, and a final batch with temperatures of 90 and 130 °C. Cerenkov images of chips showing residual activity after collection are shown in **Figure 4-48B**, and radio-TLC data is shown in **Figure 4-49**. Detailed analyses for each individual reaction are tabulated in **Table 4-22.**

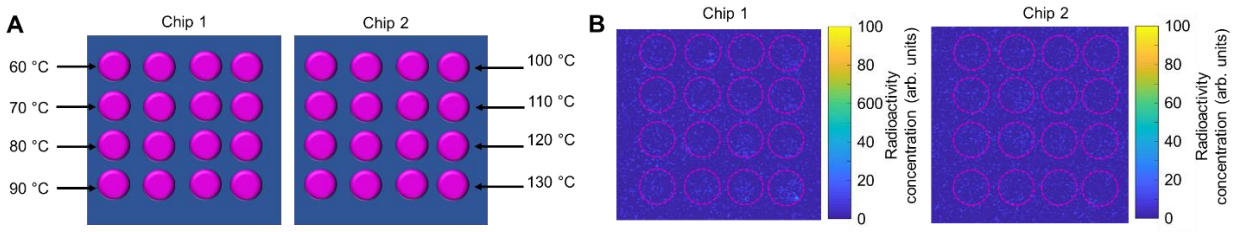

Figure 4-48. Temperature studies.
(A) Experimental setup for one batch of experiments that explored the influence of reaction temperature (8 values) on the synthesis of [^{18}F]FEPPA. (B) Cerenkov images showing the distribution of the residual activity on each chip after collection of all the crude samples. Brightness is decay-corrected to a common timepoint for all images.

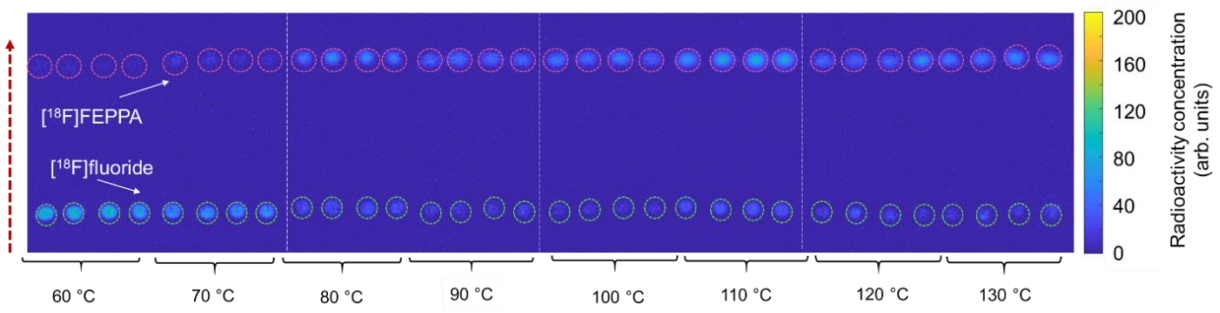

Figure 4-49. Cerenkov images of TLC plates (each containing 8 samples) after developing in the mobile phase. In this case, each TLC plate contains samples from two different temperatures (n=4 replicates each).
White dotted lines show the edges of each separate multi-sample TLC plate. Dashed circles indicate the ROIs used for analysis. The dashed red arrow indicates the direction of solvent movement during developing.

Table 4-22. Summary of data acquired when exploring the effect of temperature on the radiosyntheses of [^{18}F]FEPPA.

Temperature (°C)	Collection efficiency (%) n=4	Fluorination efficiency (%) n=4	Crude RCY (%) n=4	Activity left on chip (%) n=4
60	94.1 ± 1.6	11.9 ± 1.8	11.2 ± 1.5	2.5 ± 0.4
70	91.6 ± 1.7	22.8 ± 2.0	20.9 ± 1.7	2.1 ± 0.3
80	91.6 ± 0.9	65.1 ± 1.1	59.6 ± 1.2	1.8 ± 0.2
90	92.7 ± 1.5	77.5 ± 1.6	71.8 ± 1.8	1.7 ± 0.2
100	93.8 ± 1.5	81.3 ± 1.5	76.3 ± 2.6	1.0 ± 0.2
110	92.9 ± 1.9	83.0 ± 1.4	77.1 ± 2.0	1.0 ± 0.3
120	91.4 ± 1.0	75.5 ± 1.8	69.0 ± 1.5	1.2 ± 0.2
130	90.6 ± 1.1	75.2 ± 2.7	68.1 ± 3.0	1.6 ± 0.1

4.7.8.1 Comparison to literature methods

Table 4-23. Comparison of optimized droplet conditions to literature reports for conventional and flow-chemistry synthesis of [^{18}F]FEPPA.

	This work (2021)	Chang et al.[162] (2021)	Dahl et al.[167] (2019)	Vignal et al.[163] (2018)	Berroteran-Infante et al.[164] (2018)
Synthesizer type	Microscale (droplet format)	Macroscale	Microscale (flow format)	Macroscale	Macroscale
Base type	$TBAHCO_3$	K_{222} / K_2CO_3	K_{222} / $KHCO_3$	K_{222} / K_2CO_3	K_{222} / K_2CO_3
Base amount (nmol)	240	28000/ 20000	2000/2000	40000/22000	58000/32000
Precursor amount (nmol)	240	9000	9000	9000	12000
Reaction solvent	thexyl alcohol: MeCN (1:1 v/v)	MeCN	MeCN	MeCN	MeCN
Reaction volume (mL)	0.008	0.6	0.2	1	0.5
Temperature (°C)	90	90	80	90	90
Reaction time (min)	2	10	10	10	10
Starting activity (MBq [mCi])	13.8 [0.375]	N.R.	3700 [100]	N.R.	N.R.
Fluorination efficiency (%)	88.5 ± 0.9 (n=4)	N.R.	N.R.	N.R.	N.R.
Crude RCY (decay-corrected; %)	80.7 ± 1.2 (n=4)	N.R.	N.R.	N.R.	N.R.
Activity yield (%)	53 (n=1)	30 ± 2 (n=8)	29*	34 ± 2 (n=17)	38 ± 3 (n=15)
RCY (decay-corrected; %)	67 (n=1)	50 ± 2 (n=8)	51 ± 6 (n=3)*	48 ± 2 (n=17)	46 ± 3 (n=15)
Synthesis time (min)	30	80	55*	55	30

* Isolated yield without formulation
N.R. = not reported.

4.7.9 Representation of chromatograms

4.7.9.1 [^{18}F]Flumazenil

Crude [^{18}F]Flumazenil was injected in HPLC to isolate the product (**Figure 4-50A**). A subsequent injection was performed to confirm purity (**Figure 4-50B**), and a co-injection with

Flumazenil reference standard was performed to confirm product identity (**Figure 4-50C**). The crude product showed minimal UV impurities.

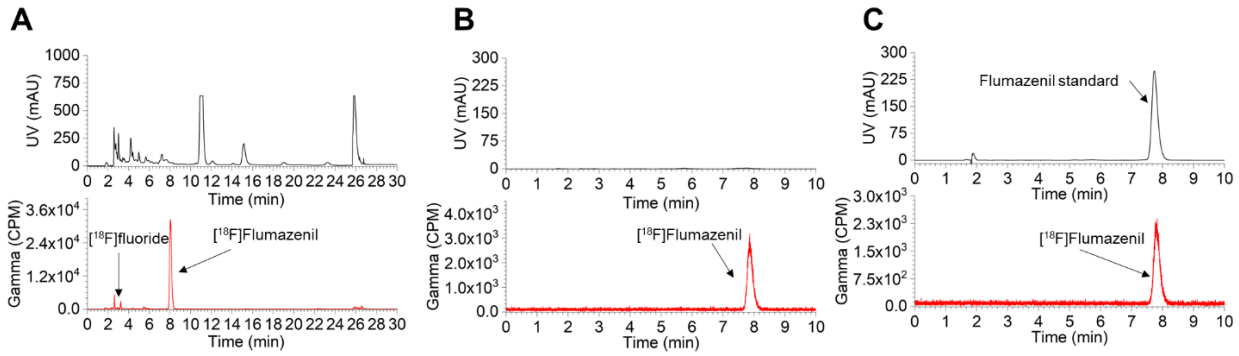

Figure 4-50. HPLC chromatograms of [^{18}F]Flumazenil.
(A) Crude product. (B) Isolated product. (C) Co-injection with reference standard.

4.7.9.2 [^{18}F]PBR06

Crude [^{18}F]PBR06 was injected in HPLC to isolate the product (**Figure 4-51A**). A subsequent injection was performed to confirm purity (**Figure 4-51B**), and a co-injection with PBR06 reference standard was performed to confirm product identity (**Figure 4-51C**). The crude product showed minimal UV impurities.

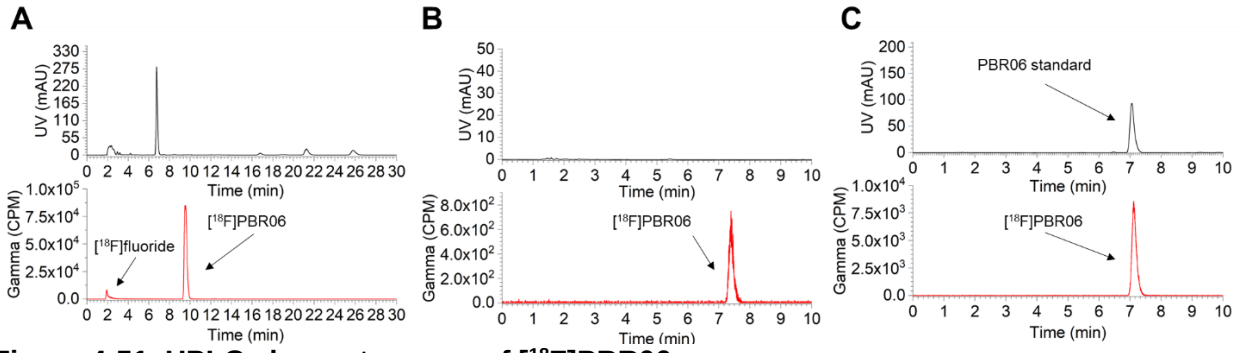

Figure 4-51. HPLC chromatograms of [^{18}F]PBR06.
(A) Crude product. (B) Isolated product. (C) Co-injection with reference standard.

4.7.9.3 [^{18}F]Fallypride

Crude [^{18}F]Fallypride was injected in HPLC to isolate the product (**Figure 4-52A**). A subsequent injection was performed to confirm purity (**Figure 4-52B**), and a co-injection with

Fallypride reference standard was performed to confirm product identity (**Figure 4-52C**). The crude product showed minimal UV impurities.

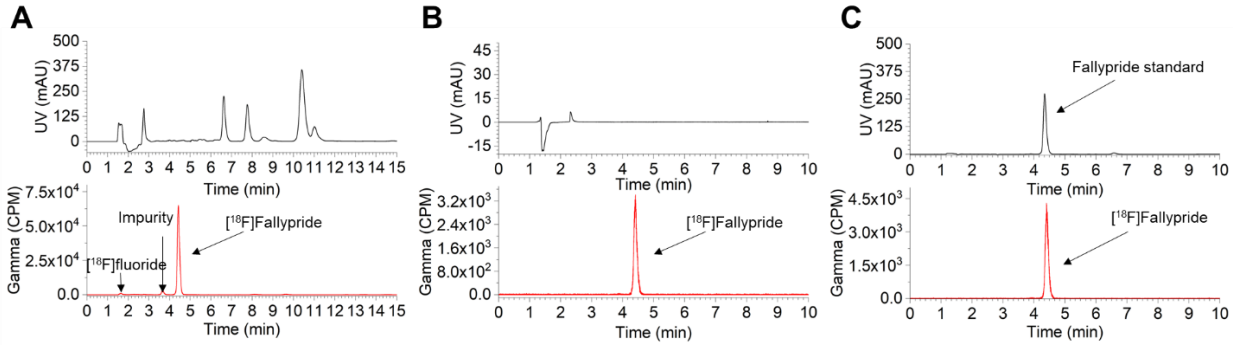

Figure 4-52. HPLC chromatograms of [^{18}F]Fallypride.
(A) Crude product. (B) Isolated product. (C) Co-injection with reference standard.

4.7.9.4 [^{18}F]FEPPA

Crude [^{18}F]FEPPA was injected in HPLC to isolate the product (**Figure 4-53A**). A subsequent injection was performed to confirm purity (**Figure 4-53B**), and a co-injection with FEPPA reference standard was performed to confirm product identity (**Figure 4-53C**). The crude product showed minimal UV impurities.

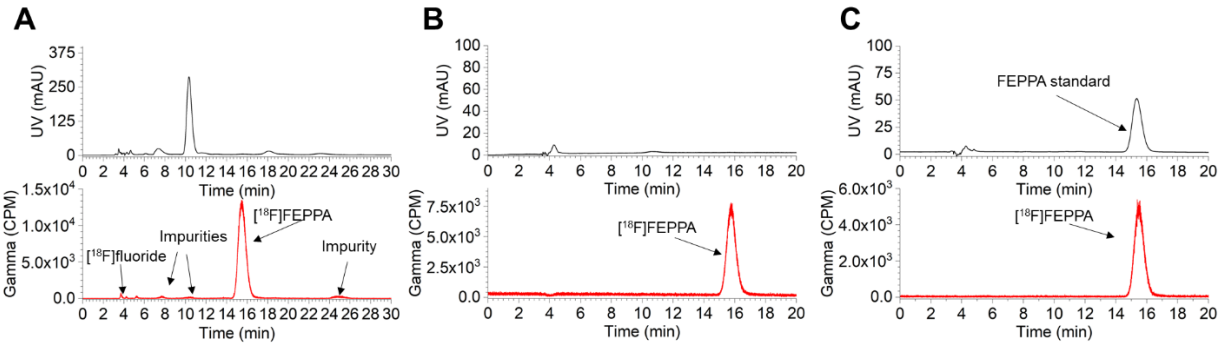

Figure 4-53. HPLC chromatograms of [^{18}F]FEPPA.
(A) Crude product. (B) Isolated formulated product. (C) Co-injection with reference standard.

4.7.10 Clinical-scale radiosynthesis

Summaries of high activity droplet syntheses of [^{18}F]PBR06 carried out with different starting activity are shown in **Table 4-24** and **Figure 4-54.**

Table 4-24. Synthesis performance of [^{18}F]PBR06 at increased activity levels.

Starting activity (MBq [mCi])	Number of replicates	Collection efficiency (%)	Fluorination efficiency (%)	Crude RCY (%)
14.1 [0.38]	n=4	95.8 ± 3.5	96.5 ± 0.9	92.4 ± 3.0
651 [17.6]	n=1	94.0	87.1	81.0
1120 [30.3]	n=1	90.3	80.9	73.0
2200 [59.7]	n=1	90.9	68.6	62.4
2390 [64.7]	n=1	89.5	88.7	71.5
2960 [80.8]	n=1	91.0	79.3	72.1
3170 [85.6]	n=1	90.3	65.6	59.2

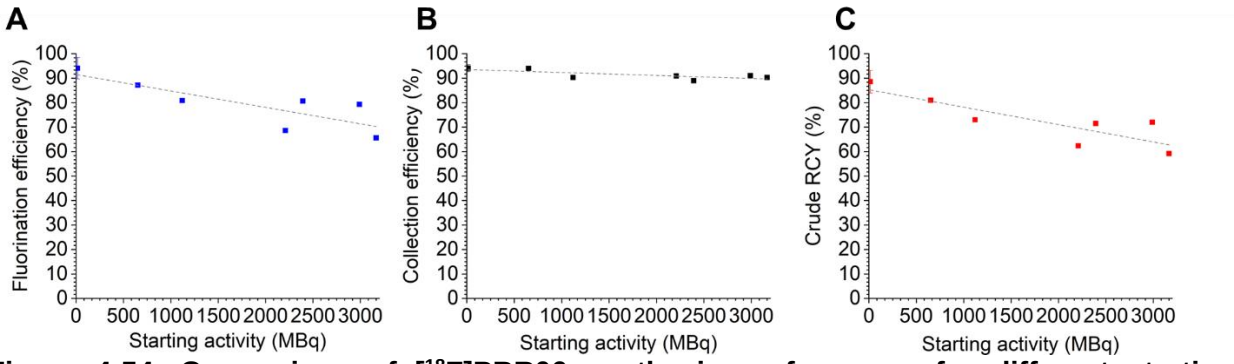

Figure 4-54. Comparison of [^{18}F]PBR06 synthesis performance for different starting activities.

(A) Fluorination efficiency. (B) Collection efficiency. (C) Crude RCY.

Chapter 5: A base free, universal [^{18}F]fluoride concentration and purification method for scale-up of microscale reactions to GBq levels

5.1 Introduction

Positron emission tomography (PET) has become an indispensable method for patient diagnostics, monitoring response to drug treatment, and developing new therapeutics[175]. PET uses biologically active molecules tagged with a short-lived positron-emitting radioisotopes that allow dynamic *in vivo* measurements of specific biochemical processes. The majority of such PET radiopharmaceuticals with regulatory approval and in clinical trials are labeled with F-18, due to its wide availability, high positron decay ratio (97%), moderate half-life (109.8 min), and good imaging resolution[6]. Preparation of these compounds is expensive due to the high cost of the radiosynthesizer, radiation shielded facilities, reagents and radioisotope for each batch, and skilled personnel needed to operate the equipment.

For more than a decade, there has been an increase in the use of microreactors for the performance of radiochemical reactions due to the substantial cost reduction on production through the lower consumption of expensive reagents, small system footprint, and possible reduction of shielding[25,62]. In addition, increase in yield can be increased due to rapid mixing of reagents, short evaporation times, and higher concentration of radionucleotide[62]. While there have been several prototypes that leverage the advantages of microfluidics for PET radiopharmaceuticals, most focus on production for preclinical use[52,58,176,177]. Recently, activity scale-up has been shown using a miniature trap and release process for the increase of activity on microdroplet reactions (e.g., up to 20 clinical doses of [^{18}F]Fallypride)[35,45,50,60]. Another method that allowed the increase of activity on microdroplets was the dispensing and drying of relatively large amounts of activity by loading 30 µL droplets onto the chip, evaporating them, and repeating until the desired activity is concentrated on the chip (e.g., up to 2 clinical doses of [^{18}F]FET and

[^{18}F]Florobetaben[139]). Subsequent reactions were performed in 10 µL volumes, utilizing 4 mm reactor droplet trap reactors[139].

While both methods successfully enabled the production of clinical doses using a microfluidic chip, the results showed that with the increase of starting activity there was a decrease in the radiochemical yield of the reactions. The use of the microscale concentration method for the production of [^{18}F]Fallypride at high activities (ranging from 3.7 GBq to 41 GBq [0.10 Ci to 1.1 Ci]) showed a decrease in the crude RCY from 65% to 25% as the overall starting activity increased. The one factor that led to the decrease in the overall crude RCY was the drop in fluorination efficiency from 90% to 40%[60]. Furthermore, utilizing microscale concentrations methods, increased activity scales led to lower [^{18}F]fluoride trapping on QMA resin (from ~94% to ~63%)[60]. While mock experiments using KF showed 100% trapping efficiency with a mock sample of 37 MBq (1 Ci) (i.e., 50 µM KF) with the mass of 3 mg of QMA resin[60], the experiments with 37 GBq of activity showed that 3 mg of QMA only trapped ~63% of the activity.

The concentration of activity on chip via the dispensing and drying method allowed the desired amount of activity to be use without any losses during the concentration process. To increase the amount of starting activity on chip using the dispensing and drying method, more volume from the activity source needs to be dried on the reaction site. However, similar observations on the decrease of overall crude RCY for the production of [^{18}F]FET, [^{18}F]FBB, and [^{18}F]BPR06 were observed[139,178]. In the case of [^{18}F]FET the overall crude RCY was reduced (from ~70% to ~40%) by the decrease in both the collection efficiency and fluorination efficiency as the starting activity increased from 0.2 to 4 GBq. Similarly, [^{18}F]FBB showed a decrease in the overall crude RCY from ~60% to ~40% as activity amount increases (from 0.02 to 4 GBq) due to the decrease in collection and fluorination efficiency[139]. The dispensing and drying method to increase the amount of starting activity was also applied to the synthesis of [^{18}F]PBR06, while no decrease on the collection efficiency was observed as the amount of staring activity increased like in the cases of [^{18}F]FET and [^{18}F]FBB (due to the lack of deprotection step), the fluorination efficiency

of the reaction decreased from ~97% at 14.1 MBq (0.38 mCi) to ~65% at 3170 MBq (85.6 mCi), which led to the overall decrease of the crude RCY from ~90% at low activity to ~60% at high activities[178].

Many potential reasons for this decrease in observed yield could be due to: radiolytic degradation, stochiometric change in the precursor to contaminant [^{19}F]fluoride species, increased concentration of contaminant anionic impurities, increased concentration of any residual cationic impurities in the [^{18}F]fluoride solution introduced into the reactor. (i) Radiolysis is the process of chemical bond cleavage caused by radiation mediated by radicals, which can lead to the reduction in yield of the desired radiolabeled molecule and the formation of side products[34,179,180]. The degree of radiolysis is related to the activity concentration in solution and the geometry of the activity volume[181]. (ii) As activity is scaled up contaminant concentrations of [^{19}F]fluoride species can begin to outweigh the concentration of [^{18}F]fluoride, leading to a stochiometric precursor ratio that could have a significant [18F]fluoride labelled product yield impact[182]. Since reaction conditions are optimized at lower activities (i.e., 15MBq [0.41 mCi])[178] and therefore lower source volumes, the conditions may no longer be optimal when the total amount of source is increased by orders of magnitude. (iii) Anionic impurities could be in abundances large enough to outcompete fluoride, labelling precursor and reducing the overall fluoride reactivity. (iv) It has been noted that metal contaminants are produced during bombardment of [^{18}O]water in a cyclotron for [^{18}F]fluoride production[183]. For example, inorganic cationic impurities that come from parts of the target (body, foils) during the bombardment can dramatically decrease the synthesis yield by either reacting with the [^{18}F]fluoride to produce insoluble salts or to reduce its nucleophilicity[184].

In this chapter we explore approaches to look at these factors independently with the aim of determine the cause(s) of reduced yield so that it can be address for reaction scale-up. As part of this study, we develop an improved method for [^{18}F]fluoride concertation that can enhance the

removal of contaminants while remaining fast and able to concentrate arbitrary activity volumes into 100-80 µL that can rapidly be loaded and dried on the microdroplet chips. Compared to previous QMA methods, it involves additional cartridges and filtration steps to remove impurities, and also uses a volatile base for elution that enables “base free” elution of [^{18}F]fluoride to better decouple the fluoride concentration process from the downstream reaction, enabling base type and amount to be optimized independently for each tracer synthesis.

5.2 Materials and Methods

5.2.1 Materials

Anhydrous acetonitrile (MeCN, 99.8%), 2,3-dimethyl-2-butanol (thexyl alcohol, 98%), 4,7,13,16,21,24-hexaoxa-1,10-diazabicyclo[8.8.8]hexacosane (K_{222}, 98%), triethylamine (TEA, 99%), trifluoroacetic acid (TFA, >99%), tetrahydrofluran (THF, >99.9%, inhibitor-free), hexanes (95%), dichloromethane (DCM, >99.8%), acetone (99.5%), ammonium formate (NH_4HCO_2: 97%), ethylene glycol (99.8%) and potassium carbonate (K_2CO_3, 99.995%), and Chelex 100 (Sodium form, 50-100 mesh) resin were purchased from Sigma-Aldrich (St. Louis, MO, USA). Kimwipe (1-ply, cellulose) was purchased from Fisher Scientific (Pittsburgh, PA, USA). Strong cation exchange resin (SCX; 35-60 µm, 300 A) were purchased from Altech (USA). Sep-Pak Plus QMA Light cartridges (37-55 µm particle size) were purchased from Water Corporation (Milford, MA, USA). PTFE tubing (1/8” OD, 1/16” ID; 1530L. 1/16” OD, 0.04” ID; 1517L, 1/16” OD, 0.01” ID; 1529L) was purchased from IDEX Health and Science (Wallingford, CT, USA). n-butanol (n-BuOH, 99%) was purchased from Alfa Aesar (Ward Hill, MA, USA). Tetrabutylammonium bicarbonate ($TBAHCO_3$, 75mM in ethanol), 2-((2,5-dimethoxybenzyl)(2-phenoxyphenyl)amino)-2-oxoethyl 4-methylbenzenesulfonate ([^{18}F]PBR06 precursor, >95%), 2-fluoro-N-(2-methoxy-5-methoxybenzyl)-N-(2-phenoxyphenyl)acetamide (reference standard for [^{18}F]PBR06, >95%), tosyl fallypride (fallypride precursor, >90%), Fallypride (reference standard, >95%), acetamide, N-[2-[2-[[(4-methylphenyl)sylfonyl]oxy]ethoxy]phenyl]methyl]-N-(4-phenoxy-3-pyridinyl)

([^{18}F]FEPPA precursor, >90%), and N-acetyl-N-(2-fluoroethoxybenzyl)-2-pehonoxy-5-pyridinamine (reference standard for [^{18}F]FEPPA, >95%) were purchased from ABX Advanced Biochemical Compounds (Radeberg, Germany). DI water was obtained from a Milli-Q water purification system (EMD Millipore Corporation, Berlin, Germany). No-carrier-added [^{18}F]fluoride was produced by the (p, n) reaction of [^{18}O]H_2O (98% isotopic purity, Huayi Isotopes Co., Changshu, Jiangsu, China) in an RDS-111 cyclotron (Siemens, Knoxville, TN, USA) at 11 MeV, using a 1.2 mL silver target with havar foil.

5.2.2 Methods

5.2.2.1 Ionic Exchange Theory

Previous reports have shown that various metal impurities arise during the production of [^{18}F]fluoride in medical cyclotrons[185,186]. In addition to the ubiquitously used quaternary methylammonium (QMA) cartridge to trap and release fluoride in conventional systems, strong cation exchange (SCX) cartridges are also used in many cases such as aluminum fluoride (AlF) chemistry[187,188]. Reagents prior to addition to the metal fluoride complex, need to be depleted of trace metals that can be introduced through their various production methods.

SCX cartridges have previously been used in conjunction with microscale [^{18}F]fluoride concentration to eliminate contaminants that could interfere with trapping on the QMA micro-cartridge[60]. However, because SCX resin primarily interacts with positively charged basic compounds such as amines or cations (1+ charge), we sought to enhance this approach with additional resin to remove multivalent metal ions in greater specificity. Chelex consists of a stryrine-divinylbenzene copolymer functionalized with iminodiacetate ions that act as chelator groups for the binding of polyvalent metal ions, with high specificity to divalent cations. It is important to note that Chelex resin utilized in its sodium form cannot be used on its own or downstream of the SCX, since Na^+ would be displaced for each trapped metal ion. This Na^+ can interfere with the efficiency of the downstream radiofluorination reactions, due to the nucleophilicity of Na^+ to fluoride. Thus, Chelex resin was placed upstream of the SCX cartridge.

The SCX cartridge in its H^+ form, allows the efficient exchange of Na^+ which will not interfere with downstream radiofluorination.

[^{18}F]fluoride, and contaminant species are first directed through the Chelex resin, capturing polyvalent cations, and releasing Na+. [^{18}F]fluoride, anionic impurities, monovalent cations, and Na^+ ions are then directed through the SCX resin. This SCX resin captures monovalent cations, exchanging H^+. [^{18}F]fluoride, anionic impurities, and H^+ are then directed to the QMA. The QMA traps the [^{18}F]fluoride and anionic impurities. Sequential washing of the QMA, ensures that residual cationic contaminants are removed prior to the concentration of [^{18}F]fluoride. Cationic species (e.g., K^+ (from K_2CO_3), and TBA^+ (from $TBAHCO_3$)) are often then mixed with phase transfer catalysts (K_{222} or TBA^+) to release [^{18}F]fluoride in a nucleophilic form suitable for radiofluorination.

5.2.2.2 Remote [^{18}F]fluoride processing

A remote processing apparatus was developed to allow the processing of [^{18}F]fluoride (**Figure 5-1**). A series of vials can be pressurized with an external N_2 source, then flow paths can be effectively switched with the use of a selector valve for different processes. In the initial trapping process, the source vial is pressurized (~18 psi) and directed though the Chelex, SCX into an intermediate vial. Once the cartridges are blown dry, a secondary vial downstream of the eluent path is pressurized (~18 psi), to direct the activity through the QMA path. The activity in the trapping configuration, passes through the QMA, through line 1 of the selector valve, and into a vial marked for waste. To wash the path of this initial trapping, both pressure to the source and vial downstream of the eluent are reduced to 0. Preloaded water (1 mL), is pressurized ahead of the source vial, filling the source vial for rinsing the path length previously used. The source once full is pressurized (~18 psi), and the water is directed through the Chelex and SCX cartridges, into the intermediate hold vial. The vial downstream of the eluent is pressurized, directing water through the QMA and line 1 of the selector valve into waste. Nitrogen is directed through the line

to ensure complete drying of the QMA cartridge prior to elution of the concentrated activity. Pressure to the various vails is halted, and eluent is loaded remotely outside of the hot cell into the eluent vial (~100 µL). The eluent vial is sealed, then pressurized (~18 psi), delivering the eluent to the vial used previously for pressurization downstream, and into the intermediate vial. The line through the valve selector is switched to line 2, that is directly connected to an empty vial for capture of the concentrated activity. The eluent in the intermediate vial through pressurization is then directed through the QMA, through the selector valve and into the empty vial. To ensure complete recovery of the eluent solution through the path length, the vial downstream of the eluent vial is additionally pressurized (~18 psi), for an additional minute. The system is completely depressurized until recovery of the concentrated activity.

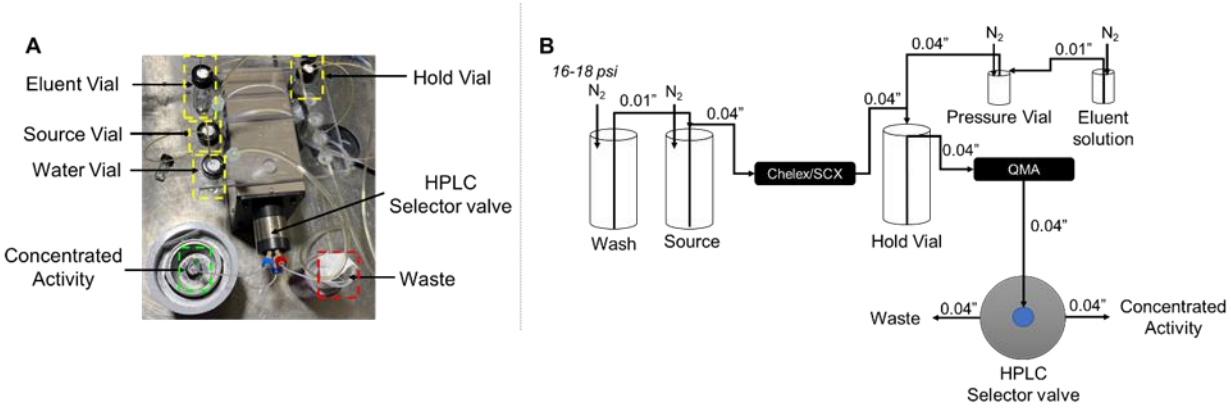

Figure 5-1. Trap and release apparatus for the removal of metallic contaminants and concentration of [^{18}F]fluoride.
(A) Photograph of the apparatus set up showing the placement of vials for the trap and release process of activity. (B) Schematic of the apparatus indicating the liquid direction throughout the system, the inner diameter of the connected PTFE tubing, and the vials where N_2 pressure was applied for the movement of the liquid.

5.2.2.3 Reagent preparation

Eluent solution (100 µL) was composed of 20 nmol/µL of TEA (aq.). [^{18}F]PBR06 precursor stock solution contained 20 mM precursor in a 1:1 v/v mixture of thexyl alcohol and MeCN. [^{18}F]Fallypride stock solution contained 39 mM of precursor in a 1:1 (v/v) mixture of theyxl alcohol and MeCN. [^{18}F]FEPPA stock solution contained 30 mM of precursor in a 1:1 (v/v) mixture of theyxl alcohol and MeCN. The collection solution for [^{18}F]PBR06, [^{18}F]Fallypride, and [^{18}F]FEPPA

was a 9:1 v/v mixture of MeOH and H_2O. 240 nmol of $TBAHCO_3$ base phase transfer catalyst was added to the concentrated activity volume after processing (i.e., the amount needed for the droplet-based synthesis of these 3 tracers[178]). TLC mobile phases for each tracer were similar to those reported in **Chapter 4**.

5.2.2.4 Micro-cartridge fabrication

Cationic impurities were removed with 10 mg of Chelex resin and 30 mg of SCX resin, which were packed into an 8” length of 1/8” OD 1/16” ID PTFE tubing. A small Kimwipe was torn and inserted into the tubing segment to act as a frit. Using a needle cleaning rod from a spinal needle (Quincke Spinal Needle, BD Biosciences, San Jose, CA, USA) it was positioned at about 7” away from the inlet and secured within the tubing by pinching the tube just downstream of the frit. A slurry of the SCX resin was prepared by adding 30 mg of the resin in 500 µL of ion chromatography (IC) grade water (Sigma-Aldrich, St. Louis, MO, USA). A syringe fitting was connected to the exit of the tubing, and a 1 mL syringe was connected to pull the slurry from the inlet side of the tubing. After complete, the resin container was filled with an additional 1 mL of IC water and the procedure repeated. A second frit was then inserted upstream of the SCX resin bed. A slurry of Chelex resin was prepared by dispersing 10 mg of the resin in 500 µL of IC water, repeating the packing procedure detailed above. A final frit was inserted upstream of the Chelex resin, secured by deforming the tubing upstream of this frit. (Resin masses for both Chelex and SCX ranged from 3 mg to 30 mg during the optimization phase.) The QMA cartridges were prepared in a similar fashion with 9 mg of resin packing into 1/16” OD, 0.04” ID tubing (3 to 9 mg were explored during optimization).

The purchased QMA resin consisted of quaternary methylammonium groups prepared with a bicarbonate counter ion. While complete conversion of the HCO_3^- form to the HO^- form is impossible, we treated the QMA resin (~1 g) with 1 N NaOH (10 mL) for 20 min. in a glass beaker with a stir bar. The treated resin was then transferred to an SPE tube fitted with a polyethylene

filter (20 µm), then rinsed with 3x 20 mL of IC water. At the end of this washing volume, the pH of the exiting water was tested to confirm a range of 6-7. The resin packed in the SPE tube was dried with N_2 (10 psi) for 60 min. Dried resin could be recovered from the SPE tube by gently tapping the tube into a capture falcon tube. QMA micro-cartridges were packed just prior to use to avoid the potential for microbial contamination. Conversion of the QMA was performed to avoid the deposition of bicarbonate salt residues, that could poison downstream radiofluorination. **Figure 5-2** shows that the residue of QMA resin in the HCO_3^- form, leaves increasing deposits as a function of base mass used during the elution process. When the QMA is in the HO^- form, this salt deposition is not observed.

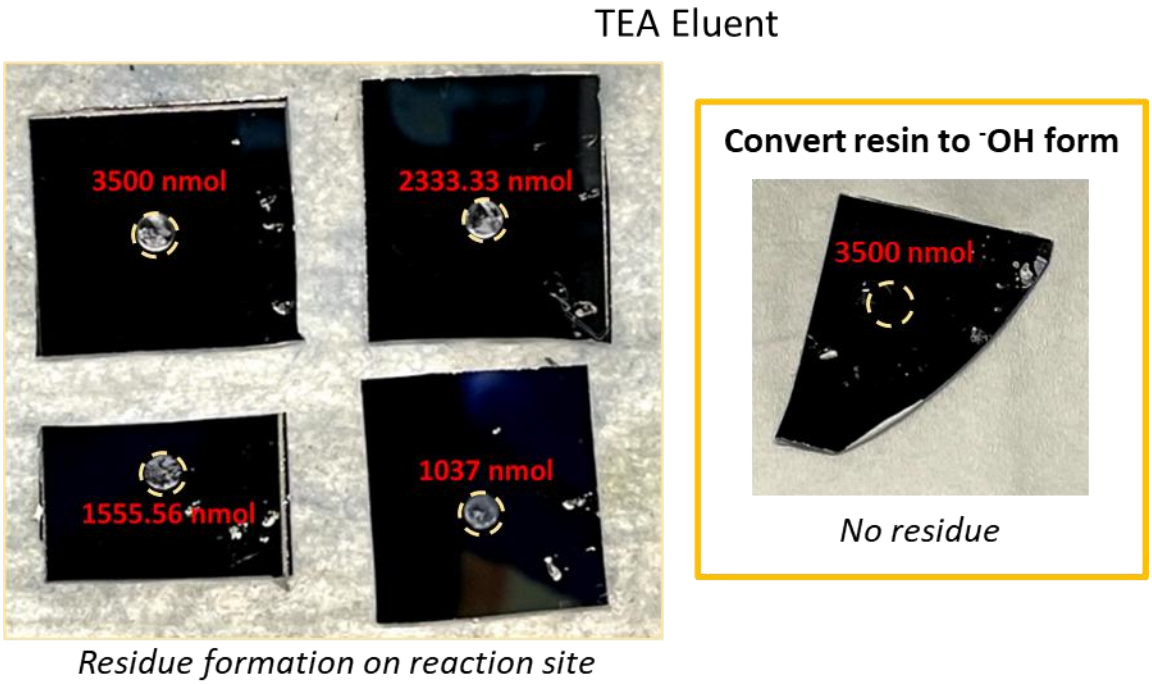

Figure 5-2. Residue formation on reaction site after elution of activity through QMA micro-cartridge using different amounts of TEA.
Four chips on the left show the formation of white residue on the reaction site after drying activity volume eluted using 3500-1037 nmol of TEA, activity was eluted through QMA micro-cartridges that contained bicarbonate counter ions. Chip on the right shows the reaction site after drying the activity eluted through a QMA that was treated to contain hydroxyl counter ions, no residue was shown when using high amounts of TEA. Yellow circles show the reaction site on the chip.

5.2.2.5 Micro-cartridge trapping visualization studies

To optimize the resin amount of QMA needed for efficient [^{18}F]fluoride trapping, were Cerenkov luminescence imaging (CLI) was used. The QMA micro-cartridge was taped into the field of view (FOV) of the Cerenkov setup (**Figure 5-3**) to observe the distribution of radioactivity on cartridges in real-time during trapping, washing, and elution of the [^{18}F]fluoride. Additional measurements of waste activity, residual source vial activity, the eluted concentrated activity vial, and the residual cartridge activity were made at the end of the experiment to quantify trapping efficiency (and breakthrough), losses during washing, and elution efficiency.

Visualization of the cartridges was performed using a previously-described home-built CLI setup[101]. The cartridge was enclosed in a light-tight apparatus, then connected to its respective source (**Figure 5-3**). The source was pressurized so that it allowed a drip rate of exit solution at a rate similar to the remote apparatus described above (~1 psi). Once the vial was pressurized, the light-tight enclosure was closed, then the QMA imaged for 1 s over 100 frames. Due to the readout of the camera, each frame represents a 3 s delay (e.g., frame 1 denotes 1 s, and frame 2 denotes 4 s). Following the collection of the CLI frames, pressure through the QMA was halted, and a brightfield image was taken for 7 ms. This brightfield image, allows user section of the QMA bed for activity breakthrough analysis in the MATLAB processing described below.

The CLI frames were imported into MATLAB and processed as previously described[93]. After frame 1 is imported into MATLAB, a script was written (**Appendix 5.5.1**) that allows the selection of the brightfield image for overlay in the video file. The user after the CLI and brightfield image is overlaid, is asked to define the boundaries of the cartridge. The pixel intensity across this defined ROI is measured for each frame by the program. Overlays of the CLI and brightfield images, the pixel intensity distribution across the cartridge, and the gaussian smoothing of this profile are all written into separate video files for analysis by the user.

5.2.2.6 Micro-cartridge concentration efficiency determination

To characterize trapping and elution efficiency, various radioactivity measurements were made with a calibrated dose calibrator (CRC-25 PET, Capintec, Inc., Ramsey, NJ). For the purposes of calculations, all radioactivity measurements were decay-corrected to a common timepoint. Measurements were made of the activity in the [^{18}F]fluoride source vial before trapping ($A_{0\ source}$), activity in the source vial after trapping (A_{source}), activity in the [^{18}O]H_2O recovery vial after trapping (A_{waste}), and the collected activity after elution ($A_{collect}$). The activity on the cartridge after trapping ($A_{cartridge}$) was determined indirectly (i.e., calculated as $A_{0\ source} - (A_{waste} + A_{source})$) to minimize radiation exposure. This method also proved to be significantly more accurate than directly measuring the cartridge in the dose calibrator, presumably due the differing geometry of the cartridge compared to the vials. Trapping efficiency (%) was computed as $A_{cartridge}/(A_{0\ source} - A_{source})$. Elution efficiency (%) was calculated as $A_{collect}/A_{cartridge}$. Recovery efficiency (%), defined as the amount of activity recovered following elution relative to starting activity, was calculated as trapping efficiency x elution efficiency. Starting activity was defined as $A_{0\ source} - A_{source}$ which can be approximated as $A_{0\ source}$ since we found $A_{source} < \sim 0.1\%$ of $A_{0\ source}$.

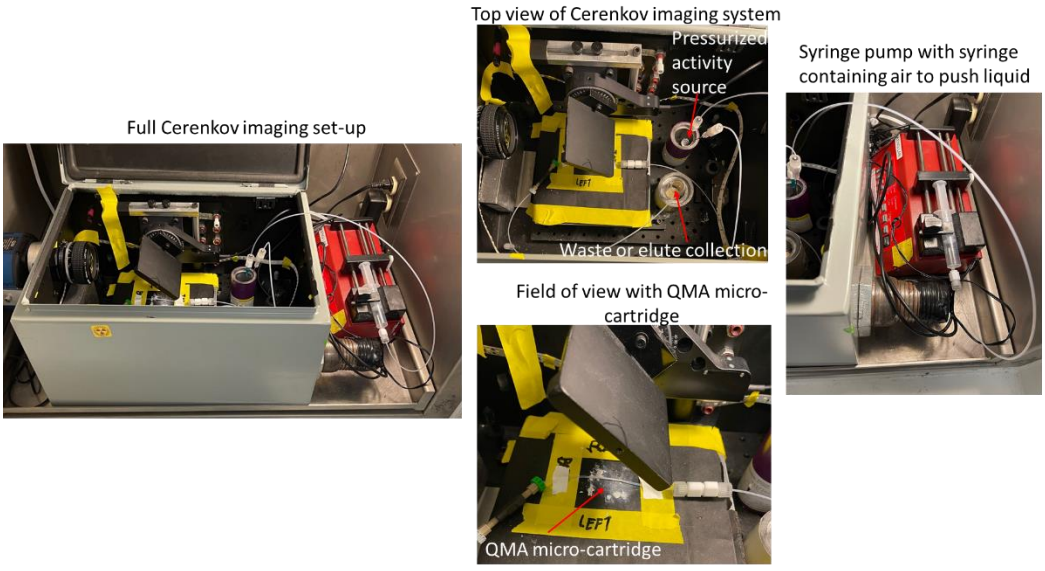

Figure 5-3. Visualization apparatus utilized for QMA mass optimization studies.

5.3 Results

5.3.1 Scale-up via increased volume of radioisotope source

In addition to examining in previous work the impact of activity scale-up (via loading multiple increments of [^{18}F]fluoride/[^{18}O]water directly from the cyclotron) on the optimized synthesis of [^{18}F]PBR06[178], we explored scaling the activity in the syntheses of [^{18}F]Fallypride and [^{18}F]FEPPA. The volume of activity solution loaded and dried on the reaction site varied from 40 to 180 µL, corresponding to activity levels of 740 to 3000 MBq (20 to 80 mCi). Activity concentration varied from day to day due to the production of different amounts of activity. **Figure 5-4** and **Table 5-1** show the trends observed for the collection efficiency, fluorination efficiency, and crude RCY for [^{18}F]Fallypride, and **Figure 5-5** and **Table 5-2** show the results for [^{18}F]FEPPA. Both radiosynthesis exhibited a decrease in overall performance with increased starting activity.

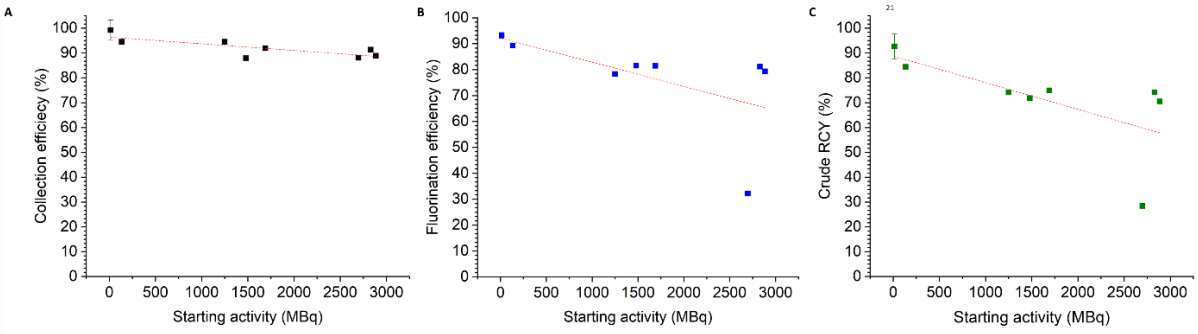

Figure 5-4. Microscale reaction performance of [^{18}F]Fallypride with variant activity scales. (A) Collection efficiency, (B) Fluorination efficiency, and (C) Crude RCY performance. Activity scale was varied by using different volumes of the radioisotope source solution.

Table 5-1. Synthesis performance of [^{18}F]Fallypride at increased activity levels.

Starting activity (MBq [mCi])	Number of replicates	Collection efficiency (%)	Fluorination efficiency (%)	Crude RCY (%)
14.1 [0.38]	n=2	99.2 ± 4.1	93.3 ± 1.1	92.7 ± 5.0
135 [3.6]	n=1	94.5	89.3	84.4
1250 [34.0]	n=1	94.9	78.3	74.2
1480 [40.0]	n=1	87.9	81.6	71.8
1690 [46.0]	n=1	91.9	81.5	74.9
2700 [73.0]	n=1	88.1	32.2	28.4
2800 [76.0]	n=1	91.3	81.2	74.2
2900 [78.0]	n=1	88.9	79.3	70.5

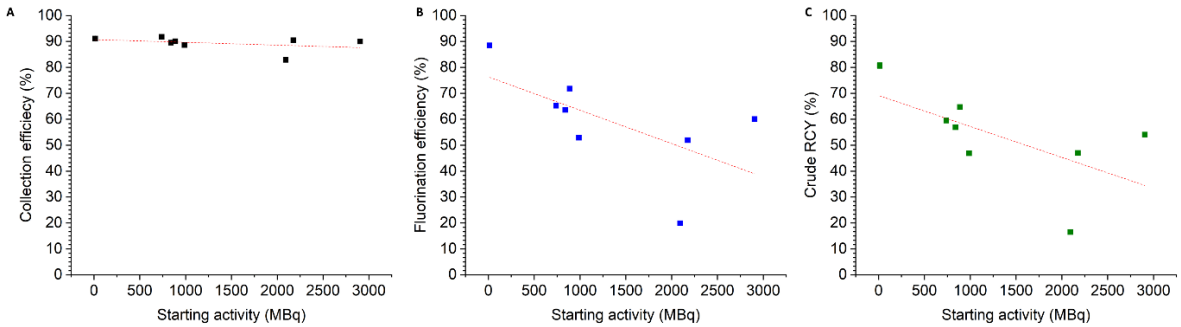

Figure 5-5. Radiosynthesis performance of [^{18}F]FEPPA with activity using microdroplets. (A) Collection efficiency, (B) Fluorination efficiency, and (C) Crude RCY performance.

Table 5-2. Synthesis performance of [^{18}F]FEPPA at increased activity levels.

Starting activity (MBq [mCi])	Number of replicates	Collection efficiency (%)	Fluorination efficiency (%)	Crude RCY (%)
14.0 [0.38]	n=2	91.1 ± 0.4	88.5 ± 0.9	80.7 ± 1.2
740 [20.0]	n=1	91.8	65.2	59.5
800 [23.0]	n=1	89.5	63.6	56.9
900 [24.0]	n=1	90.1	71.8	64.7
1000 [27.0]	n=1	88.6	52.9	46.9
2100 [57.0]	n=1	82.9	19.9	16.5
2200 [59.0]	n=1	90.5	51.9	47.0
2900 [79.0]	n=1	90.0	60.1	54.1

5.3.2 Study of impact of source volume at constant activity scale

In the previous experiments, increasing the activity was achieved using a higher volume of source activity, with multiple potential causes of the reduced reaction performance. To eliminate the impact of radiolysis, we performed similar experiments using different volumes of decayed activity source (i.e., which would have the same amount of cyclotron impurities and total fluoride as the activity solution before decay) spiked with low volumes of source (2 µL) to ensure low activity (14.1 MBq [0.38 mCi]) and 240 mol of $TBAHCO_3$. 2x2 multi-reaction microdroplet chip was used to explore 4 different such volumes (0, 50, 130, and 230 µL). For the reaction site that did not contain any decayed source, 200 µL of IC water was used instead. To perform the study, activity was loaded to the reaction site in 30 µL increments. The syntheses of [^{18}F]PBR06, [^{18}F]Fallypride, and [^{18}F]FEPPA were each performed at the difference volume scales.

We noticed an increase of white residue on the reaction site with the increase of decayed source volume (**Figure 5-6**).

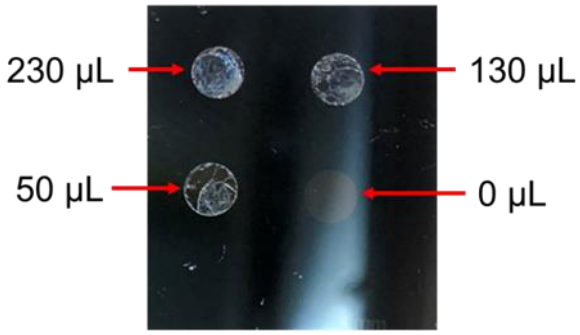

Figure 5-6. Photograph of 2x2 microdroplet chip after drying decay source volume mixed with 14.1 MBq of activity and 240 nmol of base.

This observed a decrease in reaction performance for each radiopharmaceutical as the decay source volume increased, was similar to the effects seen with drying increasingly large volumes of source. The most noticeable change was in the fluorination efficiency of each reaction though we also noticed a decrease in the collection efficiency due to loss of activity on the chip.

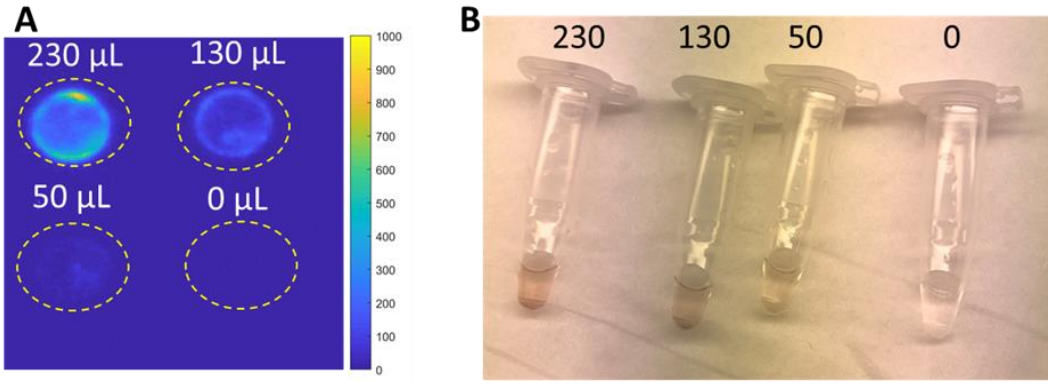

Figure 5-7. Effects of decay source volume on activity retention on chip and color of collected crude product.
(A) Cerenkov image of a 2x2 chip after collection of products. The numbers indicate the amount of decay source that was added to that reaction site. (B) Photograph of crude products after collection from its corresponding reaction sites.

The radiosynthesis results are summarized in **Figure 5-8, Table 5-3, Table 5-4** and **Table 5-5.** In the case of [^{18}F]PBR06 we noticed a decrease on crude RCY from 90% to 49% as the volume of decayed source solution increased. For [^{18}F]Fallypride, the crude RCY decreased from

87% to 23%, and for [^{18}F]FEPPA it decreased from 80% to 2%. These results show the dramatic impact on reaction performance even when the possibility of radiolysis is eliminated by using low activity levels, underscoring the need to remove impurities from [^{18}F]fluoride prior to performing scaled-up droplet reactions.

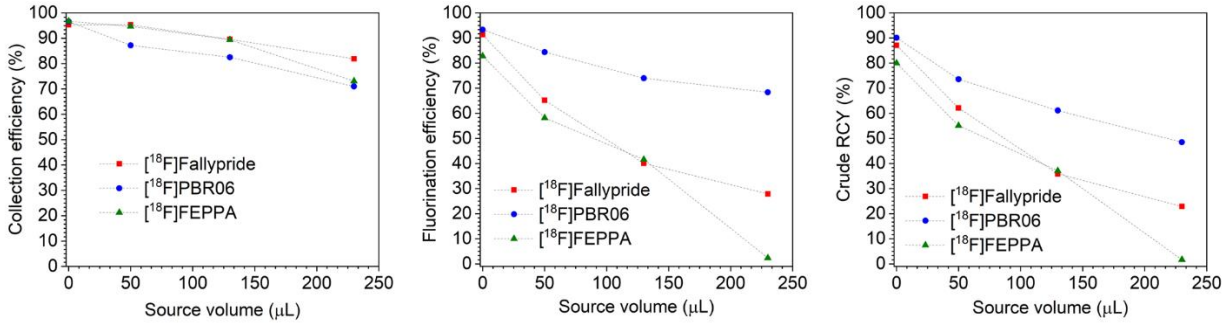

Figure 5-8. Radiosynthesis performance of 3 radiopharmaceuticals as a function of activity source volume (all performed at 14 MBq level).
(A) Collection efficiency, (B) Fluorination efficiency, and (C) Crude RCY performance.

Table 5-3. The effect of different source volumes on the reaction performance of [^{18}F]PBR-06.

Volume dried (μL)	Collection efficiency (%)	Fluorination efficiency (%)	Crude RCY (%)	Activity lost to chip (%)
230	71.0	68.4	48.5	12.4
130	82.5	74.0	61.1	
50	87.2	84.4	73.6	
0	96.6	93.3	90.1	

Table 5-4. The effect of different source volumes on the reaction performance of [^{18}F]Fallypride.

Volume dried (μL)	Collection efficiency (%)	Fluorination efficiency (%)	Crude RCY (%)	Activity lost to chip (%)
230	81.9	27.9	22.9	6.0
130	98.6	40.1	35.9	
50	95.3	65.2	62.1	
0	95.3	91.3	87.1	

Table 5-5. The effect of different source volumes on the reaction performance of [^{18}F]FEPPA.

Volume dried (µL)	Collection efficiency (%)	Fluorination efficiency (%)	Crude RCY (%)	Activity lost to chip (%)
230	73.1	2.4	1.7	7.2
130	89.4	41.6	37.1	
50	94.7	58.2	55.1	
0	96.7	82.8	80.0	

5.3.3 Determination of resin masses for trap and release process

In previous work using 3 mg microscale QMA cartridges to scale-up [^{18}F]fallypride synthesis[60], there was not only a decrease in reaction performance at higher activity scales, but also in the efficiency of trapping [^{18}F]fluoride on the cartridge. Above ~20 GBq of activity, the efficiency dropped significantly, despite mock scale-up experiments (by adding KF) suggesting much higher capacity of the 3 mg cartridge. The reduction in performance when using the large volume of the radioisotope source may be indicative that other species / contaminants are either reducing the QMA cartridge capacity or interfering with binding of [^{18}F]fluoride ions.

To more realistically simulate higher activity scales, we spiked activity (0.37 – 1.1 GBq [10-30 mCi]) amounts into 1 mL of decayed [^{18}F]fluoride in [^{18}O]H_2O which realistically simulates the effects of the higher volume of solution and contains all the impurities and same total fluoride content as a ~37 GBq (~1.0 Ci) cyclotron bombardment. Under this low activity scale, radiolysis would not be expected to impact the efficiency of the trapping process (e.g., due to the direct damage of resin). Furthermore, activity level can be eliminated as a potential variable for determining the cause for trapping efficiency issues, by keeping the activity level low, and by utilizing the same source volume.

In a preliminary test, we performed trapping of 200 µL decayed source water spiked with 0.37 GBq of activity using a 3 mg QMA micro-cartridge and found only 89% of the initial activity was retained on the cartridge after trapping and 2 washes. We explored if more resin mass would be able to retain the activity. Using a 9 mg QMA micro-cartridge, the observed trapping and wash efficiency was only 78%. Noting this poor trapping behavior, the buildup of dark coloration at the

entry port of the QMA micro-cartridge (**Figure 5-9A**) was observed, indicating the presence of significant amounts of contaminants that may interfere chemically or mechanically with trapping, perhaps leading to the surprisingly poor performance (and perhaps explaining the reduced trapping efficiency in the previous study[60]).

Next, a Chelex and SCX cartridge (30 mg Chelex, 30 mg SCX) upstream of the 9 mg QMA cartridge was tested to determine if contaminants could be removed prior to QMA trapping. This time, using 1000 µL of decayed source activity spiked with 0.37 GBq, there was no observed dark coloration in the QMA cartridge (**Figure 5-9B**), but faint traces of coloration could be observed across both the Chelex and SCX resin beds. Trapping efficiency was returned to near quantitative levels, but further optimization was performed to allow the best entrapment of [^{18}F]fluoride on the QMA cartridge (e.g., the lowest bed length utilized for trapping [^{18}F]fluoride).

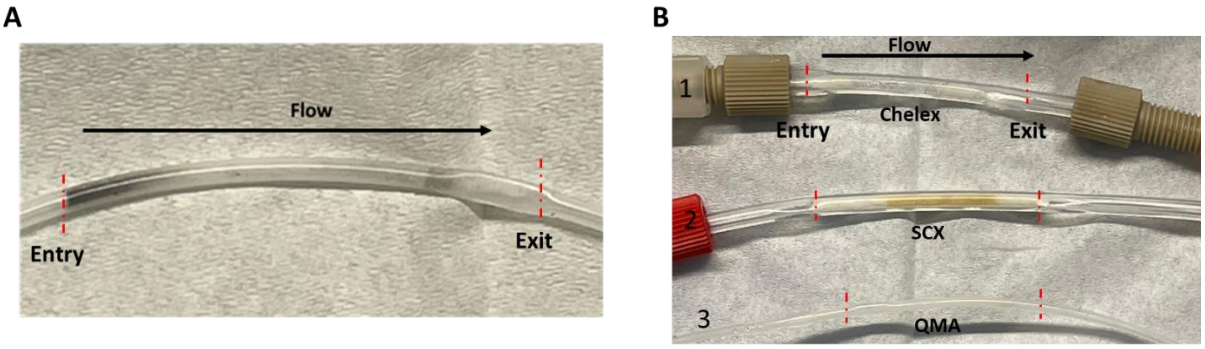

Figure 5-9. Removal of contaminants from decayed source.
(A) Photograph of QMA micro-cartridge after the passing of 200 µL of decayed source. (B) Photograph of Chelex, SCX, and QMA micro-cartridges after passing 200 µL of decayed source. Numbers indicate the order of connection and liquid direction. Dashed red lines indicate the entry and exit port points of each cartridge.

To find the optimal mass of Chelex and SCX resin to be used for purification of the [^{18}F]fluoride, we performed a series of experiments with different combinations of masses (0 to 30 mg) of each of these resins upstream of a 9 mg QMA cartridge, in which activity (1 mL of decayed source spiked with 1 GBq [30 mCi] of activity) was trapped, washed, and eluted. The activity distribution in the QMA cartridge was imaged with Cerenkov imaging and plotted as a

profile of activity along the length of the cartridge. Results are presented in **Figure 5-10**. The optimal distribution is one that is positioned as close as possible to the entrance of the cartridge (i.e., suggesting it may have additional capacity for trapping). We selected 10 mg of Chelex and 30 mg of SCX as the optimal values, which had activity distributed only along 150 pixels of the approximately 400 pixels long QMA cartridge.

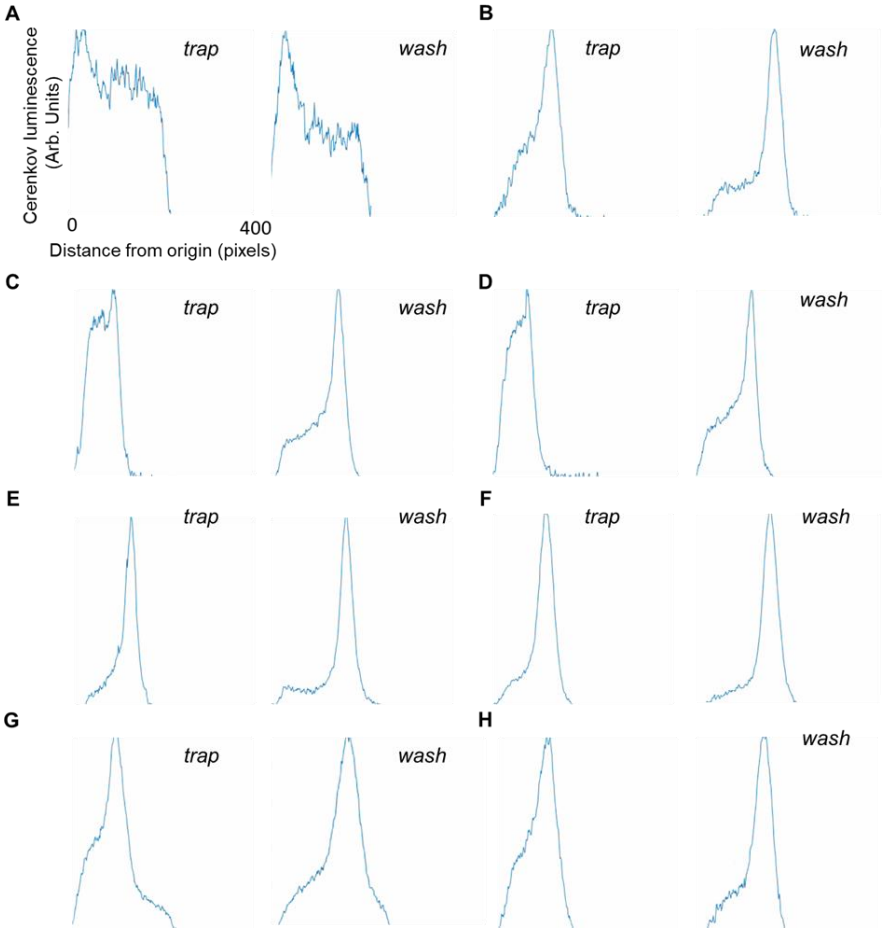

Figure 5-10. Distribution of activity trapped in a 9 mg QMA cartridge with different sized Chelex and SCX cartridges upstream. Images shown in the left of each pair is a snapshot at time 300 s for the trapping step. Images shown in the right of each pair is a snapshot in time at 300 s for the washing step.
(A) 0 mg Chelex, and 0 mg SCX. (B) 0 mg Chelex, and 30 mg SCX. (C) 3 mg Chelex, and 30 mg SCX. (D) 10 mg Chelex, and 30 mg SCX. (E) 30 mg Chelex, and 30 mg SCX. (F) 10 mg Chelex, and 10 mg SCX. (G) 30 mg Chelex, and 3 mg SCX. (H) 30 mg Chelex, and 10 mg SCX.

5.3.4 Determination of eluent for the activity release process

Previous work by Wang et al. (2020) showed that with the use of a 3 mg QMA micro-cartridge, 2 boluses of 6.2 µL (25 mM each) of $TBAHCO_3$ followed by 2 boluses of 6.2 µL water

was sufficient to elute out the trapped activity form the cartridge and perform high activity experiments of [^{18}F]Fallypride. However, the same amount of $TBAHCO_3$ was not sufficient to push out the activity trapped in a 9 mg QMA micro-cartridge (**Figure 5-11**).

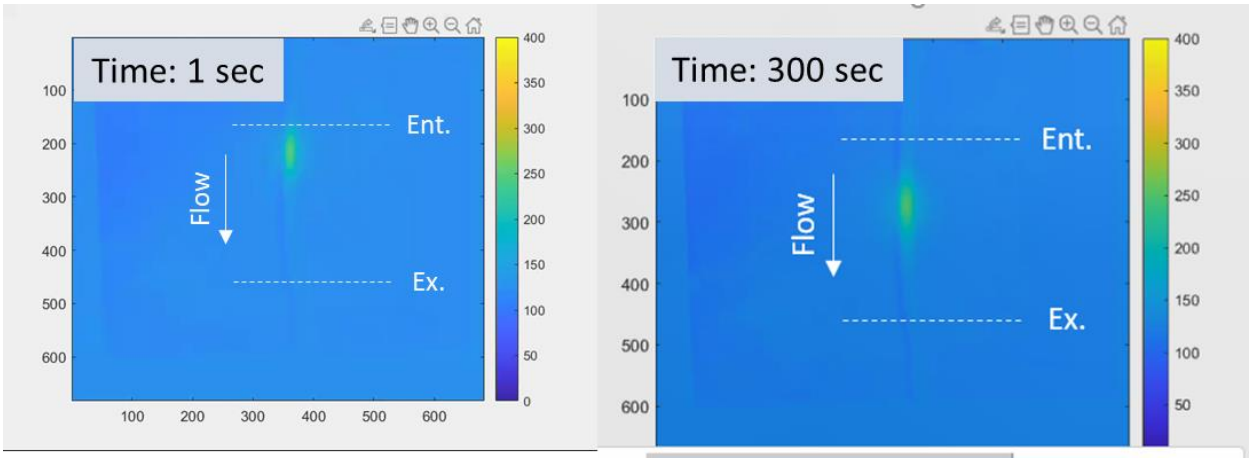

Figure 5-11. Activity distribution in a 9 mg QMA micro-cartridge with 24 µL of 30 mM of TBAHCO3 for elution. Activity moved to the middle of QMA cartridge after 300 sec but did not elute from the micro-cartridge.

A solution would be to increase the amount of $TBAHCO_3$ for the elution process, but ambiguity on the final concentration of $TBAHCO_3$ in the reaction would be difficult to control precisely. Furthermore, the addition of base would contradict many of the optimal conditions found through previous optimization studies[178], hindering reactions. Therefore, there is a need for an efficient method to elute activity without affecting the optimized concentration of $TBAHCO_3$ for downstream reactions.

Triethylamine (TEA) is a commonly used base in organic chemistry and is commonly used in radiochemistry for HPLC mobile phase preparation. TEA is a weak base with a low boiling point of 88.6 °C and does not interact with free [^{18}F]fluoride (low nucleophilicity). Recently, its use has been reported for eluting [^{18}F]fluoride from a QMA cartridge[83]. We hypothesized that TEA could provide a way to elute the activity from the cartridge and be removed by evaporation when loaded onto the reaction site prior to the downstream radiofluorination reaction – allowing a base “free” elution method. During the drying step, the optimized base concentration can be spiked to the reaction site, allowing optimized conditions to be followed for high activity reactions.

To test the effectiveness of TEA as an eluent of 0.37 GBq (10 mCi) of [^{18}F]fluoride trapped on a 9 mg QMA cartridge, a series of 10 µL boluses of 10 nmol of TEA (aq.) were passed through the cartridge and the collectivity measured (**Figure 5-12**). Most activity was eluted after 40 µL of TEA, and nearly all was eluted within 80 µL. To ensure complete elution of activity, 150 nmol of TEA was utilized for further studies. To determine if the process could be simplified, we also tried a single 80 µL with 150 nmol of TEA to ensure full elution and we achieved 90.4 ± 0.8% (n = 4) elution efficiency.

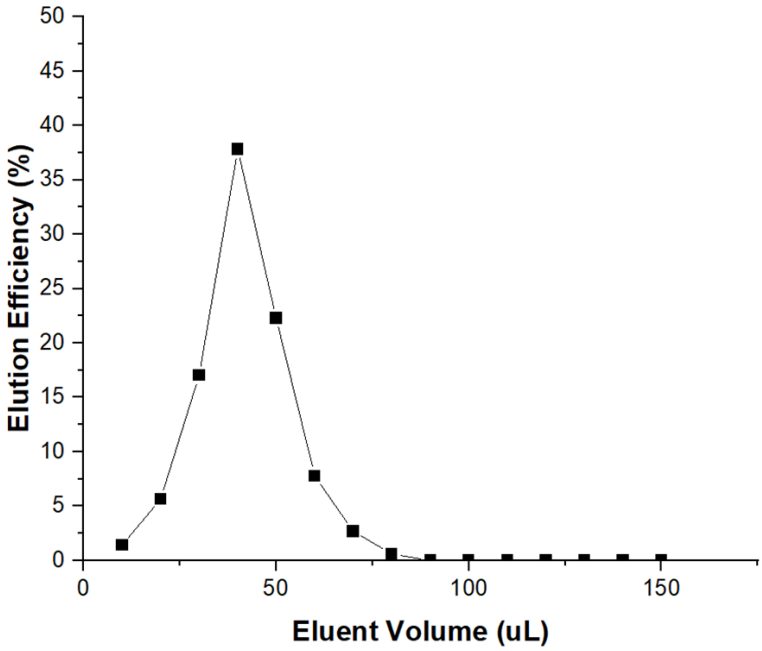

Figure 5-12. Elution efficiency of activity using plugs 10 µL of 10 nmol TEA.

Initially, we tried to load the eluted [^{18}F]fluoride in 20 µL increments, directly to the chip and evaporate at 105 °C, but found a very high loss of activity due to volatility (e.g., >90%). Likely this problem occurs because as the TEA evaporates, the solution is no longer basic, allowing [^{18}F]HF to form and escape. To address this, we mixed the concentrated activity prior to loading with the optimized concentration of base (e.g., $TBAHCO_3$) needed for the optimal conditions of the downstream radiosynthesis (For example, for the synthesis of [^{18}F]Fallypride, we added 240 nmol of $TBAHCO_3$).

Next, we optimized the amount of TEA. In theory, it should volatize during the fluoride drying step, leaving a minimal concentration that should not interfere with downstream fluorination. However, to determine the effect of residual TEA concentrations, on fluorination, a 4x4 multi-reaction microdroplet chip was used to vary the amounts of TEA (from 0 to 3500 nmol) used during the [^{18}F]fluoride drying step prior to the synthesis of [^{18}F]Fallypride. Briefly, experiments were conducted with 2 µL of activity (37 MBq [1 mCi]) loaded on each reaction site with 240 nmol of $TBAHCO_3$ and a varied amount of TEA. After drying at 105 °C for 1 min was completed, 39 mM (8 µL) of Fallypride precursor was added to each reaction and reacted for 1 min at 110 °C. Collected product was measured and analyzed via radio-TLC as previously described[93]. We noticed no adverse impact on the reaction performance with the addition of TEA (**Figure 5-13**). Considering that the residual concentration of TEA has no effect on the downstream fluorination, 2000 nmol of TEA was utilized for the elution of activity trapped on the QMA.

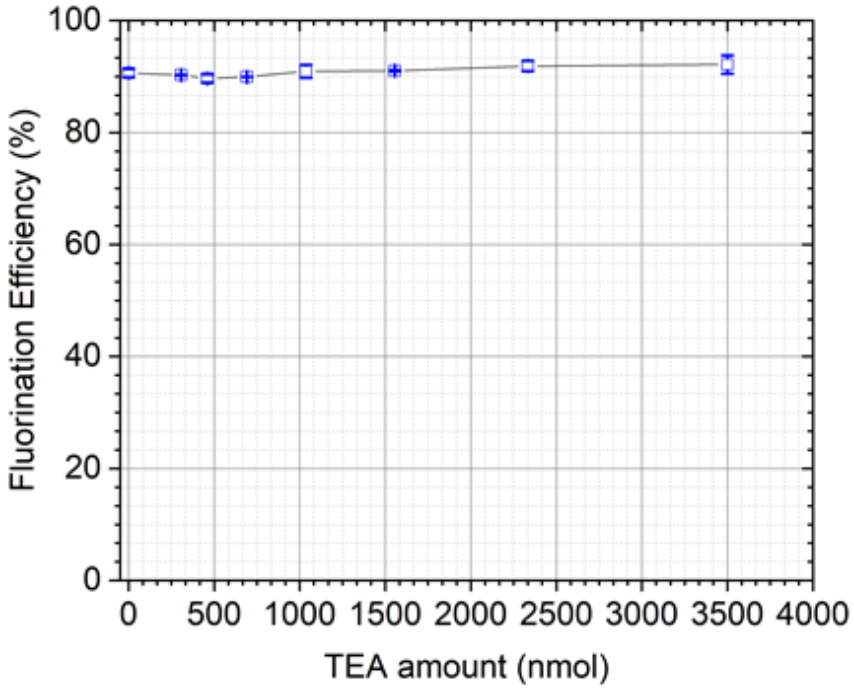

Figure 5-13. Fluorination efficiency of [^{18}F]Fallypride with different amounts of TEA (n = 2).

5.3.5 Evaluation of the full [^{18}F]fluoride purification process

Next, we combined the [^{18}F]fluoride processing with the downstream reaction. We performed an experiment with 1 mL of decayed source spiked with 185 MBq (5 mCi) in a system comprising 10 mg Chelex / 30 mg SCX and 9 mg QMA micro-cartridges. The efficiency of the concentration process in this format was >95%. Activity was then eluted using 2000 nmol of TEA (aq.) in a bolus of 100 µL. The elution efficiency of this format allowed 89%. Using a droplet chip that contained 240 nmol of $TBAHCO_3$ at the reaction site from addition with a micropipette, sequential 20 µL boluses of the eluted activity were loaded onto, and dried, on the reaction site. Next, 160 nmol of [^{18}F]PBR06 precursor in 8 µL of thexyl alcohol: MEOH (1:1 v/v) was added to the reaction site and reacted for 0.5 min at 100 °C. Product was collected with 60 µL of collection solution (9:1 MeOH: H_2O v/v) and spotted on TLC for analysis. A control reaction was performed separately with 4 µL of unprocessed [^{18}F]fluoride (18.5 MBq [0.5 mCi]). The results showed fluorination efficiency of treated decayed source to be 90.9% and the control reaction 91.7% (**Figure 5-14**), indicating that the processing method was effectively able to remove all impact of

impurities from 1 mL of decayed source solution and achieve the same high yield as a small-scale reaction.

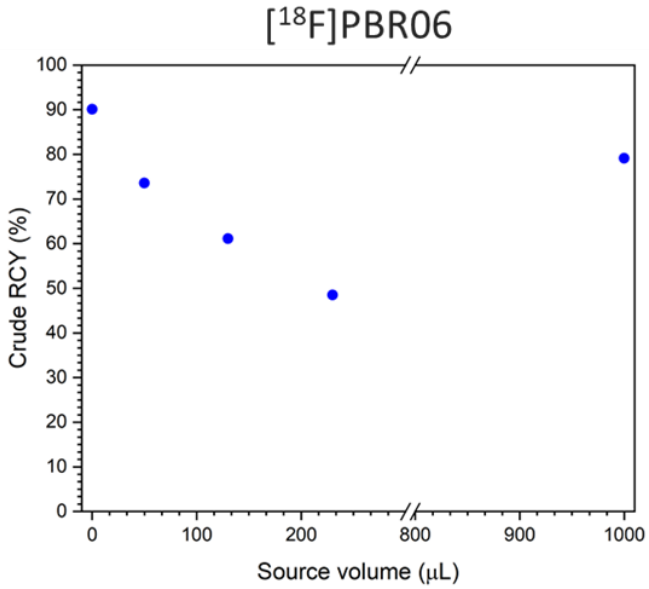

Figure 5-14. Comparison of different decay source volume effects on the synthesis of [^{18}F]PBR06 crude RCY without cartridge treatment and the effect on the crude RCY after treatment of 1 mL decay source with our serial cartridge method.

5.4 Conclusions

This chapter describes a new method for purifying and concentrating [^{18}F]fluoride suitable for use with microscale reactions. The use of 10 mg chelex and 30 mg SCX resins upstream of a 9 mg QMA resin (hydroxyl form) was able to completely remove coloration from the QMA and achieve high trapping and elution performance (trapping >95% and elution ~90%) in 80 µL of milli q water containing 150 nmol of TEA. This eluted solution can then be loaded in 20 µL increments to a droplet reaction chip (with the desired amount and type of base / phase transfer catalyst pre-loaded and dried). The yield of reactions ([^{18}F]PBR-06) exhibited identical performance whether using a tiny volume of unprocessed activity solution loaded directly to the reactor, or 1 mL of processed decayed source, processed with the novel method.

The next step is to apply this method to large volumes of non-decayed source activity, to enable loading of high activities to the droplet reactor and compare the reaction performance. With the cartridge able to remove the impact of impurities and potential stoichiometry effects (i.e. since the decayed source has the same amounts of these as non-decayed source), it will be possible to assess if and when radiolysis becomes an issue as activity scale is increased. If radiolysis is observed, radical scavengers can potentially be used to mitigate the effect.

5.5 Appendix

5.5.1 MATLAB script for real-time imaging of QMA trapping process

```
%User selects the cernkov images to be combined in video
waitfor(msgbox('Please select the Cerenkov Images in the Pop-Up Window'));
filename = uigetfile('*.*','MultiSelect', 'on');
Average_image = 0;
%The number if images is counted to loop program below
input_loop = length(filename);

%User selects the background to remove thermal read noise
waitfor(msgbox('Please select the Cerenkov Background in the Pop-Up Window'));
sample_image_folder = fullfile('C:\Users\tholl\OneDrive\Documents\MATLAB\Trials');
[filename2,sample_image_folder] = uigetfile('*.*');
imageUV = filename2;

%User selects the brightfield image to impose with cernkov captures
waitfor(msgbox('Please select the Brightfield Image in the Pop-Up Window'));
sample_image_folder = fullfile('C:\Users\tholl\OneDrive\Documents\MATLAB\Trials');
[filename3,sample_image_folder] = uigetfile('*.*');
Brightfield = filename3;

%User selects the brightfield image BKG to remove artifacts in image
waitfor(msgbox('Please select the Brightfield Background in the Pop-Up Window'));
sample_image_folder = fullfile('C:\Users\tholl\OneDrive\Documents\MATLAB\Trials');
[filename4,sample_image_folder] = uigetfile('*.*');
BrightfieldBKG = filename4;

%Convert Image to Text Array (Cell Format)
image_path = 'imageCerenkov';
%Converted Image File is Named
save_path = 'read.tiff';
%Text File is Read
backgroundCerenkov1 = textread(imageUV); %#ok<DTXTRD>
%Written into Image File
imwrite(uint16(backgroundCerenkov1), save_path);
%Raw Image of Interest
backgroundCerenkov = imread('read.tiff');

%Convert Brightfield Image to Text Array (Cell Format)
```

```
image_path = 'Brightfield';
%Converted Image File is Named
save_path = 'read.tiff';
%Text File is Read
Brightfield1 = textread(Brightfield); %#ok<DTXTRD>
%Written into Image File
imwrite(uint16(Brightfield1), save_path);
%Raw Image of Interest
Brightfield1 = imread('read.tiff');

%Convert Brightfield BKG to Text Array (Cell Format)
image_path = 'BrightfieldBKG';
%Converted Image File is Named
save_path = 'read.tiff';
%Text File is Read
BrightfieldBKG = textread(Brightfield); %#ok<DTXTRD>
%Written into Image File
imwrite(uint16(BrightfieldBKG), save_path);
%Raw Image of Interest
BrightfieldBKG = imread('read.tiff');

%Master Dark Frame is Made
imgdark = imread('masterdark.tiff');
%Dark Field Correction
img_subtraction2 = Brightfield1 - imgdark;
%Flatfield Correction from UV Plate (every element divided)
BrightfieldImage = double(img_subtraction2)./double(BrightfieldBKG);
%Median Filter Correction
BrightfieldImage = medfilt2(BrightfieldImage);
%Image is rotated from source program
BrightfieldImage = imrotate(BrightfieldImage,180);

%Adjust image brightness
imshow(BrightfieldImage);
imcontrast
uiwait(msgbox('Press Ok, once done adjusting image contrast'));
BrightfieldImage = getimage;
BrightfieldImage = imadjust(BrightfieldImage);

%Setup the total ROI for analysis
MyFigure=figure;
imshow(BrightfieldImage);

%set up the measuring tool
h = imdistline(gca);
api = iptgetapi(h);
api.setLabelVisible(false);
%pause -- you can move the edges of the segment and then press the enter key to continue
pause();
%get the distance
dist = api.getDistance();

%User is now asked to draw the single improfile line through the
%center of the lane of interest

%Cx, Cy are the initial x,y coordinates of drawn line (C), and xi,xy
```

```
%are the end coordinate of the line
waitfor(msgbox('Draw a Straight Line Through the Center of the Lane'));
figure; imshow(BrightfieldImage, [])
[CX,CY,C,xi,yi]=improfile;
close(gcf);

%The starting coordinates of the line are found
m=1;
while m<length(xi)
  if (xi(m)==xi(m+1))&(yi(m)==yi(m+1))
     xi((m+1):(end-1))=xi((m+2):end);
     yi((m+1):(end-1))=yi((m+2):end);
     xi(end)=[];
     yi(end)=[];
     warning('double values have been deleted!');
  end
  m=m+1;
end

%The total length of the line is now found based on the user
%drawn line, then the total bounds of the ROI (rectangle) are
%calculated
linescan=[];

for m=2:length(xi)
   dy=yi(m)-yi(m-1);
   dx=xi(m)-xi(m-1);
   if abs(dx)<1e-3
     if dy>0
        rotation_angle=-90;
     elseif dy<0
        rotation_angle=90;
     end
   else
        rotation_angle = (atan2(dy,dx) - atan2(0,1)) * (180/pi);
   end

%Placeholder im_log variable defined for calculations below
im_log=~(zeros(size(BrightfieldImage),'uint16')<1);

im_log(uint16(yi(m)),uint16(xi(m)))=true;
im_log(uint16(yi(m-1)),uint16(xi(m-1)))=true;

%Image is rotated so that the rectangle can be generated
im_log=bwdist(im_log)<1.2;
im_log=imrotate(im_log,rotation_angle);
[yidx,xidx]=find(im_log);

%The bounds of the rectangle are constructed -- see the PPT deck
%for outline of how this is done
if length(xidx)>1
  xmin=min(xidx);
  xmax=max(xidx);
  ymin=min(yidx);
  ymin=ymin-round(dist/2);
  height=dist;
```

```
  width=(xmax-xmin);
  ROIrect=[xmin ymin width height];
end
end

%Video file (MP4) is written and opened for collection of Cerenkov Lineplot
Video1 = VideoWriter('LinePlot','MPEG-4');
Video1.FrameRate = 3;
open(Video1);

%Video file (MP4) is written and opened for collection of overlay images
Video = VideoWriter('CerenkovFile1','MPEG-4');
Video.FrameRate = 3;
open(Video);

%Time counter is made
Count = 1;
position = [0 0];

h = waitbar(0,'Please wait ...');

for i = 1:input_loop
   close all
   f = figure('visible','off');
   img = filename{i};% Convert Image to Text Array (Cell Format)
   image_path = 'img';
   %Converted Image File is Named
   save_path = 'read.tiff';
   %Text File is Read
   img = textread(img); %#ok<DTXTRD>
   %Written into Image File
   imwrite(uint16(img), save_path);
   %Raw Image of Interest
   img1 = imread('read.tiff');

   %Master Flatfield Image
   img3 = imread('masterflat.tiff');
   %Non-Uniform Pixel Correction
   img_division = img1./img3;
   %Median Filter Correction
   img_medianfiltered = medfilt2(img_division);
   img_medianfiltered_rotated = imrotate(img_medianfiltered,180);
   imgnew = imagesc(img_medianfiltered_rotated);colorbar;

   %Automatic selection of background
   h = drawellipse('Center', [30,30], 'SemiAxes', [20,20], 'RotationAngle', 0, 'StripeColor', 'm');
   a = createMask(h); % create the binary matrix of background
   %Creation of black mask
   blackMaskedImage_bg = img_medianfiltered_rotated; % write the matrix in blackMaskImage_bg
   blackMaskedImage_bg(~a)= 0;% set elements outside ROI to be 0
   mean_bg = mean(blackMaskedImage_bg(a));% calculate mean value of elements in selected bg
region
   img_bgfiltered = img_medianfiltered_rotated - mean_bg;

   %Now, the total pixel intensity across the region is determined
   im_pi2=imrotate(img_bgfiltered,rotation_angle);
```

```
%Cerenkov image is cropped for analysis, background to follow
im_pi3_Cerenkov=imcrop(im_pi2,ROIrect);
linescan_Cerenkov=[linescan sum(im_pi3_Cerenkov)];

%Can code to normalize values here if wanted
f1 = figure('visible','off');
xlabel('Distance from Origin (Pixels)');
ylabel('Cerenkov Luminescence (Arbitrary Units)');
plot(linescan_Cerenkov/(dist+1));

%Display the time axis at top of image
a = gca;
a.Position(3) = 0.6;
Text_Str = ['Time: ', num2str(Count), ' s'];
annotation('textbox', [0.75, 0.1, 0.1, 0.1], 'String', Text_Str)
ylim([0 inf])
xlabel('Distance from Origin (mm)')
ylabel('Cerenkov Luminescence (Arbitrary Units)')
frame1 = getframe(gcf);

%Video frame is written to open file
writeVideo(Video1,frame1);
close(f1);

%Overlay of Cerenkov and Brightfield Image
f = figure('visible','off');
ax1 = axes;
imagesc(BrightfieldImage);
colormap(ax1,'gray');
ax2 = axes;
M = max(img_bgfiltered, [], 'all');
imagesc(ax2,img_bgfiltered,'alphadata', 0.65);
colormap(ax2, 'hot');
caxis(ax2,[min(nonzeros(img_bgfiltered)) max(nonzeros(img_bgfiltered))]);
ax2.Visible = 'off';
linkprop([ax1 ax2],'Position');
c = colorbar;
c.Label.String = 'Cerenkov Luminescence (Arbitrary Units)';

%Display the time axis at top of image
a = gca;
a.Position(3) = 0.53;
Text_Str = ['Time: ', num2str(Count), ' s'];
annotation('textbox', [0.75, 0.1, 0.1, 0.1], 'String', Text_Str)

%Video captures the frame
frame = getframe(gcf);

%Updated time count based on imaging program lag
Count = Count+3;

%Video frame is written to open file
writeVideo(Video,frame);

%Update waitbar
```

```
    waitbar(i/input_loop);
end

F = findall(0,'type','figure','tag','TMWWaitbar');
delete(F);

%Video is closed so it can be processed
close(Video1);
close(Video);

%Video that was written is played
implay('LinePlot.mp4')
implay('CerenkovFile1.mp4');
```

Chapter 6: Impact of aqueous phases in the analysis of radiopharmaceuticals via radio-TLC

6.1 Introduction

Positron-emission tomography (PET) is a non-invasive molecular imaging technique that harnesses radiopharmaceuticals to quantify biochemical processes *in vivo*. The radiopharmaceutical (or tracer) is a bioactive molecule labelled with a short-lived positron-emitting radionuclide. The most commonly used radionuclide is fluorine-18 due to its favorable physical and chemical properties[10,11]. Currently, most PET scans measure glucose metabolism with the radiopharmaceutical 2-[^{18}F]fluoro-2-deoxy-D-glucose ([^{18}F]FDG) to diagnose a myriad of diseases. However, additional types of scans may become more prevalent as several new PET tracers that are more specifically targeted to disease phenotypes have recently garnered clinical approval, including those targeting amyloid plaques (Neuraceq, Amyvid, Vizamyl), dysfunctional tau protein (Tauvid), prostate cancer (Axumin, Pylarify), and Parkinson's disease ([^{18}F]FDOPA)[189]. The list of new ^{18}F-labeled tracers under development also grows with the discovery of new biological targets and therapeutic strategies[190].

The successful development and production of PET tracers rely on analytical techniques such as radio-high performance liquid chromatography (radio-HPLC) and radio-thin layer chromatography (radio-TLC) to assess radiochemical conversion (during radiosynthesis development) or radiochemical purity (during quality control testing of tracers produced for clinical use). A shortcoming of radio-HPLC, however, is the propensity for retention of free [^{18}F]fluoride in the column (i.e., not reaching the detectors), which can lead to the underestimation of this species in the output chromatogram[191]. In contrast, radio-TLC does not suffer from this issue as the entirety of the TLC plate is scanned.

When using typical silica TLC plates to separate ^{18}F-labelled mixtures, [^{18}F]fluoride is usually sequestered near the origin through strong interaction with surface silanol groups, and the mobile phase moves the radiopharmaceutical away from the origin. The stationary phase, silica gel (polysilicic acid), is well known in the literature to possess the ability for acidic hydrogen bonding, basic hydrogen bonding, and dipolar interactions with analytes[73], and the mobile phase plays an important role in modulating these interactions. The reported mobile phases vary widely in literature, even for analysis of the same compound (**Table 6-1**), and we noted with interest that many studies use water as a polar mobile phase additive to enhance the migration of polar radiopharmaceutical compounds.

Table 6-1. Mobile phases reported in the literature for silica-based TLC separation of various radiopharmaceuticals.

Radiopharmaceutical	Aqueous Mobile Phase	Non-Aqueous Mobile Phase
[^{18}F]Fallypride	(60:40 MeCN: 25 mM NH_4HCO_2, 1% TEA)[36,93], (95:5 MeCN:H_2O)[149], (90:10 MeCN:H_2O)[80]	(10:90 MeOH:DCM)[83], (50:50 MeOH:EtOAc, 1% TEA)[192]
[^{18}F]FET	(80:20 MeCN:H_2O)[93,139], (67:16.5:16.5 MeCN:MeOH:H_2O)[193]	(90:10 MeOH:AcOH)[194], (67:33 Hexanes:EtOAc)[195]
[^{18}F]FBB	(90:10 MeCN:H_2O)[196]	NR
[^{18}F]FDOPA	(95:5 MeCN:H_2O)[104], (67:16.5:16.5 MeCN:MeOH:H_2O)[81]	(90:10 DCM:EtOAc)[116], (40:60 EtOAc:Et_2O)[197]
[^{18}F]FEPPA	NR	(8:10:92 MeOH:Hexanes:EtOAc)[198]
[^{18}F]FPEB	NR	(95:5 EtOAc:EtOH)[199]
[^{18}F]FLT	(95:5 MeCN:H_2O)[79,200]	(90:10 DCM:MeOH)[201]
[^{18}F]FMZ	(80:15:5 EtOAc:EtOH:H_2O)[141,142]	(80:20 EtOAc:EtOH)[147]
[^{18}F]FMISO	NR	(95:5 MeOH:NH_4)[200], (MeOH)[202]
[^{18}F]FNB	(60:40 MeCN:H_2O)[203]	NR
[^{18}F]FBA	(95:5 MeCN:H_2O)[203]	(67:33 Hexanes:EtOAc)[204]
[^{18}F]DFA	(95:5 MeCN:H_2O)[203]	NR
[^{18}F]AlF-2-AMPDA-HB	(75:25 MeCN:H_2O)[205]	NR
[^{18}F]AlF-NOTA-HL	(50:50 MeCN:H_2O)[206]	NR
[^{18}F]FTP	(20:80 MeOH: 1M NH_4OAc)[207]	NR
[^{18}F]Altanserin	(80:20 MeCN:H_2O)[173]	NR
[^{18}F]MPPF	(90:10 MeCN:H_2O)[208]	NR

NR = Not Reported

However, a drawback of using water is that it can alter the stationary phase itself through direct interactions of the water with surface silanol groups of the TLC plate. These modifications can

disrupt the possible intermolecular interactions of the surface silanol groups, impeding plate-analyte interactions and adversely affecting chromatographic behavior[209]. In fact, under some conditions, the [^{18}F]fluoride-silica interaction can be disrupted, leading to the movement of free radionuclide away from the origin, which could lead to confusion and ambiguities in the analysis of ^{18}F-radiopharmaceuticals if the TLC method is not carefully validated. We use systematic studies with different aqueous compositions to illustrate the potential detrimental impacts of using mobile phases with significant aqueous component on the radio-TLC analysis of tracers labeled with [^{18}F]fluoride and argue that the effects could also apply to tracers labelled with other radionuclides.

6.2 Materials and Methods

6.2.1 Materials

All reagents and solvents were obtained from commercial suppliers. Acetonitrile (MeCN; anhydrous, 99.8%), methanol (MeOH; anhydrous, 99.8%), water (H_2O; suitable for ion chromatography), 2,3-dimethyl-2-butanol (thexyl alcohol; anhydrous, 98%), N-methyl-2-pyrrolidone (NMP; anhydrous, 99.5%), 4,7,13,16,21,24-hexaoxa-1,10-diazabicyclo[8.8.8]hexacosane (K_{222}; 98%), and potassium carbonate (K_2CO_3; 99.995%), were purchased from Sigma-Aldrich (St. Louis, MO, USA). Tetrabutylammonium bicarbonate ($TBAHCO_3$; 75mM in ethanol), (2S)-*O*-(2′-tosyloxyethyl)-*N*-trityl-tyrosine-tert-butyl ester (TET ; precursor for [^{18}F]FET, >95%), *O*-2-fluoroethyl-L-tyrosine (FET-HCl; reference standard, >95%), ethyl-5-methyl-8-nitro-6-oxo-5,6-dihydro-4H-benzo[f]imidazo[1,5-a][1,4]diazepine-3-carboxylate (nitromazenil; precursor for [^{18}F]Flumazenil, >97%), Flumazenil (FMZ; reference standard, >99%), (S)-2,3-dimethoxy-5-[3-[[(4-methylphenyl)-sulfonyl]oxy]-propyl]-N-[[1-(2-propenyl)-2-pyrrolidinyl]methyl]-benzamide ([^{18}F]Fallypride precursor, >90%), Fallypride (reference standard, >95%), were purchased from ABX Advanced Biochemical Compounds (Radeberg, Germany). Silica gel 60 F_{254} sheets (aluminum backing, 5 cm x 20 cm) were purchased from Merck KGaA

(Darmstadt, Germany). Glass microscope slides (76.2 mm x 50.8 mm, 1 mm thick) were obtained from C&A Scientific (Manassas, VA, USA).

6.2.2 Preparation of samples of [^{18}F]fluoride and complexes

To illustrate the impact of aqueous mobile phases on the migration of [^{18}F]fluoride, several samples were prepared.

[^{18}F]fluoride samples were prepared by diluting [^{18}F]fluoride/[^{18}O]H_2O with ion chromatography-grade water to a concentration of 0.75-1.1 MBq/µL.

[^{18}F]KF/K_{222} samples were prepared by adding K_2CO_3 (0.5 mg, 3.6 µmol) and K_{222} (5 mg, 13.3 µmol) to a volume of 0.5 mL of ion chromatography grade water spiked with [18F]fluoride, yielding a 0.75-1.1 MBq/µL solution with 7.2 mM K_2CO_3 and 26.2 mM K_{222}.

[^{18}F]TBAF samples were prepared by adding $TBAHCO_3$ (75 mM; 1.2 µL, 0.7 µmol) to 99 µL of ion chromatography grade water spiked with [^{18}F]fluoride to yield a 0.75-1.1 MBq/µL solution with 7.2 mM $TBAHCO_3$.

6.2.3 Preparation of samples of [^{18}F]fluoride labeled radiopharmaceuticals

To prepare mixed samples of radiotracers and [^{18}F]fluoride, several radiopharmaceuticals were prepared using droplet radiochemistry methods on Teflon-coated silicon surface-tension trap chips as previously described[8]; except that optimal reaction conditions were altered to increase the amount of [^{18}F]fluoride in the crude reaction mixture.

Mixtures of [^{18}F]FET-intermediate/[^{18}F]TBAF were prepared by depositing an 8 µL droplet of [^{18}F]fluoride/[^{18}O]H_2O (70-90 MBq [1.9-2.5 mCi]; mixed with 240 nmol of $TBAHCO_3$) and drying at 105 °C for 1 min. Then, the fluorination step was performed by adding a 10 µL droplet containing 80 nmol of FET precursor dissolved in thexyl alcohol:MeCN (1:1; v/v) to the dried [^{18}F]fluoride residue and reacting at 90 °C for 5 min. The crude product was collected by dispensing 10 µL of MeCN to the reaction site and aspirating the volume. This process was repeated 6x for 60 µL of collected crude product.

Mixtures of [^{18}F]FMZ/[^{18}F]TBAF were prepared similarly, except that the fluorination step was performed by adding an 8 µL droplet containing 280 nmol of FMZ precursor dissolved in NMP to the dried [^{18}F]fluoride residue and reacting at 200 °C for 0.5 min.

Mixtures of [^{18}F]Fallypride/[^{18}F]TBAF were prepared similarly, except that (i) the initial [^{18}F]fluoride droplet contained 480 nmol of $TBAHCO_3$, and the fluorination step was performed by adding a 6 µL droplet containing 234 nmol of Fallypride precursor dissolved in thexyl alcohol:MeCN (1:1; v/v) to the dried [^{18}F]fluoride residue and reacting at 110 °C for 1 min.

Stock solutions of non-radioactive reference standards were prepared at 20 mM concentration. 5 mg of Fallypride standard was added to 685 µL of MeOH. 5 mg of FMZ standard was added to 825 µL of MeOH. 5 mg of FET standard was added to 1100 µL of MeOH. MeOH was chosen due to the high solubility of these reference standards (as suggested by the manufacturer), and due to its relatively low boiling point that allowed rapid drying after spotting onto the TLC plate.

6.2.4 TLC spotting, developing, and readout

TLC plates were cut (6 cm long x 3 cm wide), then marked with a pencil at 1 cm (origin line) and 5 cm (development line) from the bottom edge. 1 µL of the relevant sample was applied to the plate via a micro-pipette. In cases where radiopharmaceutical solutions were separated, an adjacent lane on the plate was spotted with the corresponding reference standard. The sample spots were then dried under a gentle stream of nitrogen for 1 min. Spotting was repeated on multiple plates to compare the effect of different mobile phases containing MeCN with different amounts of H_2O (all compositions expressed as v/v). After developing, plates were dried under a gentle stream of nitrogen for 3 min.

To better visualize the location of phase transfer catalysts ($TBAHCO_3$ and K_2CO_3/K_{222}), some plates were stained after developing by exposure for 1 min to a mixture of iodine crystals and silica gel in a sealable container[210].

Plates were visualized via Cerenkov luminescence imaging (CLI) as previously described[36,93]. Briefly, the radio-TLC plate was positioned inside a light-tight chamber, then the plate was

covered with a glass microscope slide. The Cerenkov light emission was detected by a cooled (-10 °C) scientific camera (QSI 540, Quantum Scientific Imaging, Poplarville, MS, USA) equipped with a 50 mm F/1.2 lens (Nikkor, Nikon, Tokyo, Japan) for a 60 s exposure. In addition to previously described corrections, background subtraction was further performed by selecting a small region of the image (approximate size 20 pixels) not containing any radioactive species, computing the average pixel intensity, and subtracting this average from the entire image.

After CLI imaging, the glass microscope slide was removed, and a UV lamp installed inside the light-tight chamber was illuminated while acquiring another image of the plate (7 ms exposure time). This enabled visualization of chemical species on the plate (which appear as darker bands due to indicator present on the TLC plate), as well as capturing an image of pencil markings and iodine-stained bands on the plate.

6.2.5 Analysis of TLC plates

A MATLAB program (MathWorks, Natick, MA, USA) was written to generate TLC chromatograms and display TLC plate images (**Appendix 6.6.1**). The user is first prompted to select the CLI image to be analyzed, followed by a corresponding darkfield image, and corrections are applied as previously described[101]. The program then asks the user to select a corresponding UV image, followed by selecting a flat field correction UV image (taken in advance with a blank TLC plate installed). The UV image is corrected in a similar fashion (i.e., dividing by the flat field correction image and applying 3x3 median filtering), and the user can further adjust brightness and contrast for viewing. The CLI image is then redisplayed, and the user is asked to draw a line to define the width of the widest radioactivity band, which is used as the lane width. The UV image is then redisplayed, and the user is asked to draw a line from the bottom of the TLC plate to the solvent front. The program then generates an average line profile along the lane, taking the pixel intensities versus distance from the CLI image along the user-defined centerline and averaging with adjacent lines automatically generated at 1-pixel intervals along the entirety of the selected

lane width. The program displays the final averaged line profile (chromatogram), the corrected CLI image, and the UV image.

The chromatogram was then exported and loaded in OriginPro (OrignLab, Northampton, MA, USA) to normalize the chromatograms to the highest intensity and plot groups of chromatograms. To compute the percentage of each species in a chromatogram, OriginPro was used to find the area under each band (peak) after fitting to a sum of Gaussian curves and then dividing the area corresponding to a particular band by the sum of areas for all bands.

6.3 Results

Samples of [^{18}F]fluoride (with and without phase transfer catalysts) and various crude radiopharmaceuticals with different polarities were prepared and separated on silica TLC plates with different aqueous mobile phase compositions to illustrate the effect of water on the mobilization of different species and the potential pitfalls in analysis.

6.3.1 Effect of aqueous mobile phases on migration of [^{18}F]fluoride

Samples of [^{18}F]fluoride/[^{18}O]H_2O were initially spotted on TLC plates and developed under mobile phases of increasing aqueous composition (**Figure 6-1, Table 6-2**). When the water content is low, [^{18}F]fluoride remains at the origin as expected. For ≥40% water, free [^{18}F]fluoride begins migrating away from the origin. Notably, and with great potential for ambiguity in the radio-TLC analysis of radiopharmaceuticals, two distinct bands of radioactivity are observed when using a mobile phase with ≥50% water. For ≥80% water composition, there is again only a single band observed, but it is located at the solvent front, near where the radiopharmaceutical species would be expected.

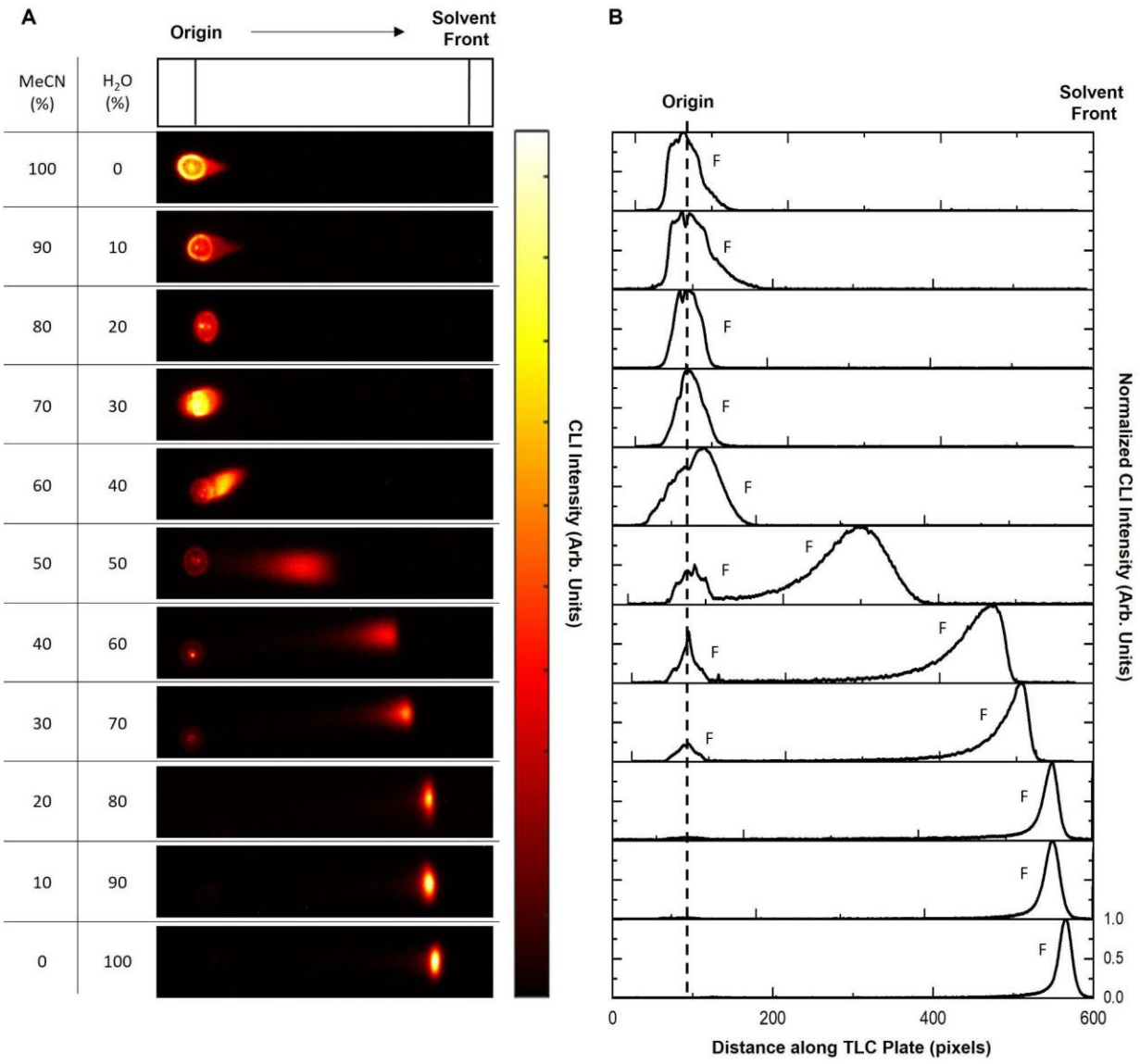

Figure 6-1. Impact of water composition in aqueous mobile phases (MeCN:H_2O) on the migration of [^{18}F]fluoride.
(A) CLI images of TLC plates. (B) TLC chromatograms generated from the CLI images. F denotes [^{18}F]fluoride.

Recognizing that phase transfer catalysts are typically used in ^{18}F-radiosyntheses, the behavior of complexed [^{18}F]fluoride was also investigated. **Figure 6-2** and **Table 6-3** shows the effects of water on the movement of [^{18}F]TBAF (i.e., [^{18}F]fluoride in the presence of $TBHACO_3$). The overall trend is similar to free [^{18}F]fluoride, though there are increased signs of chromatographic fronting and band widening for some mobile phase compositions. This fronting

may be explained because [^{18}F]fluoride and the phase transfer catalyst interact with one another yet have different migration behavior (**Figure 6-1A**). The migration of [^{18}F]KF/K_{222} (i.e., [^{18}F]fluoride in the presence of K_2CO_3 and K_{222}) was also explored (**Figure 6-6** and **Table 6-7**) and shown to behave similarly to [^{18}F]TBAF.

Table 6-2. Impact of water composition in aqueous mobile phases (MeCN:H_2O) on the retention factor (R_f) of [^{18}F]fluoride.

MeCN (%)	H_2O (%)	R_f
100	0	0.0
90	10	0.0
80	20	0.0
70	30	0.0
60	40	0.0, 0.13
50	50	0.0, 0.44
40	60	0.0, 0.76
30	70	0.0, 0.83
20	80	0.92
10	90	0.92
0	100	0.93

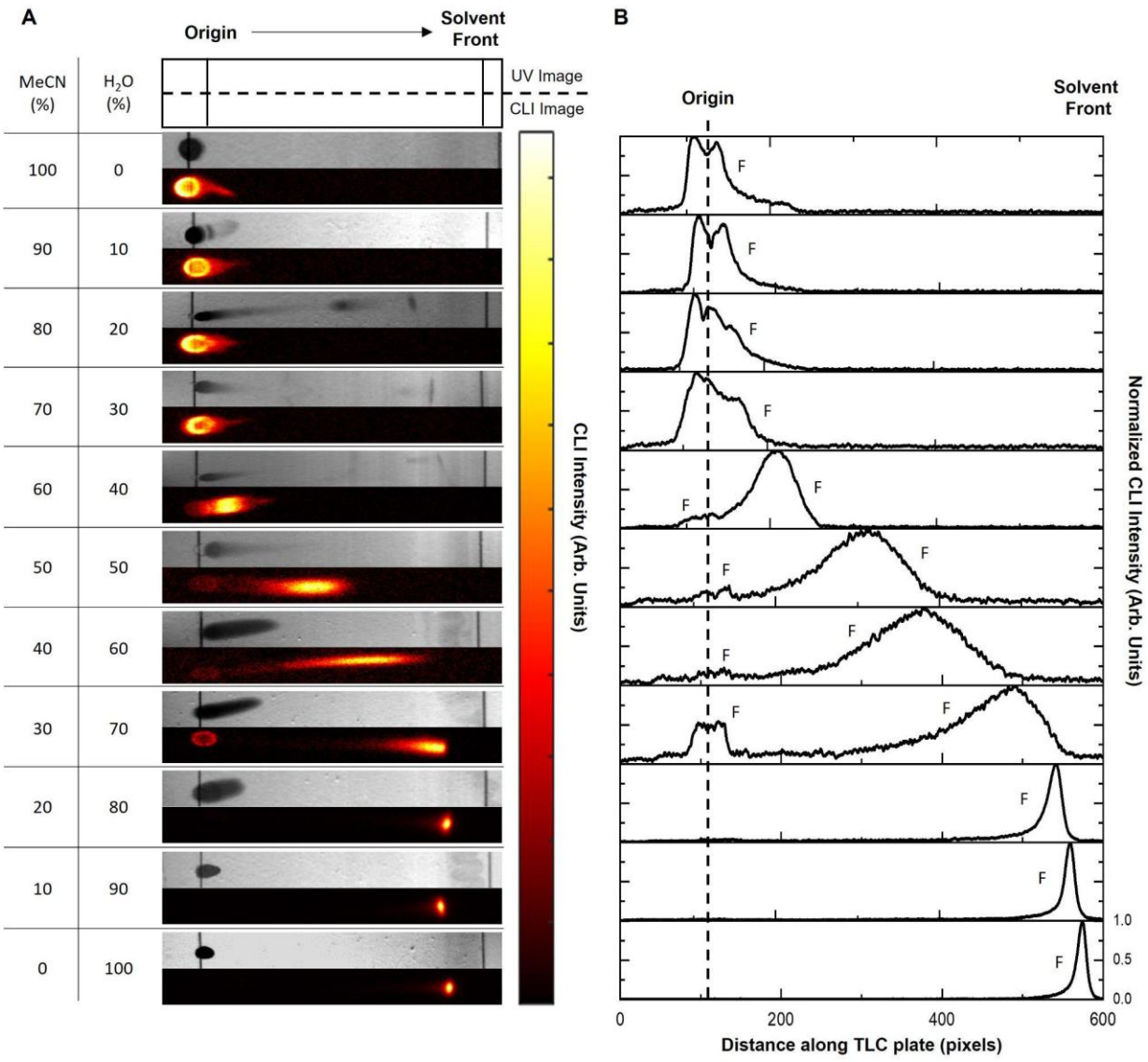

Figure 6-2.The effect of aqueous mobile phases (MeCN:H_2O) on the migration of [^{18}F]TBAF. (A) For each mobile phase composition, two images are shown: a UV image of the TLC plate stained with I_2 to visualize $TBAHCO_3$ (top), and a CLI image of a TLC plate spotted with [^{18}F]TBAF (bottom). (B) Normalized TLC chromatograms generated from the CLI images. F denotes [^{18}F]TBAF. The Supplementary Information contains an additional figure showing the migration of samples of [^{18}F]KF/K_{222}.

Table 6-3. Impact of water composition in aqueous mobile phases (MeCN:H_2O) on the R_f of [^{18}F]TBAF.

MeCN (%)	H_2O (%)	R_f
100	0	0.0
90	10	0.0
80	20	0.0
70	30	0.0
60	40	0.0, 0.16
50	50	0.0, 0.40
40	60	0.0, 0.53
30	70	0.0, 0.77
20	80	0.88
10	90	0.92
0	100	0.93

6.3.2 Effects of aqueous mobile phases on the analysis of [^{18}F]Fallypride

Noting the effects that water composition had on the chromatographic behavior of [^{18}F]fluoride and its complexes, the effect of aqueous mobile phases on the chromatographic behavior of crude [^{18}F]Fallypride samples (containing unreacted [^{18}F]TBAF) was investigated (**Figure 6-3, Table 6-4**). Interestingly, while [^{18}F]Fallypride is non-polar (cLogP = 3.3), using a mobile phase of 100% MeCN did not lead to migration away from the origin, and the [^{18}F]TBAF and [^{18}F]Fallypride bands could not be resolved. Increasing the water content to ≥20% caused the migration of [^{18}F]Fallypride toward the solvent front and allowed the bands to be resolved. However, for ≥40%

water, there was decreased migration of [^{18}F]Fallypride (and further increased mobilization of [^{18}F]TBAF), and at 50% water, there was a significant overlap of the two species. Further addition of water (≥60%) led to a reversal in the order of the bands.

Under most TLC analyses performed, the radioactivity at the origin is generally assumed to be the free radionuclide and the migrated species as the intermediate or product. Without careful assessment and validation of which bands correspond to which species, the overlapped or reversed results under the moderate or high proportion of water could introduce significant ambiguity and errors during analysis (**Figure 6-7**).

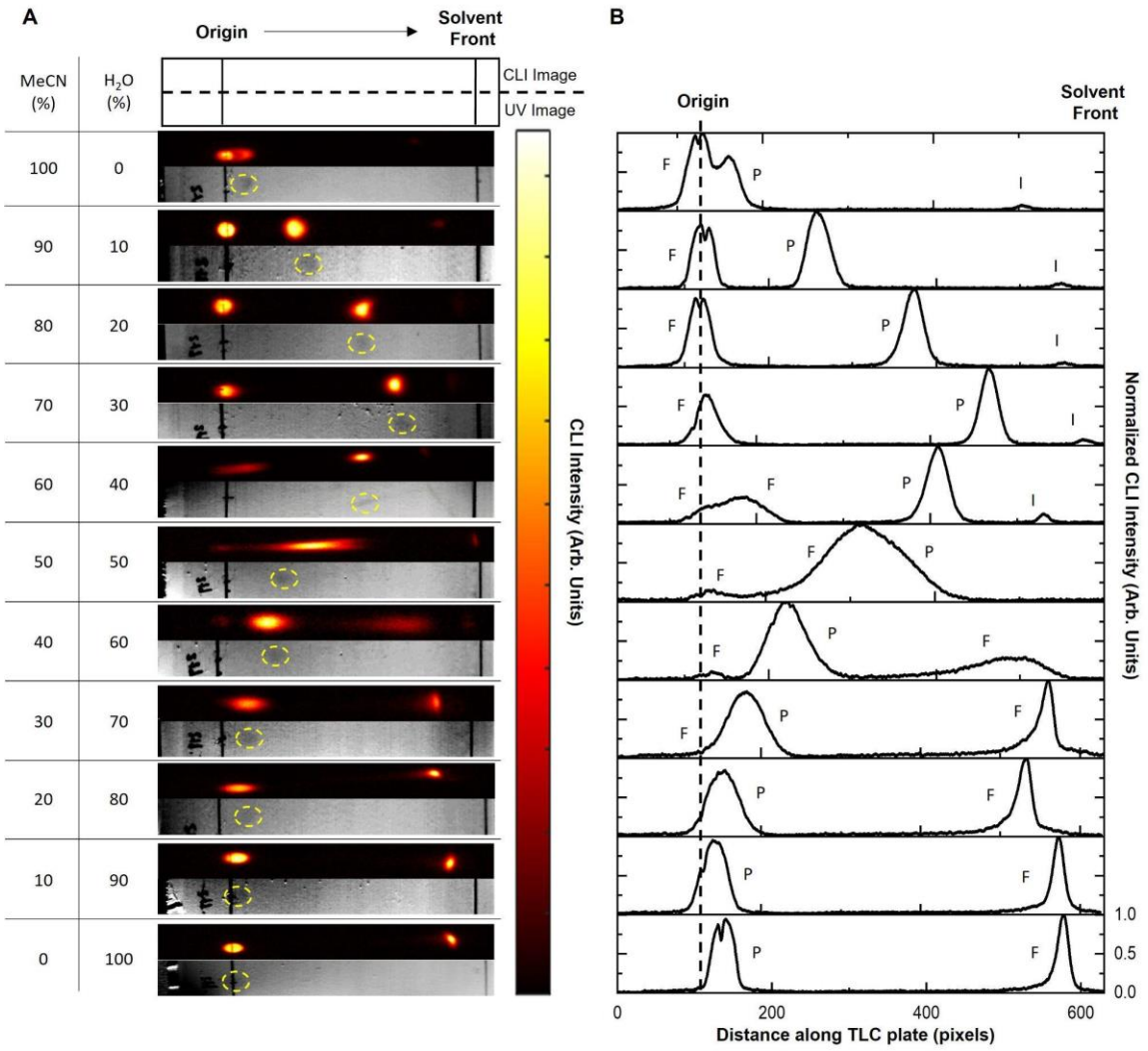

Figure 6-3. Impact of water composition in aqueous mobile phases (MeCN:H_2O) on the migration of [^{18}F]Fallypride.

(A) Images of TLC plates. For each mobile phase composition, a CLI image of the TLC plate spotted with crude [^{18}F]Fallpyride is shown (top), along with a UV image of an adjacent lane spotted with Fallypride standard (bottom). The Fallypride standard band is enclosed with a yellow dashed line for clarity. (B) Normalized TLC chromatograms generated from the CLI images. F denotes [^{18}F]TBAF, P denotes [^{18}F]Fallypride, and I denotes impurity.

Table 6-4. Impact of water composition in aqueous mobile phases (MeCN:H_2O) on the R_f of different radiochemical analytes in the crude synthesis of [^{18}F]Fallypride. The R_f of [^{18}F]Fallypride was confirmed by parallel spotting of [^{19}F]Fallypride. ND = Not discernable.

		R_f values		
MeCN (%)	H_2O (%)	[^{18}F]TBAF	[^{18}F]Fallypride	Impurity
100	0	0.0	0.07	0.75
90	10	0.0	0.27	0.84
80	20	0.0	0.50	0.86
70	30	0.0	0.68	0.90
60	40	0.0, 0.19	0.57	0.79
50	50	0.0, 0.40	0.40	ND
40	60	0.0, 0.53	0.18	ND
30	70	0.0, 0.77	0.10	ND
20	80	0.88	0.05	ND
10	90	0.92	0.0	ND
0	100	0.93	0.0	ND

6.3.3 Effects of aqueous mobile phases on the analysis of [^{18}F]Flumazenil

The effects of water composition were further investigated using samples of a more polar compound, [^{18}F]FMZ (cLogP = 1.0), containing [^{18}F]TBAF (**Figure 6-4, Table 6-5**). Though [^{18}F]FMZ is more polar than [^{18}F]Fallypride, the use of 100% MeCN led to the complete separation of [^{18}F]FMZ (near the solvent front) from [^{18}F]TBAF (at the origin). For ≥40% water, the [^{18}F]TBAF band begins to migrate away from the origin and split into two distinct radioactive bands, and for ≥60% water, mobilization of [^{18}F]FMZ begins to be adversely impacted. Significant overlap of the bands was observed using a 70% water mobile phase. Mobile phases with higher water content resulted in the migration of [^{18}F]TBAF to the solvent front, and [^{18}F]FMZ remained close to the origin. As mentioned previously, improper assumptions about the band locations could lead to significant misinterpretation of results (**Figure 6-8**).

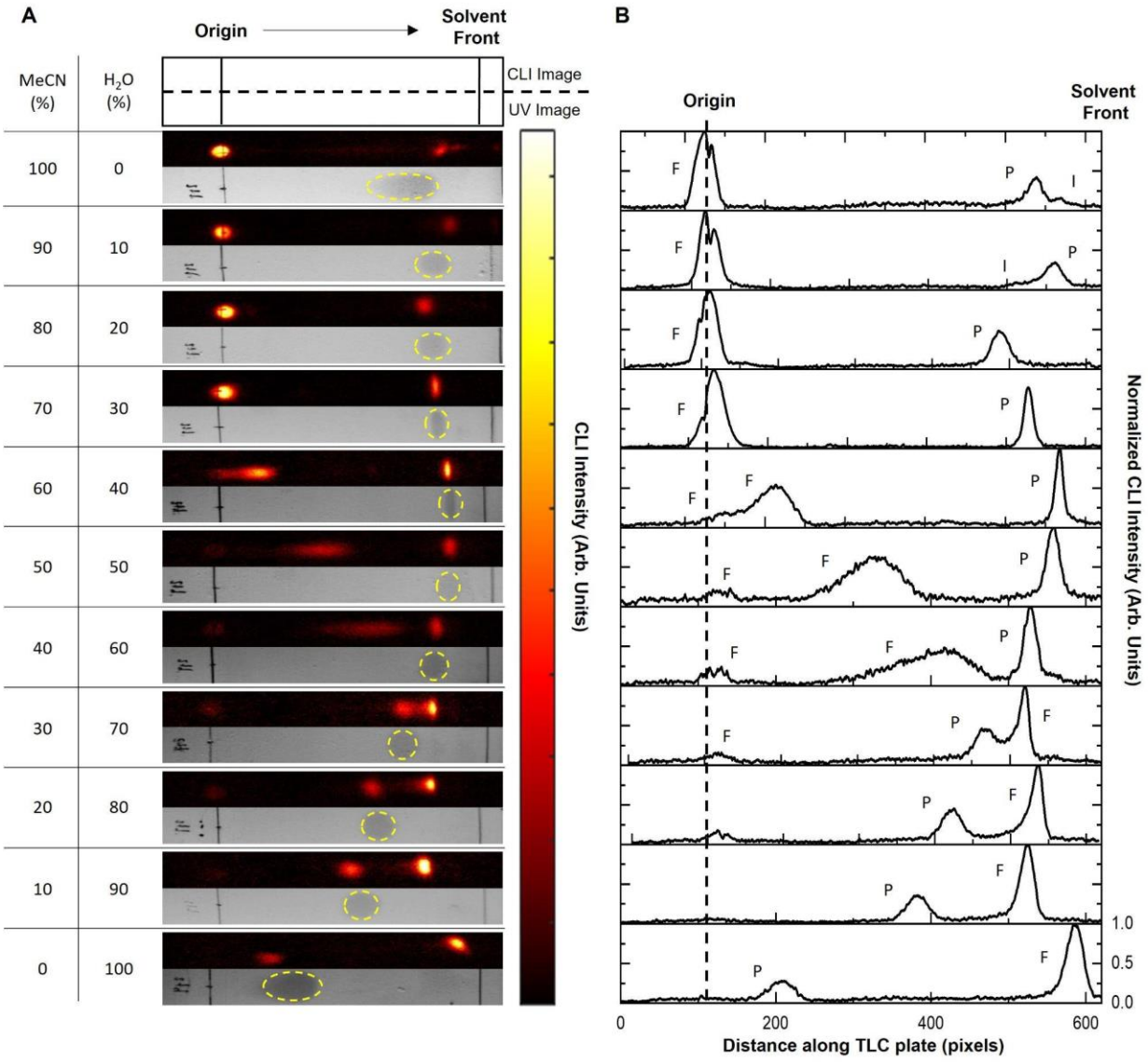

Figure 6-4. Impact of water composition in aqueous mobile phases (MeCN:H_2O) on the migration of [^{18}F]FMZ.
(A) Images of TLC plates. For each mobile phase composition, a CLI image of the TLC plate spotted with crude [^{18}F]FMZ is shown (top), along with a UV image of an adjacent lane spotted with FMZ reference standard (bottom). The FMZ standard band is enclosed with a yellow dashed line for clarity. (B) Normalized TLC chromatograms generated from the CLI images. F denotes [^{18}F]TBAF, P denotes [^{18}F]FMZ, and I denotes impurity.

Table 6-5. Impact of water composition in aqueous mobile phases (MeCN:H_2O) on the R_f of different radiochemical analytes in the crude synthesis of [^{18}F]FMZ. The R_f of [^{18}F]FMZ was confirmed by parallel spotting of [^{19}F]FMZ. ND = Not discernable.

		R_f values		
MeCN (%)	H_2O (%)	[^{18}F]TBAF	[^{18}F]FMZ	Impurity
100	0	0.0	0.84	0.89
90	10	0.0	0.89	0.79
80	20	0.0	0.78	ND
70	30	0.0	0.82	ND
60	40	0.0, 0.18	0.88	ND
50	50	0.0, 0.42	0.88	ND
40	60	0.0, 0.58	0.82	ND
30	70	0.0, 0.80	0.70	ND
20	80	0.84	0.60	ND
10	90	0.84	0.53	ND
0	100	0.93	0.18	ND

6.3.4 Effect of aqueous mobile phases on the analysis of [^{18}F]FET-intermediate

Next, the impact of aqueous mobile phases was assessed for crude mixtures of [^{18}F]FET-intermediate (cLogP = 3.9) containing [^{18}F]TBAF. Spotting of FET reference standard (cLogP = -0.9) in an adjacent lane allowed visualization of the impact of mobile phase composition on the analysis of 3 species (i.e., [^{18}F]TBAF, [^{18}F]FET-intermediate, and FET). With 100% MeCN, both [^{18}F]TBAF and FET remain at the origin, while the non-polar [^{18}F]FET-intermediate moves with the solvent front (**Figure 6-5, Table 6-6**). With ≥10% water, FET begins to move away from the origin, and with ≥40% water, [^{18}F]TBAF moves away from the origin, travelling close to FET. Interestingly, using ≥60% water impairs the mobility of the [^{18}F]FET-intermediate, which ends up closer to the origin with increasing water content, while [^{18}F]TBAF and FET remain overlapped at

the solvent front. **Figure 6-9** shows the potential for the erroneous determination of radiochemical yield if the bands were improperly identified.

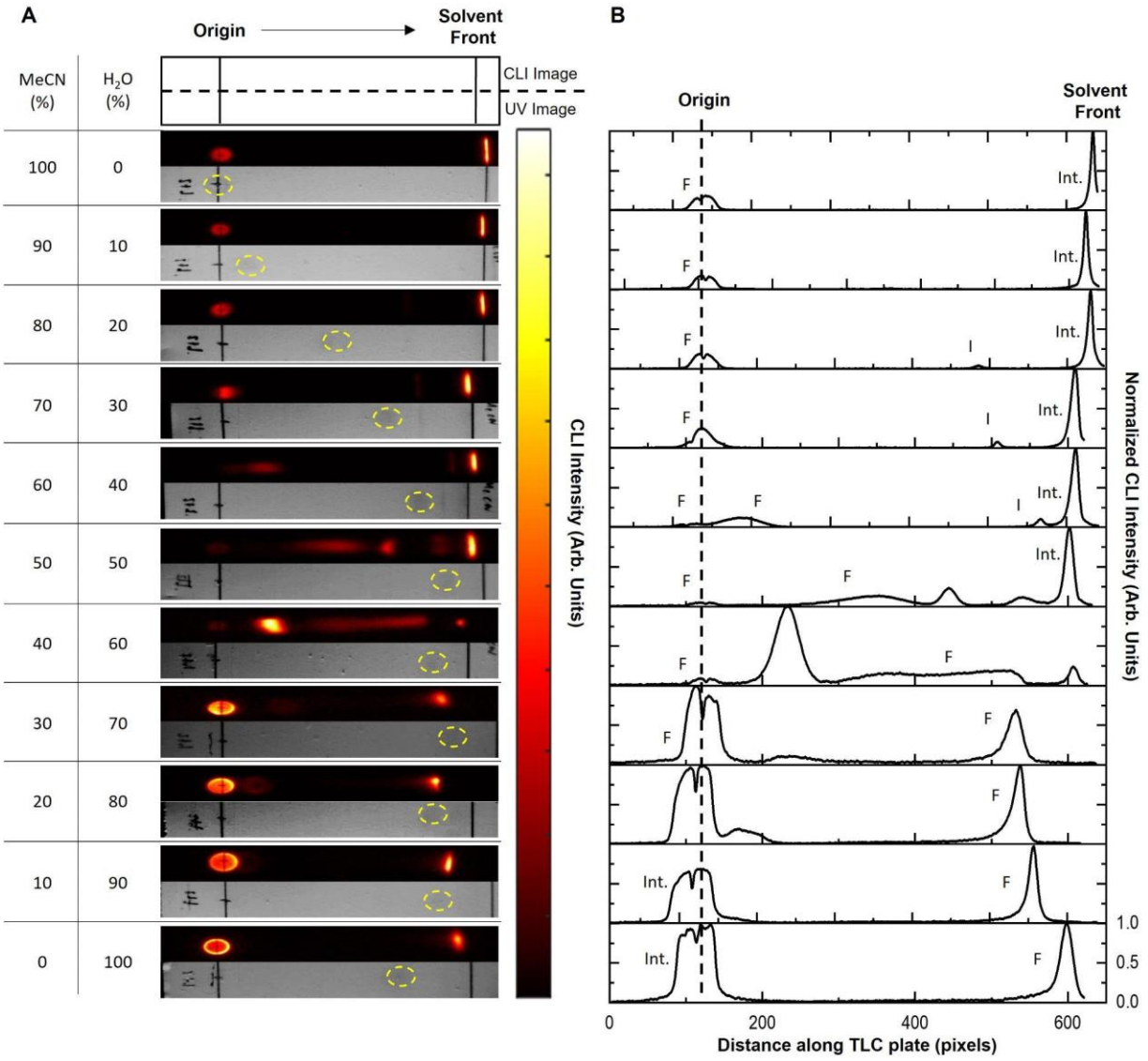

Figure 6-5. Impact of water composition in aqueous mobile phases (MeCN:H_2O) on the migration of [^{18}F]FET-intermediate and FET.
(A) Images of TLC plates. For each mobile phase composition, a CLI image of the TLC plate spotted with crude [^{18}F]FET-intermediate is shown (top), along with a UV image of an adjacent lane spotted with FET reference standard (bottom). The FET standard band is enclosed with a yellow dashed line for clarity. (B) Normalized TLC chromatograms generated from the CLI images. F denotes [^{18}F]TBAF, Int denotes [^{18}F]FET-intermediate, and I denotes impurity.

Table 6-6. Impact of water composition in aqueous mobile phases (MeCN:H_2O) on the R_f of different radiochemical analytes in the crude synthesis of [^{18}F]FET. ND = Not discernable.

		R_f values		
MeCN (%)	H_2O (%)	[^{18}F]TBAF	[^{18}F]FET-intermediate	FET
100	0	0.0	0.97	0.0
90	10	0.0	0.95	0.11
80	20	0.0	0.97	0.48
70	30	0.0	0.95	0.69
60	40	0.0, 0.13	0.95	0.79
50	50	0.0, 0.43	0.91	0.80
40	60	0.0, 0.55	ND	0.82
30	70	0.0, 0.77	ND	0.82
20	80	0.79	ND	0.81
10	90	0.82	0.0	0.76
0	100	0.90	0.0	0.71

6.4 Discussion

These findings underscore water's complex role in chromatographic selectivity and highlight two major concerns about using water as a mobile phase additive for radiopharmaceutical analysis on silica TLC plates. Firstly, the use of increasing amounts of water leads to a decreasing ability of the silica TLC plate to sequester [^{18}F]fluoride (and [^{18}F]fluoride complexes) at the origin, as well as the possibility that the [^{18}F]fluoride can form multiple bands when using a certain range of mobile phase compositions. Secondly, the water content can greatly affect the migration of the radiopharmaceutical species. Evidently, water plays a more important role in TLC plate selectivity than as a purely polar additive to affect analyte retention. These effects can lead to the overlap of bands at moderate water content and reversal of expected band positions at high water content,

potentially leading to ambiguous or inaccurate determination of radiochemical compositions if TLC methods are not carefully validated.

A possible explanation for the first observation could be that water can convert silanol groups (Si-OH; isoelectric point ~2-3) to silanolate ($Si\text{-}O^-$) groups[211]. While silanol groups can act as weak ion exchangers and bind anionic [^{18}F]fluoride, silanolate groups do not possess this ion exchange capacity[212], potentially explaining the inability of the silica plates to sequester [^{18}F]fluoride at the origin when using mobile phases with moderate to high water percentages. This change in the TLC plate may also explain the reduced migration of polar radiopharmaceuticals for mobile phases with high water content, i.e., modification of the silanol groups could lead to greater analyte affinity.

Interestingly, the water content of the mobile phase also appears to strongly influence the migration of cationic radionuclides like [^{68}Ga]Ga^{3+} on silica TLC plates. In a recent publication, researchers studied the effects of various mobile phases in the analysis of a ^{68}Ga-labeled radiopharmaceutical[213], finding that with a 50% aqueous mobile phase, [^{68}Ga]Ga^{3+} remains at the baseline, but for 100% aqueous mobile phases, [^{68}Ga]Ga^{3+} migrated with the solvent front. This trend of mobilization for cationic species also appears to be true for other radionuclides like [^{64}Cu]Cu^{2+}, which have also been shown to move with the solvent front when using purely aqueous mobile phases[214], and it is possible that similar effects could be possible for other charged radionuclides (e.g., Sc-47, Zr-89, I-124, Lu-177, Ac-225). Further study is needed to better understand the chromatographic behavior of radiometals on silica TLC plates due to the complexity of these systems (e.g., different charge states of metal ions, possible coordination of metal ions with anions or solvents, and possible coordination with the surface functional groups).

6.5 Conclusion

Via systematic studies of different TLC mobile phase compositions and different ^{18}F-labelled radiopharmaceuticals, we investigated the potential pitfalls of using water-containing mobile

phases in TLC analysis of radiopharmaceuticals on silica TLC plates. Aqueous mobile phases with ≥30% water composition led to the migration of [^{18}F]fluoride (or complexes) away from the origin, with higher water content (~50%), leading to the splitting of the [^{18}F]fluoride band, and further increase of water content pushing [^{18}F]fluoride to the solvent front. Secondarily, it was found that moderate amounts of water could hinder the migration of the radiopharmaceutical and even cause overlap with the [^{18}F]fluoride band. While water is often used as a polar mobile phase additive in radiochemical analysis, the observations in this work highlight that water has, in fact, a more complex role in chromatographic selectivity, and care is needed in radio-TLC interpretation when using mobile phases containing significant amounts of water. To avoid these complex effects, we are exploring facile methodologies for purely organic mobile phase optimization that can efficiently separate radiopharmaceuticals from radionuclides.

6.6 Appendix

Further effects observed with different percentages of water added to a mobile phase composition for the development of radiopharmaceuticals.

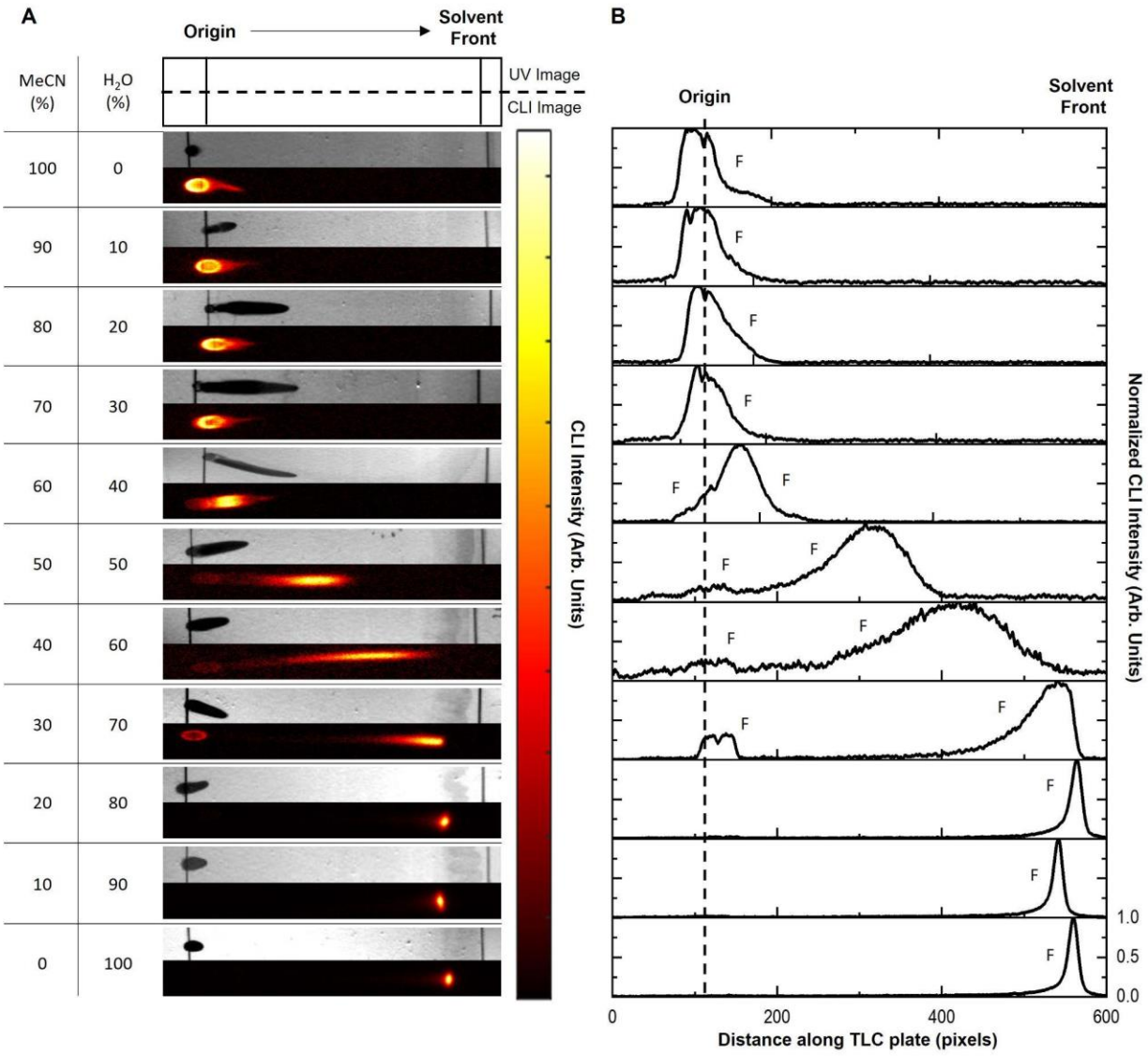

Figure 6-6. The effect of aqueous mobile phases (MeCN:H_2O) on the migration of [^{18}F]KF/K_{222}.
(A) For each mobile phase composition, two images are shown: a UV image of the TLC plate spotted with K_2CO_3/K_{222} and stained with I_2 (top) and a CLI image of a TLC plate spotted with [^{18}F]KF/K_{222} (middle). (B) TLC chromatograms generated from the CLI images. F denotes [^{18}F]KF/K_{222}.

Table 6-7. Impact of water composition in aqueous mobile phases (MeCN:H_2O) on the R_f of [^{18}F]KF/K_{222}.

MeCN (%)	H_2O (%)	R_f
100	0	0.0
90	10	0.0
80	20	0.0
70	30	0.0
60	40	0.0, 0.16
50	50	0.0, 0.40
40	60	0.0, 0.53
30	70	0.0, 0.77
20	80	0.88
10	90	0.92
0	100	0.93

A

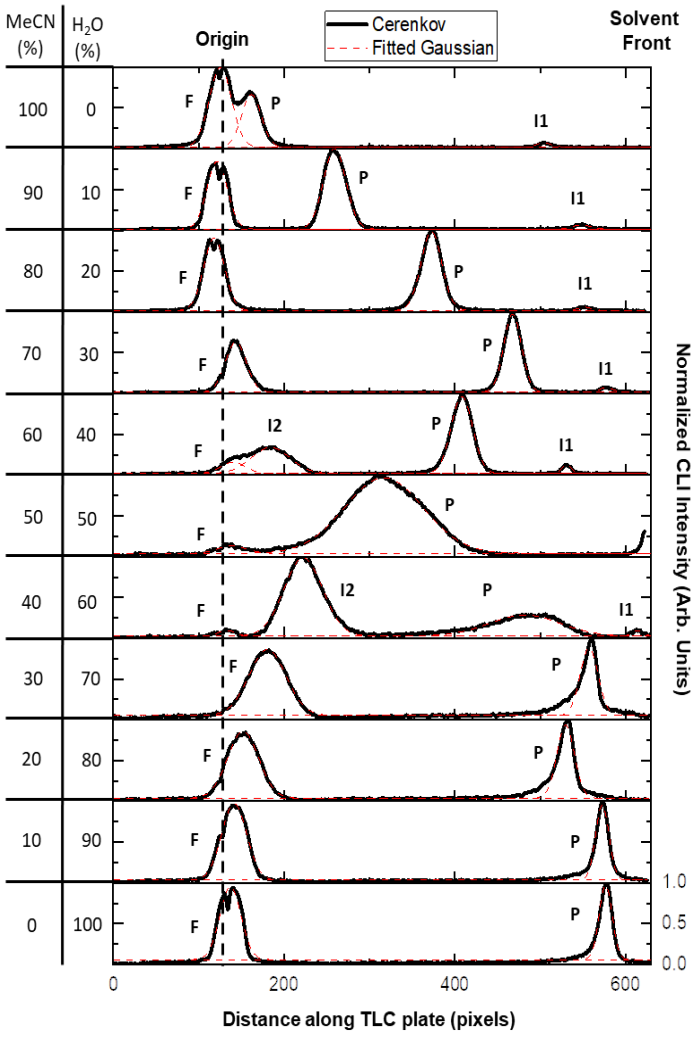

B

[18F]fluoride (%)	Impurity (%)	[18F]Fallypride (%)
62	2	36
42	2	56
43	1	56
42	2	56
9	33, 3	55
3	0	96
2	65, 1	32
62	0	38
62	0	38
62	0	38
62	0	38

Figure 6-7. The adverse impact of water-containing mobile phases in the naive calculation of fluorination efficiency for [^{18}F]Fallypride.

(A) Chromatograms of samples of [^{18}F]Fallypride/[^{18}F]TBAF separated under different compositions of MeCN:H_2O mobile phases replicated from Figure 3. Chromatograms are annotated with the following naive assignment of bands: F ([^{18}F]fluoride, assumed at origin), P (radiopharmaceutical product, confirmed with the spotting of Fallypride standard); I_i (additional band(s), naively assumed to be impurities). (B) Computed proportion of each species based on naive assumptions. The actual proportions of [^{18}F]TBAF and [^{18}F]Fallypride in the samples were 44% and 56%, respectively.

A

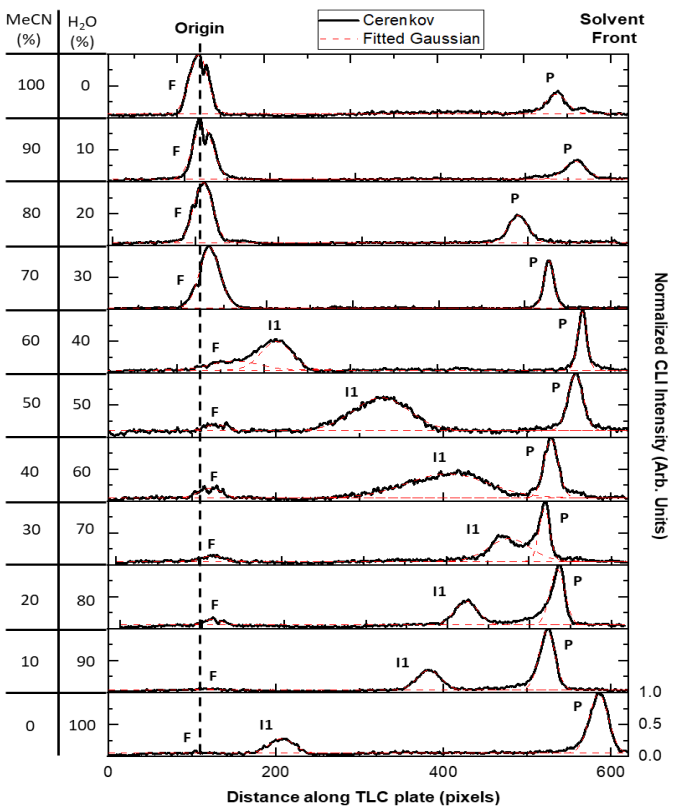

B

[^{18}F]fluoride (%)	Impurity (%)	[^{18}F]FMZ (%)
72	0	28
73	0	27
70	0	30
72	0	28
23	48	29
5	65	30
7	65	28
7	58	35
7	37	56
2	32	66
0	24	76

Figure 6-8. The adverse impact of water-containing mobile phases in the naive calculation of fluorination efficiency for [^{18}F]Flumazenil.

(A) Chromatograms of samples of [^{18}F]FMZ/[^{18}F]TBAF separated under different compositions of MeCN:H_2O mobile phases replicated from Figure 4. Chromatograms are annotated with the naive assignment of bands: F ([^{18}F]fluoride, assumed at origin), P (radiopharmaceutical product, confirmed with the spotting of FMZ standard); I_i (additional band(s), naively assumed to be impurities). (B) The computed proportion of species is based on naive assumptions. The actual proportions of [^{18}F]TBAF and [^{18}F]Fallypride in the samples were 72% and 28%, respectively.

A

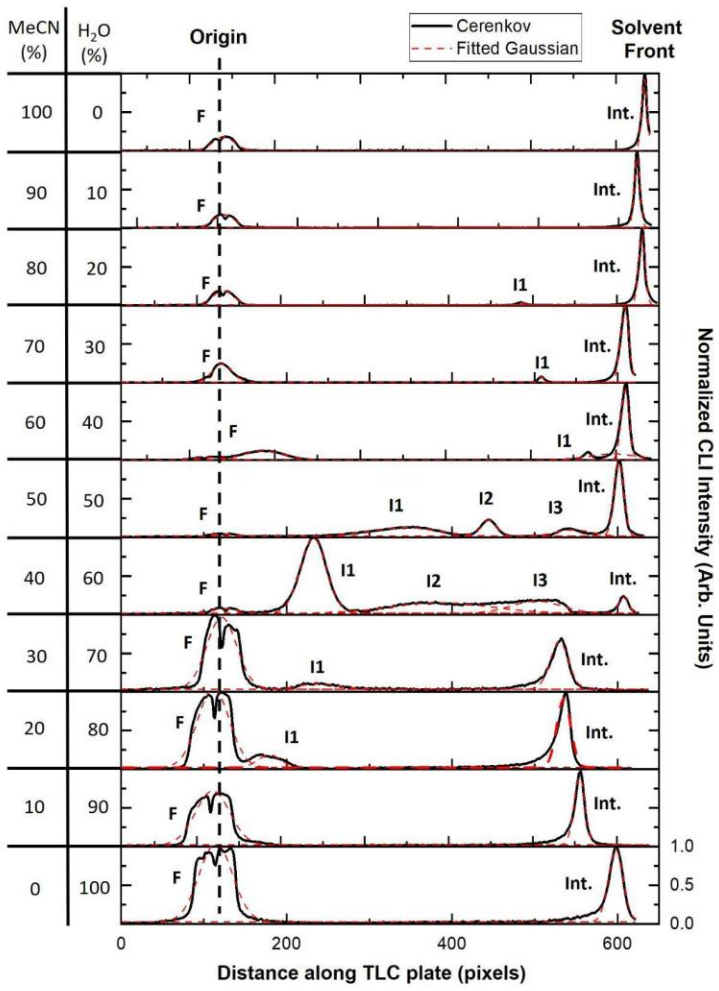

B

[18F]fluoride (%)	Impurity (%)	[18F]FET-Intermediate (%)
39	0	61
39	0	61
38	3	59
35	4	61
6	29, 21	45
3	32, 13, 12	40
3	50, 27, 16	4
67	6	27
67	8	26
71	0	29
71	0	29

Figure 6-9. The adverse impact of water-containing mobile phases in the naive calculation of fluorination efficiency for [^{18}F]FET-intermediate.
(A) Chromatograms of samples of [^{18}F]FET-intermediate/[^{18}F]TBAF separated under different compositions of MeCN:H_2O mobile phases replicated from Figure 5. Chromatograms are annotated with the naive assignment of bands: F ([^{18}F]fluoride, assumed at origin), P (radiopharmaceutical product, assumed at solvent front); I_i (additional band(s), naively assumed to be impurities). (B) The computed proportion of species is based on naive assumptions. The actual proportions of [^{18}F]TBAF and [^{18}F]FET-intermediate in the samples were 39% and 61%, respectively.

6.6.1 MATLAB Readout Script

```
%User selects the CLI image file
waitfor(msgbox('Please select the CLI Image in the Pop-Up Window'));
CLI = uigetfile('*.*');

%User selects the darkfield image file
waitfor(msgbox('Please select the darkfield image in the Pop-Up Window'));
DarkField = uigetfile('*.*');
```

```
%CLI Image Corrections

%Convert CLI image to Text Array (Cell Format)
img = textread(CLI);
imwrite(uint16(img), temp_file);
img1 = imread(temp_file);

%Convert darkfield image to Text Array (Cell Format)
backgroundCerenkov1 = textread(DarkField);
imwrite(uint16(backgroundCerenkov1), temp_file);
backgroundCerenkov = imread(temp_file);

%Darkfield Correction
img_subtraction = img1 - backgroundCerenkov;

%Flatfield correction
img3 = imread('masterflat.tiff');
img_division = img_subtraction./img3;

%Median Filter Correction
img_medianfiltered = medfilt2(img_division);

%Rotate image
img_medianfiltered_rotated = imrotate(img_medianfiltered,180);
imgnew = imagesc(img_medianfiltered_rotated);colorbar;

%Automatic selection of background
h = drawellipse('Center', [30,30], 'SemiAxes', [20,20], 'RotationAngle', 0, 'StripeColor', 'm');
a = createMask(h); % create the binary matrix of background
%Creation of black mask
blackMaskedImage_bg = img_medianfiltered_rotated; % write the matrix in blackMaskImage_bg
blackMaskedImage_bg(~a)= 0;% set elements outside ROI to be 0
mean_bg = mean(blackMaskedImage_bg(a));% calculate mean value of elements in selected bg region
img_bgfiltered1 = img_medianfiltered_rotated - mean_bg;

A = max(nonzeros(img_bgfiltered1));

%User can control the upper axis for color bar generated
titleBarCaption = 'Maximum Axis Value';
UserNumber = 2;
    while UserNumber == 2
        promptMessage = sprintf('Is the Maximum Axis Value Acceptable?')
        img_bgfiltered = imagesc(img_bgfiltered1);colormap('hot');
        caxis([0 A]);
        c = colorbar;
        c.Label.String = 'Cerenkov Luminescence (Arbitrary Units)';
        set(gca,'xtick',[]);
        set(gca,'ytick',[]);
        button = questdlg(promptMessage, titleBarCaption, 'Yes', 'No', 'Yes');
      if strcmpi(button, 'Yes')
        UserNumber = 1;
      else
        A = str2double(inputdlg('Please enter the new axis maximum', 'Axis Max'));
          while isnan(A) || fix(A) ~= A
            A = str2double(inputdlg('Please enter an INTEGER: ', 's'));
```

```
            end
        UserNumber = 2;
    end
end

%User selects the UV Image to superpose with the cerenkov image
waitfor(msgbox('Please select the UV image in the Pop-Up Window'));
Brightfield = uigetfile('*.*');

%User selects the UV flatfield image
waitfor(msgbox('Please select the UV flatfield image in the Pop-Up Window'));
BrightfieldBKG = uigetfile('*.*');

%UV Image Corrections

%Convert Brightfield Image to Text Array (Cell Format)
Brightfield1 = textread(Brightfield);
imwrite(uint16(Brightfield1), temp_file);
Brightfield1 = imread(temp_file);

%Convert Brightfield BKG to Text Array (Cell Format)
BrightfieldBKG1 = textread(BrightfieldBKG);
imwrite(uint16(BrightfieldBKG1), temp_file);
BrightfieldBKG1 = imread(temp_file);

%Flatfield correction
BrightfieldImage = double(Brightfield1)./double(BrightfieldBKG1);

%Median Filter Correction
%BrightfieldImage = medfilt2(BrightfieldImage);

%Image is rotated
BrightfieldImage = imrotate(BrightfieldImage,180);


%Show image and user selects contrast
imshow(BrightfieldImage);
imcontrast
uiwait(msgbox(['Please adjust contrast in the pop-up. Once adjusted, ' ...
    'press ok, then press ok in this box to continue:']));
BrightfieldBKG = imadjust(BrightfieldImage);
BrightfieldImage = getimage;

%Now, the line profile is computed

%CLI image now shown for drawing of ROI width
img_bgfiltered = imagesc(img_bgfiltered1);colormap('hot');
caxis([0 A]);
c = colorbar;
c.Label.String = 'Cerenkov Luminescence (Arbitrary Units)';
set(gca,'xtick',[]);
set(gca,'ytick',[]);

%User selects the lane width using measuring tool
h = imdistline(gca);
api = iptgetapi(h);
```

```
api.setLabelVisible(false);
waitfor(msgbox(['Reposition the line and its length to fit the width of the' ...
    ' region of interest (Press Enter Once Done):']));
%pause -- you can move the edges of the segment and then press the enter key to continue
pause();
%get the distance
dist = api.getDistance();

%User is now asked to draw the single improfile line through the
%center of the lane of interest

%* Cx, Cy are the initial x,y coordinates of drawn line (C)
%* xi,xy are the end coordinate of the line
waitfor(msgbox(['Draw a Straight Line Through the Center of the Lane ' ...
    '(Beginning to End):']));
figure; imshow(BrightfieldImage);
set(gca,'xtick',[]);
set(gca,'ytick',[]);
[CX,CY,C,xi,yi]=improfile;
close(gcf);

%The starting coordinates of the line are found
m=1;
while m<length(xi)
   if (xi(m)==xi(m+1))&(yi(m)==yi(m+1))
       xi((m+1):(end-1))=xi((m+2):end);
       yi((m+1):(end-1))=yi((m+2):end);
       xi(end)=[];
       yi(end)=[];
       warning('double values have been deleted!');
   end
   m=m+1;
end

%The total length of the line is now found based on the user
%drawn line, then the total bounds of the ROI (rectangle) are
%calculated
linescan=[];

for m=2:length(xi)
    dy=yi(m)-yi(m-1);
    dx=xi(m)-xi(m-1);
    if abs(dx)<1e-3
      if dy>0
         rotation_angle=-90;
      elseif dy<0
         rotation_angle=90;
      end
    else
         rotation_angle = (atan2(dy,dx) - atan2(0,1)) * (180/pi);
    end

%Placeholder im_log variable defined for calculations below
im_log=~(zeros(size(img_bgfiltered1),'uint16')<1);

im_log(uint16(yi(m)),uint16(xi(m)))=true;
```

```
im_log(uint16(yi(m-1)),uint16(xi(m-1)))=true;

%Image is rotated so that the rectangle can be generated
im_log=bwdist(im_log)<1.2;
im_log=imrotate(im_log,rotation_angle);
[yidx,xidx]=find(im_log);

%The bounds of the rectangle are constructed
if length(xidx)>1
   xmin=min(xidx);
   xmax=max(xidx);
   ymax=max(yidx);
   ymin=min(yidx);
   ymin=ymin-round(dist/2);
   height=dist;
   width=(xmax-xmin);
   ROIrect=[xmin ymin width height];
end
end

%Now, the total pixel intensity across the region is determined
im_pi2=imrotate(img_bgfiltered1,rotation_angle);

%Cerenkov image is cropped for analysis, background to follow
im_pi3_Cerenkov=imcrop(im_pi2,ROIrect);
linescan_Cerenkov=[linescan sum(im_pi3_Cerenkov)];

%Can code to normalize values here if wanted
f1 = figure;
xlabel('Distance from Origin (Pixels)');
ylabel('Cerenkov Luminescence (Arbitrary Units)');
plot(linescan_Cerenkov/(dist+1));
h = findobj(gca,'Type','line');
xData=get(h,'Xdata');
yData=get(h,'Ydata');

f = figure;
img_bgfiltered = imagesc(img_bgfiltered1);colormap('hot');
caxis([0 A]);
c = colorbar;
c.Label.String = 'Cerenkov Luminescence (Arbitrary Units)';
set(gca,'xtick', []);
set(gca,'ytick', []);

f2 = figure;
img_bgfiltered = imrotate(img_bgfiltered1, rotation_angle);
img_bgfiltered = imagesc(img_bgfiltered);colormap('hot');
rectangle(gca,'Position', ROIrect, 'EdgeColor', [1 1 1], 'LineWidth', 1, 'LineStyle','--');
F = getframe;
close(f2);

figure;
B = imrotate(F.cdata, -rotation_angle);
imshow(B);
colormap('hot');
caxis([0 A]);
```

```
c = colorbar;
c.Label.String = 'Cerenkov Luminescence (Arbitrary Units)';
set(gca,'xtick',[]);
set(gca,'ytick',[]);

figure;
imshow(BrightfieldImage);
colormap('gray');
set(gca,'xtick',[]);
set(gca,'ytick',[]);
```

Chapter 7: A rapid and systematic approach for the optimization of radio thin-layer chromatography resolution

7.1 Introduction

The importance of radiopharmaceuticals in healthcare has boomed in recent years, especially with the development and regulatory approval of several novel positron-emission tomography (PET) tracers and targeted radiotherapeutics for neuroendocrine tumors and prostate cancer, illustrating the profound potential of theranostics and personalized medicine[215–220]. There have also been significant advances in new imaging agents to study, diagnose, and aid drug development for Alzheimer's disease[221–223], and discoveries of new oncologic targets that may lead to improved diagnostics and therapies for many types of cancer[1,224]. In support of these research and clinical uses, the analysis of radiolabelled species is vital in applications encompassing the development of novel radiopharmaceuticals (e.g., synthesis optimization)[61,154,162,197,225], quality control (QC) analysis of formulated radiopharmaceuticals[75,226], and the analysis of radiometabolites[227,228]. Separation can be challenging as impurities or metabolites may be numerous, and many may have structural similarities to the radiopharmaceutical.

Radiopharmaceutical analysis is traditionally performed using chromatographic methods such as radio high-performance liquid chromatography (radio-HPLC) and radio thin-layer chromatography (radio-TLC). Though it exhibits high resolution, radio-HPLC has been criticized because species such as [^{18}F]fluoride can be trapped in the column. Thus, based on detectors at the column output, the chromatogram may not accurately reflect the actual radiochemical composition[191]. Traditional radioactivity scanning readouts used in radio-TLC circumvent this issue by assessing the entire distribution of analytes along the whole plate. However, radio-TLC can suffer from lower resolution than radio-HLPC. Imaging-based TLC readout methods can

improve readout resolution compared to scanning detectors[93,229]. Still, they may not offer improvement if the underlying chromatographic resolution of the separation process on the TLC plate is poor.

Though there is an optimum separation distance, with regards to separation efficiency and resolution, for each type of TLC plate[230], distances are often kept short in the radiochemistry field due to the strong dependence on of separation time on separation distance and the need for rapid separations when using short-lived radioisotopes. In principle, factors like stationary phase could be varied, but the radiochemistry field has predominantly used silica (normal-phase) plates[83,141,142,145,192] and, very occasionally, C18 (reverse-phase) plates[143]. This leaves mobile phase composition as the main adjustment to improve resolution.

Due to the limited knowledge of analytes (e.g., synthesis impurities or metabolites), it is often difficult to determine which mobile phases are most appropriate for crude radiopharmaceutical mixtures. Traditionally, mobile phases for radio-TLC are selected from the literature for a radiopharmaceutical structurally similar to the one of interest. Many reports use an organic solvent mixed with water (i.e., with the water added to increase migration for highly polar species) [79,173,206,208]. However, we recently showed that water could lead to the complex behavior of species on the plate[231], including migration of multiple bands corresponding to [^{18}F]fluoride (normally sequestered at the origin), and purely organic mobile phases would be preferable.

A systematic approach called PRISMA was developed to facilitate optimal mobile phase selection without needing prior knowledge about the structures and properties of analytes[232]. Herein, we describe, for the first time in radiochemistry, the use of the PRISMA method for the rapid selection of mobile phase conditions to achieve baseline separation of the desired radiopharmaceutical from both radioactive impurities (e.g., free radionuclide and other radioactive species) and UV-active non-radioactive impurities (e.g., precursor or precursor-derived impurities). While the PRISMA method is widely used in analytical chemistry laboratories, it has never, to our knowledge, been used in the radiochemistry field. This may be due to the fact that

available radio-TLC scanners only provide detection of radioactive species, which in general does not provide a sufficient number of visible high-abundance species to efficiently optimize the mobile phase. We overcome this limitation by integrating radiation detection and UV detection in a co-registered manner using multi-channel imaging-based readout of the developed TLC plates. Multiple radiopharmaceuticals with various chemical characteristics, prepared from crude radiosyntheses (which contain many impurities with high structural and chemical similarity to the desired product), are examined to illustrate the utility of the PRISMA approach.

7.2 Experimental

7.2.1 Materials

All reagents and solvents were obtained from commercial suppliers. 2,3-dimethyl-2-butanol (thexyl alcohol; anhydrous, 98%), 4,7,13,16,21,24-hexaoxa-1,10-diazabicyclo[8.8.8]hexacosane (Kryptofix 222, K222; 98%), acetic acid (AcOH; glacial, >99.9%), acetone (suitable for HPLC, >99.9%), acetonitrile (MeCN; anhydrous, 99.8%), ammonium molybdate (99.98% trace metal basis), cerium sulfate, cesium carbonate (Cs_2CO_3; 99.995%), chloroform (>99.5%, contains 100-200 ppm amylenes as stabilizer), dichloromethane (DCM; anhydrous, >99.8% contains 40-150 ppm amylene as stabilizer), diethyl ether (Et_2O; >99.9% inhibitor free), N,N-dimethylacetamide (DMA; extra dry, 99.8%), dimethylsulfoxide (DMSO; anhydrous, >99.9%), hydrochloric acid (HCl; 36.5-38%), methanol (MeOH; anhydrous, 99.8%), n-butanol (n-BuOH; anhydrous, 99.8%), n-hexane (98%), ninhydrin (used as a TLC stain), n-methyl-2-pyrrolidone (NMP; anhydrous, 99.5%), potassium carbonate (K_2CO_3; ACS grade, >99%), potassium bicarbonate ($KHCO_3$; >99.95%, trace metal basis), potassium oxalate monohydrate ($K_2C_2O_4$; ACS reagent, 99%), pyridine (anhydrous, 99.8%), sulfuric acid (99.9%), triethylamine (TEA; anhydrous, >99%), tetrahydrofuran (THF; anhydrous, >99.9% inhibitor free), tetrakispyridine copper(II) trifluoromethanesulfonate ($Cu(py)_4(OTf)_2$; 95%), toluene (anhydrous, 99.8%), and water (H_2O; suitable for ion chromatography) were purchased from Sigma-Aldrich

(St. Louis, MO, USA). (S)-2,3-dimethoxy-5-[3-[[(4-methylphenyl)-sulfonyl]oxy]-propyl]-N-[[1-(2-propenyl)-2-pyrrolidinyl]methyl]-benzamide ([^{18}F]Fallypride precursor, >95%), 5-(3-fluoropropyl)-2,3-dimethoxy-N-(((2S)-1-(2-propenyl)-2-pyrrolidinyl)methyl)benzamide (Fallypride reference standard, >95%), 2-((2,5-dimethoxybenzyl)(2-phenoxyphenyl)amino)-2-oxoethyl 4-methylbenzenesulfonate ([^{18}F]PBR-06 precursor, >95%), 2-fluoro-N-(2-methoxy-5-methoxybenzyl)-N-(2-phenoxyphenyl)acetamide (PBR-06 reference standard, >95%), acetamide, N-[2-[2-[[(4-methylphenyl)sylfonyl]oxy]ethoxy]phenyl]methyl]-N-(4-phenoxy-3-pyridinyl) ([^{18}F]FEPPA precursor, >90%), N-acetyl-N-(2-fluoroethoxybenzyl)-2-phenoxy-5-pyridinamine (FEPPA reference standard, >95%), 3-nitro-5-[2-(2-pyridinyl)ethynyl]benzonitrile ([^{18}F]FPEB precursor, >95%), 3-fluoro-5-[(pyridin-2-yl)ethynyl]benzonitrile (FPEB reference standard, >95%), ethyl-(2S)-3-[4,5-bis[(2-methylpropan-2-yl)oxycarbonyloxy]-2-trimethylstannylphenyl]-2-formamidopropanoate ([^{18}F]FDOPA precursor, >95%), (2S)-2-amino-3-(2-fluoro-4,5-dihydroxyphenyl)propanoic acid (FDOPA reference standard, >95%), and tetrabutylammonium bicarbonate ($TBAHCO_3$; 75 mM in ethanol), were purchased from ABX Advanced Biochemical Compounds (Radeberg, Germany). Silica gel 60 F_{254} sheets (aluminum backing, 5 cm x 20 cm) were purchased from Merck KGaA (Darmstadt, Germany). Silica with concentration zone (Silica 60 with diatomaceous earth zone), TLC plates, channeled F254, were purchased from Sorbtech (Norcross, GA, USA). Glass microscope slides (76.2 mm x 50.8 mm, 1 mm thick) were obtained from C&A Scientific (Manassas, VA, USA). UV-C lightbulbs (25W, 254 nm with socket) and pendant lamp sockets (light cord with on/off switch) were purchased from Amazon (Seattle, WA, USA).

No-carrier-added [^{18}F]fluoride was produced by the (p, n) reaction of [^{18}O]H_2O (98% isotopic purity, Huayi Isotopes Co., Changshu, Jiangsu, China) in an RDS-111 cyclotron (Siemens, Knoxville, TN, USA) at 11 MeV, using a 1.2-mL silver target with havar foil.

7.2.2 Preparation of radiopharmaceuticals and standard mixtures

A series of radiopharmaceuticals were prepared using droplet radiochemistry methods on Teflon-coated silicon surface tension trap chips[58,60,138] to illustrate PRISMA's ability to optimize mobile phases for radiopharmaceutical analysis. Detailed protocols for the preparation of [^{18}F]FEPPA, [^{18}F]PBR-06, [^{18}F]Fallypride, and [^{18}F]FDOPA have been previously reported[178,233].

Crude [^{18}F]FPEB was prepared by adding an 8 µL droplet of [^{18}F]fluoride/[^{18}O]H_2O (37-55 MBq [1-1.5 mCi]; mixed with 120 nmol of Cs_2CO_3 and 360 nmol of K_{222}) and drying at 105 °C for 1 min. Then, the fluorination step was performed by adding a 10 µL droplet containing 200 nmol of FPEB precursor dissolved in DMSO to the dried [^{18}F]fluoride residue and reacting at 120 °C for 5 min. The crude product was collected by dispensing 10 µL of 9:1 (v/v) MeOH:H_2O to the reaction site and aspirating the volume. This process was repeated 6x for 60 µL of collected crude product.

Stock solutions of reference standards were prepared at 20 mM concentrations. 5 mg of Fallypride was added to 685 µL of MeOH. 5 mg of PBR-06 was added to 632 µL MeOH. 5 mg of FEPPA was added to 657 µL of MeOH. 5 mg of FPEB was added to 1130 µL of MeOH. 5 mg of FDOPA was added to 1167 µL of MeOH.

7.2.3 TLC spotting, developing, and readout

TLC plates were cut (L x W, 6 cm x 3 cm), then marked with a pencil at 1 cm (origin line) and 5 cm (development line) from the bottom edge. 1 µL of the relevant crude radiopharmaceutical sample was applied to the plate via a micro-pipette. Standard and precursor samples were spotted in adjacent individual lanes. The spots were then dried under a gentle stream of nitrogen for 1 min. After development using a PRISMA-determined mobile phase (see below), the plates were dried under a gentle stream of nitrogen for 3 min and then visualized via Cerenkov luminescence imaging (CLI)[93,101] with 1 min exposure and UV imaging for 7 ms exposure, as previously reported[231].

Following CLI and UV imaging, some cases used TLC stains by dipping the developed TLC plates in the stain of interest (Hanessian stain or ninhydrin). Gentle heating of the TLC plate at 80 °C by a hot plate was used to stain the TLC plates. Hanessian stain was prepared according to the literature[234].

7.2.4 Radio-HPLC analysis of [^{18}F]Fallypride

As a performance comparison, some crude [^{18}F]Fallypride microscale reactions were analyzed with radio-TLC and radio-HPLC. The radio-HPLC system setup comprised a Smartline HPLC system (Knauer, Berlin, Germany) equipped with a degasser (Model 5050), pump (Model 1000), UV detector (254 nm; Eckert & Ziegler, Berlin, Germany), gamma-radiation detector (BFC-4100, Bioscan, Inc., Poway, CA, USA), and counter (BFC-1000; Bioscan, Inc., Poway, CA, USA). A C_{18} Gemini column was used for separations (Kinetex, 250 × 4.6 mm, 5 µm, Phenomenex, Torrance, CA, USA). Samples were separated with a mobile phase of 60% MeCN in 25 mM HN_4HCO_2 with 1% TEA (v/v) and a flow rate of 1.5 mL/min resulting in a retention time for [^{18}F]Fallypride of 5.8 min.

7.3 Methodology

7.3.1 Analysis of TLC plates

To determine the chromatographic resolution for the crude radiopharmaceutical lane on each plate, a MATLAB program with a graphical user interface (GUI) was developed (**Figure 7-5**). Initially, the user is asked to select a CLI image file. The program performs background corrections as previously described[93,101], the user can scale the image by selecting an upper-intensity value. In the next step, the user selects the corresponding UV image file and is instructed to adjust the brightness and contrast through programmed slider controls. The adjusted CLI and UV images are combined into a composite black and white image (after inverting the pixel intensities of the UV image), which is used to define the lane for the automatic generation of CLI and UV line profiles (chromatograms). To select the lane's width, the user draws a line across the broadest

chromatographic band in the composite image. Following this, the user is prompted to draw a line along the center of the lane.

To generate the CLI chromatogram, the program automatically creates a series of adjacent line profiles (image brightness versus distance along lane) at 1-pixel increments within the defined lane width and, from these, calculates an average line profile and then normalizes it to the highest intensity analyte. This user-defined line profile is then displayed, enabling the user to set a threshold height for automated peak identification to ignore background noise. The MATLAB program performs automatic peak detection on the resultant chromatogram, then fits Gaussian curves to each peak and sums these to create a single multi-Gaussian fit.

A similar process is carried out to generate the UV chromatogram, except that an additional correction is made at the end to account for uneven UV illumination along the length of the lane. In the UV image, immediately adjacent to the user-selected lane, the program captures an additional 20 'background' line profiles just adjacent to each side of the selected lane and averages them together into a single 'background' line profile, which is subtracted from the initial UV chromatogram to give the final corrected UV chromatogram.

After fitting, the MATLAB program computes the centroid and full width half maximum (FWHM) for each peak in the CLI and UV chromatograms, enabling the user to calculate the chromatographic resolution between the radiopharmaceutical and the nearest impurity.

7.3.2 PRISMA optimization

The originally reported PRISMA method[232] was applied with minor modifications. The entire optimization process could be carried out with a single batch of crude radiopharmaceutical using twenty identically-prepared TLC plates in a few hours. Each plate was spotted with three lanes: the crude radiopharmaceutical, the precursor, and the reference standard.

Step 1: solvent selection

A total of eight plates were developed with pure solvents selected from Snyder selectivity groups[73] to compare separation resolution. The pure solvents were miscible with n-hexanes

(**Table 7-4**). Based on a visual assessment of their ability to separate impurities (radioactive and non-radioactive) from the target radiopharmaceutical, three solvents (A, B, and C) exhibiting the highest degree of separation were chosen, where A, B, and C are listed in order of increasing solvent polarity.

Step 2: solvent polarity optimization

To account for the intrinsic differences in solvent polarity, solvents are all 'normalized' to the same polarity before optimizing the solvent mixture. The polarity of a mixture (S_t) is simply the volumetric average of polarities of its constituents, i.e. $S_t = x*S_X + y*S_Y$, where x and y are the volume fraction of the two component solvents, and S_X and S_Y are the polarities of each of the two component solvents. N-hexane (solvent polarity = 0) was used as a dilutant to 'normalize' the solvent polarities to the same values. Recalling that the strength of the lowest polarity pure solvent (A) is S_A, diluted forms of the three solvents A, B, and C were prepared that all had strength S_A – 0.5. Similarly, another set of three diluted solvents A, B, C, all with strength S_A - 1.0, and a third set, all with strength S_A - 1.5, were prepared. For each of the three resulting strength values (S_A – 0.5, S_A - 1.0, and S_A - 1.5), the corresponding set of three diluted solvents were mixed in a 1:1:1 ratio, designated as 333 in selectivity point (P_s) notation, where the three digits represent the volume fraction of each of the diluted solvents (i.e., volume fraction x 10 and then rounded to an integer value). 3 TLC plates were developed with these equal volume polarity-adjusted solvent mixtures. The optimal polarity was selected, so the desired radiopharmaceutical band was in the range $0.2 < R_f < 0.8$. If multiple solvent polarities mobilized the radiopharmaceutical into this range, the polarity with the greatest separation of the nearest impurity to the radiopharmaceutical was chosen for further optimization. Should none of the solvents mobilize the radiopharmaceutical to the desired range, the solvents that moved UV active impurities to the greatest degree were selected for further optimization.

Step 3: additive selection

Adding ionic pairing reagents (e.g., TEA and AcOH) can sometimes further improve separation resolution. This process was typically performed with only a few additional TLC plates. Due to the low concentration of these additives in the mobile phases, their polarities in PRISMA optimization are often treated as negligible (i.e., 0) and were included in the solvent mixture by simultaneously removing an equal volume of n-hexane from the mixture recipe[232]. Initially, the addition of each additive was tested at concentrations of 0.1%. Should the resolution or band shapes be improved (i.e., reduced tailing or fronting), proportions of 0.5% are additionally surveyed. Should additives in these low concentrations lead to no observable differences, additional concentrations at 5% are surveyed. Further optimization of the additive concentrations was dynamically determined if they led to heightened resolution of the radiopharmaceutical. (Though adding larger amounts of additives can have a non-negligible impact on the overall strength of the mixture, i.e. changing it slightly from the optimum determined in Step 2, the solvent mixture comparisons in Step 4 are all performed with the same proportion of additive and thus same overall mixture solvent strength, and useful interpolations can still be made.)

Step 4: composition optimization

Nine additional TLC plates were separated using different solvent compositions to optimize the mobile phase composition (P_S values of 100, 010, 001, 622, 262, 226, 406, 460, and 055, all at the previously selected optimal solvent strength and additive amount). The resolution was quantified for each lane. In addition to these selectivity points, we also included resolution data for the other selectivity points surveyed. We picked the mobile phase composition from this data set that gave the highest resolution, performing linear interpolation if needed (**Appendix 7.6.1**).

7.4 Results and Discussion

The PRISMA method optimized radio-TLC mobile phases for several clinically-relevant radiopharmaceuticals with varying chemical properties (**Table 7-1**).

Table 7-1. Selected radiopharmaceuticals and their calculated properties.

Radiopharmaceutical	cLogP	TPSA	H-Bond Donor Count	H-Bond Acceptor Count
[^{18}F]PBR-06	4.6	48.0	0	5
[^{18}F]FEPPA	3.6	51.7	0	5
[^{18}F]Fallypride	3.3	50.8	1	5
[^{18}F]FPEB	2.7	36.7	0	3
[^{18}F]FDOPA	-2.0	104.0	4	6

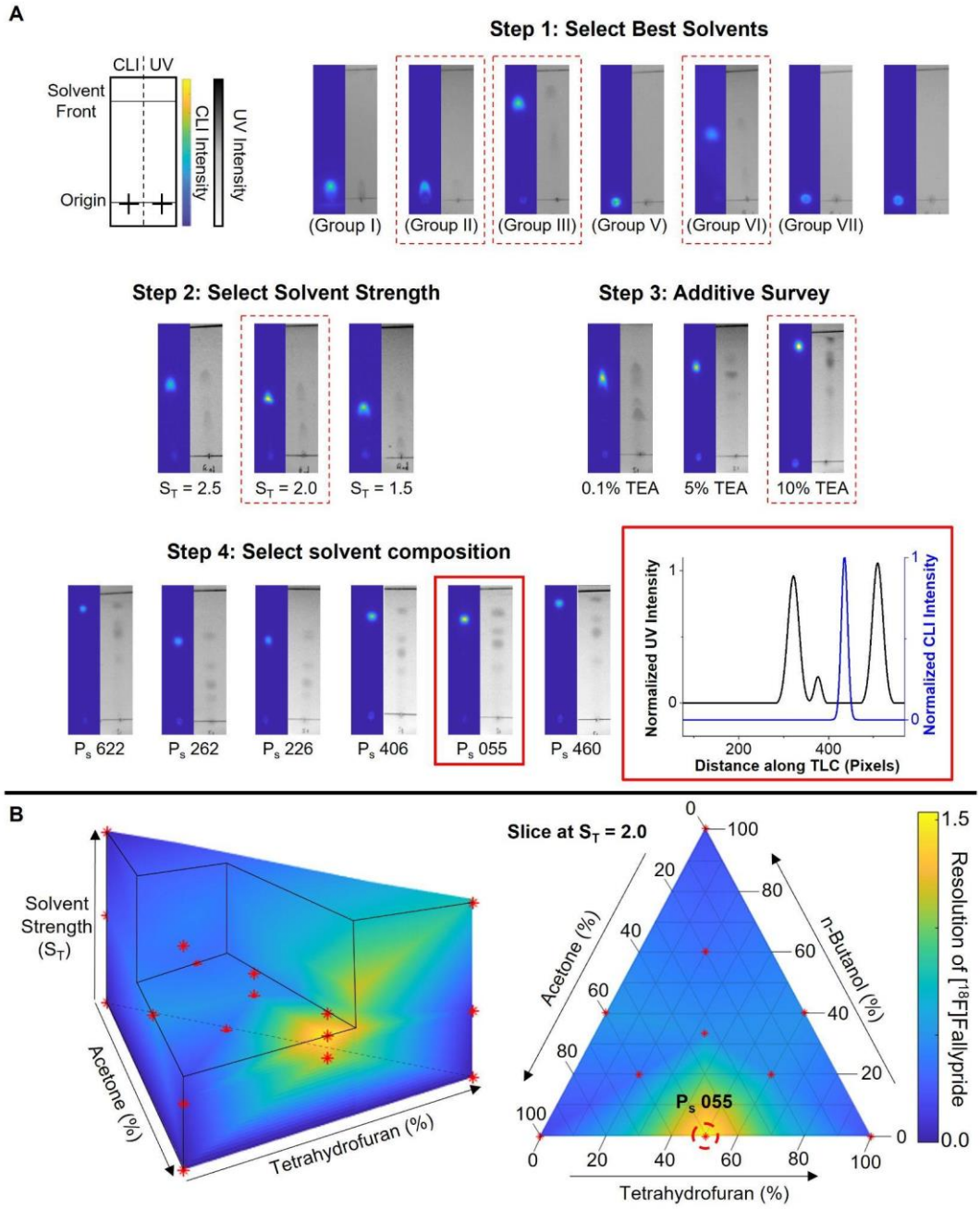

Figure 7-1. PRISMA optimization of [^{18}F]Fallypride.
(A) The PRISMA method comprises several stages of mobile phase optimization to determine conditions that provide the best resolution. TLC plates prepared with mixtures of [^{18}F]Fallypride and impurities are separated under different conditions and visualized via CLI and UV imaging. A custom software program computes the resolution between the radiopharmaceutical and the nearest impurity (radioactive or non-radioactive). Dashed red lines denote the optimal selection from each stage of the process, and the inset shows a chromatogram from the final optimized conditions. (B) The resolution is mapped as a function of mobile phase composition and solvent strength (left), and a slice of this prism taken at the optimal solvent strength (2.0) shows how resolution varies as a function of composition (right).

7.4.1 Optimization of separation of [^{18}F]Fallypride samples

Due to its moderate polarity and polar surface area, [^{18}F]Fallypride was selected as an initial model compound to undergo the PRISMA process (**Figure 7-1A**). The solvent-screening step revealed that n-BuOH (solvent A), THF (solvent B), and acetone (solvent C) provided the best separation of [^{18}F]Fallypride from impurities. Based on the minimum solvent strength of n-BuOH (3.9), the solvent polarities of 3.5, 3.0, and 2.5 were chosen for the survey at the equivolume mixture of strength-adjusted solvents (i.e., P_s = 333). While all the surveyed polarities led to the mobilization of [^{18}F]Fallypride in the R_f range of 0.2-0.8, S_t = 2.5 led to the greatest separation of [^{18}F]Fallypride from other analytes. Tailing of [^{18}F]Fallypride was observable with all mobile phases tested to this point. A possible explanation for this tailing could be ion pairing induced by interactions between the amide functional group of [^{18}F]Fallypride and surface silanol groups on the TLC plate. Different concentrations of TEA[64] were added in percentages of 0.1, 5, and 10% (v/v) to reduce ionic pairing across the plate during development. Using 10% (v/v) TEA led to well-defined bands and was used for further optimization. After surveying nine additional solvent mixtures (P_s), the optimal chromatographic resolution for [^{18}F]Fallypride from nearest impurity (R = 1.54) was found to be P_s = 055, S_t = 2.5 (**Figure 7-1B**). This selectivity point corresponds to a mobile phase composition of 31.3:24.5:34.3:10.0 (v/v) THF:acetone:n-hexanes:TEA.

7.4.2 Comparison of optimized radio-TLC to radio-HPLC

We next compared the optimized TLC method with an isocratic HPLC method. While there are limitations of comparing a normal-phase TLC method with a reversed-phased HPLC method, which furthermore have very different migration lengths, we aimed only to compare the number of resolved species (which are likely in different orders), and the relative abundance of those species. This comparison is made because normal-phase TLC and reversed-phase HPLC (with similar migration lengths as used here) are by far the most predominantly used analytical methods in radiochemistry. A crude sample of [^{18}F]Fallypride was produced under droplet-radiochemistry

conditions[178], modified to result in a low yield and high prevalence of side products. Briefly, increased $TBAHCO_3$ (300 vs. 240 nmol) was used in the [^{18}F]fluoride drying step, and the radiofluorination was performed with 100 nmol instead of 234 nmol of precursor and reacted at 140 °C for 10 min instead of 110 °C for 1 min. Interestingly, the optimized radio-TLC method separated the same number of radioactive analytes as radio-HPLC (**Figure 7-2**). We can see evidence, however, of the well-known underestimation of [^{18}F]fluoride in the radio-HPLC analysis[191]: the abundance of [^{18}F]fluoride computed from the radio-HPLC chromatogram is 71%, but, in comparison, was 95% when computed from the radio-TLC. Even more alarming, due to the underestimation of [^{18}F]fluoride, the apparent formation of [^{18}F]Fallypride calculated from the radio-HPLC chromatogram was nearly 7%, while it was <1% using radio-TLC (**Table 7-2**), suggesting more than a 7-fold error by radio-HPLC. However, if the discrepancy in the size of the [^{18}F]fluoride peaks is removed by ignoring this peak in both the radio-HPLC and radio-TLC chromatograms, the proportions of all other species are found to be similar, indicating excellent quantitative agreement between radio-HPLC and radio-TLC (with the PRISMA-optimized mobile phase).

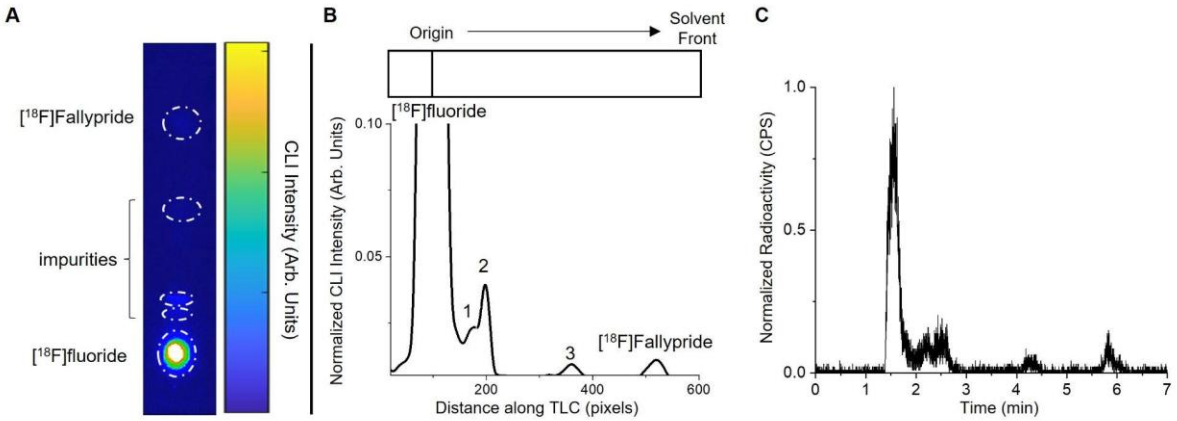

Figure 7-2. Chromatographic resolution comparison of optimized TLC against conventional isocratic HPLC.
(A) Cerenkov luminescence image of a TLC plate after spotting with a crude [^{18}F]Fallypride sample and separation via the PRISMA-optimized mobile phase. (B) TLC chromatogram was generated by taking a line profile of the Cerenkov luminescence image along the lane. The

chromatogram is truncated to better show the smaller peaks. (C) Isocratic radio-HPLC chromatogram of the same sample.

Table 7-2. Comparison of the radiochemical composition of a crude [^{18}F]Fallypride sample as determined by radio-TLC and Radio-HPLC.

	Integration (%)			
Peak	HPLC^{A}	HPLC^{B}	TLC^{A}	TLC^{B}
[^{18}F]fluoride	70.5	-	94.7	-
1	8.7	29.9	1.6	30.7
2	11.0	37.2	2.4	36.3
3	3.3	11.0	0.6	11.6
[^{18}F]Fallypride	6.5	22.0	0.8	21.3

^{A}Estimation accounts for all peaks, including [^{18}F]fluoride; ^{B}Estimation ignores [^{18}F]fluoride and is calculated solely based on other peaks

Because of the excellent agreement, it is possible to consider using an imaging-based readout of TLC plates separated according to the PRISMA-optimized mobile phase as a simpler and more rapid alternative to radio-HPLC for radiopharmaceutical analysis. If multiple samples need to be analyzed, then the advantage of radio-TLC is further magnified as multiple samples can be spotted on the same plate and separated and read out in parallel[93]. In contrast, analyzing multiple samples via radio-HPLC requires ample time for cleaning and re-equilibration between samples.

7.4.3 Comparison of literature mobile phases to PRISMA-optimized mobile phase

The separation achieved with the PRISMA-optimized mobile phase was compared to mobile phases reported in the literature for the analysis of [^{18}F]Fallypride. We produced [^{18}F]Fallypride under previously-reported droplet radiochemistry conditions[178] modified to give a moderate yield and many side products. Specifically, the amount of $TBAHCO_3$ used in the

[^{18}F]fluoride drying step was increased (from 240 to 800 nmol), and the fluorination was performed with 200 nmol instead of 234 nmol of precursor and reacted at 140 °C for 10 min instead of 110 °C for 1 min. Analysis was performed using TLC plates with pre-concentration zones, and the separation distance was extended from 4 to 5 cm to ensure the highest possible separation resolution in all cases. All lanes were spotted with 1 µL of the same crude reaction mixture**. Figure 7-3** details the mobile phases surveyed, along with the obtained CLI images and generated chromatograms. For each mobile phase, we also performed separations using only [^{18}F]TBAF (**Figure 7-7**) or [^{19}F]Fallypride (**Figure 7-8**) to confirm the R_f values of these species.

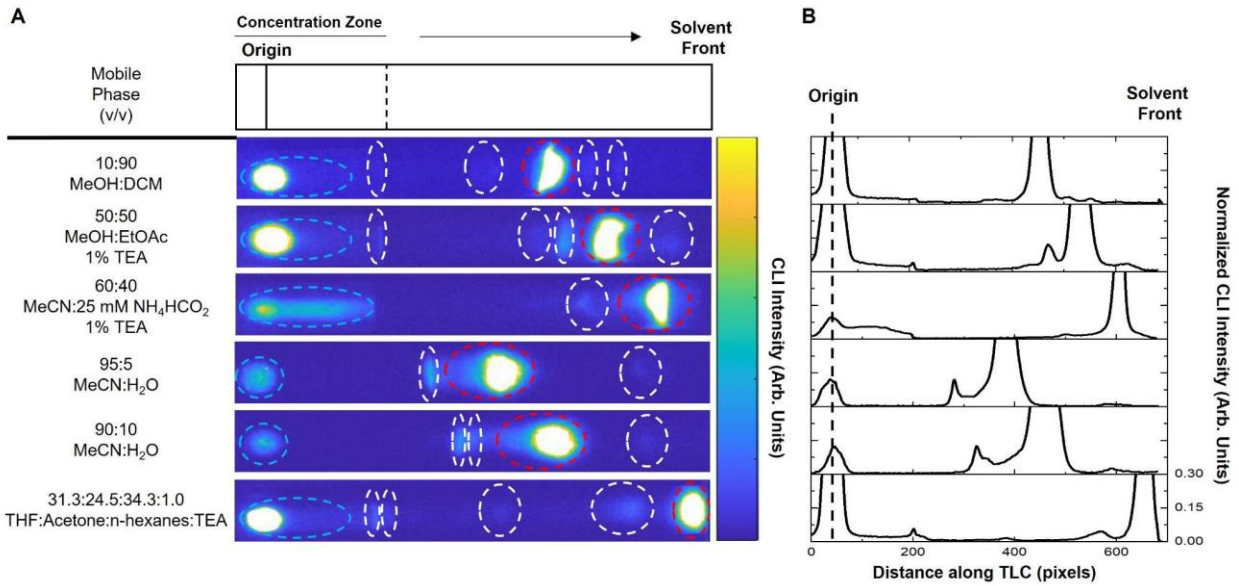

Figure 7-3. Mobile phases comparisons for the analysis of crude [^{18}F]Fallypride conversion.
(A) CLI images of TLC plates spotted with crude [^{18}F]Fallypride and developed with different mobile phases from literature (first five entries) and the PRISMA-derived mobile phase (last entry). [^{18}F]fluoride is denoted with dashed blue ellipses, side-products denoted with dashed white ellipses, and [^{18}F]Fallypride denoted with dashed red ellipses. (B) TLC chromatograms were generated by taking a line profile of the Cerenkov luminescence images. Chromatograms are truncated to better show the smaller peaks.

Abundances of species, computed from areas under peaks in the chromatograms, are summarized in **Table 7-3**. A significant disparity in the estimated abundance of [^{18}F]Fallypride and other species between different mobile phases is evident. Mobile phases with aqueous compositions (rows 3, 4, and 5) led to the greatest apparent abundance of [^{18}F]Fallypride (i.e.,

66.1%, 82.7%, and 84.7%), while purely organic mobile phases (rows 1, 2, and 6) led to a similar abundance of [^{18}F]Fallypride compared to the PRISMA optimized mobile phase (i.e., 46.5%, 47.4%, and 41.4%). The discrepancy in results obtained from the aqueous mobile phases is difficult to explain, but due to the high degree of band overlap (with a low number of resolved bands), there are likely species co-eluting with [^{18}F]Fallypride. The moderate discrepancy between the organic mobile phases suggests that the initial two literature mobile phases may result in incomplete separation of analytes, and an overlapping band may be counted with the [^{18}F]Fallypride band. Using the same crude [^{18}F]Fallypride sample, we performed a radio-HPLC separation, collected the [^{18}F]Fallypride fraction, and compared the activity to the injected activity. In addition to the high similarity between the radio-TLC and radio-HPLC chromatograms (**Figure 7-9**), the abundance of collected [^{18}F]Fallypride was 40.2%, in excellent agreement with the abundance obtained from radio-TLC using the PRISMA-optimized mobile phase.

Table 7-3. Integration of analytes detected by radio-TLC in the analysis of [^{18}F]Fallypride.

Mobile Phase (v/v)	Number of Observable Peaks	Abundance (%)						
				Impurities				Fallypride R_f
		[^{18}F]fluoride	[^{18}F]Fallypride	1	2	3	4	
10:90 MeOH:DCM[16]	6	46.7	46.5	1.7	2.0	1.3	1.8	0.65
50:50 MeOH:EtOAc 1% TEA[17]	6	43.9	47.4	0.7	1.7	4.7	1.7	0.76
60:40 MeCN:25 mM NH_4HCO_2 1% TEA[11,34]	3	30.4	66.1	3.6	-	-	-	0.87
95:5 MeCN:H_2O[19]	4	9.6	82.7	6.6	1.1	-	-	0.55
90:10 MeCN:H_2O[35]	4	6.9	84.7	4.3	2.3	-	-	0.66
31.3:24.5:34.3:1.0 THF:Acetone:n-hexanes:TEA	6	49.8	41.4	2.3	1.0	1.5	4.0	0.91

These results further underscore the problems of [^{18}F]fluoride retention on HPLC columns, which can lead to significant over-estimation errors of radiochemical species, especially low-abundance ones. Furthermore, the discrepancy when using different radio-TLC mobile phases, even for the identical sample, raises questions about the accuracy of reported results using certain mobile phases and underscores the importance of ensuring high chromatographic resolution of the analysis method.

7.4.4 Optimization of separation of [^{18}F]PBR-06 samples

For crude samples of [^{18}F]PBR-06 (**Figure 7-10**), the solvent screening step revealed that diethyl ether (solvent A), dichloromethane (solvent B), and chloroform (solvent C) exhibited the greatest separation of impurities from [^{18}F]PBR-06. Solvent polarities were normalized to 2.5, 2.0, and 1.5. With the solvents mixed in equal proportions (P_s = 333), the greatest separation of [^{18}F]PBR-06 from impurities was obtained with S_t = 2.5. Low amounts of AcOH and TEA (0.5%) were tested as chromatographic additives. The use of AcOH resulted in more observable UV-active impurities and a slightly higher chromatographic resolution for [^{18}F]PBR-06 than the use of TEA. After evaluating the impact of other mixtures of the solvents (tested at S_t = 2.5 using 0.5% AcOH (v/v)), the greatest resolution of [^{18}F]PBR-06 from nearest impurity (R = 1.84) was obtained at P_s = 333, S_t = 2.5 (**Figure 7-10**). This selectivity point corresponds to a mobile phase composition of 29.8:26.9:20.4:22.85:0.05 (v/v) diethyl ether:dichloromethane:chloroform:n-hexanes:AcOH.

7.4.5 Optimization of separation of [^{18}F]FEPPA samples

For samples of [^{18}F]FEPPA (**Figure 7-11**), the solvent screening test revealed that n-BuOH (solvent A), THF (solvent B), and acetone (solvent C) provided the best separation of [^{18}F]FEPPA from impurities. These solvents were normalized to have polarities of 3.5, 3.0, and 2.5. In equivolume mixtures (P_s = 333), S_t = 2.5 showed the greatest separation of impurities from [^{18}F]FEPPA. A screening of additives revealed heightened resolution of [^{18}F]FEPPA from impurities using 1% TEA. Further solvent mixtures were tested (at S_t = 2.5 and with the addition

of 1% TEA), and P_s = 262, S_t = 2.5 showed the greatest chromatographic resolution of [^{18}F]FEPPA from its nearest impurity (R = 2.07). This selectivity point corresponds to a mobile phase composition of 12.8:37.5:9.8:38.8:1 n-BuOH:THF:Acetone:n-hexanes:TEA (v/v).

7.4.6 Optimization of separation of [^{18}F]FDOPA samples

We next considered the two-step radiofluorination of [^{18}F]FDOPA (**Figure 7-12**), in which the crude product contains a relatively nonpolar radioactive intermediate and the highly polar [^{18}F]FDOPA product. It is notoriously difficult to separate extremely polar compounds on normal phase silica TLC plates. For this reason, it is notable that the literature for [^{18}F]FDOPA analysis cites the use of reverse phase chromatography for radio-TLC analyses[235–237]. In the solvent-screening step, [^{18}F]FDOPA could not be mobilized, but using the criteria of the furthest migration of UV impurity bands from one another, we selected n-butanol (solvent A), THF (solvent B), and acetone (solvent C). The polarity of each pure solvent was normalized to 3.5, 3.0, and 2.5. When comparing solvent strengths (at P_s = 333), S_t = 3.5 led to the greatest degree of movement for UV impurities, but S_t = 3.0 led to more distinguishable peaks and was chosen for further optimization. High percentages of chromatographic additives were tested to address the tailing across the TLC plate. The best separation was found with AcOH in 30% abundance. After comparing different solvent mixtures, P_s = 333, (at S_t = 3.0 at 30% AcOH) exhibited the greatest chromatographic resolution of [^{18}F]FDOPA from its nearest impurity (R = 1.18). This selectivity point corresponds to a mobile phase composition of 22.6:21.7:19.6:61:30 (v/v) n-butanol:THF:acetone:n-hexanes:AcOH. While baseline resolution was not achieved, the resolution achieved may be sufficient for synthesis optimization or may be improved by adapting the PRISMA method to other types of TLC plates.

7.4.7 Optimization of separation of [^{18}F]FPEB samples

Simple leaving groups in aromatic substitutions, such as NO_2 groups, are commonly used to radiofluorinate radiopharmaceuticals. It is noteworthy that the separation of these radiopharmaceuticals and precursor structures is relatively difficult using HPLC. Thus the

application of the PRISMA method to [^{18}F]FPEB (**Figure 7-13**), which is produced via S_NAR of a NO_2 leaving group, serves as a good illustration of the high-resolution capabilities of PRISMA. The solvent screening step revealed that diethyl ether (solvent A), n-BuOH (solvent B), and acetone (solvent C) yielded the greatest separation of impurities from [^{18}F]FPEB. Normalizing the polarities of the solvents to 2.5, 2.0, and 1.5, a comparison of equivolume mixtures (P_s = 333) showed that the best separation could be achieved with S_t = 1.5. Evaluation of chromatographic additives showed a minor improvement when using 1% TEA. After comparing additional solvent mixtures, the P_s = 406 mixture (with S_t = 1.5, 1% TEA) exhibited the best resolution of [^{18}F]FPEB from the nearest impurity (R = 1.71). This selectivity point corresponds to a mobile phase composition of 21.4:17.6:60.0:1.0 diethyl ether:acetone:n-hexanes:TEA (v/v).

7.4.8 Optimization of [^{18}F]FPEB radiosynthesis with high-resolution TLC analysis

As an example of how the PRISMA method can be used, we performed a high-throughput synthesis optimization of [^{18}F]FPEB using multi-reaction droplet-radiochemistry methods[178] and performed radio-TLC analysis of reactions in a multi-lane fashion[93] (8 samples per TLC plate) using the PRISMA-derived mobile phase. In the literature, harsh reaction conditions, like high temperature and base concentrations, lead to the formation of hydrolyzed impurities similar to the [^{18}F]FPEB[199,238], and HPLC analysis of crude microscale reactions (via flow-based reactor) of [^{18}F]FPEB shows closely eluting radioactive impurities[238], that may be difficult to resolve via TLC without careful optimization.

Initial microscale conditions were adapted by scaling down conditions reported in literature[239]. [^{18}F]fluoride (20-30 MBq) mixed with 500 nmol of the base was first dried at 105 °C for 1 min, and then a 10 µL droplet of precursor solution (containing 250 nmol) was added and reacted for 5 min at 140 °C. We first compared the use of different bases ($K_2C_2O_4$, K_2CO_3, $KHCO_3$, and Cs_2CO_3) and two different reaction solvents (DMSO and NMP), with n=2 replicates per condition (**Figure 7-4A**). Cs_2CO_3, in combination with DMSO, was selected for further optimization based on good RCY and low volatile loss (high collection efficiency). In optimization of the base

amount (**Figure 7-4B**), 290 nmol was selected as the best compromise of good RCY and low volatile losses. From a comparison of the impact of precursor amount (**Figure 7-4C**), a high amount of precursor is needed to improve RCY. By replotting the results as a function of the base to precursor ratio (**Figure 7-4D**), we noticed we achieved a similar yield with only 120 nmol of the precursor by lowering the amount of Cs_2CO_3 to 200 nmol. The reaction temperature was further optimized, revealing an optimal temperature of 140 °C (**Figure 7-4E**).

Under the optimized conditions, [^{18}F]FPEB could be produced in a crude RCY of ~16%, greater than other reported literature conditions (4-10%)[174,238–241]. Sixty-four reactions could be performed per day, and by employing multi-lane TLC using the optimized mobile phase, all samples each day could be analyzed within 60 min. In contrast, using radio-HPLC analysis would likely have significantly overestimated the product yield (due to loss of [^{18}F]fluoride in the column), and test reactions would have taken approximately 30-40 min each to analyze. Due to the limited half-life of F-18, only 12-16 samples could be practically analyzed each day if HPLC was used. Thus the study would have taken many more days, more batches of radioisotope (potentially adding other variables for which additional replicates are needed), and more labor hours.

7.4.9 Additional readout channels via staining

In addition to radiation readout (via Cerenkov imaging) and readout via UV imaging, additional chemical information can be gleaned from the TLC plate. Staining is a widely used method in TLC analysis that is inexpensive, can be used to detect low abundance analytes (via water-based stains like Hanessian), stain for specific functional groups (e.g., ninhydrin for the detection of amines), and detect analytes that are not UV-active. To demonstrate this principle, we employed TLC stains in the analysis of [^{18}F]PBR-06 and [^{18}F]Fallypride crude samples. In the samples of [^{18}F]PBR-06, few analytes can be visualized by UV analysis by TLC (**Figure 7-14**). Hanessian staining reveals faint traces of additional impurities near the product band. Ninhydrin staining did not reveal additional bands (**Figure 7-14**), but because it stains amine groups, this can help determine the potential identities of the bands. For [^{18}F]Fallypride, Hanessian staining

revealed no additional impurities (**Figure 7-15**). Ninhydrin staining revealed a previously unseen impurity (**Figure 7-15**).

Staining methods pose an interesting method to visualize low-abundance species and to glean additional chemical information about specific bands that could help to identify bands and improve understanding of competing reaction pathways. It is striking that the additional impurities detected via staining were well separated from the radiopharmaceutical, even though they were not visible during the PRISMA procedure to optimize the mobile phase.

7.5 Conclusions

In this study, a systematic mobile phase selection process, PRISMA, was applied to optimize TLC mobile phases to separate crude samples of radiopharmaceuticals. The PRISMA method provided a systematic framework to rapidly (<4 h) and efficiently (with only 1 batch of the crude radiopharmaceutical) reach a set of development conditions resulting in high-resolution separation without prior knowledge of impurity identities or properties. The method was successfully applied to multiple examples of diverse radiopharmaceuticals, achieving baseline separation of the radiopharmaceutical from radioactive and non-radioactive impurities. In the case of [^{18}F]Fallypride, the optimized radio-TLC method rivaled the resolution of isocratic radio-HPLC while resulting in a more accurate analysis as the method does not suffer from the issue of loss of [^{18}F]fluoride to the column of radio-HPLC. Notably, the optimized TLC conditions can be applied for synthesis optimization and potentially to portions of QC testing (e.g., radiochemical purity) or radio-metabolite studies[77,198,242–248]. UV imaging and TLC staining can reveal additional species that are not visible with the traditional use of radio-TLC. This streamlined methodology can be easily employed by radiochemistry labs, using ubiquitous materials, and enabling anyone to develop high-resolution TLC separation methods for accurate radiopharmaceutical analysis.

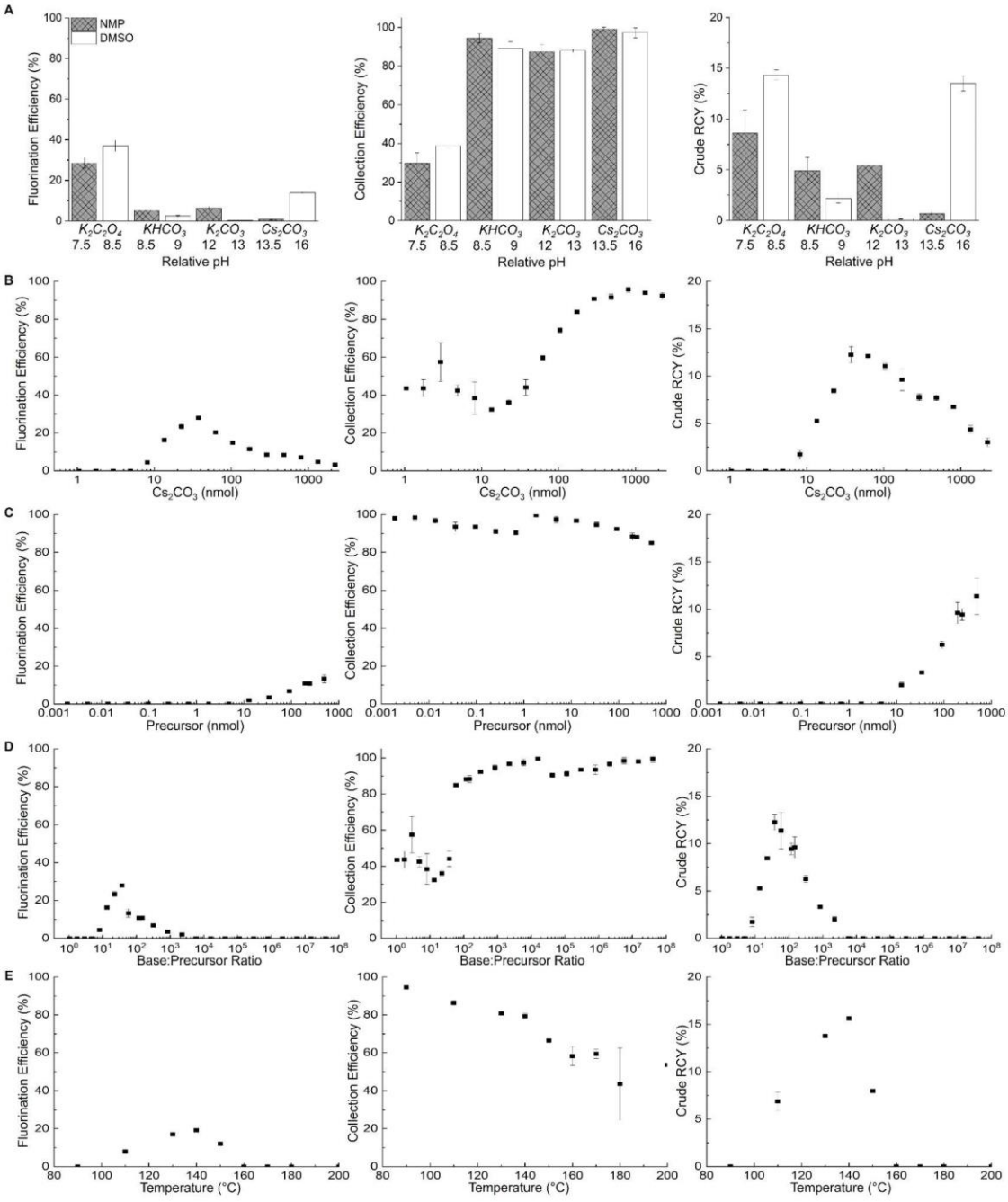

Figure 7-4. Optimization of the synthesis of [^{18}F]FPEB (n = 2), leveraging high-throughput analyses enabled by multi-lane radio-TLC using the PRISMA-optimized mobile phase. Reaction volume is 10 µL and reaction time is 5 min in all cases.

(A) Impact of different bases and two different reaction solvents. Relative pH is shown below each data point.[53] Precursor amount: 250 nmol, base amount: 500 nmol, reaction temperature: 140 °C. (B) Effect of the amount of Cs_2CO_3. Precursor amount: 250 nmol, reaction temperature: 140 °C. (C) Effect of precursor amount. Cs_2CO_3 amount: 290 nmol, reaction temperature: 140 °C. (D) Data from B and C were replotted to show the effect of the base:precursor ratio. (E) Effect of reaction temperature. Precursor amount: 200 nmol, Cs_2CO_3 amount: 120 nmol.

7.6 Appendix

Table 7-4. Solvents in Snyder selectivity groups that are miscible with n-hexanes and used for the PRISMA optimizations performed in this work.

Snyder Group Number[A]	Solvent Name	Polarity
1	diethyl ether (Et_2O)	2.8
2	n-butanol (n-BuOH)	3.9
3	tetrahydrofuran (THF)	4.0
5	dichloromethane (DCM)	3.1
6	acetone	5.1
7	toluene (PhMe)	2.4
8	chloroform ($CHCl_3$)	4.1

[A]Group 4 (Formamide) was omitted due to incompatibility with silica-based TLC, and its ability to visibly etch silica from the TLC plate. A list of all group solvents is detailed in the literature.[73]

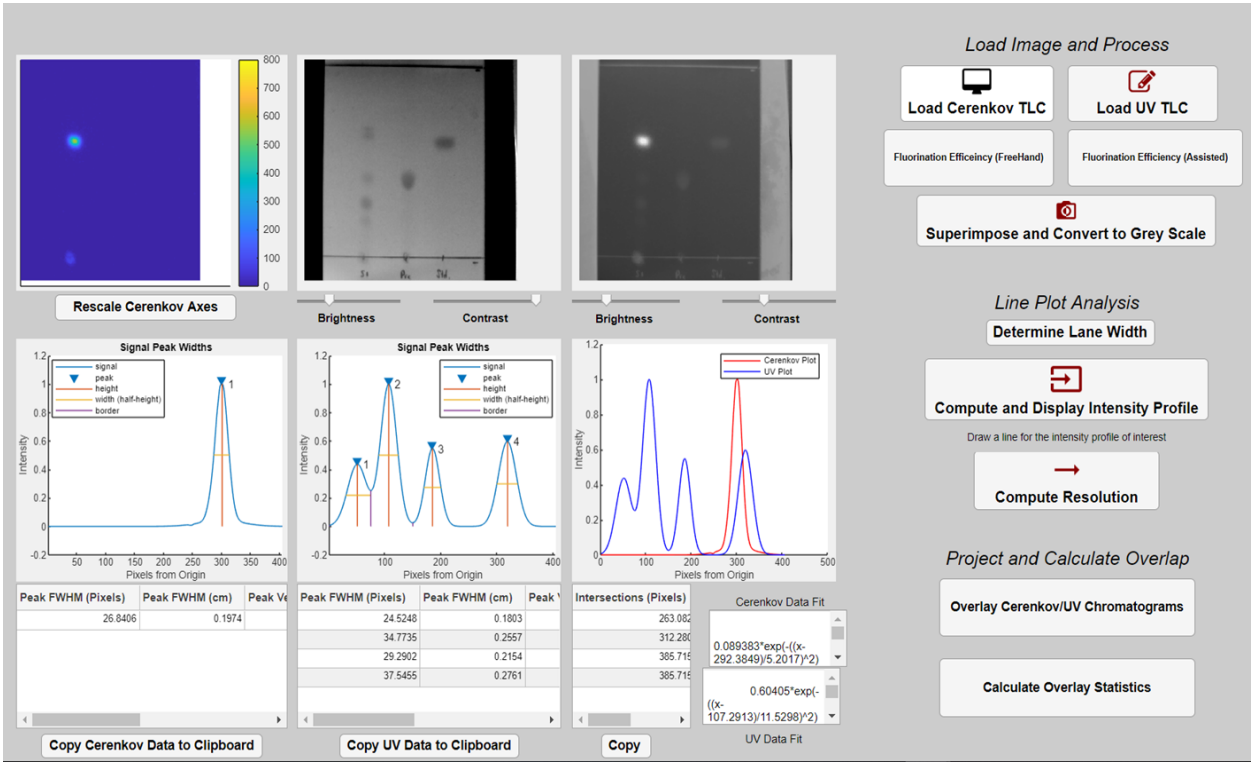

Figure 7-5. The graphical user interface of software used for analyzing TLC images.

7.6.1 PRISMA "Prism" Construction

The data resulting from the PRISMA process (described in Methods) can be visualized in a 3D representation (**Figure 7-6**). First, we draw a triangle (**Figure 7-6A**) where each side represents the volume fraction of the three pure solvents (A, B, and C) selected in Step 1. By convention, the ordering of the solvents is chosen in ascending order of solvent polarity strength. A mixture of solvents can be represented as a point within the triangle. According to the PRISMA method, selectivity point notation can be used to describe the proportion of each solvent (e.g., P_s = 622 comprises 60% solvent A, 20% solvent B, and 20% solvent C). Solvent strength is plotted on the vertical axis. Since each solvent can be diluted down to a strength of zero via n-hexanes, the available parameter space is a prism-shaped volume with the three vertical edges having lengths equal to the strength of the corresponding solvents. In our optimization process, we limit ourselves to a maximum strength corresponding to the minimum of all the solvent strengths (i.e., $\min(S_A, S_B, S_C)$) (**Figure 7-6B**).

By normalizing all 3 solvents to the same strength value, we ensure that we are working on a horizontal slice of the parameter space when varying the solvent mixture. Equivolume mixtures (P_s = 333) of solvents at three different solvents strengths are compared in Step 2 (**Figure 7-6C**). The P_s = 333 point is at the center of each triangular slice (corresponding to the three different strengths). In Step 3, chromatographic additives are considered and used in later optimization stages. The amounts of the additives are small, and they are not reflected in the 3D construction. Finally, in Step 4, we work in the triangular slice corresponding to the best strength and additives from Steps 2 and 3, and the volumetric ratio of the strength-adjusted solvents is varied. Different mixtures (i.e., selectivity points, P_s) are explored and denoted as red asterisks in **Figure 7-6D.**

For each point examined (i.e., solvent strength and composition), we compute a resolution value (between the radiopharmaceutical and its nearest impurity) and plot this as a color.

Using the resolution values from the tested points, the space's color in between points was determined by linear interpolation, and data was plotted on a triangular mesh grid with step size 0.05 (**Figure 7-6E**). The slice on which the highest resolution value occurred is shown in **Figure 7-6F**.

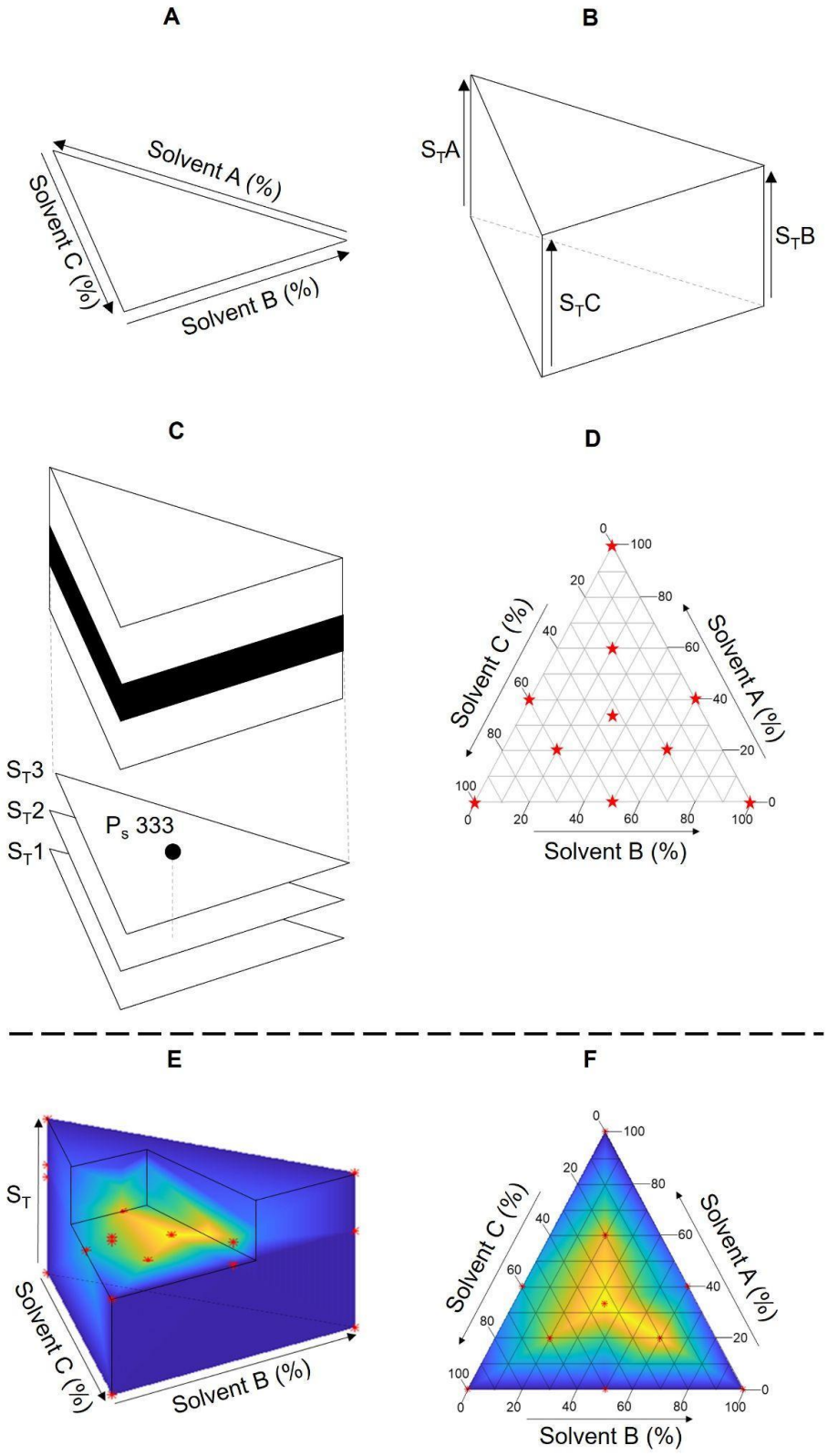

Figure 7-6. Procedure for the 3D visualization of resolution as a function of mobile phase composition.

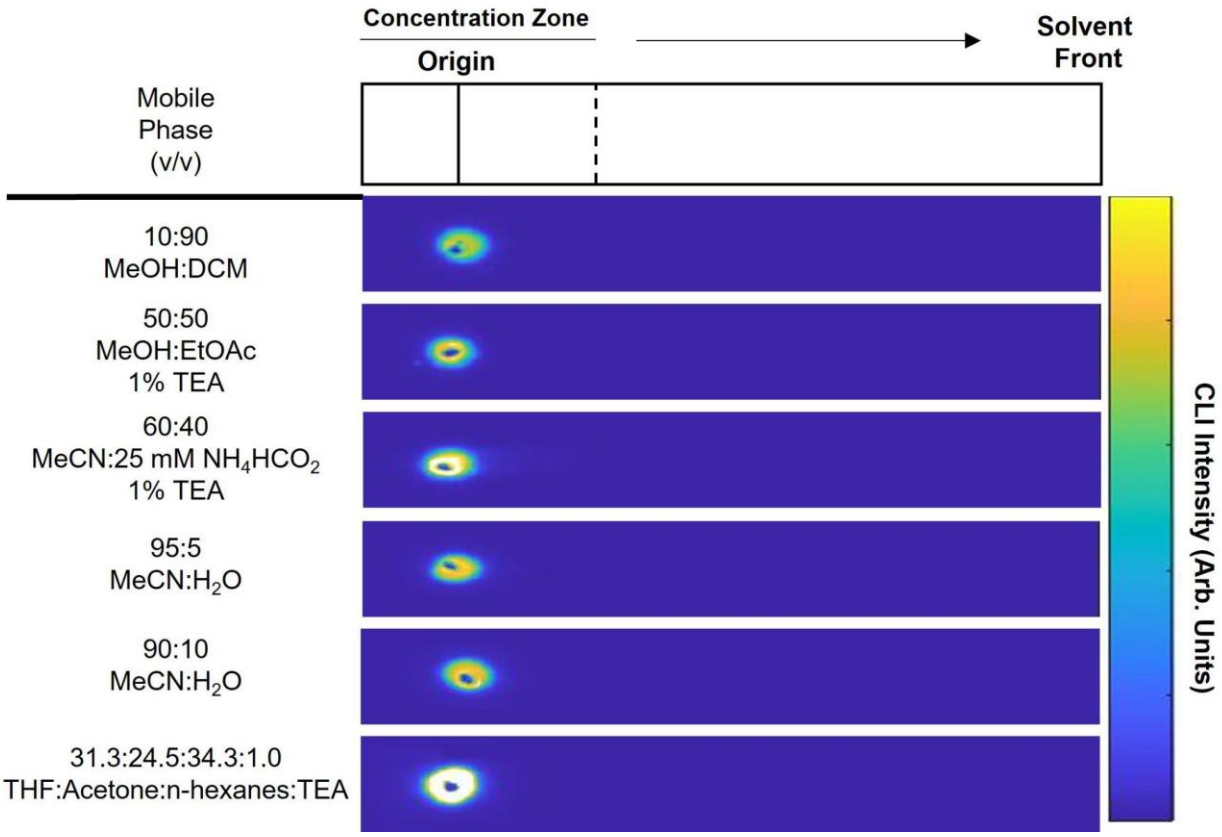

Figure 7-7. CLI images of TLC plates spotted with 1 µL crude [^{18}F]TBAF (30-50 MBq [^{18}F]fluoride, 800 nmol $TBAHCO_3$, diluted to 60 µL) developed with different [^{18}F]Fallypride mobile phases from literature (first 5 entries) and the PRISMA-derived mobile phase (last entry).

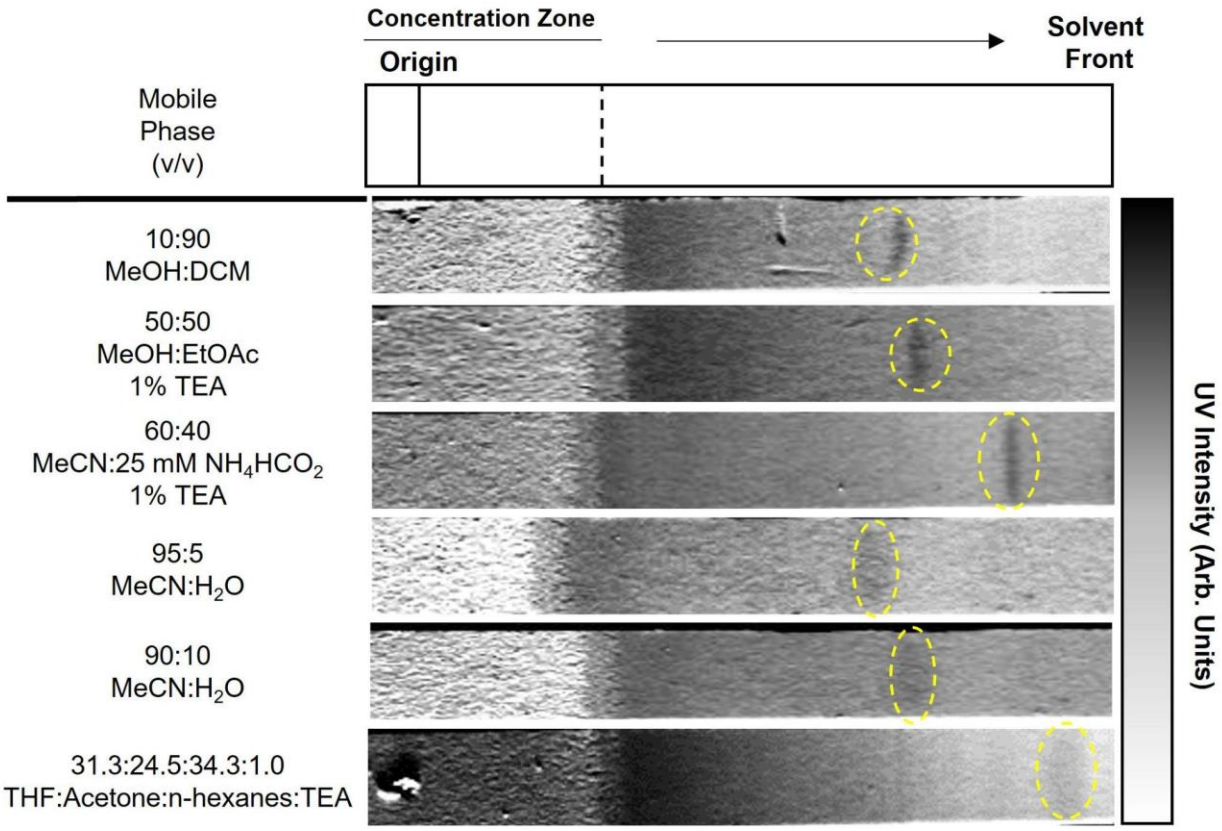

Figure 7-8. UV images of TLC plates spotted with Fallypride reference standard and developed with different mobile phases from literature (first 5 entries) and the PRISMA-derived mobile phase (last entry).

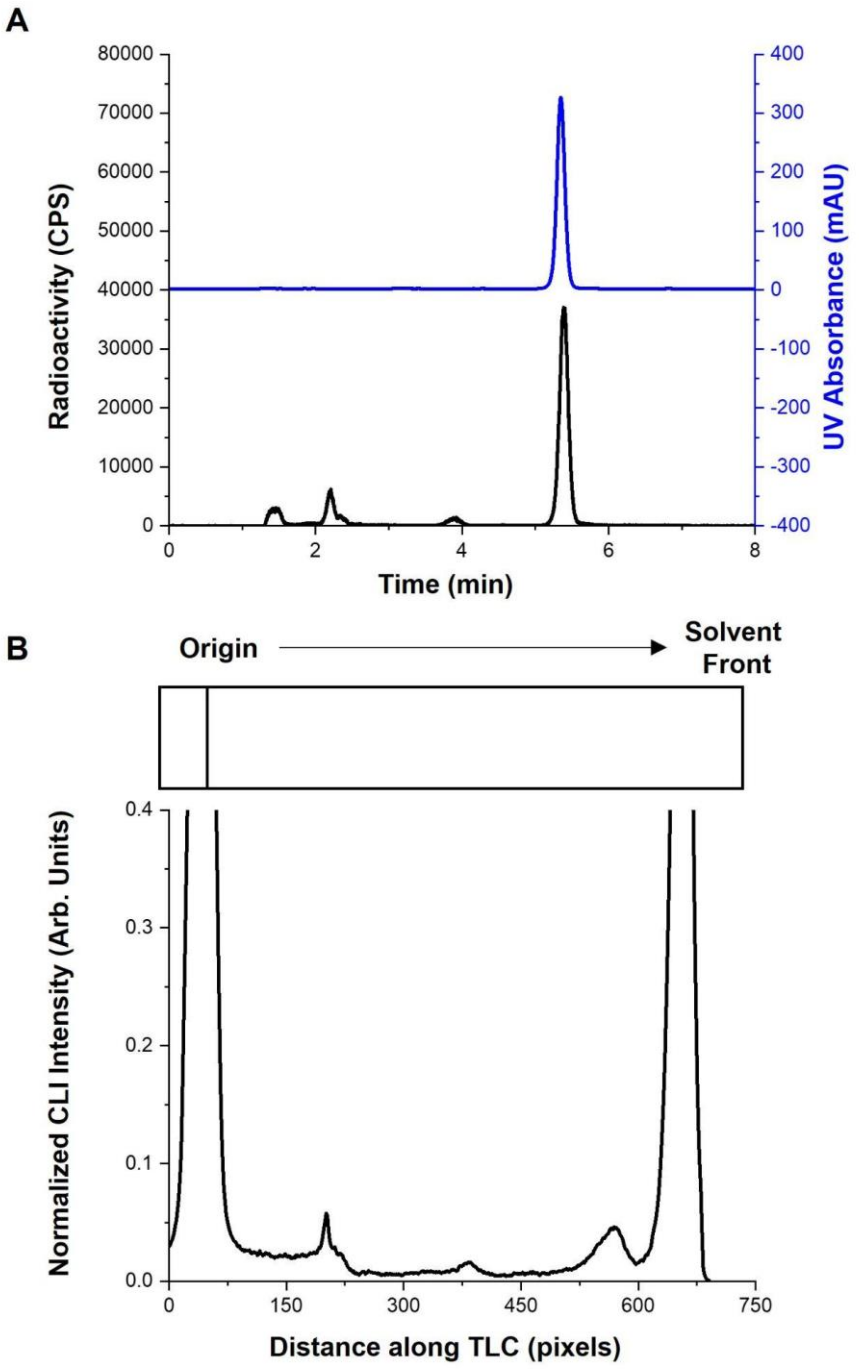

Figure 7-9. Isocratic HPLC compared to the PRISMA optimized mobile phase of a crude [^{18}F]Fallypride sample.
(A) Radio-HPLC chromatograms (Top) Standard trace of [^{19}F]Fallypride (Bottom) Crude [^{18}F]Fallypride. (B) Radio-TLC chromatograms of crude [^{18}F]Fallypride.

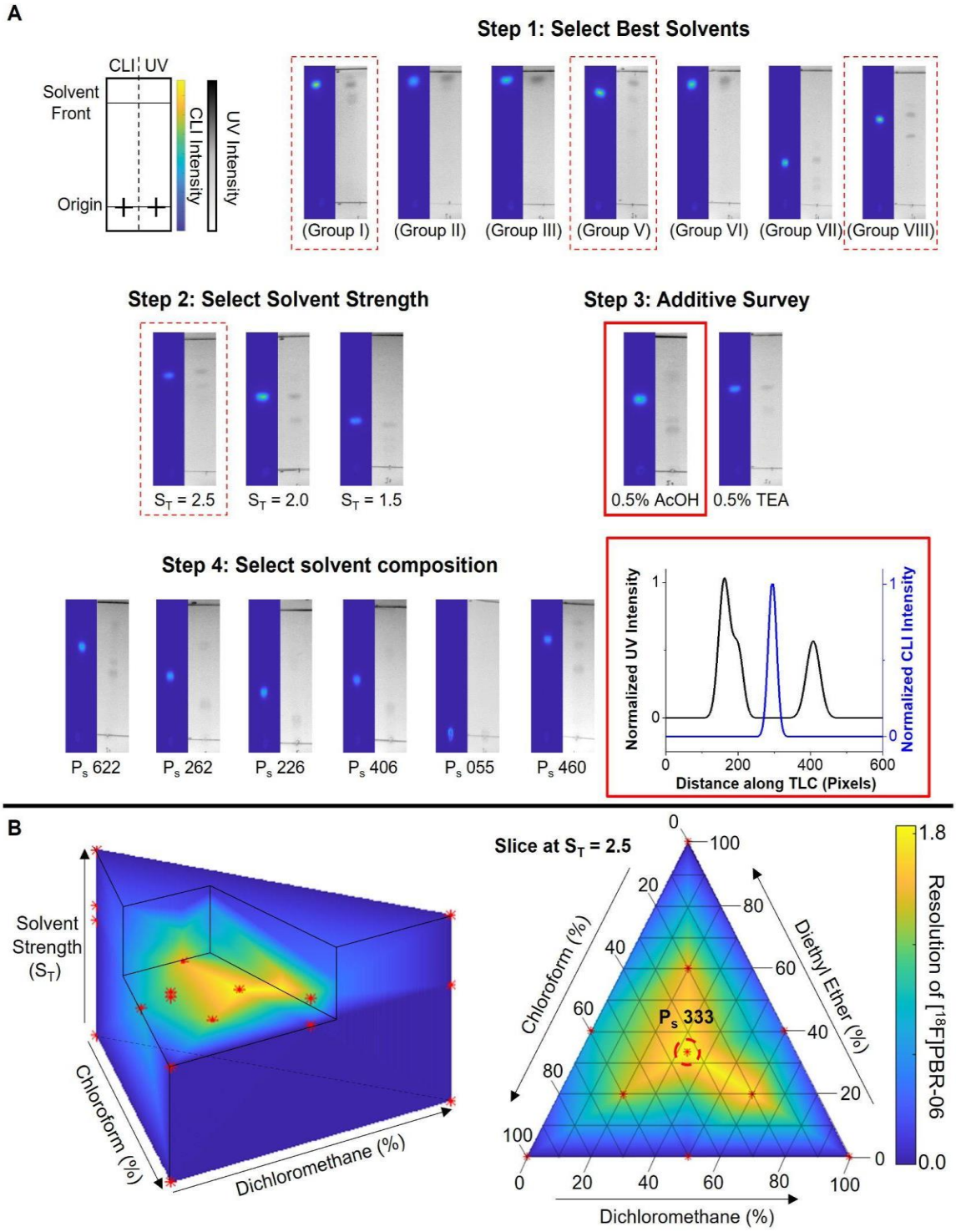

Figure 7-10. PRISMA optimization of [^{18}F]PBR-06.
(A) Results of PRISMA optimization applied to samples of [^{18}F]PBR-06. The condition(s) giving the best resolution at each step is outlined in dashed boxes. The optimal condition is outlined in solid red. (B) 3D visualization of resolution as a function of mobile phase composition.

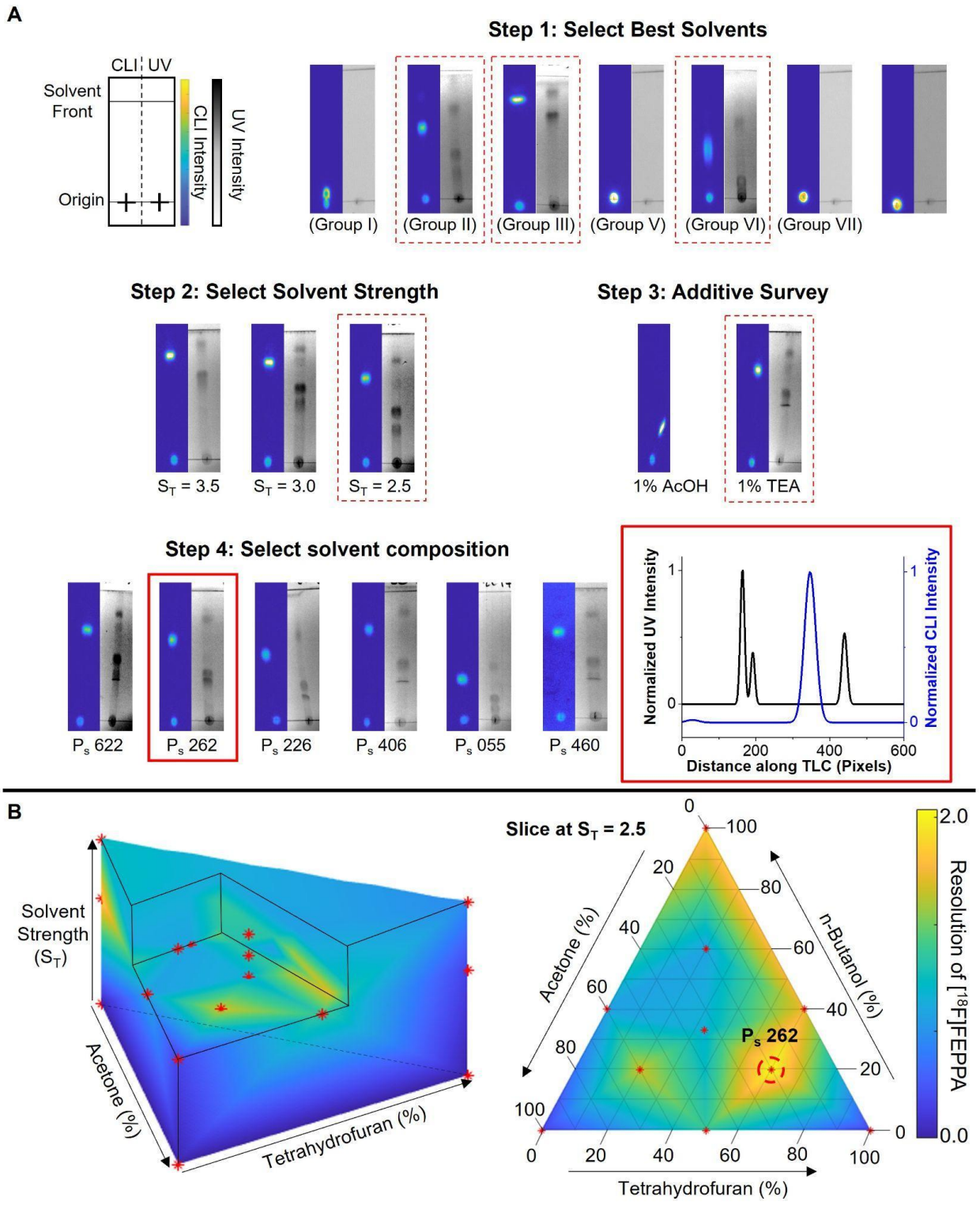

Figure 7-11. PRISMA optimization of [^{18}F]FEPPA.
(A) Results of PRISMA optimization applied to samples of [^{18}F]FEPPA. The condition(s) giving the best resolution at each step is outlined in dashed boxes. The optimal condition is outlined in solid red. (B) 3D visualization of resolution as a function of mobile phase composition.

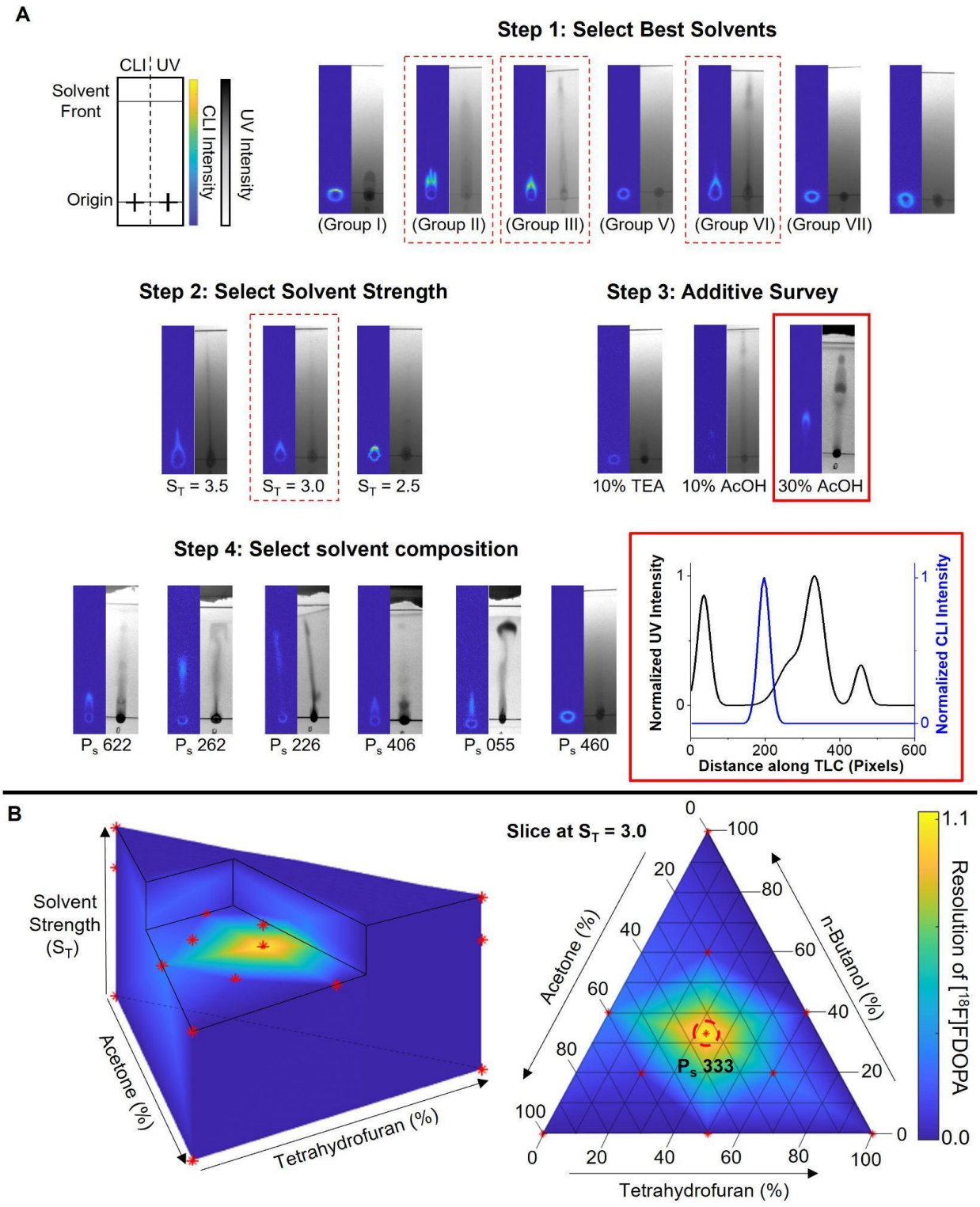

Figure 7-12. PRISMA optimization of [^{18}F]FDOPA.
(A) Results of PRISMA optimization applied to samples of [^{18}F]FDOPA. The condition(s) giving the best resolution at each step is outlined in dashed boxes. The optimal condition is outlined in solid red. (B) 3D visualization of resolution as a function of mobile phase composition.

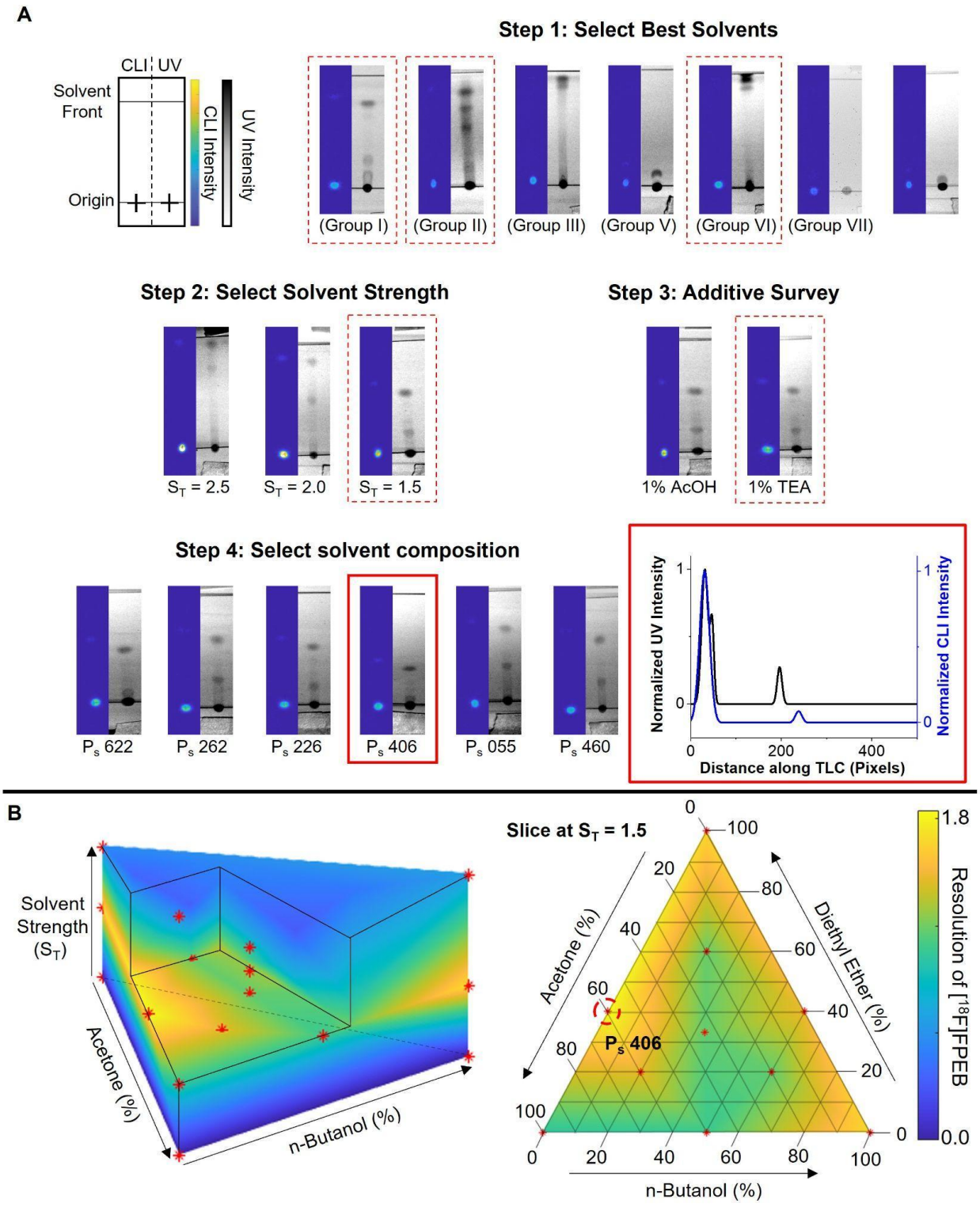

Figure 7-13. PRISMA optimization of [^{18}F]FPEB.
(A) Results of PRISMA optimization applied to samples of [^{18}F]FPEB. The condition(s) giving the best resolution at each step is outlined in dashed boxes. The optimal condition is outlined in solid red. (B) 3D visualization of resolution as a function of mobile phase composition.

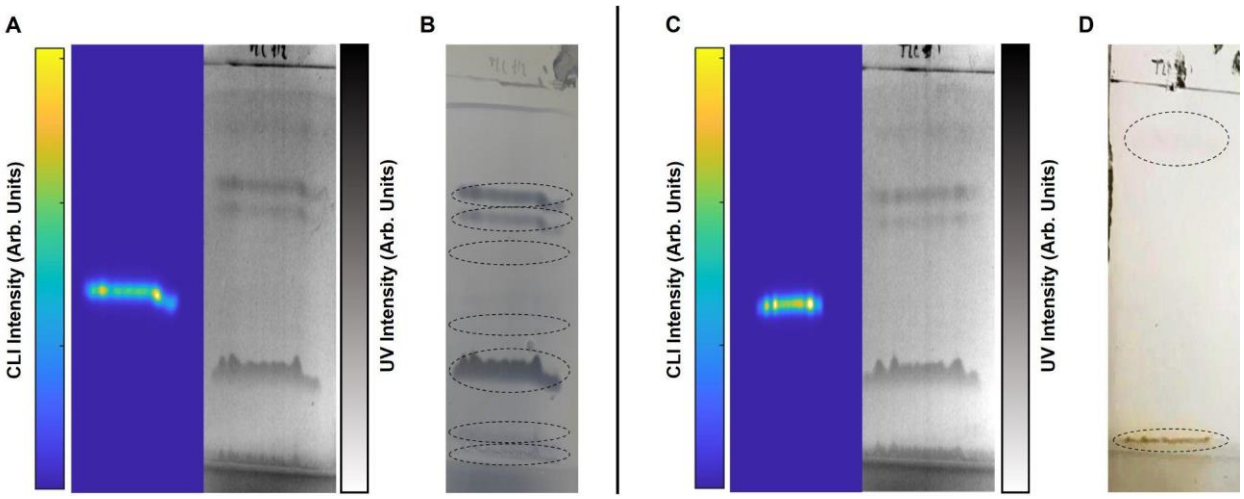

Figure 7-14. Examples of Hanessian staining possible with TLC readout.
(A) CLI and UV images of crude [^{18}F]PBR-06 reaction separated under the PRISMA-optimized TLC conditions. (B) Hanessian stain of the same TLC plate. (C) CLI and UV images of a different crude [^{18}F]PBR-06 reaction separated under the PRISMA-optimized TLC conditions. (D) Ninhydrin stain of the same TLC plate. Black dashed lines are used to denote the observable bands on the stained plates in B and D.

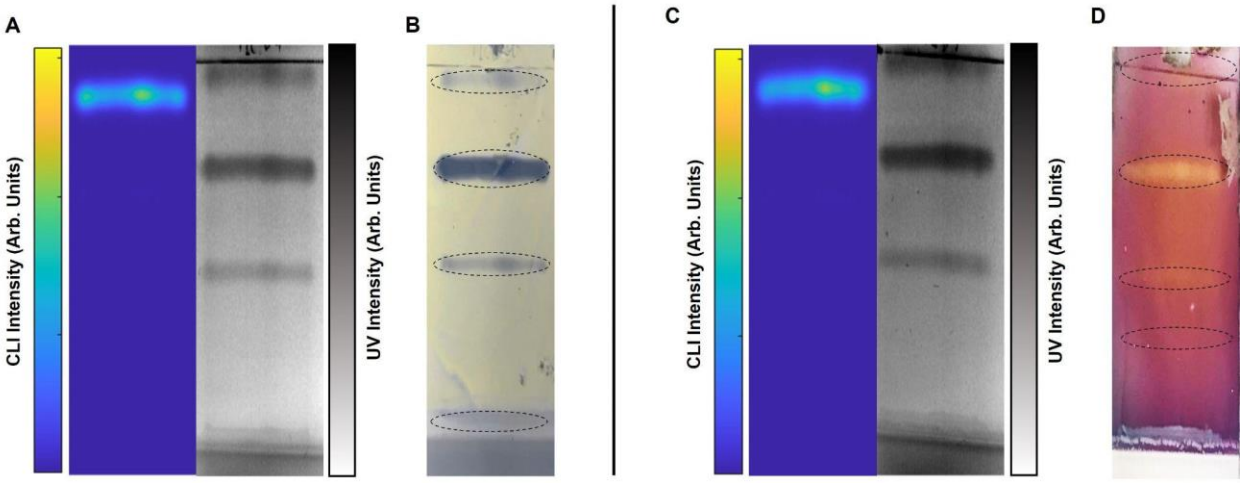

Figure 7-15. Examples of Ninhydrin staining possible with TLC readout.
(A) CLI and UV images of crude [^{18}F]Fallypride reaction separated under the PRISMA-optimized TLC conditions. (B) Hanessian stain of the same TLC plate. (C) CLI and UV images of a different crude [^{18}F]Fallypride reaction separated under the PRISMA-optimized TLC conditions. (D) Ninhydrin stain of the same TLC plate. (The pink cast across the plate may be due to incomplete drying of the TLC plate after separation, leaving residual TEA from the mobile phase.) Black dashed lines are used to denote the observable bands on the stained plate.

Chapter 8: Rapid purification and formulation of radiopharmaceuticals via thin-layer chromatography

8.1 Introduction

In the last decade, positron-emission tomography (PET) has led to many advances in disease characterization[1,2], drug development[4,249,250], and monitoring treatment efficacy for various diseases[251,252]. While numerous short-lived radionuclides may be used to label biologically active radiotracers, fluorine-18 remains by far the most common due to its high positron decay ratio (97%), short half-life (109.8 min), low positron energy (635 keV) and wide availability[10–12].

The production of 18F-labelled radiopharmaceuticals typically involves a late-stage radiofluorination method involving the reaction between [^{18}F]fluoride or a prosthetic group labelled with F-18, and a precursor, followed in some instances by the deprotection of functional groups. Subsequently, purification of the crude radiopharmaceutical is required to ensure that all unreacted precursors, reaction by-products, solvents, and other toxic reagents (e.g., phase-transfer catalysts), are removed. The high structural similarity of precursors and byproducts to radiopharmaceuticals, along with the vast precursor excess typically used in radiosyntheses to ensure efficient reaction kinetics, imposes significant challenges for the purification process.

Several chromatographic approaches are currently used to purify radiopharmaceuticals, including solid phase extraction (SPE) and high-performance liquid chromatography (HPLC). While these chromatographic methods are both versatile and compatible with a variety of stationary phases (e.g., reverse-phase C_{18}[253,254], size exclusion (SE)[255,256], and ion exchange (IEX)[257], they differ in complexity and performance. SPE is generally rapid, but separation resolution is generally regarded as low[258]. A further downside is that developing a suitable SPE-based purification protocol can take considerable time and effort. So far, SPE has only

successfully been used to purify a handful of 18F-labeled radiopharmaceuticals[55,56,259–262]. HPLC has high resolution and is used to purify the vast majority of radiotracers. Still, it is time-consuming, bulky, expensive, and often requires a downstream re-formulation process due to bio-incompatible mobile phases[263,264]. Another approach that has been used to purify radiopharmaceuticals is molecular imprinting chromatography[265]. However, this technique requires a unique stationary phase for each radiopharmaceutical and is not widely used.

Recently, our group and others have shown that microscale synthesis methods enable efficient reactions while enabling vast reduction of reagent masses[58,99,104,152,178]. Consequently, the quantity of impurities is drastically reduced, and it appears in some cases, the number of different impurities may also be reduced[138,152]. These factors may allow lower-resolution forms of purification to be employed in the purification of microscale-produced radiopharmaceuticals. For example, purification has been performed using microscale SPE for [^{18}F]FDG[55,262] and [^{18}F]FLT[56]. It has also been attempted for microfluidically-produced [^{18}F]Fallypride. Still, sufficient chemical purity was not achieved[266], suggesting that microscale and conventional SPE may have similar limitations of versatility due to the low resolution. Alternatively, our group and others have shown that conventional semi-prep HPLC columns can be replaced with analytical scale columns[60,105], enabling faster purification, higher resolution, and reduced volume of collected pure fraction (enabling faster downstream formulation). However, the continued need for a bulky and expensive instrument to perform purification undermines many of the advantages of microfluidic radiosynthesis.

To overcome these challenges, we propose using thin-layer chromatography (TLC) as a more compact, rapid, and lower-cost way to purify microfluidically-produced radiopharmaceuticals. Purification via TLC is not new and is often used in the pharmaceutical industry for the crude synthesis of candidate molecules[267]. Utilizing preparative TLC plates, crude products are separated, then the product-binding sorbent is removed from the plate and extracted in organic solutions for subsequent processing. Though separations in the pharmaceutical

industry usually involve long TLC plates and lengthy separation times, which are incompatible with the production of short-lived radiopharmaceuticals nor the goals of miniaturizing the entire radiosynthesis processes, the masses involved in batches of radiopharmaceuticals are far smaller. We hypothesized that short, analytical-scale plates might be suitable for purifying radiopharmaceuticals (**Figure 8-1**).

Radio-TLC is already widely used in radiochemistry to analyze small samples (e.g., 1 µL) of radiopharmaceuticals. By making use of high-resolution imaging-based readout (e.g., Cerenkov luminescence imaging; CLI and UV imaging), our group has recently shown that separation resolution comparable to radio-HPLC can be achieved on analytical scale TLC plates with very short separation distances (4 cm) and short separation time (<4 min)[93]. In addition to being rapid and having high resolution, TLC is very versatile. We recently adopted the PRISMA algorithm[232] for efficiently optimizing mobile phase compositions to achieve high separation of a wide variety of radiopharmaceuticals from their radioactive and non-radioactive impurities[268]. This paper shows the feasibility of using analytical-scale TLC as a compact, rapid, and high-resolution method for the purification of microfluidically-produced (i.e., low mass scale, low volume) radiopharmaceuticals.

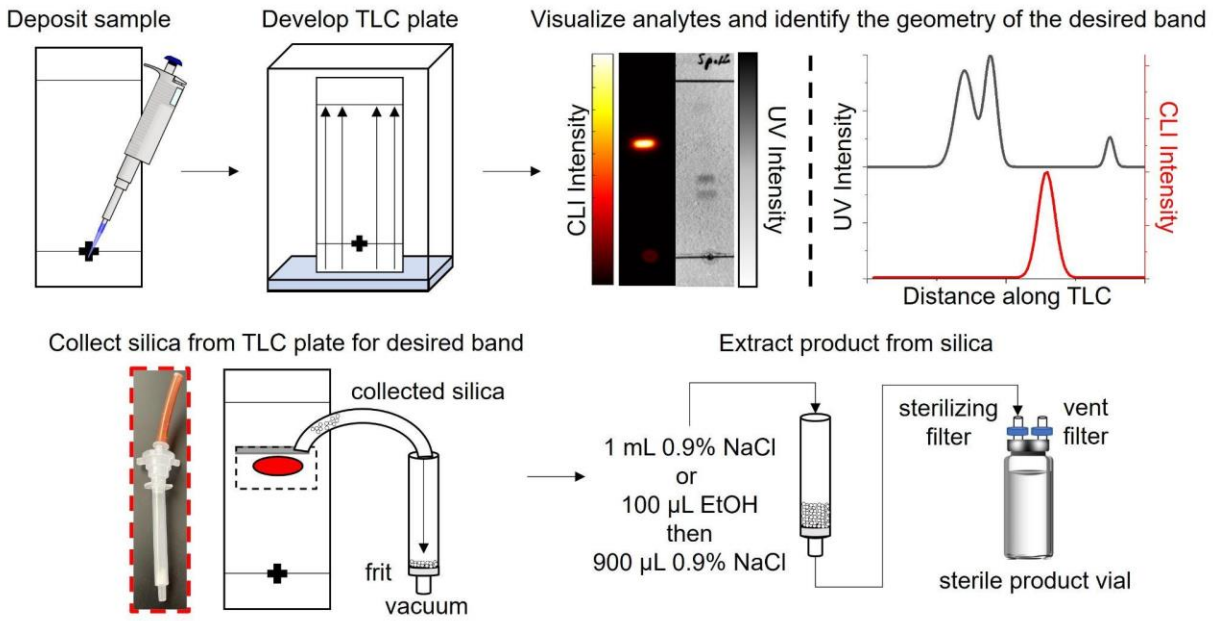

Figure 8-1. Procedure for the purification of microscale-synthesized radiopharmaceuticals using TLC.

8.2 Results

8.2.1 Performance of TLC at the scale of crude reaction mixtures

When performing TLC analysis of radiopharmaceuticals, typically, only a small sample volume (0.5 or 1.0 µL) is spotted on the plate via a capillary or pipette. In contrast, the volume of the collected crude product from microscale reactions is on the order of 40-60 µL[269], all of which need to be loaded onto the TLC plate to use this as a purification method.

We have previously used the PRISMA algorithm to establish suitable TLC mobile phases for baseline separation of [^{18}F]PBR-06 from radioactive and non-radioactive impurities in crude reaction mixtures (1 µL sample), and for [^{18}F]Fallypride from its impurities (1 µL sample)[268]. While the separation resolution is expected to suffer by increasing the sample volume and mass, the degree of resolution reduction needs to be quantified.

To study the effect of sample mass without significantly changing the size of the sample spot, we loaded samples by pipetting crude [^{18}F]PBR-06 in 1 µL increments onto the origin while heating the TLC plate with a heat gun (120 °C setting), allowing each droplet to dry (~2 s) before adding the next. For [^{18}F]PBR-06, we discovered that the chromatographic resolution of [^{18}F]PBR-

06 from its nearest impurity decreased from 2.2 to 1.0 when increasing the total volume of the spotted crude product from 6 to 60 µL. Notably, 60 µL corresponds to an entire batch of crude radiopharmaceutical. When performed manually, sample deposition with this approach took ~5 min to load a 60 µL sample.

We next tried applying the 60 µL volume in a streak rather than a single spot. Each 20 µL portion was deposited as a ~20 mm long line along the origin and then dried at 120 °C (~5 s) before applying the next streak in the same location. By spreading out the mass amount of product over a greater width of the separation medium, the chromatographic load is decreased, achieving nearly the same resolution (2.0) as the plate spotted with only 6 µL. The 60 µL sample could be deposited in <2 min by streaking.

We also tried spotting a 60 µL sample to TLC plates containing a concentration zone. A large volume can be deposited as a single spot within the concentration zone. During development, it will be concentrated into a thin line at the boundary of the concentration zone before its migration and separation within the separation zone. Using this method, the resolution was 1.7. While we expected the resolution to be similar to the streaking approach, the observed resolution may be slightly lower because the plate was an HPTLC plate, which has a thinner sorbent layer (150 µm) than the analytical plates used for other samples (250 µm).

These results are summarized in **Figure 8-2** and **Table 8-1**. Due to the high performance of the sample streaking method in conjunction with analytical TLC plates, they were used for the remainder of the study.

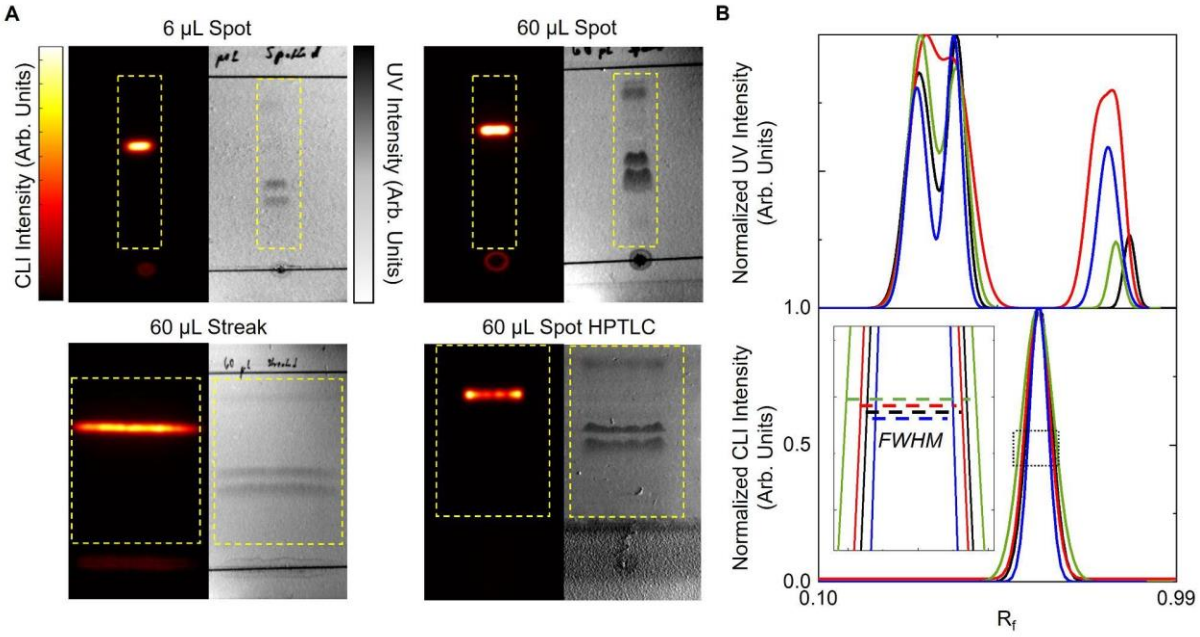

Figure 8-2. Effect of sample deposition parameters on separating [^{18}F]PBR-06 samples. (A) Images (left: CLI; right: UV) of crude [^{18}F]PBR-06 deposited on TLC plates using different volumes and application methods. Yellow lines denote the area of the image used to compute the line profiles shown in panel B, excluding the origin and solvent front lines with a strong signal in the UV images. (B) TLC chromatograms generated from the CLI and UV images. Legend: black - 6 µL spot, red - 60 µL spot, green - 60 µL streak, and blue - 60 µL spot (HPTLC plate). The inset shows a magnified view of the dashed region to highlight the full-width half maximum (FWHM).

Table 8-1. Effect of sample deposition parameters on chromatographic resolution between [^{18}F]PBR-06 and the nearest impurity.

Sample volume (µL)	Deposition method	TLC plate	Resolution
6	Spot	Analytical	2.2
60	Spot	Analytical	1.0
60	Streak	Analytical	2.0
60	Spot	HPTLC (with concentration zone)	1.7

In addition to evaluating separation resolution, losses during the sample application process were evaluated. Measurements using a calibrated ion chamber (CRC 25-PET, Capintec, Florham Park, NJ, USA) revealed ~10-20% loss of initial sample activity on the pipette tip and Eppendorf tube

originally containing the crude radiopharmaceutical. The loss could be reduced to <1% if the Eppendorf and pipette tip were rinsed with 20 µL of 9:1 MeOH:H_2O (v/v). When applied during the sample streaking method, the additional rinse volume did not effect the chromatographic resolution.

8.2.2 Efficiency of radiopharmaceutical collection from the TLC plate

After separation, the product must be collected from the plate. We elected to use a process of scraping the silica stationary phase from the plate in the region of the desired band, followed by extraction of the product into a buffer.

The effectiveness of collecting the sorbent-bound radiopharmaceutical for [^{18}F]PBR-06 and [^{18}F]Fallypride is demonstrated in **Figure 8-3**. Each TLC plate was streaked with 60 µL of crude product, developed, and then measured by a dose calibrator. A CLI image of the plate was then obtained, and the relative abundance of radiochemical species was determined using region of interest (ROI) analysis as previously described[93,101]. Combining these two measurements, we could estimate the initial quantity of radioactivity corresponding to the radiopharmaceutical product on the TLC plate. Initially, scraping of the sorbent at the position of the radiopharmaceutical band was performed via a small spatula. The sorbent (a fine powder) was collected onto weighing paper and then transferred into an SPE tube. However, using this method, >20% of the radiopharmaceutical activity (and sorbent) could be lost. Instead, we used a piece of plastic tubing with a beveled tip as the scraper. We connected the other end of the tubing through an empty SPE tube fitted with a 0.2 µm frit (Figure 8-1) to a vacuum source to capture the removed sorbent more efficiently. The entirety of the scraping process took <2 min to complete. Comparison of the collected sorbent activity of the product from the TLC plate (measured via dose calibrator) to the estimate of initial radioactivity of the radiopharmaceutical on the plate indicated that the sorbent-bound product was collected with >97% efficiency for both [^{18}F]PBR-06 and [^{18}F]Fallypride (**Table 8-2**, rows 1 and 3). Additional CLI images of the TLC plates were obtained after the scraping process. ROI analysis showed that the region of the plate corresponding to the

product contained ~0% of the initial radioactivity (**Figure 8-3**), confirming that the silica removal process is quantitative.

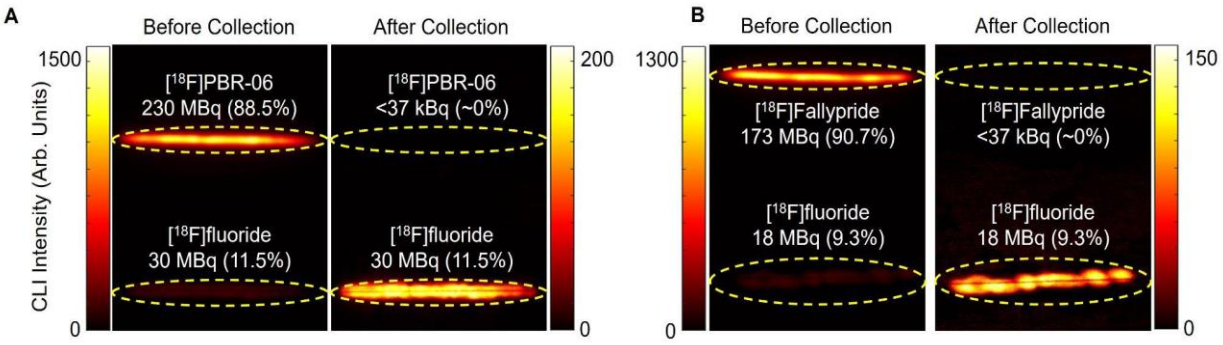

Figure 8-3. CLI images of TLC plates show the effectiveness of the stationary-phase removal step during TLC-based purification.
(A) Images of analytical TLC plate streaked with crude [^{18}F]PBR-06 before and after collection. (B) Images of analytical TLC plate streaked with crude [^{18}F]Fallypride before and after collection. Yellow bands denote ROIs used in quantifying the proportion of different radiochemical species.

Table 8-2. Performance of microscale droplet radiosyntheses coupled with the TLC-based purification and formulation. In the extraction step, Method 1 uses 1.0 mL of saline alone, and Method 2 uses 100 µL EtOH, followed by 900 µL saline. The overall collection and extraction efficiency is calculated by multiplying the silica collection efficiency by the extraction efficiency for individual runs and then averaging across replicates. The overall RCY is calculated by multiplying the crude RCY of the droplet synthesis by the silica collection efficiency and the extraction efficiency for individual runs and then averaging across replicates.

Radiotracer	Activity level (MBq)	Crude RCY of droplet synthesis (%) (n = 8)	Silica collection efficiency (%) (n = 8)	Extraction efficiency (%)		Overall collection and extraction efficiency (%)		Overall RCY (%)	
				Method 1 (n = 4)	Method 2 (n = 4)	Method 1 (n = 4)	Method 2 (n = 4)	Method 1 (n = 4)	Method 2 (n = 4)
[^{18}F]PBR-06	11	94.4 ± 1.2	98.7 ± 1.3	96.4 ± 3.4	97.9 ± 1.6	95.4 ± 4.6	96.3 ± 1.7	89.6 ± 3.9	91.3 ± 1.9
	1110-1480	91.9 ± 1.8	98.1 ± 1.1	95.6 ± 2.9	98.2 ± 0.3	94.2 ± 2.6	95.9 ± 0.9	86.7 ± 3.7	87.9 ± 1.8
[^{18}F]Fallypride	7.5	96.5 ± 1.6	97.5 ± 1.6	95.4 ± 1.1	98.4 ± 0.3	92.6 ± 2.6	96.2 ± 1.3	89.4 ± 3.7	92.9 ± 2.6
	740-1480	93.2 ± 2.5	97.5 ± 1.2	97.1 ± 1.0	97.8 ± 1.4	94.5 ± 1.9	95.6 ± 2.8	88.1 ± 3.8	89.2 ± 4.7

8.2.3 Efficiency of radiopharmaceutical collection from the TLC plate

Finally, the purified radiopharmaceutical needs to be separated from the sorbent. This is accomplished by flowing liquid through the sorbent and capturing the eluted liquid while the particles remain trapped by the frit. For this step, the output of the SPE tube (containing the sorbent-bound product) is connected through a sterilizing filter (0.2 μm) to a sterile septum-capped product vial. Vacuum is applied to a sterile filter connected to the vent port of the product vial. The end of the tubing used for scraping the sorbent is then dipped into an Eppendorf tube filled with extractant solution, effectively rinsing the sorbent collection path and eluting the radiopharmaceutical from the collected sorbent.

To avoid needing a later downstream reformulation step, we evaluated the ability to extract the product from the sorbent into biocompatible solutions. Using 100 μL of EtOH, followed by 900 μL of saline, it was possible to extract >97% of the product from the sorbent for both tracers ([^{18}F]PBR-06 and [^{18}F]Fallypride) (**Table 8-2**, rows 1 and 3). Flowing the additional 900 μL of saline through the sorbent provided a final formulated product with <10% EtOH (v/v). We also tried extracting with saline. Using 1 mL of saline, the extraction efficiency was >95% for both [^{18}F]PBR-06 and [^{18}F]Fallypride (**Table 8-2**, rows 1 and 3).

We achieved very high overall radiochemical yield (RCY) for both radiopharmaceuticals with the combination of droplet radiosynthesis and TLC-based purification/formulation (**Table 8-2**). Compared to our prior reports of droplet radiosyntheses that used analytical-scale HPLC purification (with purification efficiency of ~80%), the efficiency of the TLC purification and formulation process was significantly higher (nearly quantitative), leading to higher overall radiochemical yield. In particular, a prior report of droplet-based [^{18}F]PBR-06 production showed high crude RCY (94 ± 2%, n = 4), but due to losses during HPLC purification, the isolated RCY was only 76% (n = 1)[178], and further losses would have been expected during downstream formulation which was not performed in that study. Similarly, a prior report of droplet-based

[^{18}F]Fallypride production exhibited high crude RCY (96 ± 2%, n = 4), but due to losses during HPLC purification, the isolated yield was 78% (n=1)[58].

Notably, the entire purification and formulation process with the TLC method was very fast and took <10 min to complete (2 min for sample spotting, >4 min for TLC plate development, 2 min for silica removal, and 2 for radiopharmaceutical extraction and filtration).

8.2.4 Scale-up to clinical quantities

The ability of the TLC method to purify radiopharmaceuticals at clinically relevant levels were explored. For droplet-based radiosynthesis, scale-up is achieved by simply increasing the amount of radioactivity in the synthesis and does not require increasing the reaction mass scale[60]. For this reason, the chromatographic resolution of the TLC method should not be impaired when utilizing greater activity scales. Indeed, scaling up the amount of radioactivity led to the efficient purification of clinically relevant activity levels of [^{18}F]PBR-06 and [^{18}F]Fallypride (**Table 8-2**, lines 2 and 4). Automating the TLC purification procedure may allow more activity scales to be purified.

8.2.5 Quality control testing of purified [^{18}F]PBR-06

A series of selected key quality control (QC) tests were performed to assess the safety and purity of the radiopharmaceuticals purified (and formulated) using the TLC method. Tests performed include appearance (color, clarity), pH, residual phase transfer catalyst, residual solvents, radiochemical purity, chemical purity, and radiochemical identity.

Radiochemical and chemical analyses were performed using HPLC (**Figure 8-4**). When we initially analyzed TLC-purified [^{18}F]Fallypride (**Figure 8-5**), we noticed some impurities at early retention times in the UV channel and confirmed that these peaks come from the TLC plate itself. By pre-cleaning the TLC plates, these impurity peaks could be removed (**Figure 8-7**, **Figure 8-8**). When using pre-cleaned TLC plates, radiochemical and chemical purity standards suitable for injection were achievable.

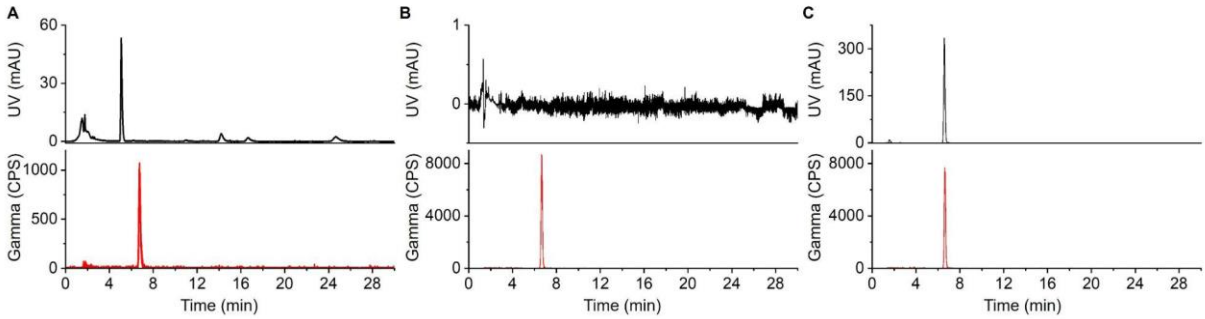

Figure 8-4. HPLC chromatograms of [^{18}F]PBR-06.
(A) Crude reaction mixture. (B) TLC-purified (and formulated) product. (C) Co-injection of TLC-purified product with the [^{19}F]PBR-06 reference standard.

The results of these and additional tests (**Appendix 8.6.1**) for three consecutive batches of TLC purified [^{18}F]PBR-06 are summarized in **Table 8-3**. The results suggest that this method could potentially be used to produce tracers for clinical use.

Due to the silica sorbent's integral role in the TLC-purification process, we were concerned that some silica could end up in the final formulation, either as small nanoparticles that pass through the frit and filter or through solubility of silica in aqueous solutions[270]. To determine levels of residual silica, we used ICP-MS to measure Si content of samples that were first digested in HNO_3 to ensure any particulate silica was captured into the solution (**Appendix 8.4.9**). Si was not detected for the formulated tracer samples (limit of detection 0.83 ng/mL). While the complete elimination of silica in the final radiopharmaceutical formulation cannot be confirmed, it can be concluded that the residual amount is extremely low.

Table 8-3. Performance and quality control testing results for three consecutive batches of [^{18}F]PBR-06.

Test	Criteria	Batch 1	Batch 2	Batch 3
Radioactivity	-	821 MBq [22.2 mCi]	744 MBq [20.1 mCi]	829 MBq [22.4 mCi]
Molar Activity	-	342 GBq/μmol	315 GBq/μmol	327 GBq/μmol
Appearance	Clear, colorless, and particulate-free	✓	✓	✓
Radiochemical Identity	Retention time ratio of radio peak vs. reference standard (0.90-1.10)	1.01	1.01	1.01
Residual $TBAHCO_3$	<104 mg/L	< 45 mg/L	< 45 mg/L	< 45 mg/L
Residual Solvents	MeCN < 410 ppm MeOH < 3000 ppm Hexanes < 290 ppm $CHCl_3$ < 60 ppm Et_2O < 5000 ppm EtOAc < 5000 ppm AcOH < 5000 ppm Thexyl alcohol < 5000 ppm	< 1 24 6 < 1 104 21 7 < 1	< 1 21 2 < 1 47 10 5 < 1	< 1 24 5 < 1 102 20 7 < 1
Radiochemical Purity	>95%	>99%	>99%	>99%
Radionuclide Identity (half-life)	105-115 min	110.4	111.7	113.8
pH	4.5-7.5	5.5	5.5	5.5
Shelf-life	Pass appearance, pH, and radiochemical purity after 120 min	✓	✓	✓

8.3 Discussion

A significant advantage of the TLC-based purification approach described is its high-speed operation. In addition to the rapid separation via TLC, for the radiopharmaceuticals tested, the

purified tracer could be recovered in saline (or a mixture with <10% EtOH), eliminating the need for a downstream reformulation step. Current microscale radio-pharmaceutical production protocols generally rely on HPLC purification followed by a separation formulation step performed via solid-phase extraction on a reversed-phase cartridge or via solvent evaporation followed by resuspension in an injectable buffer, requiring 30-60 min to complete[139,228,271]. In contrast, for the TLC purification (and formulation) method, these steps were completed in <10 min for both [^{18}F]PBR-06 and [^{18}F]Fallypride. Based on the half-life of fluoride-18, an additional 20-50 min of overall synthesis time would lead to a 12-27% loss of product. Furthermore, during HPLC and cartridge- or evaporation-based reformulation, activity losses are typically substantially higher than the 3-5% loss observed here.

We found the product band retention factors and band heights to be remarkably consistent from run to run for both the [^{18}F]PBR-06 and [^{18}F]Fallypride product bands (i.e., (R_f = 0.66 ± 0.01, band height = 0.22 ± 0.05 cm, n = 7), (R_f = 0.91 ± 0.01, band height = 0.31 ± 0.05 cm, n = 4), respectively). This allowed us to mark the TLC plate in advance with the expected position of the product band, allowing the sorbent collection without imaging the TLC plate. Batches processed in this fashion had high efficiency (low loss of product) and high chemical and radiochemical purity, equivalent to batches that relied on imaging. This observation suggests that for well-developed methods, the TLC plate imaging step can potentially be skipped, simplifying the apparatus and procedure. To use this technique reliably requires adequate separation of the desired radiopharmaceutical band from impurity bands (both radioactive and non-radioactive impurities). The mobile phases used for the separation of [^{18}F]PBR-06 and [^{18}F]Fallypride from impurities were optimized using a recently-reported methodology (PRISMA) to maximize the resolution between the radiopharmaceutical and nearest impurity[272]. This optimization algorithm provides a systematic and resource-efficient way to discover suitable mobile phases for radiopharmaceuticals and appears to have high versatility for a broad range of radiopharmaceuticals[272], suggesting that it will be possible to develop high-resolution TLC-based

methods to purify other radiotracers. Despite the presence of various organic solvents in the TLC mobile phases, GC-MS analysis revealed the amounts to be minimal and far below per-mitted amounts (**Table 8-3**). The low values are likely due to (i) the low initial volume of mobile phase "contained" within the silica in the region of the product band, (ii) the ap-plication of heat (90 °C for 30 s) to dry the TLC plate after separation, and (iii) the use of vacuum during the sorbent collection step that may further assist in the removal of any residual solvents.

An additional requirement for more widespread use would be to increase the degree of automation to simplify the process and reduce radiation exposure, especially for producing clinical scale or multi-patient batches. Simplifications could be made in the process to reduce exposure, e.g., connecting the SPE tube to the sterilizing filter at the start of the experiment and pulling vacuum through the sterile vent filter both for collecting the scraped silica into the SPE tube, as well pulling the extraction buffer through the silica. Further automation of each of the processes (sample deposition, TLC separation, and ex-traction of product) are also needed. While commercially-available systems exist for automated sample deposition in spots, lines, or other patterns (e.g., CAMAG automatic TLC sampler 4[273]), transfer of the crude radiopharmaceutical to the device, operation time, and system footprint are concerns for use in radiochemistry applications. A more practical approach may be to simply use TLC plates with concentrating zones, which would al-low the sample to be dripped at a controlled flow rate onto a single location onto a heated TLC plate rather than the more complicated process of depositing the sample in a streak pattern. The resolution obtained for [^{18}F]PBR-06 samples spotted onto concentrating-zone HPTLC plates was nearly as good as for samples streaked onto normal analytical plates and could perhaps be further optimized by comparing different types of concentrating-zone plates. Concentrating zone plates are also likely to reduce the potential dispersion effects if the streak pattern is not perfectly straight. The need for manual handling in the development process can likely be eliminated by integrating the above sample deposition approaches with commercial or custom horizontal TLC setups[274–277]. Commercially available online extraction systems also exist

for the collection of identified product bands directly from TLC plates without the need for scraping (e.g., CAMAG TLC-MS Interface 2[278], Advion Plate Express[279]), using methods such as liquid extraction. However, the manual steps for installation and alignment of TLC plates, system size, and limitations on the band geometry (that will prevent complete collection of the product species) may not be well-matched to preparative applications in the radiopharmaceutical field. A more practical approach to automation may to develop a custom apparatus with adjustable or movable flow cell placed across the product band to extract the species of interest[280,281].

Another strategy for automation may be to leverage the PRISMA procedure to develop mobile phase systems that could provide high separation resolution using other chromatography methods (e.g. silica flash chromatography), which may be easier to automate, or perhaps miniaturize using microfluidic-based systems with integrated purification media[262,282]. However, it is not clear if the resolution achieved in the column format would match that achieved in the planar TLC format, or whether a similar fast operation speed and high recovery efficiencies would be observed. Furthermore, the use of highly-UV-absorbing organic solvents could limit the ability to monitor non-radioactive impurities and obtain a pure product, and the collected radiopharmaceutical would require extensive reformulation to remove relatively large amounts of solvents, making the process more time-consuming and complicated compared to the TLC-based approach.

8.4 Materials and Methods

8.4.1 Reagents and Materials

All reagents and solvents were obtained from commercial suppliers and used without further purification. 2,3-dimethyl-2-butanol (thexyl alcohol; anhydrous, 98%), acetic acid (AcOH; glacial, >99.9%), acetone (suitable for HPLC, >99.9%), acetonitrile (MeCN, anhydrous, 99.8%), ammonium formate (NH_4HCO_2, 97%), chloroform (>99.5%, contains 100-200 ppm amylenes as a stabilizer), dichloromethane (DCM; anhydrous, >99.8% contains 40-150 ppm amylene as a

stabilizer), diethyl ether (Et_2O; >99.9% inhibitor free), ethyl acetate (EtOAc; anhydrous, 99.8%), ethyl alcohol (EtOH; 200 proof, anhydrous, >99.5%), methyl alcohol (MeOH; anhydrous, 99.8%), n-hexanes (98%), Polypropylene SPE tube with PE frits (1 mL, 20 µm porosity), Silica with concentration zone (Silica 60 with diatomaceous earth zone) HPTLC plates, tetrahydrofuran (THF; anhydrous, >99.9% inhibitor free), water (H_2O; suitable for ion chromatography) and Whatman Anotop 10 syringe filters (sterile, 0.2 um) were purchased from Sigma-Aldrich (St. Louis, MO, USA). (S)-2,3-dimethoxy-5-[3-[[(4-methylphenyl)-sulfonyl]oxy]-propyl]-N-[[1-(2-propenyl)-2-pyrrolidinyl]methyl]-benzamide ([^{18}F]Fallypride precursor, >95%), 5-(3-fluoropropyl)-2,3-dimethoxy-N-(((2S)-1-(2-propenyl)-2-pyrrolidinyl)methyl)benzamide (Fallypride reference standard, >95%), 2-((2,5-dimethoxybenzyl)(2-phenoxyphenyl)amino)-2-oxoethyl 4-methylbenzenesulfonate ([18F]PBR-06 precursor, >95%), 2-fluoro-N-(2-methoxy-5-methoxybenzyl)-N-(2-phenoxyphenyl)acetamide (PBR-06 reference standard, >95%), and tetrabutylammonium bicarbonate ($TBAHCO_3$; 75 mM in ethanol), were purchased from ABX Advanced Biochemical Compounds (Radeberg, Germany).

Silica gel 60 F_{254} sheets (aluminum backing, 5 cm x 20 cm) were purchased from Merck KGaA (Darmstadt, Germany). Glass microscope slides (76.2 mm x 50.8 mm, 1 mm thick) were obtained from C&A Scientific (Manassas, VA, USA). Saline (0.9% sodium chloride injection, USP) was obtained from Hospira Inc. (Lake Forest, IL, USA). Sodium phosphate dibasic (Na_2HPO_4-$7H_2O$) and sodium phosphate monobasic (NaH_2PO_4-H_2O) were purchased from Fisher Scientific (Thermo Fisher Scientific, Waltham, MA, USA).

No-carrier-added [^{18}F]fluoride was produced by the (p, n) reaction of [^{18}O]H_2O (98% isotopic purity, Huayi Isotopes Co., Changshu, Jiangsu, China) in an RDS-111 cyclotron (Siemens, Knoxville, TN, USA) at 11 MeV, using a 1.2-mL silver target with havar foil.

8.4.2 Preparation of radiopharmaceuticals and reference standards

[^{18}F]PBR-06 and [^{18}F]Fallypride were prepared using droplet radiochemistry methods on Teflon-coated silicon surface tension trap chips[58]. Detailed protocols for preparing these

radiotracers have been previously reported[178]. Stock solutions of reference standards were prepared at 20 mM concentrations: 5 mg of Fallypride was added to 685 µL of MeOH, and 5 mg of PBR-06 was added to 632 µL of MeOH.

8.4.3 Preparation of TLC plates

TLC plates were cut (W x H, 3 x 6 cm), then marked with horizontal pencil lines at 1 cm (origin line) and 5 cm (development line) from the bottom edge.

To eliminate impurities in the TLC plate that can contaminate the radiopharmaceutical, plates were pre-cleaned with solvent as previously described[283]. Briefly, TLC plates were submerged to the origin line in a mixture of 2:1 EtOAc: MeOH (v/v), allowed to develop for 20 min, and then heated for 1 min (at a 120 °C setting) using a heat gun (Furno 500, Wagner).

8.4.4 Sample spotting and separation

60 µL of the relevant crude radiopharmaceutical sample was applied to the plate by various methods (e.g., sequential spotting or streaking) by a micro-pipette. Spotting on analytical scale TLC plates was performed by adding 1 µL of the sample and heating with a heat gun at 120 °C (~2 s). Spotting of samples on HPTLC plates occurred with the addition of 10 µL of sample to the concentration zone, followed by drying at 120 °C (~5 s). Streaking of samples on analytical scale TLC plates were performed by deposition of 20 µL of sample in a thin streak covering ~30 mm, followed by heating at 120 °C (~5 s).

Plates were then developed in the mobile phase up to the development line. The mobile phases for [^{18}F]PBR-06 and [^{18}F]Fallypride were 29.8:26.9:20.4:22.85:0.05 (v/v) Et_2O:DCM:$CHCl_3$:n-hexanes:AcOH and 31.3:24.5:34.3:10.0 (v/v) THF:acetone:n-hexanes:TEA, respectively. After development, the plates were dried by a heat gun for 30 s at 90 °C.

8.4.5 Readout and analysis of TLC plates

The developed TLC plate was covered with a glass plate and visualized as previously reported[93] to obtain a Cerenkov luminescence image (CLI) (1 min exposure), followed by a UV image (7 ms exposure).

Images were analyzed to determine chromatographic resolution using a custom MATLAB program (Mathworks, Natick, MA, USA) with a graphical user interface (GUI) was used as previously described[268]. Briefly, the user is guided by the program to create chromatograms from the CLI and UV images, from which peak positions, widths, and resolution are calculated[268]. In the analysis, the lines drawn (for origin and solvent front) are omitted from the selected lanes since the pencil markings show up as false peaks in the UV chromatogram. The TLC chromatograms were plotted by exporting the data from the Matlab program and processing using OriginPro (OriginLab, Northampton, MA, USA).

8.4.6 Readout and analysis of TLC plates

8.4.6.1 Collection of sorbent from TLC

When performing purification, the CLI and UV images of the TLC plate were used to identify the location of the product band and nearest impurity bands. During the preparation of the TLC plate, a pencil was used to outline the expected position and size of the radiopharmaceutical band (as determined from averaging images of multiple separations from crude batches of the same radiopharmaceutical and identifying the midpoint between the radiopharmaceutical band and its nearest impurities). To scrape the sorbent from the plate, the opening of a piece of plastic tubing cut at a ~45° angle (polyurethane, 1/4“ ID, IDEX) was used. The tubing was connected to the inlet of an empty SPE tube (polypropylene, 1 mL, SigmaAldrich) that was fitted at the output end with a 10 µm frit (polyethylene, SigmaAldrich), and the output end was further connected to vacuum. While the desired region was scraped in a series of horizontal lines (raster motion), the sorbent was collected into the SPE tube. The visualization step could be omitted through the pre-calibration step of determining the margins of radiopharmaceutical collection.

8.4.6.2 Extraction of the radiopharmaceutical from sorbent

Before extraction, the sterile product vial was fitted with 2 sterile filters (Anotop, 0.2 µm), one prewetted with saline and then connected to the output of the SPE tube and one left dry (vent). The radiopharmaceutical was then eluted from the collected sorbent with biocompatible

solvents (1 mL saline, or 100 µL EtOH followed by 900 µL saline) by applying vacuum to the vent filter of the product vial and by moving the tubing 'scraper' into an Eppendorf tube filled with the desired extraction solvent. No separate re-formulation of the collected purified product was required.

8.4.7 HPLC analyses

Radio-HPLC was used to analyze crude radiopharmaceuticals and to perform tests for radiochemical and chemical purity and radiochemical identity of TLC-purified batches of radiopharmaceuticals. The radio-HPLC system setup comprised a Smartline HPLC system (Knauer, Berlin, Germany) equipped with a degasser (Model 5050), pump (Model 1000), UV detector (254 nm; Eckert & Ziegler, Berlin, Germany), gamma-radiation detector (BFC-4100, Bioscan, Inc., Poway, CA, USA), and counter (BFC-1000; Bioscan, Inc., Poway, CA, USA). A C18 Gemini column was used for separations (Kinetex, 250 × 4.6 mm, 5 µm, Phenomenex, Torrance, CA, USA). [^{18}F]PBR-06 samples were separated with a mobile phase of 60:40 (v/v) MeCN:20 mM sodium phosphate buffer (pH = 5.8) at a flow rate of 1.5 mL/min resulting in a retention time for [^{18}F]PBR-06 of 6.5 min. [^{18}F]Fallypride samples were separated with a mobile phase of 60% MeCN in 25 mM HN_4HCO_2 with 1% TEA (v/v) at a flow rate of 1.5 mL/min resulting in a retention time for [^{18}F]Fallypride of 5.8 min.

8.4.8 Quality control testing

Quality control (QC) tests were performed on 3 consecutive batches of [^{18}F]PBR-06 produced via a droplet microreactor and purified with the TLC approach described here. Testing focused primarily on color and clarity, radiochemical and chemical purity, molar activity, and residual solvent content to highlight the performance of this novel purification method. A full summary of tests and results can be found in **Appendix 8.6.1**.

8.4.9 ICP-MS analysis for silicon content

To estimate silica content in the final formulation, the amount of silicon was determined via inductively-coupled plasma mass spectrometry (ICP-MS) using a NexION 2000 (Perkin

Elmer). For each sample, an area (2.0 x 1.5 cm, WxH) was scraped from a cleaned TLC plate into an SPE tube, and 1 mL of saline was flowed through the silica and a sterile filter and collected into an Eppendorf tube for analysis. Each sample was transferred to a clean Teflon vessel for acid digestion in concentrated HNO_3 (65-70%, Trace Metal Grade, Fisher Scientific) with a supplement of H_2O_2 (30%, Certified ACS, Fisher Scientific) at 200 °C for 50 min in a microwave digestion system (Titan MPS, Perkin Elmer). Once the sample was cooled to room temperature, it was subsequently diluted to make a final volume of 10 mL by adding filtered DI H_2O for analysis. The calibration curve was established using a standard solution while the dwell time was 50 ms with thirty sweeps and three replicates with background correction. The detection limit using this procedure was 0.82 ng/mL.

8.5 Conclusions

In this feasibility study, high-resolution radio-TLC was leveraged as a means to per-form rapid purification of two clinically-relevant radiopharmaceuticals ([^{18}F]PBR-06 and [^{18}F]Fallypride) produced via droplet radiochemistry methods. Due to the high chemical and radiochemical purity and the high efficiency of product collection and formulation achieved, it is conceivable that the TLC purification method could serve as a versatile approach for the purification of microscale-produced radiopharmaceuticals. The combination of droplet radiosynthesis with TLC-based purification/formulation for the production of [^{18}F]PBR-06 led to high molar activities (≧ 300 GBq/μmol), comparing favorably to literature reports (37-222 GBq/μmol[154,284]).

Even with the higher mass loading and volume of the crude radiopharmaceutical (60 μL) compared to typical samples (0.5-1 μL), high separation resolution of the radiopharmaceutical product from radioactive and non-radioactivity impurities was achieved on the TLC plates, as visualized via CLI and UV imaging. The product collection (via sorbent collection from the plate followed by extraction) was nearly quantitative. Notably, by using injectable buffers (saline or EtOH diluted to <10% v/v in saline), the need for subsequent re-formulation is eliminated.

Consequently, radio-TLC purification (and formulation) could be completed in under 10 min. Furthermore, due to the low cost of TLC plates, one can consider the purification and formulation system to be disposable (in stark contrast to HPLC-based systems), further simplifying microscale radiosynthesis instruments, and eliminating the need for developing and validating cleaning protocols

As a proof-of-concept, several batches of [^{18}F]PBR-06 and [^{18}F]Fallypride were produced and purified at scales sufficient for clinical imaging. Critical QC tests were per-formed on multiple batches (e.g., color and clarity, chemical and radiochemical purity, molar activity, and residual solvents) and suggested the potential suitability for clinical production of the TLC purification method.

8.6 Appendix

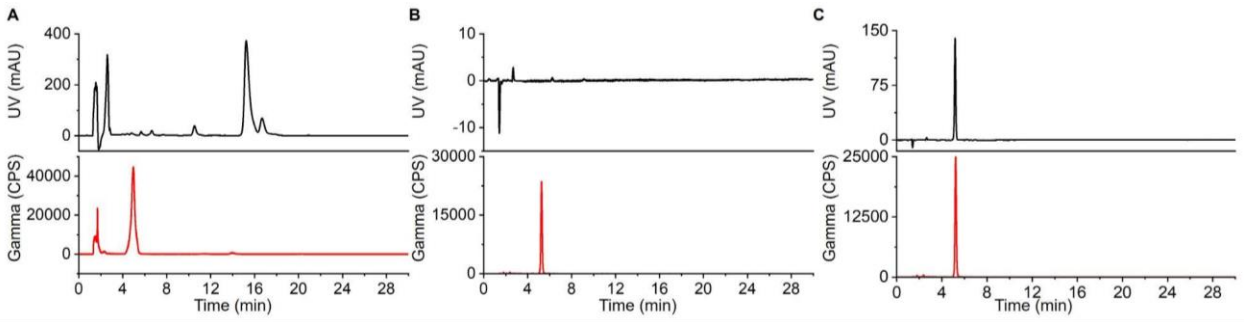

Figure 8-5. HPLC chromatograms of [^{18}F]Fallypride samples.
(A) Crude reaction product. (B) TLC-purified product. (C) Co-injection of TLC-purified product with Fallypride reference standard.

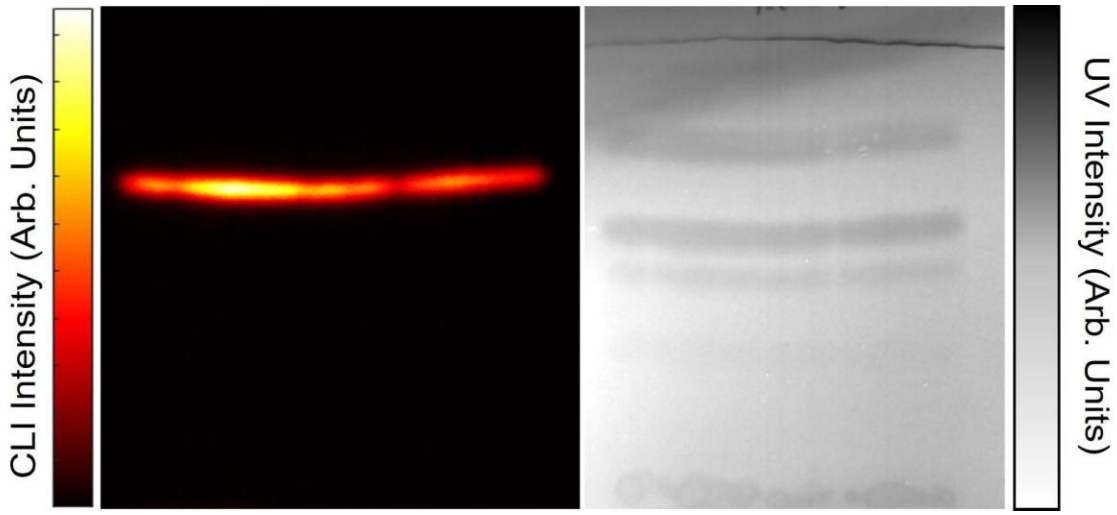

Figure 8-6. Visualization of crude [^{18}F]Fallypride streaking.
Images (Left: CLI; Right: UV) of crude [^{18}F]Fallypride deposited on TLC plates using the streaking deposition method.

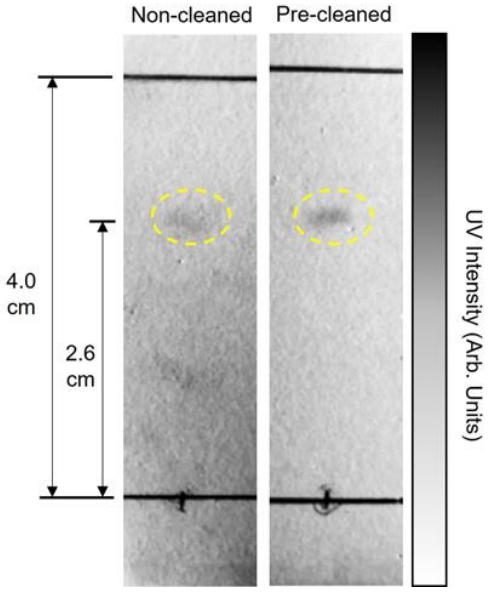

Figure 8-7. The difference between uncleaned and cleaned TLC plates.
UV images of non-cleaned and pre-cleaned TLC plates after spotting with the PBR-06 reference standard and developing in the mobile phase for [^{18}F]PBR-06. Yellow dashed circles denote the PBR-06 band. The non-cleaned plate appears to have additional regions with significant UV signals.

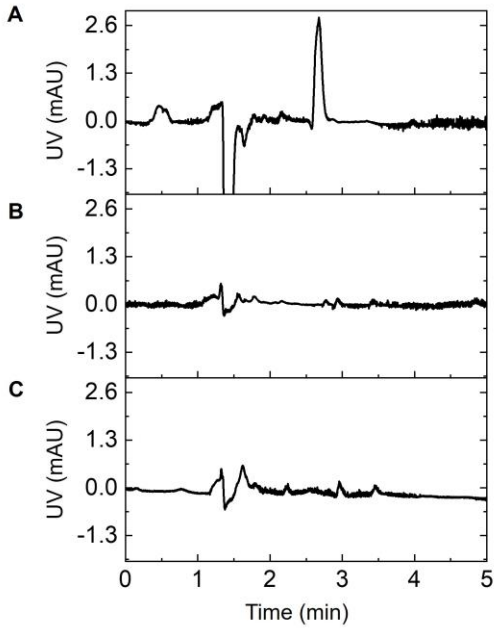

Figure 8-8. HPLC analysis (using the mobile phase for PBR-06) of mock samples obtained by silica collection and subsequent product extraction with saline from a variety of samples.
(A) non-cleaned and (B) pre-cleaned TLC plates. (C) Blank injection with fresh saline.

8.6.1 Quality control testing methods

Quality control tests for final appearance (color and clarity), radionuclide purity and identity, bacterial endotoxins, filter integrity (via bubble point test), sterility, radiochemical and chemical purity were determined as previously described[139]. The remaining QC tests were performed as described below.

8.6.1.1 Molar Activity

Molar activity was estimated by quantifying the area under the curve (AUC) of the product peak in the HPLC chromatogram (UV signal) of the purified radiopharmaceutical. AUC was converted to a molar amount using a calibration curve generated using the reference standard (Figures S5 and S6). Finally, the molar activity was computed by dividing the collected radioactivity of the product peak by the molar amount determined from the UV peak.

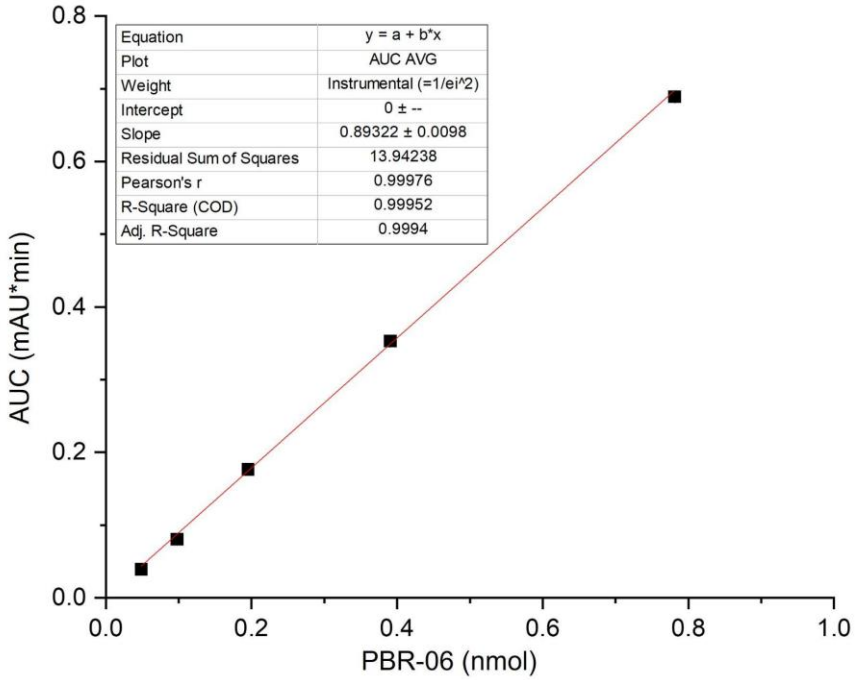

Figure 8-9. Calibration curve for PBR-06 (n = 3 for each data point).

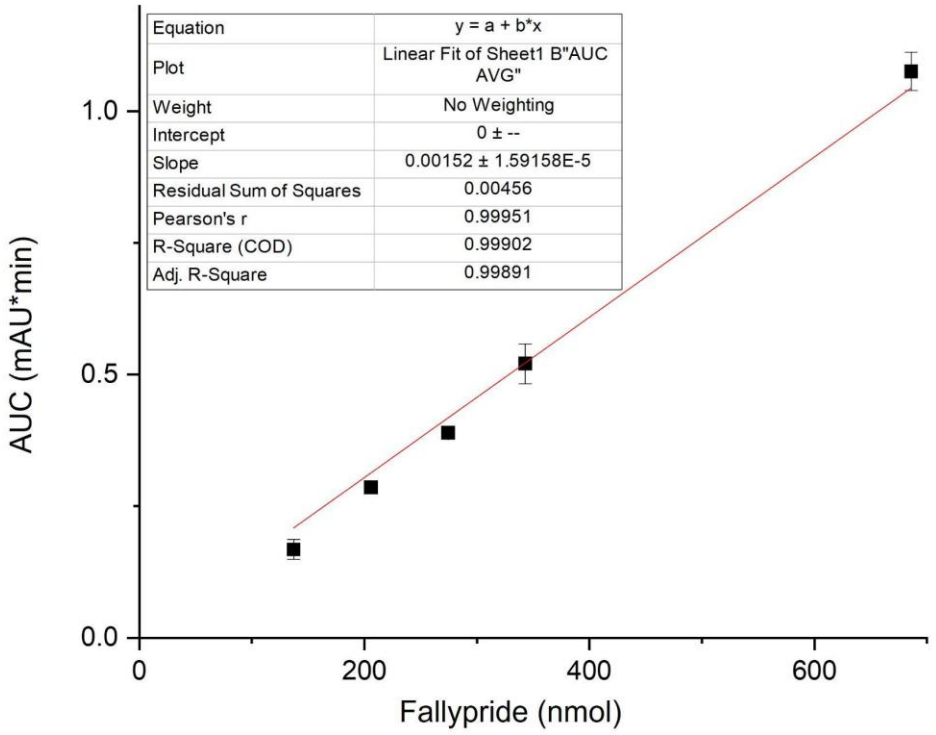

Figure 8-10. Calibration curve for Fallypride (n = 5 for each data point).

8.6.1.2 Residual $TBAHCO_3$

Residual $TBAHCO_3$ has an acceptable limit of 104 mg/L for a 1 mL formulation volume. Two assays were performed to compare the level of $TBAHCO_3$ in formulated radiopharmaceutical samples to a reference of 45 mg/L $TBAHCO_3$.

Using the method described by Kuntzsch et al.[285], 2 µL of $TBAHCO_3$ reference was spotted against formulated [^{18}F]PBR-06 and [^{18}F]Fallypride (2 µL) onto TLC plates. After drying under ambient conditions, 5 µL of 0.72 M NH_4OH (9:1 MeOH:H_2O (v/v)) was spotted on top of each sample. Dried samples were immersed in a sealed container to be subjected to staining with I_2 for a total of 2 min. Example images of these tests are shown for each radiopharmaceutical in **Figure 8-11**.

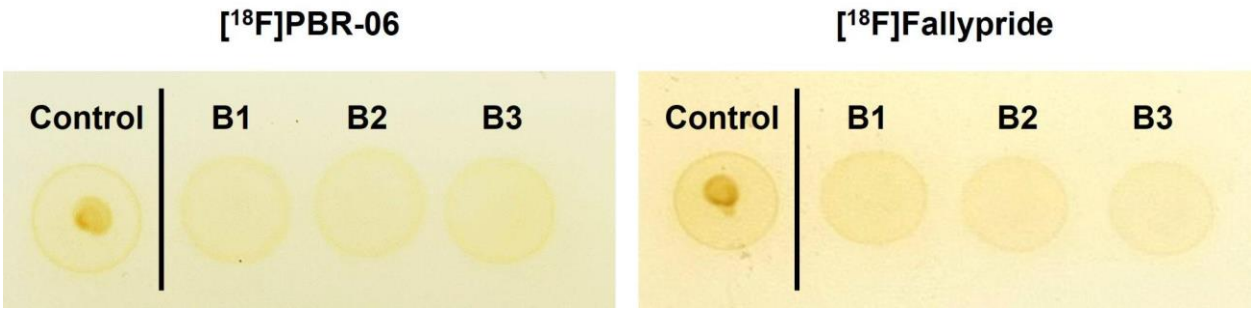

Figure 8-11. Images of iodine-stained plates to test for residual $TBAHCO_3$.
(Left) Reference (45 mg/L) compared with three batches (B1, B2, B3) of formulated [^{18}F]PBR-06. (Right) Reference compared with three batches of formulated [^{18}F]Fallypride.

Another test was performed using a recent method reported method using Dragendorf's reagent[76]. Similar to the method above, $TBAHCO_3$ reference and radiopharmaceutical samples (2 µL) were spotted on TLC plates. Plates were dried, directly dipped into the stain, and removed immediately. Heating with a heat gun (setting 170 °C) revealed $TBAHCO_3$ as a violet color, as shown in the example images in **Figure 8-12**.

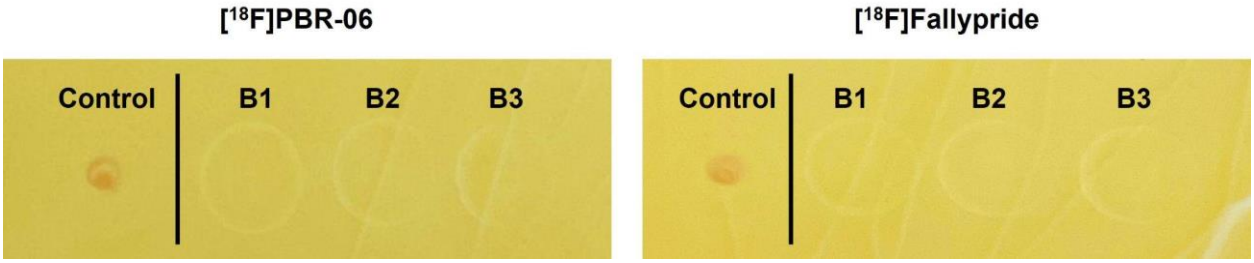

Figure 8-12. Images of Dragendorf-stained plates to test for residual $TBAHCO_3$.
(Left) Reference $TBAHCO_3$ (45 mL/L) compared with three batches (B1, B2, B3) of [^{18}F]PBR-06. (Right) Reference $TBAHCO_3$ compared with three batches of [^{18}F]Fallypride.

8.6.1.3 Residual solvent analysis

The concentration of residual solvents (MeCN, MeOH, Hexanes, $CHCl_3$, Et_2O, EtOAc, AcOH, and thexyl alcohol) was determined using gas chromatography with mass spectrometry detection (GC-MS).

GC-MS measurements were carried out using an Agilent 6890N GC, 5975 MSD, and 7683B autosampler. The instrument was controlled by Enhanced Chemstation software version E.01. The GC inlet was operated in split mode at 250 °C. UHP helium (Airgas West, Culver City, CA) was used as the carrier gas, with the flow rate set to 1.2 mL/min. GC separation was carried

out on a 30m x 250 µm x 0.25 µm DB-Wax column (Agilent J&W). The GC oven was initially held at 40 °C, heated to 100 °C at 10 °C/min, and then heated to 230 °C at 30 °C/min. The MSD was operated in the SIM mode and used EI ionization.

Instrument response for known concentrations of all pure analytes in water was measured to determine the analyte concentrations in the unknown samples. A linear relationship was observed between the known concentration values and instrument response for these standard samples. The measured analyte response values for known and unknown samples were normalized to that of isopropanol used as the internal standard.

8.6.1.4 pH

The resultant formulation was assessed via commercial pH test strips (MColopHast, EMD Millipore, Darmstadt, Germany). Chemical indicators embedded into the tape change color in response to hydroxide and hydrogen ion concentrations. Samples images are shown in **Figure 8-13**.

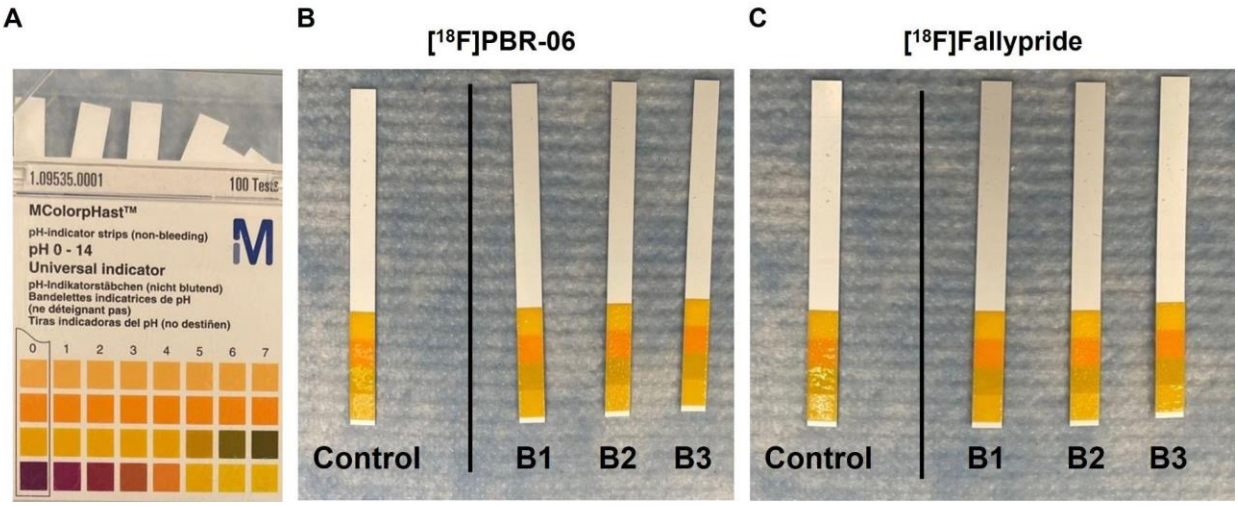

Figure 8-13. pH testing of radiopharmaceutical batches.
(A) Color scale. (B) pH tests of saline (control) and three batches (B1, B2, B3) of TLC-purified [^{18}F]PBR-06. (C) pH tests of saline and three batches of [^{18}F]Fallypride.

8.6.1.5 Radionuclidic identity

The identity of the radionuclide was determined by counting an aliquot of the formulated radiopharmaceutical in a calibrated dose calibrator over the course of 30 min. The following formula was compared to measured values to determine the radionuclidic identity:

$$T1/2 = -0.693 * (\Delta t)/ln(Af/A0)$$

where T1/2 = the half-life of the radionuclide, Δt = the change of time between two measurements, Af = final activity measured, and A0 = the initial activity measured.

8.6.1.6 Shelf-life

Radiochemical and chemical purity was assessed for batches via radio-HPLC after 120 min. A sample chromatogram for a sample of [^{18}F]PBR-06 is shown in **Figure 8-14**.

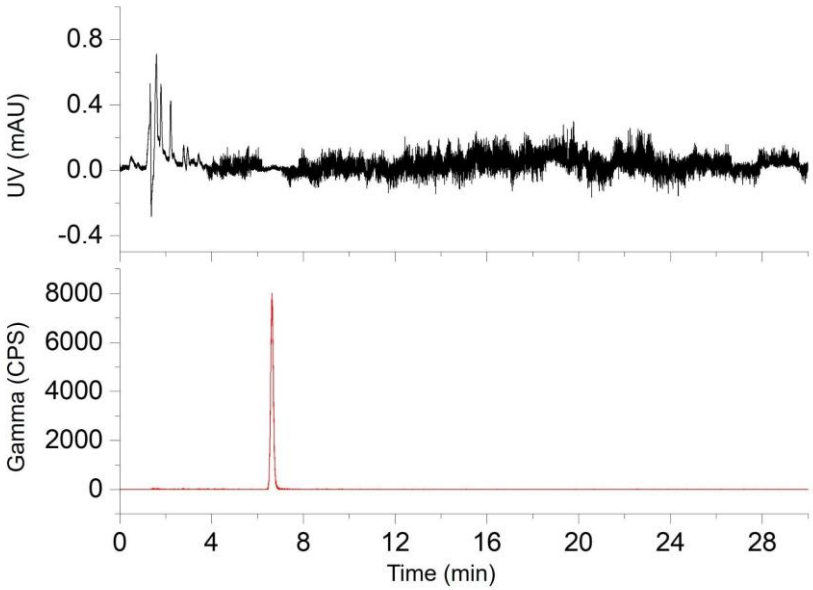

Figure 8-14. HPLC chromatogram of formulated [^{18}F]PBR-06 injected 120 min after the end of synthesis.

Chapter 9: Detection of radiometabolites in human blood using a high-performance, high-throughput thin-layer chromatography method

9.1 Introduction

Quantitative imaging with positron-emission tomography (PET) has enabled an improved understanding of pathophysiological processes[1–3], detailed monitoring of disease progression[4,5], and rapid assessment of responses to treatment over the last decade[6,7]. Using biologically-active molecules tagged with short-lived radionuclides (radiopharmaceuticals), PET allows in vivo visualization of specific physiological processes via measurement of the tissue concentration of the radiopharmaceutical throughout the body[8,286]. Many studies use the measurement of uptake normalized to injected dose and body weight (SUV) at static time points to approximate pathophysiological processes[287]. However, radiopharmaceuticals undergo complex pharmacokinetics (e.g., delivery, uptake, retention, and clearance), and PET images are unable to distinguish between radioactivity that is within the blood, in the extracellular space, specifically bound to the intended target, nonspecifically bound, or in metabolites of the radiopharmaceutical[78]. Dynamic scanning coupled with the metabolite-corrected arterial input function (AIF) must be used to distinguish these compartments and provide quantitation. Many recent studies have looked to derive AIF directly from PET images by estimating the activity concentration in the arterial blood from a blood pool (e.g., aorta, large blood vessels, or heart)[288], and, furthermore, the advent of total body PET promises to routinely allow this approach to non-invasively measure the AIF due to the heart always being in the field of view[289]. However, the image-derived AIF only allows the determination of whole blood activity and cannot account for the metabolism or binding of radiopharmaceuticals to red blood cells (RBC)[290]. Consequently,

arterial blood sampling at various time points post-injection, combined with measurements of intact tracer fraction and its free fraction, to determine the AIF remains indispensable.

However, several obstacles exist in experimentally determining the AIF, including low concentrations of radioactivity in blood samples due to the removal of radioactivity from blood to other organs over time. Furthermore, it is necessary to remove blood cells and proteins to determine the free fraction of the radiopharmaceutical in plasma[291] because this free fraction of the radiopharmaceutical is the only available population for binding the target of interest[292]. The necessary steps, including protein precipitation, unfortunately further dilute samples (e.g., a ~100 µL blood sample from a rat results in ~240 µL of processed plasma, and ~5 mL of human blood leads to ~12 mL of processed plasma)[293], necessitating high sensitivity radiation detection.

A further challenge is a need to distinguish radioactivity associated with the parent radiopharmaceutical and metabolites that can be present in plasma samples. These radiometabolites range from free radionuclides to compounds with high structural similarities to the parent compound, necessitating high-resolution chemical separation methods. Several methods (**Table 9-1**) have been used for the analysis of radiometabolites, including high-performance liquid chromatography (HPLC)[294,295], thin layer chromatography (TLC)[296,297], and solid phase extraction (SPE)[298,299] (**Figure 9-5**). The sensitivity and high resolution of HPLC make it the preferred method for metabolite analysis when combined with a scintillation detector. Nevertheless, HPLC has many disadvantages, including limited sample injection volumes[300] which are much smaller than the total volume of processed plasma, the possibility of retaining non-polar or ionic species on the column[191], which may result in overestimation of the intact radiopharmaceutical concentration, the tendency to clog the column[293], the long analysis time for each sample (including the time needed for cleaning and re-equilibration between samples)[293], and in sensitivity as a function of the time associated with the sample being passed through the detector. The use of a pre-concentration column in the “column switching”[301] HPLC technique

addresses sensitivity by enabling the injection of larger amounts of radioactivity but requires a complex HPLC setup[293]. Since samples must be processed serially, the long analysis time can be particularly problematic for the large numbers of blood samples needed to construct the AIF and/or when using short-lived PET isotopes such as C-11. One recent advance, utilizing micellular chromatography, has shown that the analysis time of plasma samples utilizing HPLC can be significantly reduced, though its adoption is limited due to complex instrumentation[302]. SPE analysis of plasma samples addresses many of the concerns by enabling the handling of large sample volumes, quick sample separation, and high sensitivity when combined with gamma counting, as well as the possibility of high-throughput analysis via parallelization. However, drawbacks of SPE include poor chromatographic resolution[303] and a need for extensive fine-tuning of washing/elution protocols to measure intact radiopharmaceuticals accurately[299]. Micellular chromatography has also been proposed for integration with SPE techniques, heightening resolution achievable, though again, its adoption is limited due to the use of specialized materials[304]. The use of TLC for analysis can provide moderate-resolution while also providing high sample throughput when coupled with autoradiography readout of multiple TLC lanes in parallel[305]. However, TLC is usually performed in small sample volumes (for example, 1 µL), meaning that only a small fraction of available plasma radioactivity is analyzed, hindering sensitivity[306]. Therefore, routine analysis of radiometabolism from a variety of widely used radiopharmaceuticals is necessary, and new methods that are rapid and easily adoptable due to the use of ubiquitous materials are warranted.

Leveraging a new approach we developed for optimizing TLC mobile phases to achieve high-resolution separations of radiopharmaceutical samples[268] and using TLC plates with concentration zones that allow much larger sample volumes (e.g., 1-2 mL) and radioactivity amounts to be deposited without affecting chromatographic resolution[307], we hypothesized that the shortcomings of the TLC radiometabolite analysis method could be overcome. We tested this hypothesis using blood samples obtained from rats and in human research participants

administered with [^{18}F]FEPPA, a ligand for the translocator protein of 18 kDa (TSPO) used as a PET biomarker for glial activation and neuroinflammation[308–310] and show that TLC can be used as a straightforward, convenient, high-resolution and high-sensitivity tool for determining the AIF.

Table 9-1. Comparison of chromatographic techniques for radiometabolite analysis at a glance.

Category	Conventional TLC	HPLC	SPE
Sample Deposition Volume	Low	Medium	High
Separation Time	High	High	Low
Analysis Time	Low	High	High
Sensitivity	Medium	Medium	High
Resolution	Low	High	Low
Method Development Time	High	High	High
Parallel Processing	Possible	Not Possible	Possible

9.2 Materials and Methods

9.2.1 Materials

2,3-dimethyl-2-butanol (thexyl alcohol; anhydrous, 98%), 4,7,13,16,21,24-hexaoxa-1,10-diazabicyclo[8.8.8]hexacosane (K_{222}; 98%), acetone (suitable for HPLC, >99.9%), acetonitrile (MeCN; anhydrous, 99.8%), Eppendorf tubes (2 mL, DNA LoBind, PCR clean), methanol (MeOH; anhydrous, 99.8%), n-butanol (n-BuOH; anhydrous, 99.8%), n-hexanes (98%), tetrahydrofuran (THF; anhydrous, >99.9% inhibitor free), and water (H2O; suitable for ion chromatography) were purchased from Sigma-Aldrich (St. Louis, MO, USA). N-[2-[2-[[(4-methylphenyl)sylfonyl]oxy]ethoxy]phenyl]methyl]-N-(4-phenoxy-3-pyridinyl) ([^{18}F]FEPPA precursor, >90%), N-acetyl-N-(2-fluoroethoxybenzyl)-2-phenoxy-5-pyridinamine (FEPPA reference standard, >95%), and tetrabutylammonium bicarbonate ($TBAHCO_3$; 75 mM in ethanol), were purchased from ABX Advanced Biochemical Compounds (Radeberg, Germany). Multi-channeled silica TLC plates (2315126C) were purchased from Sorbtech (Norcross, GA, USA). 1000 USP/mL Heparin was obtained from Sagent Pharmaceuticals

(Schaumburg, IL, USA). PTFE tubing (1/16" OD, 0.01" ID; 1529L) was purchased from IDEX Health and Science (Wallingford, CT, USA).

No-carrier-added [^{18}F]fluoride was produced via the (p, n) reaction of [^{18}O]H_2O (98% isotopic purity, Huayi Isotopes Co., Changshu, Jiangsu, China) in an RDS-111 cyclotron (Siemens, Knoxville, TN, USA) using a 1.2-mL silver target with havar foil, or in a TR-19 cyclotron using a 2 mL niobium target.

9.2.2 Preparation of [^{18}F]FEPPA

Production of [^{18}F]FEPPA was adapted from literature reports[311,312]. [^{18}F]fluoride (100-1000 mCi in 2 mL [^{18}O]H_2O) was recovered through an anion-exchange cartridge followed by elution with K_2CO_3 (3 mg) in H_2O (0.3 mL) into a pyrex glass vessel. K_{222} (10 mg) dissolved in MeCN (1 mL) was added to the vessel, and the solution was heated at 100 ± 3 °C until the liquid was fully evaporated. Azeotropic evaporation of the residual H_2O was continued by adding and drying two more 1 mL portions of MeCN. After cooling for 2-4 min, a solution of FEPPA precursor (5 mg) in MeCN (0.75 mL) was added to the dried [^{18}F]KF/K_{222} complex. The solution was reacted at 75 ± 3 °C for 20 min with N_2 bubbling, then cooled for 2-4 min, and finally, the reaction was quenched by adding H_2O (1.25 mL). The solution was injected into a 2 mL HPLC loop and purified by semipreparative HPLC (column: Phenomenex Kinetex C_{18} 5 µm, 250 mm x 10 mm; mobile phase: 1:1 v/v EtOH:H_2O; flow rate: 3 mL/min; detectors: UV 254 nm and radioactivity). The desired fraction (retention time ~9.6 – 10.2 min) was collected in a flask containing 25 mL of sterile water. The [^{18}F]FEPPA was trapped on a t-C_{18} cartridge (SepPak light, Waters), washed with 11 mL of sterile water, eluted with 0.85 mL of EtOH followed by 20 mL of sterile 0.9% saline, and passed through a sterile 0.22-µm filter (Millipore MP) into a sterile, pyrogen-free vial. Aliquots of the formulated solution were used to establish the chemical and radiochemical purity and specific activity of the final solution by analytical HPLC (column: Phenomenex Kinetex C_{18} 5 µm, 250 mm x 4.5 mm; mobile phase: 45:55 v/v MeCN:0.1 N ammonium formate; flow rate: 1.5 mL/min). In each case studied, the minimum radiochemical purity was >99% and >740 GBq/µmol.

9.2.3 Pre-clinical blood sampling

Sprague-Dawley rats (male) were injected with 59 ± 17 MBq (n = 4) [^{18}F]FEPPA with molar activities >740 GBq/μmol. Periodic arterial blood sampling was performed via cannulation of the femoral artery. At each time point (1, 3, 6, 9, 12, 15, 20, 30, 45, and 60 min), ~100 μL of blood (determined by weight) was collected using a heparin-flushed syringe into an Eppendorf tube coated with cooled heparin (4 μL, 1000 USP/mL) and stored on ice. All collected samples were processed within 10 min.

9.2.4 Clinical blood sampling

Subjects were injected with 187 ± 14 MBq [^{18}F]FEPPA (n = 5) with molar activities >740 GBq/μmol. 8 ccs of whole arterial blood was collected via a needle-free syringe (to avoid shearing forces) into 10 cc heparinized tubes and transferred onto ice. Samples were collected at 2.5, 7, 12, 20, 30, 45, 60, 90, 120, and 150 min post-injection.

9.2.5 Plasma processing procedure

Blood samples were centrifuged at 4 °C and 3,000 x g for 10 min. For each sample, the supernatant plasma was collected by a micropipette and placed into a secondary Eppendorf tube. After adding 4x (v/v) of ice-cooled MeCN, the tube was vortexed for 20 s. The samples were then recentrifuged at 4 °C and 12,000 x g for 20 min. The supernatant was collected via micropipette, leaving pelleted proteins behind.

9.2.6 Radioactivity measurements

Radioactivity measurements were made at multiple steps for each sample (i.e., initial total blood sample, blood cell pellet, total plasma, plasma protein pellet, and protein-depleted plasma). Samples were assessed via a gamma counter (Wizard 3” 1480 Automatic Gamma Counter, PerkinElmer, Waltham, MA, USA), with a blank sample counter after each set of 4 measurements (subtracting the background measurement from the measured samples). Each sample was counted for 45 s, and a calibration curve was used to convert the gamma counter output into a radioactivity amount.

Several calculations were made from these measurements at each time point. To assess red blood cell (RBC) binding of [^{18}F]FEPPA (and its metabolites), plasma to blood ratio (%) was calculated as the total plasma activity divided by the total blood activity. Binding to plasma proteins (%) was computed as the plasma protein pellet activity divided by the total plasma activity. The concentration of available [^{18}F]FEPPA at each timepoint was determined by multiplying the activity of the protein-depleted plasma by the intact fraction of [^{18}F]FEPPA (as determined below using multiple different methods) and dividing by the volume of the blood sample.

9.2.7 Determination of intact fraction via radio-TLC

To enable parallel separation of plasma samples, multi-lane TLC plates were used. Plates were placed on a 70 °C hot plate during sample deposition to enable the loading of large sample volumes. For rats, each 250-500 µL protein-depleted plasma sample was pipetted 10 µL at a time, allowing the deposited aliquot to dry before adding the next one. The total time to deposit one plasma sample was ~5-7 min. Each sample was deposited onto a dedicated lane. To accelerate the deposition process for clinical samples, we constructed an automated setup (**Figure 9-1**) for dripping multiple samples onto multiple lanes simultaneously. A pressure manifold was connected to a nitrogen source (20 psig), and each output tubing (1/8” OD, 1/16” ID) was connected via a dedicated adjustable flow restrictor (AS2211F-02006S, SMC, Noblesville, IN, USA) to pressurize a corresponding sample reservoir. Dip tubes (1/16” OD, 0.04” ID) connected to each sample reservoir were threaded through vertical holes in a custom machined plastic block and secured with 1/4"-28 fittings to align the position of the tubing outlets above the origins of the lanes on the TLC plate. The flow restrictors were adjusted beforehand to a rate of one 10 µL droplet each 5 s. Samples were dispensed in this fashion to the heated TLC plate until <5% of the initial volume remained, and then the corresponding pressure source was turned off (to prevent spraying/splashing as the final volume emerged from the dip tube).

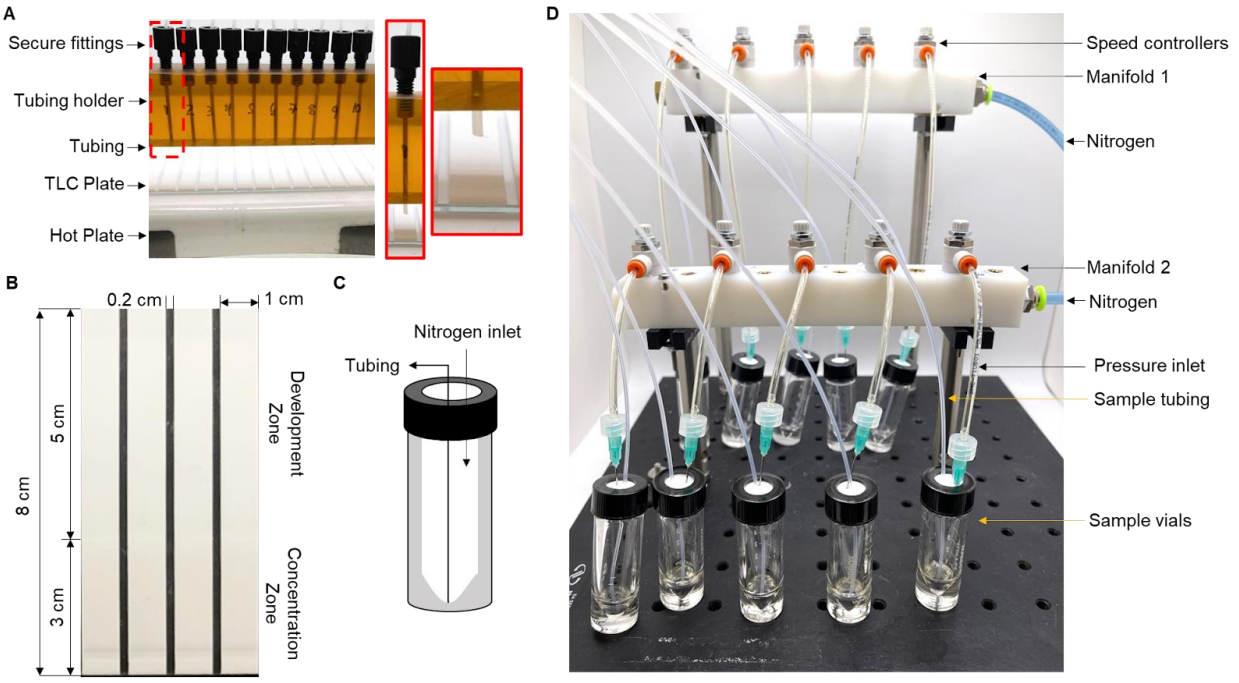

Figure 9-1. Apparatus used to automate and parallelize the deposition of plasma samples to the TLC plate.
(A) A plastic tubing holder was fabricated to secure tubing above the origin for each lane. The inlets show a zoomed view of a single tubing holder and a zoomed view of the tubing for one sample positioned above the TLC plate. (B) The channeled TLC plates with concentration zones. Only 4 lanes are shown, but we used 10 lanes sections cut from commercially-available 20-lane plates. (C) The samples are placed into v-vials and pressurized with nitrogen to enable the dripping of each sample to the TLC plate. (D) The pressure manifold system allows individual control of the nitrogen flow for each sample, enabling the deposition of 10 samples in tandem.

After the TLC plate was allowed to dry completely, it was placed in a developing chamber (LatchLid). The TLC plate was allowed to develop a total distance of 8 cm (3 cm in the concentration zone and 5 cm in the development zone) using a mobile phase of 12.8:37.5:9.8:38.8:1 v/v n-BuOH:THF:acetone:n-hexanes:TEA[268]. After developing, the TLC plate was dried by placing it on the hot plate and then cooled to room temperature. The plate was then affixed to a phosphor imaging screen (BAS-TR2025, FujiFilm Life Science, Stamford, CT, USA) and stored overnight in a light-tight enclosure. The imaging screen was then imaged with a phosphor imager (BAS-5000, FujiFilm Life Science, Stamford, CT, USA). Autoradiography images were analyzed by ImageReader (FujiFilm Life Science, Stamford, CT, USA). This software allows the selection of the number and position of lanes and generates an integrated

line profile (encompassing the width) of the pixel intensity along the length of each selected lane. Line plot profiles were exported to OriginPro (OriginLab Corporation, Northampton, MA, USA), for plotting and determining the area under the curve (AUC) for each identified analyte peak (band). Briefly, using the peak analyzer function of OriginPro, the minimum value in the chromatogram was established as the baseline subtraction value (used for the entire chromatogram correction). Bands were manually selected, and the integration window width of each selected band was automatically determined by OriginPro. The intact [^{18}F]FEPPA fraction was calculated as a function of the integrated area of the [^{18}F]FEPPA band, compared to the sum of the integrated areas of all peaks of the chromatogram.

9.2.8 Determination of intact fraction via SPE

Oasis HLB cartridges were pre-conditioned with 5 mL of EtOH and 5 mL of water. Plasma samples, without prior plasma protein precipitation, are initially mixed with 1:1 (v/v) AcOH:H_2O (volume varies with sample number), then introduced to the pre-conditioned HLB cartridge. The cartridge is then washed successively with 4 mL of 5% v/v MeOH (aq.), then 4 mL of 25% v/v MeCN (aq.) with 0.1 N ammonium formate. At the end of the elution cycle, cartridges were cut and gamma counted (GAMMA COUNTER INFO). The amount of activity remaining on the cartridge at the end of the elution cycle was compared to the initial activity in plasma and treated as the intact population of [^{18}F]FEPPA.

9.3 Results

9.3.1 Mobile phase for TLC separation

Accurate quantification of intact [^{18}F]FEPPA requires adequate separation of [^{18}F]FEPPA from radiometabolite species. Optimization of mobile phase for TLC separation of [^{18}F]FEPPA metabolites on silica analytical TLC plates was recently reported[198]. Separation of 2 µL samples was achieved using 8:10:82 (v/v) MeOH:Hexanes:EtOAc and a developing distance of 7 cm. However, significant tailing of the intact [^{18}F]FEPPA band and overlap with closely migrating

bands were observed[198]. Line profiles that featured an overlap of analytes were deconvoluted through the use of a custom MATLAB program. In a recent report, our lab used an adapted version of the PRISMA optimization algorithm to develop an alternative mobile phase for the analysis of crude reaction mixtures of [^{18}F]FEPPA (for reaction optimization) that gave excellent separation between [^{18}F]FEPPA and radioactive and non-radioactive impurities[268]. Since the mobile phase was optimized using highly similar chemical species samples, we hypothesized that it would also be suitable for analyzing radiometabolite samples. Using analytical TLC plates, with a separation distance of 4 cm, we separated crude samples (1 µL) of synthesized [^{18}F]FEPPA[178] with both mobiles phases and used Cerenkov luminescence imaging (CLI) and UV imaging(32) to visualize the plates (**Figure 9-2A** and **Figure 9-2B**). The PRISMA-optimized mobile phase had better resolution (2.07, R_f 0.73) than the literature-derived mobile phase (0.45, R_f 0.54). The PRISMA-optimized mobile phase reduced the development time (~3.8 min) compared to the literature-derived mobile phase (~6.6 min).

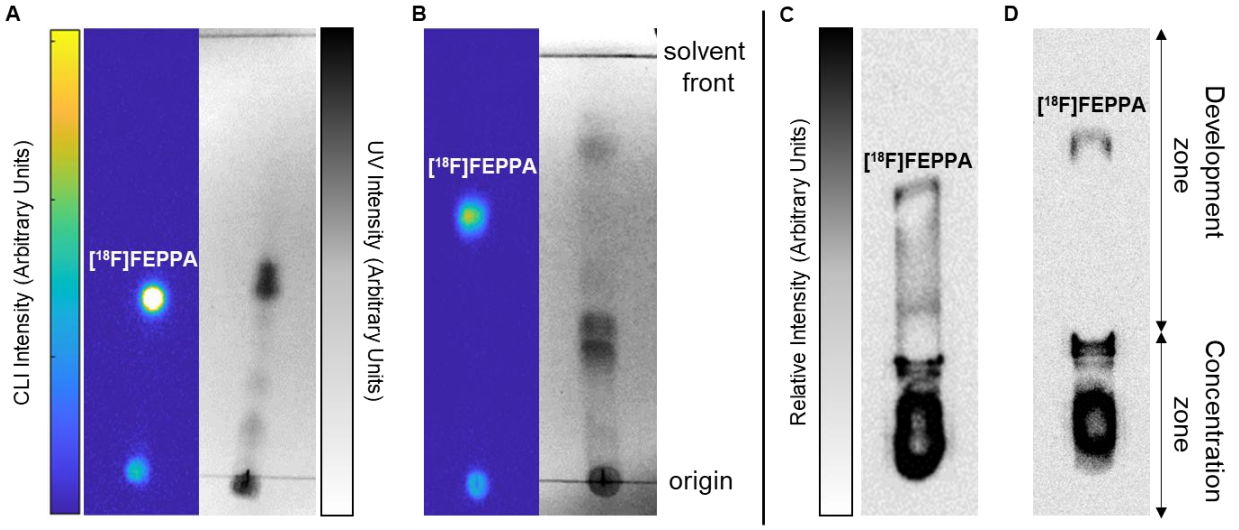

Figure 9-2. TLC resolution comparisons compared for crude radiochemical reactions and radiometabolites.
(A) Separation of crude [^{18}F]FEPPA using an optimized mobile phase reported in the literature[198] on an analytical TLC plate. The left image shows the CLI image of radioactivity distribution. The right image was captured with UV illumination to show non-radioactive species. (B) Separation of the same sample using the PRISMA-optimized mobile phase. (C) Separation of [^{18}F]FEPPA and radiometabolites in a rat plasma sample using the literature mobile phase, performed on

concentrating zone TLC plates and read out with autoradiography. (D) Separation of the same sample as C but using the PRISMA-optimized mobile phase.

Anticipating that radiometabolite samples have much lower radioactivity concentration that will not be detectable with CLI or scintillation imaging[198], we used autoradiography imaging as a higher sensitivity readout of the TLC plates. Furthermore, instead of spotting only 1 µL of each plasma sample (hundreds of µL for preclinical samples and multiple mL for clinical samples), we employed TLC plates with concentration zones. The concentration zone, made of highly porous diatomaceous earth, allows rapid evaporation of the solvent from the sample and facilitates rapid migration of species such that when separation begins, all species effectively focus to a thin line along with boundary between the concentration and separation zones, enabling high-resolution TLC separations despite the use of large sample volumes[234]. Initially, we deposited the total plasma sample (~150 µL) directly onto the concentrating zone TLC plates but found that the plate can be overloaded with proteins (**Figure 9-6**). Plasma precipitation can resolve this issue at the expense of further dilution. Using 600 µL samples of the same batch of protein-depleted plasma from a rat injected with [^{18}F]FEPPA, we again compared the two mobile phases (**Figure 9-2C** and **Figure 9-2D**) and found that the PRISMA-optimized mobile phase was able to completely resolve intact [^{18}F]FEPPA from other radiometabolites (minimum resolution = 4.5), while the literature mobile phase did not (minimum resolution = 0.9).

To enable rapid TLC analysis of many samples, we showed previously that small volumes of crude reaction mixtures can be spotted at adjacent positions with separation and readout performed simultaneously for the whole set of samples[93]. Due to the large sample volumes used here and the large pore size of the concentrating zone, very wide spacing between sample origins is needed to avoid spillover between lanes. We used commercially available TLC plates with pre-defined lanes to avoid this problem. Lanes are separated by a 2 mm gap where the sorbent material has been etched from the plate, preventing spillover from one lane to another. Using

these plates in combination with the PRISMA-optimized mobile phase, we determined the locations of the [^{18}F]fluoride (R_f = 0.00) and [^{18}F]FEPPA (R_f = 0.73) bands (**Figure 9-7**).

As a final step of method development, we assessed the detection sensitivity of the TLC method utilizing the pre-concentration zone plates used in further studies with autoradiography readout (**Figure 9-8**) and a radio-HPLC method (**Figure 9-9**). The LOD and LOQ for the TLC method were 0.014 nCi and 0.022 nCi, respectively, and for the radio-HPLC methods were 7.0 nCi and 10.5 nCi, respectively (**Figure 9-10**). Heating of the TLC plate during these studies led to no observed decomposition of [^{18}F]FEPPA. Previous studies by our lab have further shown that volatility from the TLC plates does not occur as a function of heating[268,307].

9.3.2 Analysis of pre-clinical radiometabolite samples

To evaluate the performance of the TLC method, we performed proof-of-concept studies of blood samples obtained from rats. Each 100 µL blood sample provided ~60 µL of total plasma, and after precipitation of plasma proteins, a final volume of ~240 µL. An example TLC plate surveying the fraction of intact [^{18}F]FEPPA as a function of blood sampling time is shown in **Figure 9-3A**. Remarkably, the fraction of intact [^{18}F]FEPPA showed very low variance when corresponding time points were averaged over multiple animals (**Figure 9-3B**). The computed intact fraction also agrees well (within experimental error) with published HPLC-derived data as a function of blood sampling time[311] (**Figure 9-3B**). We further assessed the role of RBC binding to determine its effect on the free fraction of [^{18}F]FEPPA in blood. A sample collection of these values in rodent and human samples spiked *ex vivo* (**Figure 9-11**) or collected from *in vivo* studies (**Figure 9-12**) are presented in **Section 9.6.5**.

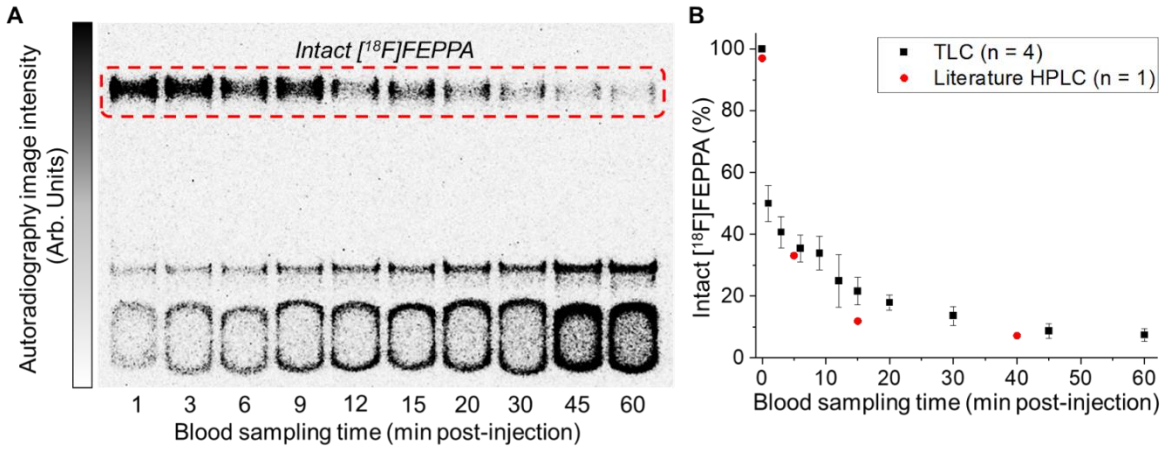

Figure 9-3. PRISMA-optimized TLC readout of pre-clinical [^{18}F]FEPPA radiometabolites. (A) An example autoradiography image of a whole multi-lane concentrating zone TLC plate spotted with plasma extracted from blood sampled at various time points from a rat injected with [^{18}F]FEPPA and separated using the PRISMA-optimized mobile phase. (B) Intact [^{18}F]FEPPA fraction plotted as a function of blood sampling time. Values derived from TLC analysis and compared with literature values derived from HPLC analysis[313]. At each time point, values are averaged across different rats.

9.3.3 Analysis of clinical radiometabolite samples

Analysis of human samples is more challenging due to the lower radiotracer concentration in blood (185 MBq for a 70 kg human, vs. 50 MBq for a 0.32 kg rat). Though 50x larger blood volumes can be sampled (e.g., 5 mL in humans vs. 100 µL in rats) to compensate for this, the final volume of processed plasma (~12 mL) is too large to deposit on the TLC plate, and only a portion of the radioactivity in each sample can be used (~2 mL). The larger sample volume, however, takes more time to deposit onto the TLC plate, and thus we developed an automated TLC spotting apparatus to enable parallel deposition of all samples (**Figure 9-1**). Using the automated sample deposition set up, up to 10 samples could be deposited in a total of 20-30 min instead of 200-300 min, which would have led to 66 - 83% radioactive decay of the samples before exposure to the autoradiography plate. A proof of concept of a TLC plate for analysis of intact [^{18}F]FEPPA from human samples is shown in **Figure 9-4A**. Analysis of [^{18}F]FEPPA fraction shows good agreement when averaged across different patients at the same time points (**Figure 9-4B**), and the TLC method shows good agreement to the SPE method (**Figure 9-4B**) and HPLC data

from the literature[313] (**Figure 9-4B**). An individual trial between the PRISMA-optimized TLC method and SPE can be found in **Figure 9-13**, also showing good agreement.

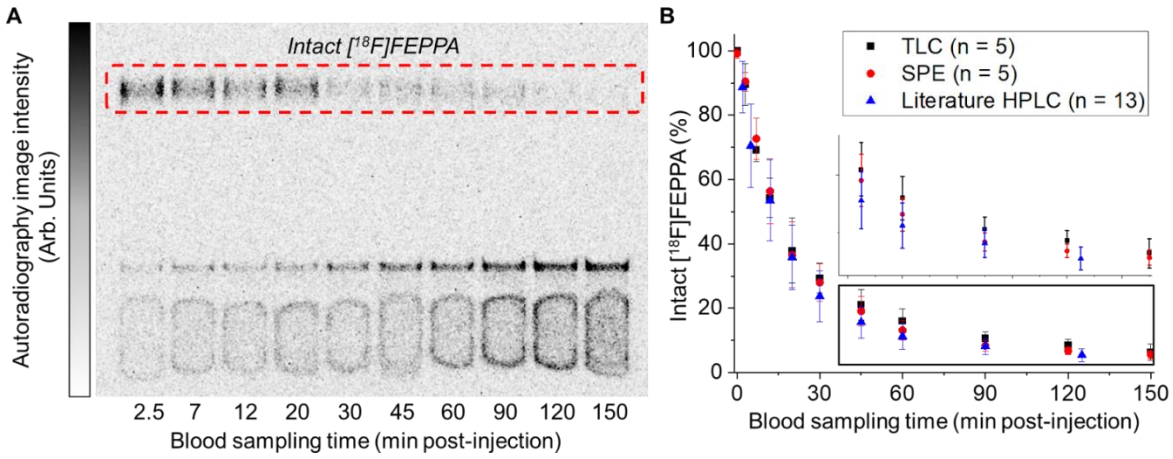

Figure 9-4. PRISMA-optimized TLC readout of clinical [^{18}F]FEPPA radiometabolites.
(A) An example autoradiography image of a whole multi-lane concentrating zone TLC plate spotted with plasma extracted from blood sampled at various time points from a human subject injected with [^{18}F]FEPPA and separated using the PRISMA-optimized mobile phase. (B) Intact [^{18}F]FEPPA fraction is shown as a function of blood sampling time. The same samples were analyzed by both TLC and SPE methods and compared with HPLC-derived data from the literature[313]. Data for each timepoint is averaged across different patients.

9.4 Discussion

The selected TLC mobile phase provided good separation of [^{18}F]FEPPA from radio-metabolites. Despite the fact that the mobile phase was optimized using crude radiosynthesis samples of [^{18}F]FEPPA (i.e., not radio-metabolite samples[198]), separation of intact [^{18}F]FEPPA from radiometabolites exhibited excellent resolution. We suspect this approach works because the PRISMA method optimizes the separation between FEPPA, its radiosynthesis precursor, and impurities formed during the radiosynthesis, many of which have very high structure similarity to FEPPA. Thus the method should also be capable of separating all metabolites (whether structurally-similar or not) of [^{18}F]FEPPA from the parent compound. The PRISMA approach is far more convenient than conventional approaches for optimizing radiometabolite mobile phases[198]. Such methods require full production and quality-control testing of the radiopharmaceutical, injection into animals or patients, blood sampling, and plasma extraction

just to generate the samples needed for the optimization study. Due to the extremely low radioactivity of each plasma sample, the number of mobile phases that can be compared is severely limited, and multiple batches of the tracer and animals would be required to perform an in-depth optimization study. Furthermore, the low activity hinders accurate quantitation of resolution, limiting the ability to distinguish between similarly-performing mobile phases. In contrast, with the PRISMA approach, the entire optimization can be performed using a single batch of crude radiopharmaceutical in just a few hours. Pre-clinical studies utilizing the method gave similar results as previously reported HPLC methods. However, in the pre-clinical HPLC analysis study, only 3-time points were conducted for analysis. This is likely due to the complexity needed to ensure quantitative analysis with HPLC, which requires collecting detected analytes for downstream gamma counting. In contrast, the TLC method described allows the ability to profile up to 20 different blood collection time points on a single commercially available plate. The ability to sample a greater number of time points could have enormous implications for the kinetic analysis of radiopharmaceuticals.

The TLC method reported here made possible the analysis of [^{18}F]FEPPA radiometabolites in clinical samples. Previous literature-TLC studies had shown analysis of [^{18}F]FEPPA in pigs[198]. The use of commercially-available concentrating zone plate allows the deposition of much larger sample volumes (up to 1-2 mL shown) than previous reports (1-10 µL [198,247,305,314–322]). With an analytical TLC plate, a large sample volume would lead to reduced resolution, but the concentrating zone effectively eliminates the impact of the initial spot size deposited on the plate. Furthermore, the availability of concentrating zone plates with inter-channel boundaries enables multiple samples to be spotted in adjacent lanes on a single TLC plate for convenient parallel development and readout. This feature makes the method more practical for studies requiring fine timepoint measurements. When combined with the automated sample deposition apparatus we developed, the whole process of sample deposition, separation, and preparation of autoradiography plate requires only 50 min of effort for the 10 samples shown

here and minimal additional time to analyze increased numbers of samples. With the dimensions and capacities of commercially available TLC plates and autoradiography plates, samples from up to 20-time points could be conveniently analyzed.

Due to the ability to deposit large volumes, the sensitivity is significantly improved compared to prior TLC-based approaches. A typical 1 µL sample spot would contain only 1 Bq of activity when analyzing preclinical (rat) samples, which is close to the LOQ of the separation and readout method we reported (0.81 Bq), and it would be very difficult to quantify the proportion of [^{18}F]FEPPA at later timepoints where significant amounts of radiometabolites were present. However, using a larger sample volume (0.3 mL), it is possible to instead load 300 Bq, far above the LOQ. This issue is heightened with samples from human subjects. In such samples, a 1 µL of the sample would contain only ~0.02 Bq, while full deposition (2 mL) enables 33.3 Bq to be loaded, which is far above the LOQ. Since our TLC method does not use the full volume of processed plasma, a smaller blood volume (~0.5 mL vs. ~5 mL) is actually needed for each time point, and potentially smaller blood volume can be drawn at each time point to minimize the physiologic impact[323] and discomfort to the patient. Furthermore, drawing less blood could significantly reduce the time and effort to draw and process blood samples.

While specialized autoradiography instruments have been proposed[198] to account for low radioactivity levels in samples, their use would be cost-prohibitive to many studies. Combining high separation resolution, high sensitivity, and high parallelism, the method offers comparative resolution to radio-HPLC and the ability to fully profile radiometabolites that are not retained as in radio-HPLC. Furthermore, the TLC method described allows heightened resolution and sensitivity over SPE approaches. While our studies focused only on the analysis of [^{18}F]FEPPA metabolites as a proof of concept, the underlying methodology could be applied to other radiopharmaceuticals. We demonstrated that the PRISMA approach could be applied to a wide range of radiopharmaceuticals[268], and the results here suggest that the approach could be used to determine optimal TLC mobile phases for radiometabolite analysis rapidly. The methods can

likely be extended to radiopharmaceuticals labeled with other isotopes. For example, autoradiography has been employed for additional positron-emitting radionuclides, including C-11, Cu-64, Ga-68, and Zr-89[324–327]. While differences in isotopes (e.g., branching ratios and half-life) will affect the determined LOD/LOQ values, this effect may be partially overcome by adjusting the autoradiography exposure time and/or sample volume deposition. The rapid separation method combined with parallel analysis would be particularly advantageous for shorter-lived radionuclides such as C-11 and Ga-68. Further use of this TLC method could find application with therapeutic radionuclides used in emerging theranostic studies[328,329] for the analysis of in vivo stability or to understand the kinetics of these radiopharmaceuticals.

9.5 Conclusions

In this study, an improved TLC-based method was developed to perform radiometabolite analysis in animal and human PET studies. The chromatographic resolution achievable with the PRISMA-optimized method was far greater than for previously reported TLC mobile phases, and in separate work, we have shown is comparable to the resolution of HPLC[268]. Importantly, because the PRISMA-optimization process is performed with the crude radiopharmaceutical, whereas the literature-derived mobile phase was developed with metabolite samples, it will be straightforward to extend this approach to other radiopharmaceuticals. The new method was used to quantify the intact [^{18}F]FEPPA fraction at 10-time points in blood samples collected from rats and humans and yielded values in agreement with the SPE and HPLC analysis methods. By using concentrating zone TLC plates, the method can accommodate much larger sample volumes than previous TLC approaches, significantly boosting sensitivity and enabling the analysis of human samples of [^{18}F]FEPPA for the first time, where the radioactivity concentration in blood is 60x lower than in rats. Compared to HPLC and SPE, the optimized TLC method is faster, more sensitive, and does not suffer the possibility of inaccuracies due to the trapping of unexpected radiochemical species on the stationary phase. Further, the ability to profile a greater throughput

of samples compared to HPLC could have enormous implications for the kinetic analysis of radiopharmaceuticals.

9.6 Appendix

9.6.1 Literature review of radiometabolite analysis methods

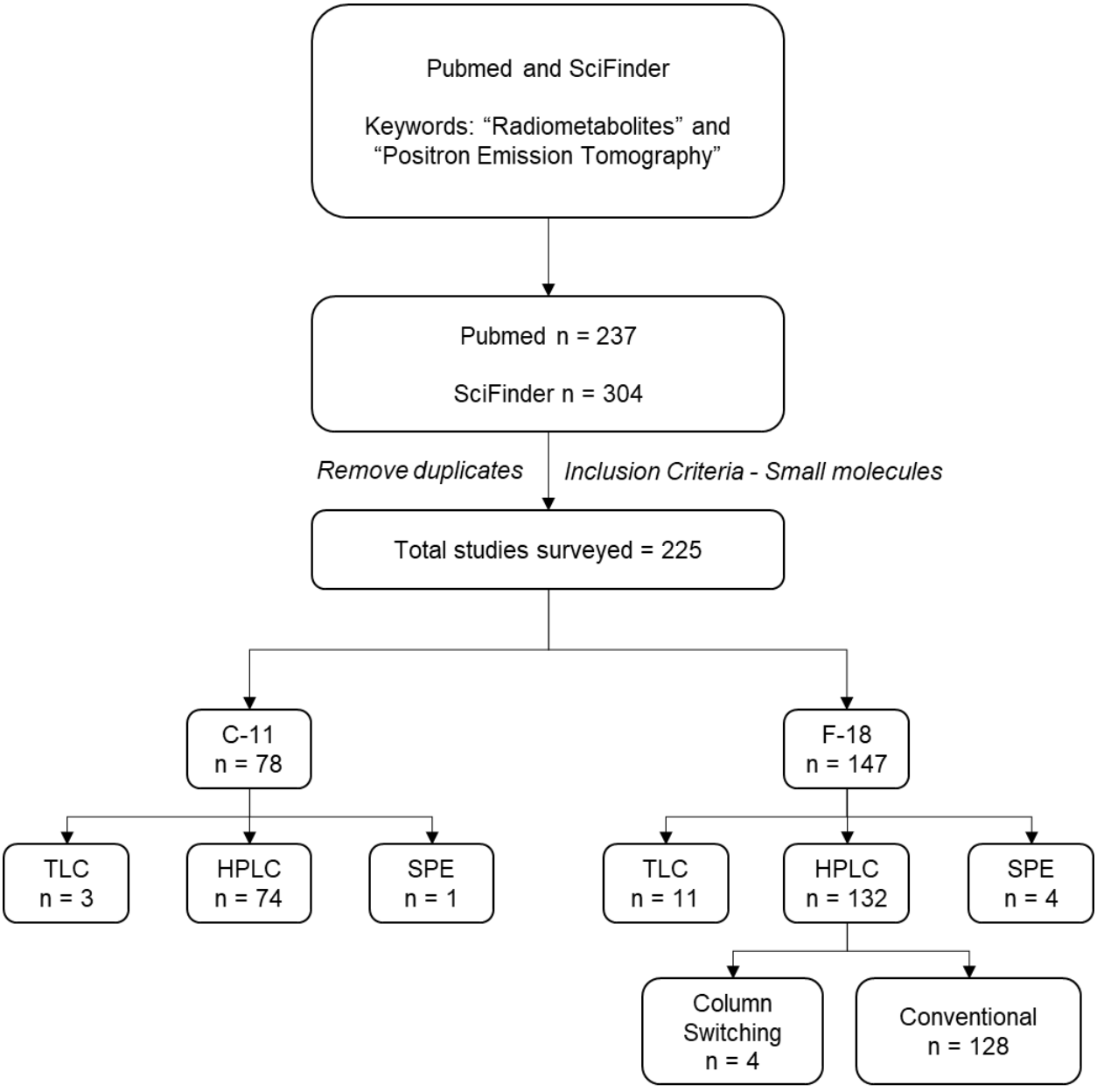

Figure 9-5. Literature survey of radiometabolite analysis. Studies are separated by radionuclide: carbon-11 and fluorine-18 No restriction was placed on the publication year.

9.6.2 Effect of plasma protein concentration on sample deposition

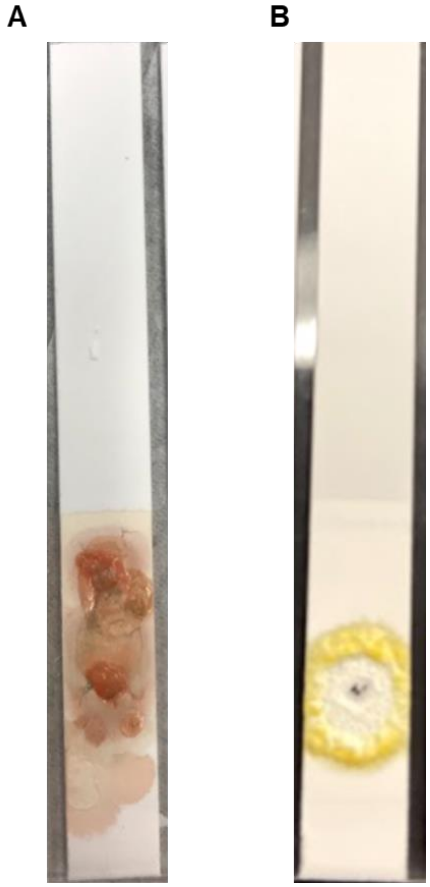

Figure 9-6. Effect on TLC plates when loaded with plasma samples containing proteins. (A) Plasma (60 µL) extracted from a hemolyzed blood sample from a rat, skipping the protein precipitation step. (B) Plasma (400 µL) extracted from a human blood sample, skipping the protein precipitation step. Protein precipitation on the face of the plate impedes the speed of development and leads to the loss of [^{18}F]FEPPA to the concentration zone.

9.6.3 Determination of [^{18}F]fluoride and [^{18}F]FEPPA

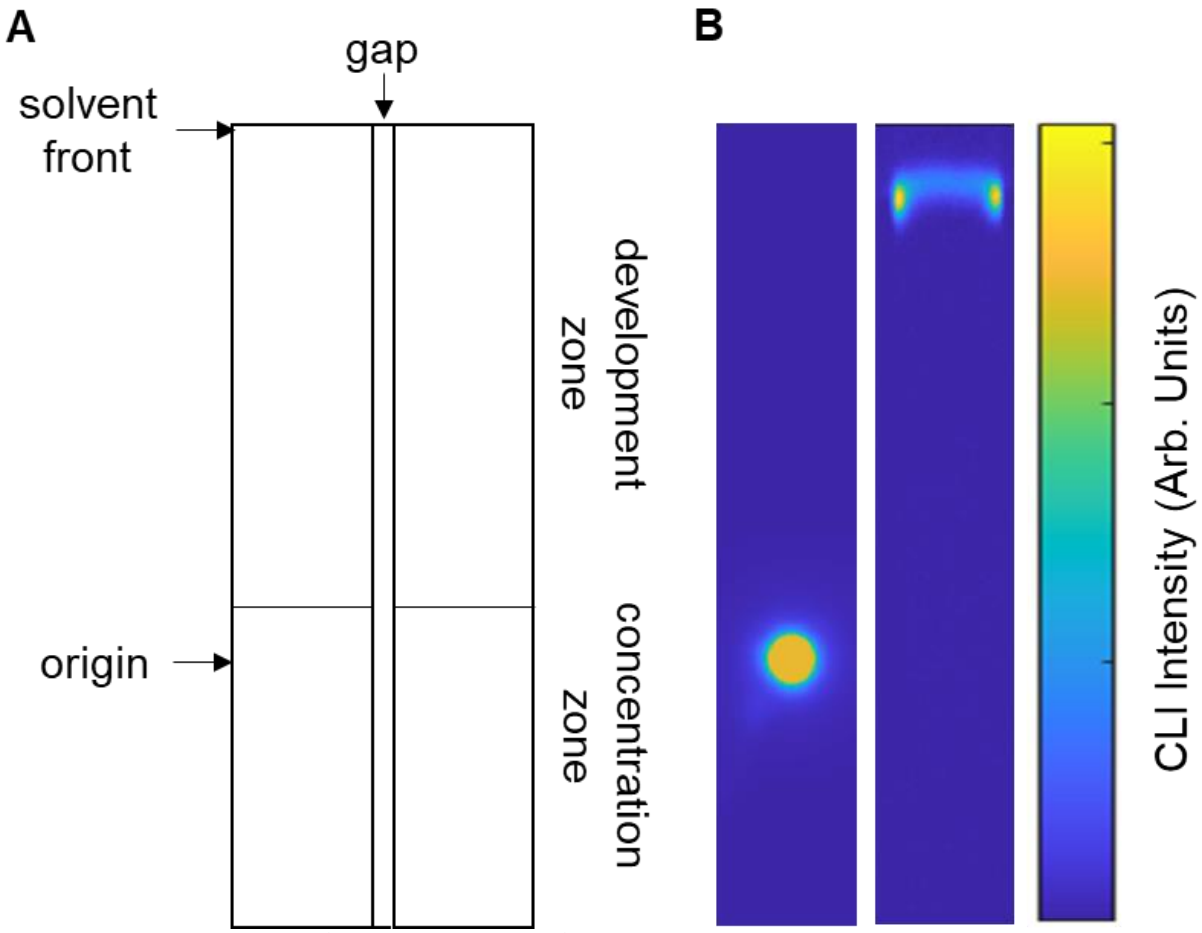

Figure 9-7. Location of [^{18}F]fluoride and [^{18}F]Fallypride bands after deposition of samples on concentrating zone TLC plates developed with the PRISMA-optimized mobile phase. TLC plates were imaged with CLI.
(A) Schematic of the TLC plate shown in panel B. (B) Left: 200 µL saline containing [^{18}F]fluoride. Right: 200 µL saline containing [^{18}F]FEPPA.

9.6.4 Determining sensitivity differences between TLC and HPLC

9.6.4.1 Limit of Detection (LOD) and Limit of Quantitation (LOQ) Studies

To compare the LOD and LOQ of the TLC and HPLC methods, [^{18}F]FEPPA was synthesized and purified via microscale methods as previously described[178]. HPLC methods[178] were used to purify and formulate [^{18}F]FEPPA in 9:1 (v/v) saline:EtOH (phosphate buffered). Serial dilutions were used to prepare [^{18}F]FEPPA in the activity range of (60-0.0001 nCi) in 200 µL sample volumes of saline. Eppendorf tubes containing the samples were measured by gamma counter before and after sample deposition (all samples profiled were deposited or injected in complete 200 µL volumes) to correct for residual activity left to the Eppendorf. Samples were subjected to radio-TLC (as described in the main text) or radio-HPLC (described in **Section 9.6.4.2**) analysis. The resulting chromatograms were assessed for their signal-to-noise ratio according to the European Pharmacopoeia definition[330]:

$$SNR = \frac{2H}{h}$$

Wherein, H denotes the height of the signal, and h denotes the height of noise in a reference frame of at least 20x the FWHM of the signal being quantitated. The LOD of this ratio is defined as 3, while the LOQ is defined as 10.

9.6.4.2 HPLC analysis of [^{18}F]FEPPA

An HPLC method was developed to allow a slow flow rate to be used to maximize the detection of [^{18}F]FEPPA, while also allowing fast analysis time by a low retention time of [^{18}F]FEPPA. The radio-HPLC system setup comprised a Smartline HPLC system (Knauer, Berlin, Germany) equipped with a degasser (Model 5050), pump (Model 1000), UV detector (254 nm; Eckert & Ziegler, Berlin, Germany), gamma-radiation detector (BFC-4100, Bioscan, Inc., Poway, CA, USA), and counter (BFC-1000; Bioscan, Inc., Poway, CA, USA). A C_{18} Gemini column was used for separations (250 × 4.6 mm, 5 µm, Phenomenex, Torrance, CA, USA). A mobile phase of 60:40 v/v MeCN:H_2O (0.1% TFA) with a flow rate of 0.6 mL/min led to a retention time for

[^{18}F]FEPPA of 7.1 min. Chromatograms were directly imported to OriginPro to determine the LOD and LOQ.

9.6.4.3 TLC analysis of [^{18}F]FEPPA

A pre-concentration zone TLC plate was used to ensure the full deposition of sample volumes, as described in the main text (**Section 9.2.7**). All parameters of sample spotting, development, and readout were mimicked according to the pre-clinical samples described to ensure the appropriate determination of the LOD and LOQ for the TLC method.

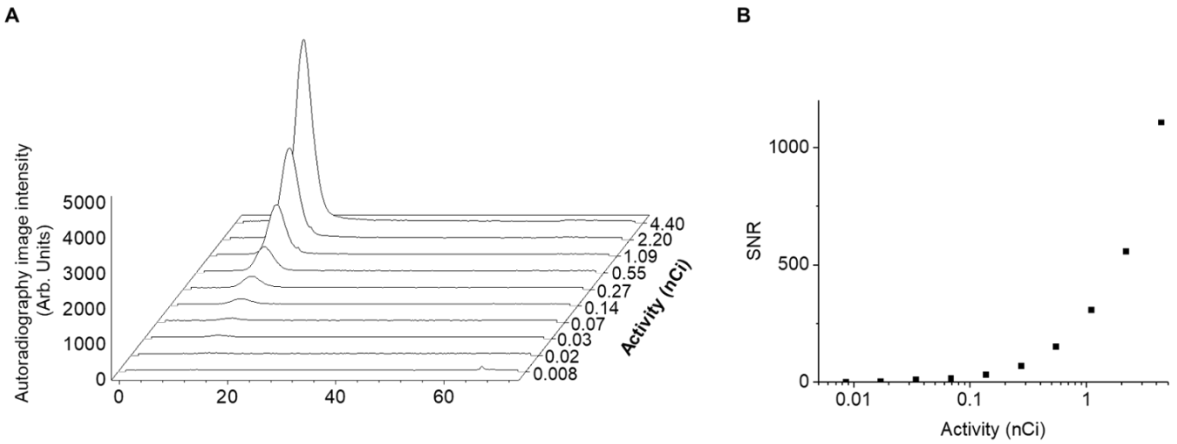

Figure 9-8. TLC analysis for the LOD and LOQ determination of [^{18}F]FEPPA.
(A) TLC chromatograms were computed from lanes of autoradiography images of developed TLC plates where each lane was spotted with 200 µL of a different concentration of purified [^{18}F]FEPPA in saline. (B) Computed signal-to-noise ratio (SNR) as a function of activity level.

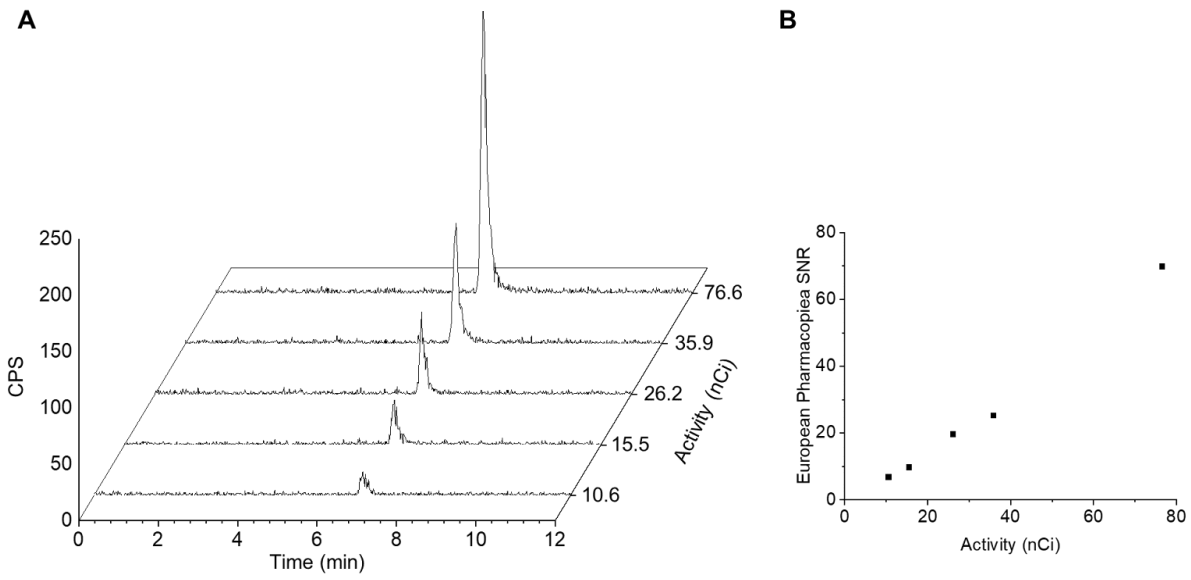

Figure 9-9. HPLC analysis for the LOD and LOQ determination of [^{18}F]FEPPA.
(A) HPLC radio-chromatograms for injections of different concentrations of purified [^{18}F]FEPPA (each sample 200 µL in saline). (B) Computed signal-to-noise ratio (SNR) as a function of activity level.

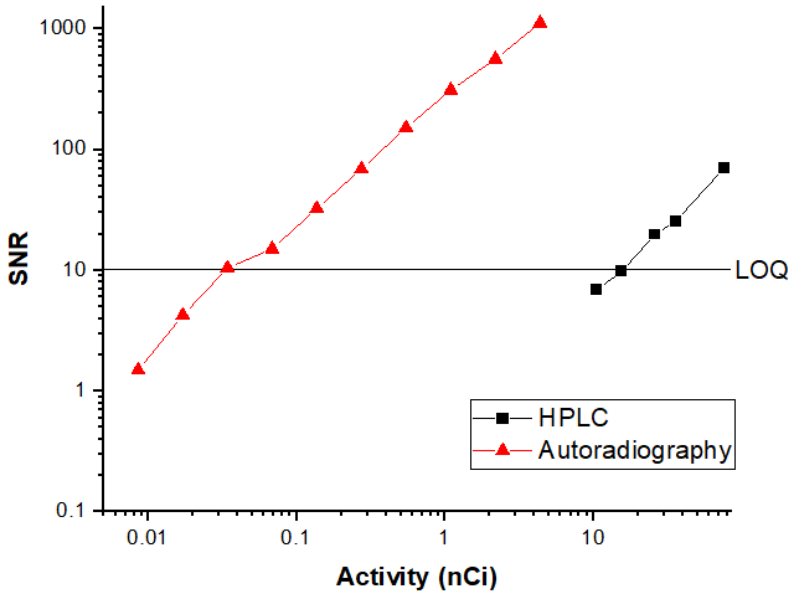

Figure 9-10. Comparison of signal-to-noise ratio (SNR) of TLC and HPLC methods.

9.6.5 Assessment of red blood cell (RBC) binding of [^{18}F]FEPPA

9.6.5.1 Ex vivo spiking of blood with formulated [^{18}F]FEPPA

To 50 µL (mouse) or 100 µL (rat or human) blood, formulated [^{18}F]FEPPA was spiked (mouse: 8 µL (90,000 CPM); rat, human: 16 µL (180,000 CPM)) in an Eppendorf tube (2 mL, DNA LoBind). Blood samples were incubated for different amounts of time (1, 10, 30, and 60 min) at 37 °C using a water bath. At the end of the incubation period, samples were quenched by adding heparin (1000 USP/mL; mouse: 15 µL; rat, human: 30 µL) and transferred to ice for further processing. All samples were centrifuged at 3,000 x g for 10 min in a cooled centrifuge (4 °C). The supernatant plasma of each sample was collected and transferred to a separate Eppendorf tube. Gamma counting of the blood pellet and plasma was performed, and the plasma:blood ratio was computed as the total activity of the plasma (not protein depleted) to the initial activity measured in blood. Data is summarized in **Figure 9-11**. After incubation, samples were also subjected to TLC analysis, but all samples showed ~100% intact [^{18}F]FEPPA.

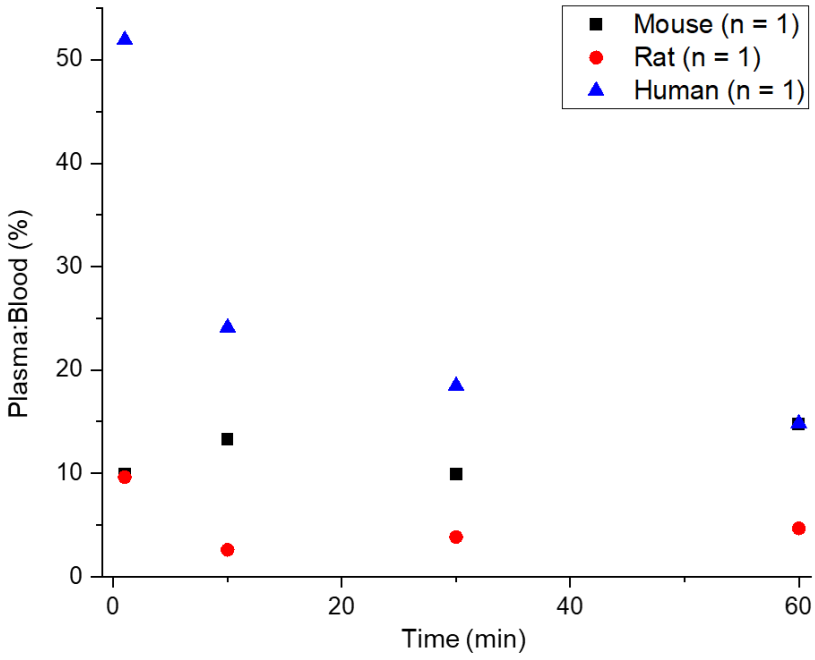

Figure 9-11. RBC binding was assessed after incubating [^{18}F]FEPPA with blood samples *ex vivo*.

9.6.5.2 In vivo analysis of RBC binding of [^{18}F]FEPPA

The degree of RBC binding was also assessed from the processed and analyzed blood samples from the in vivo studies in rats and humans described in **Sections 9.3.2-9.3.3**. Plasma:blood ratio (%) was calculated for each timepoint and averaged across the rat studies and human studies (**Figure 9-12**).

Interestingly, the degree of RBC binding differs between ex vivo and in vivo studies. In the ex vivo studies, rat blood shows high RBC binding, which, over time, differs slightly. However, in the case of the in vivo studies, the RBC binding in rats changes as a function of time, likely due to the metabolism of the [^{18}F]FEPPA. Ex vivo incubation studies of [^{18}F]FEPPA with human blood showed increased RBC binding over time. In vivo, this binding to RBC differs, possibly due to binding to peripheral targets in the body.

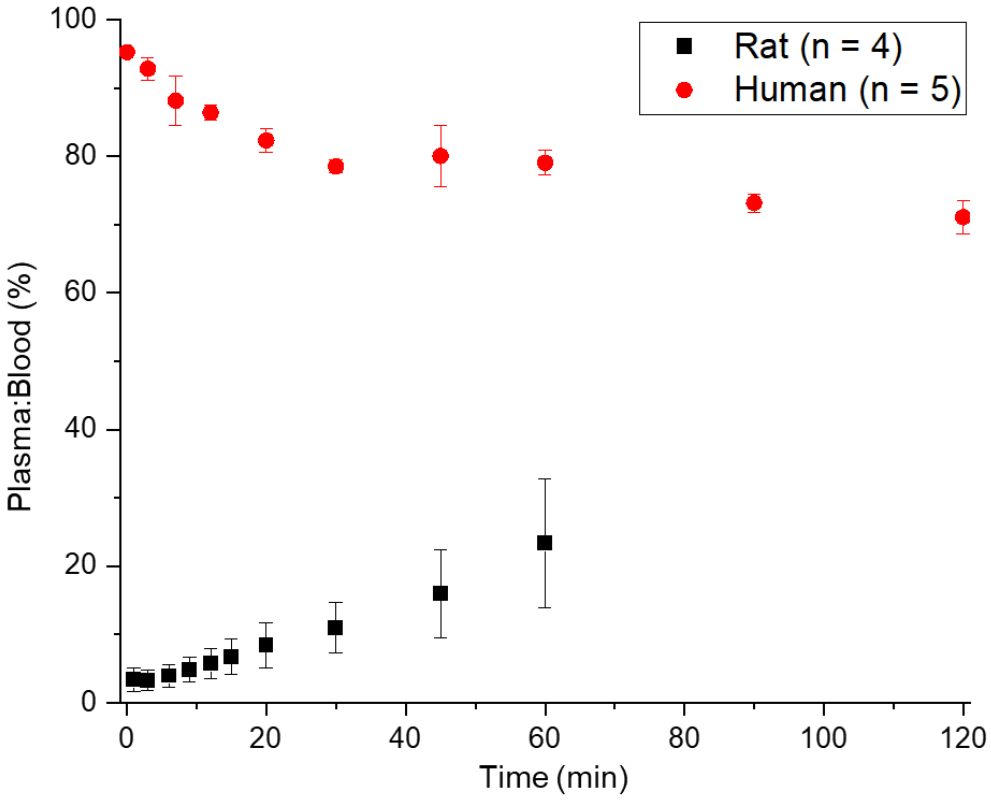

Figure 9-12. RBC binding was assessed in vivo in blood samples taken at different time points after administration of [^{18}F]FEPPA.

9.6.6 Determining the compatibility of the TLC method with SPE

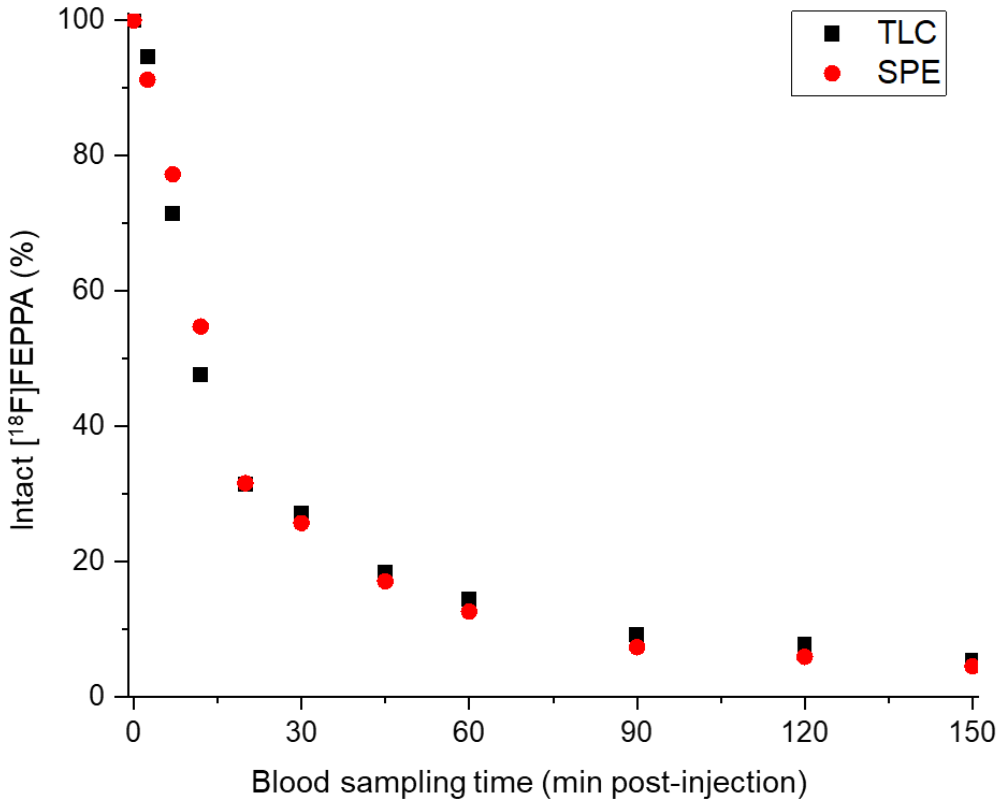

Figure 9-13. Example comparison of analysis of intact [^{18}F]FEPPA fraction from a single patient between the optimized TLC and SPE methods. All samples were divided and analyzed by the TLC and SPE methods.

Chapter 10: Electrochemical flash fluorination and radiofluorination

10.1 Introduction

Fluorinated organic compounds have distinguishing physical, biological and chemical properties with a wide range of applications in fields such as agrochemicals, pharmaceuticals and materials science.[331–333] Recently, there has been growing interest in the chemistry and properties of fluorinated organic compounds.[333–335] Fluorine gas and anhydrous HF have been broadly used for fluorination of organic compounds.[336–338] However, these chemicals are costly, highly reactive, corrosive, hazardous, and difficult to handle. There is a consensus in the community that given the wide-ranging applications of fluorine in design of bioactive molecules and molecular imaging through positron emission tomography (PET), there is still a strong demand for further development of new synthetic methodologies to expand the chemist's toolbox for easier access to a broader scope of fluorinated and radiochemical compounds.[339] There have been significant recent developments in the area of nucleophilic fluorination, a more accessible form of fluorination, and their application to radiochemistry with [^{18}F]fluoride, such as syn-thesis of aryl fluorides directly from the corresponding phenols,[340] hypervalent iodine reagents used as fluorine sources in fluorocyclization reactions,[341,342] radiofluorination of diaryl-iodonium salts and Cu-catalyzed mesityl-aryl-iodonium precursors,[343] metal-catalyzed aryl fluoride bond formation,[344] and recent reviews on these advances and their limitations.[345] Despite the development of modern fluorination techniques, many challenges still exist in terms of limited substrate scope, lack of functional group tolerance, difficulty in synthesizing the precursors and their stability, and the need for strict control of synthesis conditions. No one technique can address all the challenges for site specific fluorination. The electro-chemical approach to fluorination of stabilized cations presents a unique method for direct and very rapid fluorination in one step under mild conditions. The

method described here can target moieties such as thioethers not amenable to late-stage fluorination with existing methodologies, allowing their radio-fluorination for PET tracer development. Electrochemistry is gaining renewed prominence as a versatile tool in organic synthesis.[346,347] Electrochemical fluorination of organic compounds can be a powerful alternative technique for direct fluorination. Electrochemical oxidation can create an electron-poor carbon, potentially without the need for chemical modification, preparing the organic molecules for nucleophilic fluorination.[348,349] Fluorine atoms can be added to organic compounds in one step under mild conditions using electrochemistry, even for electron rich moieties such as aromatic and heteroaromatic rings, without the need to have leaving groups.[350,351] Traditionally, the oxidative formation of a carbocation intermediate in electroorganic synthesis has been performed in the presence of an excess of nucleophile due to the instability of the carbocations. The presence of reactive and low oxidation potential nucleophiles and products in the anodic chamber during electrolysis can limit reaction yields and scope. To overcome this problem Yoshida and co-workers developed the cation pool method, with which they could stabilize the carbocations formed during the electrochemical oxidation of carbamates by performing the electrochemical oxidation at low temperatures (-72 ˚C) followed by addition of nucleophiles such as allylsilanes post electrolysis.[352] Subsequently, the same group reported thiofluorination of alkenes and alkynes using low-temperature anodic oxidation of ArSSAr in Bu_4NBF_4/CH_2Cl_2.[353] In their process, the counter anion of the supporting electrolyte (BF_4^-), which was present during the electrolysis was also the source of fluoride. Here, for the first time, the electrochemical fluorination and radiofluorination of organic molecules using the cation pool technique is reported, where the fluoride is added post electrolysis. This approach enables the use of the cation pool method for the widely useful application of rapid and late-stage fluorination and radiochemistry. The cation pool method has tremendous potential especially for radiofluorination experiments. The excess concentration of reactive cations can provide an efficient reaction mechanism for late-stage fluorination under low fluoride concentrations encountered during radio-fluorination.[354]

Furthermore, radiochemical yield, which is reduced by decay of the radioisotope, can benefit from a rapid late-stage fluorination reaction. The cation pool can be prepared prior to cyclotron production of [^{18}F]fluoride isotope, thereby, providing a truly late-stage fluorination reaction, maximizing radiochemical yield by minimizing decay through a flash reaction of the previously prepared cations with [^{18}F]fluoride.

10.2 Materials and methods

10.2.1 Materials

2,2,2-trifluoroethanol (TFE, 99.9%, $C_2H_3F_3O$), trifluoromethanesulfonic acid (triflic acid, CF_3SO_3H, 99%), methyl (ethylthio)acetate (99%, $C_5H_{10}O_2S$) and methyl(phenylthio)acetate ($C_9H_{10}O_2S$, 99%) were purchased from Oakwood Chemical. Acetonitrile (ACN, anhydrous, 98%), tetrabutylammonium fluoride solution 1.0 M in THF (TBAF solution, ~5 wt% water), cesium fluoride (99%, CsF), Potassium fluoride (≥99.9%, KF), triethylamine trihydrofluoride (98%, (C2H5)3N·3HF) and platinum wire (99.9%) were purchased from Sigma-Aldrich. Tetrabutylammonium perchlorate (TBAP, >98.0%, $C_{16}H_{36}ClNO_4$) methyl (methylthio)acetate (>99.0%, $C_4H_8O_2S$), tetrabutylammonium tetrafluoroborate (>98.0%, $C_{16}H_{36}BF_4N$) and ptoluenesulfonic acid (>98.0%, $C_7H_8O_3S{\cdot}H_2O$) were purchased from TCI America. 2,6-Di-Tertbutyl-4-methylpyridine (98%, $C_{14}H_{23}N$) was purchased from Ark Pharm, Inc. Nafion® membrane N117, 7 mils (178 µm thickness) was purchased from Fuel Cell Earth. Analytical grade (AG) MP1M anion exchange resin was purchased from Bio-Rad.

10.2.2 Methods

In this study, a divided electrochemical cell was used for electrolysis. The anodic and cathodic chambers were separated by a Nafion membrane. Methyl (phenylthio) acetate (12 mM) was used as substrate and 2,2,2-trifluoroethanol (TFE) as solvent with different supporting electrolytes in the anodic chamber. TFE, tetrabutylammonium perchlorate (TBAP) and triflic acid were used in the cathodic chamber. 1,1,1,3,3,3-Hexafluoroiso-propanol (HFIP) has also recently been reported

as a solvent for electroorganic synthesis with a stabilizing effect on carbocation intermediates.[355–358] However, yields were negligible due to instability of fluorinated products reported here in HFIP. Previous reports on electrochemical fluorination of Methyl(phenylthio) acetate guided our choice for the substrate.[355,359] Traditional fluorination of sulfoxides have been based on fluoro-Pummerer rearrangement with DAST, electrophilic fluorination of thioethers and the combinations of chemical oxidants with nucleophilic fluorinating reagents.[360] Previous electro-chemical fluorination of thioethers were performed with excess amounts of HF salts or TBAF present in the cell during electrolysis, resulting in low fluoride conversion yield and preventing no-carrier-added fluorination.[350,361,362].

10.2.3 Results and discussion

Here, electrochemical oxidation was performed for 60 min at a constant potential of 1.6 V vs Ag wire quasi-reference electrode followed by addition of a fluoride nucleophile to the anodic chamber at the end of electrochemical oxidation. The mixture was stirred and allowed to react for 30 min while the temperature was rising to room temperature. With 168 mM of CsF, KF, Et_3Nx3HF and tetrabutylammonium fluoride (TBAF) used as fluoride (nucleophile) sources, respective yields of 4.5%,1.4%, 4% and 4.5% of methyl 2-fluoro-2-(phenylthio) acetate were obtained. The yields were quantified using gas chromatography mass spectrometry (GC-MS). **Figure 10-1** shows the schematic of the reaction and representative GC-MS chromatograms can be found in the supporting information.

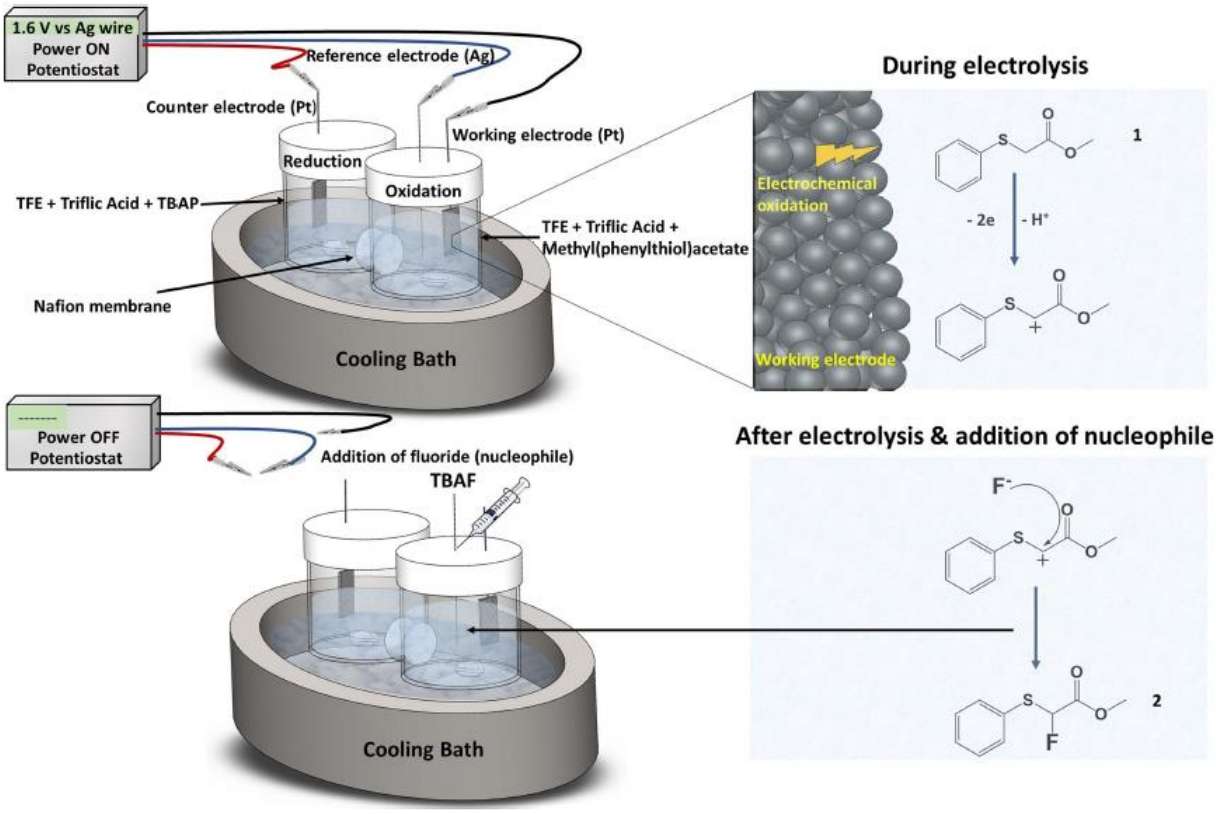

Figure 10-1. Schematic of the cation pool method for fluorination of methyl-2-(phenylthiol) acetate.

Electrolysis was repeated with TBAF at different temperatures of 21 ˚C, 0 ˚C, -20 ˚C and -40 ˚C and chemical yields of 2.2%, 4%, 6% and 3% were obtained respectively. The drop in the yield from -20 ˚C to -40 ˚C is due to the low oxidation current resulting in the slowing of precursor oxidation. 68% of the precursor was consumed when oxidation was performed at -20 ˚C, while only 12% of the precursor was consumed at -40 ˚C. -20 ˚C was chosen as the optimum temperature for further optimization. The effect of changes in supporting electrolyte on the chemical yield is shown in **Table 10-1.**

Table 10-1. Effect of supporting electrolyte on the chemical yield of 2. Electrolysis was carried out using 12 mM of 1 in TFE for 60 min at 1.6 V vs Ag wire at -20 °C followed by addition of 168 mM of TBAF post electrolysis.

Supporting electrolyte	Yield (%)
50 mM Tetrabutylammonium perchlorate (TBAP)	0
300 mM Tetrabutylammonium perchlorate (TBAP)	0
300 mM Tetrabutylammonium perchlorate + 14.2 mM triflic acid	6.0
300 mM Tetrabutylammonium tetrafluoroborate + 14.2 mM triflic acid	1.3
300 mM p-Toluenesulfonic acid + 14.2 mM triflic acid	2.0
142 mM triflic acid	12.5

It can be seen from Table 1 that TBAP alone results in negligible product formation, while addition of 14.2 mM of triflic acid increases the yield to 6%. The highest yield of 12.5% was obtained where only 142 mM of triflic acid was used without addition of salts as supporting electrolyte.

Further optimization was performed using only triflic acid as supporting electrolyte and the effect of triflic acid concentration on the yield was examined. Yields of 3.6%, 12.5% and 0% was obtained when 71 mM, 142 mM and 284 mM of triflic acid were used, respectively. The effect of precursor concentration on the product yield is presented in **Table 10-2**.

Table 10-2. Effect of precursor 1 concentration on the chemical yield of product 2. Electrolysis was carried out using precursor 1, and 142 mM of triflic acid in TFE for 60 min at 1.6 V vs Ag wire at -20 °C. 168 mM TBAF was added at the of electrochemical oxidation.

Precursor concentration (mM)	Yield (%) (n=3)
0.5	8.5±0.9
1	9.6±1.0
2	11.5±1.2
4	10.6±1.1
6	12.7±1.4
12	11.2±1.3
24	9.2±1.0

Precursor concentration changes from 0.5 mM to 24 mM resulted in only a moderate change in the yield. Due to the diminishing [^{18}F]TBAF concentration during no-carrier-added

radiochemistry experiments, the effect of lowering of TBAF concentration and ratio of TBAF to triflic acid concentration were also investigated and the results are shown in Table 10-3.

Table 10-3. Effect of TBAF concentration and TBAF concentration/tiflic acid concentration ratio on the chemical yield of product *2*. Electrolysis was carried out using 12 mM of 1 and triflic acid in TFE for 60 min at 1.6 V vs Ag wire at -20 °C. The values marked with an asterisk in the second column reflect experiments where triflic acid concentration was kept constant at 142 mM.

TBAF concentration [mM]	TBAF concentration/triflic acid concentration	Yield (%)
21	1.18	1.6
	0.15*	0.0
42	1.18	3.8
	0.30*	0.0
84	1.18	4.0
	0.60*	0.0
168	1.18*	12.5
	0.60	0.0
	2.36	3.6

It was observed that by lowering the TBAF concentration the product yield decreased to 1.5% when 21 mM of TBAF was used. It was further observed that the ratio of TBAF to triflic acid concentration plays a crucial role with optimum product yield obtained when this ratio is maintained at 1.18. This may be due to the instability of product at low pH where TBAF addition can act as a base to increase the pH of the solution.

Using the optimized parameters, radiofluorination of 1 was performed with the cation pool method with 142 mM of triflic acid and 24 mM of 1in TFE in the anodic chamber. Radio-chemical fluorination efficiencies (RCFEs) were calculated based on conversion of [^{18}F]fluoride to product 2. Initially [^{18}F]fluoride in the form of [^{18}F]TBAF was added to the anodic chamber after60 min of electrolysis, however no radio-fluorinated product was observed. Due to the diminishing TBAF concentrations in the radiochemistry experiment, addition of a non-nucleophilic base was necessary to increase the pH to 3, at which point the product was observed to be stable. To

address this challenge,5 mCi of [^{18}F]fluoride was mixed with 300 mM of 2,6-di-tert-butyl-4-methylpyridine and the mixture was added to the anodic chamber after electrolysis resulting in RCFE of 5.7±1.0% (n=3) and molar activity of 1.13±0.2 Ci/mM (n=3).Similar to cold experiments with [^{19}F]-TBAF, samples for characterization were taken 30 min after [^{18}F]fluoride addition. Notably, RCFE of 4.8±0.6% (n=3) was obtained after just 5 min post [^{18}F]fluoride addition. Successful radiofluorination of methyl 2-(methylthio) acetate and methyl 2-(ethylthio) acetate were performed using cation pool technique with same condition as above, the RCFE of 20.6±2.0% and 18.2±1.5% were obtained, respectively **Figure 10-2**.

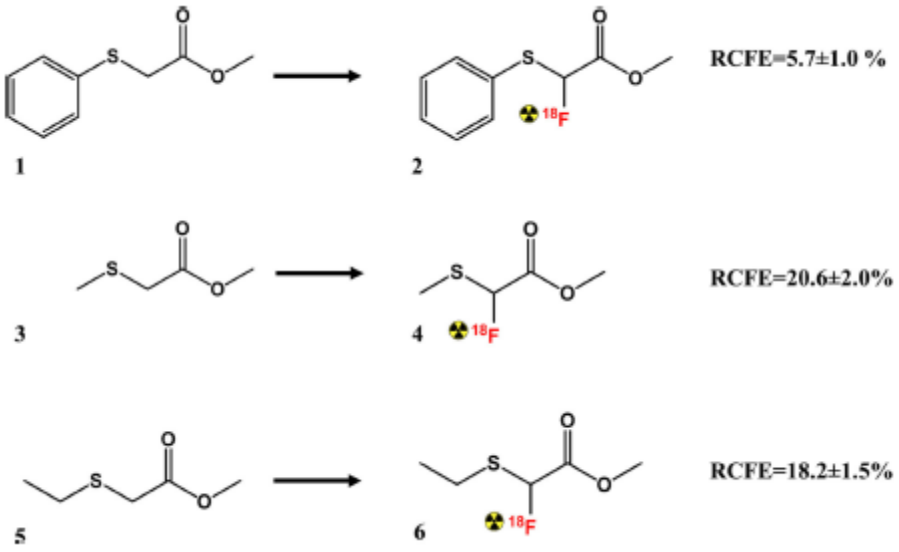

Figure 10-2. Schematic of the radiofluorination reactions.

10.3 Conclusion

In Summary, this report demonstrates a new tool for rapid late-stage fluorination and radiofluorination using the cation pool method. This is made possible through generation and pooling of stable cations under low temperature using TFE as solvent, and the subsequent fluorination reaction of carbocations with fluoride under non-oxidative conditions. Cation pool fluorination prevents further oxidation of the fluorinated product during the electrolysis and rapid late-stage radio-fluorination can minimize the losses of [^{18}F]fluoride due to radioactive decay. More in-depth studies of scope and the use of microfluidic platforms are currently in progress to

increase yields and introduce automation. Flash fluorination and radio-fluorination based on the cation pool method can be used to produce PET radiotracers and fluorinated pharmaceuticals, potentially expanding the library of fluorinated bioactive molecules available for medicinal chemistry and molecular imaging.

10.4 Appendix

10.4.1 Electrochemical synthesis

The electrochemical oxidation (the cation pool formation) and cyclic voltammetry (CV) were performed using an H shape divided 3-electrode cell with two platinum wires (length = 200 mm, diameter = 0.33 mm) as working and counter electrodes and Ag wire as quasi-reference electrode. The cathodic chamber and anodic chamber were separated by a nafion membrane. The anodic chamber contained 10 ml of TFE as solvent, methyl(phenylthio)acetate (precursor) and different supporting electrolytes such as triflic acid, tetrabutylammonium perchlorate, tetrabutylammonium tetrafluoroborate and p-toluenesulfonic acid. The cathodic chamber contained 10 ml of TFE as solvent, 300 mM tetrabutylammonium perchlorate and 757 mM of triflic acid. The reference electrode (Ag wire) was immersed in the anodic reaction mixture. The counter electrode and working electrode were cleaned before each experiment using potential cycling in 1 M sulfuric acid solution in water. The electrodes were cycled between −2 V and 2 V (2 electrode configuration) 10 times before each experiment. The electrochemical oxidation of methyl(phenylthio)acetate (carbocations formation) was performed at constant potential of 1.6 V vs Ag wire for 60 min. At the end of electrolysis, the nucleophile (TBAF) was added to the anodic chamber and allowed to react for 30 min while the reaction mixture was stirred using a magnetic stirring bar at 500 RPM and temperature was rising to the room temperature. The CVs and electrochemical oxidation experiments were performed using the Metrohm PGSTAT128N electrochemical workstation. The CVs were performed using a 200 mV/s scan rate and no stirring. **Figure 10-3** shows the CV of background (TFE + supporting electrolyte in the anodic chamber)

and CV of the cation pool reaction mixture (methyl(phenylthio)acetate + TFE + supporting electrolyte in the anodic chamber).

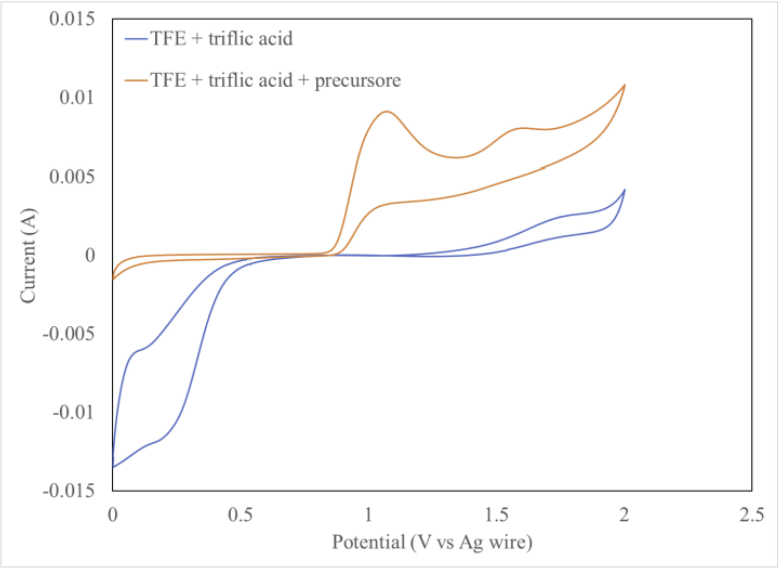

Figure 10-3. CVs of TFE and triflic acid with and without precursor (background). The CVs were run with 200 mv.s−1 scan rate at room temperature (21 °C) using a divided cell and no stirring.

It can be seen from figure A3.5.1 that the oxidation of precursor starts at 0.9 V vs Ag wire and reaches a peak at 1.08 V vs Ag wire due to the diffusion limit. The CV of the background shows very small anodic currents up to 1.5 V vs Ag wire; by increasing the potential further the background anodic current starts to increase to higher values. It also can be seen that adding the precursor to the solution can suppress the cathodic currents at potentials lower than 0.5 V vs Ag wire.

10.4.2 Gas chromatography-mass spectrometry (GC-MS) spectra

The product identification and quantification was performed using GC-MS. Mass spectra and chromatograms were carried out using an Agilent 5975C Triple-Axis Detector (TAD) inert MSD mass spectrometer coupled with an Agilent 7890A gas chromatograph. The mass spectrum was set to electron ionization mode with a voltage of 1.9 kV. The mass range was 50-250 (amu). The details of gas chromatograph's column and the method are outlined below: Inlet was set at 120 °C and had 1:10 split ratio. Oven was set to 120 °C and held for 1 min, then increased to 138 °C

at a rate of 1 °C/min and held for 15 mins. Column was Agilent 122-5532, maximum operating temperature 325 °C; 30 m length, 250 µm internal diameter and 0.25 µm film thickness. A constant flow of 1 mL/min was delivered to the transfer column. The transfer column Agilent G3185-60062, 450 °C; 0.17 m length, 100 µm internal diameter and 0 µm film thickness delivered a constant flow of 1.5 mL/min to the source. The GC-MS method had a 10 min solvent delay in order to enhance the MS filament lifetime. **Figure 10-4** is the GC-MS calibration plot used in the quantification of product 2 yield.

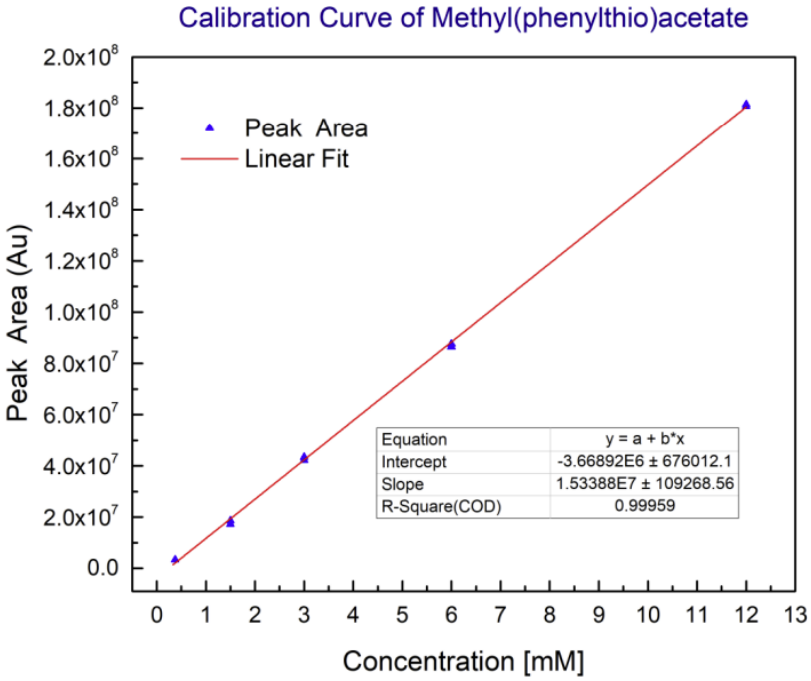

Figure 10-4. The GC calibration plot used in the quantification of formation of product 2.

Figure 10-5, Figure 10-6 and **Figure 10-7** show the GC-MS mass spectra of the products 2, 4 and 6, respectively. **Figure 10-8** shows a representative GC-MS chromatogram of the crude product.

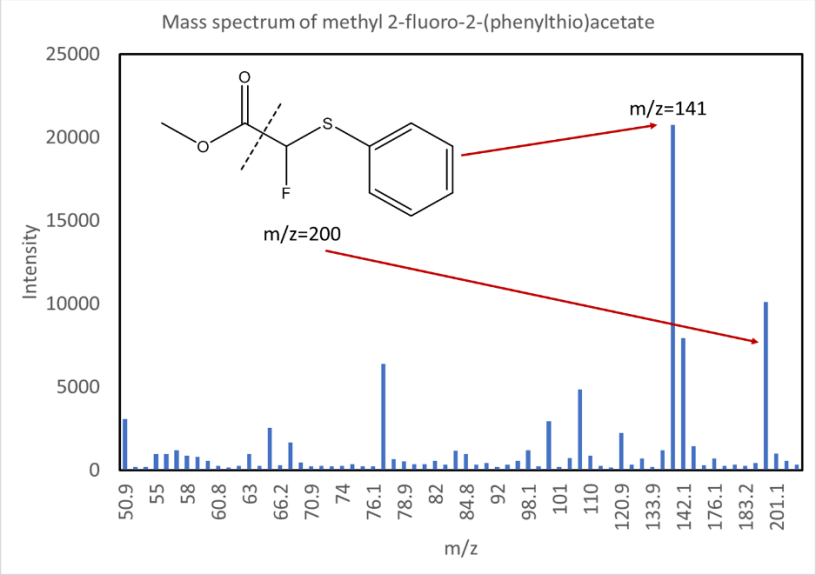

Figure 10-5. Mass spectrum of the product 2.

It can be seen from **Figure 10-8** that after electrolysis, 70% of the precursor has been consumed and no product peak can be observed at 21.7 min. The product is only observed after the injection of TBAF post electrolysis, pointing to the reaction of fluoride anions with stabilized carbocations formed during electrolysis.

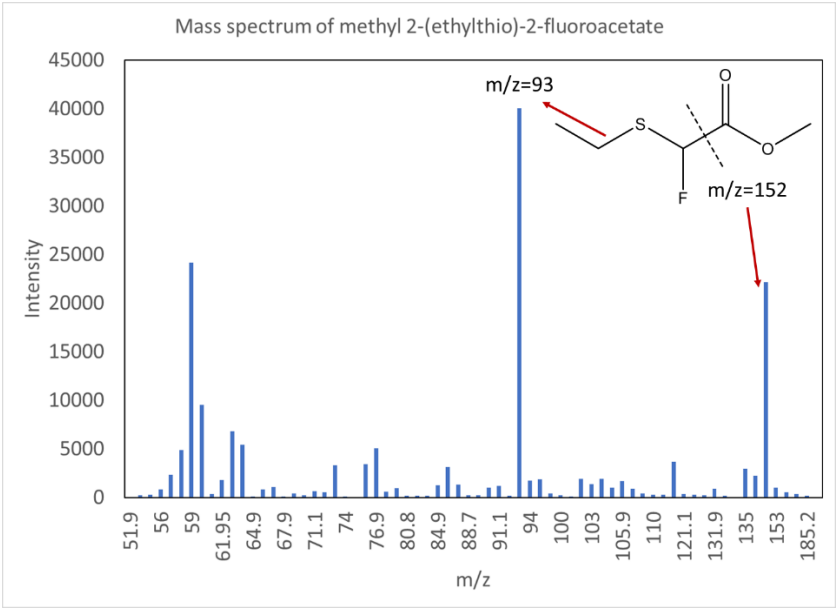

Figure 10-6. Mass Spectrum of product 4.

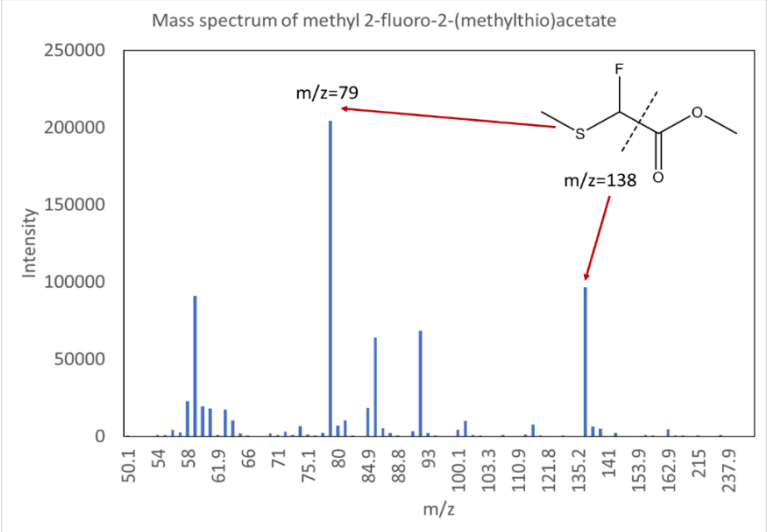

Figure 10-7. Mass spectrum of product 6.

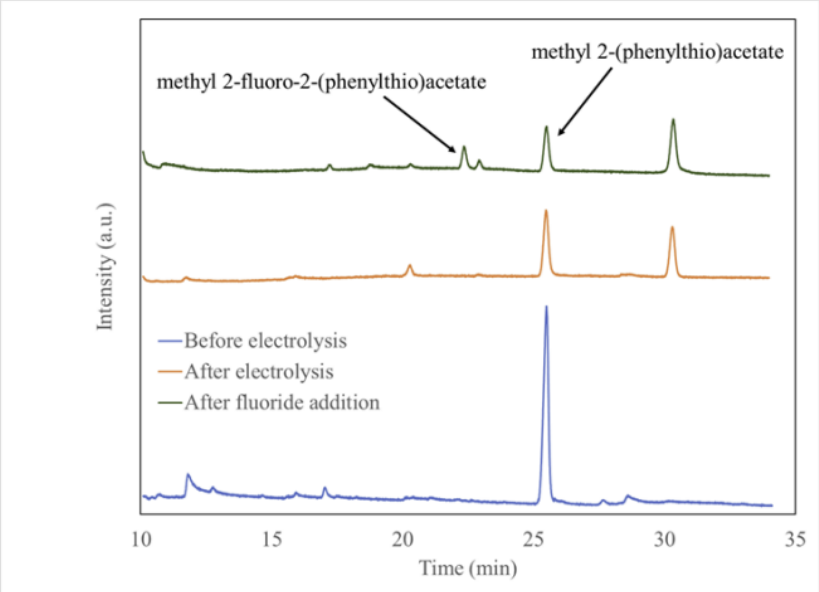

Figure 10-8. GC-MS chromatograms of the crude reaction mixture before and after electrochemical oxidation and after fluoride addition.
Electrolysis was carried out using 12 mM of 1 and 142 mM of triflic acid in TFE for 60 min at 1.6 V vs Ag wire at -20 °C. 168 mM TBAF was added at the end of electrochemical oxidation and allowed to react for 30 min while the reaction mixture was stirring and temperature was rising to the room temperature

10.4.3 Nuclear magnetic resonance (NMR) spectra

^{19}F-Nuclear-Magnetic-Resonance (^{19}F-NMR) was performed on the ^{19}F-fluorinated thioether reference standards. ^{19}F-NMR spectroscopic data were in agreement with previous reports [1-8].

Nuclear magnetic resonance spectroscopy (NMR) The identity of the product 2 was also further

characterized by ^{19}F-NMR. The 19F-NMR spectrum was obtained on a Bruker AV400 (400 MHz). 19F chemical shift is reported in parts per million (ppm) using the trifluoro acetic acid (CF3COOH) as a reference. **Figure 10-9, Figure 10-10** and **Figure 10-11** show the 19FNMR spectra of the products 2, 4 and 6, respectively. 19F-NMR spectroscopic data for products 2 and 6 were in agreement with previous reports.

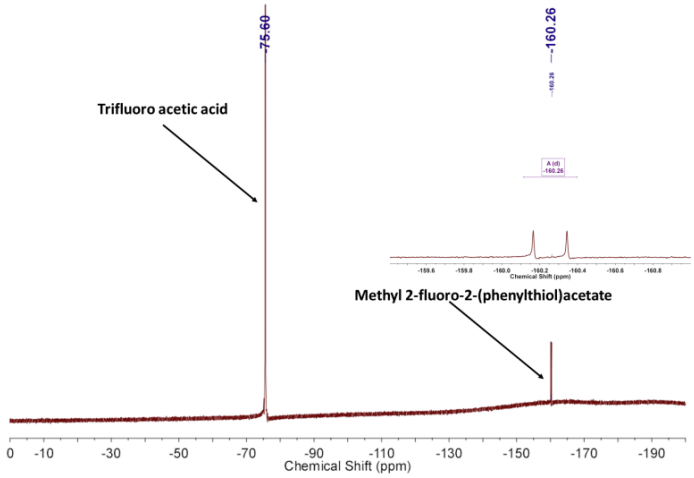

Figure 10-9. The 19F NMR of the HPLC purified product 2 plus trifluoro acetic acid as standard for further identification of the fluorinated product obtained by cation pool method.

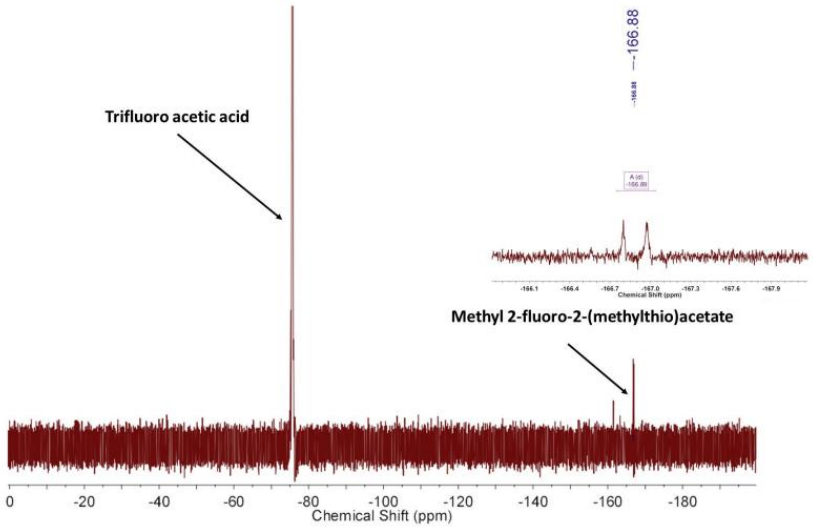

Figure 10-10. The 19F NMR of the HPLC purified product 4 plus trifluoro acetic acid as standard for further identification of the fluorinated product obtained by cation pool method.

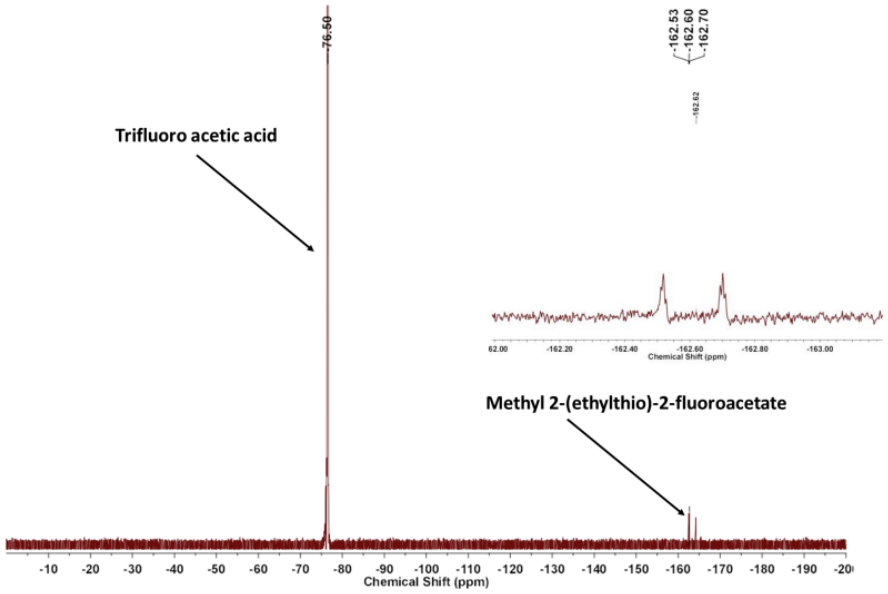

Figure 10-11. The 19F NMR of the HPLC purified product 6 plus trifluoro acetic acid as standard for further identification of the fluorinated product obtained by cation pool method.

10.4.4 Radiochemical characterization

No-carrier-added [^{18}F]-fluoride was produced by the (p,n) reaction of $^{18}O–H_2O$ (84% isotopic purity, Medical Isotopes) in a RDS-112 cyclotron (Siemens) at 11 MeV using a 1 mL tantalum target with havar foil. The radioactive isotope was trapped on analytical grade (AG) MP-1M anion exchange resin by passing through the 1 ml of bombarded $^{18}O–H_2O$. Most of the water on the resin was removed by washing with 10 mL of anhydrous ACN and drying with ultra-pure N2 for 10 min. [^{18}F]fluoride was subsequently eluted out from the cartridge with a 2 ml TFE containing 25 mM TBAP salt. In a typical experiment, approximately 5 mCi was eluted from the anion exchange cartridge in [^{18}F]-TBAF form in TFE. Radiofluorination conversion was measured using Radio-thinlayer-chromatography (radio-TLC). Radio-TLC was performed on silica plates (TLC Silica gel 60 W F254s, Merck). After dropping a sample volume (~1–5 µL) using a glass capillary, the plate was developed in the mobile phase (ACN). Chromatograms were obtained using a radio-TLC scanner (miniGita Star, Raytest). Analytical High Performance Liquid Chromatography (HPLC), equipped with a UV and gamma detector was used to determine radiochemical purity (RCP) of the radio-fluorinated product. HPLC was performed using a 1200 Series HPLC system

(Agilent Technologies) equipped with a GabiStar flow-through gamma detector (Raytest). Data acquisition and processing was performed using GINA Star Software version 5.9 Service Pack 17 (Raytest). Typically, 20 µL of radioactive sample was diluted with 180 µL of ACN and 5–20 µL of this solution was injected for HPLC analysis. Column: Synergy 4u Polar RP 80 A, 250 × 4.6 mm, 4 micron. Gradient: A = ACN; B = water; flow rate = 1.8 mL/min; 0–28 min 95% B to 45% B, 28–29 min 45% B to 5% B, 29–32 min 5% B, 32–34 min 5% B to 95% B. Radio-TLC chromatograms were used to measure radiochemical conversions (RCC). RCP and RCC were measured by dividing the area under the curve (AUC) for the desired product by the sum of AUC for all peaks. The TLC purity accounts for unreacted [^{18}F]-fluoride while the HPLC purity corrects for radiochemical side-products. The radiochemical fluorination efficiency (RCFE) was determined by the equation: RCFE = TLC RCC × HPLC RCP.

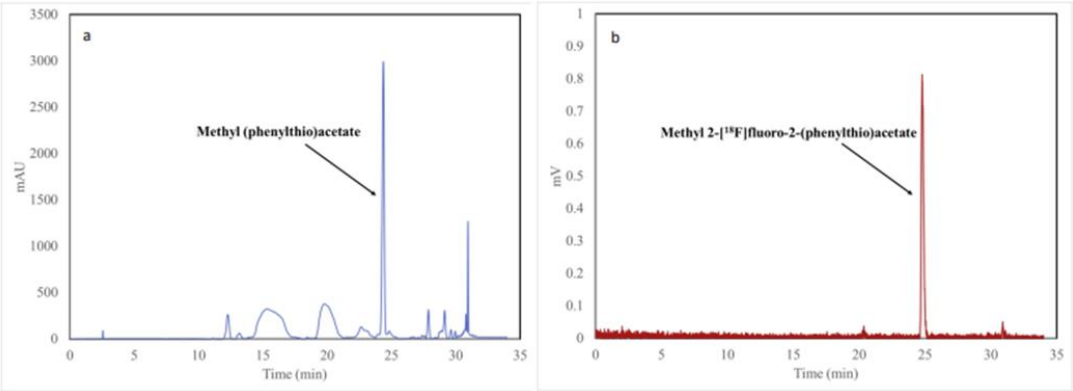

Figure 10-12. Analytical (A) UV HPLC and (B) gamma HPLC profiles of the crude sample after electrolysis.
Electrolysis was performed for 60 min at 1.6 V vs Ag wire at -20 ºC using TFE solution containing 24 mM of product 1, 142 mM of triflic acid. 2 ml of TFE solution containing 25 mM TBAP and 5 mCi [^{18}F]-fluoride was added after electrolysis was finished and the sample was taken for analysis 30 min after [^{18}F]-fluoride addition.

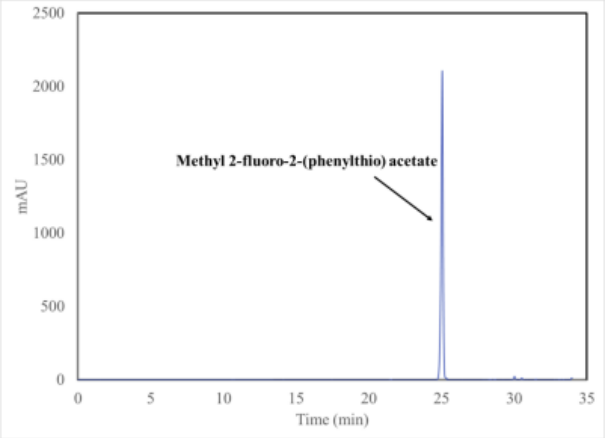

Figure 10-13. UV HPLC profile of purified product.
Electrolysis was performed for 60 min at 1.6 V vs Ag wire at -20 ºC using TFE solution containing 24 mM of product 1, 142 mM of triflic acid. 2 ml of TBAF solution was added after electrolysis was finished and the sample was HPLC purified 30 min after TBAF addition.

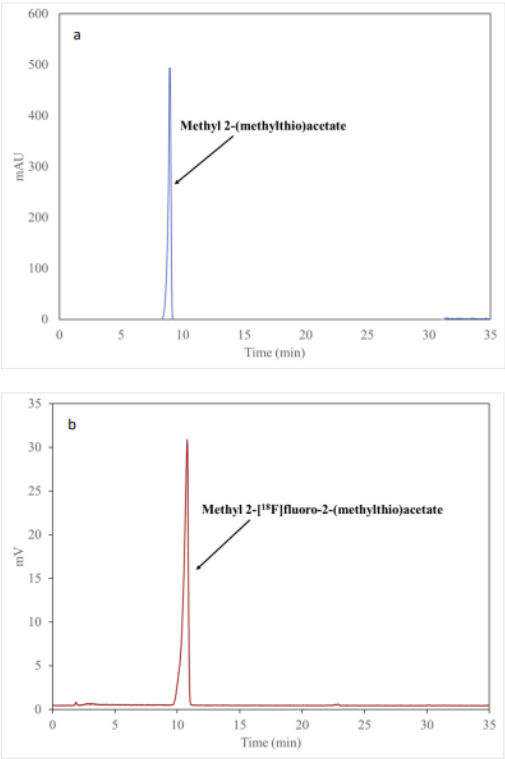

Figure 10-14. Analytical (A) UV HPLC and (B) gamma HPLC profiles of the crude sample after electrolysis.
Electrolysis was performed for 60 min at 1.6 V vs Ag wire at -20 ºC using TFE solution containing 24 mM of product 3, 142 mM of triflic acid. 2 ml of TFE solution containing 25 mM TBAP and 5 mCi 18F-fluoride was added after electrolysis was finished and the sample was taken for analysis 30 min after 18F-fluoride addition.

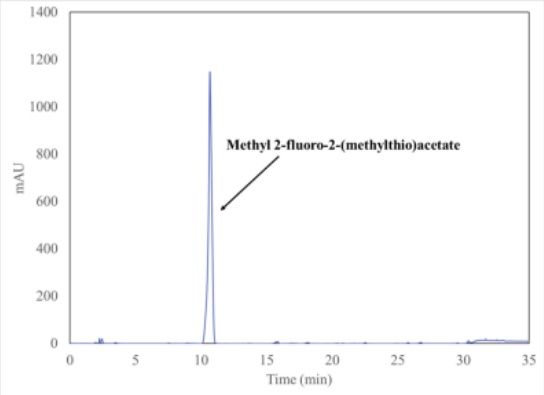

Figure 10-15. UV HPLC profile of purified product.
Electrolysis was performed for 60 min at 1.6 V vs Ag wire at -20 ºC using TFE solution containing 24 mM of product 3, 142 mM of triflic acid. 2 ml of TBAF solution was added after electrolysis was finished and the sample was HPLC purified 30 min after TBAF addition.

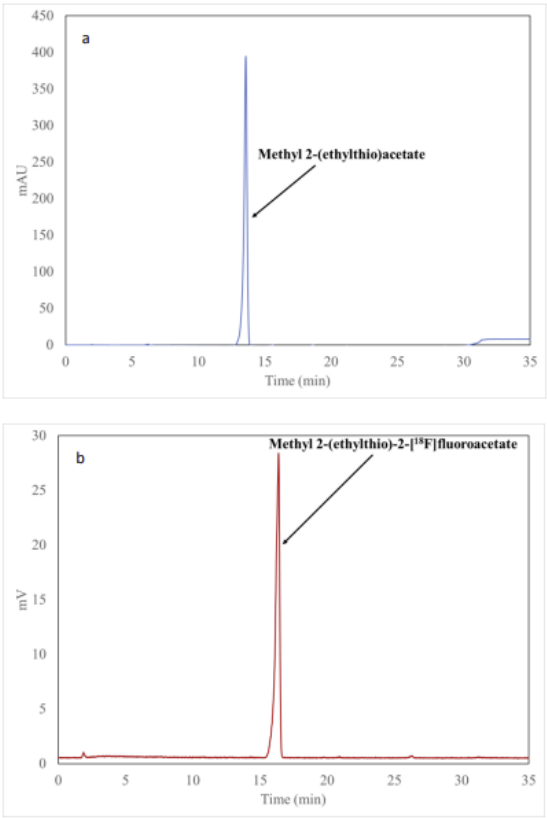

Figure 10-16. Analytical (A) UV HPLC and (B) gamma HPLC profiles of the crude sample after electrolysis.
Electrolysis was performed for 60 min at 1.6 V vs Ag wire at -20 ºC using TFE solution containing 24 mM of product 5, 142 mM of triflic acid. 2 ml of TFE solution containing 25 mM TBAP and 5 mCi [^{18}F]-fluoride was added after electrolysis was finished and the sample was taken for analysis 30 min after [^{18}F]-fluoride addition.

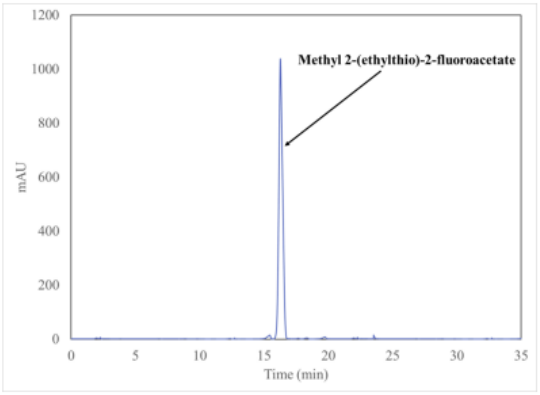

Figure 10-17. UV HPLC profile of purified product.
Electrolysis was performed for 60 min at 1.6 V vs Ag wire at -20 ºC using TFE solution containing 24 mM of product 5, 142 mM of triflic acid. 2 ml of TBAF solution was added after electrolysis was finished and the sample was HPLC purified 30 min after TBAF addition.

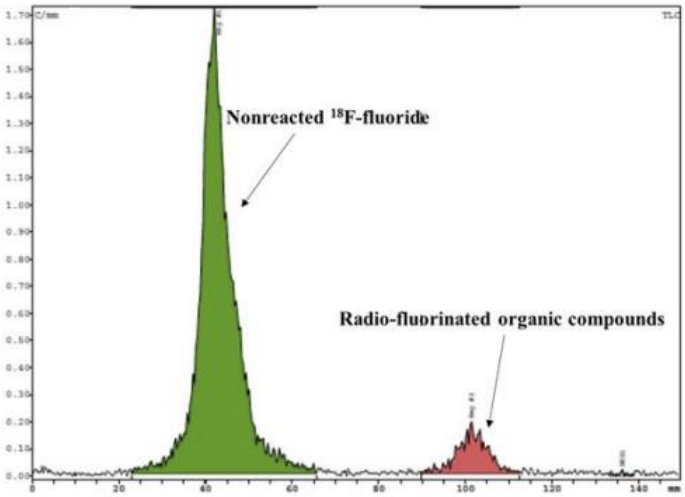

Figure 10-18. Gamma TLC of the crude sample post radio-electrochemical synthesis.
Electrolysis was performed for 60 min at 1.6 V vs Ag wire at -20 ºC using TFE solution containing 24 mM of product 1, 142 mM of triflic acid. 2 ml of TFE solution containing 25 mM TBAP and 5 mCi [^{18}F]-fluoride was added after electrolysis was finished and the sample was taken for analysis 30 min after [^{18}F]fluoride addition.

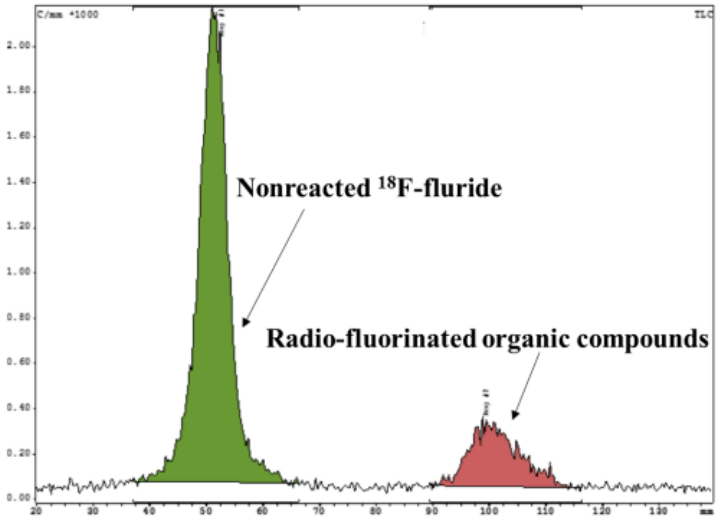

Figure 10-19. Gamma TLC of the crude sample post radio-electrochemical synthesis. Electrolysis was performed for 60 min at 1.6 V vs Ag wire at -20 ºC using TFE solution containing 24 mM of product 3, 142 mM of triflic acid. 2 mL of TFE solution containing 25 mM TBAP and 5 mCi [^{18}F]-fluoride was added after electrolysis was finished and the sample was taken for analysis 30 min after [^{18}F]-fluoride addition.

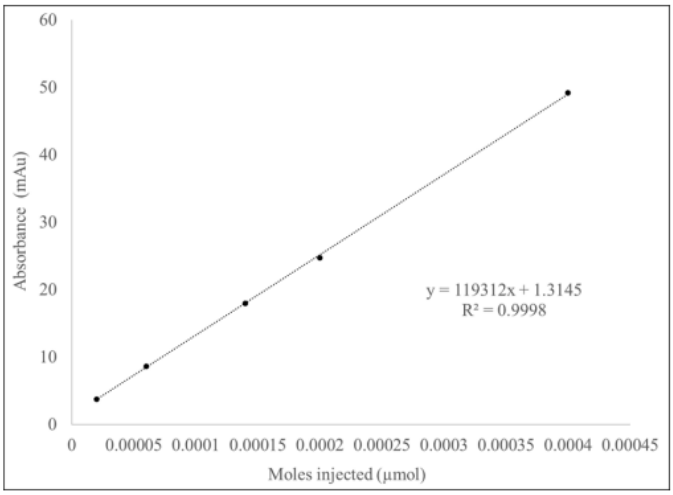

Figure 10-20. Calibration curve of UV absorbance vs. molar mass.

Chapter 11: Electrochemical radiofluorination of thioethers

11.1 Introduction

Positron Emission Tomography (PET) is an established molecular imaging technology widely used for the visualization of biological processes in clinical and research settings[363]. This technology relies on radioactively labeled molecules, called tracers. Fluorine-18 is the most frequently used radionuclide in PET due to its wide availability, physical half-life (t1/2 = 109.8 min), which closely matches biological half-life of many small molecules, and its favorable decay characteristics for imaging. Importantly, [^{18}F]fluoride is routinely produced in a no-carrier-added (NCA) form, that is, without added stable ^{19}F-species. Tracer formulations prepared from NCA [^{18}F]fluoride[364] contain only nanomolar quantities of the physiologically active molecule. This low amount allows for imaging without perturbing the biochemical process under investigation. If ^{19}F-carrier is added for production purposes, product molar activity (Am – amount of radioactivity per mole of product) is decreased and total amount of physiologically active tracer in the final formulation is increased. Low Am formulations can lead to saturation of the biological target under investigation and is suitable for only a handful of applications. Thioethers are attractive scaffolds for PET tracer development yet approaches for their radiolabeling are limited. Examples of biologically relevant thioethers include radiolabeled methionine and cysteine, which are important in elucidating amino acid metabolism in multiple diseases[365–367]. The strongly nucleophilic sulfur atom hinders the use of weakly nucleophilic [^{18}F]fluoride in labeling reactions. Due to this interference, methionine radiolabeling mostly relies on electrophilic agents based on [^{11}C]carbon, a suboptimal choice due to 20 min half-life of this isotope. Despite these limitations, [^{11}C]-methionine has demonstrated significant clinical utility[368], urging further development in this area[369]. Several pharmaceuticals in clinical use contain thioether scaffolds and can be potentially radiolabeled by electrochemical radiofluorination if appropriately protected precursors are

synthesized[368,370]. Among them are nucleotide receptor antagonist Ticagrelor[371], antiretroviral Nelfinavir[372], and a urate transporter inhibitor Lesinurad[373]. Using [^{18}F] fluoride for radiolabeling of thioethers remains an important but elusive target.

11.2 Materials and methods

11.2.1 Materials

Chemicals were purchase from commercial sources and used without further purification. Tetrabutylammonium perchlorate (TBAP, >99%, for electrochemical analysis) was purchased from Fluka. Tetraethylammonium fluoride tetrahydrofluoride (>97%) and Pyridinium pToluenesulphonate (>98%) were purchased from TCI. Methyl 2-(phenylthio)acetate (99%) was purchased from Alfa Aesar. Acetonitrile (ACN, anhydrous, >99.8%) and pToluenesulphonic Acid (99%) were purchased from Agros Organics. Methyl 2-(methylthio)acetate (>98%), 2-(Phenylthiol)acetonitrile (98%), diethyl ((phenylthio)methyl)phosphonate (96%), Dimethoxyethane (DME) (>99%) and Trifluoroethanol (TFE) (>99%) were purchased from Fisher. Trifluoromethanesulfonic acid (Triflic Acid) (99.5%) and Methyl 2-(ethylsulfanyl)acetate (99%) were purchased from Oakwood Chemical. Ethanol (200 proof, anhydrous) was purchased from Decon. 2-(Phenylthiol)acetamide (97%) was purchased from Synthonix. Hexafluoroisopropanol (HFIP) (99%) was purchased from VWR International. All water used was purified to 18MΩ and passed through a 0.1 mm filter. No-carrier-added [18F]fluoride was produced using [18O]H2O (84% isotopic purity, Medical Isotopes) in a RDS-112 cyclotron (Siemens) from a 11 MeV bombardment with a 1 mL tantalum target with havar foil.

11.2.2 Experimental methods

11.2.2.1 Carrier added electrochemical fluorination procedure

The carrier added experiments were performed to produce the ^{19}F-labelled thioether reference standards. Electrolysis was performed at an oxidation potential of 1.9V. The electrochemical solution contained 50 mM thioether precursor, 50 mM TBAP and 100 mM tetraethylammonium

fluoride tetrahydrofluoride. A 30 mL single chamber electrochemical cell was used with 20 mL of solution using ACN as the solvent. An oil bath was used to set the temperature to 70°C. Electrolysis was performed for 60 mins with stirring at 600 rpm using a three-electrode system under a constant potential mode controlled by an Autolab128 potentiostat-galvanostat (Metrohm USA). Alternating pulses were applied to reduce passivation of the electrodes. The oxidation pulse was held for 60 seconds and a reduction pulse of -0.6V for 6 seconds. Platinum wire was used for the working and counter electrodes. Silver wire was used as a pseudo reference electrode.

The crude electrochemical solution after electrolysis was concentrated using a C18 SPE cartridge (Waters). The crude was added to 500 mL of water, stirred and then trapped on the C18 cartridge. 100 mL of water was then passed through the cartridge and dried with N_2 for 10 mins. The organics with the ^{19}F-labelled product were then eluted with 1 mL of ethanol, which was mixed with 1 mL of water. The resulting mixture was transferred into the loading loop of the HPLC followed by water (0.5 mL) and injected onto the HPLC column for purification. This was performed with our previously reported radio-electrochemical fluorination platform HPLC separation subunit. Column: (Phenomenex, Gemini 5u C18 110A, 250 × 10 mm); gradient A = ACN (0.1% TFA); B = water (0.1% TFA); flow rate = 5 mL/min; 0 min 95% B, 0–30 min 95%-40% B. The product containing fraction was collected in ~4–5 mL. The collected fraction was then concentrated using a C18 CPE cartridge by adding 20x volume of water, mixing and then trapping the product on the cartridge. 100 mL of water was then passed through the cartridge and it was dried for 10 mins with N_2. The product standards were then eluted with 1 mL of ethanol. The thioether product standards were identified using GC-MS and NMR as described below. The HPLC retention times of the ^{19}F labelled thioether product standards was used to verify the NCA-ECF ^{18}F labelled products.

11.2.2.2 No-carrier added electrochemical [^{18}F]fluorination procedure

No-carrier-added ^{18}F-fluoride was produced by the (p,n) reaction of $^{18}O–H_2O$ (84% isotopic purity, Medical Isotopes) in a RDS-112 cyclotron (Siemens) at 11 MeV using a 1 mL tantalum target with havar foil. The radioactive isotope was trapped on analytical grade (AG) MP-1M anion exchange resin by passing through the 1 ml of bombarded $^{18}O–H_2O$. The cartridge was built using PEEK tubing with SPE frits (Agilent) on both ends containing 5 mg of the anion exchange resin. The cartridge was dried with a stream of ultra-pure N_2 for 5 mins followed by 3 mL of anhydrous ACN. The cartridge was further dried with a stream of N_2 for 5 mins. ^{18}F-fluoride was subsequently eluted off the cartridge with 1 mL of TFE containing 50 mM Bu_4NClO_4 and used in the electrochemical fluorinations. In a typical experiment, approximately 5 mCi of no-carrier-added ^{18}F-fluoride was eluted from the anion exchange cartridge in ^{18}F-TBAF form in TFE.

The electrochemical reaction cell volume was 1.5 mL. Electrolysis was performed for 30 mins. The solvent used was trifluoroethanol (TFE). No $Et_4NF{\cdot}4HF$ was added. Electrolysis was performed at an oxidation potential of 1.9V with 1.5 mL 50 mM thioether precursor, 50 mM TBAP and in TFE at 70°C for 30 mins and stirring at 600 rpm under a constant – potential mode controlled by an Autolab128 potentiostat-galvanostat (Metrohm USA). The cell used alternating pulses to reduce passivation of the electrodes. The oxidation pulse was held for 60 seconds and cleaning pulse of -0.6V for 6 seconds. Pt was used for the working and counter electrodes. Ag wire was used as a pseudo reference electrode.

11.3 Results and discussion

In this paper we report no-carrier-added electrochemical fluorination (NCA-ECF) of a range of thioethers (**Figure 11-1**).

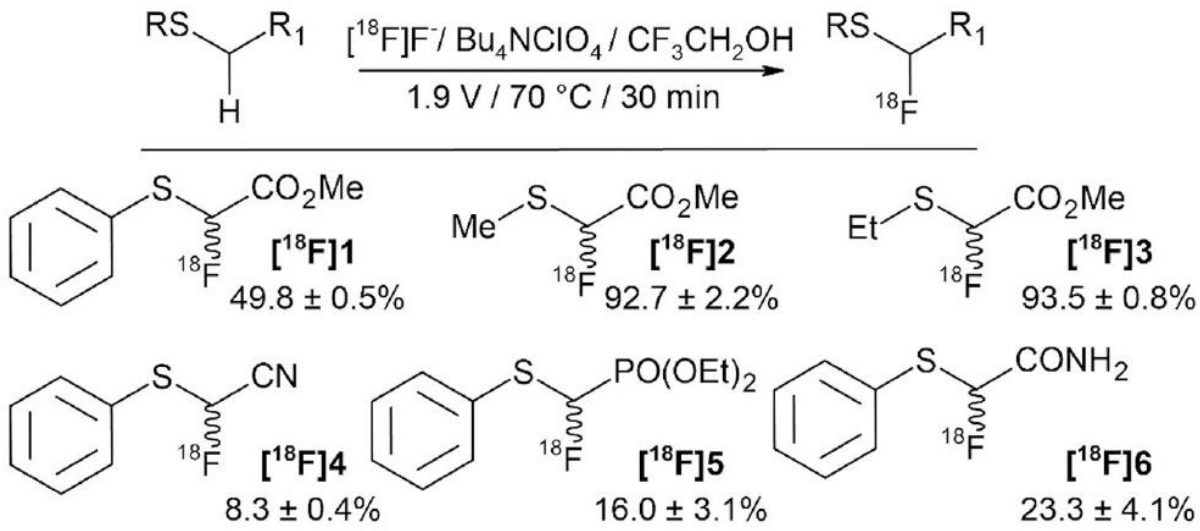

Figure 11-1. Scope of the NCA-ECF. Radiofluorination was performed on platinum electrodes under potentiostatic conditions.
Radiochemical yield is reported as an average of three experiments.

This success is enabled by electrochemical methodology, which to the best of our knowledge, is the first report of electrochemical production of NCA radiotracers in quantities typically used in clinical settings. Outside of radiochemistry, electrochemical methods offer a unique approach to the fluorination of thioethers[348,374–377]. Unfortunately, it relies on excess of (HF)n salts and thus cannot yield NCA products. Fuchigami et al. first proposed a mechanism for the electrochemical fluorination (ECF) of thioethers[378,379] (**Figure 11-2**).

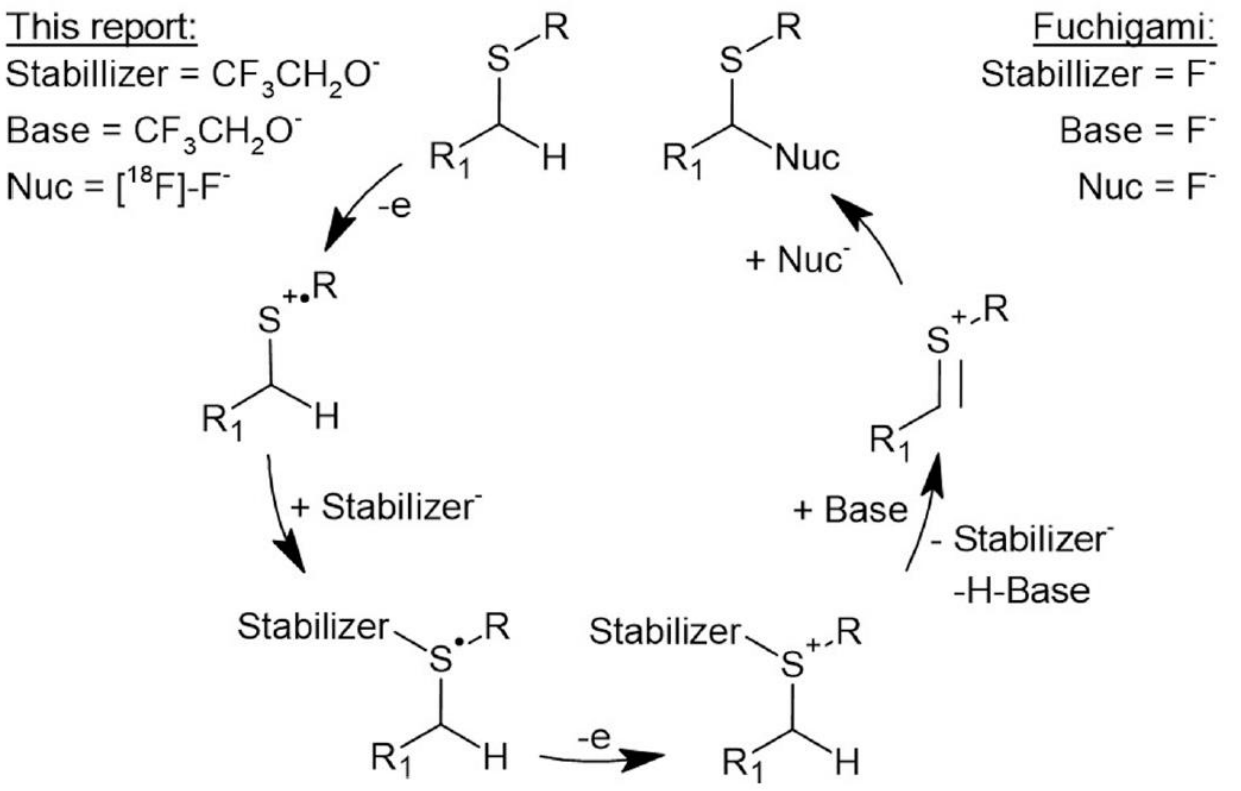

Figure 11-2. Proposed mechanism for the NCA-ECF compared to Fuchigami mechanism.

In this mechanism, fluoride plays a 3-fold role: it stabilizes the radical cation intermediate after first oxidative step, acts as a base in the elimination step and as a nucleophile to produce the α-fluorinated sulfide[380]. There is a clear need for an excess of fluoride for this reaction to proceed in good yields[381]. The use of fluorinating agents that are not HF-based is still very rare[382]. In previous reports, we applied the Fuchigami methodology for the electrochemical 18F-fluorination of a model compound, methyl-2-(phenylthio)acetate[356,358]. Predictably, only low Am product was produced and lowering HF concentration reduced Radiochemical Yield (RCY) without significant gain in Am. We hypothesized that an auxiliary reagent could be used to replace fluoride in two roles that it plays in the Fuchigami mechanism: to stabilize the radical intermediate and to act as Lewis base. This study reports the successful search for a Brønsted acid that plays a role of this auxiliary reagent and facilitates no-carrier-added electrochemical radiofluorination (NCA-ECF). summarizes RCY, [^{18}F]fluoride conversion (Radiochemical Conversion, RCC; assessed with

radio-TLC) and radiochemical purity (RCP; assessed with radio-HPLC) in a series of experiments exploring radiolabelling conditions of methyl(phenylthiol) acetate.

Table 11-1. NCA-ECF of Precursor 1 Using Potential Auxillary Groups (average of 3 experiments).

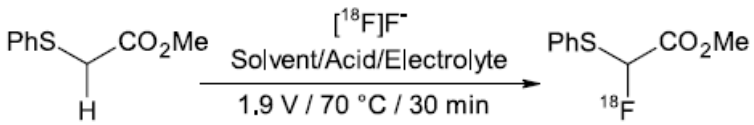

#	Solvent	Acid (mM)	Electrolyte (50 mM)	RCC,%	RCP, %	RCY, %
1	MeCN	–	TBAP	18.9 ± 0.8	2.2 ± 0.1	0.5 ± 0.1
2	DME	–	TBAP	0	0	0
3	TFE	–	TBAP	59.3 ± 1.0	84.1 ± 2.1	49.8 ± 0.5
4	HFIP	–	TBAP	58.1 ± 4.4	27.2 ± 0.4	15.8 ± 1.4
5	TFE	–	PPTS	70.5 ± 1.9	21.9 ± 0.6	15.4 ± 1.8
6	MeCN	–	PPTS	62.6 ± 7.7	6.1 ± 1.2	3.9 ± 1.2
7	TFE	–	TBA-OTf	30.9 ± 1.8	79.9 ± 1.3	24.7 ± 1.8
8	MeCN	–	TBA-OTf	0	0	0
9	TFE	2 mM TfOH	TBAP	27.5 ± 1.5	84.2 ± 4.1	23.2 ± 2.1
10	TFE	10 mM TfOH	TBAP	2.4 ± 0.1	13.5 ± 0.8	0.3 ± 0.1
11	MeCN	2 mM TfOH	TBAP	0	0	0
12	MeCN	10 mM TfOH	TBAP	0	0	0
13	TFE	2 mM TsOH	TBAP	35.8 ± 0.4	71.1 ± 1.7	25.5 ± 0.3
14	TFE	10 mM TsOH	TBAP	15.9 ± 0.5	85.8 ± 2.6	13.7 ± 0.8
15	MeCN	2 mM TsOH	TBAP	0	0	0
16	MeCN	10 mM TsOH	TBAP	0	0	0

PPTS= Pyridinium p-Toluenesulfonate; TBA-OTf= Bu_4N^+ $CF_3SO_3^-$; TfOH= CF_3SO_3H; TBAP= Bu_4NClO_4.

To establish a baseline yield, NCA-ECF of [^{18}F]**1** in acetonitrile (MeCN) with tetrabutylammonium perchlorate (TBAP) as the electrolyte was investigated. The non-isolated, decay-corrected RCY of the reaction was 0.5 ± 0.2% (*n* = 3; **Table 11-1**, entry 1). Using

dimethoxyethane (DME) as a solvent failed to produce any radioactive products (Table A4.1, entry 2) despite its reported ability to solvate quaternary ammonium cations, thereby increasing the availability of fluoride for ECF[383,384]. We explored the use of relatively weak nucleophilic triflate (OTf) and tosylate (OTs) additives in an attempt to provide stability for the cation-radical without competing with [^{18}F]fluoride nucleophile[385]. TBAP was replaced with either pyridinium tosylate or Bu4N-OTf in the NCA synthesis of [^{18}F]**1**. While the use of OTf yielded no product (**Table 11-1** entry 8), a more nucleophilic[386] OTs additive led to an observed RCY of 3.9 ± 1.2% (*n* = 3): an order of magnitude increase from that observed with TBAP. This led us to hypothesize that using triflic or toluenesulfonic acids instead of their salts might have a beneficial effect. In this way, respective conjugate bases would form after cathodic reduction of acidic protons in situ. However, low pH was previously reported to diminish product yields in ECF[356], leading us to examine two concentrations of TfOH and pTSA (2 mM, 10 mM). Unfortunately, these studies did not lead to product formation. In search of additives that would be more nucleophilic than OTs, yet only modestly competitive with [^{18}F]fluoride species, we discovered that Eberson suggested use of trifluoroethanol (TFE) and hexafluoroisopropanol (HFIP) for stabilization of radical cations[387]. These solvents are known to have high dielectric constants, low polarizabilities and propensities to solvate competing anions thereby increasing the cationic intermediate lifetime[360,361,387–389]. Recently, fluorination of thioethers has been successfully demonstrated in these solvents[390]. This data encouraged us to try TFE and HFIP in NCA-ECF. This strategy proved to be fruitful and good conversion of [^{18}F] fluoride in the NCA synthesis of [^{18}F]**2** was observed with TFE and HFIP as the solvent and TBAP as the electrolyte. Whereas in the case of HFIP, considerable amounts of unknown byproducts were formed, with TFE, the vast majority of [^{18}F]fluoride incorporation resulted in the formation of the desired product [^{18}F]**2**. It is likely that the byproducts are formed through formation of perfluorinated ethers previously described[391]. The observed RCY of 49.8 ± 1.0% with TFE as the solvent marked a breakthrough in the NCA-ECF of thioethers. In a series of follow-up experiments, the previously investigated triflate and tosylate compounds (pTS,

TBATF, TfOH and pTSA) were retested as additives to the solvent TFE, resulting in reduced formation of [^{18}F]**2** as compared to the use of neat TFE. The promising results with TFE as the solvent can be explained by the proposed fluoro-Pummerer-type mechanism. **Figure 11-2** presents a combined illustration of commonly accepted fluoro-Pummerer mechanism (**Figure 11-2**, right) and its modification that we suggest to explain the no-carrier added reaction reported here (**Figure 11-2**, left). Trifluoroethanolate enhanced by reduction of TFE on the cathode in the single chamber cell, acts as a promoting agent in the fluoro-Pummerer-type rearrangement. TFE and HFIP alcoholates stabilize the sulfur carbocation after the first anodic oxidation. Following the second anodic oxidation reaction, fluorinated alcoholate abstracts proton in the α-position to sulfur forming a sulfonium ion. The latter can react with either [^{18}F]fluoride or competing nucleophiles to yield the desired product or an auxiliary-ether, respectively. Indeed, a substantial amount of the auxiliary-ether was observed using GC–MS[356]. HFIP alcoholate seems to have weaker stabilizing effect on the sulfur carbocation as suggested by the increased formation of undesired side products. TFE is likely to extend the cation intermediate lifetime, thereby increasing the probability of the nucleophilic attack at diminishing NCA concentrations of fluoride. In a limited study of the scope of this approach, NCA-ECF of several thioethers in TFE was performed (**Figure 11-1**). Excellent RCYs were observed in the formation of [^{18}F]**2** and [^{18}F]**3**. Notably, both respective substrates lack the phenyl group adjacent to sulfur as compared to substrate 1. Poor RCY was observed in the formation of [^{18}F]**4**. The nitrile group potentially exerts a destabilizing effect on the sulfonium/carbenium cation resulting in the formation of unidentified radiochemical side products. A similar trend was seen in case of [^{18}F]**5** with the second lowest RCY within the scope, likely caused by electron withdrawing properties of the phosphonate group. The NCA-ECF of 2-(phenylthio) acetamide to yield [^{18}F]**6** is notable since the primary amide has an oxidation potential similar to that of sulfur. The fact that this transformation proceeds without the protection of the primary amide illustrates the versatility of this methodology, in that a wider range of thioethers can potentially be fluorinated without prior modification. A complete radiosynthesis of [^{18}F]**2** that

includes the HPLC isolation of the final product was performed. Up to 700 MBq of [^{18}F]**2** were synthesized within 90 min from the end of bombardment in 88 ± 3% isolated RCY and RCP of >95%. Am ranged from 4.7 to 5.3 GBq/μmol, representing >100x increase compared to previous reports on electrochemical radiofluorination, and approaching values observed in other NCA techniques[82].

11.4 Conclusion

This is the first example of no-carrier added radiofluorination of thioethers. The methodology tolerates a range of functional groups, including unprotected amides. This methodology offers the possibility to produce high Am ^{18}F-fluorinated thioethers as tracers for PET imaging. Further research is underway to increase the yield of NCA-ECF and extending the scope beyond thioethers and to biologically relevant molecules.

11.5 Appendix

11.5.1 Synthesis parameter optimization

The NCA procedure described in section 4 was used for all experiments with the changes annotated in tables S1 and S2. The experimental results of the NCA-ECF using the precursor Methyl (phenylthio) Acetate **1** are tabulated in **Table 11-2** and **Table 11-3**. **Table 11-2** contains the experiments to optimize the electrochemical reaction for time and temperature. The optimal temperature was 70°C and time was 30 mins. **Table 11-3** summarizes results for alternative auxiliary groups in the fluoro-Pummerer mechanism to facilitate NCA-ECF with ACN and TFE were used as solvents in these experiments. The only successful fluorination in ACN was performed using Pyridinium pToluenesulfonate (PPTS) with an RCY of 3.9$\pm$1.2% (n=3). Triflic Acid (TfOH) and pToluenesulphonic Acid (TsOH) both reduced RCY in TFE. PPTS and Tetrabutylammonium Trifluoromethanesulfonate (TBA-OTf) also resulted in reduced RCY in TFE compared to using TBAP.

Table 11-2. NCA-ECF optimization of 1 in TFE (n=3).

Time (mins)	Temp (°C)	RCC	RCP	RCY
10	70	34.5±5.2%	90.5±3.5%	31.4±5.9%
30	70	59.3±1.0%	84.1±2.1%	49.8±0.5%
60	70	57.5±1.4%	34.7±4.9%	19.9±2.3%
30	25	21.2±2.6%	91.9±0.7%	19.4±2.2%

Trifluoroethanol (TFE).

Table 11-3. NCA-ECF of 1 Testing of Possible Auxiliary Groups (n=3).

Solvent	Acid (mM)	Electrolyte (50 mM)	RCC	RCP	RCY
TFE	-	PPTS	70.5±1.9%	21.9±0.6%	15.4±1.8%
ACN	-	PPTS	62.6±7.7%	6.1±1.2%	3.9±1.2%
TFE	-	TBA-OTf	30.9±1.8%	79.9±1.3%	24.7±1.8%
ACN	-	TBA-OTf	0%	0%	0%
TFE	2mM TfOH	TBAP	27.5±1.5%	84.2±4.1%	23.2±2.1%
TFE	10mM TfOH	TBAP	2.4±0.1%	13.5±0.8%	0.3±0.1%
ACN	2 mM TfOH	TBAP	0%	0%	0%
ACN	10 mM TfOH	TBAP	0%	0%	0%
TFE	2 mM TsOH	TBAP	35.8+0.4%	71.1+1.7%	25.5±0.3%
TFE	10 mM TsOH	TBAP	15.9±0.5%	85.8+2.6%	13.7±0.8%
ACN	2mM TsOH	TBAP	0%	0%	0%
ACN	10 mM TsOH	TBAP	0%	0%	0%

Acetonitrile (ACN). Pyridinium pToluenesulfonate (PPTS). Tetrabutylammonium trifluoromethanesulfonate (TBA-OTf). Triflic Acid (TfOH). pToluenesulphonic Acid (TsOH). Tetrabutylammonium Perchlorate (TBAP).

11.5.2 Molar activity calculations

NCA-ECF was performed to synthesize the radiofluorinated product methyl 2-[^{18}F]fluoro-2-(methylthio)acetate ([^{18}F]3) as described above. TLC and HPLC Analysis were performed on product. Due to the similarity of the absorbance of the fluorinated and non-fluorinated molecules

and the slow decomposition of the synthesized non-radioactive reference, a more precise known concentration of the precursor was used to measure UV absorbance vs. molar mass. A calibration curve of the UV absorbance at 205 nm was used to determine the concentration of the radiofluorinated product after NCA-ECF. Curves were obtained using a linear-least square fit of absorbance versus molar mass spanning the expected mass range. Molar activity was calculated by dividing the radioactivity of the injected sample by the molar mass (as determined from the AUC for the UV peak and the calibration curve). The radioactivity was determined by a well counter (Capintec Inc.) and corrected for RCC determined by TLC and RCP determined by HPLC. All results were corrected for radioactive decay. A molar activity (Am) example calculation is shown below.

$$\frac{\mathbf{570}\ \mu\boldsymbol{Ci}}{\mathbf{4.2}\ \mu\dfrac{\boldsymbol{mol}}{\boldsymbol{Lit}} \times \mathbf{100}\ \mu\boldsymbol{l}} = \mathbf{1.36}\ \boldsymbol{Ci}/\mu\boldsymbol{mol}$$

11.5.3 HPLC analysis

HPLC chromatograms of the carrier added electrochemical syntheses for the fluorinated standards are shown in the graph below.

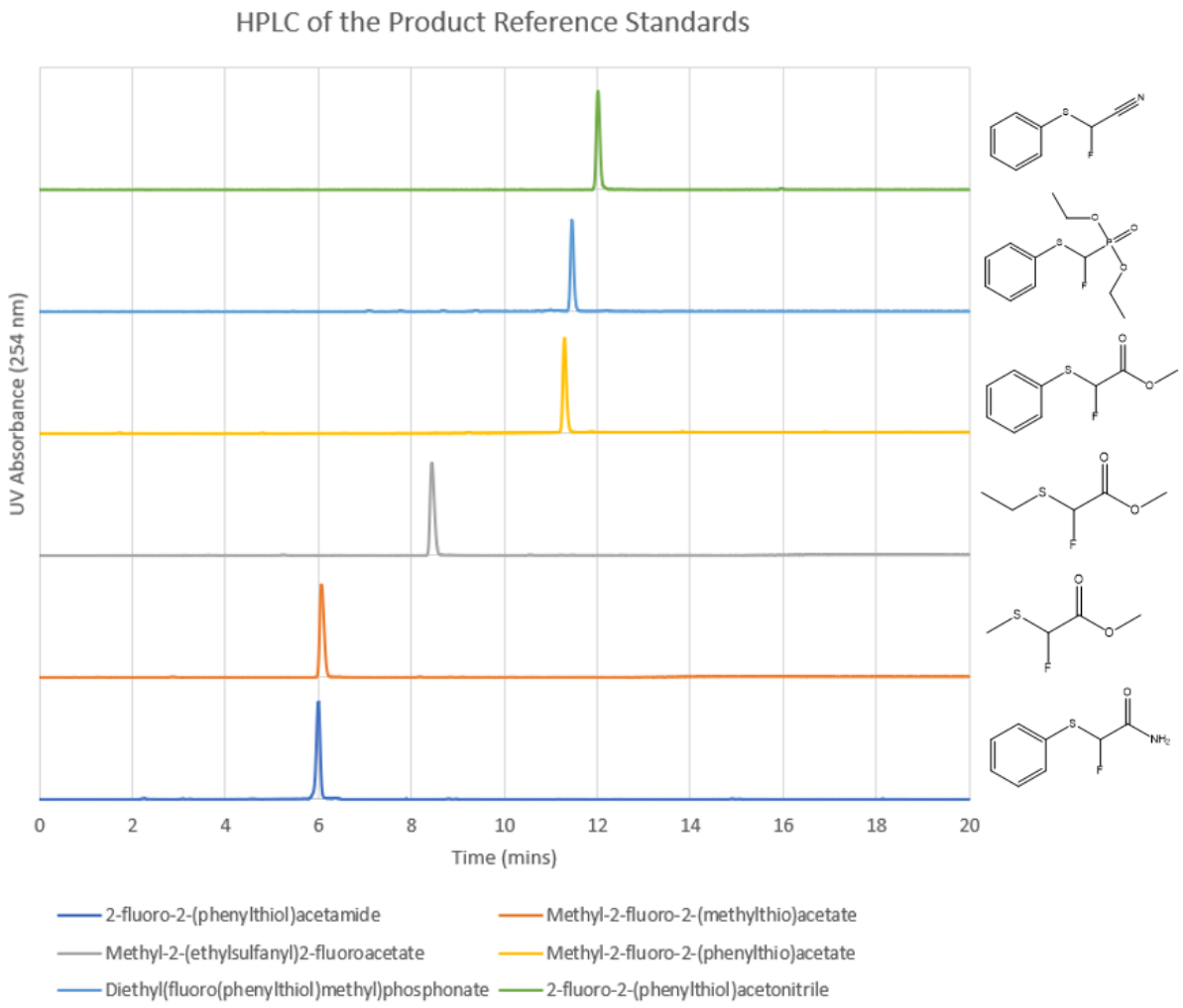

Figure 11-3. HPLC chromatograms of different thioether molecules.

The crude HPLC of the NCA-ECF UV and gamma chromatograms using each of the 6 thioether precursors are shown below. The procedure for the NCA-ECF is described above. The top chromatogram of each graph is the gamma signal from ^{18}F-labelled molecules with the gamma peak of the product highlighted with an arrow. The bottom chromatogram of each graph is the UV (205 nm) of the molecules produced during electrolysis. The remaining precursor is highlighted with an arrow.

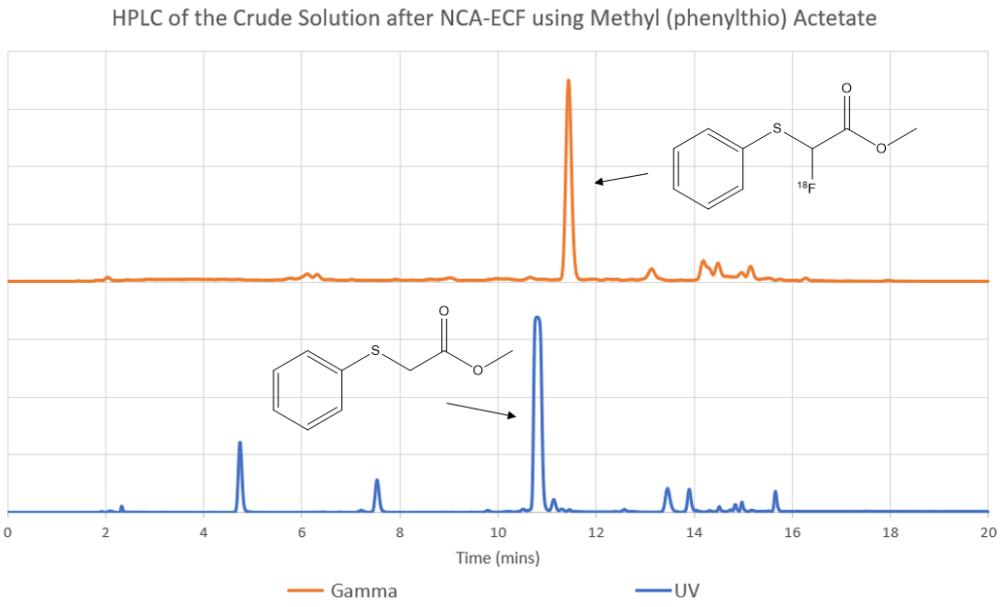

Figure 11-4. HPLC chromatogram of crude methyl(phenylthiol)acetate.

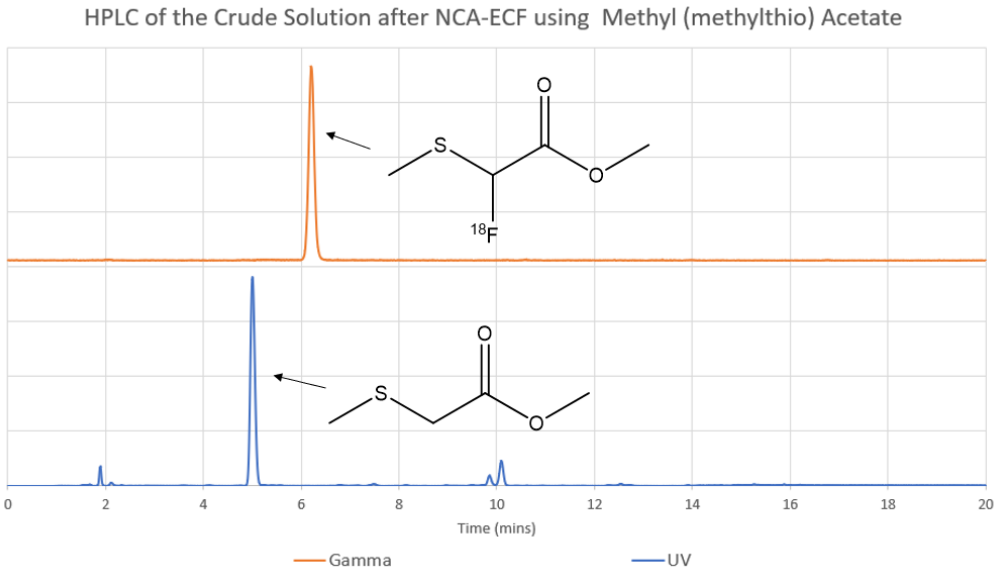

Figure 11-5. HPLC chromatogram of crude methyl(methylthiol)acetate.

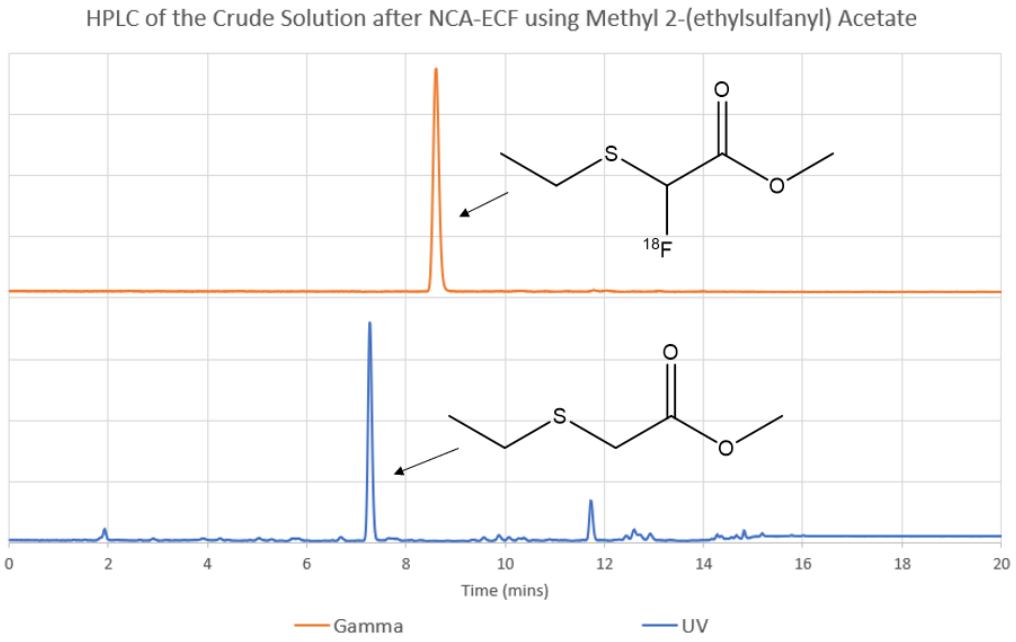

Figure 11-6. HPLC chromatogram of crude methyl 2-(ethylsulfanyl)acetate.

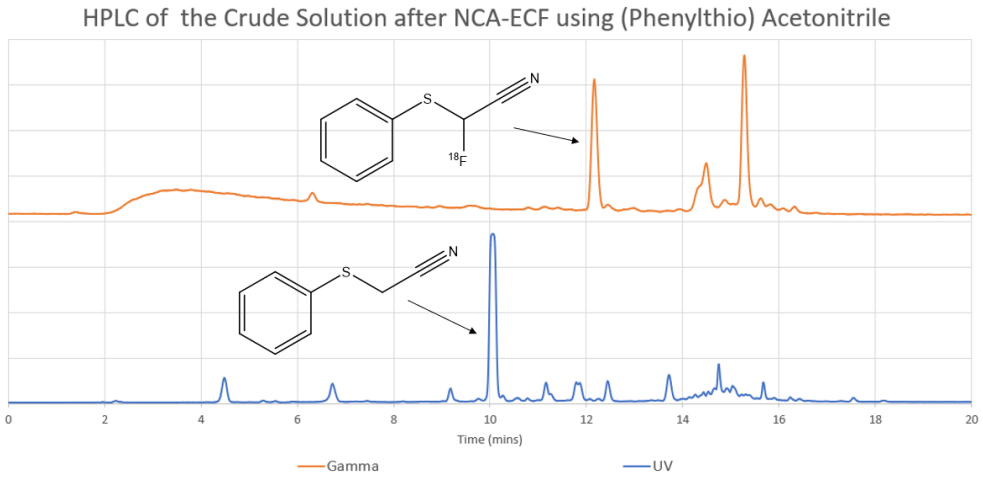

Figure 11-7. HPLC chromatogram of crude methyl 2-(ethylsulfanyl)acetate.

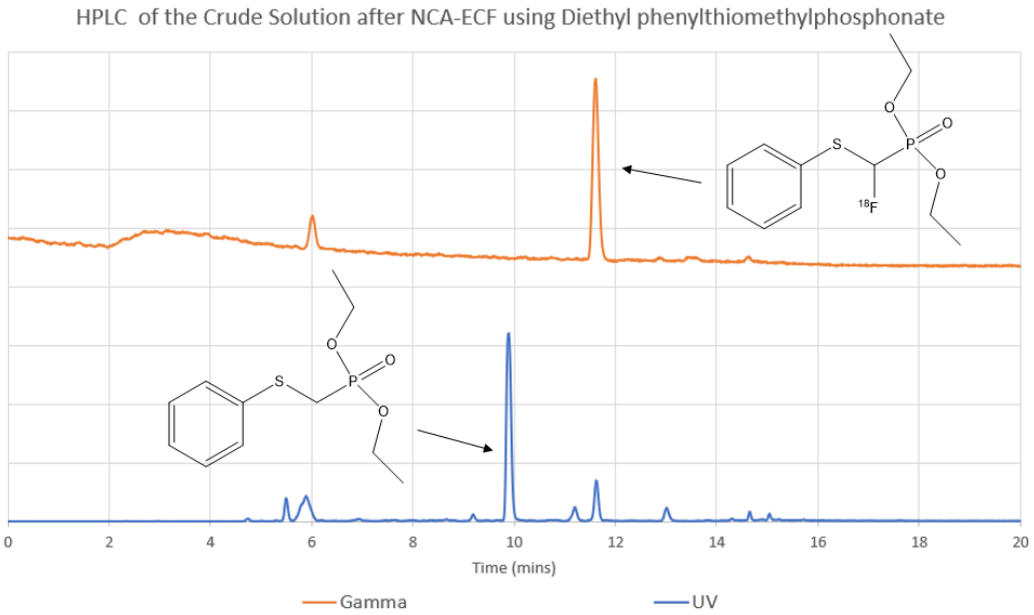

Figure 11-8. HPLC chromatogram of crude diethyl phenylthiomethylphosphonate.

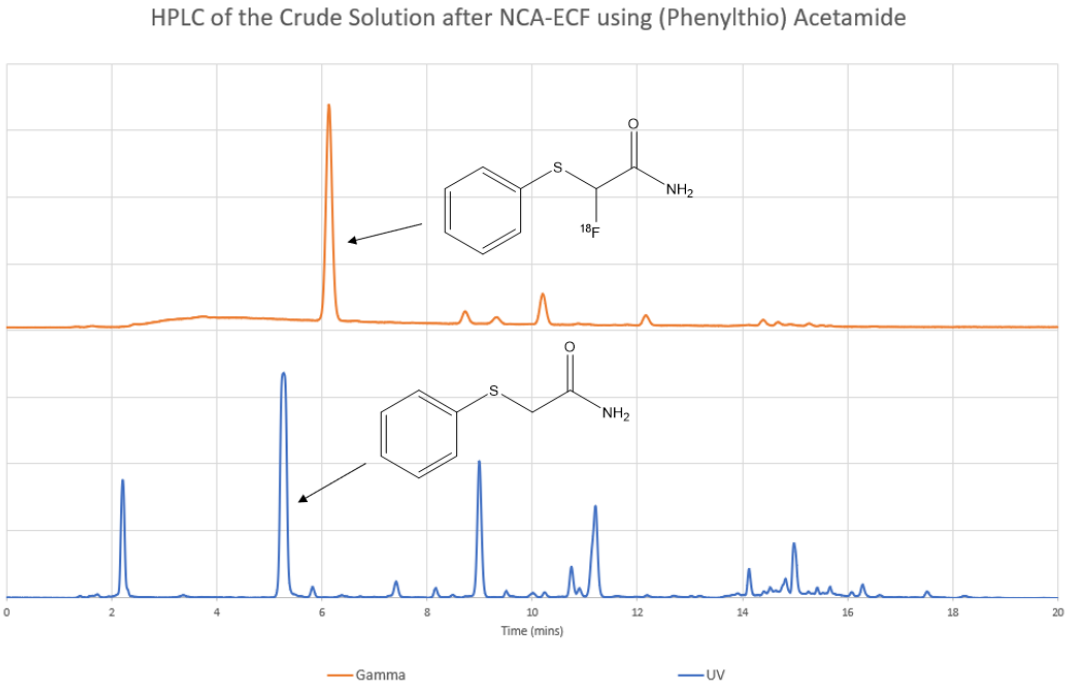

Figure 11-9. HPLC chromatogram of crude (phenylthiol)acetamide.

Chapter 12: In vivo imaging of mitochondrial membrane potential in non-small cell lung cancer

12.1 Main

Mitochondria are required for lung tumorigenesis as was shown in a *Kras*^{G12D} driven genetically engineered mouse model (GEMM) of lung cancer[392]. Therefore we used *Kras*^{G12D} mutant, *Lkb1* deficient (*Kras/Lkb1*) GEMMs to perform ^{18}FBnTP PET imaging on lung tumors *in vivo*[393,394]. ^{18}FBnTP is a positively charged lipophilic cation that localizes to the negatively charged mitochondrial inner membrane in a voltage-dependent manner[395,396]. The probe has most frequently been studied in rodent and canine myocardium to detect myocardial infarction[397,398] and in cancer cell xenografts as a surrogate marker of apoptosis following cytotoxic treatment with chemotherapy agents[399]. While mass spectroscopy based approaches have been used to study $\Delta\Psi$[400], no study to date has used ^{18}FBnTP PET to measure mitochondrial $\Delta\Psi$ using autochthonous murine models of lung cancer. We first synthesized ^{18}FBnTP as previously described[358] and performed PET imaging on lung tumors in *Kras/Lkb1* mice ten weeks post tumor induction. We identified both ^{18}FBnTP positive lung tumors and heart (**Figure 12-1a**). We then performed biodistribution analysis of tissues by either measuring gamma counts or percent injected dose per gram (%ID/g) and confirmed high uptake of the tracer in the heart, liver and intestine as well as low uptake in normal lung, skeletal muscle and brain (**Figure 12-1b-c**). Analysis of ^{18}FBnTP PET imaged *Kras/Lkb1* mice identified two distinct populations of lung tumors distinguished by either high or low ^{18}FBnTP uptake (**Figure 12-1d-e**). Interestingly, we confirmed that tumors with high ^{18}FBnTP avidity segregated with lung adenocarcinomas (ADCs) while lung squamous cell carcinomas (SCC) tumors had uniformly lower avidity for ^{18}FBnTP (**Figure 12-1d**). We confirmed lung tumor histology by staining tumors for cytokeratin 5 (CK5) to mark SCC and thyroid transcription factor 1 (TTF1) or surfactant protein C (SP-C) to identify ADCs (**Figure 12-1f**).

We suspected that lung SCC with low ^{18}FBnTP uptake had low mitochondrial content thus explaining the reduced ΔΨ and ^{18}FBnTP uptake. We stained tumors for the pan mitochondrial marker Tom20 and confirmed similar staining intensities for both lung ADC and SCC (**Figure 12-1f**). We performed additional analysis of the mitochondrial membrane proteins Tom20, 40, 70 and Tim23 in lung ADC and SCC from KL mice and showed that ADCs (SP-C:actin ratio >0.5) had no discernable difference in expression of these proteins as compared to SCC (SP-C:actin ratio <0.5) (**Figure 12-5**). These results demonstrate both tumor subtypes have similar mitochondrial content but a two-fold difference in ^{18}FBnTP affinity (**Figure 12-1d**).

We next sought to validate 18F-BnTP as a voltage-sensitive marker of both ΔΨ and oxidative phosphorylation (OXPHOS) by treating cells with the mitochondrial complex I inhibitor phenformin, which dissipates ΔΨ and inhibits OXPHOS[401] (**Figure 12-2a**). Short-term phenformin treatment of the human lung ADC cell line A549 or the mouse lung ADC line L3161C (derived from a *Kras^{G12D};p53$^{-/-}$;Lkb1$^{-/-}$* mouse) significantly reduced ΔΨ in a dose dependent manner as measured by TMRE staining (**Figure 12-2b, e**). The flow cytometry gating parameters for TMRE analysis and cell viability following acute phenformin treatment are represented in **Figure 12-6a-c**. Likewise, acute treatment of A549 cells with phenformin significantly reduced ^{18}FBnTP uptake similar to results with TMRE staining (**Figure 12-2c**). We next demonstrated that loss of ΔΨ induced by phenformin also resulted in a significant reduction of cellular OXPHOS in both A549 and L3161C cells as measured by respirometry (**Figure 12-2d, f**). Lastly, we treated L3161C cells with oligomycin, a complex V ATPase inhibitor, which induces increased ΔΨ. We detected a significant increase in TMRE and ^{18}FBnTP uptake following oligomycin treatment while ΔΨ was significantly reduced following the addition of the mitochondrial uncoupler FCCP (**Figure 12-2g, h**; **Figure 12-6b**) matching a response equal to the *in vivo* probe MitoClick[400]. Acute treatment with oligomycin +/- FCCP did not affect cell viability (**Figure 12-6d**). These results demonstrate that ^{18}FBnTP is a voltage sensitive probe that detected changes in ΔΨ and OXPHOS in mouse and human lung cancer cells.

We next measured ^{18}FBnTP uptake in lung tumors of *Kras/Lkb1* GEMMs before and after treatment with either phenformin or vehicle (saline) as described in **Figure 12-2i**. Representative PET images show reduced ^{18}FBnTP uptake in lung tumors following phenformin treatment (**Figure 12-2j**). Treatment groups showed no significant difference in ^{18}FBnTP uptake values before start of the treatment (**Figure 12-2k**) but showed a significant reduction in ^{18}FBnTP uptake in the mice that received phenformin (**Figure 12-2l**). We further quantified the fold change in ^{18}FBnTP uptake following treatment and show that phenformin induced a significant drop in tracer uptake compared to vehicle treated mice (**Figure 12-2m**). We performed three independent experiments in *Kras/Lkb*1 mice that showed a significant reduction in ^{18}FBnTP uptake in phenformin treated lung tumors compared to those treated with vehicle alone (**Figure 12-2n**). Because *Kras/Lkb1* tumors are sensitive to phenformin[394] it is possible that reduced ^{18}FBnTP uptake was due to phenformin induced cell death. Therefore, we stained phenformin and vehicle treated tumors for cleaved caspase 3 and Ki67 and found no evidence of phenformin induced apoptosis or reduced cell viability (**Figure 12-7a-d**). This data agrees with previously published studies in which only a longer duration of phenformin treatment between 4-8 weeks resulted in cellular apoptosis[394,402]. Measurement of phenformin by mass spectrometry in lung tumor tissue from KL mice showed a significant increase in phenformin in tumors from treated mice as compared to tumors treated with vehicle (**Figure 12-8**).

We then investigated whether ^{18}FBnTP could selectively measure changes in $\Delta\Psi$ and OXPHOS in vivo following treatment with a broader panel of ETC inhibitors. The complex I inhibitors included metformin, phenformin, or rotenone, which all reduce $\Delta\Psi$ and suppress OXPHOS[394,401,403] as well as the complex V inhibitor oligomycin, which induces an increase in $\Delta\Psi$. We used an orthotopic mouse model in which we transthoracically implanted L3161C lung tumour cells into the left lobe of syngeneic recipient mice **Figure 12-3a** to profile mitochondrial $\Delta\Psi$ in lung tumours. Notably, this enabled us to spatially localize a single lung tumour in the left lobe of the mouse and perform PET imaging of ^{18}F-BnTP in mouse lung ADC tumours (**Figure**

12-7f–h). We measured ^{18}F-BnTP uptake in these orthotopically implanted mice after acute treatment for 4 h with either oligomycin or rotenone[404] (**Figure 12-3a**). We used a safely tolerated dose of rotenone (0.5 mg kg−1) or oligomycin (0.25 mg kg−1) below the toxic dose range[405]. Uptake of ^{18}F-BnTP in lung tumours was significantly increased after the delivery of oligomycin, whereas rotenone treatment significantly reduced ^{18}F-BnTP uptake (**Figure 12-3b**). Our results demonstrate that ^{18}F-BnTP PET detected acute changes in mitochondrial ΔΨ in lung tumours after inhibition of respiratory complexes I or V.

At a cellular level metformin, like phenformin, inhibits mitochondrial complex I resulting in reduced OXPHOS[406–408], and is broadly used world wide to clinically manage type 2 diabetes[409]. Yet, despite decades of clinical use and research on metformin there has been no definitive biomarker established to measure its direct inhibition of complex I activity in vivo. We therefore sought to determine if ^{18}FBnTP PET could measure changes in the ΔΨ of lung tumors following systemic treatment of mice with metformin (**Figure 12-3f**). Our results show that ^{18}FBnTP uptake in lung tumors was significantly reduced in the mice that received metformin compared to the vehicle treated mice (**Figure 12-3g**). Metformin is a less potent inhibitor of complex I than phenformin and as expected it had slightly less inhibition of ^{18}FBnTP uptake than did phenformin (**Figure 12-3 f,g**). Histological analysis of tumors treated with biguanides confirmed that neither metformin nor phenformin induced apoptosis, cell death or significantly altered tumor growth measured by CC3 and Ki67, respectively (**Figure 12-9b**). These results confirm that ^{18}FBnTP imaging can accurately detected a loss of ΔΨ following delivery of metformin.

We next sought to perform a rescue experiment using the Saccharomyces cerevisiae NADH dehydrogenase (ND1), which oxidizes NADH similar to mammalian mitochondrial complex I. Expression of the yeast ND1 protein enables cells to bypass complex I inhibition rendering them insensitive to metformin or phenformin[408,410]. Expression of ND1 in the L3161C tumor line conferred resistance to phenformin as L3161C-ND1 cells maintained higher OXPHOS following phenformin treatment as compared to cells expressing the vector alone (**Figure 12-9c-d**). We

then performed ^{18}FBnTP PET imaging on L3161C-vector and L3161C-ND1 tumors treated with phenformin. ND1 expressing L3161C tumors were resistant to phenformin and showed no loss of ^{18}FBnTP uptake as compared to vector expressing L3161C tumors (**Figure 12-9e**). Vehicle treated L3161C-ND1 and vector tumors were both positive for ^{18}FBnTP uptake (**Figure 12-9f**). Our results demonstrate that ^{18}FBnTP imaging allows for selective measurement of ΔΨ and OXPHOS in lung tumors following inhibition with multiple complex I inhibitors.

NSCLC is marked by genetic, metabolic and histological heterogeneity in tumors[411–413]. We next sought to perform multi-tracer PET imaging on *Kras/Lkb1* mice using both ^{18}FBnTP and [^{18}F]Fluoro-2-deoxyglucose (^{18}F-FDG) PET tracers as a means to non-invasively profile glucose metabolism with ^{18}F-FDG and mitochondrial ΔΨ with ^{18}FBnTP. Multi-tracer PET imaging of *Kras/Lkb1* lung tumors revealed distinct metabolic heterogeneity between lung tumors in which we identified three distinct tumor populations (**Figure 12-4a**). Glycolytic tumors denoted as type "A" represent tumors positive for ^{18}F-FDG with low uptake of ^{18}FBnTP, tumors denoted as type "B" represent tumors positive for ^{18}FBnTP with low uptake of ^{18}F-FDG negative and tumors denoted as type "C" represent tumors with uptake of both ^{18}FBnTP and ^{18}F-FDG tracers (**Figure 12-4a**). Histological analysis of PET imaged lung tumors revealed that type A tumors were SCC marked by positive CK5-TTF1staining. Conversely, type B and C tumors were both positive for TTF1 and absent of CK5 staining confirming ADC histology (**Figure 12-10a,b**).

Both lung ADC and SCC showed distinct ^{18}FBnTP and ^{18}F-FDG profiles suggesting these tumor subtypes may have distinct bioenergetic profiles. Previous studies have shown that lung SCC tumors from *Kras/Lkb1* mice are refractory to phenformin, which suggested that lung SCC tumors may harbor intrinsic defects in complex I that modulate response to complex I inhibition[402,414]. Supporting this, a study of mitochondrial proteins in human NSCLC identified that late stage lung carcinomas have reduced expression of NDUFS1 and NDUFV1, which are complex I subunits involved in the transfer of electrons from NADH (**Figure 12-11a**)[415]. The authors showed that reduced NDUFS1 gene and protein expression correlated with lower overall

survival of NSCLC patients. Therefore, we performed a PET guided biochemical analysis of Ndufs1 and Ndufv1 in lung ADCs and SCCs in *Kras/Lkb1* mice. We identified that ^{18}FBnTP^{NEG} / ^{18}F-FDG^{POS} SCC tumors (shown in red) had a marked reduction in Ndfus1 and Ndufv1 proteins as compared to ^{18}FBnTP^{POS} / ^{18}F-FDG^{NEG} ADCs (shown in blue) (**Figure 12-4b,c**; **Figure 12-11b-d**). We analyzed Ndfus1 and Ndufv1 proteins in lung ADC and SCC tumors from *Kras/Lkb1* mice across four independent experiments and discovered that SCCs (red boxes) had a consistent reduction in Ndfus1 as compared to ADCs (blue boxes) (**Figure 12-4d**; **Figure 12-11e** and **Figure 12-12**). Lung ADC and SCC were distinguished by the presence or absence of SP-C protein and immunoblots for Tom20, Tom40, Tom70 or Tim23 showed similar distribution of mitochondrial content between SCC and ADC tumors (**Figure 12-4c,d**; **Figure 12-11e**).

We next examined the NDUFS1 and NDUFV1 proteins in the human lung ADC cell line A549 and lung SCC line RH2. Identical to mouse lung tumors, we identified a decrease in levels of both the NDUFS1 and V1 proteins in RH2 cells compared to A549 cells (**Figure 12-4e**). Functional analysis of mitochondrial $\Delta\Psi$ in human and mouse ADC and SCC cell lines demonstrated that the SCC tumor cells had a significantly reduced $\Delta\Psi$ to that of ADC cells (**Figure 12-4f**; **Figure 12-13a**). RH2 cells had significantly reduced oxygen consumption rate and a significantly increased extracellular acidification rate compared to A549 cells (**Figure 12-4g,h**). Analysis of complex I in coomassie stained blue native gels showed that RH2 cells had lower complex I levels than A549 (**Figure 12-4i**). In addition, RH2 cells had significantly reduced complex I activity as compared to A549 cells (**Figure 12-4j**). These results suggest that $\Delta\Psi$ and complex I activity may be predictive of response to complex I inhibition – with lung ADC cells predicted to have increased sensitivity compared to lung SCC cells. We demonstrated that both human and mouse lung ADC cell lines were in fact more sensitive to phenformin at low doses compared to lung SCCs lines (**Figure 12-4k**; **Figure 12-13b**).

Spurred by the ability to use multi-tracer PET imaging to detect metabolic heterogeneity across multiple tumors, we next asked whether ^{18}FBnTP and ^{18}F-FDG PET imaging could detect

metabolic heterogeneity within an individual lung tumor. We identified heterogeneous uptake of both ^{18}FBnTP and ^{18}F-FDG in lung nodules from *Kras/Lkb1* mice as represented in **Figure 12-4l**. Histological analysis of the tumor revealed that the ^{18}F-FDG avid region was positive for the SCC tumor marker CK5 and had elevated expression of Glut1 thus explaining the elevated ^{18}F-FDG uptake. In contrast, the ^{18}FBnTP avid region that stained positive for the ADC marker TTF1 and negative for CK5 had low expression of Glut1 thus explaining the low ^{18}F-FDG uptake **(Figure 12-4m,n**; **Figure 12-14**). These results demonstrate that multi-tracer PET imaging with ^{18}FBnTP and ^{18}F-FDG was able to identify distinct mitochondrial and metabolic heterogeneity within individual lung tumors. Our study represents a novel and non-invasive approach to using ^{18}FBnTP PET imaging to profile mitochondrial ΔΨ and functional mitochondrial heterogeneity within NSCLC. We detected distinct mitochondrial ΔΨ and complex I activity profiles in lung SCC and ADCs tumors that were predictive of response to phenformin. With complex I inhibitors such as IACS-010759 poised to enter testing in clinical trials[416], our results suggest ^{18}FBnTP may function as a noninvasive biomarker to differentiate tumors that will be sensitive or resistant to complex I inhibition. ^{18}FBnTP PET imaging represents a valuable resource not only to the field of cancer metabolism but one that can be extended to other fields actively investigating mitochondrial activity in aging, physiology, and disease.

12.2 Methods

12.2.1 Cell culture

Cells were maintained at 37 °C in a humidified incubator with 5% CO_2. A549 cells were obtained from ATCC. The RH2 lung cancer cell line was previously established in our laboratories. All cell lines were routinely tested and confirmed to be free of Mycoplasma using the LookOut Mycoplasma PCR Detection Kit (Sigma). Cells were grown in Dulbecco's modified Eagle's medium (DMEM) plus 5% fetal bovine serum (Hyclone) and 1% penicillin/streptomycin (Gibco).

12.2.2 Studies in genetically engineered mouse models

We performed studies with the genetically engineered mouse model of lung cancer, in which KrasLSL-G12D mice (which carry a loxP-Stop-loxP sequence followed by the KrasG12D point mutation allele) were crossed with Lkb1-deficient (Lkb1lox/lox) and R26-LuciferaseLSL (which carry a loxP-Stop-loxP sequence followed by luciferase at the Rosa26 locus) mice, to generate KrasG12D;Lkb1−/−;R26LSL-Luc (KL) mice, as previously described[414]. In brief, lung tumours were induced by intranasal administration of 5 × 105 transduction units of Lenti-PGK-Cre (FCT071, Kerafast) and developed nearly 100% lung adenocarcinomas, as previously described[394,414]. KL mice that inhaled Lenti-PGK-Cre were used in studies with phenformin treatment. For studies in which mice were imaged with both ^{18}F-BnTP and ^{18}F-FDG probes, KL mice inhaled Cre-expressing adenovirus (Adeno-Cre), which leads to development of both ADC and SCC tumours. For all treatments, KL mice were imaged with ^{18}F-BnTP and sorted into two groups based on the tumour maximum percentage injected dose per gram (%ID/g) values. Then, the values were normalized to the maximum %ID/g uptake of the heart, so that two groups would have similar matched maximum %ID/g values, as described in ‘PET–CT imaging studies’. Treatment was initiated on the same day or the next day after ^{18}F-BnTP imaging. Mice were treated with 125 mg kg−1 day−1 phenformin for 5 days or 15 mg kg−1 day−1 IACS-010759 for 12 days. The drugs were delivered by oral gavage. All experimental procedures that were performed on mice were approved by the UCLA Animal Research Committee (ARC). Mice were euthanized before the ARC-approved end points were reached; none of the tumours exceeded maximum ARC-defined volumes. Both male and female mice were used in all experiments and no preference in mouse gender was given for any of the studies.

12.2.3 Studies in syngeneic mice

We established the L3161C mouse cell line from a lung tumour dissected from a KrasG12D;p53−/−;Lkb1−/− (KPL) mouse. After resection, the tumour was minced and incubated in collagenase/dispase (10269638001, Sigma) for 3 h. Cells were filtered using a 70-μm strainer,

centrifuged, resuspended in DMEM with 5% FBS and plated in a 6-cm dish. The next day, medium was changed and cells that attached were cultured. We confirmed that the L3161C cell line was ADC by implanting cells into syngeneic mice, detecting lung tumours and staining with H&E and CK5 and TTF1. For some experiments, L3161C cells expressed pBabe or pBabe-NDI (from Addgene plasmid 72876,) as previously described[410]. For imaging studies, 1 × 105 L3161C cells suspended in 20 µl PBS were implanted into the left lung lobe via transthoracic injection. Two weeks after injection, mice were imaged by computed tomography. Mice with similar sized tumours were used for ^{18}F-BnTP imaging. For treatment studies, syngeneic mice were imaged with ^{18}F-BnTP, and split into two groups (three groups for **Figure 12-3b**) based on tumour maximum %ID/g, such that maximum %ID/g values of tumours in both groups would be similar, as described in 'PET–CT imaging studies'. Treatment was then initiated for the specified time. Mice were treated with a single dose of 0.25 mg kg−1 oligomycin or 0.5 mg kg−1 rotenone; both drugs were delivered by intraperitoneal injection. For other studies, mice were treated with 125 mg kg−1 day−1 phenformin or 500 mg kg−1 day−1 metformin for 5 days; both drugs were delivered by oral gavage in the morning. After imaging, mice were euthanized and tissue was obtained. For some experiments, lungs were fixed with 10% neutral buffered formalin overnight; for other experiments, lung tumor nodules were rapidly dissected, snap-frozen in liquid nitrogen and stored at −80 °C.

12.2.4 [^{18}F]FBnTP synthesis

The radiotracer ^{18}F-BnTP was synthesized as previously described[358]. The three-pot, four-step synthesis of ^{18}F-BnTP was performed using the automated radiochemical synthesizer ELIXYS FLEX/CHEM (Sofie Biosciences). The no-carrier-added [^{18}F]fluoride was produced from the (p, n) reaction of [^{18}O]H_2O with an RDS-112 11 MeV cyclotron (Siemens) in a 1-ml tantalum target with Havar foil. [^{18}F]Fluoride in water was pushed through a strong cation-exchange (SCX) cartridge and trapped on a QMA cartridge. [^{18}F]Fluoride was then eluted with a solution of Kryptofix 222 (10 mg, 27 µmol) and K_2CO_3 (1 mg, 7 µmol) in an acetonitrile:water (3:5, 0.8 ml)

mixture. Azeotropic evaporation was performed at 110 °C under a stream of nitrogen (7 p.s.i.) to remove excess water using acetonitrile. The 4-trimethylammoniumbenzaldehyde trifluoromethansulfonate (5 mg) precursor was solvated in DMSO (0.8 ml), added to the reactor vial containing the dried [^{18}F]fluoride and allowed to react at 90 °C for 5 min with stirring. The resulting 4-[^{18}F]fluorobenzaldehyde (^{18}F-FBA) mixture was diluted with water containing 1% (w/v) Na-ascorbate solution (5 ml total) and passed through an Oasis WCX cartridge (41 kPa) for 1.5 min. The WCX cartridge was dried with nitrogen (138 kPa) for 1 min and eluted with DCM (3 ml). The mixture was passed through a glass column containing $NaBH_4 \cdot (Al_2O_3)x$ (350 mg) on the top half portion and K_2CO_3 (2 g) on the bottom half portion for a flow-through reduction of ^{18}F-FBA to 4-[^{18}F]fluorobenzyl alcohol (^{18}F-FBnOH), which was directed to the second reactor vial (21 kPa). A subsequent elution and rinsing of the column was performed using DCM (1 ml, containing 0.2% (v/v) of water; 21 kPa). The mixture containing ^{18}F-FBnOH was reacted with Ph_3PBr_2 (100 mg) in DCM (1.1 ml) at 35 °C for 10 min resulting in the formation of 4-[^{18}F]fluorobenzyl bromide (^{18}F-FBnBr). The resulting mixture was passed through a silica cartridge and directed towards the third reactor vial (14 kPa). A solution of PPh3 (3 mg) in ethanol (0.6 ml) was added, followed by removal of most of the DCM under vacuum and a stream of nitrogen (21 kPa) at 45 °C for 6.5 min while stirring. Ethanol (1 ml) was added and the mixture was evaporated to approximately 0.5 ml under vacuum and a stream of nitrogen (48 kPa) at 80 °C for 2.5 min while stirring. The mixture was reacted at 160 °C for 5 min in a sealed position, which converted the ^{18}F-FBnBr to the desired ^{18}F-FBnTP. The reaction vial was cooled to 35 °C and diluted with water (3 ml) while stirring. The mixture was passed through a Sep-Pak Plus Accell CM cartridge (55 kPa) and the cartridge was washed with ethanol (20 ml). The product was released with 2% ethanol in saline plus 0.5% (w/v) Na-ascorbate (10 ml) and passed through a sterile filter into a vented sterile vial. Under optimized conditions, the resulting ^{18}F-FBnTP PET tracer was obtained in AY of 1.4–2.2 GBq starting from 9.4 to 12.0 GBq [^{18}F]fluoride in 90–92 min (radiochemical yield = 28.6 ± 5.1% with n = 3). Molar activities ranged from 80 to 99 GBq μmol^{-1} (end of synthesis) and radiochemical purity was >99%.

12.2.5 PET-CT imaging studies

All PET–CT imaging was performed on KL mice or syngeneic mice transthoracically implanted with L3161C using either single tracer imaging with ^{18}F-BnTP or dual radiotracer imaging with ^{18}F-BnTP and ^{18}F-FDG, as previously described[413,414]. To reduce variability between mice imaged with ^{18}F-BnTP, the maximum %ID/g for each tumour was normalized to maximum %ID/g of heart, as indicated in the figures. For waterfall plots in **Figure 12-2g**, **Figure 12-3b, d, e** and **Figure 12-8c, d,** we calculated the percentage change in the uptake of the ^{18}F-BnTP probe after treatment relative to before treatment, using maximum %ID/g of the tumour that was normalized to maximum %ID/g of the heart for each mouse.

12.2.6 Respirometry analysis

Experiments were conducted on a Seahorse XF96 Extracellular Flux Analyzer (Agilent Technologies) to measure oxygen consumption rate (OCR) and extracellular acidification rate. L3161C, A549 or RH2 cells were seeded into an XF96 microplate at density of 12,000–15,000 cells per well. Cells were plated in growth medium and maintained overnight in a tissue culture incubator (37 °C, 5% CO_2). On the day of the experiment, assay medium (Seahorse XF Base Medium supplemented with 2 mM L-glutamine, 1 mM pyruvate and 10 mM glucose) was freshly prepared. The cells were washed twice with assay medium and brought to a final volume of 175 µl per well. The XF96 plate was placed in a 37 °C incubator without CO2 for 30 min before loading the plate into the instrument. Injection of compounds during the assay included: the mitochondrial ATP synthase inhibitor oligomycin (final concentration 2 µM); the chemical uncoupler FCCP (final concentration 1 µM); and the complex I inhibitors rotenone (final concentration 2 µM) and phenformin (final concentration 1 mM); and the complex III inhibitor antimycin A (final concentration 2 µM). At the conclusion of the assay, the cells were fixed with 4% paraformaldehyde, stained with Hoechst, and cell number per well was determine based on nuclei number using an Operetta High-Content Imaging System (PerkinElmer). OCRs were normalized to cell number per well. Activity of complex I was measured in permeabilized cells using XF PMP

assay where complex I dependent OCR was measured by determining OCR in the presence of pyruvate and malate (as substrates for complex I) before and after addition of rotenone (complex I inhibitor).

12.2.7 Measurement of mitochondrial ΔΨ

Experiments were conducted by analysing TMRE fluorescence using flow cytometry. A549 and L3161C cells were collected on the day of the assay and 500,000 cells were aliquoted into a microcentrifuge tube. Cells were resuspended in 0.5 ml DMEM and 5% FBS with different concentrations of phenformin, oligomycin or FCCP as indicated. Cells were incubated in a tissue culture incubator (37 °C, 5% CO_2) for 2 h. After 2 h incubation, medium with TMRE was added to tubes, such that final concentration of TMRE was 7 nM and concentrations of phenformin, oligomycin and FCCP were constant. Cells were incubated for an additional 1 h in a tissue culture incubator (37 °C, 5% CO_2). Cells were washed twice in phenol-red-free DMEM and cellular fluorescence was acquired with a BD LSRII analyser at UCLA Flow Cytometry Core. Data were analysed with Flowing Software.

12.2.8 In vitro [^{18}F]FBnTP uptake assay

On the day of the assay, cells were trypsinized, collected in DMEM plus 5% FBS and counted. Then, 1,000,000 cells were aliquoted into a microcentrifuge tube, resuspended in 0.5 ml medium containing DMEM and 5% FBS plus vehicle, 1 mM phenformin, 8 μM oligomycin or 8 μM oligomycin with 4 μM FCCP. Cells were incubated in a tissue culture incubator (37 °C, 5% CO_2) for 2 h. After 2 h incubation, 0.5 ml of media with ^{18}F-BnTP was added to tubes, such that final concentration of ^{18}F-BnTP was 10 μCi ml^{-1} and concentrations of phenformin, oligomycin and FCCP were constant. Cells were incubated for a further 1 h in a tissue culture incubator (37 °C, 5% CO_2). The uptake was terminated by centrifugation at 4 °C (134g, 5 min). Cells were washed twice with cold media. After the final wash, cell pellet was resuspended in 500 μl of media, and 300 μl was used in a gamma counter, while 100 μl was used to count viable cells using ViCell counter (Beckman). Counts per minute were normalized to viable cells.

12.2.9 Immunohistochemistry

After the fixation step in 10% neutral buffered formalin overnight, lungs were transferred to 70% ethanol and further processing and embedding was done by the Translational Pathology Core Laboratory at UCLA. The following antibodies were used: anti-CK5 (EP1601Y) (Abcam, ab52635 1:100), anti-TTF1 (8G7G3/1) (DAKO, 1:1,000), anti-Ki67 (SP6) (Thermo-Scientific, RM-9106-S1, 1:200), anti-GLUT1 (Alpha Diagnostic, GT11-A, 1:400), anti-cleaved caspase 3 (CST, 9664, 1:1,000). Slides were scanned onto a ScanScope AT (Aperio Technologies). Digital slides were analysed with Definiens and QuPath software.

12.2.10 Western blot analysis

Whole-cell lysates from lung tumours isolated from mice were prepared as previously described7. In brief, tumours were homogenized in buffer containing phosphatase and protease inhibitors (20 mM Tris pH 7.5, 150 mM NaCl, 1% Triton X-100, 50 mM sodium fluoride, 1 mM EDTA, 1 mM EGTA, 2.5 mM pyrophosphate, 1 mM sodium orthovanadate, protease inhibitor tablet), centrifuged and the supernatant was normalized, aliquoted and stored in −80 °C freezer. Lysates were separated on 4–12% Bis-Tris protein gels (Thermo), transferred to PVDF membrane and probed with the following antibodies: SP-C (1:5,000, AB3786 Milipore); GLUT1 (1:2,000, GT11-A, Alpha Diagnostic); NDUFS1 (1:2,000, ab169540, Abcam); NDUFS1 (1:2,000, sc-271510, Santa Cruz); NDUSV1 (1:500, sc-100566, Santa Cruz), NDUFV2 (1:2,000, sc-271620, Santa Cruz), TOM20 (1:10,000, FL-145, Santa Cruz), TOM40 (1:2,000, 18409-1-AP, Proteintech); TOM70 (1:2,000, 14528-1-AP, Proteintech); TIM23 (1:2,000, 11123-1-AP, Proteintech); actin (1:8,000, 4970 and 3700, Cell Signaling Technology). Intensity of bands was quantified using Image J.

12.2.11 Blue native gel

Blue native (BN)–PAGE was performed as previously described30 with minor modifications. In brief, mitochondria (100 μg protein) were solubilized for 15 min with digitonin using a 6 g:1 g digitonin:protein ratio. Insoluble material was removed by centrifugation at 21,000g

for 30 min at 4 °C, the soluble component was combined with BN–PAGE loading dye and separated on a 3–13% acrylamide–bisacrylamide precast BN–PAGE gel. For separation, cathode buffer (15 mM Bis-Tris, pH 7.0, and 50 mM tricine) containing 0.02% (w/v) Coomassie blue G was used until the dye front had reached approximately one-third of the way through the gel before exchange with cathode buffer lacking Coomassie blue G. Anode buffer contained 50 mM Bis-Tris (pH 7.0). Native complexes were separated at 4 °C at 110 V for 1 h, followed by 12 mA constant current. Thyroglobulin (669 kDa), ferritin (440 kDa), catalase (232 kDa), lactate dehydrogenase (140 kDa), and bovine serum albumin (BSA 67 kDa) were used as markers (GE Healthcare).

12.2.12 Liquid chromatography-mass spectroscopy

Tumours were homogenized with a Tissue Master (Omni international) in 1 ml chilled 80% methanol. Tumour suspensions were spun down at 4 °C for 5 min at 17,000g, and the top layer taken as extracted metabolites. The volume equivalent of 1 mg of tumour was transferred into glass vials and the samples were dried with a EZ2-Elite lyophilizer (Genevac). Dried metabolites were resuspended in 100 µl of 50%:50% acetonitrile:dH2O solution; 10 µl of these suspensions were injected per analysis. Samples were run on a Vanquish (Thermo Scientific) UHPLC system with mobile phase A (5 mM ammonium acetate, pH 9.9) and mobile phase B (acetonitrile). Separation was achieved at a 200 µl min−1 flow rate on a Luna 3mm NH2 100A (150 × 2.0 mm) at 40 °C with a gradient going from 15% A to 95% A in 18 min followed by an 11 min isocratic step. The UHPLC was coupled to a Q-Exactive (Thermo Scientific) mass analyser running in positive mode at 3.5 kV with an MS1 resolution of 70,000. Metabolites were identified using exact mass (MS1), retention time, and fragmentation patterns (MS2) at normalized collision energy 35. Quantification was performed via area under the curve (AUC) integration of MS1 ion chromatograms with the MZmine 2 software package. For the quantification of absolute moles of phenformin, one tumour from the vehicle group was selected to provide a representative tumour small molecular matrix. The volume equivalent of 1 mg of this tumour was distributed into several glass vials and 10 µl of pure aqueous phenformin standards (0.1–0.5 mM) was added to these

samples to span the possible range of phenformin concentrations. From this point on, samples were treated as described above. AUC values from the phenformin standards were used to fit a linear regression model that related MS1 AUC to the moles of phenformin present. The linear regression equation was used to convert MS1 AUC to moles of phenformin in all tumour samples and expressed relative to the tissue mass of each tumour.

12.2.13 Statistical analysis

The in vivo experiments were analysed using analysis of variance (ANOVA) models to evaluate the main effects of the two treatment types on the various quantitative outcome measures. Categorical outcomes were compared between groups with Fisher's exact test. The sample size of 7–10 KL mice per group provided a 99% power to detect differences in the outcomes of percentage CC3, Ki67 and 18F-BnTP %ID/g positivity, based on the observed results previously described7, assuming a two-sample t-test (a simplification of the ANOVA analysis plan) with a two-sided 0.05 significance level.

Mouse experiments involving imaging of KL mice with ^{18}F-BnTP were repeated with three separate cohorts several months apart. For imaging studies with both genetically engineered mouse models and syngeneic mice, after basal ^{18}F-BnTP imaging, mice were split into two groups (three cohorts for **Figure 12-3b**) based on maximum %ID/g values, such that maximum %ID/g values of tumours in both groups would be similar after normalization to the maximum probe uptake in the heart. Variation is indicated using standard deviation or standard error of the mean as described. Differences between groups were determined using unpaired two-tailed t-test or one-way ANOVA if more than two groups were compared. Western blot analysis of mitochondrial markers was completed on lung nodules isolated from three separate cohorts of mice.

Investigators were not blinded to the allocations for treatment groups. This is because allocations to the groups were done on the basis of the maximum uptake of the ^{18}F-BnTP probe, which was calculated using AMIDE computer software. Maximum uptake values were based on the percentage injected doses of the ^{18}F-BnTP probe, which were calculated independently of the

investigators. Regions of interest were defined for tumour and heart by investigators, and were used to calculate the maximal uptake value. Regions of interest were independently reviewed by two authors and verified in a blinded manner. For the histological analysis, quantification of the Ki67 and CC3 staining was done using automated morphometric Definiens software that defines positive and negative staining regions using established algorithms before analysis. Histological analysis was verified in a blinded review.

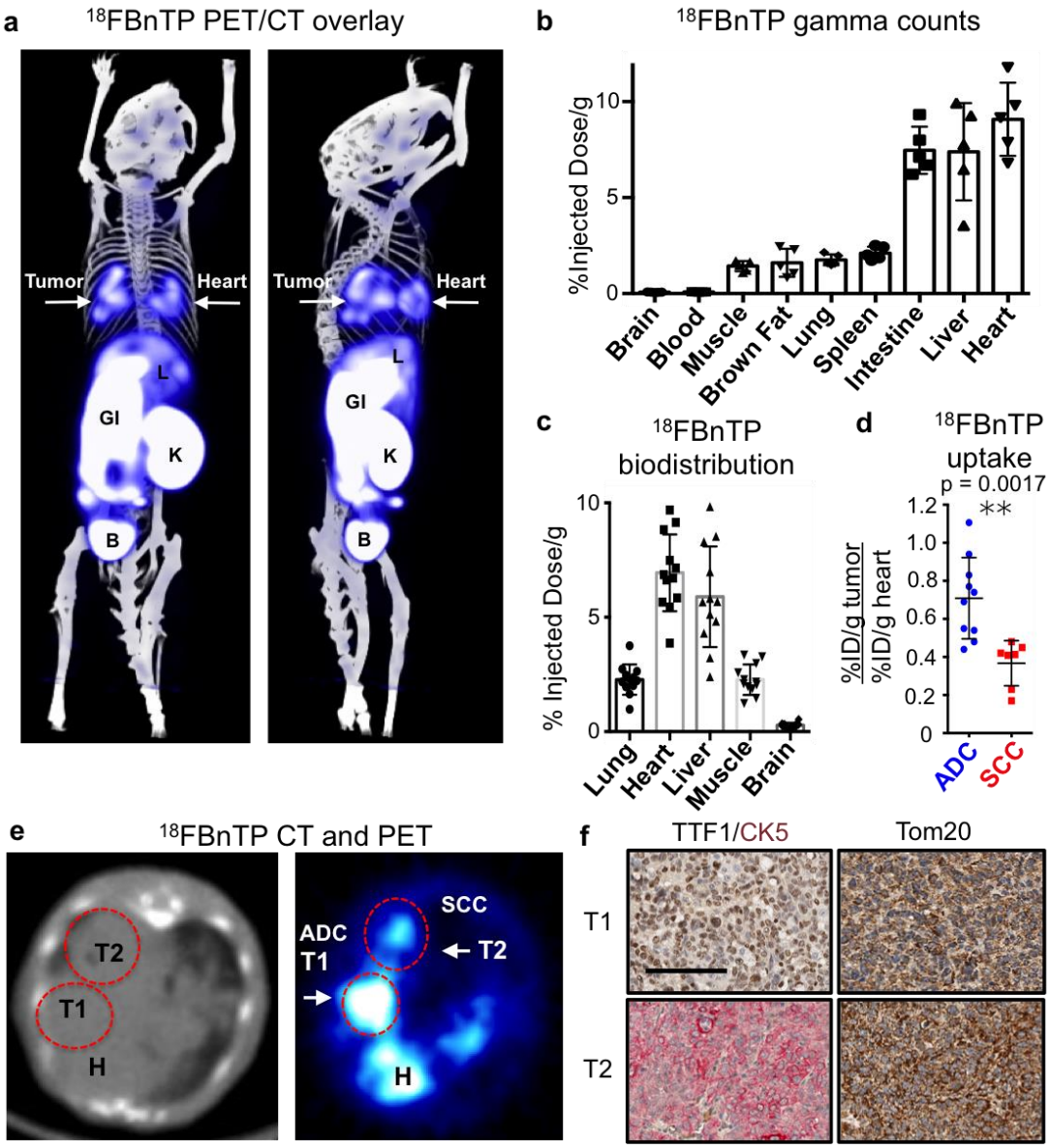

Figure 12-1. ^{18}FBnTP PET imaging and biodistribution analysis of Kras/Lkb1 lung tumors identified differential uptake between lung adenocarcinomas (ADC) and squamous cell carcinomas (SCC).

a PET/CT overlay of a *Kras/Lkb1* mouse with lung tumors, imaged with ^{18}FBnTP probe. Right panel is rotated 90° compared to left panel. Heart and Tumor are indicated by arrows. L – liver; GI – gastrointestinal tract; K – Kidney; B – Bladder. **b** Biodistribution of ^{18}FBnTP probe in tissue from wild type FVB mice measured by gamma counter *ex vivo* after 1 hr uptake (n = 5 mice). **c** Biodistribution of the ^{18}FBnTP probe in normal tissue of *Kras/Lkb1* mice measured by % injected dose/gram after 1 hr uptake (n = 5 mice). **d** ^{18}FBnTP uptake in lung ADC and SCC from *Kras/Lkb1* mice (n = 5 mice, n = 10 ADC tumors, n = 7 SCC tumors). **e** Representative transverse image of the heart and lungs of a *Kras/Lkb1* mouse imaged with CT (left panel) and ^{18}FBnTP (right panel). H – heart, T1 – adenocarcinoma (ADC), T2- squamous cell carcinoma (SCC). **f** IHC staining of T1 and T2 tumors from panel d. TTF1 – thyroid transcription factor 1; CK5 – keratin 5; Tom20 – translocase of outer membrane 20. Scale bar = 100 μm. The data are represented as the mean +/- SD. Statistical significance (**p<0.01) was calculated using unpaired two-tailed t-test.

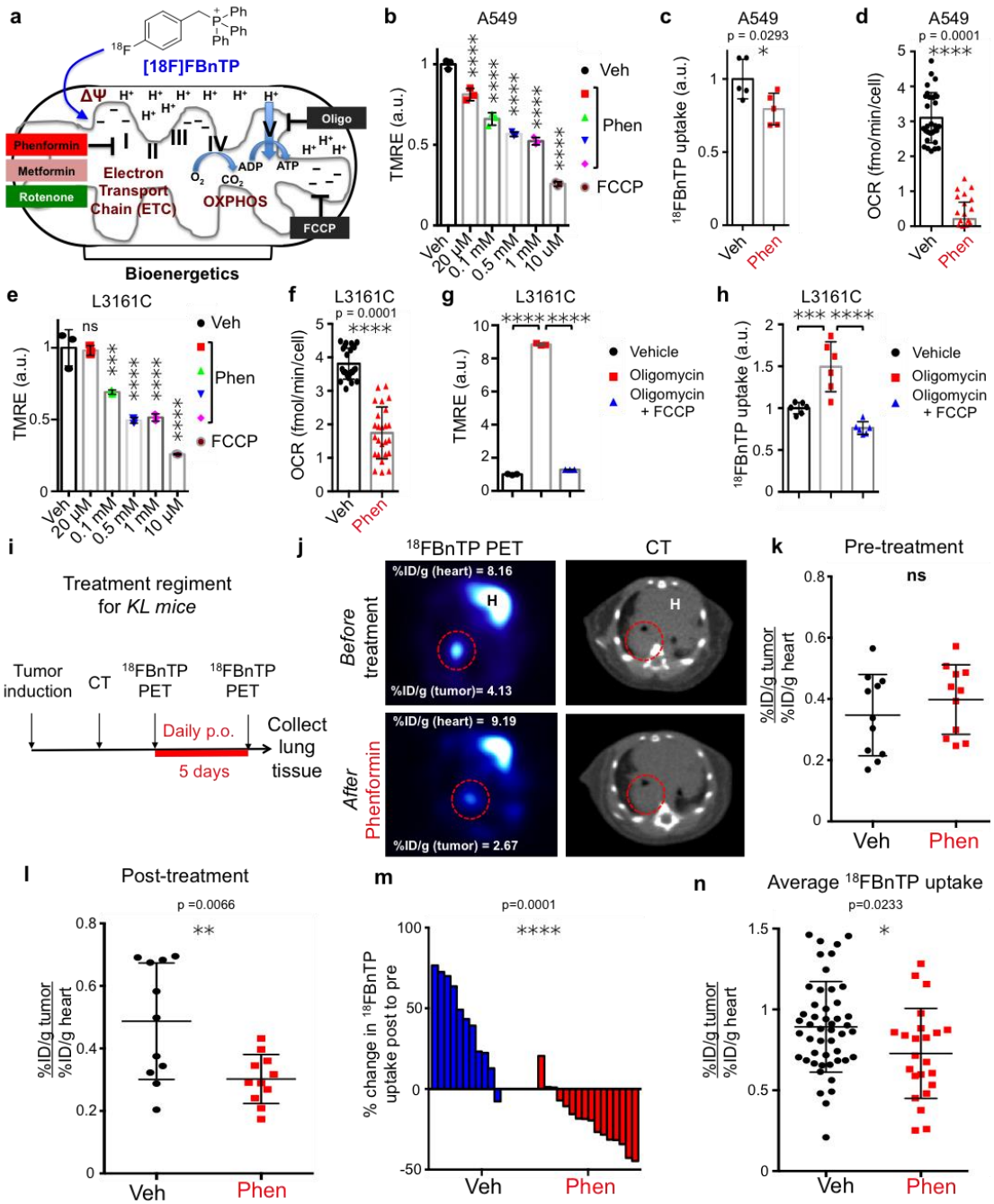

Figure 12-2. Treatment of Kras/Lkb1 GEMMs with the complex I inhibitor phenformin suppresses ^{18}FBnTP uptake in lung tumors.

a Schematic drawing representing voltage dependent uptake of 18FBnTP into the mitochondria. Bioenergetics driven by electron transport chain (ETC), and oxidative phosphorylation (OXPHOS) are shown. **b** TMRE measurements in A549 cells treated with indicated concentrations of Phenformin or FCCP for 3 hr (n = 3 replicates). **c** Uptake of 18FBnTP measured by gamma counter in A549 cells treated with 1 mM Phenformin for 3 hr (n = 5 replicates). **d** Oxygen consumption rate (OCR) per cell measured in A549 cells treated acutely with 1 mM Phenformin for 45 min (n = 25 technical replicates). **e** TMRE measurements in mouse cell line L3161C treated with indicated concentrations of Phenformin or FCCP for 3 hr (n = 3 replicates). **f** OCR per cell measured in mouse tumor line L3161C treated acutely with 1 mM Phenformin for 45 min (n = 25

technical replicates). **g** TMRE measurements in mouse cell line L3161C treated with Vehicle, 8 μM Oligomycin, or 8 μM Oligomycin + 4 μM FCCP for 3 hr (n = 3 replicates). **h** Uptake of 18FBnTP probe measured by gamma counter in mouse cell line L3161C treated with Vehicle, 8 μM Oligomycin, or 8 μM Oligomycin + 4 μM FCCP for 3 hr (n = 6 replicates). **i** Schematic drawing of imaging and treatment regiments for Kras/Lkb1 mice treated with 125 mg/kg/day Phenformin. **j** Representative images from a Kras/Lkb1 mouse before (top panel) and after (bottom panel) treatment for 5 days with 125 mg/kg/day Phenformin. Values for maximum percent injected dose (%ID/g) for the heart and tumor are indicated. H - heart. **k** Quantification of maximum percent injected dose (%ID/g) for tumors in Vehicle (Veh) and Phenformin (Phen) groups before treatment (Pre-treatment). Each dot represents an individual tumor; n = 11 Vehicle and Phenformin groups. **l** Quantification of 18FBnTP uptake for tumors in Veh and Phen groups after treatment (Post-treatment) with 125 mg/kg/day Phenformin for 5 days. Each dot represents individual tumor; n = 11 Vehicle and Phenformin groups. **m** Waterfall plot for % change in probe uptake post-treatment to pre-treatment for mice treated with Veh or Phen for 5 days. Each bar represents an individual tumor. **n** Average 18FBnTP uptake in Kras/Lkb1 mice after 5 day treatment with Vehicle (Veh) (n = 48 tumors; 10 mice) or Phenformin (Phen) (n = 23 tumors; 10 mice). Each dot represents individual tumor. The data are represented as the mean +/- SD. Statistical significance (*$p<0.05$; **$p<0.01$; ***$p<0.001$; ****$p<0.0001$; ns, not significant) was calculated using unpaired two-tailed t-test or one-way ANOVA (for b, e, g, h). Experiments in b-g were performed twice; experiment in h was performed once.

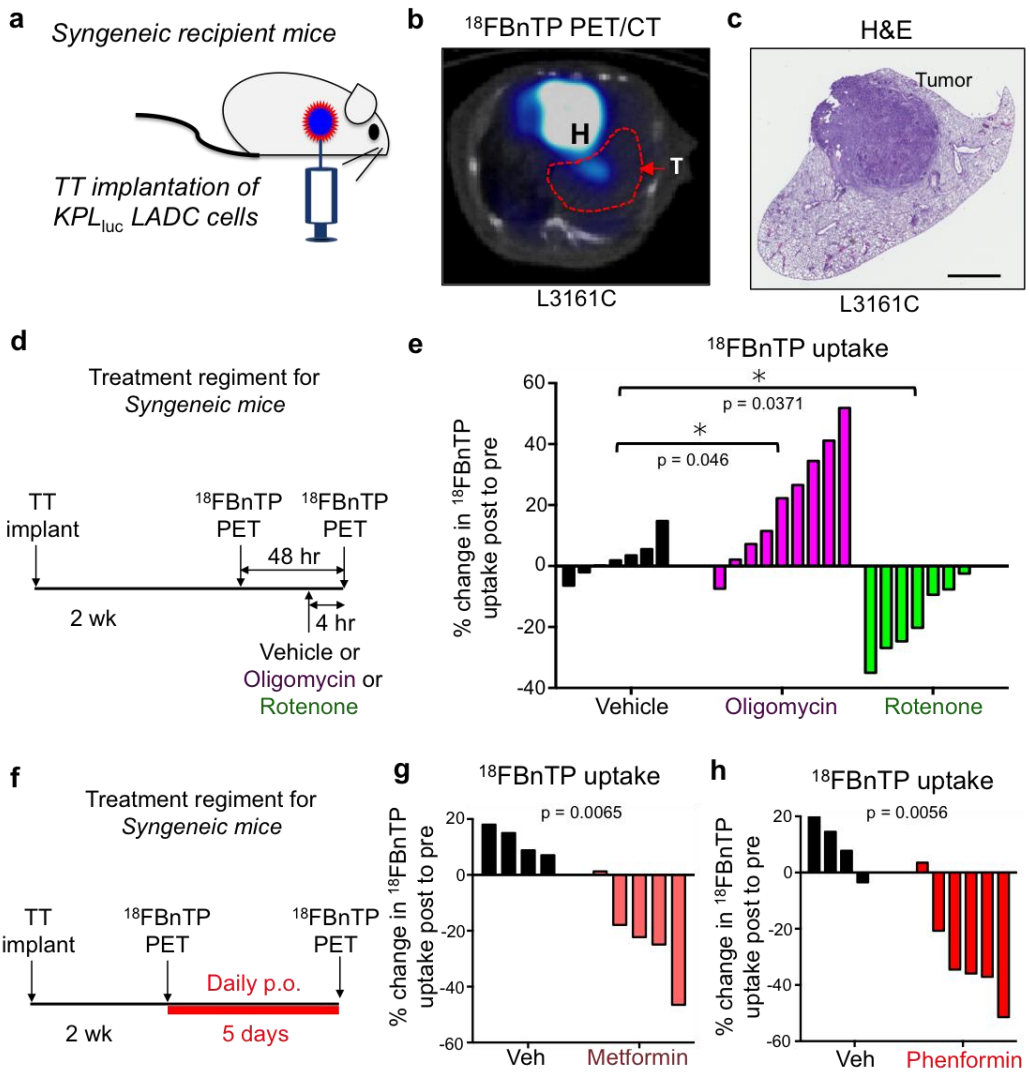

Figure 12-3. ^{18}FBnTP detects mitochondrial complex I inhibition in vivo.
a Schematic drawing of the transthoracic (TT) implantation of KPL lung adenocarcinoma (ADC) cells into syngeneic recipient mouse. **b** Representative ^{18}FBnTP PET/CT overlay of a tumor formed by transthoracically implanted L3161C cell line. H – heart, T – tumor. **c** H&E slide of a tumor formed by transthoracically implanted L3161C cell line. Scale bar = 2 mm. **d** Schematic drawing of the treatment and imaging regiment for syngeneic mice implanted transthoracically (TT) with L3161C cell line and treated with a single dose of Vehicle or Oligomycin or Rotenone. **e** Waterfall plot for % change in ^{18}FBnTP uptake post-treatment to pre-treatment for mice treated with a single dose of Vehicle (n = 7 mice) or 0.25 mg/kg Oligomycin (n = 9 mice) or 0.5 mg/kg Rotenone (n = 7 mice). Statistical significance (*p<0.05) was calculated using one way ANOVA. **f** Schematic drawing of the treatment and imaging regiment for syngeneic mice implanted transthoracically with L3161C cell line and treated with Vehicle or Complex I inhibitor for the indicated time. **g** Waterfall plot for % change in 18FBnTP uptake post-treatment to pre-treatment for mice treated with Vehicle (n = 4 mice) or 500 mg/kg Metformin (n = 5 mice) for 5 days. **h** Waterfall plot for % change in 18FBnTP uptake post-treatment to pre-treatment for mice treated with Vehicle (n = 4 mice) or 125 mg/kg Phenformin (n = 6 mice) for 5 days. Experiments in e, g, and h were performed once. Statistical significance for g and h was calculated using unpaired two-tailed t-test.

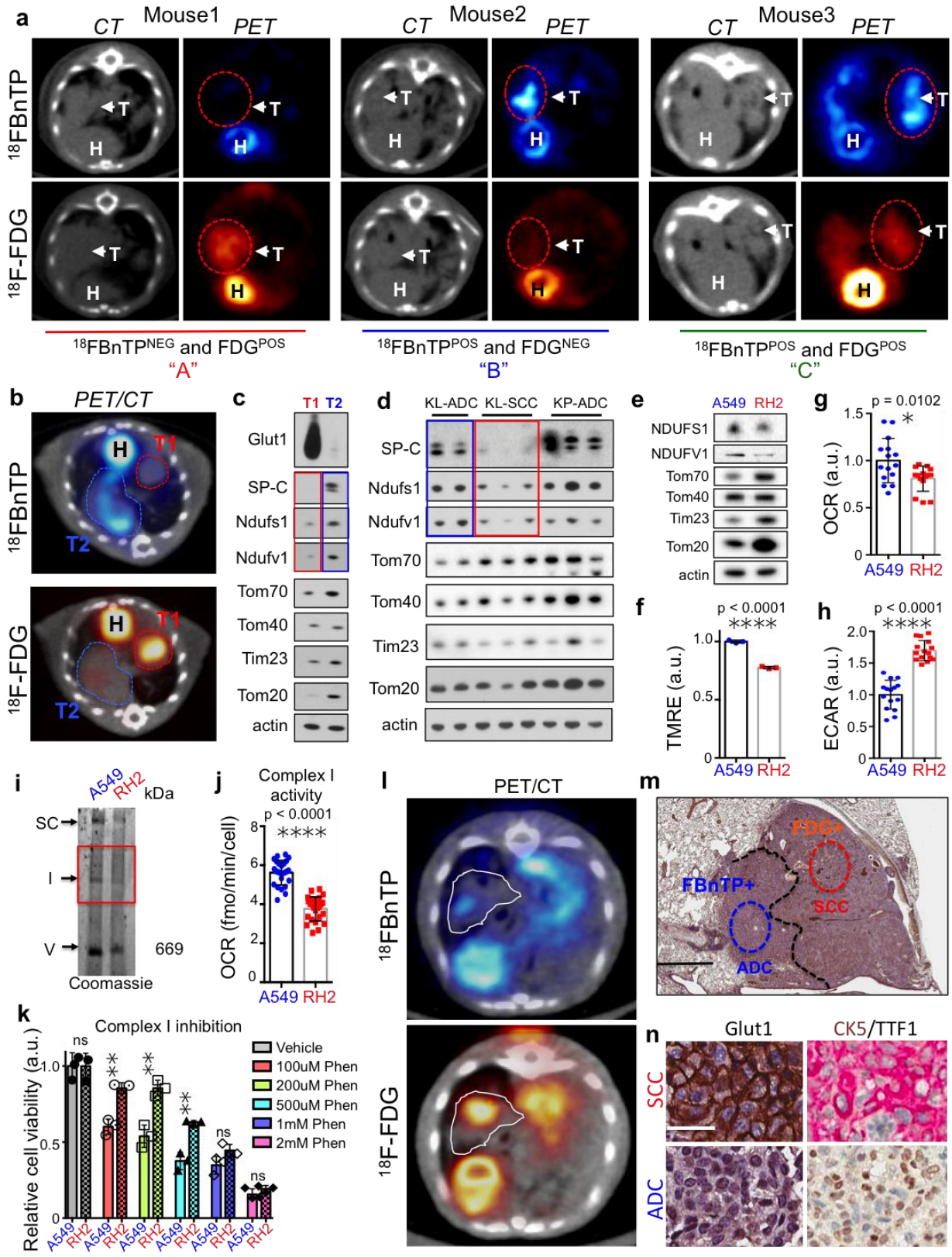

Figure 12-4. Multi-tracer PET imaging of lung tumors in Kras/Lkb1 mice with of ^{18}FBnTP and ^{18}F-FDG.

a Representative PET images of Kras/Lkb1 mice imaged with ^{18}FBnTP and ^{18}F-FDG on sequential days. Top panel shows CT and ^{18}FBnTP image and bottom panel shows CT and ^{18}F-FDG image. H - heart, T - tumor; tumors are indicated by arrows and circled. **b** PET/CT images of a Kras/Lkb1 mouse with two tumors, T1 and T2. Top panel – ^{18}FBnTP/CT overlay, bottom panel – ^{18}F-FDG/CT overlay. H – heart. **c** Western blot of tumors T1 and T2 isolated from mouse imaged in b and probed with indicated antibodies. **d** Western blot from tumors isolated from Kras/Lkb1 (KL) or Kras/p53 (KP) mice was probed with indicated antibodies. **e** Whole cell lysates from adenocarcinoma cell line A549 and squamous cell carcinoma cell line RH2 were probed with indicated antibodies. **f** TMRE measurement comparing A549 and RH2 (n = 3 replicates) human cell lines. **g** Basal oxygen consumption rate (OCR) per cell was measured in A549 and RH2 cell lines (n = technical 15 replicates). **h** Extracellular acidification rate (ECAR) was measured in A549 and RH2 cell line (n = technical 15 replicates). **i** Coomassie staining of mitochondria isolated from A549 and RH2 cells separated on blue native gel. SC – supercomplex, I – complex I, V – complex V. **j** Complex I activity was evaluated by measuring oxygen consumption rate (OCR) per cell in A549 and RH2 cell lines (n = technical 25 replicates) when cells were using pyruvate and malate as substrates. **k** Cell viability of A549 and RH2 cell lines (n = 3 replicates) was measured in the presence of indicated concentrations of phenformin for 48 hr. **l** Transverse view of a Kras/Lkb1 mouse imaged with ^{18}FBnTP PET/CT (left panel) and ^{18}F-FDG PET/CT (right panel). H - heart, tumor is outlined by the dotted line. **m** H&E stain of the PET imaged tumor. Tumor histology is indicated as ADC or SCC. Scale bar = 1.0 mm. **n** representative images of Glut1 (left panel) and CK5/TTF1 (right panel) stained tumor. Scale bar = 25 μm. The data are represented as the mean +/- SD. Statistical significance (*p<0.05; **p<0.01; ***p<0.001; ****p<0.0001; ns, not significant) was calculated using unpaired two-tailed t-test. Experiments in e-k were performed twice.

12.3 Appendix

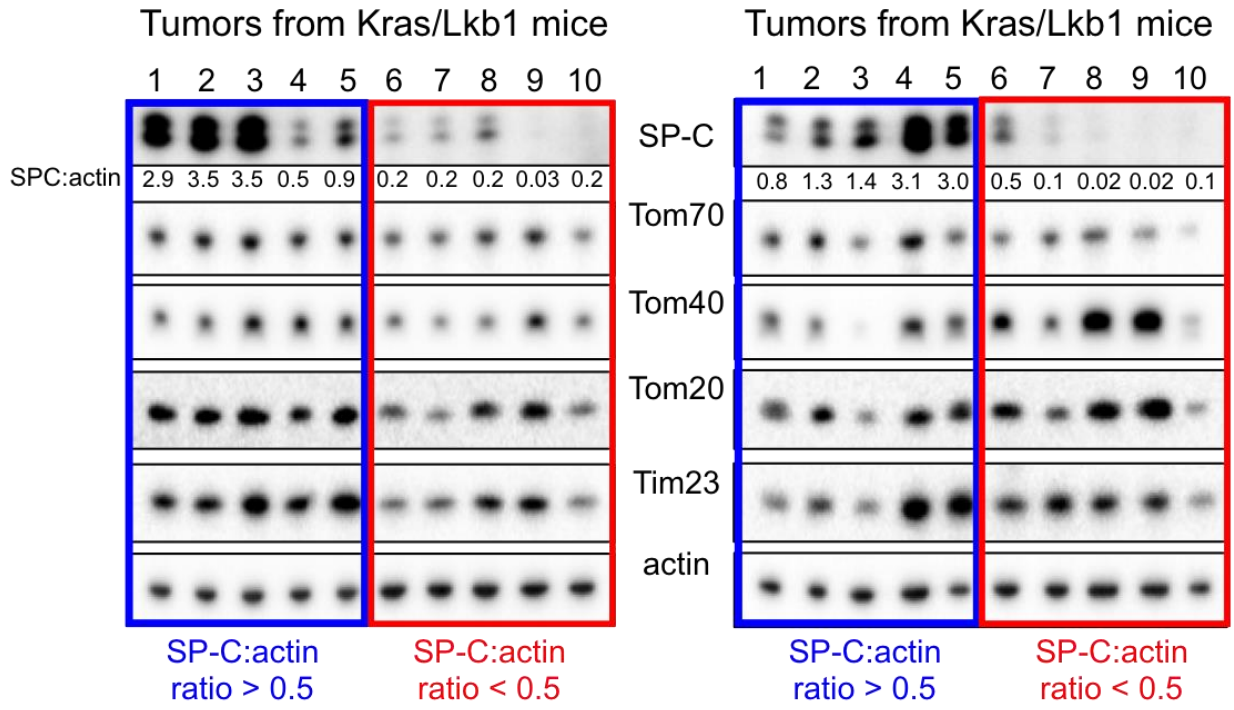

Figure 12-5. Mitochondrial markers in Kras/Lkb1 mouse lung tumors.
Whole cell lysates from lung tumors isolated from Kras/Lkb1 mice were immunoblotted with indicated antibodies. Tumors with high levels of surfactant protein C (SP-C:actin > 0.5) are defined

as adenocarcinomas (blue box), while tumors with lower levels of SP-C (SP-C:actin < 0.5) are defined as squamous cell carcinomas (red box).

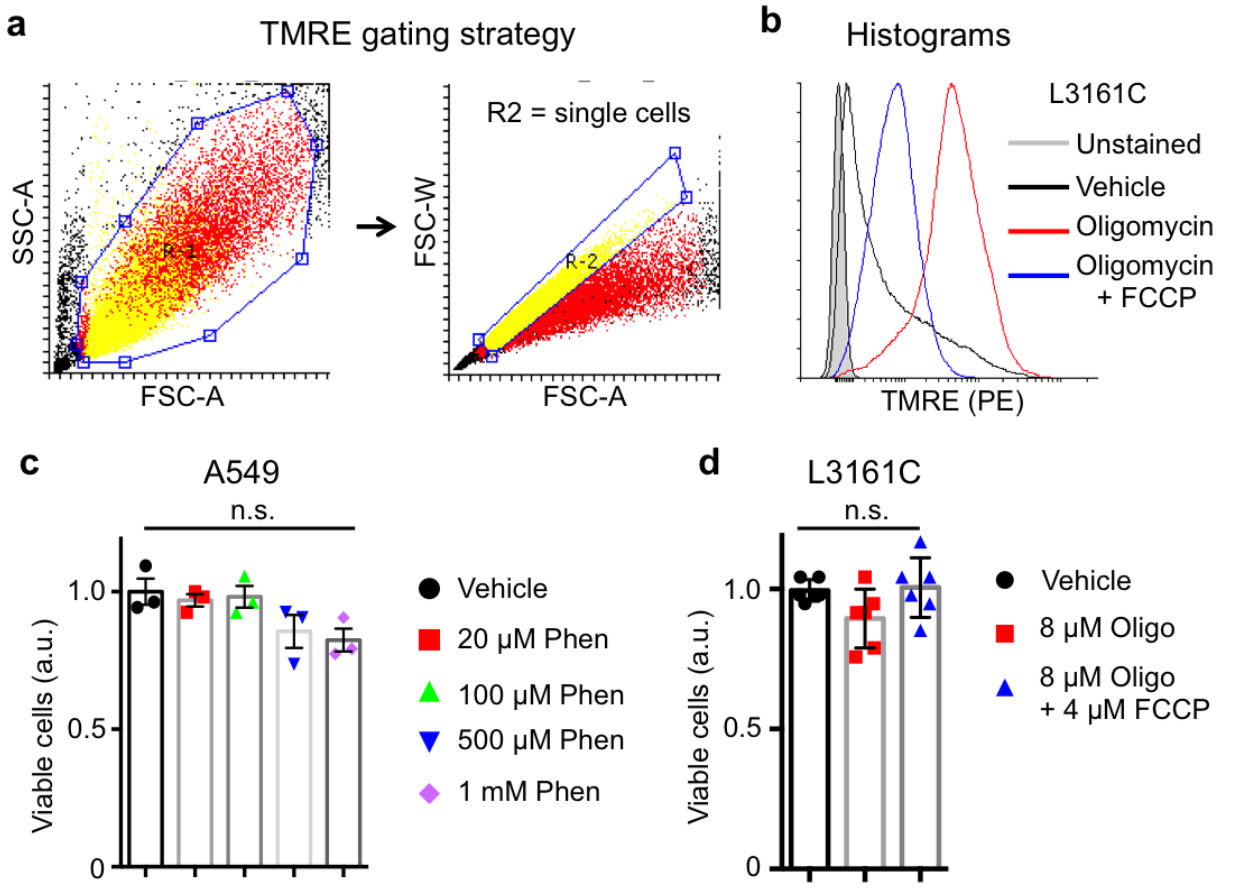

Figure 12-6. Flow cytometry data from L3161C cells stained with TMRE.
a Gating strategy used for quantification of TMRE signal. The R2 – region representing single cells was used for quantification of the TMRE signal. **b** Overlay histogram showing shifts in TMRE signal in L3161C cells strained with Vehicle, 8 μM Oligomycin, and 8 μM Oligomycin + 4 μM FCCP. **c** Viability of A549 cells treated for 3 hr with vehicle or increasing doses of phenformin. **d** Viability of L3161C cells treated for 3 hr with vehicle or oligomycin +/- FCCP. The data are represented as the mean +/- SD. Statistical significance (*p<0.05; **p<0.01; ***p<0.001; ****p<0.0001; ns, not significant) was calculated using one-way ANOVA. Experiments in c and d were repeated once.

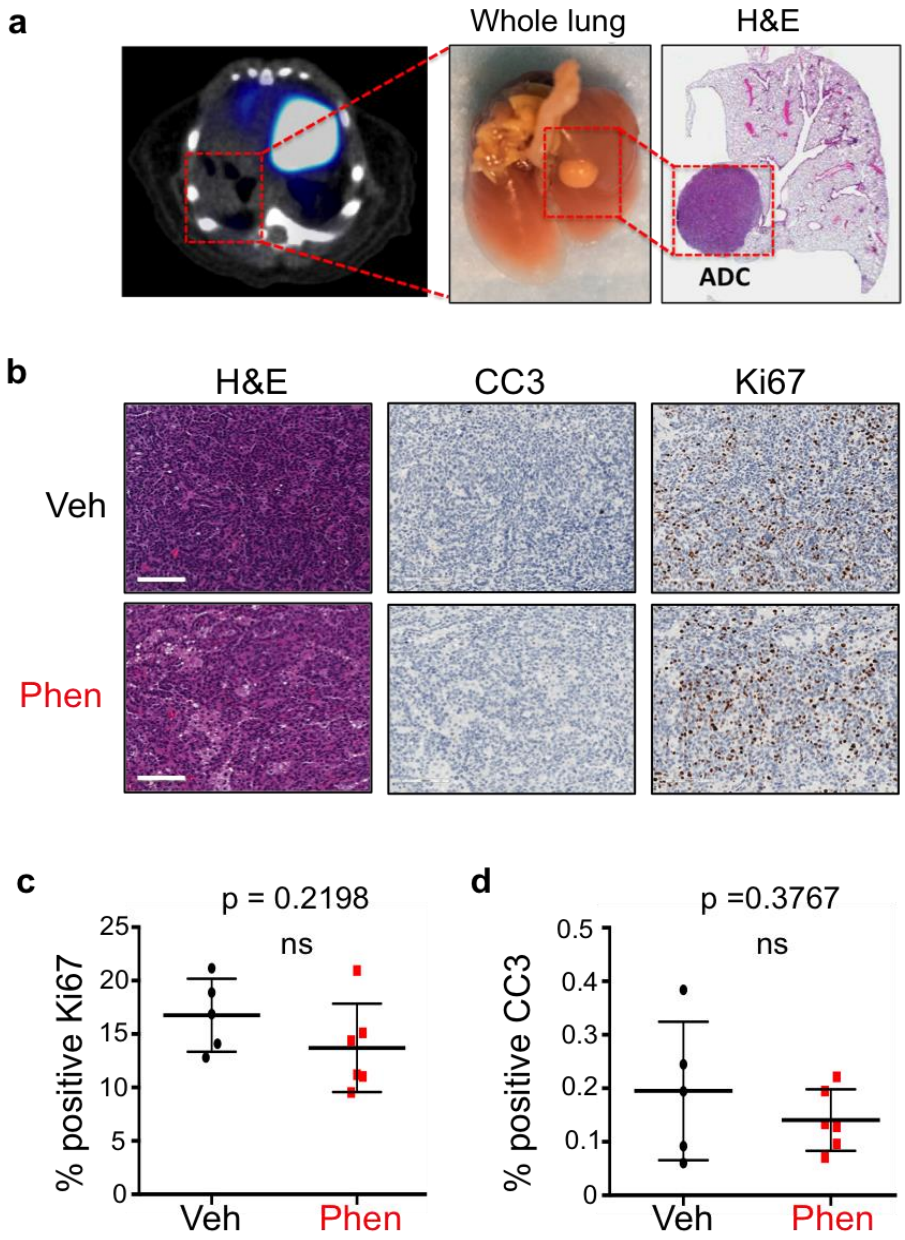

Figure 12-7. Short-term treatment with phenformin does not induced changes in proliferation or apoptosis.

a Transverse ^{18}FBnTP/CT overlay (left panel), image of the whole mouse lung after treatment with phenformin (middle panel), H&E stain of a lung lobe with associated adenocarcinoma (ADC) tumor (right panel). **b** Representative slides stained with H&E (left panel), Cleaved Caspase 3 (middle panel), and Ki67 (right panel) from tumors from Kras/Lkb1 mice treated with Vehicle (top panel) or Phenformin (bottom panel). Scale bar = 100 μm. **c** Quantification of staining for Ki67 (left panel) and **d** Cleaved Caspase 3 (right panel) for tumors from Kras/Lkb1 mice treated with Vehicle (n = 5 mice) or Phenformin (n = 5 mice). The data are represented as the mean +/- SD. Statistical significance (*p<0.05; **p<0.01; ***p<0.001; ****p<0.0001; ns, not significant) was calculated using unpaired two-tailed t-test.

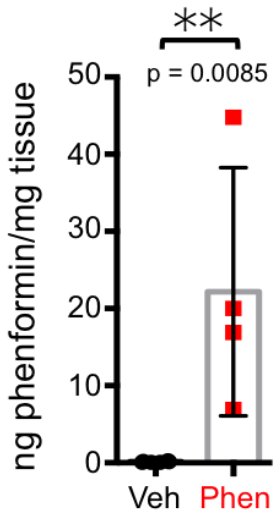

Figure 12-8. Detection of phenformin in lung tumors by mass spectrometry.
Phenformin was quantified using liquid chromatography/mass spectroscopy in lung tumors isolated from Kras/Lkb1 mice. Tumors were isolated from mice treated with Vehicle (saline) (n = 6) or 100-200 mg/kg Phenformin (n = 4) by oral gavage for 5 days. This experiment was repeated once. The data are represented as the mean +/- SD. Statistical significance (*p<0.05; **p<0.01; ***p<0.001; ****p<0.0001; ns, not significant) was calculated using unpaired two-tailed t-test.

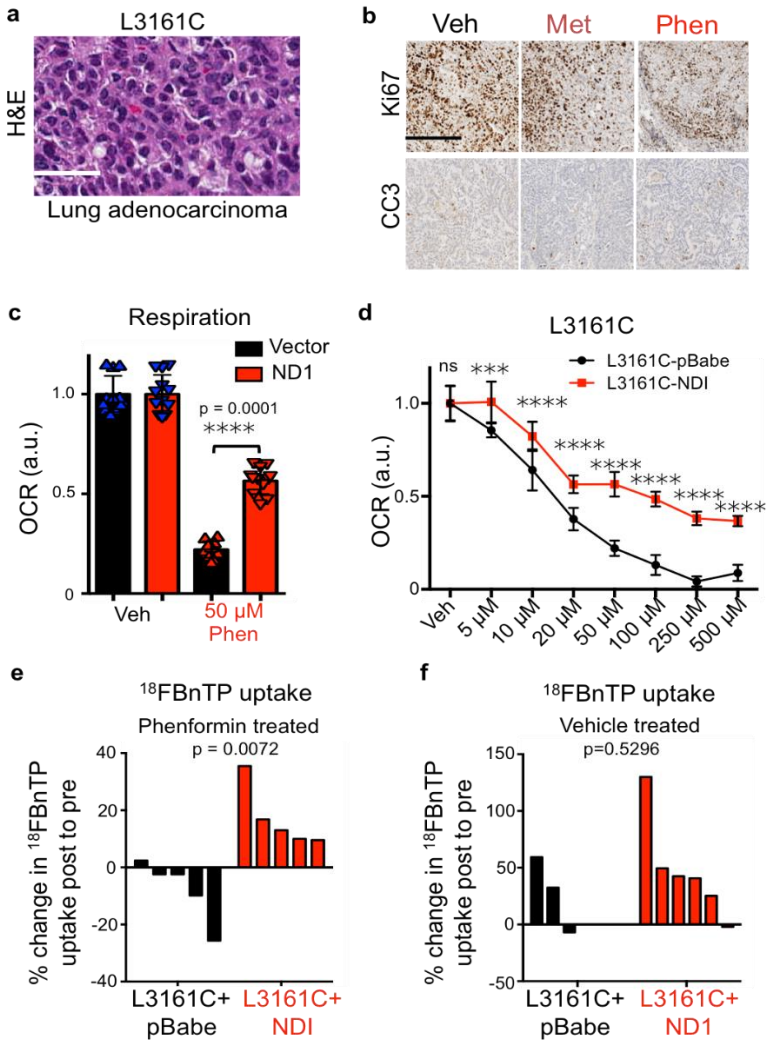

Figure 12-9. In vitro and in vivo analysis of the mouse lung adenocarcinoma cell line L3161C.

a H&E staining of a lung ADC from L3161C mouse tumor cell line. Scale bar = 25 μm. **b** Representative slides stained with Ki67 (top panel), and Cleaved Caspase 3 (bottom panel) from tumors formed by transthoracically transplanted L3161C cells that were treated with Vehicle, Metformin, Phenformin or Rotenone. Scale bar = 200 μm. **c** Basal OCR rate per cell for L3161C-pBabe (black) (n = 6-12 replicates) and L3161C-ND1 cells (red) (n = 12 replicates) treated with 50 μM Phenformin for 24 hr. **d** Basal OCR rate per cell for L3161C-pBabe (black) (n = 6-12 replicates) and L3161C-ND1 cells (red) (n = 12 replicates) treated with indicated concentrations of Phenformin for 24 hr. This experiment was repeated once. The data are represented as the mean +/- SD. Statistical significance (***p<0.001; ****p<0.0001; ns, not significant) was calculated using one way ANOVA. **e** Waterfall plot for % change in ^{18}FBnTP uptake post-treatment to pre-treatment for mice transthoracically transplanted with L3161C cells expressing empty vector (L3161C+pBabe) (n = 5 mice) or expressing ND1 (L3161C+ND1) (n = 5 mice) and treated with 125 mg/kg/day Phenformin for 5 days. e, Waterfall plot of % change in ^{18}FBnTP uptake in tumors formed by transthoracically transplanted L3161C-pBabe (n = 3 mice) or L3161C-ND1 cells (n = 6 mice) that were treated with Vehicle for 5 days. Experiments in e and f were preformed once.

Statistical significance (*p<0.05; **p<0.01; ***p<0.001; ****p<0.0001; ns, not significant) was calculated using unpaired two-tailed t-test.

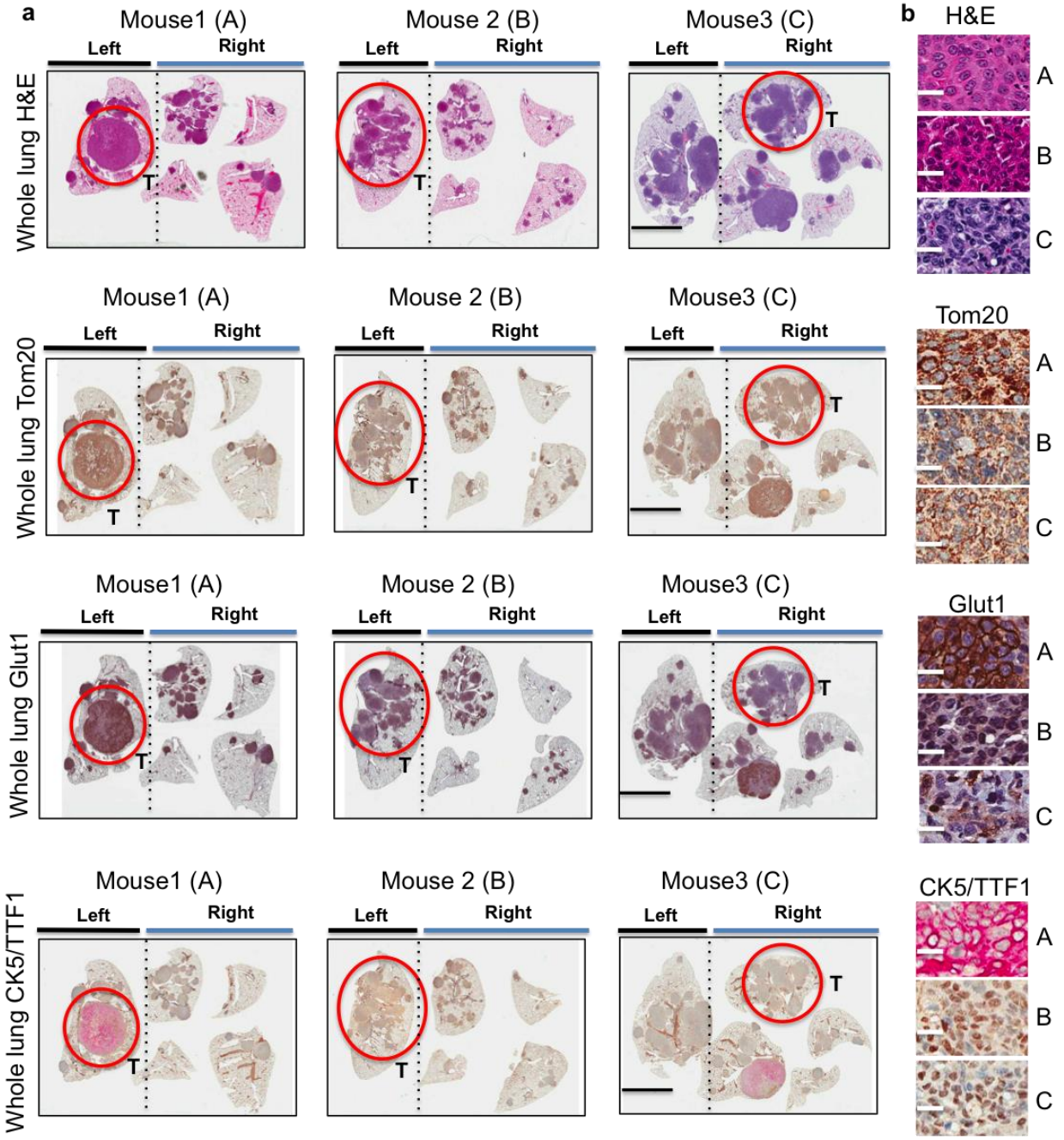

Figure 12-10. IHC markers in lung tumors from Kras/Lkb1 mice.
a Whole lungs from Mouse 1, Mouse 2 and Mouse 3 stained for H&E or antibodies against Tom20, Glut1 or CK5-TTF1. Scale bar = 5 mm. **b** Representative images from tumor circled in red were stained with H&E or the indicated antibodies. Scale bar = 25 μm.

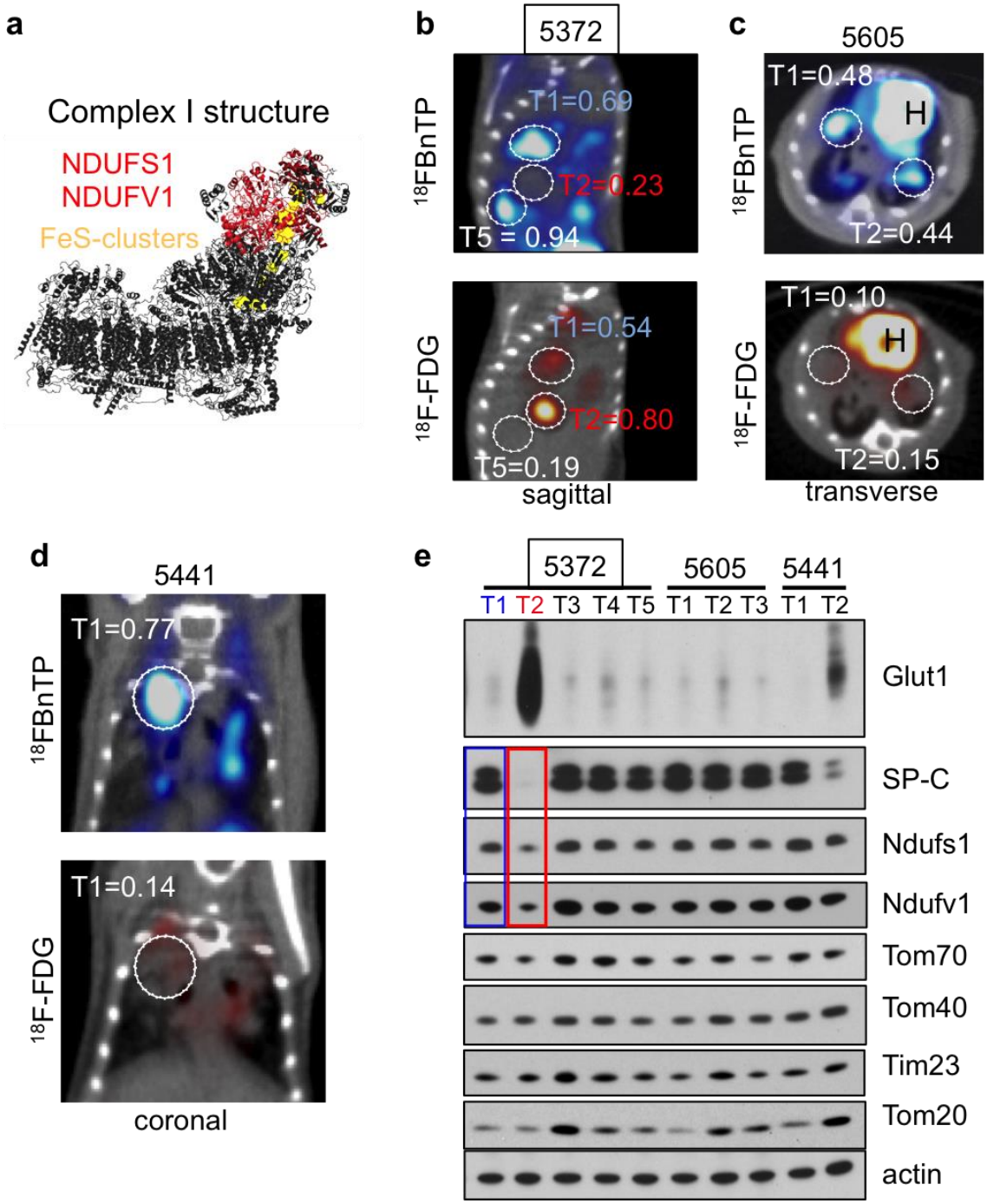

Figure 12-11. PET/CT and biochemical analysis of Kras/Lkb1 tumors.
a-d PET/CT images from Kras/Lkb1 mice that were imaged on sequential days with ^{18}FBnTP (top panel) and ^{18}F-FDG (bottom panel). Tumors are circled, H – heart. Maximum %ID/g uptake value for each tumor normalized to the maximum %ID/g uptake in the heart is indicated **e** Western blot analysis from lung nodules that were isolated from mice imaged in **a-d**. Two lung tumors from mouse 5372 (imaged in b) are shown – T2 in red (high ^{18}F-FDG and Glut1 levels; low ^{18}FBnTP and low Ndufs1 and Ndufv1 levels); and T5 in blue (low ^{18}F-FDG and Glut1 levels; high ^{18}FBnTP and high Ndufs1 and Ndufv1 levels).

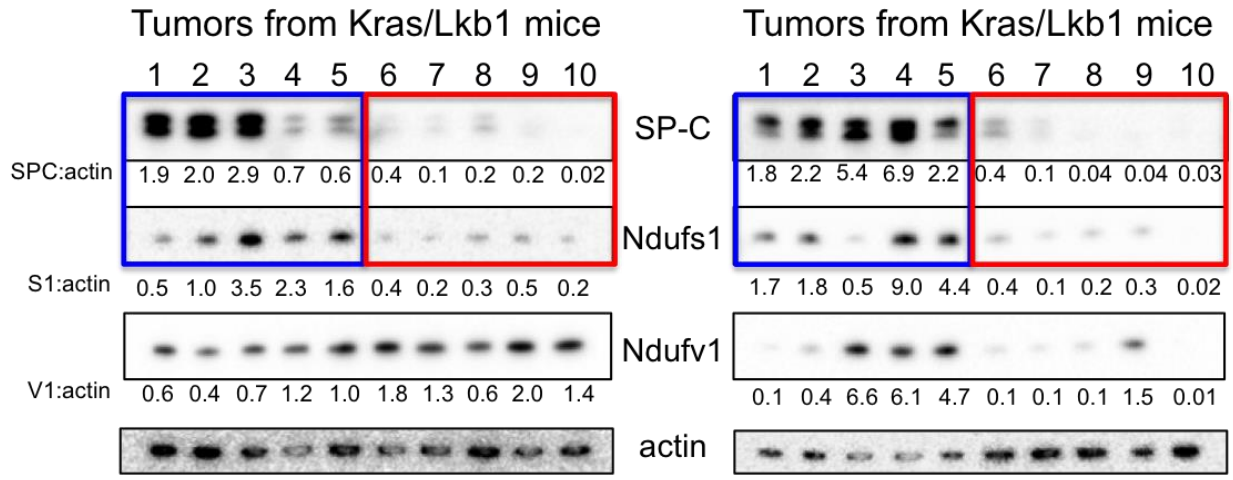

Figure 12-12. Differential Ndufs1 protein expression between ADC and SCC Kras/Lkb1 tumors.
Whole cell lysates from lung tumors isolated from Kras/Lkb1 mice were immunoblotted with the indicated antibodies.

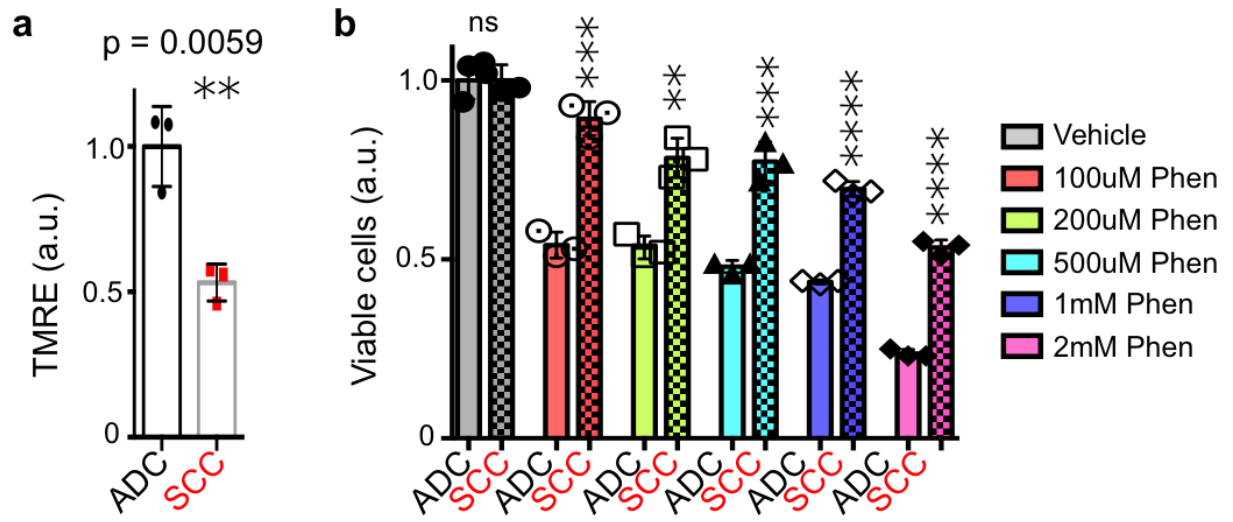

Figure 12-13. Sensitivity of mouse lung cell lines to phenformin.
a TMRE measurement comparing mouse adenocarcinoma cell line and mouse squamous cell carcinoma cell lines (n = 3 replicates). **b** Cell viability of mouse adenocarcinoma cell line and mouse squamous cell carcinoma cell line (n = 3 replicates) was measured in the presence of indicated concentrations of Phenformin for 48 hr. The data are represented as the mean +/- SD. Statistical significance (*p<0.05; **p<0.01; ***p<0.001; ****p<0.0001; ns, not significant) was calculated using unpaired two-tailed t-test. Experiments were repeated twice.

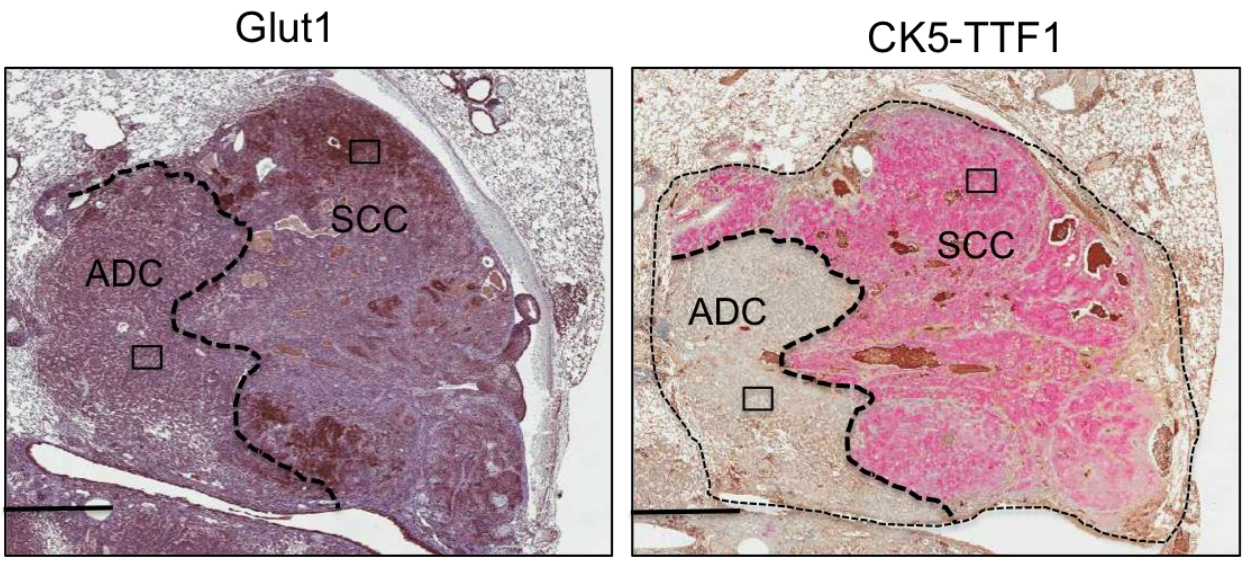

Figure 12-14. IHC staining on a Kras/Lkb1 tumor with ADC-SCC mixed histology.
Glut1 (left) and CK5-TTF1 (right) staining were performed on an ADC-SCC mixed tumor from a Kras/Lkb1 mouse. Tissue segmentation demarks ADC from SCC regions. Boxes indicated where representative 40X images were captured. Scale bar = 1.0 mm.

Chapter 13: 3-dimensional mapping of mitochondrial networks defines diverse bioenergetic phenotypes in lung cancer

13.1 Main

13.1.1 Introduction

Mitochondria are critical to the governance of metabolism and bioenergetics in cancer cells. The mitochondria form highly organized networks, in which the structure of their outer and inner membranes defines their bioenergetic capacity. However, in vivo studies defining the relationship between the structural organization of mitochondrial networks and their functional bioenergetics in cancer have been limited. In this study we performed in vivo structural and functional profiling of mitochondrial networks and bioenergetic phenotypes in non-small cell lung cancer (NSCLC) using an integrated platform comprised of PET imaging, respirometry and 3-dimensional scanning block-face electron microscopy (3D SBEM). The diverse bioenergetic phenotypes and metabolic dependencies we profiled in NSCLCs aligned with distinct structural organization of mitochondrial networks. We discovered that mitochondrial networks were organized into distinct compartments within tumor cells. In tumors with high rates of oxidative phosphorylation ($OXPHOS^{HI}$) we identified peri-droplet mitochondrial networks in which mitochondria contacted lipid droplets to support respiration and fatty acid oxidation in tumor cells. In contrast, we discovered that in glycolytic tumors with low OXPHOS activity ($OXPHOS^{LO}$) glucose flux directly regulated peri-nuclear localization of mitochondria, structural remodeling and the respiratory capacity of mitochondria. Our data suggest that in NSCLC, the mitochondrial networks are compartmentalized into distinct subpopulations that govern the bioenergetic capacity within tumors.

Non-small cell lung cancer (NSCLC) is a heterogeneous disease at a histological, genetic and in particular metabolic level[411,413]. Mitochondria are essential regulators of cellular energy and

metabolism, playing a critical role in sustaining growth and survival of lung tumor cells[392]. Specifically, the mitochondria are organized into dynamic networks such that the structural architecture of their outer and inner membrane dictates cellular electron transport chain (ETC) activity and respiratory capacity[417,418]. However, our understanding of how mitochondrial networks are structurally and functionally regulated in cancer at an in vivo level is limited.

To better understand mitochondrial bioenergetics in NSCLC, we recently utilized a voltage sensitive, positron emission tomography (PET) tracer known as 4-[^{18}F]fluorobenzyl triphenylphosphonium (^{18}FBnTP)[397], to measure changes in mitochondrial membrane potential ($\Delta\Psi$) in autochthonous K-Ras driven mouse models of NSCLC[419–421]. Importantly, ^{18}FBnTP uptake in lung tumors was predictive of response to Complex I inhibitors[419]. PET imaging of NSCLC tumors in Kras-driven GEMMs identified that LUADs and LUSC had distinctly different uptake for the ^{18}FBnTP and ^{18}F-FDG tracers suggestive of functionally distinct metabolic and bioenergetic phenotypes[419]. We next sought to determine if ^{18}FBnTP uptake in lung tumors directly correlated with OXPHOS activity.

13.1.2 In vivo profiling of bioenergetics reveals distinct OXPHOS signatures among NSCLC tumor subgroups

In order to evaluate the respiratory capacity of the electron transport chain (ETC) in lung tumors, we coupled PET imaging of NSCLC tumors in genetically engineered mouse models (GEMMs) followed by *ex vivo* respirometry analysis of mitochondrial Complex I and II performed on frozen lung tumors represented in **Figure 13-1a**. Coupling PET imaging with *ex vivo* respirometry allowed for the direct measurement of Complex I (and Complex II) maximal respiratory capacity (MRC) in frozen lung tumors[422]. Representative ^{18}FBnTP and ^{18}F-FDG PET imaging of a *Kras^{G12D};p53$^{-/-}$;Lkb1$^{-/-}$* (*KPL*) mouse is shown in **Figure 13-1b**, which identified synchronous lung tumors with heterogeneous ^{18}FBnTP and ^{18}F-FDG tracer uptake values. *KPL* lung tumor 1 was observed to be ^{18}FBnTP^{HI}; ^{18}F-FDG^{LO} and predicted to have elevated Complex I and II activity characteristic of an OXPHOS^{HI} signature. In comparison, the *KPL* lung tumor 2,

which was ^{18}F-BnTP^{LO}; ^{18}F-FDG^{HI} was predicted to have reduced Complex I and II activity characteristic of an OXPHOS^{LO} signature (**Figure 13-1b**). We performed *ex vivo* respirometry on *KPL* tumors 1 and 2 and observed a 3-fold upregulation in Complex I and Complex II MRC in the ^{18}FBnTP^{HI} tumor 1 compared to the ^{18}F-BnTP^{LO} tumor 2 (**Figure 13-1c**). We confirmed the histology of all lung tumors by immunoblot analysis of protein expression of SP-C and GLUT1 in whole cell lysates of lung tumors as well as immunohistochemical (IHC) co-staining of tumors for TTF1 and cytokeratin 5 (CK5) as previously described[413]. Tumor histology confirmed that *KPL* tumor 1 was LUAD and tumor 2 was LUSC based on surfactant protein C (SP-C) and glucose transporter 1 (GLUT1) protein expression[413,418]. We then examined mitochondrial respiration in LUAD and LUSC tumors from a larger cohort of *KPL* mice and found a significant increase in Complex I MRC in ^{18}FBnTP^{HI} LUADs as compared to ^{18}F-BnTP^{LO} LUSCs (**Figure 13-1d**). We obtained similar results performing a PET guided ex vivo respirometry analysis on LUAD and LUSC tumors from KL mice.

In order to determine if the differences in Complex I and Complex II MRC were intrinsic to lung tumor histology as opposed to tumor genotype we examined GEMMs from five different genetic backgrounds. These included – the *KPL* GEMMs as well as *Kras^{G12D}; Lkb1$^{-/-}$* (*KL*), *Kras^{G12D};p53$^{-/-}$* (*KP*), *Kras^{G12D}* (Kras) *and Lkb1$^{-/-}$;p53$^{-/-}$;Pten$^{-/-}$* (LPP) mice. Of note, the *KPL, KL* and *LPP* GEMMs develop both LUAD and LUSC subtypes, while K and KP GEMMs develop exclusively LUADs. We identified a direct and significant correlation between ^{18}FBnTP uptake and Complex I and Complex II MRC in NSCLC tumors (**Figure 13-1e**). Importantly, the LUAD and LUSC tumor subtypes segregated into two distinct populations in which LUADs had a higher ^{18}FBnTP uptake and Complex I and Complex II MRC as compared to LUSCs (**Figure 13-1e**). Conversely, ^{18}F-FDG uptake was inversely correlated with Complex I and Complex II MRC in LUAD and LUSC tumors and again these tumors subtypes separated into two distinct populations (**Figure 13-1f**).

We next evaluated whether the differences in OXPHOS activity and glucose flux observed in mouse tumors were conserved in human LUAD and LUSC tumors as well. We measured significantly higher Complex I and II MRC in tumor xenografts from LUAD cell lines H1975 and A549 as compared to tumors from LUSC cell line RH2 or the head and neck squamous cell carcinoma (HNSCC) cell line Tu686 (**Figure 13-1g**). We tested A549 vs A549 Rho cell lines in tumor xenografts as a control. The A549 Rho cells lacked ETC complex proteins compared to wildtype A549 cells. Additionally, A549 Rho tumors had reduced ^{18}FBnTP uptake and significantly lower Complex I and Complex II MRC in xenografts from a control A549 Rho cell line that were established using ethidium bromide treatment[423]. We next measured ^{18}FBnTP and ^{18}F-FDG uptake in OXPHOS^{HI} H1975 and OXPHOS^{LO} RH2 mouse tumor xenografts and confirmed that H1975 had a significantly higher ^{18}FBnTP uptake compared to RH2 tumors (**Figure 13-1h**). Conversely, RH2 tumors had significantly higher ^{18}F-FDG uptake than H1975 tumors (**Figure 13-1i**). Collectively, these results showed that ^{18}FBnTP uptake correlates with Complex I activity in mouse and human lung tumors. By coupling ^{18}FBnTP and ^{18}F-FDG PET imaging with ex vivo respirometry it is now possible to distinguish bioenergetic signatures in tumors and distinguish between OXPHOS^{HI} vs OXPHOS^{LO} phenotypes. While we identified a significantly higher mitochondrial respiratory capacity in LUADs as compared to LUSC, given the genetic and metabolic heterogeneity that is common to NSCLC[411], we anticipate that OXPHOS^{HI} and OXPHOS^{LO} mitochondrial phenotypes will be identified among both LUAD and LUSC subpopulations.

13.1.3 PET guided ultra-resolution 3D SBEM imaging of mitochondrial architecture in NSCLC

The distinct functional differences that we observed in mitochondrial respiration between NSCLC tumor subtypes suggested that equally distinct differences existed in the structural organization of mitochondrial networks between LUAD and LUSC tumors. To investigate this, we developed a workflow that paired functional ^{18}FBnTP and ^{18}F-FDG PET imaging with ultra-

resolution 3-dimensional serial block-face electron microscopy (3D SBEM) (**Figure 13-2a**). Pairing PET imaging with 3D SBEM enabled us to functionally image mitochondria activity in whole lung tumors and then map the ultrastructures of mitochondrial networks in tumor cells[424]. Using ^{18}FBnTP and ^{18}F-FDG PET and microCT imaging we first spatially orientated tumors and functionally distinguished tumor regions as ^{18}FBnTP^{HI}; ^{18}F-FDG^{LO} (OXPHOS^{HI}) vs ^{18}F-BnTP^{LO}; ^{18}F-FDG^{HI} (OXPHOS^{LO}) tumor regions in order to accurately guide SBEM analysis. Representative images of both transverse PET/CT scans and 3D reconstructions show lung tumors from KL mice that are either ^{18}FBnTP^{LO}; ^{18}F-FDG^{HI} (**Figure 13-2b**) or ^{18}FBnTP^{HI}; ^{18}F-FDG^{LO}.

Next, we imaged whole lungs by high resolution microCT in both ^{18}F-BnTP^{HI}; ^{18}F-FDG^{LO} and ^{18}FBnTP^{LO}; ^{18}F-FDG^{HI} lung tumors (**Figure 13-2c**). Tumors were then sectioned in half along the transverse axis (**Figure 13-2c**) with the top half of the tumor was analyzed by SBEM imaging and the bottom half of the tumor was saved for histological analysis in order to exclude any necrotic tissue and select tumor dense regions for SBEM imaging (**Figure 13-2c-e**). We quantified tumor volume and vasculature using microCT analysis and CD34 IHC staining. Our data showed no significant differences in vasculature between LUAD vs LUSC. CD34 staining showed a significant increase in CD34 in normal tissue as compared to that of tumor tissue. No significant differences in CD34 staining were identified in either lung tumor subtype (LUAD vs LUSC).

SBEM ultra-resolution imaging was then performed on the tumor blocks to generate 2-dimensional (2D) sequential image slices. Within our SBEM images we generated isotropic voxels of nanometer scale allowing comprehensive visualization of NSCLC tumors at a cellular and subcellular level. The SBEM sample volume imaged represented over 300 cells per tissue volume at a nanometer resolution of 5-6nm on the x-y axis. The enabled visualization cellular ultrastructure such as mitochondrial cristae. Serial SBEM images generated within the x-y-z-axes achieved a resolution of nanometer at 20-60nm. 2D images were stacked in order to create a 3D SBEM tumor volume (**Figure 13-2f**). Following the generation of a 3D image of the tumor we built a topographical map of the tumor's cellular landscape in order to differentiate tumor from non-

tumor cells. We performed segmentation of individual cells followed by labeling of each cell type within the tumor landscape based on morphological features of each of the cell types that included: adeno and squamous carcinomas, neutrophils, macrophages, endothelial cells and red blood cells (**Figure 13-2g,h**). These results demonstrate a successful 3D mapping of the cellular topography in NSCLC tumor subtypes in GEMMs. In LUSC, the two major cell types identified were squamous cell carcinomas (40%) and neutrophils (42%) as distinguished by their distinct subcellular structures (**Figure 13-2h**)[425–429]. A small proportion of adenomatous carcinoma and red blood cells were also observed in the LUSC tumor SBEM tissue block (**Figure 13-2h**). Identical analysis was performed on OXPHOS-proficient (^{18}FBnTP^{HI}; ^{18}F-FDG^{LO}) LUADs using the workflow described in **Figure 13-2a**. 3D SBEM analysis of LUADs identified a predominance of tumor infiltrating macrophages. The presence of neutrophils in LUSCs and macrophages in LUADs agrees with the tumor infiltrating immune cells documented within the microenvironment of each lung tumor subtype in autochthonous mouse models of NSCLC[430–433] as well as in NSCLC patients[434,435].

13.1.4 Distinct spatial and structural organization of mitochondria mark OXPHOSHI vs OXPHOSLO tumors

The functional differences in Complex I activity measured between LUAD and LUSC tumors suggested distinct differences exist in the structural and spatial organization of mitochondria in each tumor subtype. It is well described that morphological changes in mitochondrial structure impact their function. Increases in mitochondrial fission and cristae remodeling through either genetic or pharmacological perturbation results in uncoupling of mitochondrial respiration and increases in glycolytic metabolism[436,437]. We therefore analyzed mitochondrial ultrastructure and the spatial localization of mitochondria within individual tumor cells from (^{18}FBnTP^{HI}; ^{18}F-FDG^{LO}) LUADs and (^{18}FBnTP^{LO}; ^{18}F-FDG^{HI}) LUSCs. We segmented the mitochondria and nuclei in LUAD and LUSC cells. We measured a volume of 5.62x104μm^3 and

~200 intact cells in LUSC tissue and a volume of $2.75x10^5$ μm^3 and ~350 intact cells in LUAD tissues in order to generate 3D reconstructions of individual tumor cells (**Figure 13-3a**).

In order to achieve a comprehensive analysis of the large mitochondrial content within the SBEM volumes, we developed a deep learning convolutional neural network utilizing the U-Net architecture. This enabled us to achieve robust and accurate trinary segmentation of mitochondria, nucleus and background[438–440]. We first generated a ground truth annotation by performing manual labeling of mitochondria based on their morphological features. We then trained the convolutional neural networks evolved from U-shaped encoder decoder architecture adapted with Atrous Spatial Pyramid Pooling (ASPP) filters to automate trinary segmentation of the mitochondria, nucleus and background. We applied the U-NET based deep learning neural network algorithm on 200-550 serial 2D SBEM images in order to generate 3D renderings of mitochondria and nucleus in lung tumor cells. This approach provided an accurate reference of spatial distribution and enabled 3D reconstruction of images along the x, y and z axis.

We analyzed 20,000-50,000 mitochondrion per tumor section with morphological measurements taken for length, total volume, sphericity (roundness) and cristae density. We validated mitochondria prediction accuracy generated from our U-Net algorithm by pairwise comparisons to manual segmentation. The performance of trinary segmentation (mitochondria, nucleus and background) from our neural networks was measure by similarity coefficient and compared to that of ground truth (manual) segmentation. The U-Net algorithms achieved a 0.92 DICE score which translated to 92% accuracy as compared to that of manual registration. Representative images 3D reconstructions of mitochondrial networks (red) and nuclei (blue) from LUAD and LUSC cells are shown in **Figure 13-3b**. From here, 2D images of mitochondria and their IMM cristae architecture were reconstructed into 3D structures (**Figure 13-3c-e**).

In line with the distinct bioenergetic profiles measured among LUAD vs LUSC tumor cells in **Figure 13-1**, we measured equally distinct differences in mitochondrial organization and cellular localization in both tumor subtypes. Quantification of mitochondrial sphericity (roundness), length,

and volume showed that LUSC maintained mitochondrial pools characterized by fragmented and circular morphology (**Figure 13-3b, f-h**). The mitochondrial parameters graphed in the density plots (length, volume, cellular localization) showed a narrow distribution in LUSC as compared to LUADs. This narrow distribution is characteristic of a more uniform or homogenous distribution of mitochondrial structure. These results were in stark contrast to the organization of mitochondrial networks in LUADs in which the density plots showed a broad distribution of mitochondrial networks characteristic of more diverse or heterogeneous mitochondrial structures as compared to LUSC (**Figure 13-3b, f-h**). In addition to structural differences, we identified distinct variances in the spatial distribution of mitochondria between LUAD and LUSC cells. The mitochondria in LUSC localize in perinuclear clusters, whereas in LUAD the mitochondria are distributed throughout the cell and localized at both the nucleus and cytoplasm (**Figure 13-3b**). We next developed an algorithm to measure the distance of individual mitochondria from the nucleus of each cell. We then measured and quantified the distance between individual mitochondria and the nucleus in lung tumor cells. We discovered a broad distribution of mitochondria in LUAD that included a mix of perinuclear and cytoplasmic mitochondrial pools (**Figure 13-3b, k-l**). In contrast, LUSC maintained a uniform concentration of mitochondrial around the nucleus with few mitochondria localized to the cytoplasm. We also confirmed similar trend of mitochondrial morphology and spatial distribution has been conserved between *in vivo* tumor tissues and *in vitro* culture cell lines derived from mouse NSCLC tumors.

We next investigated the architecture of the cristae within LUAD and LUSC tumors. The mitochondrial cristae, which reside in the inner mitochondrial membrane (IMM) house the respiratory chain Complexes I-V that comprise the electron transport chain and serve as the site of OXPHOS and cellular bioenergetics[441–443]. Importantly, the structural organization of cristae directly impacts the bioenergetic capacity of the mitochondria[417,418,444]. We therefore analyzed and quantified the ultrastructure of the cristae architecture in LUAD and LUSC tumor cells using a Weka segmentation (Image J) program[445] (**Figure 13-3c-e**). Morphological analysis identified a

differential density and distribution of cristae structures between LUAD and LUSC (**Figure 13-3e**). We identified three cristae structures in our analysis that have been well described in both normal tissue and cancer cells. These included: 1) highly organized orthodox or lamellar cristae that we classified as Type I[446], 2) sparse and disorganized cristae that we classified at Type II[447] and 3) condensed cristae that we classified at Type III[448] represented in **Figure 13-3e**.

Our analysis revealed that LUAD cells had a heterogenous distribution of Type I, II and III cristae, whereas LUSC tumor cells had predominantly Type II and III cristae and a significant absence of Type I cristae (**Figure 13-3i**). Orthodox, lamellar cristae support robust OXPHOS activity in cells whereas disorganized and condensed cristae are associated with defects in cellular OXPHOS activity[446,448–450]. The significant reduction of Type I cristae in LUSC as compared to that of LUAD tumor cells supports the distinct bioenergetic activities that we profiled in these tumor subtypes, in which ^{18}FBnTP^{LO} LUSC tumors had significantly reduced Complex I and Complex II MRC as compared to ^{18}FBnTP^{HI} LUADs.

In order to confirm that the mitochondrial phenotypes we profiled in mouse NSCLC tumors were conserved across species, we analyzed mitochondrial structure and cellular localization in human LUAD and LUSC tumor cell lines. Analysis of mitochondrial length as measured by circularity and aspect ratio showed that OXPHOS^{HI} LUAD cell lines A549 and H1975 had significantly increased circularity and aspect ratio as compared to OXPHOS^{LO} LUSC cell lines RH2 and the HNSCC cell line Tu686 (**Figure 13-3j,k**). In addition, A549 and H1975 cells had significantly increased mitochondrial and were distributed cytoplasmic distribution as compared to RH2 and Tu686 cells whose mitochondrial were fragmented and predominantly localized to the nucleus perinuclear mitochondrial phenotype (**Figure 13-3l,m**). A549 and H1975 cells had higher cristae density and displaying predominantly type I cristae that were distributed throughout the cytoplasm compared to RH2 and Tu686 cells, whose mitochondria were primarily comprised of both type II and III cristae (**Figure 13-3n,o**). Quantitative, measurement of mitochondrial networks within NSCLCs tumors identified that OXPHOS^{LO} LUSC had a narrow gaussian distribution in all

mitochondrial parameters measured - mitochondria dynamics (length), spatial localization of mitochondria and cristae architecture. Conversely, $OXPHOS^{HI}$ LUADs displayed a broad distribution of mitochondrial dynamics, spatial localization and cristae architecture. These results demonstrate that mitochondrial networks within $OXPHOS^{LO}$ LUSC are significantly more homogeneous as compared to $OXPHOS^{HI}$ LUADs, which maintain more diverse pools of mitochondria.

13.1.5 OXPHOSHI LUADs compartmentalize mitochondrial into peri-droplet subpopulations

The broad spatial distribution of mitochondrial networks throughout the cytoplasm in $^{18}FBnTP^{HI}$, $OXPHOS^{HI}$ LUADs prompted us to investigated whether the mitochondria compartmentalize into subpopulations that support OXPHOS activity in these tumors. Compartmentalization of metabolism among tissues and within individual cells has been shown to support cellular growth through the coordinated function[451]. At an intracellular level, the mitochondria communicate with cellular organelles such as the ER and nucleus to facilitate a metabolic and survival functions in both normal and cancer cells[452–454]. We therefore examined communication of cytoplasmic mitochondria (CM) with cellular organelles. SBEM imaging and 3D reconstructions of lung tumor cells identified a vast number of lipid droplets (LDs) in $^{18}FBnTP^{HI}$, $OXPHOS^{HI}$ LUADs that was nearly absent in $^{18}FBnTP^{LO}$ LUSC (**Figure 13-4a-c**). We identified subpopulations of cytoplasmic mitochondria (CM) that contact LDs and wrapped themselves around the LDs to form peri-droplet mitochondria (PDM) (**Figure 13-3a** bottom left inset). PDMs have been described in brown adipose tissue (BAT)[455], heart[456], and skeletal muscle[457] but not in lung cancer. In BAT, PDMs directly bind to LDs in order to regulate cellular respiration, lipid production and nutrient preferences for fatty acid oxidation (FAO)[458]. Structurally, PDMs are characterized by increased fusion, organized lamellar cristae and elevated rates of respiration as compared to CM networks[458]. These results suggested that $OXPHOS^{HI}$ lung tumor cells may compartmentalize mitochondrial subpopulations to support cellular respiration.

We quantified the distribution of PDM, PNM and CM subpopulations across LUAD and LUSC tumor cells and showed a broad distribution of PDM, PNM and CM among LUADs (Figure 4d). Interestingly, PDMs were nearly absent in $^{18}FBnTP^{LO}$, $OXPHOS^{LO}$ LUSC cells. There cellular landscape was dominated by PNM and CM subpopulations (**Figure 13-4d**). In LUADs, the PDMs were characterized as hyperfused mitochondria with predominantly orthodox Type I cristae and were consistent with morphologies previously reported in BAT[458]. PDMs were interlaced through dense regions of LDs and contacted multiple LDs shown in both 2D and 3D SBEM images (**Figure 13-4e-f**). Following this, we used oil red O staining, which labels the neutral lipids (triglycerides and diacylglycerols) to confirm the presence of LDs NSCLC tumors. Oil red O staining from KrasG12D-driven GEMMs and human NSCLC xenografts showed a significant enrichment in LDs in $^{18}FBnTP^{HI}$, $OXPHOS^{HI}$ LUADs that was absent in $^{18}FBnTP^{LO}$, $OXPHOS^{LO}$ LUSCs (**Figure 13-4g-j**).

We next measured PDM in human $OXPHOS^{HI}$ LUAD vs $OXPHOS^{LO}$ LUSC cell lines. We showed that $OXPHOS^{HI}$ LUAD lines – H1975, H1651 and A549 had a significant increase in LDs and PDM formation as compared to $OXPHOS^{LO}$ squamous cell carcinoma lines RH2 and Tu686 (**Figure 13-4k-m**). Lastly, we analyzed The LUAD and LUSC Cancer Genome Atlases for gene expression of the PLIN5 and DGAT1 proteins that regulate lipid droplet biogenesis and peri-droplet mitochondrial formation. PLIN5 is a perilipin that acts as a scaffolding protein and is associated with peri-droplet mitochondrial formation in cardiac and skeletal muscle[456]. DGAT1 is an enzyme that mediates the final step of triacylglycerol synthesis, esterifying diacylglycerol to yield triacylglycerol, which is then packaged into lipid droplets[459]. We identified a significant upregulation of gene expression for both PLIN5 and DGAT1 in LUADs as compared to LUSC tumors.

PDMs have been shown to support cellular respiration through increased FAO[458]. We next examined whether the PDM compartment supported mitochondrial respiration in LUAD cells through FAO and if this was absent in PDM-deficient LUSC cells. Measurement of the percent

change in basal oxygen consumption rate (OCR) following treatment with inhibitors of pyruvate metabolism (UK-5099), glutamine metabolism (BPTES) or fatty acid oxidation (etomoxir) showed that OXPHOS-proficient LUADs cell lines utilized pyruvate, glutamine and FAO to support respiration (**Figure 13-4n**). In contrast OXPHOS-deficient squamous cell lines RH2 and Tu686 were sensitive to only pyruvate and glutamine inhibition and not reliant on FAO. We next measured cell growth of PDM-rich H1975 vs PDM-deficient RH2 cell lines following nutrient deprivation of glucose, glutamine or free fatty acids (FFA). Our results showed that restricting FFAs significantly inhibited growth of H1975 cells but not RH2 cells (**Figure 13-4o**) suggesting that cells with high PDM content are dependent on FFAs to support cellular respiration and growth. Both cells were highly dependent on glutamine as is normal for many cultured lung tumor cells[460]. Of interest, H1975 cells grew well in low glucose conditions while RH2 cells did not thus agreeing with previous studies that identified LUSC are reliant on glucose and glutamine for cell survival[413,461].

13.1.6 Glucose flux regulates mitochondrial motility and respiratory capacity in OXPHOSLO LUSC tumors

Quantitative analysis of the spatial distribution of mitochondrial subpopulations among LUSC tumors confirmed that mitochondria were predominantly populated by PNM subpopulations with Type III cristae (**Figure 13-5a,b**). The perinuclear localization of mitochondria in LUSC suggested that mitochondrial motility may be impaired thus confining the mitochondria to the nuclear region in the cell. Distribution of mitochondrial throughout the cell is regulated by mitochondrial motility. Mitochondria move along the cytoskeleton (microtubules, actin, intermediated filaments) aided by motor and adaptor and transmembrane proteins[462,463]. Notably, motor adaptors sense glucose flux via *O*-GlcNAcylation by *O*-GlcNAc Transferase (OGT) (**Figure 13-5c**). Approximately 2% of glucose imported into cells is shunted into the nutrient-sensing hexosamine biosynthetic pathway, which activates OGT[464]. The hexosamine pathway was shown to be activated in lung cancer[465] and studies in neuronal axons have shown that OGT forms a

complex on the outer mitochondrial membrane and *O*-GlcNAcylates motor adaptors in response to elevations in glucose concentration that results in arrest of mitochondrial motility[466]. Importantly, elevated glucose uptake and high glycolytic flux are hallmarks of hypermetabolic LUSC tumors[461]. We postulated that increased glycolytic flux may repress mitochondrial motility along the cytoskeleton through activation of the Hexosamine pathway and OGT functioning to confine and localize the mitochondria to the nuclear space shown in the model in **Figure 13-5c**.

We quantified mitochondrial motility by measuring the displacement of individual mitochondria over time (PMID: 15545319). Glycolytic, $OXPHOS^{LO}$ squamous cell lines had significantly reduced mitochondrial motility compared to the $OXPHOS^{HI}$ LUAD cell lines H1975 and A549 (**Figure 13-5d**). Glucose restriction in the media by either low glucose concentrations (1mM) or galactose induced significant increases in mitochondrial motility (**Figure 13-5e**). Targeted inhibition of glucose transport using the pan GLUT1/3 inhibitor KL-11743[467,468] in RH2 cells resulted in a significant increase in mitochondrial motility and distance from the nucleus in which mitochondria relocated to the cytoplasm (**Figure 13-5f-h**). We inhibited the hexosamine pathway using azaserine that inhibits glutamine-fructose-6-phosphate transaminase [isomerizing] 2 (GFPT2) and OSMI-1 that inhibits OGT as previously shown[465]. Both azaserine and OSMI-1 induced a significant increase in mitochondrial motility (**Figure 13-5i**). Additionally, KL-11743 treatment induced a stark decrease in total cellular O-GlcNAcylation (**Figure 13-5j**). Glucose restriction, azaserine treatment and siRNA knockdown of OGT led to a similar decrease in total cellular O-GlcNAcylation. Lastly, siRNA knockdown of OGT lead to a significant increase in mitochondrial motility (**Figure 13-5k**). In sum, these results demonstrate that glucose flux through the Hexosamine and OGT pathways regulate mitochondrial motility in glycolytic LUSC tumor cells.

In addition to increased motility, KL-11743 induced the elongation of mitochondrial networks shown in **Figure 13-5g**. We next investigated whether inhibition of glucose flux induced remodeling of mitochondrial cristae. KL-11743 treatment induced remodeling of cristae marked by a significant increase in organized lamellar type I cristae and a concomitant decrease in type

III cristae in RH2 cells (**Figure 13-5l-m**). Glucose restriction, inhibition of the hexosamine pathway and OGT knockdown in RH2 cells yielded identical results to KL-11743 treatment in cells in which cristae were remodeled from predominantly Type III to Type I. H1975 cells showed a modest but significant enrichment in Type I cristae after azaserine treatment or OGT knockdown. The remodeling of mitochondrial dynamics and cristae from malformed circular type II and III cristae into well-formed lamellar type I cristae in RH2 cells following KL-11743 treatment suggested an upregulation of OXPHOS activity in these cells. We measured significant increases in the maximum oxygen consumption rate (OCR max) of cells as well as increased of Complex I and Complex II activity in RH2 and to a lesser extent in H1975 cells following KL-11743 treatment, glucose restriction, azaserine treatment or OGT knockdown (**Figure 13-5n-o**). These results demonstrate that remodeling of mitochondrial dynamics and cristae induced an increase in mitochondrial respiration in glycolytic, $OXPHOS^{LO}$ RH2 cells. Lastly, we performed ^{18}FBnTP PET imaging on RH2 tumor xenografts following treatment with KL-11743. KL-11743 induced a significant increase in ^{18}FBnTP uptake compared to vehicle treated tumors (**Figure 13-5p**). We performed *ex vivo* respirometry on KL-11743 and vehicle treated RH2 tumors and showed that KL-11743 treatment induced a significant increase in Complex I and Complex II MRC as compared to vehicle (**Figure 13-5q**). These results demonstrate that glycolytic flux restricts mitochondrial motility and OXPHOS, in hypermetabolic LUSCs both *in vitro* and *in vivo*.

We next investigated the role of microtubules, actin and vimentin in the regulation of mitochondrial motility. Disruption of both microtubule and actin networks by treatment with latrunculin A or nocodazole respectively, led to a significant decrease in mitochondrial motility in both H1975 and RH2 NSCLC cell lines. In contrast, siRNA mediated knockdown of vimentin in H1975 or RH2 cells led to a significant increase in mitochondrial motility. We next confirmed that both latrunculin A and nocodazole treatment induced a significant decrease in the distance of mitochondria from the nucleus resulting in an enrichment of peri-nuclear mitochondria, whereas knockdown of vimentin led to a significant increase in H1975 and RH2 cells. Lastly, we measured

basal OCR after disruption of the cytoskeleton componentry. We identified that latrunculin A and nocodazole treatment induced a significant decrease and that vimentin knockdown induced a significant increase in in basal OCR in H1975 and RH2 cells. These results suggest that both microtubules and active networks support mitochondrial motility, cytoplasmic distribution of mitochondria and respiratory capacity while vimentin functions in an antagonistic and suppressive manner.

13.1.7 Glucose flux regulates mitochondrial motility and respiratory capacity in OXPHOSLO LUSC tumors

In summary, we present an *in vivo* structural and functional analysis of mitochondrial networks and bioenergetic phenotypes across NSCLC tumor subtypes in both mouse and human tumors. The *ex vivo* respirometry we performed on lung tumors identified significant increases in Complex I respiratory activity in ^{18}FBnTP positive LUAD as compared to glycolytic, LUSCs with low ^{18}FBnTP uptake. These results underscore the diversity of bioenergetic activity among NSCLC tumor subtypes. A recent study defined that ubiquinol oxidization is required for lung tumor growth, highlighting a critical role of Complex III and the ETC in lung tumorigenesis[469]. Collectively, this study and our work profiling respiration dependencies underscore the importance of mapping respiratory chain dependencies across NSCLC subtypes. The functional diversity we discovered between LUADs and LUSCs accurately predicted distinct structural mitochondrial phenotypes among lung tumor subtypes demonstrating that mitochondrial structure impacts its function. PET-guided 3D SBEM analysis successfully identified structural and spatial distribution of mitochondrial networks within ^{18}FBnTP positive LUADs. In contrast, we identified that ^{18}FBnTP negative LUSC retain uniform structural and spatial organization of their mitochondria that is metabolically regulated by glucose flux. The broad diversity of mitochondrial phenotypes intrinsic to LUADs suggests that these tumors possess an innate metabolic and bioenergetic flexibility that is distinct from LUSCs. We identified a previously unrecognized mechanism of metabolic

compartmentalization in LUADs in which populations of PDM exist that support mitochondrial respiration in tumor cells.

The closely regulated and uniform mitochondrial networks we profiled in LUSCs corresponded with reduced metabolic flexibility in these tumors compared to that of LUADs. LUSC were more reliant on glucose and glutamine metabolism to support OXPHOS and less so on FAO, while LUADs utilized glucose, glutamine and fatty acids to support cellular respiration. This suggests a therapeutic window may exist to selectively target metabolism lung tumors with homogeneous mitochondrial phenotypes and limited metabolic flexibility. We have demonstrated that LUSCs are dependent on glucose and glutamine metabolism and are selectively sensitive to inhibition of these pathways[413,459]. Structure-and-function studies defining the relationship between mitochondrial architecture and metabolic dependencies may hold promise as strategies to profile metabolic liabilities unique to lung cancer subtypes. We anticipate that coupling PET imaging with 3D SBEM will have dynamic applications beyond that of lung cancer and enrich our understanding of how mitochondrial bioenergetics impact human disease.

13.2 Methods

13.2.1 Cell culture

Cells were cultured in Dulbecco's modified Eagle's medium (DMEM; Thermo Fisher Scientific) supplemented with 10% fetal bovine serum (FBS) (Hyclone) and 1% penicillin/streptomycin (Gibco). A549 cells and H1975 cells were obtained from ATCC. The lung squamous cell line (human) RH2 were established in the laboratory of Dr. Steven Dubinett (UCLA). The head and neck squamous cell line (human) Tu686 was a gift from Maie St.John laboratory (UCLA). The mouse lung squamous cell line derived from Mouse 5 (LPP) and mouse lung adenocarcinoma cell line derived from Mouse 4 (LPP) were established in our laboratory. After resecting the tumor tissues, they were minced with razors and digested with collagenase/dispase (Sigma). Lysate was filtered through 70 μm cell strained. Dissociated single cells were centrifuged and

resuspended in DMEM (10% FBS). Plate the cells in tissue culture dished and medium change until there were enough colonies to expand the culture. All cells were grown at 37°C in 5% CO2 in a humidified incubator, and Mycoplasma tested using the LookOut Mycoplasma PCR Detection Kit (Sigma).

13.2.2 Genetically engineered mouse models (GEMMs) of lung tumor

We employed 5 GEMMs in this study: (1) Kras-Lox-Stop-Lox-G12D; Rosa26-Lox-Stop-Lox-Luc (Kras); (2) Kras-Lox-Stop-Lox-G12D; Lkb1 Lox/Lox; Rosa26-Lox-Stop-Lox-Luc mice (KL); (3) Kras-Lox-Stop-Lox-G12D; p53 Lox/Lox; Rosa26-Lox-Stop-Lox-Luc mice (KP); (4) Kras-Lox-Stop-Lox-G12D; Lkb1 Lox/Lox; p53 Lox/Lox; Rosa26-Lox-Stop-Lox-Luc mice (KPL); (5) Lkb1 Lox/Lox; p53 Lox/Lox; Pten Lox/Lox; Rosa26-Lox-Stop-Lox-Luc mice (LPP). Lung tumors were induced by Ad5-CMV-Cre (VVC-U of Iowa-1174) or LentiCre (Kerafast) delivered intranasally as described previously[394]. Tumor growth was routinely monitored by bioluminescence imaging using IVIS imager (PerkinElmer). All animal experiments were approved by Animal Research Committee (ARC) and performed following ARC protocols and requirements. Lung tumors from different GEMM mice were collected by snap freezing in liquid nitrogen. Snap frozen samples were stored at -80 °C until respirometry assay and Western blotting analysis.

13.2.3 Subcutaneous implantation in NSG mice

A549, H1975, A549 Rho, RH2 and Tu686 cells were cultured *in vitro* under the condition described above. Cells were collected and suspended in PBS, then mixed with Matrigel Membrane Matrix (Corning) and implanted subcutaneously on the flanks of NSG mice (2-4 $\times$ 10*6 cells/flank). For the treatment study of GLUT1/3 inhibitor KL-11743 (C6), mice were treated with C6 (100mg/kg) delivered by oral gavage for 8 days. Subcutaneous tumors were either snap frozen in liquid nitrogen or fixed in 10% formalin overnight. Snap frozen samples were stored at -80 °C until respirometry assay. Formalin fixed samples were sent to Translational Pathology Core Laboratory (TPCL) at UCLA for embedding and sectioning.

13.2.4 18F-FBnTP synthesis

The procedures of synthesizing radio-active^{18}F-FBnTP probe was performed as previously described[257,419].

13.2.5 PET/CT imaging

The procedures of PET/CT imaging and analysis was performed as previously described[59,61]. PET signals were measured by % injected dose (ID)/gram (g) after 1h uptake and normalized to heart signal. The ratio of ^{18}FBnTP uptake %ID/g (tumor) to %ID/g (heart) $\geq$ 0.5 is defined as ^{18}FBnTP^{HI}; a ratio < 0.5 is defined as ^{18}FBnTP^{LO}. The ratio of ^{18}F-FDG uptake %ID/g (tumor) to %ID/g (heart) $\geq$ 0.2 is defined as ^{18}F-FDG^{HI}; ratio < 0.2 is defined as ^{18}F-FDG^{LO} tumor[438].

13.2.6 Ex vivo respirometry analysis on frozen tissues

Tumor tissues were isolated from genetically engineered mouse models of lung cancer and snap frozen using liquid nitrogen. Frozen samples were stored in -80°C until use in the Seahorse experiments. Frozen tissues were thawed on ice and homogenized in MAS buffer (70mM sucrose, 220mM mannitol, 5mM KH_2PO_4, 5mM $MgCl_2$, 1mM EGTA, 2mM HEPES pH 7.4) with protease inhibitor cocktail (Roche). Homogenates were centrifuged at 1,000g for 10 minutes at 4°C and supernatant was collected. Protein concentrations were determined by BCA assay kit (Thermo Fisher). Lysates (12µg/well for human samples and 6µg/well for mouse samples) were loaded into Seahorse XF96 microplate in MAS buffer (20µL each well) and centrifuged at 2,000g for 5 minutes at 4°C. After centrifugation the volume was increased to 150µL by adding 130µL MAS containing cytochrome c (10µg/mL). At port A, substrates of NADH (1mM) were injected to determine the respiratory capacity of mitochondrial Complex I; succinate (5mM) + rotenone (2µM) were injected to determine the respiratory capacity of mitochondrial Complex II. Following substrate injections were loaded: port B: rotenone (2µM) + antimycin (4µM); port C: TMPD (0.5mM) + ascorbic acid (1mM); port D: azide (50mM). OCR rates were measured using Seahorse XF96 Extracellular Flux Analyzer (Agilent Technologies) and normalized to mitochondrial content quantified by MitoTracker Deep Red staining (Thermo Fisher).

13.2.7 In vitro respirometry analysis on cultured cells

Cells were seeded into Seahorse XF96 microplate prior to the assay and maintained in tissue culture incubator (37°C in 5% CO2) to reach 90-100% density before running Seahorse assay. To measure Complex I and Complex II respiratory capacity, cells were permeabilized with 5nM XF Plasma Membrane Permeabilizer (PMP, Agilent) and analyzed as described above in *ex vivo* tissues. Permeabilized cells were started in State 3 with substrates of pyruvate (5mM) + malate (0.5mM) and 4mM ADP for respiration-driven through Complex I; succinate (5mM) + rotenone (2µM) and 4mM ADP for Complex II. Following State 3 measurements injections included: port A: oligomycin (2µM); ports B and C: FCCP (B: 0.75µM and C: 1.35µM); port D: rotenone (2µM) + antimycin (2µM).

To measure OCR and ECAR rates, cells were washed twice and incubated with freshly prepared assay medium (Seahorse XF Base Medium + 2mM L-glutamine + 1mM Pyruvate + 10mM glucose) for 30 minutes. The substrates were injected in the order of oligomycin (2µM), FCCP (0.75/1.35µM), rotenone (2µM) + antimycin A (2µM).

Cell count (per well) was determined by nuclei number which were stained with Hoechst and quantified by Operetta High-Content Imaging System (PerkinElmer). OCR and ECAR rates were normalized to cell count per well.

13.2.8 Whole animal perfusion and tissue fixation

Fixative solution (2% paraformaldehyde, 2.5% glutaradehyde, 0.15M cacodylate and 2mM Ca^{2+}) was freshly prepared every time. Animals were anesthetized by ketamine (200mg/kg) / xylazine (10mg/kg) delivered by intraperitoneal injection. Anesthesia took effect after several minutes. The depth of anesthesia was tested using tail pinch and paw prick and ensured the breathing did not stop. The body cavity was cut with scissors and followed by cutting up midline to sternum. Heart was exposed and needle was placed into left ventricle then right atrium was snipped with iridectomy scissors. The animal was perfused for 30 seconds at the flow speed of 8mL/minute with Ringer's solution supplemented with 2% xylocaine and 1000U herapin. Then valve on the

pump was switched on to fixative solution and perfused for 5-8 minutes. After continuous perfusion, mouse lung tumor was harvested, placed in ice-cold fixative solution and fixed overnight in the fridge. Fixed tissues were washed 3 times with 0.15M cacodylate buffer (2mM Ca^{2+}) and stored in the same buffer at 4 °C until further processing.

13.2.9 Sample preparation for SBEM imaging

Post-fixed tissues of mouse lung tumor were washed in 0.15M cacodylate buffer (2mM Ca^{2+}). Tissues were stained for 1 hour with 2% osmium and 1.5% potassium ferrocyanide in 0.15M cacodylate buffer (2mM Ca^{2+}). Tissues were washed 5 times (5 minutes each time) with ddH_2O, then Placed in filtered TCH buffer (0.05g thiocarbohydrazide in 10mL ddH_2O) for 20 minutes at room temperature (RT). Tissues were washed 5 times (5 minutes each time) with ddH_2O and then stained with 2% osmium in ddH_2O for 30 minutes at RT. Following that, tissues were stained with 2% uranyl acetate overnight at RT and lead aspartate solution (0.66% (w/v) lead in 0.03M aspartic acid) for 30 minutes in 60°C oven. Tissues were dehydrated in serial ice-cold ethanol (70%, 90% and 100%) and ice-cold acetone after washing in ddH_2O. Tissues were then embedded in serial Durcupan resin (50%, 75%, 100%) and solidified in 60°C oven for 2 days.

13.2.10 Sample preparation for SBEM imaging

SBEM volumes were collected on a Zeiss Gemini 300 microscope equipped with a Gatan 3View 2XP microtome system. The volumes were collected at 2.5 kV using a 30μm aperture, the gun in analytic mode, and the beam in high current mode. Focal charge compensation with nitrogen gas was used to mitigate charging artifacts. The dwell time was 1 microsecond. The pixel size was either 5 or 6 nm, and the Z step size was always 50 nm. Following data collection, the images were converted to .mrc format and cross correlation was used to for rigid image alignment of the slices using the IMOD image processing package[470].

13.2.11 Sample preparation for SBEM imaging

MicroCT imaging was performed on a Zeiss Versa 510 microscope. The wet lung specimens were imaged with no contrast staining in buffer at 40 kV, using 360 degrees of specimen rotation and collecting 801 projection images. The pixel size was 11.5μm. Specimens stained for SBEM and embedded in epoxy were imaged at 80 kV, using 360 degrees of specimen rotation and collecting 1601 projection images. The pixel size was between 5-8μm.

13.2.12 3D visualization and analysis of SBEM images

Individual cells were segmented using Amira software (Thermo Scientific). Sequential SBEM images were processed with median filter and contrast adjustment to enhance the appearance of intracellular space. Interactive thresholding was applied to distinguish cellular and extracellular space and generate binary images. Binary images were processed with Separate Object algorithm to fragment cells without clear extracellular boundaries. Connected Components algorithm was applied to create individual labels for each identified cell. Segmented individual cells in each stack are visualized with a voxelization rendering.

13.2.13 Machine learning based segmentation of nucleus and mitochondria in SBEM images

We propose a method to segment nuclei (class 1) and mitochondria (class 2) from the background (class 0) in a 3D SBEM volume. Our method takes individual slices from the volume (2D images) as input and predicts the segmentation for the slices independently. To perform the segmentation, we propose to learn a deep neural network which is a function which takes an image as input and outputs a confidence map corresponding to each class. The class with the highest response is chosen for each pixel to yield the segmentation map for each slice. Specifically, we chose an encoder-decoder architecture based on U-Net[470], with 3 modifications. (i) We use ResNet[471] blocks (with 32, 64, 128, 256 and 256 filters) instead of standard convolutional blocks. (ii) Since mitochondria are small objects, we chose to limit spatial downsampling to $\frac{1}{8}$th of the original image. To do so, we remove max-pooling operations after the 3rd layer. (iii) We used an Atrous Spatial

Pyramid Pooling (ASPP)[472] layer with strides 6, 12, 18, 24 as the last layer of our encoder to increase the field of view of our filters. All weights use random uniform initialization, and we used leaky-ReLU activations. Our model is trained using the standard cross-entropy loss and is optimized using Adam[473] with $\beta_1 = 0.9$ and $\beta_2 = 0.999$. We used an initial learning rate of 1×10^{-4} and decreased it to 1×10^{-5} after 150 epoch for a total of 200 epochs. We use a batch size of 8 and resize each image to 768×768. We perform random horizontal and vertical flips, rotations between $[-20°, 20°]$, zero-mean additive gaussian noise with standard deviation of 0.08, and crop sizes up to 90% of the image height and width as data augmentation. Each augmentation has a 50% probability of being applied. We train our model on 10 densely labeled images, and reserve 3 images for validation. Training takes ≈ 8 hours on an Nvidia GTX 1080 GPU, and inference takes ≈ 11 ms per 2D image. Our segmentation model achieves a 0.92 DICE score and a 0.86 IoU across all classes.

13.2.14 Machine learning based segmentation of nucleus and mitochondria in SBEM images

We composed the volumes by stacking individual network predictions for all slices. We used 3D connected components with 26-connectivity to aggregate instances independently on nuclei and mitochondria predictions and removed objects smaller than 30 voxels. To quantify the distance between mitochondria and nucleus surface we computed the centroid of each nuclear and mitochondrion prediction, and used the centroids to assign each mitochondria to the closest nuclei. We then reported the distance between the nucleus' centroid and the centroids of all mitochondria assigned to it. Mitochondrial length is measured by the TEASAR algorithm [ref], which is a fully automatic tree structure extraction method, to skeletonize each mitochondrion. We interpreted the skeletons as adjacency matrices which define 3D undirected graphs. The length was computed as the longest path in the graph. Quantification of mitochondrial volume is to derive a closed triangular mesh for every mitochondrion in the predicted volume through the 3D marching cubes algorithm. We then computed the volume inside the mesh by summing the

volumes of the tetrahedra which compose it. We also quantified the sphericity of mitochondria given the mesh obtained through marching cubes (described above) and the corresponding enclosed volume, we just need the surface area of the mesh to compute sphericity. The surface area of the mesh is computed as the sum of the surface areas of the triangles that compose it, which allowed us to compute the sphericity for the mitochondria.

13.2.15 Quantification of distance between mitochondria and nucleus in fluorescent images

Given the center of a mitochondria, we want to find its minimum distance to the surface of a nucleus, which is segmented as an ellipse. The result can be obtained by solving a constrained optimization problem using Lagrange multiplier. The original ellipse of nucleus is tilted by a degree θ and is centered at an arbitrary coordinate (h,k). To ease the computation, we translate and rotate the original ellipse to a standard ellipse that is centered at (0,0) with major axis aligned with the x-axis and the minor axis aligned with the y-axis. The center of the mitochondria follows the same transformation. Through substitution and rearranging the terms, the objective function is a fourth degree polynomial, which has at most four possible roots that satisfy the criteria. We then choose the coordinate (x,y) on the ellipse that has the minimal distance to the target nucleus.

13.2.16 Immunohistochemistry

The procedures of immunohistochemistry staining and analysis was performed as previously described [2]. Tissue slides were probed with following antibodies: CD34 (1:800, ab8158 Abcam); TTF-1 (1:1000, M3575 Dako); Cytokeratin 5 (1:1000, ab52635 Abcam).

13.2.17 Oil Red O Staining

The oil red o staining was performed following the protocols of commercial kit (StatLab, KTOROPT). Frozen tissues were fixed by O.C.T compound (Fisher HealthCare) and sectioned at Translational Pathology Core Laboratory (UCLA). The frozen tissue sections were fixed in 10% formalin for 5min, then rinsed in distilled water. Slides were immersed in propylene glycol for 2min followed by immersing in preheated oil red o solution at 60°C for 6min. Slides were then washed

in 85% propylene glycol for 1min and running distilled water for 1min. The nuclei were stained with Modified Mayer's Hematoxylin for 1min and rinsed in distilled water for 1min. The slides were mounted with aqueous medium and covered with coverslip.

13.2.18 Western Blotting

Whole cell lysates of lung tumors isolated from GEMMs were generated by homogenizing snap frozen tumor tissues in lysis buffer (20mM Tris pH 7.5, 150mM NaCl, 1% (v/v) Triton X-100, 50mM sodium fluoride, 1mM EDTA, 1mM EGTA, 2.5mM pyrophosphate, 1mM sodium orthovanadate, complete protease inhibitor cocktail). Whole cell lysates were centrifuged at 2,000g for 5 minutes and supernatants were transferred to empty tubes. Supernatants were stored at -80°C until use. Whole cell lysates of *in vitro* cultured cells were generated by homogenizing in SDS lysis buffer (100mM Tris pH 7.5, 100mM NaCl, 1% SDS, protease inhibitor cocktail) followed by heat inactivation at 90°C for 10 minutes. Protein concentration was determined by BCA assay (Thermo Fisher). Lysates were run on 4-12% Bis-Tris gels (Thermo Fisher) to separate the proteins, then transferred to PVDF membrane. Membranes were stained with Poceau S to confirm transfer efficiency. Membranes were then probed with following antibodies: SP-C (1:5000, AB3786 Milipore); Glut1 (1:2000, GT11-A, Alpha Diagnostic); Ndufs1 (1:1000, ab169540, abcam); O-Linked N-Acetylglucosamine (1:1000, ab2739, Abcam); SDHA (1:1000, 5839, Cell Signaling Technology); SDHC (1:1000, ab155999, Abcam); Actin (1:5000, A3853, Sigma); Tubulin (1:2500, T9026, Sigma).

13.2.19 Mitochondrial Motility and Mitochondrial Cristae analysis

2×10*5 cells were plated per well into CELLview 4-compartment glass-bottom tissue culture dishes (Greiner Bio-One) 48 hours prior to the imaging section, and maintained in tissue culture incubator (37°C in 5% CO2). Cells were stained with TMRE (15nM, Thermo Fisher) for 1h to analyze mitochondrial motility, and 10-*N*-nonyl acridine orange (100nM, Thermo Fisher) for 1-3h to analyze mitochondrial cristae. Live cell imaging was performed on the Zeiss LSM 880 with

Airyscan using the alpha Plan-Apochromat 100x/1.46 Oil DIC M27 objectives. Images were deconvoluted by Airyscan Processing in ZEN software. Image analysis was performed using ImageJ (Fiji) in the order of: background subtraction, crop region of interest, adjust thresholds and measure parameters. Mitochondrial motility was analyzed using Motility Journal w/ Percent Threshold developed in Dr. Orian Shirihai laboratory. The algorithm takes the mitochondrial area in the first frame, and it pseudocolors them green. Then it takes the mitochondrial area in the second frame, third frame, and so on, and pseudocolors them red. Then, for each time point, the algorithm overlays the green and red time points, making a yellow region where there is overlap between the two channels. For each time point, there is a green, red, and yellow value. The algorithm takes these values and computes: (green + red)/yellow. There is a value for each time point, and when the algorithm has computed the value for each of the frames in the video, it takes the slope of the values. Therefore, the actual number that you get from the algorithm represents the slope of [(green + red)/yellow] for each of the time points in the movie. Of course, values closer to zero mean there is less mitochondrial displacement. Mitochondrial cristae structure was analyzed using macros designed for cristae segmentation and quantification which have been described previously[445,449].

13.2.20 Statistical analysis

Statistical analyses were performed on GraphPad Prism 9. Differences between groups were determined using unpaired two-tailed t-test or one-way ANOVA if more than two groups were compared. For treatment studies, Dunnett test was employed to compare every mean to a control mean. For non-treatment studies, Tukey test was used to compare every mean to every other mean.

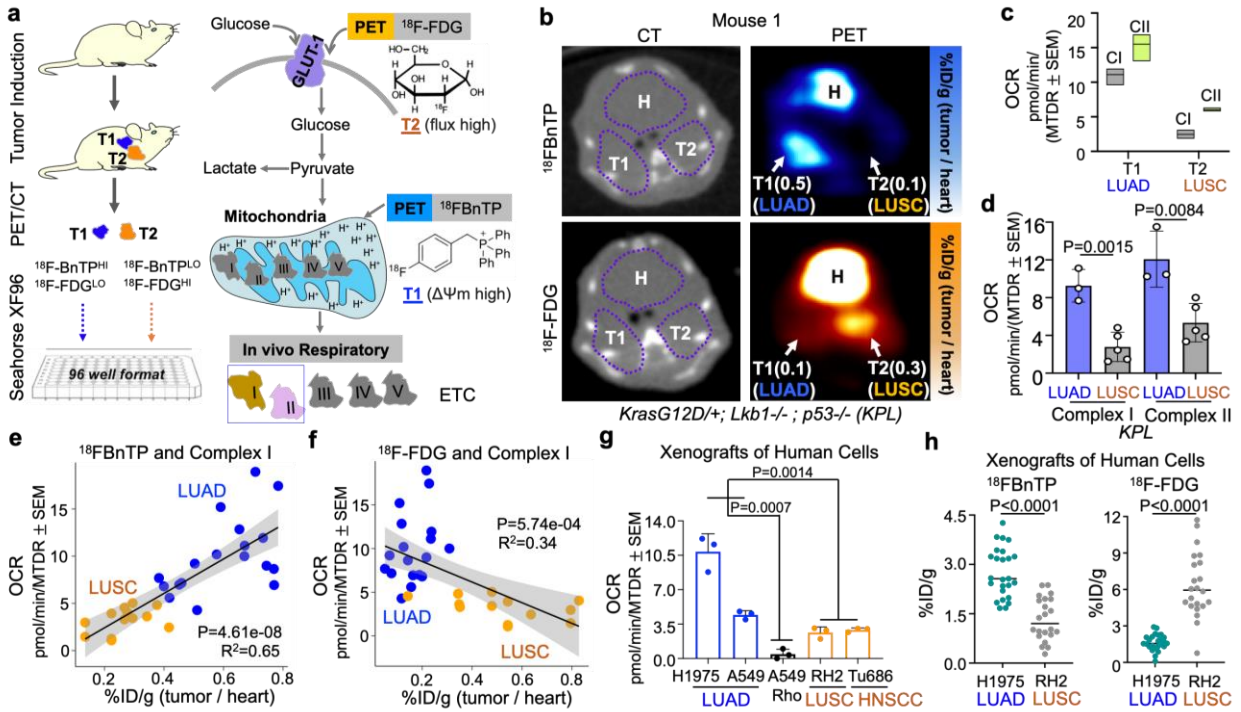

Figure 13-1. Functional in vivo imaging of OXPHOS defined heterogeneous respiratory chain activities among NSCLC subtypes.

a, Schematic depicting experimental workflow of dual-probe PET imaging with ^{18}FBnTP and ^{18}F-FDG tracers followed by respirometry on frozen tumor samples measuring mitochondrial Complex I (CI) and Complex II (CII) maximal respiration capacity (MRC). **b,** Representative transverse image of the heart and lung tumors of mouse 1 (KPL) imaged with CT (left panel) and PET (right panel) probed with ^{18}FBnTP (top) and ^{18}F-FDG (bottom). H-heart, T1 is LUAD, T2 is LUSC **c,** MRC of mitochondrial CI and CII isolated from frozen tissues of T1 and T2 in mouse 1. Data are mean ± s.e.m. (n = 3 technical replicates). **d,** MRC of CI and CII in LUAD and LUSC from KPL mice (n = 8 tumors, 3 LUAD tumors and 5 LUSC tumors. Unpaired two-tailed t-test. **e,f,** Scatter plot with regression line showing %ID/g of PET tracers versus CI MRC of tumors from KPL, KL, Kras, KP and LPP mice (n=30 tumors, 18 LUAD tumors (blue dots) and 12 LUSC tumors (yellow? dark yellow? dots)). F-statistics. **g,** MRC of CI isolated from frozen xenograft tumors established from human LUAD, LUSC, and HNSCC cell lines; data are mean ± s.e.m. (n = 15 total subcutaneous tumors, n = 3 biological replicates (xenografts) per cell line); One-way ANOVA, Tukey test. **h,i,** ^{18}FBnTP and ^{18}F-FDG uptake of subcutaneous xenografts of human LUAD and LUSC cell lines. Unpaired two-tailed t-test.

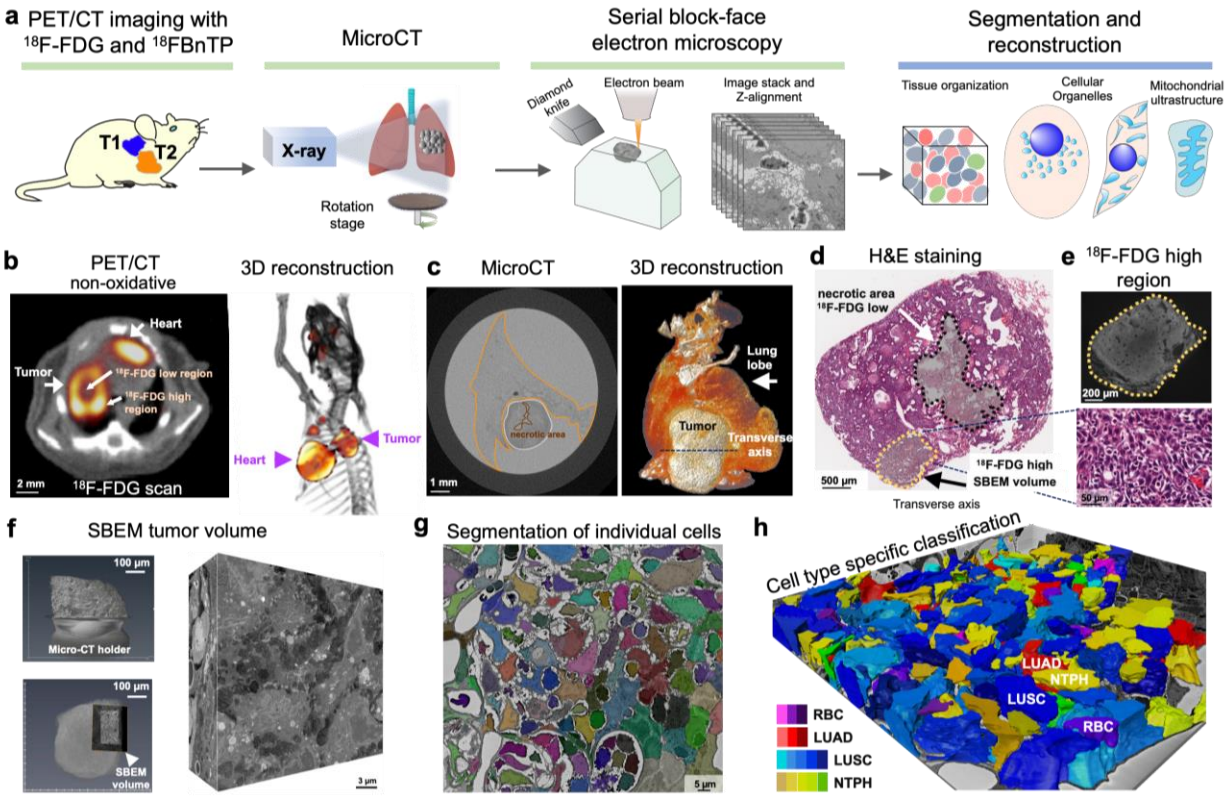

Figure 13-2. Functional super-resolution mapping of mitochondrial architecture in lung tumors using PET and 3D SBEM imaging.

a, Overview of serial block-face electron (SBEM) imaging and reconstruction on tumor regions orientated by microCT and functionally characterized by dual-probe PET imaging. **b,** Identification of ^{18}F-FDG high and ^{18}F-FDG low regions in transverse and 3D rendered PET/CT overlayed image. Synchronous LUSC tumor was isolated from KL mouse. Heart and tumor are indicated by arrows. **c,** MicroCT image and 3D reconstruction showing the position of tumor (white outlined) in the lung lobe (orange outlined). Dense tumor region is distinguished from tissue sparse necrotic area (brown outlined) within the tumor based on tissue density. **d,** Hematoxylin and eosin (H&E) slide of whole tumor adjacent to the section processed for high-resolution microCT and SBEM imaging, scale bar 500μm. **e,** High-resolution microCT image of selected SBEM region with high ^{18}F-FDG signal. Representative H&E staining was from matched SBEM region. **f,** Left panel: 3D rendering of high-resolution microCT images, scale bar 100μm; Right panel: 3D rendering of SBEM images, scale bar 4μm. **g,** Segmentation of individual cell in SBEM volume using Amira, individual cells were labelled with different colors. **h,** Whole-volume SBEM landscape composed with LUSC (different shades of blue), neutrophils (NTPH, different shades of yellow), red blood cells (RBC, different shades of purple) and LUAD (different shades of red).

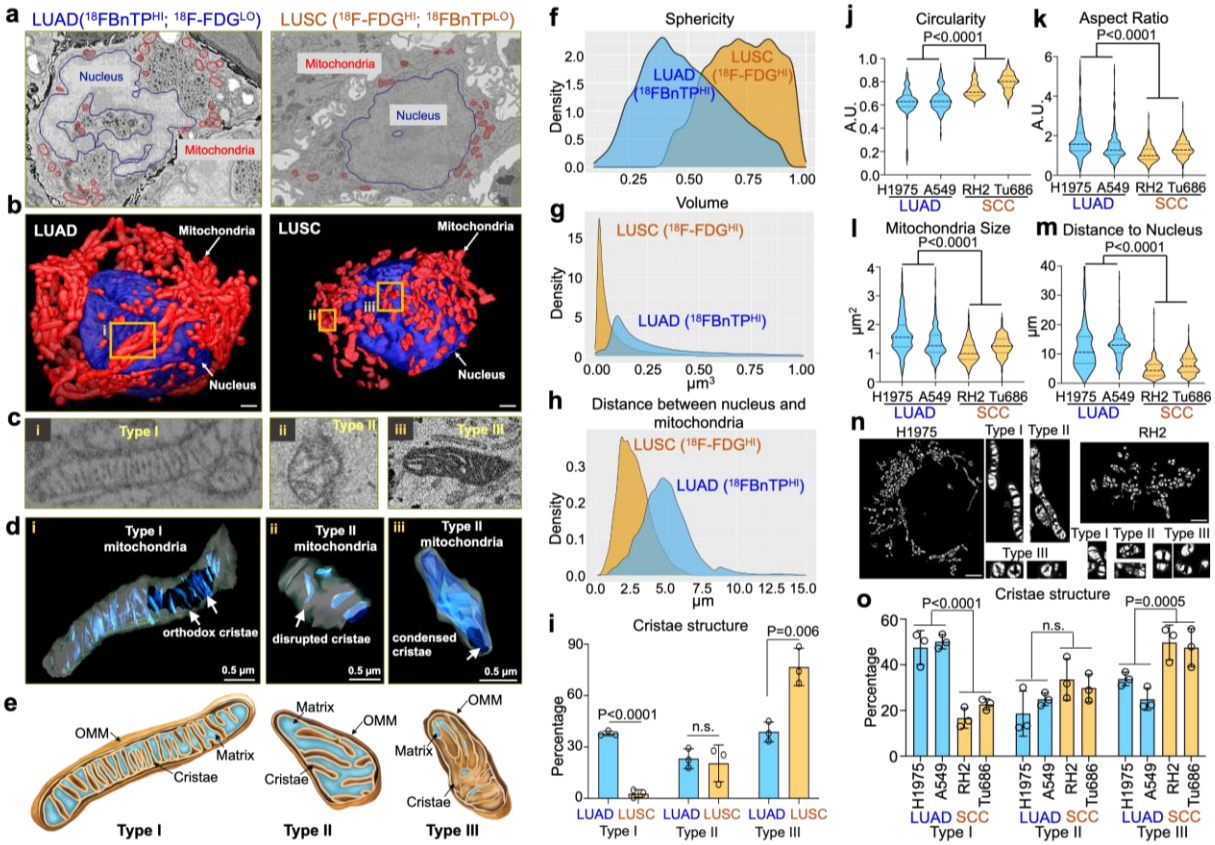

Figure 13-3. Conserved spatial and structural mitochondrial phenotypes identified in ^{18}FBnTP positive and negative lung tumors.

a,b, Representative 2D SBEM images and 3D reconstruction of nuclei and mitochondria from ^{18}FBnTP^{HI} ^{18}F-FDG^{LO} LUAD (left) and ^{18}FBnTP^{LO} ^{18}F-FDG^{HI} LUSC (right) cells, scale bar 5μm. **c,d,** Representative 2D SBEM images and 3D reconstruction of mitochondrial cristae structures defined as type I, II and III from cells shown in **a** and **b**. **e,** Schematic illustration of mitochondrial ultrastructure including outer mitochondrial membrane (OMM), matrix and cristae defined as type I, II and III. **f-h,** Density plots of mitochondrion sphericity, volume enclosed within meshed surface, and distance between meshed nucleus surface and each meshed mitochondrial surface. n > 50,000 mitochondria (approximately 250 cells) from LUAD SBEM volume and n > 22,000 mitochondria (approximately 170 cells) from LUSC SBEM volume were analyzed. **i,** percentage of type I, II and III cristae structure in ^{18}FBnTP^{HI} ^{18}F-FDG^{LO} LUAD and ^{18}FBnTP^{LO} ^{18}F-FDG^{HI} LUSC cells, n > 1,000 mitochondria per SBEM volume were analyzed. Data are mean ± s.e.m. Unpaired two-tailed t-test. **j-m,** Violin plots of mitochondrial shape descriptors (circularity, aspect ratio), mitochondrial size (area) and spatial distribution descriptors (distance relative to nucleus) in human LUAD cell lines (H1975, A549), LUSC cell line (RH2) and HNSCC cell line (Tu686). Data are from n = 3 biological replicates, n = 100 cells per replicate, One-way ANOVA, Tukey test. **n,** Representative mitochondrial cristae structure stained with NAO and segmented by Weka segmentation (ImageJ) in human LUAD cell line (H1975) and human LUSC cell line (RH2). Examples of defined type I, II and III cristae structure were shown in both cell lines. **o,** percentage of type I, II and III cristae structure in in human LUAD cell lines (H1975, A549), LUSC cell line (RH2) and HNSCC cell line (Tu686). Data are from n = 3 biological replicates, n = 100 cells per replicate, One-way ANOVA, Tukey test.

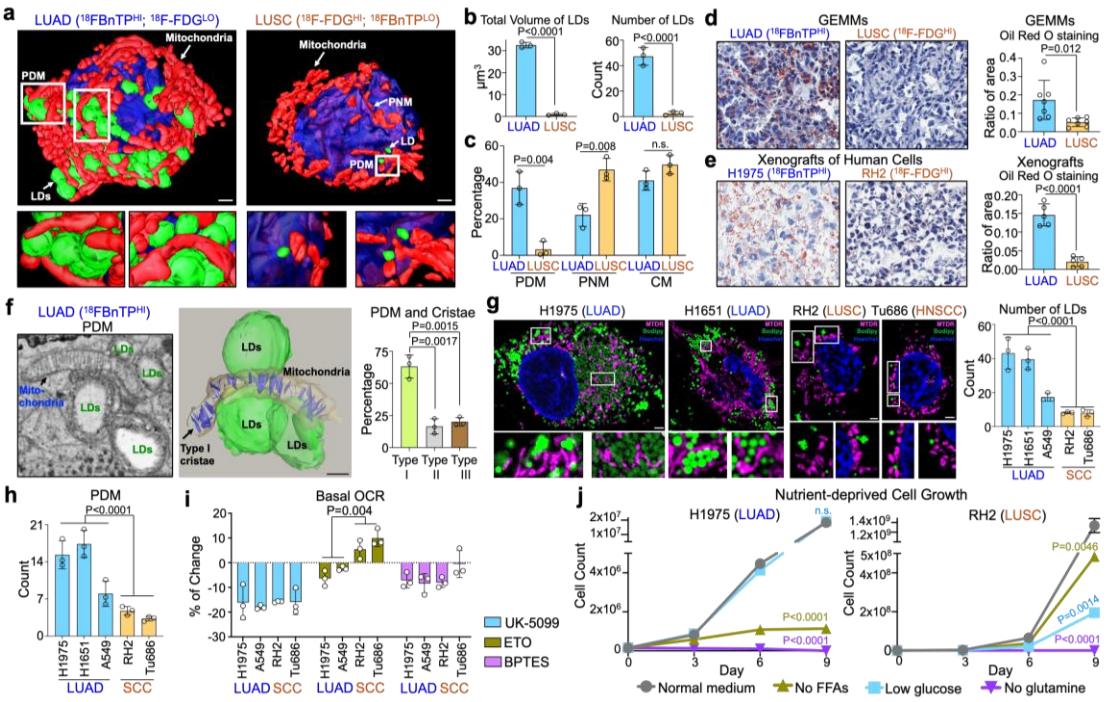

Figure 13-4. OXPHOS-proficient LUADs are enriched for peri-droplet mitochondrial subpopulations and rely on fatty acid oxidation to support cellular respiration and survival. **a,** Representative 3D reconstruction of lipid droplets (green), mitochondria (red) and nucleus (blue) from ^{18}FBnTP^{HI} ^{18}F-FDG^{LO} LUAD (left) and ^{18}FBnTP^{LO} ^{18}F-FDG^{HI} LUSC (right) SBEM volumes, scale bar 4μm. Peri-lipid mitochondria (PDM) and peri-nuclear mitochondria (PNM) are indicated by white arrow and white box. The interaction and contact sites between lipid droplets (LDs) and mitochondria are shown with the zoomed-in images with white box. **b,c,** Quantification of total volume (left panel) and total number (right panel) of LDs, and percentage of PDM, PNM and cytoplasmic mitochondria (CM) in ^{18}FBnTP^{HI} ^{18}F-FDG^{LO} LUAD and ^{18}FBnTP^{LO} ^{18}F-FDG^{HI} LUSC SBEM volumes. Data are mean ± s.e.m., n = 3 biologically independent samples. Unpaired two-tailed t-test. **d,e,** (left) Representative images of oil red o and hematoxylin staining on LUAD and LUSC tumors isolated from GEMMs (KL) and Xenografts of human cells. (right) Quantification of oil red o staining density relative to hematoxylin staining in LUAD and LUSC tumors dissociated from GEMMs (Kras, KL, KP, KPL) and Xenografts of human cells (LUAD: H1975, A549, H1651; LUSC: RH2; HNSCC: Tu686). Unpaired two-tailed t-test. **f,** (left) Representative 2D SBEM image and 3D reconstruction showing PDM and associated cristae structure, scale bar 2μm. (right) Percentage of type I, II and III cristae in PDM. Data are mean ± s.e.m., n = 3 biologically independent samples. Unpaired two-tailed t-test. **g,** Representative fluorescent images stained with MitoTracker DeepRed (MTDR), bodipy and Hoechst in *in vitro* cultured human cells, scale bar 2μm. **g** (right) and **h**, average number of LDs and PDM in human LUAD and SCC cell lines. Data are from n = 3 biological replicates, n = 100 cells per replicate. Unpaired two-tailed t-test. **i,** Percentage of change in basal OCR in human LUAD and SCC cells in response to UK-5099, ETO and BPTES treatments. Data are mean ± s.e.m., n = 3 biologically independent samples. One-way ANOVA, Tukey test. **j,** cell count of H1975 and RH2 cells proliferating under the conditions of normal medium (25mM glucose), no free fatty acids (FFAs), low glucose (12mM) and no glutamine medium. Data are mean ± s.e.m., n = 3 biologically independent samples. Unpaired two-tailed t-test.

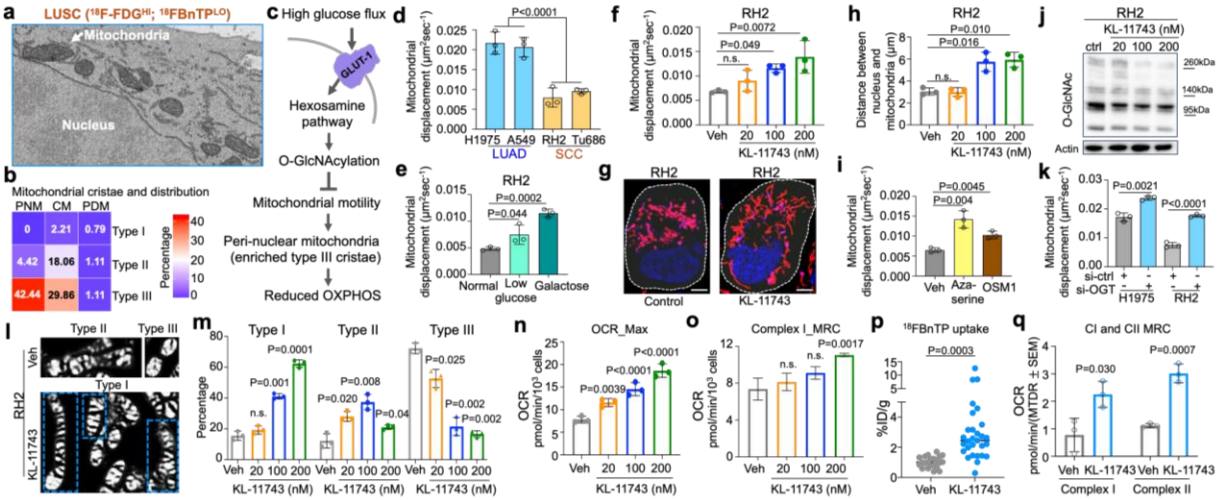

Figure 13-5. Glucose metabolism regulates mitochondrial motility and remodeling of the cristae to suppress mitochondrial respiration in OXPHOS-deficient LUSC tumors.

a, (top) Representative 2D SBEM image showing PNM and associated type III cristae in ^{18}FBnTP^{LO} ^{18}F-FDG^{HI} LUSC. b, Heat map showing the percentage of mitochondrial population classified by spatial distribution and cristae structure. n > 1,000 mitochondria per SBEM volume were analyzed. Data are mean value from n = 3 biologically independent samples. **c,** Diagram of glucose flux driven hexosamine biosynthetic pathway and our hypothesized model of mitochondrial cristae remodeling and OXPHOS function. **c,** Mitochondrial motility in *in vitro* cultured human LUAD (H1975, A549), LUSC (RH2) and HNSCC (Tu686) cell lines. Data are mean ± s.e.m. (n = 3 biological replicates and n = 50 cells per replicate), one-way ANOVA, Tukey test. **d,** Mitochondrial motility in RH2 cells treated with indicated concentrations of KL-11743 for 72h. Data are mean ± s.e.m. (n = 3 biological replicates, and n = 50 cells per replicate), one-way ANOVA, Dunnett test. **e,** Representative fluorescent image of RH2 cells stained with MTDR and DAPI (blue) of RH2 cells after treatment of KL-11743 (200nM) for 72h, scale bar 4μm. **f,** Quantification of spatial distribution descriptors (distance relative to nucleus) in RH2 cells after treatment of KL-11743 at indicated concentrations for 72h. Data are mean ± s.e.m. (n = 3 biological replicates, and n = 100 cells per replicate), one-way ANOVA, Dunnett test. **g,i,** (**g**) Mitochondrial motility in RH2 cells after treatment of hexosamine biosynthetic pathway inhibitors azaserine (0.5μM) and OSM1 (25μM) for 72h. (**i**) Mitochondrial motility in RH2 and H1975 cells treated with si-ctrl and si-OGT for 72h. Data are mean ± s.e.m. (n = 3 biological replicates, and n = 50 cells per replicate), unpaired two-tailed t-test. **h,** Western blot of RH2 cells treated with indicated concentrations of KL-11743 for 72h was probed with indicated antibodies. **j,** Representative fluorescent images stained with NAO and followed by Weka segmentation (ImageJ) in RH2 cells treated with KL-11743 (200nM) for 72h. **k,** Percentage of type I, II, III cristae structure in RH2 cells treated with indicated concentrations of KL-11743. Data are mean ± s.e.m. (n = 3 biological replicates, and n > 500 mitochondria per replicate. **l,m,** Mitochondria OCR-max and MRC of CI in RH2 cells treated with indicated concentrations of KL-11743 for 72h. Data are mean ± s.e.m., n = 3 biologically independent samples, one-way ANOVA, Dunnett test. **n,** ^{18}FBnTP uptake of subcutaneous xenografts of human LUSC (RH2) treated with KL-11743 (100mg/kg, 10 days). Unpaired two-tailed t-test. o, MRC of CI and CII frozen subcutaneous xenografts of human LUSC (RH2) treated with KL-11743 (100mg/kg, 10 days). Data are mean ± s.e.m. (n = 3 subcutaneous tumors per condition), unpaired two-tailed t-test.

Chapter 14: Outlook

Chapter 1 of this dissertation discussed the many challenges surrounding the production of PET radiopharmaceuticals in a manner that would ensure availability of a wide range of radiopharmaceuticals. While many advances in the literature surrounding the use of microfluidic devices have been described in recent years, many approaches feature complex or expensive microfluidic chips that would unlikely be amenable to use as disposable devices. (Disposability is an enormous advantage for operational simplicity and obviates the need to develop and validate system cleaning protocols, which can be complicated if using a single system to prepare multiple radiotracers.) One recent development by our group features a simple Teflon-coated silicon microfluidic chip with a surface tension trap for droplet reactions. Initial reports utilizing these microvolume droplet reactors have shown that conventional radiochemical yields of radiopharmaceuticals in macroscale reactors can be reproduced, while providing many advantages. Due to the lower volume scale utilized, reagent cost is reduced, specific activity heightened, and the purification scale (and purification time) are substantially reduced. Automation of the microvolume droplet reactor system has also been shown, featuring a small physical footprint that could allow the possibility for self-shielding and housing the setup away from radiopharmacies and instead within clinics or imaging centers for on-site, on-demand production of PET radiopharmaceuticals. All these observed benefits hint at the possibility that soon, the cost-effective on-demand production of PET radiopharmaceuticals may be achievable.

Current generations of the droplet radiosynthesizer of our lab require the need for an analytical HPLC system for purification of synthesized radiopharmaceuticals. The TLC method we show in **Chapter 8** showed that purification and reformulation of radiopharmaceuticals could be performed in an alternative format. The successful application of this method with [^{18}F]Fallypride, and [^{18}F]PBR-06 was shown at clinical dose scales. The use of this method could allow a smaller

footprint and cost of the overall droplet radiosynthesizer. We expect that the PRISMA method shown in **Chapter 7** could be applied to other radiopharmaceuticals, but this would need to be demonstrated further. In addition, the ability to truly replace HPLC would require further development in automation; some of these ideas were covered in **Section 8.5**.

The PRISMA method we showed in **Chapter 7** combined with multi-lane TLC readout, allows for high-throughput analysis of radiopharmaceuticals. This concept was shown with a series of 5 diverse radiopharmaceuticals. In combination with multi-reaction chips, this is a complete solution for high-throughput optimization, where hundreds of reactions can be performed in a matter of a few days. This optimization could be followed by production in a droplet-based automated radiosynthesizer. This methodology could be further applied to adapt macroscale protocols to microscale system to take advantage of microscale production, or tackle optimization of difficult syntheses.

The TLC-based radiometabolite method discussed in **Chapter 9** solved the problems of previous TLC-based approaches, and now offers advantages over HPLC and SPE. The PRISMA approach allows ease of optimization with diverse radiopharmaceuticals. The apparatus allows straightforward use and could be adopted for routine clinical use that would have advantages of (i) reduced effort to prepare and analyze samples, (ii) lower blood volume needed per timepoint, (iii) higher sensitivity. The method would find great use in radiopharmaceuticals that have lower plasma availability. Notably, the method due to its high sensitivity could be extended to later timepoints, or isotopes with lower positron-branching ratio. Methods to fully automate this promising technique are warranted.

References

(1) Dendl, K.; Koerber, S. A.; Kratochwil, C.; Cardinale, J.; Finck, R.; Dabir, M.; Novruzov, E.; Watabe, T.; Kramer, V.; Choyke, P. L.; Haberkorn, U.; Giesel, F. L. FAP and FAPI-PET/CT in Malignant and Non-Malignant Diseases: A Perfect Symbiosis? *Cancers* **2021**, *13* (19), 4946. https://doi.org/10.3390/cancers13194946.

(2) Berti, V.; Osorio, R. S.; Mosconi, L.; Li, Y.; Santi, S. D.; Leon, M. J. de. Early Detection of Alzheimer's Disease with PET Imaging. *NDD* **2010**, *7* (1–3), 131–135. https://doi.org/10.1159/000289222.

(3) Deleye, S.; Waldron, A.-M.; Verhaeghe, J.; Bottelbergs, A.; Wyffels, L.; Broeck, B. V.; Langlois, X.; Schmidt, M.; Stroobants, S.; Staelens, S. Evaluation of Small-Animal PET Outcome Measures to Detect Disease Modification Induced by BACE Inhibition in a Transgenic Mouse Model of Alzheimer Disease. *J Nucl Med* **2017**, *58* (12), 1977–1983. https://doi.org/10.2967/jnumed.116.187625.

(4) Eckelman, W. C. The Use of Positron Emission Tomography in Drug Discovery and Development. In *Positron Emission Tomography: Basic Sciences*; Bailey, D. L., Townsend, D. W., Valk, P. E., Maisey, M. N., Eds.; Springer: London, 2005; pp 327–341. https://doi.org/10.1007/1-84628-007-9_17.

(5) Knowles, S. M.; Tavare, R.; Zettlitz, K. A.; Rochefort, M. M.; Salazar, F.; Jiang, Z. K.; Reiter, R. E.; Wu, A. M. Applications of ImmunoPET: Using 124I-Anti-PSCA A11 Minibody for Imaging Disease Progression and Response to Therapy in Mouse Xenograft Models of Prostate Cancer. *Clin Cancer Res* **2014**, clincanres.1452.2014. https://doi.org/10.1158/1078-0432.CCR-14-1452.

(6) Cherry, S. R. Fundamentals of Positron Emission Tomography and Applications in Preclinical Drug Development. *The Journal of Clinical Pharmacology* **2001**, *41* (5), 482–491. https://doi.org/10.1177/00912700122010357.

(7) Hargreaves, R. The Role of Molecular Imaging in Drug Discovery and Development. *Clinical Pharmacology & Therapeutics* **2008**, *83* (2), 349–353. https://doi.org/10.1038/sj.clpt.6100467.

(8) Alauddin, M. M. Positron Emission Tomography (PET) Imaging with 18F-Based Radiotracers. *American Journal of Nuclear Medicine and Molecular Imaging* **2012**, *2* (1), 55–76.

(9) Bailey, D. L.; Karp, J. S.; Surti, S. Physics and Instrumentation in PET. In *Positron Emission Tomography: Basic Sciences*; Bailey, D. L., Townsend, D. W., Valk, P. E., Maisey, M. N., Eds.; Springer: London, 2005; pp 13–39. https://doi.org/10.1007/1-84628-007-9_2.

(10) Banister, S.; Roeda, D.; Dolle, F.; Kassiou, M. Fluorine-18 Chemistry for PET: A Concise Introduction. *Current Radiopharmaceuticals* **2010**, *3* (2), 68–80. https://doi.org/10.2174/1874471011003020068.

(11) Jacobson, O.; Kiesewetter, D. O.; Chen, X. Fluorine-18 Radiochemistry, Labeling Strategies and Synthetic Routes. *Bioconjugate Chem.* **2015**, *26* (1), 1–18. https://doi.org/10.1021/bc500475e.

(12) Brooks, A. F.; Makaravage, K. J.; Wright, J.; Sanford, M. S.; Scott, P. J. H. Fluorine-18 Radiochemistry. In *Handbook of Radiopharmaceuticals*; John Wiley & Sons, Ltd, 2020; pp 251–289. https://doi.org/10.1002/9781119500575.ch8.

(13) *PET exam number United States 2020*. Statista. https://www.statista.com/statistics/962242/pet-examinations-in-united-states-total-number/ (accessed 2022-11-04).

(14) Escalona, S.; Blasco, J. A.; Reza, M. M.; Andradas, E.; Gómez, N. A Systematic Review of FDG-PET in Breast Cancer. *Med Oncol* **2010**, *27* (1), 114–129. https://doi.org/10.1007/s12032-009-9182-3.

(15) Cuaron, J.; Dunphy, M.; Rimner, A. Role of FDG-PET Scans in Staging, Response Assessment, and Follow-up Care for Non-Small Cell Lung Cancer. *Front. Oncol.* **2013**, *2*, 208. https://doi.org/10.3389/fonc.2012.00208.
(16) Fletcher, J. W.; Djulbegovic, B.; Soares, H. P.; Siegel, B. A.; Lowe, V. J.; Lyman, G. H.; Coleman, R. E.; Wahl, R.; Paschold, J. C.; Avril, N.; Einhorn, L. H.; Suh, W. W.; Samson, D.; Delbeke, D.; Gorman, M.; Shields, A. F. Recommendations on the Use of 18F-FDG PET in Oncology. *J. Nucl. Med.* **2008**, *49* (3), 480–508. https://doi.org/10.2967/jnumed.107.047787.
(17) Keng, P. Y.; Esterby, M.; van Dam, R. M. Emerging Technologies for Decentralized Production of PET Tracers. In *Positron Emission Tomography - Current Clinical and Research Aspects*; Hsieh, C.-H., Ed.; InTech: Rijeka, Croatia, 2012; pp 153–182.
(18) Keppler, J. S.; Conti, P. S. A Cost Analysis of Positron Emission Tomography. *American Journal of Roentgenology* **2001**, *177* (1), 31–40. https://doi.org/10.2214/ajr.177.1.1770031.
(19) Saha, G. B. Design and Cost of PET Center. In *Basics of PET Imaging: Physics, Chemistry, and Regulations*; Saha, P., Gopal B., Ed.; Springer International Publishing: Cham, 2016; pp 227–239. https://doi.org/10.1007/978-3-319-16423-6_12.
(20) Rensch, C.; Jackson, A.; Lindner, S.; Salvamoser, R.; Samper, V.; Riese, S.; Bartenstein, P.; Wängler, C.; Wängler, B. Microfluidics: A Groundbreaking Technology for PET Tracer Production? *Molecules* **2013**, *18* (7), 7930–7956. https://doi.org/10.3390/molecules18077930.
(21) Pascali, G.; Matesic, L. How Far Are We from Dose On Demand of Short-Lived Radiopharmaceuticals? In *Perspectives on Nuclear Medicine for Molecular Diagnosis and Integrated Therapy*; Kuge, Y., Shiga, T., Tamaki, N., Eds.; Springer Japan, 2016; pp 79–92. https://doi.org/10.1007/978-4-431-55894-1_6.
(22) Razzaq, T.; Kappe, C. O. Continuous Flow Organic Synthesis under High-Temperature/Pressure Conditions. *Chemistry – An Asian Journal* **2010**, *5* (6), 1274–1289. https://doi.org/10.1002/asia.201000010.
(23) Wiles, C.; Watts, P. Continuous Flow Reactors, a Tool for the Modern Synthetic Chemist. *Eur. J. Org. Chem.* **2008**, 1655–1671.
(24) Arima, V.; Watts, P.; Pascali, G. Microfluidics in Planar Microchannels: Synthesis of Chemical Compounds On-Chip. In *Lab-on-a-Chip Devices and Micro-Total Analysis Systems*; Castillo-León, J., Svendsen, W. E., Eds.; Springer International Publishing, 2015; pp 197–239.
(25) Pascali, G.; Watts, P.; Salvadori, P. A. Microfluidics in Radiopharmaceutical Chemistry. *Nuclear Medicine and Biology* **2013**, *40* (6), 776–787. https://doi.org/10.1016/j.nucmedbio.2013.04.004.
(26) Zeng, D.; Desai, A. V.; Ranganathan, D.; Wheeler, T. D.; Kenis, P. J. A.; Reichert, D. E. Microfluidic Radiolabeling of Biomolecules with PET Radiometals. *Nuclear Medicine and Biology* **2013**, *40* (1), 42–51. https://doi.org/10.1016/j.nucmedbio.2012.08.012.
(27) Wright, B. D.; Whittenberg, J.; Desai, A.; DiFelice, C.; Kenis, P. J. A.; Lapi, S. E.; Reichert, D. E. Microfluidic Preparation of a 89Zr-Labeled Trastuzumab Single-Patient Dose. *J Nucl Med* **2016**, *57* (5), 747–752. https://doi.org/10.2967/jnumed.115.166140.
(28) Pfaff, S.; Philippe, C.; Pichler, V.; Hacker, M.; Mitterhauser, M.; Wadsak, W. Microfluidic 68 Ga-Labeling: A Proof of Principle Study. *Dalton Transactions* **2018**, *47* (17), 5997–6004. https://doi.org/10.1039/C8DT00158H.
(29) Liu, Z.; Schaap, K. S.; Ballemans, L.; Zanger, R. de; Blois, E. de; Rohde, M.; Oehlke, E. Measurement of Reaction Kinetics of [177Lu]Lu-DOTA-TATE Using a Microfluidic System. *Dalton Trans.* **2017**, *46* (42), 14669–14676. https://doi.org/10.1039/C7DT01830D.
(30) De Leonardis, F.; Pascali, G.; Salvadori, P. A.; Watts, P.; Pamme, N. On-Chip Pre-Concentration and Complexation of [18F]Fluoride Ions via Regenerable Anion Exchange Particles for Radiochemical Synthesis of Positron Emission Tomography Tracers. *Journal*

of Chromatography A **2011**, *1218* (29), 4714–4719. https://doi.org/16/j.chroma.2011.05.062.
(31) Arima, V.; Pascali, G.; Lade, O.; Kretschmer, H. R.; Bernsdorf, I.; Hammond, V.; Watts, P.; Leonardis, F. D.; Tarn, M. D.; Pamme, N.; Cvetkovic, B. Z.; Dittrich, P. S.; Vasovic, N.; Duane, R.; Jaksic, A.; Zacheo, A.; Zizzari, A.; Marra, L.; Perrone, E.; Salvadori, P. A.; Rinaldi, R. Radiochemistry on Chip: Towards Dose-on-Demand Synthesis of PET Radiopharmaceuticals. *Lab Chip* **2013**, *13* (12), 2328–2336. https://doi.org/10.1039/C3LC00055A.
(32) Saiki, H.; Iwata, R.; Nakanishi, H.; Wong, R.; Ishikawa, Y.; Furumoto, S.; Yamahara, R.; Sakamoto, K.; Ozeki, E. Electrochemical Concentration of No-Carrier-Added [18F]Fluoride from [18O]Water in a Disposable Microfluidic Cell for Radiosynthesis of 18F-Labeled Radiopharmaceuticals. *Applied Radiation and Isotopes* **2010**, *68* (9), 1703–1708. https://doi.org/10.1016/j.apradiso.2010.02.005.
(33) Wong, R.; Iwata, R.; Saiki, H.; Furumoto, S.; Ishikawa, Y.; Ozeki, E. Reactivity of Electrochemically Concentrated Anhydrous [18F]Fluoride for Microfluidic Radiosynthesis of 18F-Labeled Compounds. *Applied Radiation and Isotopes* **2012**, *70* (1), 193–199. https://doi.org/10.1016/j.apradiso.2011.09.022.
(34) Keng, P. Y.; Sergeev, M.; van Dam, R. M. Advantages of Radiochemistry in Microliter Volumes. In *Perspectives on Nuclear Medicine for Molecular Diagnosis and Integrated Therapy*; Kuge, Y., Shiga, T., Tamaki, N., Eds.; Springer Japan, 2016; pp 93–111. https://doi.org/10.1007/978-4-431-55894-1_7.
(35) Keng, P. Y.; van Dam, R. M. Digital Microfluidics: A New Paradigm for Radiochemistry. *Mol. Imag.* **2015**, *14*, 579–594.
(36) Sergeev, M.; Lazari, M.; Morgia, F.; Collins, J.; Javed, M. R.; Sergeeva, O.; Jones, J.; Phelps, M. E.; Lee, J. T.; Keng, P. Y.; Dam, R. M. van. Performing Radiosynthesis in Microvolumes to Maximize Molar Activity of Tracers for Positron Emission Tomography. *Communications Chemistry* **2018**, *1* (1), 10. https://doi.org/10.1038/s42004-018-0009-z.
(37) Chyng-Yann Shiue; Joanna S. Fowler; Alfred P. Wolf; Masazumi Watanabe; Carroll D. Arnett. Synthesis and Specific Activity Determinations of No-Carrier-Added Fluorine-18-Labeled Neuroleptic Drugs. *J Nucl Med* **1985**, *26* (2), 181–186.
(38) Hume, S. P.; Gunn, R. N.; Jones, T. Pharmacological Constraints Associated with Positron Emission Tomographic Scanning of Small Laboratory Animals. *European Journal of Nuclear Medicine and Molecular Imaging* **1998**, *25*, 173–176. https://doi.org/10.1007/s002590050211.
(39) Jagoda, E. M.; Vaquero, J. J.; Seidel, J.; Green, M. V.; Eckelman, W. C. Experiment Assessment of Mass Effects in the Rat: Implications for Small Animal PET Imaging. *Nuclear Medicine and Biology* **2004**, *31* (6), 771–779. https://doi.org/10.1016/j.nucmedbio.2004.04.003.
(40) Reichert, D. E. A Digital Revolution in Radiosynthesis. *J Nucl Med* **2014**, *55* (2), 181–182. https://doi.org/10.2967/jnumed.113.132498.
(41) Knapp, K.-A.; Nickels, M. L.; Manning, H. C. The Current Role of Microfluidics in Radiofluorination Chemistry. *Mol Imaging Biol* **2019**. https://doi.org/10.1007/s11307-019-01414-6.
(42) Lee, C.-C.; Sui, G.; Elizarov, A.; Shu, C. J.; Shin, Y.-S.; Dooley, A. N.; Huang, J.; Daridon, A.; Wyatt, P.; Stout, D.; Kolb, H. C.; Witte, O. N.; Satyamurthy, N.; Heath, J. R.; Phelps, M. E.; Quake, S. R.; Tseng, H.-R. Multistep Synthesis of a Radiolabeled Imaging Probe Using Integrated Microfluidics. *Science* **2005**, *310* (5755), 1793–1796. https://doi.org/10.1126/science.1118919.
(43) Unger, M. A.; Chou, H.-P.; Thorsen, T.; Scherer, A.; Quake, S. R. Monolithic Microfabricated Valves and Pumps by Multilayer Soft Lithography. *Science* **2000**, *288* (5463), 113–116. https://doi.org/10.1126/science.288.5463.113.

(44) Melin, J.; Quake, S. R. Microfluidic Large-Scale Integration: The Evolution of Design Rules for Biological Automation. *Annu. Rev. Biophys. Biomol. Struct.* **2007**, *36* (1), 213–231. https://doi.org/10.1146/annurev.biophys.36.040306.132646.

(45) Elizarov, A. M.; van Dam, R. M.; Shin, Y. S.; Kolb, H. C.; Padgett, H. C.; Stout, D.; Shu, J.; Huang, J.; Daridon, A.; Heath, J. R. Design and Optimization of Coin-Shaped Microreactor Chips for PET Radiopharmaceutical Synthesis. *J Nucl Med* **2010**, *51* (2), 282–287. https://doi.org/10.2967/jnumed.109.065946.

(46) Tseng, W.-Y.; Cho, J. S.; Ma, X.; Kunihiro, A.; Chatziioannou, A.; van Dam, R. M. Toward Reliable Synthesis of Radiotracers for Positron Emission Tomography in PDMS Microfluidic Chips: Study and Optimization of the [18F] Fluoride Drying Process. In *Technical Proceedings of the 2010 NSTI Nanotechnology Conference and Trade Show*; CRC Press: Anaheim, CA, 2010; Vol. 2, pp 472–475.

(47) van Dam, R. M.; Elizarov, A. M.; Ball, C. E.; Shen, C. K.-F.; Padgett, H.; Kolb, H.; Rolland, J.; Diener, L.; Williams, D.; Edgecombe, B.; Jeffries, J.; Stoianova, D.; Stephen, T.; Motamedi, F.; Heath, J. R. Automated Microfluidic-Chip-Based Stand-Alone Instrument for the Synthesis of Radiopharmaceuticals on Human-Dose Scales. In *Technical Proceedings of the 2007 NSTI Nanotechnology Conference and Trade Show*; Santa Clara, CA, 2007; Vol. 3, pp 300–303.

(48) Bejot, R.; Elizarov, A. M.; Ball, E.; Zhang, J.; Miraghaie, R.; Kolb, H. C.; Gouverneur, V. Batch-Mode Microfluidic Radiosynthesis of N-Succinimidyl-4-[18F]Fluorobenzoate for Protein Labelling. *J Label Compd Radiopharm* **2011**, *54* (3), 117–122. https://doi.org/10.1002/jlcr.1826.

(49) Yokell, D. L.; Leece, A. K.; Lebedev, A.; Miraghaie, R.; Ball, C. E.; Zhang, J.; Kolb, H.; Elizarov, A.; Mahmood, U. Microfluidic Single Vessel Production of Hypoxia Tracer 1H-1-(3-[18F]-Fluoro-2-Hydroxy-Propyl)-2-Nitro-Imidazole ([18F]-FMISO). *Appl Radiat Isot* **2012**, *70* (10), 2313–2316. https://doi.org/10.1016/j.apradiso.2012.05.022.

(50) Lebedev, A.; Miraghaie, R.; Kotta, K.; Ball, C. E.; Zhang, J.; Buchsbaum, M. S.; Kolb, H. C.; Elizarov, A. Batch-Reactor Microfluidic Device: First Human Use of a Microfluidically Produced PET Radiotracer. *Lab Chip* **2012**, *13* (1), 136–145. https://doi.org/10.1039/C2LC40853H.

(51) Keng, P. Y.; Chen, S.; Ding, H.; Sadeghi, S.; Shah, G. J.; Dooraghi, A.; Phelps, M. E.; Satyamurthy, N.; Chatziioannou, A. F.; Kim, C.-J. "CJ"; van Dam, R. M. Micro-Chemical Synthesis of Molecular Probes on an Electronic Microfluidic Device. *PNAS* **2012**, *109* (3), 690–695. https://doi.org/10.1073/pnas.1117566109.

(52) Chen, S.; Javed, M. R.; Kim, H.-K.; Lei, J.; Lazari, M.; Shah, G. J.; Dam, M. van; Keng, P. Y.; Kim, C.-J. Radiolabelling Diverse Positron Emission Tomography (PET) Tracers Using a Single Digital Microfluidic Reactor Chip. *Lab Chip* **2014**, *14*, 902–910. https://doi.org/10.1039/C3LC51195B.

(53) Javed, M. R.; Chen, S.; Lei, J.; Collins, J.; Sergeev, M.; Kim, H.-K.; Kim, C.-J.; van Dam, R. M.; Keng, P. Y. High Yield and High Specific Activity Synthesis of [18F]Fallypride in a Batch Microfluidic Reactor for Micro-PET Imaging. *Chem. Commun.* **2014**, *50* (10), 1192–1194. https://doi.org/10.1039/C3CC47616B.

(54) Javed, M. R.; Chen, S.; Kim, H.-K.; Wei, L.; Czernin, J.; Kim, C.-J. "CJ"; Dam, R. M. van; Keng, P. Y. Efficient Radiosynthesis of 3′-Deoxy-3′-18F-Fluorothymidine Using Electrowetting-on-Dielectric Digital Microfluidic Chip. *J Nucl Med* **2014**, *55* (2), 321–328. https://doi.org/10.2967/jnumed.113.121053.

(55) Koag, M. C.; Kim, H.-K.; Kim, A. S. Efficient Microscale Synthesis of [18F]-2-Fluoro-2-Deoxy-d-Glucose. *Chemical Engineering Journal* **2014**, *258*, 62–68. https://doi.org/10.1016/j.cej.2014.07.077.

(56) Koag, M. C.; Kim, H.-K.; Kim, A. S. Fast and Efficient Microscale Radiosynthesis of 3′-Deoxy-3′-[18F]Fluorothymidine. *Journal of Fluorine Chemistry* **2014**, *166*, 104–109. https://doi.org/10.1016/j.jfluchem.2014.07.033.
(57) Fiel, S. A.; Yang, H.; Schaffer, P.; Weng, S.; Inkster, J. A. H.; Wong, M. C. K.; Li, P. C. H. Magnetic Droplet Microfluidics as a Platform for the Concentration of [18F]Fluoride and Radiosynthesis of Sulfonyl [18F]Fluoride. *ACS Appl. Mater. Interfaces* **2015**, *7* (23), 12923–12929. https://doi.org/10.1021/acsami.5b02631.
(58) Wang, J.; Chao, P. H.; van Dam, R. M. Ultra-Compact, Automated Microdroplet Radiosynthesizer. *Lab Chip* **2019**, No. 19, 2415–2424. https://doi.org/10.1039/C9LC00438F.
(59) Lisova, K.; Sergeev, M.; Evans-Axelsson, S.; Stuparu, A. D.; Beykan, S.; Collins, J.; Jones, J.; Lassmann, M.; Herrmann, K.; Perrin, D.; Lee, J. T.; Slavik, R.; van Dam, R. M. Microscale Radiosynthesis, Preclinical Imaging and Dosimetry Study of [18F]AMBF3-TATE: A Potential PET Tracer for Clinical Imaging of Somatostatin Receptors. *Nuclear Medicine and Biology* **2018**, *61*, 36–44. https://doi.org/10.1016/j.nucmedbio.2018.04.001.
(60) Wang, J.; Chao, P. H.; Slavik, R.; van Dam, R. M. Multi-GBq Production of the Radiotracer [18F]Fallypride in a Droplet Microreactor. *RSC Adv.* **2020**, *10* (13), 7828–7838. https://doi.org/10.1039/D0RA01212B.
(61) Rios, A.; Wang, J.; Chao, P. H.; Dam, R. M. van. A Novel Multi-Reaction Microdroplet Platform for Rapid Radiochemistry Optimization. *RSC Adv.* **2019**, *9* (35), 20370–20374. https://doi.org/10.1039/C9RA03639C.
(62) Wang, J.; van Dam, R. M. High-Efficiency Production of Radiopharmaceuticals via Droplet Radiochemistry: A Review of Recent Progress. *Mol Imaging* **2020**, *19*, 1–21. https://doi.org/10.1177/1536012120973099.
(63) *Chromatography of Mycotoxins, Volume 54 - 1st Edition*. https://www.elsevier.com/books/chromatography-of-mycotoxins/betina/978-0-444-81521-7 (accessed 2022-11-03).
(64) Fried, B.; Sherma, B. *Thin-Layer Chromatography, Revised And Expanded*; CRC Press: Boca Raton, 1999.
(65) Santiago, M.; Strobel, S. Chapter Twenty-Four - Thin Layer Chromatography. In *Methods in Enzymology*; Lorsch, J., Ed.; Laboratory Methods in Enzymology: Cell, Lipid and Carbohydrate; Academic Press, 2013; Vol. 533, pp 303–324. https://doi.org/10.1016/B978-0-12-420067-8.00024-6.
(66) *Chromatography-A Century of Discovery 1900-2000.The Bridge to The Sciences/Technology, Volume 64 - 1st Edition*. https://www.elsevier.com/books/chromatography-a-century-of-discovery-1900-2000the-bridge-to-the-sciences-technology/gehrke/978-0-444-50114-1 (accessed 2022-11-04).
(67) Cummins, P. M.; Rochfort, K. D.; O'Connor, B. F. Ion-Exchange Chromatography: Basic Principles and Application. In *Protein Chromatography: Methods and Protocols*; Walls, D., Loughran, S. T., Eds.; Methods in Molecular Biology; Springer: New York, NY, 2017; pp 209–223. https://doi.org/10.1007/978-1-4939-6412-3_11.
(68) Urh, M.; Simpson, D.; Zhao, K. Chapter 26 Affinity Chromatography: General Methods. In *Methods in Enzymology*; Burgess, R. R., Deutscher, M. P., Eds.; Guide to Protein Purification, 2nd Edition; Academic Press, 2009; Vol. 463, pp 417–438. https://doi.org/10.1016/S0076-6879(09)63026-3.
(69) Ó'Fágáin, C.; Cummins, P. M.; O'Connor, B. F. Gel-Filtration Chromatography. In *Protein Chromatography: Methods and Protocols*; Walls, D., Loughran, S. T., Eds.; Methods in Molecular Biology; Springer: New York, NY, 2017; pp 15–25. https://doi.org/10.1007/978-1-4939-6412-3_2.
(70) Phillips, T. M.; Corradini, D. *Handbook of HPLC, Second Edition*; CRC PressINC, 2010.

(71) Berezkin, V. G. Contributions from N.A. Izmailov and M.S. Schraiber to the Development of Thin-Layer Chromatography (On the 70th Anniversary of the Publication of the First Paper on Thin-Layer Chromatography). *J Anal Chem* **2008**, *63* (4), 400–404. https://doi.org/10.1134/S1061934808040163.
(72) Stahl, E. History of the Development of Thin-Layer Chromatography. In *Thin-Layer Chromatography: A Laboratory Handbook*; Bolliger, H. R., Brenner, M., Gänshirt, H., Mangold, H. K., Seiler, H., Stahl, E., Waldi, D., Stahl, E., Eds.; Springer: Berlin, Heidelberg, 1965; pp 1–4. https://doi.org/10.1007/978-3-662-01031-0_1.
(73) Snyder, L. Solvent Selectivity in Normal-Phase TLC. *J Planar Chromatogr* **2008**, *21* (5), 315–323. https://doi.org/10.1556/JPC.21.2008.5.1.
(74) Coenen, H. H.; Gee, A. D.; Adam, M.; Antoni, G.; Cutler, C. S.; Fujibayashi, Y.; Jeong, J. M.; Mach, R. H.; Mindt, T. L.; Pike, V. W.; Windhorst, A. D. Consensus Nomenclature Rules for Radiopharmaceutical Chemistry — Setting the Record Straight. *Nuclear Medicine and Biology* **2017**, *55* (Supplement C), v–xi. https://doi.org/10.1016/j.nucmedbio.2017.09.004.
(75) Fermi, E. Quality Control of PET Radiopharmaceuticals. In *Molecular Imaging: Radiopharmaceuticals for PET and SPECT*; Springer Berlin Heidelberg, 2009; pp 197–204.
(76) Tanzey, S. S.; Mossine, A. V.; Sowa, A. R.; Torres, J.; Brooks, A. F.; Sanford, M. S.; Scott, P. J. H. A Spot Test for Determination of Residual TBA Levels in 18F-Radiotracers for Human Use Using Dragendorff Reagent. *Anal. Methods* **2020**, *12* (41), 5004–5009. https://doi.org/10.1039/D0AY01565B.
(77) Matusch, A.; Meyer, P. T.; Bier, D.; Holschbach, M. H.; Woitalla, D.; Elmenhorst, D.; Winz, O. H.; Zilles, K.; Bauer, A. Metabolism of the A1 Adenosine Receptor PET Ligand [18F]CPFPX by CYP1A2: Implications for Bolus/Infusion PET Studies. *Nuclear Medicine and Biology* **2006**, *33* (7), 891–898. https://doi.org/10.1016/j.nucmedbio.2006.07.006.
(78) Bui, L.; Kitkungvan, D.; Roby, A. E.; Nguyen, T. T.; Gould, K. L. Pitfalls in Quantitative Myocardial PET Perfusion II: Arterial Input Function. *J Nucl Cardiol* **2020**, *27* (2), 397–409. https://doi.org/10.1007/s12350-020-02074-8.
(79) Lazari, M.; Collins, J.; Shen, B.; Farhoud, M.; Yeh, D.; Maraglia, B.; Chin, F. T.; Nathanson, D. A.; Moore, M.; Dam, R. M. van. Fully Automated Production of Diverse 18F-Labeled PET Tracers on the ELIXYS Multireactor Radiosynthesizer Without Hardware Modification. *J. Nucl. Med. Technol.* **2014**, *42* (3), 203–210. https://doi.org/10.2967/jnmt.114.140392.
(80) Lu, S.; Giamis, A. M.; Pike, V. W. Synthesis of [18F]Fallypride in a Micro-Reactor: Rapid Optimization and Multiple-Production in Small Doses for Micro-PET Studies. *Curr Radiopharm* **2009**, *2* (1), 1–13.
(81) Wang, Y. X.; Zhang, L.; Tang, G. H.; Yin, D. Z. An Improved Enantioselective Synthesis of No-Carrier-Added (NCA) 6-[18F]FLUORO-L-DOPA. *Journal of Labelled Compounds and Radiopharmaceuticals* **2001**, *44* (S1), S866–S867. https://doi.org/10.1002/jlcr.25804401304.
(82) Collins, J.; Waldmann, C. M.; Drake, C.; Slavik, R.; Ha, N. S.; Sergeev, M.; Lazari, M.; Shen, B.; Chin, F. T.; Moore, M.; Sadeghi, S.; Phelps, M. E.; Murphy, J. M.; van Dam, R. M. Production of Diverse PET Probes with Limited Resources: 24 18F-Labeled Compounds Prepared with a Single Radiosynthesizer. *Proceedings of the National Academy of Sciences* **2017**, *114* (43), 11309–11314. https://doi.org/10.1073/pnas.1710466114.
(83) Inkster, J. a. H.; Akurathi, V.; Sromek, A. W.; Chen, Y.; Neumeyer, J. L.; Packard, A. B. A Non-Anhydrous, Minimally Basic Protocol for the Simplification of Nucleophilic 18 F-Fluorination Chemistry. *Scientific Reports* **2020**, *10* (1), 6818 (9 pages). https://doi.org/10.1038/s41598-020-61845-y.
(84) Othman, N.; Talib, Y.; Kamal, W. H. B. W. Imaging Scanner Usage in Radiochemical Purity Test. *Nuclear Technical Convention* **2011**.
(85) Ettlinger, D. E.; Häusler, D.; Wadsak, W.; Girschele, F.; Sindelar, K. M.; Mien, L.-K.; Ungersböck, J.; Viernstein, H.; Kletter, K.; Dudczak, R.; Mitterhauser, M. Metabolism and

Autoradiographic Evaluation of [18F]FE@CIT: A Comparison with [123I]β-CIT and [123I]FP-CIT. *Nuclear Medicine and Biology* **2008**, *35* (4), 475–479. https://doi.org/10.1016/j.nucmedbio.2008.02.008.

(86) Jeon, S. J.; Kim, K. M.; Lim, I.; Song, K.; Kim, J. G. Pixelated Scintillator-Based Compact Radio Thin Layer Chromatography Scanner for Radiopharmaceuticals Quality Control. *J. Inst.* **2017**, *12* (11), T11003. https://doi.org/10.1088/1748-0221/12/11/T11003.

(87) Maneuski, D.; Giacomelli, F.; Lemaire, C.; Pimlott, S.; Plenevaux, A.; Owens, J.; O'Shea, V.; Luxen, A. On the Use of Positron Counting for Radio-Assay in Nuclear Pharmaceutical Production. *Applied Radiation and Isotopes* **2017**, *125* (Supplement C), 9–14. https://doi.org/10.1016/j.apradiso.2017.03.021.

(88) Decristoforo, C.; Zaknun, J.; Kohler, B.; Oberladstaetter, M.; Riccabona, G. The Use of Electronic Autoradiography in Radiopharmacy. *Nuclear Medicine and Biology* **1997**, *24* (4), 361–365. https://doi.org/10.1016/S0969-8051(97)00055-3.

(89) Gillies, J. M.; Prenant, C.; Chimon, G. N.; Smethurst, G. J.; Perrie, W.; Hamblett, I.; Dekker, B.; Zweit, J. Microfluidic Reactor for the Radiosynthesis of PET Radiotracers. *Applied Radiation and Isotopes* **2006**, *64* (3), 325–332. https://doi.org/10.1016/j.apradiso.2005.08.007.

(90) Fujibayashi, Y.; Cutler, C.; Anderson, C.; McCarthy, D.; Jones, L.; Sharp, T.; Yonekura, Y.; Welch, M. Comparative Studies of Cu-64-ATSM and C-11-Acetate in an Acute Myocardial Infarction Model: Ex Vivo Imaging of Hypoxia in Rats. *Nuclear Medicine and Biology* **1999**, *26* (1), 117–121. https://doi.org/10.1016/S0969-8051(98)00049-3.

(91) von Guggenberg, E.; Penz, B.; Kemmler, G.; Virgolini, I.; Decristoforo, C. Comparison of Different Methods for Radiochemical Purity Testing of [99mTc-EDDA-HYNIC-D-Phe1,Tyr3]-Octreotide. *Applied Radiation and Isotopes* **2006**, *64* (2), 194–200. https://doi.org/10.1016/j.apradiso.2005.07.019.

(92) Park, J. C.; An, G. I.; Park, S.-I.; Oh, J.; Kim, H. J.; Ha, Y. S.; Wang, E. K.; Kim, K. M.; Kim, J. Y.; Lee, J.; Welch, M. J.; Yoo, J. Luminescence Imaging Using Radionuclides: A Potential Application in Molecular Imaging. *Nuclear Medicine and Biology* **2011**, *38* (3), 321–329. https://doi.org/10.1016/j.nucmedbio.2010.09.003.

(93) Wang, J.; Rios, A.; Lisova, K.; Slavik, R.; Chatziioannou, A. F.; van Dam, R. M. High-Throughput Radio-TLC Analysis. *Nuclear Medicine and Biology* **2020**, *82–83*, 41–48. https://doi.org/10.1016/j.nucmedbio.2019.12.003.

(94) Ciarrocchi, E.; Belcari, N. Cerenkov Luminescence Imaging: Physics Principles and Potential Applications in Biomedical Sciences. *EJNMMI Physics* **2017**, *4* (1), 14. https://doi.org/10.1186/s40658-017-0181-8.

(95) Matthews, P. M.; Rabiner, E. A.; Passchier, J.; Gunn, R. N. Positron Emission Tomography Molecular Imaging for Drug Development. *Br J Clin Pharmacol* **2012**, *73* (2), 175–186. https://doi.org/10.1111/j.1365-2125.2011.04085.x.

(96) Piel, M.; Vernaleken, I.; Rösch, F. Positron Emission Tomography in CNS Drug Discovery and Drug Monitoring. *J. Med. Chem.* **2014**, *57* (22), 9232–9258. https://doi.org/10.1021/jm5001858.

(97) Cherry, S. R.; James A. Sorenson; Michael E. Phelps. *Physics in Nuclear Medicine*, 4th ed.; Elsevier saunders: Philadelphia, PA, USA, 2012.

(98) Knapp, K.-A.; Nickels, M. L.; Manning, H. C. The Current Role of Microfluidics in Radiofluorination Chemistry. *Mol Imaging Biol* **2020**, *22* (3), 463–475. https://doi.org/10.1007/s11307-019-01414-6.

(99) Wang, J.; Chao, P. H.; Hanet, S.; Dam, R. M. van. Performing Multi-Step Chemical Reactions in Microliter-Sized Droplets by Leveraging a Simple Passive Transport Mechanism. *Lab Chip* **2017**, *17* (24), 4342–4355. https://doi.org/10.1039/C7LC01009E.

(100) Pascali, G.; Matesic, L.; Collier, T. L.; Wyatt, N.; Fraser, B. H.; Pham, T. Q.; Salvadori, P. A.; Greguric, I. Optimization of Nucleophilic 18F Radiofluorinations Using a Microfluidic

Reaction Approach. *Nat. Protocols* **2014**, *9* (9), 2017–2029. https://doi.org/10.1038/nprot.2014.137.
(101) Dooraghi, A. A.; Keng, P. Y.; Chen, S.; Javed, M. R.; Kim, C.-J. "CJ"; Chatziioannou, A. F.; van Dam, R. M. Optimization of Microfluidic PET Tracer Synthesis with Cerenkov Imaging. *Analyst* **2013**, *138* (19), 5654–5664. https://doi.org/10.1039/C3AN01113E.
(102) Collins, J.; Waldmann, C. M.; Drake, C.; Slavik, R.; Ha, N. S.; Sergeev, M.; Lazari, M.; Shen, B.; Chin, F. T.; Moore, M.; Sadeghi, S.; Phelps, M. E.; Murphy, J. M.; Dam, R. M. van. Production of Diverse PET Probes with Limited Resources: 24 ^{18}F-Labeled Compounds Prepared with a Single Radiosynthesizer. *PNAS* **2017**, *114* (43), 11309–11314. https://doi.org/10.1073/pnas.1710466114.
(103) Lisova, K.; Chen, B. Y.; Wang, J.; Fong, K. M.-M.; Clark, P. M.; van Dam, R. M. Rapid, Efficient, and Economical Synthesis of PET Tracers in a Droplet Microreactor: Application to O-(2-[18F]Fluoroethyl)-L-Tyrosine ([18F]FET). *EJNMMI radiopharm. chem.* **2019**, *5* (1), 1. https://doi.org/10.1186/s41181-019-0082-3.
(104) Wang, J.; Holloway, T.; Lisova, K.; van Dam, R. M. Green and Efficient Synthesis of the Radiopharmaceutical [18F]FDOPA Using a Microdroplet Reactor. *React. Chem. Eng.* **2020**, *5* (2), 320–329. https://doi.org/10.1039/C9RE00354A.
(105) Lisova, K.; Wang, J.; Rios, A.; van Dam, R. M. Adaptation and Optimization of [F-18] Florbetaben ([F-18] FBB) Radiosynthesis to a Microdroplet Reactor. In *Journal of Labelled Compounds & Radiopharmaceuticals*; WILEY 111 RIVER ST, HOBOKEN 07030-5774, NJ USA, 2019; Vol. 62, pp S353–S354.
(106) Fischman, A. J. Role of [18F]-Dopa–PET Imaging in Assessing Movement Disorders. *Radiologic Clinics of North America* **2005**, *43* (1), 93–106. https://doi.org/10.1016/j.rcl.2004.08.002.
(107) Schiepers, C.; Chen, W.; Cloughesy, T.; Dahlbom, M.; Huang, S.-C. 18F-FDOPA Kinetics in Brain Tumors. *J Nucl Med* **2007**, *48* (10), 1651–1661. https://doi.org/10.2967/jnumed.106.039321.
(108) Chen, W.; Silverman, D. H. S.; Delaloye, S.; Czernin, J.; Kamdar, N.; Pope, W.; Satyamurthy, N.; Schiepers, C.; Cloughesy, T. 18F-FDOPA PET Imaging of Brain Tumors: Comparison Study with 18F-FDG PET and Evaluation of Diagnostic Accuracy. *J Nucl Med* **2006**, *47* (6), 904–911.
(109) Becherer, A.; Szabó, M.; Karanikas, G.; Wunderbaldinger, P.; Angelberger, P.; Raderer, M.; Kurtaran, A.; Dudczak, R.; Kletter, K. Imaging of Advanced Neuroendocrine Tumors with 18F-FDOPA PET. *J Nucl Med* **2004**, *45* (7), 1161–1167.
(110) Jager, P. L.; Chirakal, R.; Marriott, C. J.; Brouwers, A. H.; Koopmans, K. P.; Gulenchyn, K. Y. 6-L-18F-Fluorodihydroxyphenylalanine PET in Neuroendocrine Tumors: Basic Aspects and Emerging Clinical Applications. *Journal of Nuclear Medicine* **2008**, *49* (4), 573–586. https://doi.org/10.2967/jnumed.107.045708.
(111) Minn, H.; Kauhanen, S.; Seppänen, M.; Nuutila, P. 18F-FDOPA: A Multiple-Target Molecule. *J Nucl Med* **2009**, *50* (12), 1915–1918. https://doi.org/10.2967/jnumed.109.065664.
(112) Koopmans, K. P.; Sluiter, W. J. Chapter 4 Staging of Carcinoid Tumours with 18F-DOPA PET: A Prospective, Diagnostic Accuracy Study. 15.
(113) de Vries, E. F. J.; Luurtsema, G.; Brüssermann, M.; Elsinga, P. H.; Vaalburg, W. Fully Automated Synthesis Module for the High Yield One-Pot Preparation of 6-[18F]Fluoro-l-DOPA. *Applied Radiation and Isotopes* **1999**, *51* (4), 389–394. https://doi.org/10.1016/S0969-8043(99)00057-3.
(114) Pretze, M.; Wängler, C.; Wängler, B. 6-[^{18}F]Fluoro-L-DOPA: A Well-Established Neurotracer with Expanding Application Spectrum and Strongly Improved Radiosyntheses. *Biomed Res Int* **2014**, *2014*, e674063. https://doi.org/10.1155/2014/674063.

(115) Zischler, J.; Kolks, N.; Modemann, D.; Neumaier, B.; Zlatopolskiy, B. D. Alcohol-Enhanced Cu-Mediated Radiofluorination. *Chem. Eur. J.* **2017**, *23* (14), 3251–3256. https://doi.org/10.1002/chem.201604633.
(116) Libert, L. C.; Franci, X.; Plenevaux, A. R.; Ooi, T.; Maruoka, K.; Luxen, A. J.; Lemaire, C. F. Production at the Curie Level of No-Carrier-Added 6-18F-Fluoro-l-Dopa. *J Nucl Med* **2013**, *54* (7), 1154–1161. https://doi.org/10.2967/jnumed.112.112284.
(117) Kuik, W.-J.; Kema, I. P.; Brouwers, A. H.; Zijlma, R.; Neumann, K. D.; Dierckx, R. A. J. O.; DiMagno, S. G.; Elsinga, P. H. In Vivo Biodistribution of No-Carrier-Added 6-18F-Fluoro-3,4-Dihydroxy-L-Phenylalanine (18F-DOPA), Produced by a New Nucleophilic Substitution Approach, Compared with Carrier-Added 18F-DOPA, Prepared by Conventional Electrophilic Substitution. *J Nucl Med* **2015**, *56* (1), 106–112. https://doi.org/10.2967/jnumed.114.145730.
(118) Chao, P. H.; Lazari, M.; Hanet, S.; Narayanam, M. K.; Murphy, J. M.; van Dam, R. M. Automated Concentration of [18F]Fluoride into Microliter Volumes. *Applied Radiation and Isotopes* **2018**, *141*, 138–148. https://doi.org/10.1016/j.apradiso.2018.06.017.
(119) Chao, P. H.; Wang, J.; Van Dam, R. M. A Fully Automated Radiosynthesis Platform for Scalable Production and Purification of PET Tracers. In *Proceedings of the 22nd International Conference on Miniaturized Systems for Chemistry and Life Sciences*; Royal Society of Chemistry: Kaohsiung, Taiwan, 2018; pp 1155–1158.
(120) Carroll, M. A.; Nairne, J.; Smith, G.; Widdowson, D. A. Radical Scavengers: A Practical Solution to the Reproducibility Issue in the Fluoridation of Diaryliodonium Salts. *Journal of Fluorine Chemistry* **2007**, *128* (2), 127–132. https://doi.org/10.1016/j.jfluchem.2006.10.018.
(121) Aggarwal, R.; Wei, X.; Kim, W.; Small, E. J.; Ryan, C. J.; Carroll, P.; Cooperberg, M.; Evans, M. J.; Hope, T. Heterogeneous Flare in Prostate-Specific Membrane Antigen Positron Emission Tomography Tracer Uptake with Initiation of Androgen Pathway Blockade in Metastatic Prostate Cancer. *European Urology Oncology* **2018**, *1* (1), 78–82. https://doi.org/10.1016/j.euo.2018.03.010.
(122) Ma, W. W.; Jacene, H.; Song, D.; Vilardell, F.; Messersmith, W. A.; Laheru, D.; Wahl, R.; Endres, C.; Jimeno, A.; Pomper, M. G.; Hidalgo, M. [18F]Fluorodeoxyglucose Positron Emission Tomography Correlates With Akt Pathway Activity but Is Not Predictive of Clinical Outcome During MTOR Inhibitor Therapy. *J Clin Oncol* **2009**, *27* (16), 2697–2704. https://doi.org/10.1200/JCO.2008.18.8383.
(123) Seo, Y. J.; Kang, Y.; Muench, L.; Reid, A.; Caesar, S.; Jean, L.; Wagner, F.; Holson, E.; Haggarty, S. J.; Weiss, P.; King, P.; Carter, P.; Volkow, N. D.; Fowler, J. S.; Hooker, J. M.; Kim, S. W. Image-Guided Synthesis Reveals Potent Blood-Brain Barrier Permeable Histone Deacetylase Inhibitors. *ACS Chem. Neurosci.* **2014**, *5* (7), 588–596. https://doi.org/10.1021/cn500021p.
(124) Airas, L.; Nylund, M.; Rissanen, E. Evaluation of Microglial Activation in Multiple Sclerosis Patients Using Positron Emission Tomography. *Front. Neurol.* **2018**, *9*. https://doi.org/10.3389/fneur.2018.00181.
(125) Roelcke, U.; Wyss, M. T.; Nowosielski, M.; Rudà, R.; Roth, P.; Hofer, S.; Galldiks, N.; Crippa, F.; Weller, M.; Soffietti, R. Amino Acid Positron Emission Tomography to Monitor Chemotherapy Response and Predict Seizure Control and Progression-Free Survival in WHO Grade II Gliomas. *Neuro-Oncology* **2016**, *18* (5), 744–751. https://doi.org/10.1093/neuonc/nov282.
(126) Wang, Y. T.; Edison, P. Tau Imaging in Neurodegenerative Diseases Using Positron Emission Tomography. *Curr Neurol Neurosci Rep* **2019**, *19* (7), 45. https://doi.org/10.1007/s11910-019-0962-7.

(127) Bruton, L.; Scott, P. J. H. Automated Synthesis Modules for PET Radiochemistry. In *Handbook of Radiopharmaceuticals*; John Wiley & Sons, Ltd, 2020; pp 437–456. https://doi.org/10.1002/9781119500575.ch13.
(128) Zhang, X.; Dunlow, R.; Blackman, B. N.; Swenson, R. E. Optimization of 18F-Syntheses Using 19F-Reagents at Tracer-Level Concentrations and Liquid Chromatography/Tandem Mass Spectrometry Analysis: Improved Synthesis of [18F]MDL100907. *Journal of Labelled Compounds and Radiopharmaceuticals* **2018**, *61* (5), 427–437. https://doi.org/10.1002/jlcr.3606.
(129) Shevlin, M. Practical High-Throughput Experimentation for Chemists. *ACS Med. Chem. Lett.* **2017**, *8* (6), 601–607. https://doi.org/10.1021/acsmedchemlett.7b00165.
(130) Santanilla, A. B.; Regalado, E. L.; Pereira, T.; Shevlin, M.; Bateman, K.; Campeau, L.-C.; Schneeweis, J.; Berritt, S.; Shi, Z.-C.; Nantermet, P.; Liu, Y.; Helmy, R.; Welch, C. J.; Vachal, P.; Davies, I. W.; Cernak, T.; Dreher, S. D. Nanomole-Scale High-Throughput Chemistry for the Synthesis of Complex Molecules. *Science* **2015**, *347* (6217), 49–53. https://doi.org/10.1126/science.1259203.
(131) Krska, S. W.; DiRocco, D. A.; Dreher, S. D.; Shevlin, M. The Evolution of Chemical High-Throughput Experimentation To Address Challenging Problems in Pharmaceutical Synthesis. *Acc. Chem. Res.* **2017**, *50* (12), 2976–2985. https://doi.org/10.1021/acs.accounts.7b00428.
(132) Matesic, L.; Kallinen, A.; Greguric, I.; Pascali, G. Dose-on-Demand Production of Diverse 18F-Radiotracers for Preclinical Applications Using a Continuous Flow Microfluidic System. *Nuclear Medicine and Biology* **2017**, *52*, 24–31. https://doi.org/10.1016/j.nucmedbio.2017.05.004.
(133) Liu, K.; Lepin, E. J.; Wang, M.-W.; Guo, F.; Lin, W.-Y.; Chen, Y.-C.; Sirk, S. J.; Olma, S.; Phelps, M. E.; Zhao, X.-Z.; Tseng, H.-R.; van Dam, R. M.; Wu, A. M.; Shen, C. K.-F. Microfluidic-Based 18F-Labeling of Biomolecules for Immuno–Positron Emission Tomography. *Mol Imaging* **2011**, *10* (3), 168–176. https://doi.org/10.2310/7290.2010.00043.
(134) Chen, Y.-C.; Liu, K.; Shen, C. K.-F.; van Dam, R. M. On-Demand Generation and Mixing of Liquid-in-Gas Slugs with Digitally Programmable Composition and Size. *J. Micromech. Microeng.* **2015**, *25* (8), 084006. https://doi.org/10.1088/0960-1317/25/8/084006.
(135) Iwata, R.; Pascali, C.; Terasaki, K.; Ishikawa, Y.; Furumoto, S.; Yanai, K. Minimization of the Amount of Kryptofix 222 - KHCO3 for Applications to Microscale 18F-Radiolabeling. *Appl Radiat Isot* **2017**, *125*, 113–118. https://doi.org/10.1016/j.apradiso.2017.04.021.
(136) Laube, M.; Wodtke, R.; Kopka, K.; Kniess, T.; Pietzsch, J. 18F-Chemistry in HPLC Vials - a Microliter Scale Radiofluorination Approach. *Nuclear Medicine and Biology* **2021**, *96–97*, S61. https://doi.org/10.1016/S0969-8051(21)00367-X.
(137) Lazari, M.; Irribarren, J.; Zhang, S.; van Dam, R. M. Understanding Temperatures and Pressures during Short Radiochemical Reactions. *Applied Radiation and Isotopes* **2016**, *108*, 82–91. https://doi.org/10.1016/j.apradiso.2015.12.037.
(138) Wang, J.; Holloway, T.; Lisova, K.; Dam, R. M. van. Green and Efficient Synthesis of the Radiopharmaceutical [18F]FDOPA Using a Microdroplet Reactor. *React. Chem. Eng.* **2019**. https://doi.org/10.1039/C9RE00354A.
(139) Lisova, K.; Wang, J.; Hajagos, T. J.; Lu, Y.; Hsiao, A.; Elizarov, A.; van Dam, R. M. Economical Droplet-Based Microfluidic Production of [18F]FET and [18F]Florbetaben Suitable for Human Use. *Sci Rep* **2021**, *11* (1), 20636. https://doi.org/10.1038/s41598-021-99111-4.
(140) Andersson, J. D.; Matuskey, D.; Finnema, S. J. Positron Emission Tomography Imaging of the γ-Aminobutyric Acid System. *Neuroscience Letters* **2019**, *691*, 35–43. https://doi.org/10.1016/j.neulet.2018.08.010.

(141) Vaulina, D.; Nasirzadeh, M.; Gomzina, N. Automated Radiosynthesis and Purification of [18F]Flumazenil with Solid Phase Extraction. *Applied Radiation and Isotopes* **2018**, *135*, 110–114. https://doi.org/10.1016/j.apradiso.2018.01.008.
(142) Nasirzadeh, M.; Vaulina, D. D.; Kuznetsova, O. F.; Gomzina, N. A. A Novel Approach to the Synthesis of [18F]Flumazenil, a Radioligand for PET Imaging of Central Benzodiazepine Receptors. *Russ Chem Bull* **2016**, *65* (3), 794–800. https://doi.org/10.1007/s11172-016-1376-1.
(143) Mandap, K. S.; Ido, T.; Kiyono, Y.; Kobayashi, M.; Lohith, T. G.; Mori, T.; Kasamatsu, S.; Kudo, T.; Okazawa, H.; Fujibayashi, Y. Development of Microwave-Based Automated Nucleophilic [18F]Fluorination System and Its Application to the Production of [18F]Flumazenil. *Nuclear Medicine and Biology* **2009**, *36* (4), 403–409. https://doi.org/10.1016/j.nucmedbio.2009.01.011.
(144) Massaweh, G.; Schirrmacher, E.; la Fougere, C.; Kovacevic, M.; Wängler, C.; Jolly, D.; Gravel, P.; Reader, A. J.; Thiel, A.; Schirrmacher, R. Improved Work-up Procedure for the Production of [18F]Flumazenil and First Results of Its Use with a High-Resolution Research Tomograph in Human Stroke. *Nuclear Medicine and Biology* **2009**, *36* (7), 721–727. https://doi.org/10.1016/j.nucmedbio.2009.05.008.
(145) Ryzhikov, N. N.; Seneca, N.; Krasikova, R. N.; Gomzina, N. A.; Shchukin, E.; Fedorova, O. S.; Vassiliev, D. A.; Gulyás, B.; Hall, H.; Savic, I.; Halldin, C. Preparation of Highly Specific Radioactivity [18F]Flumazenil and Its Evaluation in Cynomolgus Monkey by Positron Emission Tomography. *Nuclear Medicine and Biology* **2005**, *32* (2), 109–116. https://doi.org/10.1016/j.nucmedbio.2004.11.001.
(146) Moon, B. S.; Kil, H. S.; Park, J. H.; Kim, J. S.; Park, J.; Chi, D. Y.; Lee, B. C.; Kim, S. E. Facile Aromatic Radiofluorination of [18F]Flumazenil from Diaryliodonium Salts with Evaluation of Their Stability and Selectivity. *Org. Biomol. Chem.* **2011**, *9* (24), 8346–8355. https://doi.org/10.1039/C1OB06277H.
(147) Ryzhikov, N. N.; Gomzina, N. A.; Fedorova, O. S.; Vasil'ev, D. A.; Kostikov, A. P.; Krasikova, R. N. Preparation of [18F]Flumazenil, a Potential Radioligand for PET Imaging of Central Benzodiazepine Receptors, by Isotope Exchange. *Radiochemistry* **2004**, *46* (3), 290–294. https://doi.org/10.1023/B:RACH.0000031692.63830.85.
(148) Gomzina, N. A.; Zaitsev, V. V.; Krasikova, R. N. Optimization of Nucleophilic Fluorination Step in the Synthesis of Various Compounds Labelled with Fluorine-18 for Their Use as Pet Radiotracers. *Journal of Labelled Compounds and Radiopharmaceuticals* **2001**, *44* (S1), S895–S897. https://doi.org/10.1002/jlcr.25804401314.
(149) Lazari, M.; Quinn, K. M.; Claggett, S. B.; Collins, J.; Shah, G. J.; Herman, H. E.; Maraglia, B.; Phelps, M. E.; Moore, M. D.; Dam, R. M. van. ELIXYS - a Fully Automated, Three-Reactor High-Pressure Radiosynthesizer for Development and Routine Production of Diverse PET Tracers. *EJNMMI Res* **2013**, *3* (1), 52. https://doi.org/10.1186/2191-219X-3-52.
(150) Doi, H.; Goto, M.; Suzuki, M. Pd0-Mediated Rapid C-[18F]Fluoromethylation by the Cross-Coupling Reaction of a [18F]Fluoromethyl Halide with an Arylboronic Acid Ester: Novel Method for the Synthesis of a 18F-Labeled Molecular Probe for Positron Emission Tomography. *BCSJ* **2012**, *85* (11), 1233–1238. https://doi.org/10.1246/bcsj.20120151.
(151) Zarrad, F.; Zlatopolskiy, B. D.; Krapf, P.; Zischler, J.; Neumaier, B. A Practical Method for the Preparation of 18F-Labeled Aromatic Amino Acids from Nucleophilic [18F]Fluoride and Stannyl Precursors for Electrophilic Radiohalogenation. *Molecules* **2017**, *22* (12). https://doi.org/10.3390/molecules22122231.
(152) Lisova, K.; Wang, J.; Chao, P. H.; van Dam, R. M. A Simple and Efficient Automated Microvolume Radiosynthesis of [18F]Florbetaben. *EJNMMI Radiopharmacy and Chemistry* **2020**, *5* (1), 30. https://doi.org/10.1186/s41181-020-00113-w.

(153) Simmons, D. A.; James, M. L.; Belichenko, N. P.; Semaan, S.; Condon, C.; Kuan, J.; Shuhendler, A. J.; Miao, Z.; Chin, F. T.; Longo, F. M. TSPO–PET Imaging Using [18F]PBR06 Is a Potential Translatable Biomarker for Treatment Response in Huntington's Disease: Preclinical Evidence with the P75NTR Ligand LM11A-31. *Hum Mol Genet* **2018**, *27* (16), 2893–2912. https://doi.org/10.1093/hmg/ddy202.
(154) Wang, M.; Gao, M.; Miller, K. D.; Zheng, Q.-H. Synthesis of [11C]PBR06 and [18F]PBR06 as Agents for Positron Emission Tomographic (PET) Imaging of the Translocator Protein (TSPO). *Steroids* **2011**, *76* (12), 1331–1340. https://doi.org/10.1016/j.steroids.2011.06.012.
(155) Zhang, H.; Xiao, J.; Zhou, J.; Tan, H.; Hu, Y.; Mao, W.; Fu, Z.; Lin, Q.; Shi, H.; Cheng, D. 18F-PBR06 PET/CT Imaging for Evaluating Atherosclerotic Plaques Linked to Macrophage Infiltration. *Nucl Med Commun* **2019**, *40* (4), 370–376. https://doi.org/10.1097/MNM.0000000000000978.
(156) Siessmeier, T.; Zhou, Y.; Buchholz, H.-G.; Landvogt, C.; Vernaleken, I.; Piel, M.; Schirrmacher, R.; Rösch, F.; Schreckenberger, M.; Wong, D. F.; Cumming, P.; Gründer, G.; Bartenstein, P. Parametric Mapping of Binding in Human Brain of D2 Receptor Ligands of Different Affinities. *J Nucl Med* **2005**, *46* (6), 964–972.
(157) Vandehey, N. T.; Moirano, J. M.; Converse, A. K.; Holden, J. E.; Mukherjee, J.; Murali, D.; Nickles, R. J.; Davidson, R. J.; Schneider, M. L.; Christian, B. T. High-Affinity Dopamine D2/D3 PET Radioligands 18F-Fallypride and 11C-FLB457: A Comparison of Kinetics in Extrastriatal Regions Using a Multiple-Injection Protocol. *J Cereb Blood Flow Metab* **2010**, *30* (5), 994–1007. https://doi.org/10.1038/jcbfm.2009.270.
(158) Timofeeva, D. S.; Ofial, A. R.; Mayr, H. Kinetics of Electrophilic Fluorinations of Enamines and Carbanions: Comparison of the Fluorinating Power of N–F Reagents. *J. Am. Chem. Soc.* **2018**, *140* (36), 11474–11486. https://doi.org/10.1021/jacs.8b07147.
(159) Cacace, F.; Speranza, M.; Wolf, A. P.; Macgregor, R. R. Nucleophilic Aromatic Substitution; Kinetics of Fluorine-18 Substitution Reactions in Polyfluorobenzenes. Isotopic Exchange between 18F− and Polyfluorobenzenes in Dimethylsulfoxide. A Kinetic Study. *Journal of Fluorine Chemistry* **1982**, *21* (2), 145–158. https://doi.org/10.1016/S0022-1139(00)81238-5.
(160) Valera, F. E.; Quaranta, M.; Moran, A.; Blacker, J.; Armstrong, A.; Cabral, J. T.; Blackmond, D. G. The Flow's the Thing…Or Is It? Assessing the Merits of Homogeneous Reactions in Flask and Flow. *Angewandte Chemie International Edition* **2010**, *49* (14), 2478–2485. https://doi.org/10.1002/anie.200906095.
(161) Aroh, K. C.; Jensen, K. F. Efficient Kinetic Experiments in Continuous Flow Microreactors. *React. Chem. Eng.* **2018**, *3* (1), 94–101. https://doi.org/10.1039/C7RE00163K.
(162) Chang, C.-W.; Chiu, C.-H.; Lin, M.-H.; Wu, H.-M.; Yu, T.-H.; Wang, P.-Y.; Kuo, Y.-Y.; Huang, Y.-Y.; Shiue, C.-Y.; Huang, W.-S.; Yeh, S. H.-H. GMP-Compliant Fully Automated Radiosynthesis of [18F]FEPPA for PET/MRI Imaging of Regional Brain TSPO Expression. *EJNMMI Res* **2021**, *11* (1), 26. https://doi.org/10.1186/s13550-021-00768-9.
(163) Vignal, N.; Cisternino, S.; Rizzo-Padoin, N.; San, C.; Hontonnou, F.; Gelé, T.; Declèves, X.; Sarda-Mantel, L.; Hosten, B. [18F]FEPPA a TSPO Radioligand: Optimized Radiosynthesis and Evaluation as a PET Radiotracer for Brain Inflammation in a Peripheral LPS-Injected Mouse Model. *Molecules* **2018**, *23* (6), 1375. https://doi.org/10.3390/molecules23061375.
(164) Berroterán-Infante, N.; Balber, T.; Fürlinger, P.; Bergmann, M.; Lanzenberger, R.; Hacker, M.; Mitterhauser, M.; Wadsak, W. [18F]FEPPA: Improved Automated Radiosynthesis, Binding Affinity, and Preliminary in Vitro Evaluation in Colorectal Cancer. *ACS Med. Chem. Lett.* **2018**, *9* (3), 177–181. https://doi.org/10.1021/acsmedchemlett.7b00367.
(165) Vasdev, N.; Green, D. E.; Vines, D. C.; McLarty, K.; McCormick, P. N.; Moran, M. D.; Houle, S.; Wilson, A. A.; Reilly, R. M. Positron-Emission Tomography Imaging of the TSPO with

[18F]FEPPA in a Preclinical Breast Cancer Model. *Cancer Biotherapy and Radiopharmaceuticals* **2013**, *28* (3), 254–259. https://doi.org/10.1089/cbr.2012.1196.
(166) Setiawan, E.; Wilson, A. A.; Mizrahi, R.; Rusjan, P. M.; Miler, L.; Rajkowska, G.; Suridjan, I.; Kennedy, J. L.; Rekkas, P. V.; Houle, S.; Meyer, J. H. Role of Translocator Protein Density, a Marker of Neuroinflammation, in the Brain During Major Depressive Episodes. *JAMA Psychiatry* **2015**, *72* (3), 268. https://doi.org/10.1001/jamapsychiatry.2014.2427.
(167) Dahl, K.; Garcia, A.; Stephenson, N. A.; Vasdev, N. "In-Loop" 18F-Fluorination: A Proof-of-Concept Study. *Journal of Labelled Compounds and Radiopharmaceuticals* **2019**, *62* (7), 292–297. https://doi.org/10.1002/jlcr.3751.
(168) Gu, Z.; Taschereau, R.; Vu, N. T.; Prout, D. L.; Silverman, R. W.; Lee, J. T.; Chatziioannou, A. F. Performance Evaluation of G8, a High-Sensitivity Benchtop Preclinical PET/CT Tomograph. *Journal of Nuclear Medicine* **2019**, *60* (1), 142–149. https://doi.org/10.2967/jnumed.118.208827.
(169) Gu, Z.; Taschereau, R.; Vu, N. T.; Prout, D. L.; Lee, J.; Chatziioannou, A. F. Performance Evaluation of HiPET, a High Sensitivity and High Resolution Preclinical PET Tomograph. *Phys. Med. Biol.* **2020**, *65* (4), 045009. https://doi.org/10.1088/1361-6560/ab6b44.
(170) Jones, J.; Rios, A.; Chao, P.; Wang, J.; van Dam, R. M. High-Throughput Microdroplet Radiochemistry Platform to Accelerate Radiotracer Development. In *Journal of Labelled Compounds & Radiopharmaceuticals*; 2019; Vol. 62, pp S350–S351.
(171) Bowden, G. D.; Pichler, B. J.; Maurer, A. A Design of Experiments (DoE) Approach Accelerates the Optimization of Copper-Mediated 18 F-Fluorination Reactions of Arylstannanes. *Scientific Reports* **2019**, *9* (1), 11370. https://doi.org/10.1038/s41598-019-47846-6.
(172) Calderwood, S.; Collier, T. L.; Gouverneur, V.; Liang, S. H.; Vasdev, N. Synthesis of 18F-Arenes from Spirocyclic Iodonium(III) Ylides via Continuous-Flow Microfluidics. *Journal of Fluorine Chemistry* **2015**, *178*, 249–253. https://doi.org/10.1016/j.jfluchem.2015.08.006.
(173) Ungersboeck, J.; Philippe, C.; Haeusler, D.; Mitterhauser, M.; Lanzenberger, R.; Dudczak, R.; Wadsak, W. Optimization of [11C]DASB-Synthesis: Vessel-Based and Flow-through Microreactor Methods. *Applied Radiation and Isotopes* **2012**, *70* (11), 2615–2620. https://doi.org/10.1016/j.apradiso.2012.08.001.
(174) Liang, S. H.; Yokell, D. L.; Jackson, R. N.; Rice, P. A.; Callahan, R.; Johnson, K. A.; Alagille, D.; Tamagnan, G.; Collier, T. L.; Vasdev, N. Microfluidic Continuous-Flow Radiosynthesis of [18F]FPEB Suitable for Human PET Imaging. *Med. Chem. Commun.* **2014**, *5* (4), 432–435. https://doi.org/10.1039/C3MD00335C.
(175) Kelloff, G. J.; Krohn, K. A.; Larson, S. M.; Weissleder, R.; Mankoff, D. A.; Hoffman, J. M.; Link, J. M.; Guyton, K. Z.; Eckelman, W. C.; Scher, H. I.; O'Shaughnessy, J.; Cheson, B. D.; Sigman, C. C.; Tatum, J. L.; Mills, G. Q.; Sullivan, D. C.; Woodcock, J. The Progress and Promise of Molecular Imaging Probes in Oncologic Drug Development. *Clin Cancer Res* **2005**, *11* (22), 7967–7985. https://doi.org/10.1158/1078-0432.CCR-05-1302.
(176) Elizarov, A. M. Microreactors for Radiopharmaceutical Synthesis. *Lab Chip* **2009**, *9* (10), 1326–1333.
(177) Pascali, G.; Mazzone, G.; Saccomanni, G.; Manera, C.; Salvadori, P. A. Microfluidic Approach for Fast Labeling Optimization and Dose-on-Demand Implementation. *Nuclear Medicine and Biology* **2010**, *37* (5), 547–555. https://doi.org/16/j.nucmedbio.2010.03.006.
(178) Rios, A.; Holloway, T. S.; Chao, P. H.; De Caro, C.; Okoro, C. C.; van Dam, R. M. Microliter-Scale Reaction Arrays for Economical High-Throughput Experimentation in Radiochemistry. *Sci Rep* **2022**, *12* (1), 10263. https://doi.org/10.1038/s41598-022-14022-2.
(179) Búriová, E.; Macášek, F.; Melichar, F.; Kropáček, M.; Procházka, L. Autoradiolysis of the 2-Deoxy-2-[18F]Fluoro-D-Glucose Radiopharmaceutical. *Journal of Radioanalytical and Nuclear Chemistry* **2005**, *264* (3), 595–602.

(180) Jacobson, M. S.; Dankwart, H. R.; Mahoney, D. W. Radiolysis of 2-[18F]Fluoro-2-Deoxy-d-Glucose ([18F]FDG) and the Role of Ethanol and Radioactive Concentration. *Applied Radiation and Isotopes* **2009**, *67* (6), 990–995. https://doi.org/10.1016/j.apradiso.2009.01.005.
(181) Rensch, C.; Waengler, B.; Yaroshenko, A.; Samper, V.; Baller, M.; Heumesser, N.; Ulin, J.; Riese, S.; Reischl, G. Microfluidic Reactor Geometries for Radiolysis Reduction in Radiopharmaceuticals. *Applied Radiation and Isotopes* **2012**, *70* (8), 1691–1697. https://doi.org/10.1016/j.apradiso.2012.03.004.
(182) Iwata, R.; Terasaki, K.; Ishikawa, Y.; Harada, R.; Furumoto, S.; Yanai, K.; Pascali, C. A Concentration-Based Microscale Method for 18F-Nucleophilic Substitutions and Its Testing on the One-Pot Radiosynthesis of [18F]FET and [18F]Fallypride. *Applied Radiation and Isotopes* **2020**, 109361. https://doi.org/10.1016/j.apradiso.2020.109361.
(183) Hess, E.; Takács, S.; Scholten, B.; Tárkányi, F.; Coenen, H. H.; Qaim, S. M. Excitation Function of the 18O(p,n)18F Nuclear Reaction from Threshold up to 30 MeV. *Radiochimica Acta* **2001**, *89* (6), 357–362. https://doi.org/10.1524/ract.2001.89.6.357.
(184) Asti, M.; Grassi, E.; Sghedoni, R.; De Pietri, G.; Fioroni, F.; Versari, A.; Borasi, G.; Salvo, D. Purification by Ozonolysis of 18O Enriched Water after Cyclotron Irradiation and the Utilization of the Purified Water for the Production of [18F]-FDG (2-Deoxy-2-[18F]-Fluoro-d-Glucose). *Applied Radiation and Isotopes* **2007**, *65* (7), 831–835. https://doi.org/10.1016/j.apradiso.2007.03.003.
(185) Kilian, K.; Chabecki, B.; Kiec, J.; Kunka, A.; Panas, B.; Wójcik, M.; Pękal, A. Synthesis, Quality Control and Determination of Metallic Impurities in 18F-Fludeoxyglucose Production Process. *Reports of Practical Oncology & Radiotherapy* **2014**, *19*, S22–S31. https://doi.org/10.1016/j.rpor.2014.03.001.
(186) Bowden, L.; León Vintró, L.; Mitchell, P. I.; O'Donnell, R. G.; Seymour, A. M.; Duffy, G. J. Radionuclide Impurities in Proton-Irradiated [18O]H2O for the Production of 18F−: Activities and Distribution in the [18F]FDG Synthesis Process. *Applied Radiation and Isotopes* **2009**, *67* (2), 248–255. https://doi.org/10.1016/j.apradiso.2008.10.015.
(187) Allott, L.; Pieve, C. D.; Turton, D. R.; Smith, G. A General [18F]AlF Radiochemistry Procedure on Two Automated Synthesis Platforms. *React. Chem. Eng.* **2017**, *2* (1), 68–74. https://doi.org/10.1039/C6RE00204H.
(188) *The aluminium-[18F]fluoride revolution: simple radiochemistry with a big impact for radiolabelled biomolecules | EJNMMI Radiopharmacy and Chemistry | Full Text*. https://ejnmmipharmchem.springeropen.com/articles/10.1186/s41181-021-00141-0 (accessed 2022-11-06).
(189) *Drugs@FDA: FDA-Approved Drugs*. https://www.accessdata.fda.gov/scripts/cder/daf/ (accessed 2022-07-18).
(190) Centre National de la Recherche Scientifique. *^{18}F-Database of Imaging Radiolabelled Compounds (DIRAC)*. ^{18}F-Database of Imaging Radiolabelled Compounds (DIRAC). http://www.iphc.cnrs.fr/dirac/ (accessed 2013-02-22).
(191) Ory, D.; Van den Brande, J.; de Groot, T.; Serdons, K.; Bex, M.; Declercq, L.; Cleeren, F.; Ooms, M.; Van Laere, K.; Verbruggen, A.; Bormans, G. Retention of [18F]Fluoride on Reversed Phase HPLC Columns. *Journal of Pharmaceutical and Biomedical Analysis* **2015**, *111*, 209–214. https://doi.org/10.1016/j.jpba.2015.04.009.
(192) Ismail, R.; Irribarren, J.; Javed, M. R.; Machness, A.; van Dam, M.; Keng, P. Y. Cationic Imidazolium Polymer Monoliths for Efficient Solvent Exchange, Activation and Fluorination on a Continuous Flow System. *RSC Advances* **2014**, *4* (48), 25348–25356. https://doi.org/10.1039/c4ra04064c.
(193) Wessmann, S. H.; Henriksen, G.; Wester, H.-J. Cryptate Mediated Nucleophilic 18F-Fluorination without Azeotropic Drying. *Nuklearmedizin* **2012**, *51* (01), 1–8. https://doi.org/10.3413/Nukmed-0425-11-08.

(194) Bogni, A.; Laera, L.; Cucchi, C.; Iwata, R.; Seregni, E.; Pascali, C. An Improved Automated One-Pot Synthesis of O-(2-[18F]Fluoroethyl)-L-Tyrosine ([18F]FET) Based on a Purification by Cartridges. *Nuclear Medicine and Biology* **2019**, *72–73*, 11–19. https://doi.org/10.1016/j.nucmedbio.2019.05.006.
(195) Wang, M.-W.; Yin, D.-Z.; Zhang, L.; Zhou, W.; Wang, Y.-X. Remote-Controlled Module-Assisted Synthesis of O-(2-[18F]Fluoroethyl)-L-Tyrosine as Tumor PET Tracer Using Two Different Radiochemical Routes. *Nuclear Science and Techniques* **2006**, *17* (3), 148–153. https://doi.org/10.1016/S1001-8042(06)60029-8.
(196) Wang, H.; Guo, X.; Jiang, S.; Tang, G. Automated Synthesis of [18F]Florbetaben as Alzheimer's Disease Imaging Agent Based on a Synthesis Module System. *Applied Radiation and Isotopes* **2013**, *71* (1), 41–46. https://doi.org/10.1016/j.apradiso.2012.09.014.
(197) Shen, B.; Ehrlichmann, W.; Uebele, M.; Machulla, H.-J.; Reischl, G. Automated Synthesis of n.c.a. [18F]FDOPA via Nucleophilic Aromatic Substitution with [18F]Fluoride. *Applied Radiation and Isotopes* **2009**, *67* (9), 1650–1653. https://doi.org/10.1016/j.apradiso.2009.03.003.
(198) Li, F.; Hicks, J. W.; Yu, L.; Desjardin, L.; Morrison, L.; Hadway, J.; Lee, T.-Y. Plasma Radio-Metabolite Analysis of PET Tracers for Dynamic PET Imaging: TLC and Autoradiography. *EJNMMI Research* **2020**, *10* (1), 141 (12 pages). https://doi.org/10.1186/s13550-020-00705-2.
(199) Stephenson, N. A.; Holland, J. P.; Kassenbrock, A.; Yokell, D. L.; Livni, E.; Liang, S. H.; Vasdev, N. Iodonium Ylide Mediated Radiofluorination of 18F-FPEB and Validation for Human Use. *J Nucl Med* **2015**, *56* (3), 489–492. https://doi.org/10.2967/jnumed.114.151332.
(200) Nandy, S. K.; Rajan, M. G. R. Fully Automated and Simplified Radiosynthesis of [18F]-3′-Deoxy-3′-Fluorothymidine Using Anhydro Precursor and Single Neutral Alumina Column Purification. *J Radioanal Nucl Chem* **2009**, *283* (3), 741–748. https://doi.org/10.1007/s10967-009-0429-4.
(201) Lee, S. J.; Oh, S. J.; Chi, D. Y.; Kil, H. S.; Kim, E. N.; Ryu, J. S.; Moon, D. H. Simple and Highly Efficient Synthesis of 3′-Deoxy-3′-[18F]Fluorothymidine Using Nucleophilic Fluorination Catalyzed by Protic Solvent. *Eur J Nucl Med Mol Imaging* **2007**, *34* (9), 1406–1409. https://doi.org/10.1007/s00259-007-0391-8.
(202) Akula, M. R.; Collier, T. L.; Blevins, D. W.; Kabalka, G. W.; Osborne, D. Sequential Preparation of [18F]FLT and [18F]FMISO Employing Advion NanoTek® Microfluidic Synthesis System. *Advances in Molecular Imaging* **2019**, *9* (4), 53–59. https://doi.org/10.4236/ami.2019.94008.
(203) Collins, J.; Waldmann, C. M.; Drake, C.; Slavik, R.; Ha, N. S.; Sergeev, M.; Lazari, M.; Shen, B.; Chin, F. T.; Moore, M.; Sadeghi, S.; Phelps, M. E.; Murphy, J. M.; van Dam, R. M. Production of Diverse PET Probes with Limited Resources: 24 18F-Labeled Compounds Prepared with a Single Radiosynthesizer. *Proceedings of the National Academy of Sciences* **2017**, *114* (43), 11309–11314. https://doi.org/10.1073/pnas.1710466114.
(204) Zarganes-Tzitzikas, T.; Clemente, G. S.; Elsinga, P. H.; Dömling, A. MCR Scaffolds Get Hotter with 18F-Labeling. *Molecules* **2019**, *24* (7), 1327. https://doi.org/10.3390/molecules24071327.
(205) Russelli, L.; Martinelli, J.; De Rose, F.; Reder, S.; Herz, M.; Schwaiger, M.; Weber, W.; Tei, L.; D'Alessandria, C. Room Temperature Al18F Labeling of 2-Aminomethylpiperidine-Based Chelators for PET Imaging. *ChemMedChem* **2020**, *15* (3), 284–292. https://doi.org/10.1002/cmdc.201900652.
(206) Yu, H.-M.; Chan, C.-H.; Yang, C.-H.; Hsia, H.-T.; Wang, M.-H. Hexavalent Lactoside Labeled with [18F]AlF for PET Imaging of Asialoglycoprotein Receptor. *Applied Radiation and Isotopes* **2020**, *162*, 109199. https://doi.org/10.1016/j.apradiso.2020.109199.

(207) Shih, I.-H.; Duan, X.-D.; Kong, F.-L.; Williams, M. D.; Yang, K.; Zhang, Y.-H.; Yang, D. J. Automated Synthesis of 18F-Fluoropropoxytryptophan for Amino Acid Transporter System Imaging. *BioMed Research International* **2014**, *2014*, 492545. https://doi.org/10.1155/2014/492545.
(208) Koivula, T.; Laine, J.; Lipponen, T.; Perhola, O.; Kämäräinen, E.-L.; Bergström, K.; Solin, O. Assessment of Labelled Products with Different Radioanalytical Methods: Study on 18F-Fluorination Reaction of 4-[18F]Fluoro-N-[2-[1-(2-Methoxyphenyl)-1-Piperazinyl]Ethyl-N-2-Pyridinyl-Benzamide (p-[18F]MPPF). *J Radioanal Nucl Chem* **2010**, *286* (3), 841–846. https://doi.org/10.1007/s10967-010-0802-3.
(209) Johnson, A. R.; Vitha, M. F. Chromatographic Selectivity Triangles. *Journal of Chromatography A* **2011**, *1218* (4), 556–586. https://doi.org/10.1016/j.chroma.2010.09.046.
(210) Cardinale, J.; Martin, R.; Remde, Y.; Schäfer, M.; Hienzsch, A.; Hübner, S.; Zerges, A.-M.; Marx, H.; Hesse, R.; Weber, K.; Smits, R.; Hoepping, A.; Müller, M.; Neels, O. C.; Kopka, K. Procedures for the GMP-Compliant Production and Quality Control of [18F]PSMA-1007—A Next Generation Radiofluorinated Tracer for the Detection of Prostate Cancer. **2017**. https://doi.org/10.20944/preprints201708.0057.v1.
(211) Wiegmann, J. The Chemistry of Silica. Solubility, Polymerization, Colloid and Surface Properties, and Biochemistry. Von RALPH K. ILER. New York/Chichester/Brisbane/Toronto: John Wiley & Sons 1979. XXIV, 866 S., Lwd., £ 39.50. *Acta Polymerica* **1980**, *31* (6), 406–406. https://doi.org/10.1002/actp.1980.010310623.
(212) Dalstein, L.; Potapova, E.; Tyrode, E. The Elusive Silica/Water Interface: Isolated Silanols under Water as Revealed by Vibrational Sum Frequency Spectroscopy. *Physical Chemistry Chemical Physics* **2017**, *19* (16), 10343–10349. https://doi.org/10.1039/C7CP01507K.
(213) Eppard, E.; Homann, T.; de la Fuente, A.; Essler, M.; Rösch, F. Optimization of Labeling PSMA ^{HBED} with Ethanol-Postprocessed ^{68} Ga and Its Quality Control Systems. *J Nucl Med* **2017**, *58* (3), 432–437. https://doi.org/10.2967/jnumed.116.177634.
(214) Jeong, S.; Park, J. Y.; Cha, M. G.; Chang, H.; Kim, Y.; Kim, H.-M.; Jun, B.-H.; Lee, D. S.; Lee, Y.-S.; Jeong, J. M.; Lee, Y.-S.; Jeong, D. H. Highly Robust and Optimized Conjugation of Antibodies to Nanoparticles Using Quantitatively Validated Protocols. *Nanoscale* **2017**, *9* (7), 2548–2555. https://doi.org/10.1039/C6NR04683E.
(215) Hofman, M. S.; Kong, G.; Neels, O. C.; Eu, P.; Hong, E.; Hicks, R. J. High Management Impact of Ga-68 DOTATATE (GaTate) PET/CT for Imaging Neuroendocrine and Other Somatostatin Expressing Tumours. *Journal of Medical Imaging and Radiation Oncology* **2012**, *56* (1), 40–47. https://doi.org/10.1111/j.1754-9485.2011.02327.x.
(216) Baum, R. P.; Kulkarni, H. R. THERANOSTICS: From Molecular Imaging Using Ga-68 Labeled Tracers and PET/CT to Personalized Radionuclide Therapy - The Bad Berka Experience. *Theranostics* **2012**, *2* (5), 437–447. https://doi.org/10.7150/thno.3645.
(217) Graf, J.; Pape, U.-F.; Jann, H.; Denecke, T.; Arsenic, R.; Brenner, W.; Pavel, M.; Prasad, V. Prognostic Significance of Somatostatin Receptor Heterogeneity in Progressive Neuroendocrine Tumor Treated with Lu-177 DOTATOC or Lu-177 DOTATATE. *Eur J Nucl Med Mol Imaging* **2020**, *47* (4), 881–894. https://doi.org/10.1007/s00259-019-04439-9.
(218) Bräuer, A.; Grubert, L. S.; Roll, W.; Schrader, A. J.; Schäfers, M.; Bögemann, M.; Rahbar, K. 177Lu-PSMA-617 Radioligand Therapy and Outcome in Patients with Metastasized Castration-Resistant Prostate Cancer. *Eur J Nucl Med Mol Imaging* **2017**, *44* (10), 1663–1670. https://doi.org/10.1007/s00259-017-3751-z.
(219) Carlucci, G.; Ippisch, R.; Slavik, R.; Mishoe, A.; Blecha, J.; Zhu, S. 68Ga-PSMA-11 NDA Approval: A Novel and Successful Academic Partnership. *Journal of Nuclear Medicine* **2021**, *62* (2), 149–155. https://doi.org/10.2967/jnumed.120.260455.

(220) Keam, S. J. Piflufolastat F 18: Diagnostic First Approval. *Mol Diagn Ther* **2021**, *25* (5), 647–656. https://doi.org/10.1007/s40291-021-00548-0.
(221) Chiaravalloti, A.; Danieli, R.; Lacanfora, A.; Palumbo, B.; Caltagirone, C.; Schillaci, O. Usefulness of 18F Florbetaben in Diagnosis of Alzheimer's Disease and Other Types of Dementia. *Curr Alzheimer Res* **2017**, *14* (2), 154–160. https://doi.org/10.2174/1567205013666160620114309.
(222) Filippi, L.; Chiaravalloti, A.; Bagni, O.; Schillaci, O. 18F-Labeled Radiopharmaceuticals for the Molecular Neuroimaging of Amyloid Plaques in Alzheimer's Disease. *Am J Nucl Med Mol Imaging* **2018**, *8* (4), 268–281.
(223) Lohith, T. G.; Bennacef, I.; Vandenberghe, R.; Vandenbulcke, M.; Salinas, C. A.; Declercq, R.; Reynders, T.; Telan-Choing, N. F.; Riffel, K.; Celen, S.; Serdons, K.; Bormans, G.; Tsai, K.; Walji, A.; Hostetler, E. D.; Evelhoch, J. L.; Laere, K. V.; Forman, M.; Stoch, A.; Sur, C.; Struyk, A. Brain Imaging of Alzheimer Dementia Patients and Elderly Controls with 18F-MK-6240, a PET Tracer Targeting Neurofibrillary Tangles. *J Nucl Med* **2019**, *60* (1), 107–114. https://doi.org/10.2967/jnumed.118.208215.
(224) Treglia, G.; Muoio, B.; Roustaei, H.; Kiamanesh, Z.; Aryana, K.; Sadeghi, R. Head-to-Head Comparison of Fibroblast Activation Protein Inhibitors (FAPI) Radiotracers versus [18F]F-FDG in Oncology: A Systematic Review. *International Journal of Molecular Sciences* **2021**, *22* (20), 11192. https://doi.org/10.3390/ijms222011192.
(225) Laat, B. de; Leurquin-Sterk, G.; Celen, S.; Bormans, G.; Koole, M.; Laere, K. V.; Casteels, C. Preclinical Evaluation and Quantification of 18F-FPEB as a Radioligand for PET Imaging of the Metabotropic Glutamate Receptor 5. *J Nucl Med* **2015**, jnumed.115.162636. https://doi.org/10.2967/jnumed.115.162636.
(226) Dahlbom, M. PET Calibration, Acceptance Testing, and Quality Control. In *Basic Science of PET Imaging*; Springer, Cham, 2017; pp 229–255. https://doi.org/10.1007/978-3-319-40070-9_10.
(227) Peyronneau, M.-A.; Saba, W.; Goutal, S.; Kuhnast, B.; Dollé, F.; Bottlaender, M.; Valette, H. [18F]Fallypride: Metabolism Studies and Quantification of the Radiotracer and Its Radiometabolites in Plasma Using a Simple and Rapid Solid-Phase Extraction Method. *Nuclear Medicine and Biology* **2013**, *40* (7), 887–895. https://doi.org/10.1016/j.nucmedbio.2013.06.003.
(228) Patt, M.; Schildan, A.; Barthel, H.; Becker, G.; Schultze-Mosgau, M. H.; Rohde, B.; Reininger, C.; Sabri, O. Metabolite Analysis of [18F]Florbetaben (BAY 94-9172) in Human Subjects: A Substudy within a Proof of Mechanism Clinical Trial. *J Radioanal Nucl Chem* **2010**, *284* (3), 557–562. https://doi.org/10.1007/s10967-010-0514-8.
(229) Ha, Y. S.; Lee, W.; Jung, J.-M.; Soni, N.; Pandya, D. N.; An, G. I.; Sarkar, S.; Lee, W. K.; Yoo, J. Visualization and Quantification of Radiochemical Purity by Cerenkov Luminescence Imaging. *Anal. Chem.* **2018**, *90* (15), 8927–8935. https://doi.org/10.1021/acs.analchem.8b01098.
(230) Spangenberg, B.; Poole, C. F.; Weins, C. Theoretical Basis of Thin Layer Chromatography (TLC). In *Quantitative Thin-Layer Chromatography: A Practical Survey*; Spangenberg, B., Poole, C. F., Weins, C., Eds.; Springer: Berlin, Heidelberg, 2011; pp 13–52. https://doi.org/10.1007/978-3-642-10729-0_2.
(231) Laferriere-Holloway, T. S.; Rios, A.; Van Dam, R. M. Detrimental Impact of Aqueous Mobile Phases in 18F-Labelled Radiopharmaceutical Analysis via Radio-TLC. *RSC Analytical Methods* **Submitted**.
(232) Nyiredy, S. Planar Chromatographic Method Development Using the PRISMA Optimization System and Flow Charts. *Journal of Chromatographic Science* **2002**, *40* (10), 553–563. https://doi.org/10.1093/chromsci/40.10.553.

(233) Lu, Y.; van Dam, R. M. First Microvolume Metal-Mediated Synthesis of [18F]FDOPA in a Microreactor [ABSTRACT]. *Nuclear Medicine and Biology* **2021**, *96–97*, S15–S16. https://doi.org/10.1016/S0969-8051(21)00291-2.
(234) Cai, L. Thin Layer Chromatography. *Current Protocols Essential Laboratory Techniques* **2014**, *8* (1), 6.3.1-6.3.18. https://doi.org/10.1002/9780470089941.et0603s08.
(235) Huang, Y.-Y.; Tzen, K.-Y.; Liu, Y.-L.; Chiu, C.-H.; Tsai, C.-L.; Wen, H.-P.; Tang, K.-H.; Liu, C.-C.; Shiue, C.-Y. Impact of Residual 18F-Fluoride in 18F-FDOPA for the Diagnosis of Neuroblastoma. *Ann Nucl Med* **2015**, *29* (6), 489–498. https://doi.org/10.1007/s12149-015-0970-x.
(236) Huang, Y.-Y.; Poniger, S.; Tsai, C.-L.; Tochon-Danguy, H. J.; Ackermann, U.; Yen, R.-F. Three-Step Two-Pot Automated Production of NCA [18F]FDOPA with FlexLab Module. *Applied Radiation and Isotopes* **2020**, *158*, 108871. https://doi.org/10.1016/j.apradiso.2019.108871.
(237) Nanabala, R.; Pillai, M. R. A.; Gopal, B. Experience of 6-l-[18F]FDOPA Production Using Commercial Disposable Cassettes and an Automated Module. *Nucl Med Mol Imaging* **2022**, *56* (3), 127–136. https://doi.org/10.1007/s13139-022-00742-w.
(238) Varlow, C.; Murrell, E.; Holland, J. P.; Kassenbrock, A.; Shannon, W.; Liang, S. H.; Vasdev, N.; Stephenson, N. A. Revisiting the Radiosynthesis of [18F]FPEB and Preliminary PET Imaging in a Mouse Model of Alzheimer's Disease. *Molecules* **2020**, *25* (4), 982. https://doi.org/10.3390/molecules25040982.
(239) Wang, J.-Q.; Tueckmantel, W.; Zhu, A.; Pellegrino, D.; Brownell, A.-L. Synthesis and Preliminary Biological Evaluation of 3-[18F]Fluoro-5-(2-Pyridinylethynyl)Benzonitrile as a PET Radiotracer for Imaging Metabotropic Glutamate Receptor Subtype 5. *Synapse* **2007**, *61* (12), 951–961. https://doi.org/10.1002/syn.20445.
(240) Sullivan, J. M.; Lim, K.; Labaree, D.; Lin, S.; McCarthy, T. J.; Seibyl, J. P.; Tamagnan, G.; Huang, Y.; Carson, R. E.; Ding, Y.-S.; Morris, E. D. Kinetic Analysis of the Metabotropic Glutamate Subtype 5 Tracer [18F]FPEB in Bolus and Bolus-Plus-Constant-Infusion Studies in Humans. *J Cereb Blood Flow Metab* **2013**, *33* (4), 532–541. https://doi.org/10.1038/jcbfm.2012.195.
(241) Lim, K.; Labaree, D.; Li, S.; Huang, Y. Preparation of the Metabotropic Glutamate Receptor 5 (MGluR5) PET Tracer [18F]FPEB for Human Use: An Automated Radiosynthesis and a Novel One-Pot Synthesis of Its Radiolabeling Precursor. *Applied Radiation and Isotopes* **2014**, *94*, 349–354. https://doi.org/10.1016/j.apradiso.2014.09.006.
(242) Jin, Z.-H.; Furukawa, T.; Sogawa, C.; Claron, M.; Aung, W.; Tsuji, A. B.; Wakizaka, H.; Zhang, M.-R.; Boturyn, D.; Dumy, P.; Fujibayashi, Y.; Saga, T. PET Imaging and Biodistribution Analysis of the Effects of Succinylated Gelatin Combined with L-Lysine on Renal Uptake and Retention of 64Cu-Cyclam-RAFT-c(-RGDfK-)4 in Vivo. *European Journal of Pharmaceutics and Biopharmaceutics* **2014**, *86* (3), 478–486. https://doi.org/10.1016/j.ejpb.2013.11.006.
(243) Kokic, M.; Honer, M.; Kessler, L. J.; Grauert, M.; Schubiger, P. A.; Ametamey, S. M. Synthesis and in Vitro and in Vivo Evaluation of [11c]Methyl-Biii277cl for Imaging the Pcp-Binding Site of the Nmda Receptor by Pet. *Journal of Receptors and Signal Transduction* **2002**, *22* (1–4), 123–139. https://doi.org/10.1081/RRS-120014591.
(244) Kuang, Y.; Salem, N.; Corn, D. J.; Erokwu, B.; Tian, H.; Wang, F.; Lee, Z. Transport and Metabolism of Radiolabeled Choline in Hepatocellular Carcinoma. *Mol. Pharmaceutics* **2010**, *7* (6), 2077–2092. https://doi.org/10.1021/mp1001922.
(245) Kuang, Y.; Wang, F.; Corn, D. J.; Tian, H.; Lee, Z. Metabolism of Radiolabeled Methionine in Hepatocellular Carcinoma. *Mol Imaging Biol* **2014**, *16* (1), 44–52. https://doi.org/10.1007/s11307-013-0678-z.
(246) Roivainen, A.; Någren, K.; Hirvonen, J.; Oikonen, V.; Virsu, P.; Tolvanen, T.; Rinne, J. O. Whole-Body Distribution and Metabolism of [N-Methyl-11C](R)-1-(2-Chlorophenyl)-N-(1-

Methylpropyl)-3-Isoquinolinecarboxamide in Humans; an Imaging Agent for in Vivo Assessment of Peripheral Benzodiazepine Receptor Activity with Positron Emission Tomography. *Eur J Nucl Med Mol Imaging* **2009**, *36* (4), 671–682. https://doi.org/10.1007/s00259-008-1000-1.

(247) Tang, D.; Li, J.; Buck, J. R.; Tantawy, M. N.; Xia, Y.; Harp, J. M.; Nickels, M. L.; Meiler, J.; Manning, H. C. Evaluation of TSPO PET Ligands [18F]VUIIS1009A and [18F]VUIIS1009B: Tracers for Cancer Imaging. *Mol Imaging Biol* **2017**, *19* (4), 578–588. https://doi.org/10.1007/s11307-016-1027-9.

(248) Steinmetz, A. The Broad Scope of Cesium Salts in Organic Chemistry. *Catalysts Cesium from Acros Organics* **2011**, 3–11.

(249) Aboagye, E. O.; Price, P. M.; Jones, T. In Vivo Pharmacokinetics and Pharmacodynamics in Drug Development Using Positron-Emission Tomography. *Drug Discovery Today* **2001**, *6* (6), 293–302. https://doi.org/10.1016/S1359-6446(01)01684-1.

(250) Bhattacharyya, S. Application of Positron Emission Tomography in Drug Development. *Biochem Pharmacol (Los Angel)* **2012**, *1* (6), 1000e128. https://doi.org/10.4172/2167-0501.1000e128.

(251) Avril, S.; Muzic, R. F.; Plecha, D.; Traughber, B. J.; Vinayak, S.; Avril, N. 18F-FDG PET/CT for Monitoring of Treatment Response in Breast Cancer. *J Nucl Med* **2016**, *57* (Suppl 1), 34S-39S. https://doi.org/10.2967/jnumed.115.157875.

(252) Weber, W. A.; Figlin, R. Monitoring Cancer Treatment with PET/CT: Does It Make a Difference? *J Nucl Med* **2007**, *48* (1_suppl), 36S – 44.

(253) Füchtner, F.; Angelberger, P.; Kvaternik, H.; Hammerschmidt, F.; Simovc, B. P.; Steinbach, J. Aspects of 6-[18F]Fluoro-L-DOPA Preparation: Precursor Synthesis, Preparative HPLC Purification and Determination of Radiochemical Purity. *Nuclear Medicine and Biology* **2002**, *29* (4), 477–481. https://doi.org/10.1016/S0969-8051(02)00298-6.

(254) Boothe, T. E.; Emran, A. M. The Role of High Performance Liquid Chromatography in Radiochemical/Radiopharmaceutical Synthesis and Quality Assurance. In *New Trends in Radiopharmaceutical Synthesis, Quality Assurance, and Regulatory Control*; Emran, A. M., Ed.; Springer US: Boston, MA, 1991; pp 409–422. https://doi.org/10.1007/978-1-4899-0626-7_38.

(255) Wester, H. J.; Schottelius, M. Fluorine-18 Labeling of Peptides and Proteins. In *PET Chemistry*; Schubiger, P. A., Lehmann, L., Friebe, M., Eds.; Ernst Schering Research Foundation Workshop; Springer Berlin Heidelberg, 2007; pp 79–111.

(256) *Size Exclusion Chromatography: Principles and Methods*; 18-1022-18 AL; GE Healthcare, 2014. https://proteins.gelifesciences.com/~/media/protein-purification-ib/documents/handbooks/size-exclusion-chromatography-handbook.pdf.

(257) Waldmann, C. M.; Gomez, A.; Marchis, P.; Bailey, S. T.; Momcilovic, M.; Jones, A. E.; Shackelford, D. B.; Sadeghi, S. An Automated Multidose Synthesis of the Potentiometric PET Probe 4-[^{18}F]Fluorobenzyl-Triphenylphosphonium ([^{18}F]FBnTP). *Mol Imaging Biol* **2018**, *20* (2), 205–212. https://doi.org/10.1007/s11307-017-1119-1.

(258) Simpson, N. J. K. *Solid-Phase Extraction: Principles, Techniques, and Applications*; CRC Press, 2000.

(259) Dewkar, G. K.; Sundaresan, G.; Lamichhane, N.; Hirsch, J.; Thadigiri, C.; Collier, T.; Hartman, M. C. T.; Vaidyanthan, G.; Zweit, J. Microfluidic Radiosynthesis and Biodistribution of [18F] 2-(5-Fluoro-Pentyl)-2-Methyl Malonic Acid. *Journal of Labelled Compounds and Radiopharmaceuticals* **2013**, *56* (5), 289–294. https://doi.org/10.1002/jlcr.3016.

(260) Nandy, S. K.; Rajan, M. G. R. Simple, Column Purification Technique for the Fully Automated Radiosynthesis of [18F]Fluoroazomycinarabinoside ([18F]FAZA). *Applied Radiation and Isotopes* **2010**, *68* (10), 1944–1949. https://doi.org/10.1016/j.apradiso.2010.04.011.

(261) Lee, S. J.; Hyun, J. S.; Oh, S. J.; Yu, K. H.; Ryu, J. S. Development of a New Precursor-Minimizing Base Control Method and Its Application for the Automated Synthesis and SPE Purification of [18F]Fluoromisonidazole ([18F]FMISO). *Journal of Labelled Compounds and Radiopharmaceuticals* **2013**, *56* (14), 731–735. https://doi.org/10.1002/jlcr.3115.
(262) Tarn, M. D.; Pascali, G.; De Leonardis, F.; Watts, P.; Salvadori, P. A.; Pamme, N. Purification of 2-[18F]Fluoro-2-Deoxy-d-Glucose by on-Chip Solid-Phase Extraction. *J Chromatogr A* **2013**, *1280*, 117–121. https://doi.org/10.1016/j.chroma.2013.01.032.
(263) Lazarus, C. R. Formulation of Radiopharmaceuticals. In *Radionuclide Imaging in Drug Research*; Wilson, C. G., Hardy, J. G., Frier, M., Davis, S. S., Eds.; Springer Netherlands: Dordrecht, 1982; pp 61–73. https://doi.org/10.1007/978-94-011-9728-1_5.
(264) Lau, J.; Rousseau, E.; Kwon, D.; Lin, K.-S.; Bénard, F.; Chen, X. Insight into the Development of PET Radiopharmaceuticals for Oncology. *Cancers* **2020**, *12* (5), 1312. https://doi.org/10.3390/cancers12051312.
(265) Turiel, E.; Martin-Esteban, A. Molecularly Imprinted Polymers: Towards Highly Selective Stationary Phases in Liquid Chromatography and Capillary Electrophoresis. *Analytical and Bioanalytical Chemistry* **2004**, *378* (8), 1876–1886. https://doi.org/10.1007/s00216-003-2331-1.
(266) Zhang, X.; Liu, F.; Knapp, K.-A.; Nickels, M. L.; Manning, H. C.; Bellan, L. M. A Simple Microfluidic Platform for Rapid and Efficient Production of the Radiotracer [18F]Fallypride. *Lab Chip* **2018**, *18* (9), 1369–1377. https://doi.org/10.1039/C8LC00167G.
(267) Wood, J. L.; Steiner, R. R. Purification of Pharmaceutical Preparations Using Thin-Layer Chromatography to Obtain Mass Spectra with Direct Analysis in Real Time and Accurate Mass Spectrometry. *Drug Testing and Analysis* **2011**, *3* (6), 345–351. https://doi.org/10.1002/dta.293.
(268) Holloway, T.; Rios, A.; Okoro, C.; van Dam, R. M. Replacing High-Performance Liquid Chromatography (HPLC) with High-Resolution Thin Layer Chromatography (TLC) for Rapid Radiopharmaceutical Analysis [ABSTRACT]. *Nuclear Medicine and Biology* **2021**, *96–97*, S63. https://doi.org/10.1016/S0969-8051(21)00370-X.
(269) Wang, J.; van Dam, R. M. Economical Production of Radiopharmaceuticals for Preclinical Imaging Using Microdroplet Radiochemistry. In *Biomedical Engineering Technologies: Volume 1*; Ossandon, M. R., Baker, H., Rasooly, A., Eds.; Methods in Molecular Biology; Springer US: New York, NY, 2022; pp 813–828. https://doi.org/10.1007/978-1-0716-1803-5_43.
(270) King, EarlJ. THE SOLUBILITY OF SILICA. *The Lancet* **1938**, *231* (5987), 1236–1238. https://doi.org/10.1016/S0140-6736(00)89813-X.
(271) Rominger, A.; Brendel, M.; Burgold, S.; Keppler, K.; Baumann, K.; Xiong, G.; Mille, E.; Gildehaus, F.-J.; Carlsen, J.; Schlichtiger, J.; Niedermoser, S.; Wängler, B.; Cumming, P.; Steiner, H.; Herms, J.; Haass, C.; Bartenstein, P. Longitudinal Assessment of Cerebral β-Amyloid Deposition in Mice Overexpressing Swedish Mutant β-Amyloid Precursor Protein Using 18F-Florbetaben PET. *J Nucl Med* **2013**, *54* (7), 1127–1134. https://doi.org/10.2967/jnumed.112.114660.
(272) Laferriere-Holloway, T. S.; Rios, A.; Lu, Y.; Okoro, C. C.; van Dam, R. M. A Rapid and Systematic Approach for the Optimization of Radio Thin-Layer Chromatography Resolution. *Journal of Chromatography A* **2022**, 463656. https://doi.org/10.1016/j.chroma.2022.463656.
(273) *CAMAG® Automatic TLC Sampler 4 (ATS 4)*. https://www.camag.com/product/camag-automatic-tlc-sampler-4-ats-4 (accessed 2022-11-11).
(274) Arup, U.; Ekman, S.; Lindblom, L.; Mattsson, J.-E. High Performance Thin Layer Chromatography (HPTLC), an Improved Technique for Screening Lichen Substances. *The Lichenologist* **1993**, *25* (1), 61–71. https://doi.org/10.1006/lich.1993.1018.

(275) Tuzimski, T. Basic Principles of Planar Chromatography and Its Potential for Hyphenated Techniques. In *High-Performance Thin-Layer Chromatography (HPTLC)*; Srivastava, M., Ed.; Springer: Berlin, Heidelberg, 2011; pp 247–310. https://doi.org/10.1007/978-3-642-14025-9_14.
(276) *CAMAG® Horizontal Developing Chamber*. https://www.camag.com/product/camag-horizontal-developing-chamber (accessed 2022-11-12).
(277) Hałka-Grysińska, A.; Dzido, T. H.; Sitarczyk, E.; Klimek-Turek, A.; Chomicki, A. A New Semiautomatic Device with Horizontal Developing Chamber for Gradient Thin-Layer Chromatography. *Journal of Liquid Chromatography & Related Technologies* **2016**, *39* (5–6), 257–263. https://doi.org/10.1080/10826076.2016.1163177.
(278) *CAMAG® TLC-MS Interface 2*. https://www.camag.com/product/camag-tlc-ms-interface-2 (accessed 2020-06-12).
(279) *Plate Express Automated TLC Plate Reader - Advion X Interchim*. Advion. https://www.advion.com/products/plate-express/ (accessed 2022-11-11).
(280) Läufer, K.; Lehmann, J.; Petry, S.; Scheuring, M.; Schmidt-Schuchardt, M. Simple, Inexpensive System for Using Thin-Layer Chromatography for Micro-Preparative Purposes. *Journal of Chromatography A* **1994**, *684* (2), 370–373. https://doi.org/10.1016/0021-9673(94)00571-0.
(281) Pasilis, S. P.; Van Berkel, G. J. Atmospheric Pressure Surface Sampling/Ionization Techniques for Direct Coupling of Planar Separations with Mass Spectrometry. *Journal of Chromatography A* **2010**, *1217* (25), 3955–3965. https://doi.org/10.1016/j.chroma.2009.10.064.
(282) Gerhardt, R. F.; Peretzki, A. J.; Piendl, S. K.; Belder, D. Seamless Combination of High-Pressure Chip-HPLC and Droplet Microfluidics on an Integrated Microfluidic Glass Chip. *Anal. Chem.* **2017**, *89* (23), 13030–13037. https://doi.org/10.1021/acs.analchem.7b04331.
(283) Kagan, I. A.; Flythe, M. D. Thin-Layer Chromatographic (TLC) Separations and Bioassays of Plant Extracts to Identify Antimicrobial Compounds. *J Vis Exp* **2014**, No. 85, 51411. https://doi.org/10.3791/51411.
(284) Lartey, F. M.; Ahn, G.-O.; Shen, B.; Cord, K.-T.; Smith, T.; Chua, J. Y.; Rosenblum, S.; Liu, H.; James, M. L.; Chernikova, S.; Lee, S. W.; Pisani, L. J.; Tirouvanziam, R.; Chen, J. W.; Palmer, T. D.; Chin, F. T.; Guzman, R.; Graves, E. E.; Loo, B. W. PET Imaging of Stroke-Induced Neuroinflammation in Mice Using [18F]PBR06. *Mol Imaging Biol* **2014**, *16* (1), 109–117. https://doi.org/10.1007/s11307-013-0664-5.
(285) Kuntzsch, M.; Lamparter, D.; Bruggener, N.; Muller, M.; Kienzle, G. J.; Reischl, G. Development and Successful Validation of Simple and Fast TLC Spot Tests for Determination of Kryptofix® 2.2.2 and Tetrabutylammonium in 18F-Labeled Radiopharmaceuticals. *Pharmaceuticals (Basel)* **2014**, *7* (5), 621–633. https://doi.org/10.3390/ph7050621.
(286) Ametamey, S. M.; Honer, M.; Schubiger, P. A. Molecular Imaging with PET. *Chem. Rev.* **2008**, *108* (5), 1501–1516. https://doi.org/10.1021/cr0782426.
(287) Lammertsma, A. A. Forward to the Past: The Case for Quantitative PET Imaging. *J Nucl Med* **2017**, *58* (7), 1019–1024. https://doi.org/10.2967/jnumed.116.188029.
(288) Mabrouk, R.; Rusjan, P. M.; Mizrahi, R.; Jacobs, M. F.; Koshimori, Y.; Houle, S.; Ko, J. H.; Strafella, A. P. Image Derived Input Function for [18F]-FEPPA: Application to Quantify Translocator Protein (18 KDa) in the Human Brain. *PLOS ONE* **2014**, *9* (12), e115768. https://doi.org/10.1371/journal.pone.0115768.
(289) Cherry, S. R.; Jones, T.; Karp, J. S.; Qi, J.; Moses, W. W.; Badawi, R. D. Total-Body PET: Maximizing Sensitivity to Create New Opportunities for Clinical Research and Patient Care. *Journal of Nuclear Medicine* **2018**, *59* (1), 3–12. https://doi.org/10.2967/jnumed.116.184028.

(290) Meikle, S. R.; Sossi, V.; Roncali, E.; Cherry, S. R.; Banati, R.; Mankoff, D. A.; Jones, T.; James, M. L.; Sutcliffe, J.; Ouyang, J.; Petibon, Y.; Ma, C.; Fakhri, G. E.; Surti, S.; Karp, J. S.; Badawi, R. D.; Yamaya, T.; Akamatsu, G.; Schramm, G.; Rezaei, A.; Nuyts, J.; Fulton, R. R.; Kyme, A. Z.; Lois, C.; Sari, H.; Price, J.; Boellaard, R.; Jeraj, R.; Bailey, D. L.; Eslick, E. M.; Willowson, K. P.; Dutta, J. Quantitative PET in the 2020s: A Roadmap. *Phys. Med. Biol.* **2020**. https://doi.org/10.1088/1361-6560/abd4f7.

(291) Farde, L.; Eriksson, L.; Blomquist, G.; Halldin, C. Kinetic Analysis of Central [11C]Raclopride Binding to D2-Dopamine Receptors Studied by PET—A Comparison to the Equilibrium Analysis. *J Cereb Blood Flow Metab* **1989**, *9* (5), 696–708. https://doi.org/10.1038/jcbfm.1989.98.

(292) Hashimoto, H.; Kawamura, K.; Takei, M.; Igarashi, N.; Fujishiro, T.; Shiomi, S.; Watanabe, R.; Muto, M.; Furutsuka, K.; Ito, T.; Yamasaki, T.; Yui, J.; Nemoto, K.; Kimura, Y.; Higuchi, M.; Zhang, M.-R. Identification of a Major Radiometabolite of [11C]PBB3. *Nuclear Medicine and Biology* **2015**, *42* (12), 905–910. https://doi.org/10.1016/j.nucmedbio.2015.08.006.

(293) Moein, M. M.; Nakao, R.; Amini, N.; Abdel-Rehim, M.; Schou, M.; Halldin, C. Sample Preparation Techniques for Radiometabolite Analysis of Positron Emission Tomography Radioligands; Trends, Progress, Limitations and Future Prospects. *TrAC Trends in Analytical Chemistry* **2019**, *110*, 1–7. https://doi.org/10.1016/j.trac.2018.10.019.

(294) Takano, A.; Uz, T.; Garcia-Segovia, J.; Tsai, M.; Lahu, G.; Amini, N.; Nakao, R.; Jia, Z.; Halldin, C. A Nonhuman Primate PET Study: Measurement of Brain PDE4 Occupancy by Roflumilast Using (R)-[11C]Rolipram. *Mol Imaging Biol* **2018**, *20* (4), 615–622. https://doi.org/10.1007/s11307-018-1168-0.

(295) Stepanov, V.; Takano, A.; Nakao, R.; Amini, N.; Miura, S.; Hasui, T.; Kimura, H.; Taniguchi, T.; Halldin, C. Development of Two Fluorine-18 Labeled PET Radioligands Targeting PDE10A and in Vivo PET Evaluation in Nonhuman Primates. *Nuclear Medicine and Biology* **2018**, *57*, 12–19. https://doi.org/10.1016/j.nucmedbio.2017.10.004.

(296) Ma, Y.; Kiesewetter, D. O.; Lang, L.; Der, M.; Huang, B.; Carson, R. E.; Eckelman, W. C. Determination of [18F]FCWAY, [18F]FP-TZTP, and Their Metabolites in Plasma Using Rapid and Efficient Liquid-Liquid and Solid Phase Extractions. *Nuclear Medicine and Biology* **2003**, *30* (3), 233–240. https://doi.org/10.1016/S0969-8051(02)00452-3.

(297) Katsifis, A.; Loc'h, C.; Henderson, D.; Bourdier, T.; Pham, T.; Greguric, I.; Lam, P.; Callaghan, P.; Mattner, F.; Eberl, S.; Fulham, M. A Rapid Solid-Phase Extraction Method for Measurement of Non-Metabolised Peripheral Benzodiazepine Receptor Ligands, [18F]PBR102 and [18F]PBR111, in Rat and Primate Plasma. *Nuclear Medicine and Biology* **2011**, *38* (1), 137–148. https://doi.org/10.1016/j.nucmedbio.2010.07.008.

(298) Fairclough, M.; McMahon, A.; Barnett, E.; Matthews, J.; Brown, C. A.; Jones, A. A Highly Reproducible Method for the Measurement of [6-O-Methyl-11C]Diprenorphine and Its Radio-Metabolites Based on Solid-Phase Extraction and Radio-High-Pressure Liquid Chromatography. *Journal of Labelled Compounds and Radiopharmaceuticals* **2021**, *64* (1), 30–39. https://doi.org/10.1002/jlcr.3886.

(299) Liang, S. H.; Holland, J. P.; Stephenson, N. A.; Kassenbrock, A.; Rotstein, B. H.; Daignault, C. P.; Lewis, R.; Collier, L.; Hooker, J. M.; Vasdev, N. PET Neuroimaging Studies of [18F]CABS13 in a Double Transgenic Mouse Model of Alzheimer's Disease and Non-Human Primates. *ACS Chem Neurosci* **2015**, *6* (4), 535–541. https://doi.org/10.1021/acschemneuro.5b00055.

(300) Kozlowski, E. S.; Dalterio, R. A. Analyte Solvent and Injection Volume as Variables Affecting Method Development in Semipreparative Reversed-Phase Liquid Chromatography. *Journal of Separation Science* **2007**, *30* (14), 2286–2292. https://doi.org/10.1002/jssc.200700099.

(301) Vasdev, N.; Collier, T. L. Design and Prototype of an Automated Column-Switching HPLC System for Radiometabolite Analysis. *Pharmaceuticals* **2016**, *9* (3), 51. https://doi.org/10.3390/ph9030051.
(302) Nakao, R.; Halldin, C. “Mixed” Anionic and Non-Ionic Micellar Liquid Chromatography for High-Speed Radiometabolite Analysis of Positron Emission Tomography Radioligands. *Journal of Chromatography A* **2013**, *1281*, 54–59. https://doi.org/10.1016/j.chroma.2013.01.071.
(303) Hennion, M.-C. Solid-Phase Extraction: Method Development, Sorbents, and Coupling with Liquid Chromatography. *Journal of Chromatography A* **1999**, *856* (1), 3–54. https://doi.org/10.1016/S0021-9673(99)00832-8.
(304) Nakao, R.; Halldin, C. A Simplified Radiometabolite Analysis Procedure for PET Radioligands Using a Solid Phase Extraction with Micellar Medium. *Nuclear Medicine and Biology* **2013**, *40* (5), 658–663. https://doi.org/10.1016/j.nucmedbio.2013.02.007.
(305) Tan, P. Z.; Baldwin, R. M.; Van Dyck, C. H.; Al-Tikriti, M.; Roth, B.; Khan, N.; Charney, D. S.; Innis, R. B. Characterization of Radioactive Metabolites of 5-HT2A Receptor PET Ligand [18F]Altanserin in Human and Rodent. *Nucl Med Biol* **1999**, *26* (6), 601–608. https://doi.org/10.1016/s0969-8051(99)00022-0.
(306) Sherma, J.; Fried, B. *Handbook of Thin-Layer Chromatography*; CRC Press, 2003.
(307) Holloway, T.; Rios, A.; Okoro, C.; van Dam, R. M. Thin Layer Chromatography for Rapid Purification and Reformulation of Microfluidically-Produced Radiopharmaceuticals [ABSTRACT]. *Nuclear Medicine and Biology* **2021**, *96–97*, S63–S64. https://doi.org/10.1016/S0969-8051(21)00371-1.
(308) Hafizi, S.; Da Silva, T.; Gerritsen, C.; Kiang, M.; Bagby, R. M.; Prce, I.; Wilson, A. A.; Houle, S.; Rusjan, P. M.; Mizrahi, R. Imaging Microglial Activation in Individuals at Clinical High Risk for Psychosis: An In Vivo PET Study with [18F]FEPPA. *Neuropsychopharmacol.* **2017**, *42* (13), 2474–2481. https://doi.org/10.1038/npp.2017.111.
(309) Hafizi, S.; Tseng, H.-H.; Rao, N.; Selvanathan, T.; Kenk, M.; Bazinet, R. P.; Suridjan, I.; Wilson, A. A.; Meyer, J. H.; Remington, G.; Houle, S.; Rusjan, P. M.; Mizrahi, R. Imaging Microglial Activation in Untreated First-Episode Psychosis: A PET Study With [18F]FEPPA. *Am J Psychiatry* **2017**, *174* (2), 118–124. https://doi.org/10.1176/appi.ajp.2016.16020171.
(310) Suridjan, I.; Rusjan, P. M.; Voineskos, A. N.; Selvanathan, T.; Setiawan, E.; Strafella, A. P.; Wilson, A. A.; Meyer, J. H.; Houle, S.; Mizrahi, R. Neuroinflammation in Healthy Aging: A PET Study Using a Novel Translocator Protein 18kDa (TSPO) Radioligand, [18F]-FEPPA. *NeuroImage* **2014**, *84*, 868–875. https://doi.org/10.1016/j.neuroimage.2013.09.021.
(311) Wilson, A. A.; Garcia, A.; Parkes, J.; McCormick, P.; Stephenson, K. A.; Houle, S.; Vasdev, N. Radiosynthesis and Initial Evaluation of [18F]-FEPPA for PET Imaging of Peripheral Benzodiazepine Receptors. *Nuclear Medicine and Biology* **2008**, *35* (3), 305–314. https://doi.org/10.1016/j.nucmedbio.2007.12.009.
(312) *Automated Production of [18F]FEPPA as a Neuroinflammation Imaging Agent | Journal of Nuclear Medicine*. https://jnm.snmjournals.org/content/57/supplement_2/1033 (accessed 2022-11-03).
(313) *Feasibility study of TSPO quantification with [18F]FEPPA using population-based input function | PLOS ONE*. https://journals.plos.org/plosone/article?id=10.1371/journal.pone.0177785 (accessed 2022-11-02).
(314) Nakaoka, T.; Uetake, Y.; Kaneko, K.; Niwa, T.; Ochiai, H.; Irie, S.; Suezaki, Y.; Otsuka, N.; Hayashinaka, E.; Wada, Y.; Cui, Y.; Maeda, K.; Kusuhara, H.; Sugiyama, Y.; Hosoya, T.; Watanabe, Y. Practical Synthesis of [18F]Pitavastatin and Evaluation of Hepatobiliary Transport Activity in Rats by Positron Emission Tomography. *Mol. Pharmaceutics* **2020**, *17* (6), 1884–1898. https://doi.org/10.1021/acs.molpharmaceut.9b01284.

(315) Keller, T.; Krzyczmonik, A.; Forsback, S.; Picón, F. R. L.; Kirjavainen, A. K.; Takkinen, J.; Rajander, J.; Cacheux, F.; Damont, A.; Dollé, F.; Rinne, J. O.; Haaparanta-Solin, M.; Solin, O. Radiosynthesis and Preclinical Evaluation of [18F]F-DPA, A Novel Pyrazolo[1,5a]Pyrimidine Acetamide TSPO Radioligand, in Healthy Sprague Dawley Rats. *Mol Imaging Biol* **2017**, *19* (5), 736–745. https://doi.org/10.1007/s11307-016-1040-z.
(316) Wiese, C.; Große Maestrup, E.; Galla, F.; Schepmann, D.; Hiller, A.; Fischer, S.; Ludwig, F.-A.; Deuther-Conrad, W.; Donat, C. K.; Brust, P.; Büter, L.; Karst, U.; Wünsch, B. Comparison of in Silico, Electrochemical, in Vitro and in Vivo Metabolism of a Homologous Series of (Radio)Fluorinated Σ1 Receptor Ligands Designed for Positron Emission Tomography. *ChemMedChem* **2016**, *11* (21), 2445–2458. https://doi.org/10.1002/cmdc.201600366.
(317) Tietz, O.; Wuest, M.; Marshall, A.; Glubrecht, D.; Hamann, I.; Wang, M.; Bergman, C.; Way, J. D.; Wuest, F. PET Imaging of Cyclooxygenase-2 (COX-2) in a Pre-Clinical Colorectal Cancer Model. *EJNMMI Research* **2016**, *6* (1), 37. https://doi.org/10.1186/s13550-016-0192-9.
(318) Sephton, S. M.; Herde, A. M.; Mu, L.; Keller, C.; Rüdisühli, S.; Auberson, Y.; Schibli, R.; Krämer, S. D.; Ametamey, S. M. Preclinical Evaluation and Test–Retest Studies of [18F]PSS232, a Novel Radioligand for Targeting Metabotropic Glutamate Receptor 5 (MGlu5). *Eur J Nucl Med Mol Imaging* **2015**, *42* (1), 128–137. https://doi.org/10.1007/s00259-014-2883-7.
(319) Koudih, R.; Gilbert, G.; Dhilly, M.; Abbas, A.; Barré, L.; Debruyne, D.; Sobrio, F. Radiolabelling of 1,4-Disubstituted 3-[18F]Fluoropiperidines and Its Application to New Radiotracers for NR2B NMDA Receptor Visualization. *Org. Biomol. Chem.* **2012**, *10* (42), 8493–8500. https://doi.org/10.1039/C2OB26378E.
(320) Fischer, C. R.; Müller, C.; Reber, J.; Müller, A.; Krämer, S. D.; Ametamey, S. M.; Schibli, R. [18F]Fluoro-Deoxy-Glucose Folate: A Novel PET Radiotracer with Improved in Vivo Properties for Folate Receptor Targeting. *Bioconjugate Chem.* **2012**, *23* (4), 805–813. https://doi.org/10.1021/bc200660z.
(321) Moerlein, S. M.; Perlmutter, J. S. Binding of 5-(2′-[18F]Fluoroenthyl)Flumazenil to Central Benzodiazepine Receptors Measured in Living Baboon by Positron Emission Tomography. *European Journal of Pharmacology* **1992**, *218* (1), 109–115. https://doi.org/10.1016/0014-2999(92)90153-U.
(322) Paquette, M.; Phoenix, S.; Ouellet, R.; Langlois, R.; van Lier, J. E.; Turcotte, É. E.; Bénard, F.; Lecomte, R. Assessment of the Novel Estrogen Receptor PET Tracer 4-Fluoro-11β-Methoxy-16α-[18F]Fluoroestradiol (4FMFES) by PET Imaging in a Breast Cancer Murine Model. *Mol Imaging Biol* **2013**, *15* (5), 625–632. https://doi.org/10.1007/s11307-013-0638-7.
(323) Weber, B.; Burger, C.; Biro, P.; Buck, A. A Femoral Arteriovenous Shunt Facilitates Arterial Whole Blood Sampling in Animals. *Eur J Nucl Med* **2002**, *29* (3), 319–323. https://doi.org/10.1007/s00259-001-0712-2.
(324) Bundy, D. C. Autoradiography. *Current Protocols in Protein Science* **1997**, *10* (1), 10.11.1-10.11.6. https://doi.org/10.1002/0471140864.ps1011s10.
(325) Escorcia, F. E.; Steckler, J. M.; Abdel-Atti, D.; Price, E. W.; Carlin, S. D.; Scholz, W. W.; Lewis, J. S.; Houghton, J. L. Tumor-Specific Zr-89 Immuno-PET Imaging in a Human Bladder Cancer Model. *Mol Imaging Biol* **2018**, *20* (5), 808–815. https://doi.org/10.1007/s11307-018-1177-z.
(326) Maybody, M.; Grewal, R. K.; Healey, J. H.; Antonescu, C. R.; Fanchon, L.; Hwang, S.; Carrasquillo, J. A.; Kirov, A.; Farooki, A. Ga-68 DOTATOC PET/CT-Guided Biopsy and Cryoablation with Autoradiography of Biopsy Specimen for Treatment of Tumor-Induced Osteomalacia. *Cardiovasc Intervent Radiol* **2016**, *39* (9), 1352–1357. https://doi.org/10.1007/s00270-016-1350-1.

(327) Hansen, A. E.; Kristensen, A. T.; Jørgensen, J. T.; McEvoy, F. J.; Busk, M.; van der Kogel, A. J.; Bussink, J.; Engelholm, S. A.; Kjær, A. 64Cu-ATSM and 18FDG PET Uptake and 64Cu-ATSM Autoradiography in Spontaneous Canine Tumors: Comparison with Pimonidazole Hypoxia Immunohistochemistry. *Radiation Oncology* **2012**, *7* (1), 89. https://doi.org/10.1186/1748-717X-7-89.
(328) Gomes Marin, J. F.; Nunes, R. F.; Coutinho, A. M.; Zaniboni, E. C.; Costa, L. B.; Barbosa, F. G.; Queiroz, M. A.; Cerri, G. G.; Buchpiguel, C. A. Theranostics in Nuclear Medicine: Emerging and Re-Emerging Integrated Imaging and Therapies in the Era of Precision Oncology. *RadioGraphics* **2020**, *40* (6), 1715–1740. https://doi.org/10.1148/rg.2020200021.
(329) Turner, J. H. Recent Advances in Theranostics and Challenges for the Future. *BJR* **2018**, 20170893. https://doi.org/10.1259/bjr.20170893.
(330) *European Pharmacopoeia*, 11th ed.; Council of Europe: Strasbourg, France, 2022.
(331) Campbell, M. G.; Mercier, J.; Genicot, C.; Gouverneur, V.; Hooker, J. M.; Ritter, T. Bridging the Gaps in 18F PET Tracer Development. *Nat Chem* **2016**, *9* (1), 1–3. https://doi.org/10.1038/nchem.2693.
(332) Tang, P.; Wang, W.; Ritter, T. Deoxyfluorination of Phenols. *J. Am. Chem. Soc.* **2011**, *133* (30), 11482–11484. https://doi.org/10.1021/ja2048072.
(333) Lewandowski, G.; Meissner, E.; Milchert, E. Special Applications of Fluorinated Organic Compounds. *J Hazard Mater* **2006**, *136* (3), 385–391. https://doi.org/10.1016/j.jhazmat.2006.04.017.
(334) O'Hagan, D. Fluorine in Health Care: Organofluorine Containing Blockbuster Drugs. *Journal of Fluorine Chemistry* **2010**, *131* (11), 1071–1081. https://doi.org/10.1016/j.jfluchem.2010.03.003.
(335) Champagne, P. A.; Desroches, J.; Hamel, J.-D.; Vandamme, M.; Paquin, J.-F. Monofluorination of Organic Compounds: 10 Years of Innovation. *Chem Rev* **2015**, *115* (17), 9073–9174. https://doi.org/10.1021/cr500706a.
(336) Villalba, G.; Ayres, R. U.; Schroder, H. Accounting for Fluorine: Production, Use, and Loss. *Journal of Industrial Ecology* **2007**, *11* (1), 85–101. https://doi.org/10.1162/jiec.2007.1075.
(337) Gillis, E. P.; Eastman, K. J.; Hill, M. D.; Donnelly, D. J.; Meanwell, N. A. Applications of Fluorine in Medicinal Chemistry. *J. Med. Chem.* **2015**, *58* (21), 8315–8359. https://doi.org/10.1021/acs.jmedchem.5b00258.
(338) Purser, S.; Moore, P. R.; Swallow, S.; Gouverneur, V. Fluorine in Medicinal Chemistry. *Chem Soc Rev* **2008**, *37* (2), 320–330. https://doi.org/10.1039/b610213c.
(339) Chambers, R. D.; Parsons, M.; Sandford, G.; Bowden, R. Electrophilic Fluorination at Saturated Sites. *Chem. Commun.* **2000**, No. 11, 959–960. https://doi.org/10.1039/B001624L.
(340) Rozen, S. Elemental Fluorine: Not Only for Fluoroorganic Chemistry! *Acc. Chem. Res.* **1996**, *29* (5), 243–248. https://doi.org/10.1021/ar950106c.
(341) Kohlhepp, S. V.; Gulder, T. Hypervalent Iodine(III) Fluorinations of Alkenes and Diazo Compounds: New Opportunities in Fluorination Chemistry. *Chem. Soc. Rev.* **2016**, *45* (22), 6270–6288. https://doi.org/10.1039/C6CS00361C.
(342) Rotstein, B. H.; Stephenson, N. A.; Vasdev, N.; Liang, S. H. Spirocyclic Hypervalent Iodine(III)-Mediated Radiofluorination of Non-Activated and Hindered Aromatics. *Nat Commun* **2014**, *5* (1), 4365. https://doi.org/10.1038/ncomms5365.
(343) Ichiishi, N.; Brooks, A. F.; Topczewski, J. J.; Rodnick, M. E.; Sanford, M. S.; Scott, P. J. H. Copper-Catalyzed [18F]Fluorination of (Mesityl)(Aryl)Iodonium Salts. *Org Lett* **2014**, *16* (12), 3224–3227. https://doi.org/10.1021/ol501243g.
(344) Furuya, T.; Kamlet, A. S.; Ritter, T. Catalysis for Fluorination and Trifluoromethylation. *Nature* **2011**, *473* (7348), 470–477. https://doi.org/10.1038/nature10108.

(345) Preshlock, S.; Tredwell, M.; Gouverneur, V. (18)F-Labeling of Arenes and Heteroarenes for Applications in Positron Emission Tomography. *Chem Rev* **2016**, *116* (2), 719–766. https://doi.org/10.1021/acs.chemrev.5b00493.
(346) Wiebe, A.; Gieshoff, T.; Möhle, S.; Rodrigo, E.; Zirbes, M.; Waldvogel, S. R. Electrifying Organic Synthesis. *Angew Chem Int Ed Engl* **2018**, *57* (20), 5594–5619. https://doi.org/10.1002/anie.201711060.
(347) Möhle, S.; Zirbes, M.; Rodrigo, E.; Gieshoff, T.; Wiebe, A.; Waldvogel, S. R. Modern Electrochemical Aspects for the Synthesis of Value-Added Organic Products. *Angew Chem Int Ed Engl* **2018**, *57* (21), 6018–6041. https://doi.org/10.1002/anie.201712732.
(348) Fuchigami, T.; Inagi, S. Selective Electrochemical Fluorination of Organic Molecules and Macromolecules in Ionic Liquids. *Chem Commun (Camb)* **2011**, *47* (37), 10211–10223. https://doi.org/10.1039/c1cc12414e.
(349) Sawamura, T.; Takahashi, K.; Inagi, S.; Fuchigami, T. Electrochemical Fluorination Using Alkali-Metal Fluorides. *Angewandte Chemie International Edition* **2012**, *51* (18), 4413–4416. https://doi.org/10.1002/anie.201200438.
(350) Lebedev, A.; Jiao, J.; Lee, J.; Yang, F.; Allison, N.; Herschman, H.; Sadeghi, S. Radiochemistry on Electrodes: Synthesis of an 18F-Labelled and in Vivo Stable COX-2 Inhibitor. *PLOS ONE* **2017**, *12* (5), e0176606. https://doi.org/10.1371/journal.pone.0176606.
(351) He, Q.; Wang, Y.; Alfeazi, I.; Sadeghi, S. Electrochemical Nucleophilic Synthesis of Di-Tert-Butyl-(4-[18F]Fluoro-1,2-Phenylene)-Dicarbonate. *Appl Radiat Isot* **2014**, *92*, 52–57. https://doi.org/10.1016/j.apradiso.2014.06.013.
(352) Yoshida, J.; Suga, S.; Suzuki, S.; Kinomura, N.; Yamamoto, A.; Fujiwara, K. Direct Oxidative Carbon−Carbon Bond Formation Using the “Cation Pool” Method. 1. Generation of Iminium Cation Pools and Their Reaction with Carbon Nucleophiles. *J. Am. Chem. Soc.* **1999**, *121* (41), 9546–9549. https://doi.org/10.1021/ja9920112.
(353) Fujie, S.; Matsumoto, K.; Suga, S.; Yoshida, J. Thiofluorination of Carbon–Carbon Multiple Bonds Using Electrochemically Generated ArS(ArSSAr) $^{+}$ BF_4^{-}. *Chem. Lett.* **2009**, *38* (12), 1186–1187. https://doi.org/10.1246/cl.2009.1186.
(354) Javed, M. R.; Chen, S.; Lei, J.; Collins, J.; Sergeev, M.; Kim, H.-K.; Kim, C.-J.; Dam, R. M. van; Keng, P. Y. High Yield and High Specific Activity Synthesis of [18F]Fallypride in a Batch Microfluidic Reactor for Micro-PET Imaging. *Chem. Commun.* **2014**, *50* (10), 1192–1194. https://doi.org/10.1039/C3CC47616B.
(355) Leroux, F.; Jeschke, P.; Schlosser, M. α-Fluorinated Ethers, Thioethers, and Amines: Anomerically Biased Species. *Chem. Rev.* **2005**, *105* (3), 827–856. https://doi.org/10.1021/cr040075b.
(356) Balandeh, M.; Waldmann, C.; Shirazi, D.; Gomez, A.; Rios, A.; Allison, N.; Khan, A.; Sadeghi, S. Electrochemical Fluorination and Radiofluorination of Methyl(Phenylthio)Acetate Using Tetrabutylammonium Fluoride (TBAF). *J Electrochem Soc* **2017**, *164* (9), G99–G103. https://doi.org/10.1149/2.0941709jes.
(357) Chen, H.; Hu, Z.; Zhang, J.; Liang, G.; Xu, B. A Modified Fluoro-Pummerer Reaction with DAST and NIS for Synthesis of β-Amino-α-Fluoro-Sulfides from Corresponding β-Amino-Sulfides. *Tetrahedron* **2015**, *71* (14), 2089–2094. https://doi.org/10.1016/j.tet.2015.02.049.
(358) Waldmann, C. M.; Lebedev, A.; Allison, N.; Sadeghi, S. An Automated Synthesizer for Electrochemical 18F-Fluorination of Organic Compounds. *Appl Radiat Isot* **2017**, *127*, 245–252. https://doi.org/10.1016/j.apradiso.2017.06.028.
(359) Elsler, B.; Wiebe, A.; Schollmeyer, D.; Dyballa, K. M.; Franke, R.; Waldvogel, S. R. Source of Selectivity in Oxidative Cross-Coupling of Aryls by Solvent Effect of 1,1,1,3,3,3-Hexafluoropropan-2-Ol. *Chemistry – A European Journal* **2015**, *21* (35), 12321–12325. https://doi.org/10.1002/chem.201501604.

(360) Kirste, A.; Nieger, M.; Malkowsky, I. M.; Stecker, F.; Fischer, A.; Waldvogel, S. R. Ortho-Selective Phenol-Coupling Reaction by Anodic Treatment on Boron-Doped Diamond Electrode Using Fluorinated Alcohols. *Chemistry – A European Journal* **2009**, *15* (10), 2273–2277. https://doi.org/10.1002/chem.200802556.
(361) Waldvogel, S. R.; Lips, S.; Selt, M.; Riehl, B.; Kampf, C. J. Electrochemical Arylation Reaction. *Chem. Rev.* **2018**, *118* (14), 6706–6765. https://doi.org/10.1021/acs.chemrev.8b00233.
(362) Colomer, I.; Chamberlain, A. E. R.; Haughey, M. B.; Donohoe, T. J. Hexafluoroisopropanol as a Highly Versatile Solvent. *Nat Rev Chem* **2017**, *1* (11), 1–12. https://doi.org/10.1038/s41570-017-0088.
(363) Phelps, M. E. Positron Emission Tomography Provides Molecular Imaging of Biological Processes. *PNAS* **2000**, *97* (16), 9226–9233. https://doi.org/10.1073/pnas.97.16.9226.
(364) Deng, X.; Rong, J.; Wang, L.; Vasdev, N.; Zhang, L.; Josephson, L.; Liang, S. H. Chemistry for Positron Emission Tomography: Recent Advances in 11C-, 18F-, 13N-, and 15O-Labeling Reactions. *Angewandte Chemie International Edition* **2019**, *58* (9), 2580–2605. https://doi.org/10.1002/anie.201805501.
(365) Glaudemans, A. W. J. M.; Enting, R. H.; Heesters, M. A. A. M.; Dierckx, R. A. J. O.; van Rheenen, R. W. J.; Walenkamp, A. M. E.; Slart, R. H. J. A. Value of 11C-Methionine PET in Imaging Brain Tumours and Metastases. *Eur J Nucl Med Mol Imaging* **2013**, *40* (4), 615–635. https://doi.org/10.1007/s00259-012-2295-5.
(366) Huang, T.; Tang, G.; Wang, H.; Nie, D.; Tang, X.; Liang, X.; Hu, K.; Yi, C.; Yao, B.; Tang, C. Synthesis and Preliminary Biological Evaluation of S-11C-Methyl-d-Cysteine as a New Amino Acid PET Tracer for Cancer Imaging. *Amino Acids* **2015**, *47* (4), 719–727. https://doi.org/10.1007/s00726-014-1899-4.
(367) Nuñez, R.; Macapinlac, H. A.; Yeung, H. W. D.; Akhurst, T.; Cai, S.; Osman, I.; Gonen, M.; Riedel, E.; Scher, H. I.; Larson, S. M. Combined 18F-FDG and 11C-Methionine PET Scans in Patients with Newly Progressive Metastatic Prostate Cancer. *J Nucl Med* **2002**, *43* (1), 46–55.
(368) Ilardi, E. A.; Vitaku, E.; Njardarson, J. T. Data-Mining for Sulfur and Fluorine: An Evaluation of Pharmaceuticals To Reveal Opportunities for Drug Design and Discovery. *J. Med. Chem.* **2014**, *57* (7), 2832–2842. https://doi.org/10.1021/jm401375q.
(369) Neal, T. R.; Apana, S.; Berridge, M. S. Improved Synthesis of [18F]Fluoromethyl Tosylate, a Convenient Reagent for Radiofluoromethylations. *Journal of Labelled Compounds and Radiopharmaceuticals* **2005**, *48* (8), 557–568. https://doi.org/10.1002/jlcr.949.
(370) Scott, K. A.; Njardarson, J. T. Analysis of US FDA-Approved Drugs Containing Sulfur Atoms. *Top Curr Chem (Z)* **2018**, *376* (1), 5. https://doi.org/10.1007/s41061-018-0184-5.
(371) Shinde, G. B.; Mahale, P. K.; Padaki, S. A.; Niphade, N. C.; Toche, R. B.; Mathad, V. T. An Efficient and Safe Process for the Preparation of Ticagrelor, a Platelet Aggregation Inhibitor via Resin-NO2 Catalyzed Formation of Triazole Ring. *SpringerPlus* **2015**, *4* (1), 493. https://doi.org/10.1186/s40064-015-1299-6.
(372) Albizati, K. F.; Babu, S.; Birchler, A.; Busse, J. K.; Fugett, M.; Grubbs, A.; Haddach, A.; Pagan, M.; Potts, B.; Remarchuk, T.; Rieger, D.; Rodriguez, R.; Shanley, J.; Szendroi, R.; Tibbetts, T.; Whitten, K.; Borer, B. C. A Synthesis of the HIV-Protease Inhibitor Nelfinavir from d-Tartaric Acid. *Tetrahedron Letters* **2001**, *42* (37), 6481–6485. https://doi.org/10.1016/S0040-4039(01)01338-7.
(373) Meng, Q.; Zhao, T.; Kang, D.; Huang, B.; Zhan, P.; Liu, X. The Development of an Effective Synthetic Route of Lesinurad (RDEA594). *Chemistry Central Journal* **2017**, *11* (1), 86. https://doi.org/10.1186/s13065-017-0316-y.
(374) Fuchigami, T.; Tajima, T. Highly Selective Electrochemical Fluorination of Organic Compounds in Ionic Liquids. *Journal of Fluorine Chemistry* **2005**, *126* (2), 181–187. https://doi.org/10.1016/j.jfluchem.2004.11.003.

(375) Khan, Z. U. H.; Kong, D.; Chen, Y.; Muhammad, N.; Khan, A. U.; Khan, F. U.; Tahir, K.; Ahmad, A.; Wang, L.; Wan, P. Ionic Liquids Based Fluorination of Organic Compounds Using Electrochemical Method. *Journal of Industrial and Engineering Chemistry* **2015**, *31*, 26–38. https://doi.org/10.1016/j.jiec.2015.06.007.
(376) Noel, M.; Suryanarayanan, V.; Chellammal, S. A Review of Recent Developments in the Selective Electrochemical Fluorination of Organic Compounds. *Journal of Fluorine Chemistry* **1997**, *83* (1), 31–40. https://doi.org/10.1016/S0022-1139(96)03564-6.
(377) Dawood, K. M. Electrolytic Fluorination of Organic Compounds. *Tetrahedron* **2004**, *7* (60), 1435–1451.
(378) Konno, A.; Nakagawa, K.; Fuchigami, T. New Mechanistic Aspects of Anodic Monofluorination of Halogenoalkyl and Alkyl Phenyl Sulphides. *J. Chem. Soc., Chem. Commun.* **1991**, No. 15, 1027–1029. https://doi.org/10.1039/C39910001027.
(379) Fuchigami, T.; Shimojo, M.; Konno, A. Electrolytic Partial Fluorination of Organic Compounds. 17. Regiospecific Anodic Fluorination of Sulfides Bearing Electron-Withdrawing Substituents at the Position .Alpha. to the Sulfur Atom. *J. Org. Chem.* **1995**, *60* (11), 3459–3464. https://doi.org/10.1021/jo00116a037.
(380) Hugenberg, V.; Haufe, G. Fluoro-Pummerer Rearrangement and Analogous Reactions. *Journal of Fluorine Chemistry* **2012**, *143*, 238–262. https://doi.org/10.1016/j.jfluchem.2012.06.015.
(381) Bur, S. K.; Padwa, A. The Pummerer Reaction: Methodology and Strategy for the Synthesis of Heterocyclic Compounds. *Chem. Rev.* **2004**, *104* (5), 2401–2432. https://doi.org/10.1021/cr020090l.
(382) Wigman, B.; Lee, W.; Wei, W.; Houk, K. N.; Nelson, H. M. Electrochemical Fluorination of Vinyl Boronates through Donor-Stabilized Vinyl Carbocation Intermediates**. *Angewandte Chemie International Edition* **2022**, *61* (12), e202113972. https://doi.org/10.1002/anie.202113972.
(383) Fuchigami, T. Unique Solvent Effects on Selective Electrochemical Fluorination of Organic Compounds. *Journal of Fluorine Chemistry* **2007**, *128* (4), 311–316. https://doi.org/10.1016/j.jfluchem.2006.11.015.
(384) Hou, Y.; Fuchigami, T. Electrolytic Partial Fluorination of Organic Compounds XL. Solvent Effects on Anodic Fluorination of Heterocyclic Sulfides. *J. Electrochem. Soc.* **2000**, *147* (12), 4567. https://doi.org/10.1149/1.1394102.
(385) Jacobson, O.; Kiesewetter, D. O.; Chen, X. Fluorine-18 Radiochemistry, Labeling Strategies and Synthetic Routes. *Bioconjug Chem* **2015**, *26* (1), 1–18. https://doi.org/10.1021/bc500475e.
(386) Stang, P. J.; Anderson, A. G. Hammett and Taft Substituent Constants for the Mesylate, Tosylate, and Triflate Groups. *J. Org. Chem.* **1976**, *41* (5), 781–785. https://doi.org/10.1021/jo00867a007.
(387) Eberson, L.; Hartshorn, M. P.; Persson, O.; Radner, F. Making Radical Cations Live Longer. *Chem. Commun.* **1996**, No. 18, 2105–2112. https://doi.org/10.1039/CC9960002105.
(388) Eberson, L.; Hartshorn, M. P.; Persson, O. 1,1,1,3,3,3-Hexafluoropropan-2-Ol as a Solvent for the Generation of Highly Persistent Radical Cations. *J. Chem. Soc., Perkin Trans. 2* **1995**, No. 9, 1735–1744. https://doi.org/10.1039/P29950001735.
(389) Shuklov, I. A.; Dubrovina, N. V.; Börner, A. Fluorinated Alcohols as Solvents, Cosolvents and Additives in Homogeneous Catalysis. *Synthesis* **2007**, *2007* (19), 2925–2943. https://doi.org/10.1055/s-2007-983902.
(390) Shida, N.; Takenaka, H.; Gotou, A.; Isogai, T.; Yamauchi, A.; Kishikawa, Y.; Nagata, Y.; Tomita, I.; Fuchigami, T.; Inagi, S. Alkali Metal Fluorides in Fluorinated Alcohols: Fundamental Properties and Applications to Electrochemical Fluorination. *J. Org. Chem.* **2021**, *86* (22), 16128–16133. https://doi.org/10.1021/acs.joc.1c00692.

(391) Röckl, J. L.; Dörr, M.; Waldvogel, S. R. Electrosynthesis 2.0 in 1,1,1,3,3,3-Hexafluoroisopropanol/Amine Mixtures. *ChemElectroChem* **2020**, *7* (18), 3686–3694. https://doi.org/10.1002/celc.202000761.
(392) Weinberg, F.; Hamanaka, R.; Wheaton, W. W.; Weinberg, S.; Joseph, J.; Lopez, M.; Kalyanaraman, B.; Mutlu, G. M.; Budinger, G. R. S.; Chandel, N. S. Mitochondrial Metabolism and ROS Generation Are Essential for Kras-Mediated Tumorigenicity. *Proceedings of the National Academy of Sciences* **2010**, *107* (19), 8788–8793. https://doi.org/10.1073/pnas.1003428107.
(393) Ji, H.; Ramsey, M. R.; Hayes, D. N.; Fan, C.; McNamara, K.; Kozlowski, P.; Torrice, C.; Wu, M. C.; Shimamura, T.; Perera, S. A.; Liang, M.-C.; Cai, D.; Naumov, G. N.; Bao, L.; Contreras, C. M.; Li, D.; Chen, L.; Krishnamurthy, J.; Koivunen, J.; Chirieac, L. R.; Padera, R. F.; Bronson, R. T.; Lindeman, N. I.; Christiani, D. C.; Lin, X.; Shapiro, G. I.; Jänne, P. A.; Johnson, B. E.; Meyerson, M.; Kwiatkowski, D. J.; Castrillon, D. H.; Bardeesy, N.; Sharpless, N. E.; Wong, K.-K. LKB1 Modulates Lung Cancer Differentiation and Metastasis. *Nature* **2007**, *448* (7155), 807–810. https://doi.org/10.1038/nature06030.
(394) Shackelford, D. B.; Abt, E.; Gerken, L.; Vasquez, D. S.; Seki, A.; Leblanc, M.; Wei, L.; Fishbein, M. C.; Czernin, J.; Mischel, P. S.; Shaw, R. J. LKB1 Inactivation Dictates Therapeutic Response of Non-Small Cell Lung Cancer to the Metabolism Drug Phenformin. *Cancer Cell* **2013**, *23* (2), 143–158. https://doi.org/10.1016/j.ccr.2012.12.008.
(395) *Characterization of membrane potential-dependent uptake of the novel PET tracer 18F-fluorobenzyl triphenylphosphonium cation | SpringerLink*. https://link.springer.com/article/10.1007/s00259-007-0500-8 (accessed 2022-10-28).
(396) *Mitochondria-Targeted Small Molecule Therapeutics and Probes | Antioxidants & Redox Signaling*. https://www.liebertpub.com/doi/10.1089/ars.2011.3969?url_ver=Z39.88-2003&rfr_id=ori%3Arid%3Acrossref.org&rfr_dat=cr_pub++0pubmed (accessed 2022-10-28).
(397) Madar, I.; Ravert, H. T.; Du, Y.; Hilton, J.; Volokh, L.; Dannals, R. F.; Frost, J. J.; Hare, J. M. Characterization of Uptake of the New PET Imaging Compound 18F-Fluorobenzyl Triphenyl Phosphonium in Dog Myocardium. *Journal of Nuclear Medicine* **2006**, *47* (8), 1359–1366.
(398) Kim, D.-Y.; Kim, H.-S.; Le, U. N.; Jiang, S. N.; Kim, H.-J.; Lee, K.-C.; Woo, S.-K.; Chung, J.; Kim, H.-S.; Bom, H.-S.; Yu, K.-H.; Min, J.-J. Evaluation of a Mitochondrial Voltage Sensor, (18F-Fluoropentyl)Triphenylphosphonium Cation, in a Rat Myocardial Infarction Model. *J Nucl Med* **2012**, *53* (11), 1779–1785. https://doi.org/10.2967/jnumed.111.102657.
(399) Madar, I.; Huang, Y.; Ravert, H.; Dalrymple, S. L.; Davidson, N. E.; Isaacs, J. T.; Dannals, R. F.; Frost, J. J. Detection and Quantification of the Evolution Dynamics of Apoptosis Using the PET Voltage Sensor 18F-Fluorobenzyl Triphenyl Phosphonium. *Journal of Nuclear Medicine* **2009**, *50* (5), 774–780. https://doi.org/10.2967/jnumed.108.061283.
(400) Logan, A.; Pell, V. R.; Shaffer, K. J.; Evans, C.; Stanley, N. J.; Robb, E. L.; Prime, T. A.; Chouchani, E. T.; Cochemé, H. M.; Fearnley, I. M.; Vidoni, S.; James, A. M.; Porteous, C. M.; Partridge, L.; Krieg, T.; Smith, R. A. J.; Murphy, M. P. Assessing the Mitochondrial Membrane Potential in Cells and In Vivo Using Targeted Click Chemistry and Mass Spectrometry. *Cell Metabolism* **2016**, *23* (2), 379–385. https://doi.org/10.1016/j.cmet.2015.11.014.
(401) Dykens, J. A.; Jamieson, J.; Marroquin, L.; Nadanaciva, S.; Billis, P. A.; Will, Y. Biguanide-Induced Mitochondrial Dysfunction Yields Increased Lactate Production and Cytotoxicity of Aerobically-Poised HepG2 Cells and Human Hepatocytes in Vitro. *Toxicology and Applied Pharmacology* **2008**, *233* (2), 203–210. https://doi.org/10.1016/j.taap.2008.08.013.
(402) Li, F.; Han, X.; Li, F.; Wang, R.; Wang, H.; Gao, Y.; Wang, X.; Fang, Z.; Zhang, W.; Yao, S.; Tong, X.; Wang, Y.; Feng, Y.; Sun, Y.; Li, Y.; Wong, K.-K.; Zhai, Q.; Chen, H.; Ji, H. LKB1 Inactivation Elicits a Redox Imbalance to Modulate Non-Small Cell Lung Cancer

Plasticity and Therapeutic Response. *Cancer Cell* **2015**, *27* (5), 698–711. https://doi.org/10.1016/j.ccell.2015.04.001.
(403) Giordano, S.; Lee, J.; Darley-Usmar, V. M.; Zhang, J. Distinct Effects of Rotenone, 1-Methyl-4-Phenylpyridinium and 6-Hydroxydopamine on Cellular Bioenergetics and Cell Death. *PLoS ONE* **2012**, *7* (9), e44610. https://doi.org/10.1371/journal.pone.0044610.
(404) Singer, T. P.; Ramsay, R. R. The Reaction Sites of Rotenone and Ubiquinone with Mitochondrial NADH Dehydrogenase. *Biochimica et Biophysica Acta (BBA) - Bioenergetics* **1994**, *1187* (2), 198–202. https://doi.org/10.1016/0005-2728(94)90110-4.
(405) Caboni, P.; Sherer, T. B.; Zhang, N.; Taylor, G.; Na, H. M.; Greenamyre, J. T.; Casida, J. E. Rotenone, Deguelin, Their Metabolites, and the Rat Model of Parkinson's Disease. *Chem. Res. Toxicol.* **2004**, *17* (11), 1540–1548. https://doi.org/10.1021/tx049867r.
(406) Bridges, H. R.; Jones, A. J. Y.; Pollak, M. N.; Hirst, J. Effects of Metformin and Other Biguanides on Oxidative Phosphorylation in Mitochondria. *Biochem J* **2014**, *462* (3), 475–487. https://doi.org/10.1042/BJ20140620.
(407) Owen, M. R.; Doran, E.; Halestrap, A. P. Evidence That Metformin Exerts Its Anti-Diabetic Effects through Inhibition of Complex 1 of the Mitochondrial Respiratory Chain. *Biochem J* **2000**, *348 Pt 3*, 607–614.
(408) Wheaton, W. W.; Weinberg, S. E.; Hamanaka, R. B.; Soberanes, S.; Sullivan, L. B.; Anso, E.; Glasauer, A.; Dufour, E.; Mutlu, G. M.; Budigner, G. S.; Chandel, N. S. Metformin Inhibits Mitochondrial Complex I of Cancer Cells to Reduce Tumorigenesis. *Elife* **2014**, *3*, e02242. https://doi.org/10.7554/eLife.02242.
(409) Sanchez-Rangel, E.; Inzucchi, S. E. Metformin: Clinical Use in Type 2 Diabetes. *Diabetologia* **2017**, *60* (9), 1586–1593. https://doi.org/10.1007/s00125-017-4336-x.
(410) Birsoy, K.; Possemato, R.; Lorbeer, F. K.; Bayraktar, E. C.; Thiru, P.; Yucel, B.; Wang, T.; Chen, W. W.; Clish, C. B.; Sabatini, D. M. Metabolic Determinants of Cancer Cell Sensitivity to Glucose Limitation and Biguanides. *Nature* **2014**, *508* (7494), 108–112. https://doi.org/10.1038/nature13110.
(411) Hensley, C. T.; Faubert, B.; Yuan, Q.; Lev-Cohain, N.; Jin, E.; Kim, J.; Jiang, L.; Ko, B.; Skelton, R.; Loudat, L.; Wodzak, M.; Klimko, C.; McMillan, E.; Butt, Y.; Ni, M.; Oliver, D.; Torrealba, J.; Malloy, C. R.; Kernstine, K.; Lenkinski, R. E.; DeBerardinis, R. J. Metabolic Heterogeneity in Human Lung Tumors. *Cell* **2016**, *164* (4), 681–694. https://doi.org/10.1016/j.cell.2015.12.034.
(412) *Spatial and temporal diversity in genomic instability processes defines lung cancer evolution | Science*. https://www.science.org/doi/10.1126/science.1253462 (accessed 2022-10-28).
(413) Momcilovic, M.; Bailey, S. T.; Lee, J. T.; Fishbein, M. C.; Braas, D.; Go, J.; Graeber, T. G.; Parlati, F.; Demo, S.; Li, R.; Walser, T. C.; Gricowski, M.; Shuman, R.; Ibarra, J.; Fridman, D.; Phelps, M. E.; Badran, K.; John, M. S.; Bernthal, N. M.; Federman, N.; Yanagawa, J.; Dubinett, S. M.; Sadeghi, S.; Christofk, H. R.; Shackelford, D. B. The GSK3 Signaling Axis Regulates Adaptive Glutamine Metabolism in Lung Squamous Cell Carcinoma. *Cancer Cell* **2018**, *33* (5), 905-921.e5. https://doi.org/10.1016/j.ccell.2018.04.002.
(414) Momcilovic, M.; McMickle, R.; Abt, E.; Seki, A.; Simko, S. A.; Magyar, C.; Stout, D. B.; Fishbein, M. C.; Walser, T. C.; Dubinett, S. M.; Shackelford, D. B. Heightening Energetic Stress Selectively Targets LKB1-Deficient Non–Small Cell Lung Cancers. *Cancer Research* **2015**, *75* (22), 4910–4922. https://doi.org/10.1158/0008-5472.CAN-15-0797.
(415) Su, C.-Y.; Chang, Y.-C.; Yang, C.-J.; Huang, M.-S.; Hsiao, M. The Opposite Prognostic Effect of NDUFS1 and NDUFS8 in Lung Cancer Reflects the Oncojanus Role of Mitochondrial Complex I. *Sci Rep* **2016**, *6* (1), 31357. https://doi.org/10.1038/srep31357.
(416) Molina, J. R.; Sun, Y.; Protopopova, M.; Gera, S.; Bandi, M.; Bristow, C.; McAfoos, T.; Morlacchi, P.; Ackroyd, J.; Agip, A.-N. A.; Al-Atrash, G.; Asara, J.; Bardenhagen, J.; Carrillo, C. C.; Carroll, C.; Chang, E.; Ciurea, S.; Cross, J. B.; Czako, B.; Deem, A.; Daver, N.; de

Groot, J. F.; Dong, J.-W.; Feng, N.; Gao, G.; Gay, J.; Do, M. G.; Greer, J.; Giuliani, V.; Han, J.; Han, L.; Henry, V. K.; Hirst, J.; Huang, S.; Jiang, Y.; Kang, Z.; Khor, T.; Konoplev, S.; Lin, Y.-H.; Liu, G.; Lodi, A.; Lofton, T.; Ma, H.; Mahendra, M.; Matre, P.; Mullinax, R.; Peoples, M.; Petrocchi, A.; Rodriguez-Canale, J.; Serreli, R.; Shi, T.; Smith, M.; Tabe, Y.; Theroff, J.; Tiziani, S.; Xu, Q.; Zhang, Q.; Muller, F.; DePinho, R. A.; Toniatti, C.; Draetta, G. F.; Heffernan, T. P.; Konopleva, M.; Jones, P.; Di Francesco, M. E.; Marszalek, J. R. An Inhibitor of Oxidative Phosphorylation Exploits Cancer Vulnerability. *Nat Med* **2018**, *24* (7), 1036–1046. https://doi.org/10.1038/s41591-018-0052-4.

(417) Perkins, G. A.; Ellisman, M. H.; Fox, D. A. Three-Dimensional Analysis of Mouse Rod and Cone Mitochondrial Cristae Architecture: Bioenergetic and Functional Implications. *Mol Vis* **2003**, *9*, 60–73.

(418) Gilkerson, R. W.; Selker, J. M. L.; Capaldi, R. A. The Cristal Membrane of Mitochondria Is the Principal Site of Oxidative Phosphorylation. *FEBS Lett* **2003**, *546* (2–3), 355–358. https://doi.org/10.1016/s0014-5793(03)00633-1.

(419) Momcilovic, M.; Jones, A.; Bailey, S. T.; Waldmann, C. M.; Li, R.; Lee, J. T.; Abdelhady, G.; Gomez, A.; Holloway, T.; Schmid, E.; Stout, D.; Fishbein, M. C.; Stiles, L.; Dabir, D. V.; Dubinett, S. M.; Christofk, H.; Shirihai, O.; Koehler, C. M.; Sadeghi, S.; Shackelford, D. B. In Vivo Imaging of Mitochondrial Membrane Potential in Non-Small-Cell Lung Cancer. *Nature* **2019**, *575* (7782), 380–384. https://doi.org/10.1038/s41586-019-1715-0.

(420) Pelletier-Galarneau, M.; Detmer, F. J.; Petibon, Y.; Normandin, M.; Ma, C.; Alpert, N. M.; El Fakhri, G. Quantification of Myocardial Mitochondrial Membrane Potential Using PET. *Curr Cardiol Rep* **2021**, *23* (6), 70. https://doi.org/10.1007/s11886-021-01500-8.

(421) Madar, I.; Naor, E.; Holt, D.; Ravert, H.; Dannals, R.; Wahl, R. Brown Adipose Tissue Response Dynamics: In Vivo Insights with the Voltage Sensor 18F-Fluorobenzyl Triphenyl Phosphonium. *PLOS ONE* **2015**, *10* (6), e0129627. https://doi.org/10.1371/journal.pone.0129627.

(422) Acin-Perez, R.; Benador, I. Y.; Petcherski, A.; Veliova, M.; Benavides, G. A.; Lagarrigue, S.; Caudal, A.; Vergnes, L.; Murphy, A. N.; Karamanlidis, G.; Tian, R.; Reue, K.; Wanagat, J.; Sacks, H.; Amati, F.; Darley-Usmar, V. M.; Liesa, M.; Divakaruni, A. S.; Stiles, L.; Shirihai, O. S. A Novel Approach to Measure Mitochondrial Respiration in Frozen Biological Samples. *The EMBO Journal* **2020**, *39* (13), e104073. https://doi.org/10.15252/embj.2019104073.

(423) Morais, R.; Zinkewich-Péotti, K.; Parent, M.; Wang, H.; Babai, F.; Zollinger, M. Tumor-Forming Ability in Athymic Nude Mice of Human Cell Lines Devoid of Mitochondrial DNA1. *Cancer Research* **1994**, *54* (14), 3889–3896.

(424) Perez, A. J.; Seyedhosseini, M.; Deerinck, T. J.; Bushong, E. A.; Panda, S.; Tasdizen, T.; Ellisman, M. H. A Workflow for the Automatic Segmentation of Organelles in Electron Microscopy Image Stacks. *Front Neuroanat* **2014**, *8*, 126. https://doi.org/10.3389/fnana.2014.00126.

(425) *Carcinomas of the Lung: An Ultrastructural and Immunocytochemical Study | American Journal of Clinical Pathology | Oxford Academic*. https://academic.oup.com/ajcp/article-abstract/80/1/6/1792083 (accessed 2022-10-28).

(426) Robinson, J. M.; Kobayashi, T.; Seguchi, H.; Takizawa, T. Evaluation of Neutrophil Structure and Function by Electron Microscopy: Cytochemical Studies. *J Immunol Methods* **1999**, *232* (1–2), 169–178. https://doi.org/10.1016/s0022-1759(99)00174-x.

(427) Mooi, W. J.; Dingemans, K. P.; Wagenaar, S. Sc.; Hart, A. A. M.; Wagenvoort, C. A. Ultrastructural Heterogeneity of Lung Carcinomas: Representativity of Samples for Electron Microscopy in Tumor Classification. *Human Pathology* **1990**, *21* (12), 1227–1234. https://doi.org/10.1016/S0046-8177(06)80035-3.

(428) Lucattelli, M.; Cavarra, E.; de Santi, M. M.; Tetley, T. D.; Martorana, P. A.; Lungarella, G. Collagen Phagocytosis by Lung Alveolar Macrophages in Animal Models of Emphysema. *Eur Respir J* **2003**, *22* (5), 728–734. https://doi.org/10.1183/09031936.03.00047603.
(429) Obiditsch-Mayer, I.; Breitfellner, G. Electron Microscopy in Cancer of the Lung. *Cancer* **1968**, *21* (5), 945–951. https://doi.org/10.1002/1097-0142(196805)21:5<945::aid-cncr2820210519>3.0.co;2-n.
(430) Xu, C.; Fillmore, C. M.; Koyama, S.; Wu, H.; Zhao, Y.; Chen, Z.; Herter-Sprie, G. S.; Akbay, E. A.; Tchaicha, J. H.; Altabef, A.; Reibel, J. B.; Walton, Z.; Ji, H.; Watanabe, H.; Jänne, P. A.; Castrillon, D. H.; Rustgi, A. K.; Bass, A. J.; Freeman, G. J.; Padera, R. F.; Dranoff, G.; Hammerman, P. S.; Kim, C. F.; Wong, K.-K. Loss of Lkb1 and Pten Leads to Lung Squamous Cell Carcinoma with Elevated PD-L1 Expression. *Cancer Cell* **2014**, *25* (5), 590–604. https://doi.org/10.1016/j.ccr.2014.03.033.
(431) Koyama, S.; Akbay, E. A.; Li, Y. Y.; Aref, A. R.; Skoulidis, F.; Herter-Sprie, G. S.; Buczkowski, K. A.; Liu, Y.; Awad, M. M.; Denning, W. L.; Diao, L.; Wang, J.; Parra-Cuentas, E. R.; Wistuba, I. I.; Soucheray, M.; Thai, T.; Asahina, H.; Kitajima, S.; Altabef, A.; Cavanaugh, J. D.; Rhee, K.; Gao, P.; Zhang, H.; Fecci, P. E.; Shimamura, T.; Hellmann, M. D.; Heymach, J. V.; Hodi, F. S.; Freeman, G. J.; Barbie, D. A.; Dranoff, G.; Hammerman, P. S.; Wong, K.-K. STK11/LKB1 Deficiency Promotes Neutrophil Recruitment and Proinflammatory Cytokine Production to Suppress T-Cell Activity in the Lung Tumor Microenvironment. *Cancer Research* **2016**, *76* (5), 999–1008. https://doi.org/10.1158/0008-5472.CAN-15-1439.
(432) Nagaraj, A. S.; Lahtela, J.; Hemmes, A.; Pellinen, T.; Blom, S.; Devlin, J. R.; Salmenkivi, K.; Kallioniemi, O.; Mäyränpää, M. I.; Närhi, K.; Verschuren, E. W. Cell of Origin Links Histotype Spectrum to Immune Microenvironment Diversity in Non-Small-Cell Lung Cancer Driven by Mutant Kras and Loss of Lkb1. *Cell Rep* **2017**, *18* (3), 673–684. https://doi.org/10.1016/j.celrep.2016.12.059.
(433) Mollaoglu, G.; Jones, A.; Wait, S. J.; Mukhopadhyay, A.; Jeong, S.; Arya, R.; Camolotto, S. A.; Mosbruger, T. L.; Stubben, C. J.; Conley, C. J.; Bhutkar, A.; Vahrenkamp, J. M.; Berrett, K. C.; Cessna, M. H.; Lane, T. E.; Witt, B. L.; Salama, M. E.; Gertz, J.; Jones, K. B.; Snyder, E. L.; Oliver, T. G. The Lineage-Defining Transcription Factors SOX2 and NKX2-1 Determine Lung Cancer Cell Fate and Shape the Tumor Immune Microenvironment. *Immunity* **2018**, *49* (4), 764-779.e9. https://doi.org/10.1016/j.immuni.2018.09.020.
(434) Kargl, J.; Busch, S. E.; Yang, G. H. Y.; Kim, K.-H.; Hanke, M. L.; Metz, H. E.; Hubbard, J. J.; Lee, S. M.; Madtes, D. K.; McIntosh, M. W.; Houghton, A. M. Neutrophils Dominate the Immune Cell Composition in Non-Small Cell Lung Cancer. *Nat Commun* **2017**, *8*, 14381. https://doi.org/10.1038/ncomms14381.
(435) Eruslanov, E. B.; Bhojnagarwala, P. S.; Quatromoni, J. G.; Stephen, T. L.; Ranganathan, A.; Deshpande, C.; Akimova, T.; Vachani, A.; Litzky, L.; Hancock, W. W.; Conejo-Garcia, J. R.; Feldman, M.; Albelda, S. M.; Singhal, S. Tumor-Associated Neutrophils Stimulate T Cell Responses in Early-Stage Human Lung Cancer. *J Clin Invest* **2014**, *124* (12), 5466–5480. https://doi.org/10.1172/JCI77053.
(436) Rehman, J.; Zhang, H. J.; Toth, P. T.; Zhang, Y.; Marsboom, G.; Hong, Z.; Salgia, R.; Husain, A. N.; Wietholt, C.; Archer, S. L. Inhibition of Mitochondrial Fission Prevents Cell Cycle Progression in Lung Cancer. *FASEB J* **2012**, *26* (5), 2175–2186. https://doi.org/10.1096/fj.11-196543.
(437) Seo, B. J.; Choi, J.; La, H.; Habib, O.; Choi, Y.; Hong, K.; Do, J. T. Role of Mitochondrial Fission-Related Genes in Mitochondrial Morphology and Energy Metabolism in Mouse Embryonic Stem Cells. *Redox Biology* **2020**, *36*, 101599. https://doi.org/10.1016/j.redox.2020.101599.

(438) Mg, H.; C, C.; L, T.; D, B.; S, P.; Ea, B.; M, M.; R, A.; Tj, D.; St, P.; Mh, E. CDeep3M-Plug-and-Play Cloud-Based Deep Learning for Image Segmentation. *Nature methods* **2018**, *15* (9). https://doi.org/10.1038/s41592-018-0106-z.
(439) *U-Net: deep learning for cell counting, detection, and morphometry | Nature Methods*. https://www.nature.com/articles/s41592-018-0261-2 (accessed 2022-10-28).
(440) Shelhamer, E.; Long, J.; Darrell, T. Fully Convolutional Networks for Semantic Segmentation. *IEEE Trans Pattern Anal Mach Intell* **2017**, *39* (4), 640–651. https://doi.org/10.1109/TPAMI.2016.2572683.
(441) Davies, K. M.; Strauss, M.; Daum, B.; Kief, J. H.; Osiewacz, H. D.; Rycovska, A.; Zickermann, V.; Kühlbrandt, W. Macromolecular Organization of ATP Synthase and Complex I in Whole Mitochondria. *Proceedings of the National Academy of Sciences* **2011**, *108* (34), 14121–14126. https://doi.org/10.1073/pnas.1103621108.
(442) *Supercomplex Assembly Determines Electron Flux in the Mitochondrial Electron Transport Chain | Science*. https://www.science.org/doi/10.1126/science.1230381 (accessed 2022-10-28).
(443) Chaban, Y.; Boekema, E. J.; Dudkina, N. V. Structures of Mitochondrial Oxidative Phosphorylation Supercomplexes and Mechanisms for Their Stabilisation. *Biochimica et Biophysica Acta (BBA) - Bioenergetics* **2014**, *1837* (4), 418–426. https://doi.org/10.1016/j.bbabio.2013.10.004.
(444) S, C.; C, F.; Me, S.; T, V.; R, Q.-C.; M, C.; S, C.; V, C.; A, C.; Lc, G.; E, P.-C.; L, S.; P, F.-S.; Ja, E.; L, S. Mitochondrial Cristae Shape Determines Respiratory Chain Supercomplexes Assembly and Respiratory Efficiency. *Cell* **2013**, *155* (1). https://doi.org/10.1016/j.cell.2013.08.032.
(445) Segawa, M.; Wolf, D. M.; Hultgren, N. W.; Williams, D. S.; van der Bliek, A. M.; Shackelford, D. B.; Liesa, M.; Shirihai, O. S. Quantification of Cristae Architecture Reveals Time-Dependent Characteristics of Individual Mitochondria. *Life Sci Alliance* **2020**, *3* (7), e201900620. https://doi.org/10.26508/lsa.201900620.
(446) Perkins, G. A.; Renken, C. W.; Frey, T. G.; Ellisman, M. H. Membrane Architecture of Mitochondria in Neurons of the Central Nervous System. *J Neurosci Res* **2001**, *66* (5), 857–865. https://doi.org/10.1002/jnr.10050.
(447) Mootha, V. K.; Wei, M. C.; Buttle, K. F.; Scorrano, L.; Panoutsakopoulou, V.; Mannella, C. A.; Korsmeyer, S. J. A Reversible Component of Mitochondrial Respiratory Dysfunction in Apoptosis Can Be Rescued by Exogenous Cytochrome c. *The EMBO Journal* **2001**, *20* (4), 661–671. https://doi.org/10.1093/emboj/20.4.661.
(448) Scalettar, B. A.; Abney, J. R.; Hackenbrock, C. R. Dynamics, Structure, and Function Are Coupled in the Mitochondrial Matrix. *Proceedings of the National Academy of Sciences* **1991**, *88* (18), 8057–8061. https://doi.org/10.1073/pnas.88.18.8057.
(449) Wolf, D. M.; Segawa, M.; Kondadi, A. K.; Anand, R.; Bailey, S. T.; Reichert, A. S.; van der Bliek, A. M.; Shackelford, D. B.; Liesa, M.; Shirihai, O. S. Individual Cristae within the Same Mitochondrion Display Different Membrane Potentials and Are Functionally Independent. *The EMBO Journal* **2019**, *38* (22), e101056. https://doi.org/10.15252/embj.2018101056.
(450) Mannella, C. A. Structure and Dynamics of the Mitochondrial Inner Membrane Cristae. *Biochim Biophys Acta* **2006**, *1763* (5–6), 542–548. https://doi.org/10.1016/j.bbamcr.2006.04.006.
(451) *Compartmentalized metabolism supports midgestation mammalian development | Nature*. https://www.nature.com/articles/s41586-022-04557-9 (accessed 2022-10-28).
(452) *Structural and functional features and significance of the physical linkage between ER and mitochondria | Journal of Cell Biology | Rockefeller University Press*. https://rupress.org/jcb/article/174/7/915/44577/Structural-and-functional-features-and (accessed 2022-10-28).

(453) Quirós, P. M.; Mottis, A.; Auwerx, J. Mitonuclear Communication in Homeostasis and Stress. *Nat Rev Mol Cell Biol* **2016**, *17* (4), 213–226. https://doi.org/10.1038/nrm.2016.23.
(454) Lewis, S. C.; Uchiyama, L. F.; Nunnari, J. ER-Mitochondria Contacts Couple MtDNA Synthesis with Mitochondrial Division in Human Cells. *Science* **2016**, *353* (6296), aaf5549. https://doi.org/10.1126/science.aaf5549.
(455) Boutant, M.; Kulkarni, S. S.; Joffraud, M.; Ratajczak, J.; Valera-Alberni, M.; Combe, R.; Zorzano, A.; Cantó, C. Mfn2 Is Critical for Brown Adipose Tissue Thermogenic Function. *The EMBO Journal* **2017**, *36* (11), 1543–1558. https://doi.org/10.15252/embj.201694914.
(456) Wang, H.; Sreenivasan, U.; Hu, H.; Saladino, A.; Polster, B. M.; Lund, L. M.; Gong, D.-W.; Stanley, W. C.; Sztalryd, C. Perilipin 5, a Lipid Droplet-Associated Protein, Provides Physical and Metabolic Linkage to Mitochondria. *J Lipid Res* **2011**, *52* (12), 2159–2168. https://doi.org/10.1194/jlr.M017939.
(457) Tarnopolsky, M. A.; Rennie, C. D.; Robertshaw, H. A.; Fedak-Tarnopolsky, S. N.; Devries, M. C.; Hamadeh, M. J. Influence of Endurance Exercise Training and Sex on Intramyocellular Lipid and Mitochondrial Ultrastructure, Substrate Use, and Mitochondrial Enzyme Activity. *Am J Physiol Regul Integr Comp Physiol* **2007**, *292* (3), R1271-1278. https://doi.org/10.1152/ajpregu.00472.2006.
(458) Benador, I. Y.; Veliova, M.; Mahdaviani, K.; Petcherski, A.; Wikstrom, J. D.; Assali, E. A.; Acín-Pérez, R.; Shum, M.; Oliveira, M. F.; Cinti, S.; Sztalryd, C.; Barshop, W. D.; Wohlschlegel, J. A.; Corkey, B. E.; Liesa, M.; Shirihai, O. S. Mitochondria Bound to Lipid Droplets Have Unique Bioenergetics, Composition, and Dynamics That Support Lipid Droplet Expansion. *Cell Metab* **2018**, *27* (4), 869-885.e6. https://doi.org/10.1016/j.cmet.2018.03.003.
(459) Smith, S. J.; Cases, S.; Jensen, D. R.; Chen, H. C.; Sande, E.; Tow, B.; Sanan, D. A.; Raber, J.; Eckel, R. H.; Farese, R. V. Obesity Resistance and Multiple Mechanisms of Triglyceride Synthesis in Mice Lacking Dgat. *Nat Genet* **2000**, *25* (1), 87–90. https://doi.org/10.1038/75651.
(460) Davidson, S. M.; Papagiannakopoulos, T.; Olenchock, B. A.; Heyman, J. E.; Keibler, M. A.; Luengo, A.; Bauer, M. R.; Jha, A. K.; O'Brien, J. P.; Pierce, K. A.; Gui, D. Y.; Sullivan, L. B.; Wasylenko, T. M.; Subbaraj, L.; Chin, C. R.; Stephanopolous, G.; Mott, B. T.; Jacks, T.; Clish, C. B.; Vander Heiden, M. G. Environment Impacts the Metabolic Dependencies of Ras-Driven Non-Small Cell Lung Cancer. *Cell Metabolism* **2016**, *23* (3), 517–528. https://doi.org/10.1016/j.cmet.2016.01.007.
(461) Goodwin, J.; Neugent, M. L.; Lee, S. Y.; Choe, J. H.; Choi, H.; Jenkins, D. M. R.; Ruthenborg, R. J.; Robinson, M. W.; Jeong, J. Y.; Wake, M.; Abe, H.; Takeda, N.; Endo, H.; Inoue, M.; Xuan, Z.; Yoo, H.; Chen, M.; Ahn, J.-M.; Minna, J. D.; Helke, K. L.; Singh, P. K.; Shackelford, D. B.; Kim, J.-W. The Distinct Metabolic Phenotype of Lung Squamous Cell Carcinoma Defines Selective Vulnerability to Glycolytic Inhibition. *Nat Commun* **2017**, *8*, 15503. https://doi.org/10.1038/ncomms15503.
(462) Varadi, A.; Johnson-Cadwell, L. I.; Cirulli, V.; Yoon, Y.; Allan, V. J.; Rutter, G. A. Cytoplasmic Dynein Regulates the Subcellular Distribution of Mitochondria by Controlling the Recruitment of the Fission Factor Dynamin-Related Protein-1. *J Cell Sci* **2004**, *117* (Pt 19), 4389–4400. https://doi.org/10.1242/jcs.01299.
(463) Koutsopoulos, O. S.; Laine, D.; Osellame, L.; Chudakov, D. M.; Parton, R. G.; Frazier, A. E.; Ryan, M. T. Human Miltons Associate with Mitochondria and Induce Microtubule-Dependent Remodeling of Mitochondrial Networks. *Biochim Biophys Acta* **2010**, *1803* (5), 564–574. https://doi.org/10.1016/j.bbamcr.2010.03.006.
(464) Hart, G. W. Nutrient Regulation of Signaling and Transcription. *J Biol Chem* **2019**, *294* (7), 2211–2231. https://doi.org/10.1074/jbc.AW119.003226.
(465) Kim, J.; Lee, H. M.; Cai, F.; Ko, B.; Yang, C.; Lieu, E. L.; Muhammad, N.; Rhyne, S.; Li, K.; Haloul, M.; Gu, W.; Faubert, B.; Kaushik, A. K.; Cai, L.; Kasiri, S.; Marriam, U.; Nham, K.;

Girard, L.; Wang, H.; Sun, X.; Kim, J.; Minna, J. D.; Unsal-Kacmaz, K.; DeBerardinis, R. J. The Hexosamine Biosynthesis Pathway Is a Targetable Liability in KRAS/LKB1 Mutant Lung Cancer. *Nat Metab* **2020**, *2* (12), 1401–1412. https://doi.org/10.1038/s42255-020-00316-0.

(466) *Glucose Regulates Mitochondrial Motility via Milton Modification by O-GlcNAc Transferase: Cell*. https://www.cell.com/cell/fulltext/S0092-8674(14)00728-4?_returnURL=https%3A%2F%2Flinkinghub.elsevier.com%2Fretrieve%2Fpii%2FS0092867414007284%3Fshowall%3Dtrue (accessed 2022-10-28).

(467) Liu, K. G.; Kim, J.-I.; Olszewski, K.; Barsotti, A. M.; Morris, K.; Lamarque, C.; Yu, X.; Gaffney, J.; Feng, X.-J.; Patel, J. P.; Poyurovsky, M. V. Discovery and Optimization of Glucose Uptake Inhibitors. *J Med Chem* **2020**, *63* (10), 5201–5211. https://doi.org/10.1021/acs.jmedchem.9b02153.

(468) Olszewski, K.; Barsotti, A.; Feng, X.-J.; Momcilovic, M.; Liu, K. G.; Kim, J.-I.; Morris, K.; Lamarque, C.; Gaffney, J.; Yu, X.; Patel, J. P.; Rabinowitz, J. D.; Shackelford, D. B.; Poyurovsky, M. V. Inhibition of Glucose Transport Synergizes with Chemical or Genetic Disruption of Mitochondrial Metabolism and Suppresses TCA Cycle-Deficient Tumors. *Cell Chem Biol* **2022**, *29* (3), 423-435.e10. https://doi.org/10.1016/j.chembiol.2021.10.007.

(469) Martínez-Reyes, I.; Cardona, L. R.; Kong, H.; Vasan, K.; McElroy, G. S.; Werner, M.; Kihshen, H.; Reczek, C. R.; Weinberg, S. E.; Gao, P.; Steinert, E. M.; Piseaux, R.; Budinger, G. R. S.; Chandel, N. S. Mitochondrial Ubiquinol Oxidation Is Necessary for Tumour Growth. *Nature* **2020**, *585* (7824), 288–292. https://doi.org/10.1038/s41586-020-2475-6.

(470) Ronneberger, O.; Fischer, P.; Brox, T. U-Net: Convolutional Networks for Biomedical Image Segmentation. In *Medical Image Computing and Computer-Assisted Intervention – MICCAI 2015*; Navab, N., Hornegger, J., Wells, W. M., Frangi, A. F., Eds.; Lecture Notes in Computer Science; Springer International Publishing: Cham, 2015; pp 234–241. https://doi.org/10.1007/978-3-319-24574-4_28.

(471) He, K.; Zhang, X.; Ren, S.; Sun, J. Deep Residual Learning for Image Recognition. arXiv December 10, 2015. https://doi.org/10.48550/arXiv.1512.03385.

(472) Chen, L.-C.; Papandreou, G.; Kokkinos, I.; Murphy, K.; Yuille, A. L. DeepLab: Semantic Image Segmentation with Deep Convolutional Nets, Atrous Convolution, and Fully Connected CRFs. *IEEE Trans Pattern Anal Mach Intell* **2018**, *40* (4), 834–848. https://doi.org/10.1109/TPAMI.2017.2699184.

(473) Kingma, D. P.; Ba, J. Adam: A Method for Stochastic Optimization. arXiv January 29, 2017. https://doi.org/10.48550/arXiv.1412.6980.